

Subduction zone metamorphism: Timescales and emergence in the geological record

Renée Jade Tamblyn

Department of Earth Sciences
School of Physical Sciences
The University of Adelaide

This thesis is submitted in fulfilment of the requirements for the degree of Doctor of Philosophy

March, 2021

Abstract 8

Declaration 10

Acknowledgements 11

Publications arising from this project 12

Chapter 1: Introduction and thesis outline 15

High-pressure low-temperature metamorphism 16

Methodology of interrogated subduction zone assemblages 17

Mineral equilibria forward modelling 18

Geochronology 19

The timescales and behaviour of subducted rocks 19

Exhumation in subduction systems 20

The emergence of subduction metamorphism on Earth 21

Eclogites 23

Blueschists 24

Coesite and diamond 24

Lawsonite 24

Thesis outline 25

Chapter 2 25

Chapter 3 26

Chapter 4 26

Chapter 5 27

Chapter 6 28

Chapter 7 28

References 29

Chapter 2: Blueschist from the Mariana forearc records long-lived residence of material in the subduction channel 41

Abstract 44

Introduction 44

Background 46

Geology and geometry of the IBM system 46

Previous studies of blueschists from the Mariana forearc drill sites 48

Methods 50

Results 51

Petrography 51

Zircon and rutile geochronology 56

Mineral equilibria forward modelling 56

Protolith constraints 57

Discussion 58

Conclusions 63

Acknowledgements 64

References 64

Chapter 3: Subduction and accumulation of lawsonite eclogite and garnet blueschist in eastern Australia 71

Abstract 74

Introduction 74

Geological setting 76

Samples 78

RB11: lawsonite eclogite 78

RB12: garnet blueschist 79

Analytical methods 81

Electron Probe Micro Analyses and X-Ray mapping 81

Lu–Hf and Sm–Nd geochronology 81

U–Pb geochronology 82

Phase equilibria forward modelling 82

Results 84

Electron Probe Micro Analyses 84

LA–ICP–MS mapping 87

Lu–Hf and Sm–Nd geochronology 87

U–Pb geochronology 87

Phase equilibria forward modelling 90

Discussion 93

Timing of high-pressure metamorphism at Port Macquarie 93

Pressure-temperature conditions during metamorphism 99

Tectonic framework for high-pressure metamorphism in East Gondwana 101

Accumulation of high-pressure products and spatial translation during slab rollback 103

Conclusions 105

Acknowledgements 106

References 106

Chapter 4: Resubduction of lawsonite eclogite within a serpentinite-filled subduction channel 117

Abstract 120

Introduction 120

Geological setting 121

The Southern New England Orogen 121

Tectonic framework on the high-pressure rocks and the Tasmanides 122

High-pressure metamorphism and mélange formation in the SNEO 123

Petrography 124

Methods 128

Electron Probe Micro Analyses and mapping 128

Phase equilibrium forward modelling 128

U–Pb titanite geochronology 128

Ar–Ar phengite geochronology 129

Rb–Sr phengite geochronology 129

LA–ICP–QQQ mapping 129

Results 130

Electron Probe Micro Analyses and mapping 130

Phase equilibrium forward modelling 134

Stage 1 136

Stage 2 140

U–Pb titanite geochronology 141

Ar–Ar phengite geochronology 142

Rb–Sr phengite geochronology 143

LA–ICP–QQQ isotope mapping 143

Discussion 143

Petrological evidence for reburial of the lawsonite eclogite 145

Origin of oscillatory garnet zoning and the possible role of fluids 146

P–T conditions of reburial 147

Timing of reburial 148

Examples of other burial cycles 152

Subduction channel dynamics 152

Conclusions 154

Acknowledgements 154

References 154

Chapter 5: The 2 Ga eclogites of central Tanzania: Directly linking age and metamorphism 165

Abstract 168

Introduction 168

Geological background 169

Samples 173

T01-40 173

T06-09 173

A previous eclogitic assemblage 176

Methods 176

Q450 Scanning Electron Microscopy 176

Electron Probe Micro Analyses and X-Ray mapping 177

LA–ICP–MS garnet spot analyses and mapping 177

Garnet Lu–Hf geochronology 177

Zircon U–Pb geochronology and trace elements 177

Rutile U–Pb geochronology and trace elements 178

Mineral equilibria modelling 179

Results 180

Electron Probe Micro Analyses and X-Ray mapping 180

Garnet REE LA–ICP–MS maps 182

Garnet Lu–Hf geochronology 184

Zircon U–Pb geochronology and trace elements 186

Rutile U–Pb geochronology 188

Ti in zircon and Zr in rutile thermometry 188

Mineral equilibria modelling 191

Discussion 195

Timing of eclogite-facies metamorphism 195

P–T conditions during subduction 196

Garnet zoning and thermal histories of the retrogressed eclogites 198

Tectonic model for formation of the Usagaran retrogressed eclogites 200

Conclusions 203

Acknowledgements 204

References 204

Chapter 6: Mantle heating at ca. 2 Ga driven by crustal growth: Evidence from granites and eclogites 213

Abstract 216

Introduction 216

Methods 217

Geochemical analyses and filtering 217

Mineral equilibria forward modelling 217

Province age-area analysis 217

The P–T sensitive geochemistry of granites 217

Thermal insulation of the mantle by continental crust 220

Preservation of subduction-related eclogites 222

The balance of crustal growth and mantle temperature 224

Acknowledgements 224

References 224

Chapter 7: Discussion and conclusions 229

Discussion and conclusions 230

Complex behaviour of HP–LT rocks in the subduction channel 230

The emergence of modern-style subduction in the Earth 231

Reconciling the records 234

The power of datasets 234

Future directions 237

Limitations of collection of geochronological data in HP–LT assemblages 237

Tying geodynamic modelling to petrochronological studies 237

Interrogating combined datasets to fully understand the evolution of the Earth 238

References 239

Appendix 1: Companion study to Chapter 5 245

Appendix 2: Supplementary materials for Chapter 2 311

Appendix 3: Supplementary materials for Chapter 3 323

Appendix 4: Supplementary materials for Chapter 5 339

Appendix 5: Supplementary materials for Chapter 5 381

Appendix 6: Supplementary materials for Chapter 6 421

Abstract

Eclogites and blueschists are the primary recorders of processes that occur within subduction zones. Their mineralogy can be used to determine their pressure-temperature-time (*P–T–t*) evolution during burial to mantle depths, which in turn illuminates information about plate tectonics, subduction channel dynamics, and the thermal state of the mantle. This thesis uses high-pressure rocks as a tool to investigate subduction systems through time, from blueschist formed in a currently active subduction zone to the emergence of eclogites ca. 2 billion years ago.

Of ongoing debate are the durations that materials can remain trapped in subduction channels, and the *P–T–t* paths they experience. Numerical modelling has predicted complex behaviour, such as accumulation and cycling of high-pressure low-temperature (HP–LT) rocks within the subduction channel, but there are few rock systems preserved clearly documenting this process. This thesis presents work on two locations of long-lived entrapment of HP–LT rocks, from a currently active subduction zone, the Izu-Bonin-Mariana system, and a palaeosubduction system in Eastern Australia. In the Mariana system, a fragment of blueschist was subducted at ca. 50 Ma and entrapped within the subduction system until its recent eruption in a serpentinite-volcano. In Eastern Australia, blocks of lawsonite eclogite and garnet blueschist were formed and accumulated at ca. 490 Ma and 470 Ma respectively. Further work identified two cycles of metamorphism in the lawsonite eclogite, with a second burial event taking place after partial exhumation within the subduction channel over 40 My.

Subduction in the recent Earth can involve very cool thermal gradients (< 250 °C/GPa), although the earliest recognised instances of modern-style subduction occured along warmer thermal gradients. Eclogites from the Usagaran Belt in central Tanzania are amongst the oldest in the world, forming at ca. 2 Ga. They were buoyantly exhumed within metapelitic lithologies within ca. 6 Myr. They, along with other eclogites across the African Palaeoproterozoic orogens, demonstrate the transition from a warm subduction regime to the establishment of modern-style subduction on Earth.

While the *P–T–t* evolutions of HP–LT rocks hold information about geodynamics, a fascinating topic is the emergence of subduction-style rocks in the geological record. Although there is debate around the timing of the first HP–LT rocks, eclogites widely emerge in the geological record from ca. 2.2–1.8 Ga, and then disappear until the Mesoproterozoic. Mantle temperatures were possibly too warm before ca. 2.2 Ga to allow the creation and/or preservation of eclogites. However, the subsequent ca. 0.7 Ga gap in the geological record is of interest. Coincident with this emergence, the global granite record shows in-

creases in Y and heavy rare earth elements (HREEs), and decreases in Sr and Eu at ca. 2 Ga. These changes are explained by increasing temperatures associated with granite generation. This warming event is proposed to have been driven by crustal growth from ca. 2–1.8 Ga, which increased thermal insulation of the mantle. Warmer temperatures in the mantle prohibited the preservation of eclogites, until secular cooling of the mantle overcame the insulating effect at ca 1.1 Ga.

I certify that this work contains no material which has been accepted for the award of any other degree or diploma in my name, in any university or other tertiary institution and, to the best of my knowledge and belief, contains no material previously published or written by another person, except where due reference has been made in the text. In addition, I certify that no part of this work will, in the future, be used in a submission in my name, for any other degree or diploma in any university or other tertiary institution without the prior approval of the University of Adelaide and where applicable, any partner institution responsible for the joint-award of this degree.

I acknowledge that copyright of published works contained within this thesis resides with the copyright holder(s) of those works.

I also give permission for the digital version of my thesis to be made available on the web, via the University's digital research repository, the Library Search and also through web search engines, unless permission has been granted by the University to restrict access for a period of time.

I acknowledge the support I have received for my research through the provision of an Australian Government Research Training Program Scholarship.

05/03/2021

Renée Jade Tamblyn Date

I thank my supervisors, Martin, Laura and Dave, for your support academically and personally over the years. Martin, thank you for taking me to see some of the most amazing places and geology, for challenging me and for the many (many) fruitful geological discussions. Also, thank you for giving me the opportunity and support to pursue the PhD topic that I truly wanted to. Laura, thank you for your wisdom and always flawless guidance, and for the coffees. Dave, thank you for always thoughtfully answering my questions and being one swift email away.

The friendships I have found in the PhDs, postdocs and staff of Mawson are too plentiful and special in their own ways to list here. From Aldermann room beers, to field trips, demonstrating, coffees, lunches, camping trips, hallway hellos, nights out… the comradeship and social bond built in this group is truly exceptional. I must thank Georgie, Mitchell, Morgan and Jack, you have given me endless support and friendship and I can't imagine these years without you.

The CERG tank occupants and visitors, Mitchell, Dillon, Brad, Claire, Kiara, Xiaofang, Jie, you all made life in the basement colourful and wonderful. I want to thank Alex, Mitchell, Jack, Derrick and others for many geological ideas and discussions. Thank you to the amazing people at Adelaide Microscopy, Sarah, Ben, Dave, Aoife and Ken, but also sorry about all the last-minute analysis and carbon coating.

To my family, Dad, Mum and Mitchell. I am truly lucky to have been supported so well and given some of the best opportunities in life. Mum, for always telling me I could achieve whatever I wanted. Dad, for fostering my love of science.

Finally, to Travis. I am not sure I would be here in one piece without your absolutely relentless care and love. I wouldn't want anyone else by my side, and I am beyond excited for what our future brings us.

Publications arising from this thesis

Peer reviewed journal articles

Blueschist from the Mariana forearc records long-lived residence of material in the subduction channel (2019). **R. Tamblyn**, T. Zack, A.K. Schmitt, M. Hand, D. Kelsey, L. Morrissey, S. Pabst, I. Savov. *Earth and Planetary Science Letters,* 519, 171-181

Subduction and accumulation of lawsonite eclogite and garnet blueschist in eastern Australia (2020). **R. Tamblyn**, M. Hand, D. Kelsey, R. Anczkiewicz, D. Och. *Journal of Metamorphic Geology*, 38(2), 157-182.

Resubduction of lawsonite eclogite in serpentinite-filled subduction channel (2020). **R. Tamblyn**, M. Hand, L. Morrissey, T. Zack, G. Phillips, D. Och. *Contributions to Mineralogy and Petrology,* 175 (8), 1-22

The 2 Ga eclogites of Central Tanzania: Directly linking age and metamorphism (2020). **R. Tamblyn**, D. Brown, M. Hand, L. Morrissey, C. Clark, R. Anczkiewicz. *Lithos,* 380–38, 105890

Thermobarometric constraints on burial and exhumation of 2-billion-year-old eclogites and their metapelitic hosts (2020). D. Brown, **R. Tamblyn**, M. Hand, L. Morrissey. *Precambrian Research,* 105833

Mantle heating at ca. 2 Ga driven by crustal growth: Evidence from granites and eclogites (*in review*). **R. Tamblyn**, D. Hasterok, M. Hand, M. Gard. *Geology*

In-situ Lu–Hf geochronology of garnet, apatite and xenotime by LA ICP MS/MS (*in review*). A. Simpson, S. Gilbert, **R. Tamblyn**, M. Hand, C. Spandler, J. Gillespie, A. Nixon, S. Glorie. *Chemical Geology*

Conference presentations

The emergence of eclogites linked to global arc chemistry change at ca. 2 Ga (2021). **R. Tamblyn**, D. Hasterok, M. Hand, M. Gard. *Australian Earth Sciences Convention.*

Mantle heating at ca. 2 Ga driven by crustal growth: Evidence from granites and eclogites (2020). **R. Tamblyn**, D. Hasterok, M. Hand, M. Gard. *Geological Society of Australia Earth Sciences Student Symposium, South Australia.*

The 2 Ga eclogites of central Tanzania: Directly linking age and metamorphism (2020). **R. Tamblyn**, D. Brown, M. Hand, L. Morrissey, C. Clark, R. Anczkiewicz. *Goldschmidt.*

Long-lived zircon growth in trapped eclogite (2020). M. Hand, **R. Tamblyn**, D. Zivak, T. Raimondo. *European Geosciences Union General Assembly.*

Cycling of eclogite in the Southern New England Orogen, Australia (2019). **R. Tamblyn**, M. Hand, L. Morrissey, T. Zack, G. Phillips, D. Och. *Geological Society of Australia Earth Sciences Student Symposium, South Australia.*

Evidence for resubduction of lawsonite-eclogite during return flow, eastern Australia (2019). **R. Tamblyn**, M. Hand, L. Morrissey, T. Zack, G. Phillips, D. Och. *The Institute for Geoscience Research Conference, Curtin University.*

Palaeoproterozoic eclogites: exhumation and burial convolution of Pt histories (2019). D. Brown, **R. Tamblyn**, M. Hand, L. Morrissey. *European Geosciences Union General Assembly.*

Dating diagenesis using authigenic titanite (2019). M. Bockmann, M. Hand., **R. Tamblyn.**, P. Kolesik, C. Clark, N. Tucker. *European Geosciences Union General Assembly.*

Resubduction of lawsonite-eclogite during return flow, eastern Australia (2019). **R. Tamblyn**, M. Hand, L. Morrissey, T. Zack, G. Phillips, D. Och. *Biennial meeting of the Specialist Group for Structural Geology and Tectonics, Australia.*

There and back: recording metamorphism in the Western Gneiss Complex (2019) . T. Romyn, M. Hand, **R. Tamblyn**, C. Clark, K. Barovich. *Biennial meeting of the Specialist Group for Structural Geology and Tectonics, Australia.*

Cambrian eclogite-facies metamorphism in the central Transantarctic Mountains, East Antarctica: extending the record of early Palaeozoic high-pressure metamorphism along the eastern Gondwanan margin (2019). D. Brown, M. Hand, L. Morrissey, **R. Tamblyn**, J. Goodge. *Biennial meeting of the Specialist Group for Structural Geology and Tectonics, Australia.*

Metamorphic conditions of blueschist erupted from serpentinite-mud volcanism in the Mariana forearc (2018). **R. Tamblyn**, T. Zack, A.K. Schmitt, M. Hand, D. Kelsey, L. Morrissey, S. Pabst, I. Savov. *European Geosciences Union General Assembly.*

Metamorphic conditions of blueschist from mud volcanoes in the Mariana trench (2018). **R. Tamblyn**, T. Zack, A.K. Schmitt, M. Hand, D. Kelsey, L. Morrissey, S. Pabst, I. Savov. *Geological Society of Australia Earth Sciences Student Symposium, South Australia.*

In-situ LA–ICP–MS Rb–Sr dating of phengite in eclogites (2018). **R. Tamblyn**, M. Hand, L. Morrissey, T. Zack, G. Phillips, D. Och. *Australian Geoscience Council Convention*

Fast eclogite to granulite metamorphism in the Usagaran Belt in the early Palaeoproterozoic (2018). **R. Tamblyn**, D. Brown, M. Hand, L. Morrissey. *Granulites and Granulites.*

Long distance transport of eclogite and blueschist during early Pacific Ocean subduction rollback (2017) . **R. Tamblyn**, M. Hand, D. Kelsey, G. Phillips, R. Anczkiewicz, D. Och. *European Geosciences Union General Assembly.*

Long-lived high-pressure metamorphism encodes durations of subduction and slab retreat (2017). **R. Tamblyn**, M. Hand, D. Kelsey, G. Phillips, R. Anczkiewicz, D. Och. *The Institute for Geoscience Research Conference, Curtin University.*

The emergence of high-pressure low-temperature metamorphism on Earth (2017). **R. Tamblyn**, M. Hand, D, Kelsey, L. Morrissey. *The Dorothy Hill Women in Geosciences Symposium, Australia.*

Chapter 1:
Introduction and thesis outline

1. High-pressure low-temperature metamorphism

The pressure-temperature-time (*P–T–t*) evolution experienced by metamorphic rocks is encoded in their mineralogy and chemistry. Interpreting this evolution gives information about the physical and chemical conditions recorded in the crust but also the upper mantle, which in turn allows us to unravel the tectonic and geodynamic processes operating on Earth through time. Convergent plate processes are arguably the most dramatic expression of plate tectonics and provide important insights into how tectonic processes have evolved through time.

Subduction is a convergent plate margin process, by which an oceanic or continental tectonic plate is thrust under another into the mantle (Fig. 1). During this process, isotherms in the subducting plate are depressed into the mantle, resulting in low temperatures at high pressures (Fig. 1; 2). This style of high-pressure low-temperature (HP–LT) metamorphism produces eclogite and blueschist facies mineral assemblages, which can only be achieved via subduction. It is through the identification of these diagnostic mineral assemblages that workers have been able to recognise palaeo-subduction systems on Earth, and decipher information about the physiochemical conditions and temporal patterns of subduction zones through history.

While some form of plate tectonics has been argued to have begun as early as ca. 4 Ga (Condie and Pease, 2008; Maruyama et al., 2018), the emergence of modern-style subduction (i.e. cool, one-sided subduction; Fig. 1) is more enigmatic. Petrological arguments for the beginning of modern-style subduction include the emergence and distribution of HP–LT assemblages in the geological record (Ernst, 1972; Grambling, 1975; Liou et al., 1990; Maruyama et al., 1996; Stern, 2005; Tsujimori et al., 2006; Brown, 2006; Brown, 2007; Brown, 2010; Tsujimori and Ernst, 2014; Holder et al., 2018; Brown and Johnson, 2018; Stern, 2018; Brown et al., 2020a; Brown et al., 2020b; Palin et al., 2020.) These assemblages indicate modern-style subduction began at ca. 2.1 Ga. Since the establishment of modern-style subduction, HP–LT rocks have been the primary recorders of a variety of subduction zone processes, including but not limited to: fluid transport and release, element cycling, palaeo seismicity, slab breakoff and rollback, and collision (e.g. Spandler et al., 2003; Hermann et al., 2006; Angiboust et al., 2014; Viete et al., 2018; Tamblyn et al., 2019).

An alternative way to probe subduction zone processes is through numerical geodynamic modelling (e.g. Geyra et al., 2002; Yomato et al., 2007; van Keken et al., 2008; Sizova et al., 2010; Gerya, 2011; Li, 2014; Leng and Mao, 2015; Sizova et al., 2015; Ruh et al., 2018; van Keken et al., 2018;

Leng and Huang, 2018; Peacock, 2020). In this approach, modellers seek to explore and reproduce physical processes that occur in the real Earth. These models of subduction must be tied to observations from exhumed HP–LT rocks in order to test their validity. For example, numerical models suggest channel flow in subduction zones is a common process (Gerya et al., 2002; Krebs et al., 2008; Làzaro et al., 2009; Peacock, 2020), however few examples of this process have been recognised in the geological record. Therefore, the investigation of the metamorphic evolution of HP–LT rocks also aims to support or refute numerical models, and vice versa.

2. Methodology for interrogating subduction zone assemblages

Rocks retrieved from subduction systems are typically mafic in composition, and are relics of the mid-ocean ridge basalt (MORB), which made up the top layer of the subducting oceanic crust. Felsic, pelitic and ultramafic material is also commonly returned from subduction systems, however these compositions are somewhat limited in the extent to which they can mineralogically record high-pressure conditions (e.g. Proyer, 2003). Metamorphism of basaltic and gabbroic rocks however can produce eclogites and blueschists, the defining HP–LT assemblages (Fig. 2). Eclogites contain the diagnostic mineral assemblage garnet and omphacite (sodic clinopyroxene), while blueschists are generally dominated by sodic amphibole, including the diagnostic mineral glaucophane.

Certain key metamorphic minerals in HP–LT assemblages are critical to unlocking the *P*–*T*–*t* histories of subduction-related rocks. Mineral assemblages as well as the chemical compositions of the minerals are integral to interpreting mineral

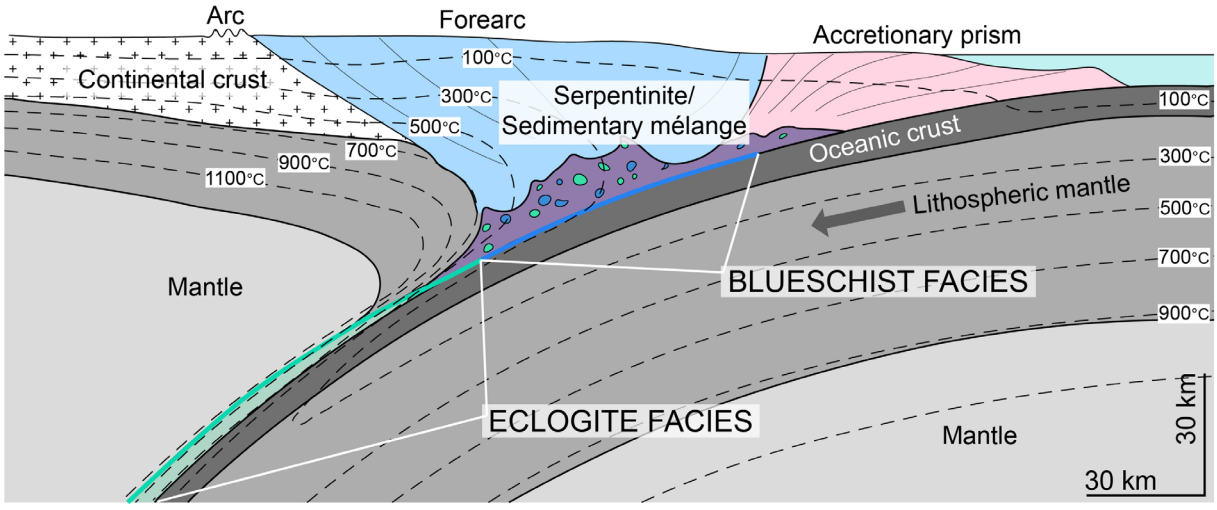


Figure 1: Schematic cross-section through an oceanic subduction system, after Tsujimori et al. (2006). Hypothetical isotherms are shown as black dashed lines, and are depressed into the mantle by the cool, subducting slab. Exotic blocks of HP–LT assemblages are shown hosted in mélange.

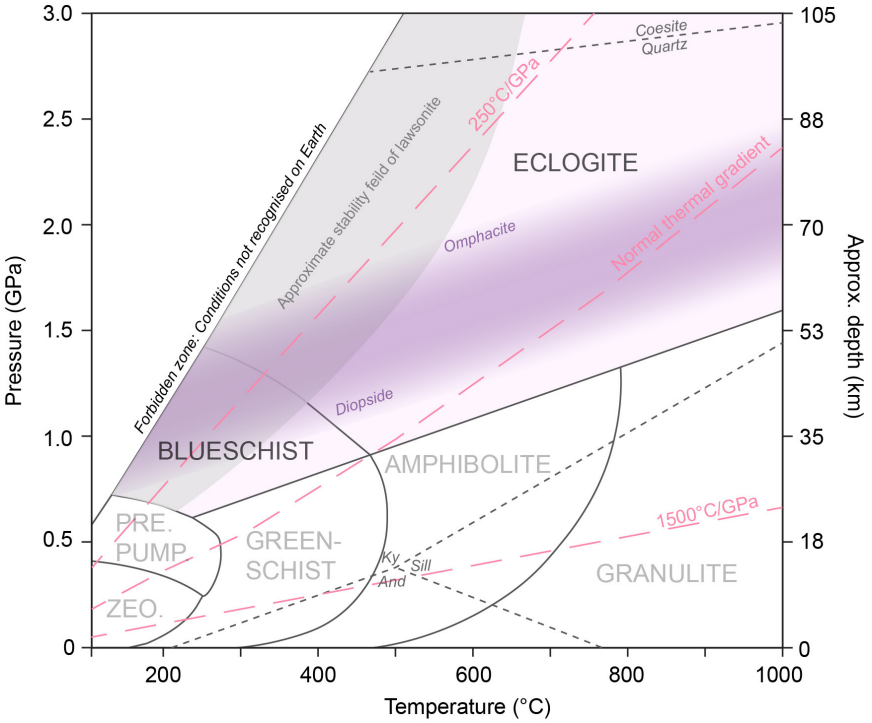


Figure 2: Approximate pressure-temperature conditions of the metamorphic facies. Geotherms are shown as pink dashed lines. Approximate transitions of key phases are shown in grey dashed lines. Approximate location of the diopside to omphacite transition is shown in purple, but is dependant on bulk rock composition.

equilibria models, which allow the *P*–*T* evolution of the sample to be identified. Major and accessory minerals can also sequester radiogenic elements, which allow the timing of their growth (via geochronology) to be obtained. The combination of these techniques is called petrochronology. This thesis applies petrochronological techniques to several subduction-related rocks of varying age and from different localities.

2.1 Mineral equilibria forward modelling

Mineral equilibria forward modelling, or *P*–*T* modelling, is a robust method to interrogate and interpret the metamorphic evolution of HP–LT rocks. *P*–*T* models (or pseudosections) are constructed, mainly to explore variations in pressure, temperature and compositional space. Importantly, models are created for specific bulk rock compositions or binary compositional ranges, allowing exploration into restricted or local rock mineral assemblages, as well as examining other factors such as fluid uptake or influx and oxidation state (e.g. Marmo et al., 2002; Evans, 2004; Lanari and Engi, 2017; Hyppolito et al., 2019). Additionally, the modal proportions and chemical compositions of modelled minerals can be used to further identify the prograde, peak and retrograde evolution of metamorphic rocks (e.g. Pearce et al., 2015; Yakmchuk et al., 2017). Finally, *P*–*T* models can be created to interrogate fundamental processes in the crust, by taking average compositions of rocks of interest and modelling them to understand global processes in Earth's history (e.g.

Wei and Clarke, 2011; Palin et al., 2016; Johnson et al., 2017).

2.2 Geochronology

Traditionally, the dating of eclogite and blueschist facies mineral assemblages has been challenging. A lack of U-rich geochronometers, such as monazite or zircon, has limited the application of conventional geochronologic techniques. Because of this, methods such as MC-ICP-MS Lu–Hf analysis of garnet and lawsonite have become common practice in dating mafic HP–LT assemblages (e.g. Anczkiewicz et al., 2004; Herwartz et al., 2012; Smit et al., 2013; Mulcahy et al., 2009; Mulcahy et al., 2014; Vervoort, 2015). However, more recently, the refinement and development of new analytical methods has opened new avenues to measure the isotopic compositions of minerals. For example, the development of the in-situ Rb–Sr method via laser ablation has allowed the dating of micas, a common mineral in high-pressure assemblages (Zack and Hogmalm, 2016; Hogmalm et al., 2017; Redaa et al., 2021). The analysis of U–Pb isotopes as well as trace element compositions of accessory minerals such as rutile, titanite and zircon has also opened avenues to date eclogites and blueschists, with the added bonus of obtaining information about the temperature of mineral growth (Watson et al., 2006; Ferry and Watson, 2007; Tomkins et al., 2007). In-situ approaches also have the strength of targeting different mineralogical and textural domains within assemblages or minerals themselves, for example targeting growth zoning.

3. The timescales and behaviour of subducted rocks

The mechanisms by which eclogites and blueschists are exhumed from depth is part of ongoing work and debate, as these assemblages are denser than the surrounding crust and upper mantle and therefore are usually lost to the mantle. The durations of metamorphism and exhumation experienced by subducted rocks has also been a point of contention in the metamorphic community (Guillot et al., 2009; Agard et al., 2009; Agard et al., 2018). For example, it is a traditionally held viewpoint that fast exhumation is required to preserve HP–LT assemblages (Brown, 2007; Tsujimori et al., 2006; Li, 2020). However prolonged timescales of prograde and retrograde metamorphism are commonly reported (e.g. Làzaro et al., 2009). Timescales of exhumation are primarily dependant on the style of tectonics operating during subduction, as this will determine the input material and rheology of the subduction channel (Fig. 3; Peacock, 2020). Additionally, the age of subducting plate, the age of the subduction system, the rate of subduction, the dip of the subducting slab, the degree of mechanical coupling between the upper and lower plates, and the magnitude of shear heating and fluid input all control the thermal and chemical structure of a subduction system (Peacock, 1996;

Gerya et al., 2002; Stern, 2002; Peacock, 2003; Agard et al., 2009; Guillot et al., 2009; Peacock, 2020). Due to the difficulties in imaging modern subduction systems, these parameters are generally estimated from fossil subduction systems. As such, the processes and timescales of exhumation, which are dependent on the thermal and chemical structures of subduction zones, remain somewhat enigmatic.

3.1. Exhumation in subduction systems

Exhumation of mafic eclogite and blueschist lithologies in continental systems, i.e. systems where a significant portion of the subducting material is continental in origin, is commonly thought to be driven by the buoyancy of the continental material (e.g. Hacker et al., 2003; Warren et al., 2008a; Warren et al., 2008b; Warren, 2013; Sizova et al., 2014; Petersen and Buck, 2015). In many cases, eclogite or blueschist facies mafic boudins are found encased in felsic or metapelitic material, for example in the Western Gneiss Complex of Norway. This relationship can be explained by either i) HP–LT rocks becoming exhumed from the subduction channel and being emplaced into accretionary or continental material; or ii) HP–LT rocks sharing the same subduction history as the encasing pelitic/felsic material and being exhumed coherently. The latter interpretation tends to be favoured, in which the negative buoyancy of the less dense continental material is thought to aid exhumation, often assisted by slab breakoff or upper plate extension (Petersen and Buck, 2015; Brown et al., 2020). A key feature of these exhumation processes is that they generally occur on short timescales, with the lower plate moving at rates of up to ~ 35 mm/y (Fig. 3; Rubatto and Hermann, 2001; Warren et al., 2013; Agard et al., 2009).

In oceanic systems, common tectonic relationships include large mafic slices of HP–LT assemblages, interpreted to reflect the exhumation of a coherent slab of oceanic crust, or boudins of mafic HP–LT assemblages hosted by serpentinite or sedimentary material, interpreted to reflect complex mixing within the subduction channel (Agard et al., 2009; Guillot et al., 2011; Agard et al., 2018; Zhang, 2020; Festa et al., 2020). Coherent slices of metamorphosed oceanic crust can be tectonically stacked, and may preserve metamorphic conditions which rarely exceed upper blueschist facies, e.g. the Zagros blueschists (Agard et al., 2011; Angiboust et al., 2016). The mechanism for their exhumation may be the subduction of large asperities (e.g., seamounts) or underthrusting of more buoyant material into the subduction channel, which promotes exhumation of oceanic crust to shallower depths (Angiboust et al., 2016). The rate this occurs at may be slow to moderate, for example the exhumation velocity of the Zagros blueschists is estimated to be around 3–4 mm/y (Fig. 3; Monié and Agard, 2009; Agard et al, 2009). The formation and subsequent exhuma-

tion of subduction mélanges, where eclogite and blueschist boudins or lenses are encased in serpentinite or metasedimentary matrixes, may be an extremely long-lived process. In eastern Cuba, HP–LT rocks are formed over a timespan of ca. 55 M.y., and exhumed at varying rates between 2 and 5 mm/y (Fig. 3; Krebs et al., 2008; Làzaro et al., 2009; Agard et al., 2009; Blanco-Quintero et al., 2011). In this context, exhumation is driven by buoyancy of the hydrated serpentinite matrix combined with circulation of material within the subduction channel, referred to as return flow (Cloos, 1982; Cloos and Shreve, 1988a; Cloos and Shreve, 1988b; Gerya et al., 2002).

Returned blocks of HP–LT assemblages as well as other subduction products may have diverse *P–T–t* histories, which sample different physical conditions throughout the subduction zones history (Krebs et al., 2008; Làzaro et al., 2009; Fornash et al., 2016; Pourteau et al., 2019). An added complexity of material behaviour during return flow is that HP–LT blocks may become cycled, and experience multiple burial events within the subduction channel (e.g. Garcia-Casco et al., 2002; Kabir and Takasu, 2010; Blanco-Quintero et al., 2011; Li et al., 2016). This behaviour has been predicted by numerical modelling (Gerya et al., 2002), but there are few fossil subduction terranes where long-lived entrapment and cycling have been identified and well constrained.

Despite the diversity in the discussed exhumation mechanisms for subduction systems, it appears that all HP–LT rocks are exhumed to shallow crustal levels in pulses, which only occur over a restricted timeframe of the subduction systems total history (Agard et al., 2009; Agard et al., 2011; Rutte et al., 2020; van Keken et al., 2018). This punctuated exhumation may be due to periodic decoupling of the upper and lower plates, weakening in the subduction channel, or introduction of asperities into the subduction system (Warren et

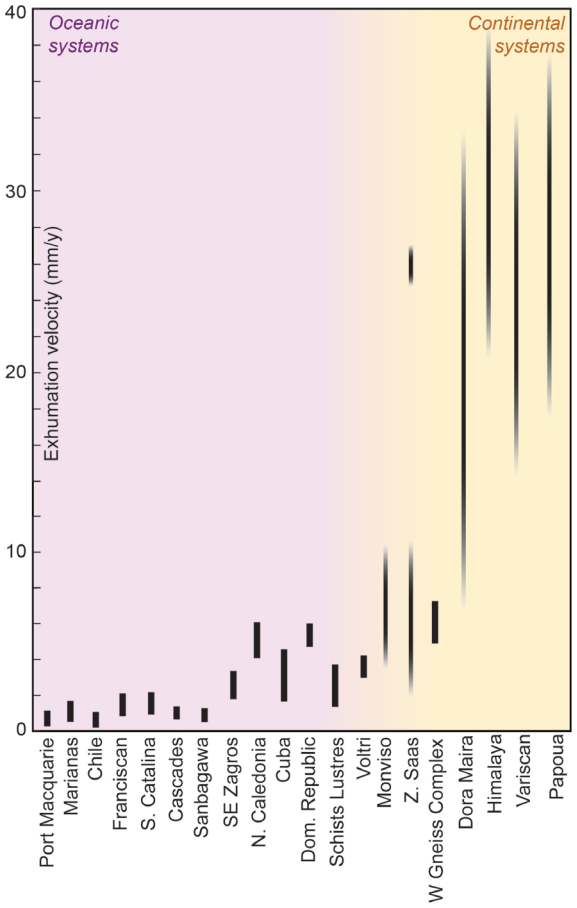


Figure 3: Exhumation velocities of HP–LT terranes and rocks, updated from Agard et al. (2009). Timescales are based on geochronology of peak-retrograde mineral assemblages, which usually reflects the greatest depth reached by the rock to its residence at shallow-mid crustal levels.

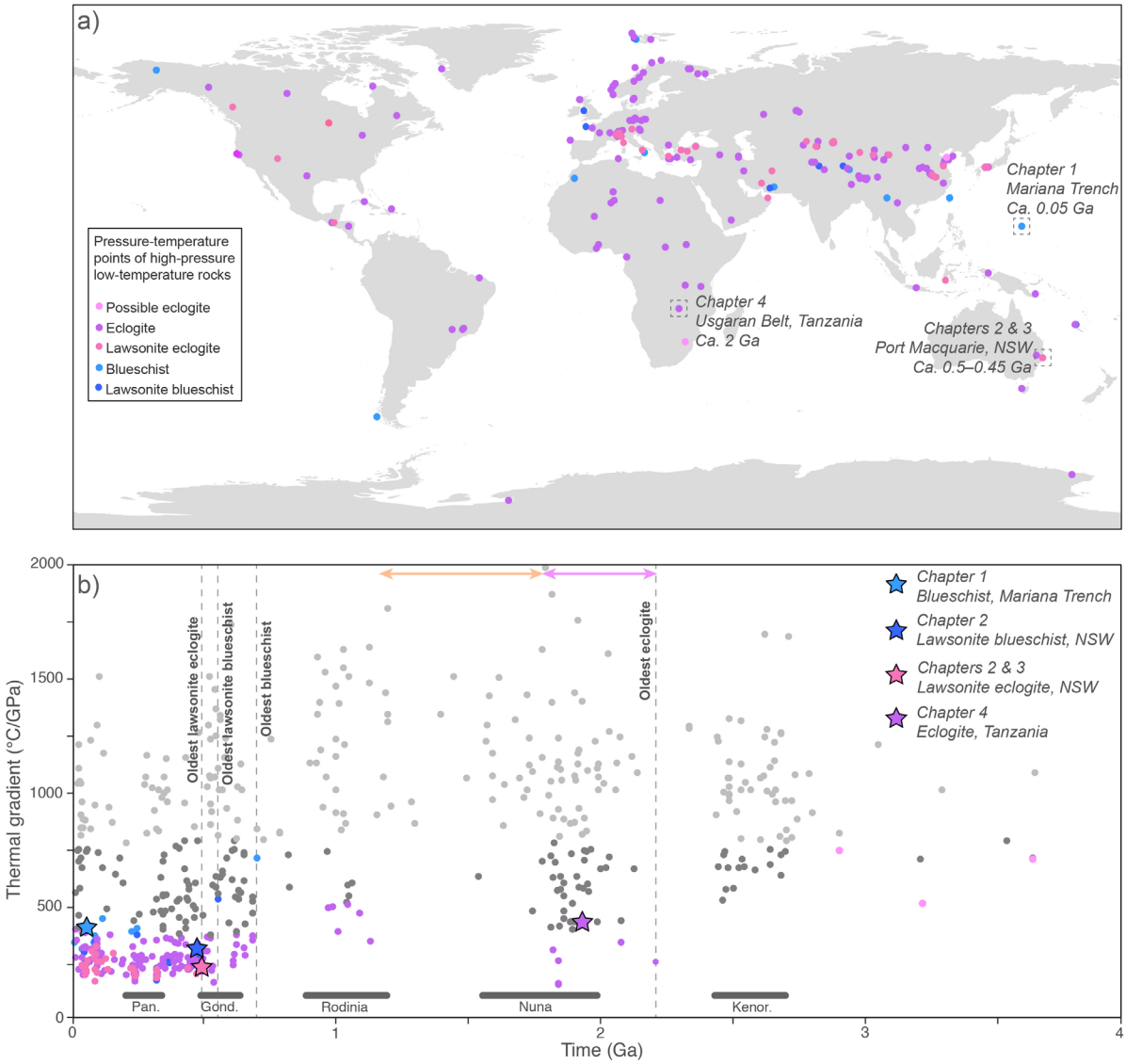


Figure 4: HP–LT rocks in the geological record. a) Geographic locations of various HP–LT assemblages on Earth. Rocks studied in this thesis are outlined by grey dashed boxes. b) Thermal gradients of metamorphic rocks through time, after Brown et al. (2020). Granulites are shown in pale grey, amphibolites are shown in dark grey. Pale grey line indicates the LOWESS curve through all metamorphic data through time (Brown et al., 2020). Supercontinents are shown along the x-axis. Contributions of this thesis are marked in coloured stars. Pink arrow indicates the first widespread emergence of eclogite, orange arrow indicates the subsequent absence of eclogites in the geological record.

al., 2008; Agard et al., 2009; Warren, 2013; Agard et al., 2018; Rutte et al., 2020).

4. The emergence of subduction metamorphism on Earth

The distribution of HP–LT assemblages through Earth's history has been of long-standing interest to geoscientists (Fig 4; Ernst, 1972; Grambling, 1975; Liou et al., 1990; Maruyama et al., 1996; Stern, 2005; Tsujimori et al., 2006; Brown, 2006; Brown, 2007; Brown, 2010; Brown, 2014; Tsuji-

mori and Ernst, 2014; Holder et al., 2018; Brown and Johnson, 2018; Brown et al., 2020a; Brown et al., 2020b; Palin et al., 2020). Eclogites, blueschists and *P–T* sensitive minerals such as coesite, diamond and lawsonite appear gradually throughout the metamorphic record (Fig. 3). The progressive emergence of these thermally-sensitive mineral assemblages through time may reflect a progressive cooling of the mantle (Tsujimori et al., 2006; Brown, 2006; Brown, 2007; Brown, 2010; Brown, 2014; Tsujimori and Ernst, 2014; Holder et al., 2018; Brown and Johnson, 2018; Brown et al., 2020a; Brown et al., 2020b). However, there are also arguments that this pattern may represent the issue of preservation in the geological record, as HP–LT assemblages can be retrogressed or remetamorphosed after exhumation into the crust (Brown, 2006; Brown and Johnson, 2018). Regardless, the distribution of these rocks through time warrants investigation.

4.1 Eclogites

Subduction-related eclogites are defined in this thesis as eclogites that have an affinity to a subduction system, whether this be through MORB-like whole rock chemistry or their geological/tectonic setting. Subduction-related eclogites unambiguously emerge in the geological record in the Palaeoproterozoic, from ca. 2.1–1.8 Ga (Fig. 4). Some of these old eclogites are found in the Eburnian-Transamazonian Orogen in Cameroon (Loose and Schenk, 2018), the Congo Craton (François et al., 2018), the Usagaran Orogen in Tanzania (Möller et al., 1995; Collins et al., 2004; Brown et al,. 2020; Tamblyn et al., 2021), the Snowbird Tectonic Zone in Canada (Baldwin et al., 2014), the Belomorian Province in Russia (Herwartz et al., 2012; Yu et al., 2019), the Ubendian Orogen in Tanzania (Boniface et al., 2012), the Trans-Hudson Orogen in North America (Weller and St-Onge, 2017), the North China Craton (Xu et al., 2018) and the Nagssugtoqidian Orogen in Greenland (Glassely et al., 2014; Müller et al., 2018). These eclogites tend to record warm thermal gradients, and exhume through the amphibolite to granulite facies. Generally, it has been argued the emergence of eclogites at this time was due to the cooling of the mantle, and possibly aided by the increase in preservation potential of subduction-related rocks during the assembly of Nuna (Zhao et al., 2004; Brown et al., 2020). Numerical modelling (Sizova et al., 2010; Sizova et al., 2014) has shown that mantle temperatures of approximately 180 °C above present day values will inhibit the creation and/or exhumation of eclogite-facies rocks into the crust, due to the propensity for shallow break-off of the subducting slab. Therefore, it seems likely that the temperature of the mantle exerted a first order control on the formation of modern-style subduction systems and therefore the appearance of eclogites in the geological record.

Following this initial emergence, there is an ab-

sence of eclogite-facies rocks in the geological record, until ca. 1.1 Ga (orange arrow in Fig. 4). There is another small gap in the record after the formation of the supercontinent Rodinia, and then a continuous record of eclogites to the present day. These gaps may represent preservation issues related to the formation of the supercontinents, or may represent fluctuations in mantle conditions.

4.2 Blueschists

The oldest blueschists on Earth are found in the Bou Azzer inlier of Morocco (Hefferan et al., 2002), and the Aksu blueschist terrane in the Tarim Craton, China (Zhu et al., 2011; Xia et al., 2019). The Bou Azzer blueschists are part of the Anti-Atlas and Transaharan Pan African orogen, the timing of their formation is poorly known, and could be between ca. 750–600 Ma (Hefferan et al., 2002). Similarly, the Aksu blueschist terrane in the Tarim Craton is interpreted to have formed at ca. 750 Ma (Yong et al., 2019). The formation of these terranes has been heralded as the emergence of modern subduction and even plate tectonics on Earth (Stern, 2005; 2018). However, more generally they are thought to reflect progressive cooling of the mantle during the Neoproterozoic (Maruyama et al., 1996; Brown, 2006; 2007; Brown and Johnson, 2018). Further work characterising the *P*–*T*–*t* histories of ancient blueschists may be helpful in understanding if progressive cooling is recorded in blueschist facies assemblages through time.

4.3 Coesite and diamond

Ultrahigh-pressure (UHP) metamorphism is recorded in metamorphic rocks by coesite, a polymorph of quartz, and diamond, a polymorph of carbon (Ernst and Liou, 2008; Schertl and O'Brien, 2013; Gilotti, 2013). Coesite is stable at a minimum pressure of around 3 GPa, and diamond at a minimum of around 4 GPa, reflecting depths well into the mantle (Schertl and O'Brien, 2013; Gilotti, 2013). UHP minerals are usually found in continental subduction or collisional terranes, although some cases are known from oceanic systems (Gilotti, 2013; Aulbach et al., 2016). In order to preserve UHP minerals, they are usually encased within a strong host mineral that protects the inclusion from retrogression during decompression, and also from any interaction with fluid (Gilotti, 2013; Sonin et al., 2019). The oldest coesite-bearing eclogitic rocks are from northeast Brazil (ca. 630 Ma; Santos et al., 2015) and northern Mali (ca. 620 Ma; Jahn et al., 2001). The oldest diamond-bearing orogenic rocks are ca. 530 Ma and are found in the Kokchetav Massif in northern Kazakhstan (Schertl and Sobolev, 2013). Therefore, the emergence of UHP metamorphism is broadly coeval with the abundant emergence of blueschists and eclogites during the Neoproterozoic (Fig. 3).

4.4 Lawsonite

Lawsonite contains ~ 11 wt% H_2O and as such is an important mineral for transporting fluids in subduction zones (Tsujimori et al,. 2006; Tsujimori and Ernst). It only forms along very cool thermal gradients in the blueschist and eclogite facies (Fig. 2). As such, it is diagnostic of cold conditions during subduction, and has only been preserved on Earth for the last ca. 560 million years (Fig 4; Tsujimori et al,. 2006; Tsujimori and Ernst, 2014; Whitney et al., 2020). Lawsonite can contain significant amounts of trace elements such as REEs, Sr, U and Pb, which can be used to track fluid evolution and release in subduction systems (Fornash et al., 2019; Whitney et al., 2020). Its rarity in the geological record has been attributed to its thermal sensitivity, requiring extremely cool conditions to form and be preserved during exhumation (< ~ 250 °C/GPa; Tsujimori et al,. 2006; Tsujimori and Ernst, 2014; Whitney et al., 2020; Chapman and Clark, 2020). The oldest lawsonite-bearing blueschists are found in the Anglesey blueschist belt of Wales (ca. 560–550 Ma; Dallmeyer and Gibbons, 1987), and the oldest lawsonite bearing eclogite is found in Port Macquarie, in eastern Australia (ca. 505 Ma; Tamblyn et al., 2020).

5. Thesis outline

The central aim of this thesis is to investigate the *P–T–t* histories of HP–LT rocks from various stages in the history of modern-style subduction on Earth (Fig. 4). Petrochronological methods are used to constrain the timing and duration of subduction and exhumation. Mineral assemblage modelling is used to constrain the thermal gradients and *P–T* paths experienced during subduction. These methods then allow interpretation of the geodynamic regime responsible for these processes, and contribute to the global dataset of subduction-related rocks. Chapters 2 and 3 focus on the timescales of metamorphism and entrapment of subduction products, firstly in a modern subduction system, and then in a fossil subduction system. Chapter 4 investigates the complex behaviour of entrapped materials during convective flow within the subduction channel. Chapter 5 focusses on one of the oldest examples of subduction-related metamorphism, in rocks that experienced a different style of metamorphism compared to rocks in younger systems, such as those in Chapters 2–4. Finally, Chapter 6 examines patterns in the appearance and disappearance of HP–LT assemblages in the metamorphic record, and compares these to the igneous rock record, to uncover large-scale patterns and processes in the Earth through the last 2 billion years, including mantle temperature and crustal growth.

Chapter 2

Chapter 2 is published in Earth and Planetary Science Letters as: Tamblyn, R., Zack, T., Schmitt,

A.K., Hand, M., Kelsey, D., Morrissey, L., Pabst, S. and Savov, I.P. (2019). "Blueschist from the Mariana forearc records long-lived residence of material in the subduction channel." Earth and Planetary Science Letters, 519, pp.171-181.

This chapter investigates a blueschist chip erupted from a serpentinite mud volcano in the forearc of the Izu-Bonin-Mariana subduction system. This system is currently active and is the only known location on Earth where subduction zone products are presently being transported to the surface. Zircon and rutile geochronology indicates that the blueschist chip formed ca. 50 M.y. ago, during the early stages of subduction of the Pacific oceanic plate. Mineral equilibria modelling indicates the blueschist experienced warm subduction zone thermal gradients of approximately 370 °C/GPa, supporting this interpretation. The blueschist was also buried to approximately 45 km deep, before its exhumation to a position approximately 25 km deep, below the serpentinite volcano. It is interpreted to have been exhumed via channel flow within the subduction system. The maximum age of the serpentinite volcano is ca. 4 Ma, meaning that the chip must have been stored within the subduction channel for at least ca. 46 M.y. This example from a modern subduction system proves that serpentinite-hosted HP–LT rocks may become trapped in subduction zones, and record long-lived P–T–t histories as subduction continues.

Chapter 3

Chapter 3 is published in the Journal of Metamorphic Geology as: Tamblyn, R., Hand, M., Kelsey, D., Anczkiewicz, R. and Och, D. (2020). "Subduction and accumulation of lawsonite eclogite and garnet blueschist in eastern Australia." Journal of Metamorphic Geology, 38(2), pp.157-182.

In this chapter, the metamorphic histories of exotic blocks of lawsonite eclogite and garnet blueschist in serpentinite mélange from Port Macquarie, eastern Australia, are investigated. Lu–Hf and Sm–Nd garnet and U–Pb zircon show the lawsonite eclogite assemblage formed at ca. 500 Ma, but the garnet blueschist formed later, at ca. 470 Ma. Lawsonite eclogite formed at conditions of approximately 2.7 GPa and 590 °C, and garnet blueschist formed at conditions of approximately 2.0 GPa and 550 °C. This data indicate the two metamorphic blocks underwent burial at different times and to different depths within the subduction channel, and must have become mixed together in serpentinite during their post-peak evolution. This buoyant serpentinite is also the probable cause of their exhumation via channel flow. Additionally, their residence in a younger Devonian–Carboniferous orogen on the margin of eastern Australia suggests they were entrapped within the subduction channel for up to ca. 250 Ma, experiencing east-ward directed transport as

the subduction channel rolled back. This study shows that thermal durations recorded by oceanic HP–LT rocks may be long, and that these rocks can experience transport as subducting slabs migrate during that time.

Chapter 4

Chapter 4 is published in Contributions to Mineralogy and Petrology as: Tamblyn, R., Hand, M., Morrissey, L., Zack, T., Phillips, G. and Och, D. (2020). "Resubduction of lawsonite eclogite within a serpentinite-filled subduction channel." Contributions to Mineralogy and Petrology, 175(8), pp.1-22.

Chapter 4 focuses on the block of lawsonite eclogite previously examined in Chapter 3. Further detailed investigation into the petrology of the lawsonite eclogite revealed several mineral assemblages, suggesting the eclogite is polymetamorphic, i.e. experienced multiple burial events. An initial burial cycle is identified by the garnet and lawsonite Lu–Hf data from Chapter 3, which suggests these minerals formed at ca. 490 Ma. Revisiting of the petrography of the garnets indicates two generations of growth, with ca. 490 Ma garnet containing possible evidence of reaching coesite facies. Matrix minerals however formed at ca. 450 Ma, as dated by U–Pb titanite, Ar–Ar phengite and in-situ Rb–Sr phengite geochronology. Mineral equilibria modelling suggests the P–T path following by the eclogite was two tight hairpin loops along a cold thermal gradient which preserved pristine lawsonite. The cycling occurred over ca. 50 m.y., supporting predictions that HP–LT rocks may record complex behaviours during convective flow over prolonged timeframes in subduction systems.

Chapter 5

Chapter 5 is published in Lithos as: Tamblyn, R., Brown, D., Hand, M., Morrissey, L., Clark, C. and Anczkiewicz, R. (2020). "The 2 Ga eclogites of Central Tanzania: Directly linking age and metamorphism." Lithos, p.105890.

This chapter investigates the metamorphic histories of two eclogites from the Usagaran Belt in central Tanzania. It is accompanied by a related paper which can be found in the supplementary chapter, which investigates the pelitic lithologies that encase the eclogites. Lu–Hf garnet geochronology dates subduction-related metamorphism at ca. 1994 Ma, supported by rutile and zircon U–Pb data. Mineral equilibria modelling and thermometry suggest the eclogites reached minimum conditions of approximately 1.8 GPa and 800 °C, implying warm conditions during subduction. The eclogites were then retrogressed to amphibolite–granulite conditions during exhumation. Exhumation likely occurred during slab breakoff driven buoyancy of the oceanic crust and sur-

rounding pelitic material, over a relatively short timeframe of ca. 6 M.y.. Several eclogites of similar age and P–T conditions are found throughout nearby African orogens, suggesting the existence of a large modern-style subduction system in the Palaeoproterozoic.

A companion study to this can be found in Appendix 1 and is published as: Brown, D.A., Tamblyn, R., Hand, M. and Morrissey, L.J. (2020). Thermobarometric constraints on burial and exhumation of 2-billion-year-old eclogites and their metapelitic hosts. Precambrian Research, 347, p.105833.

This study examines the pelitic lithologies which encase the Usagaran eclogites, as well as two other eclogite-facies mafic rocks. Mineral equilibria modelling shows that while the encasing pelites preserve apparently low-pressure assemblages, they were subducted along with the mafic rocks to pressures of approximately 1.7 GPa. This study supports that the thermal conditions in the subducting crust were warm. A tectonic regime involving crustal thickening during subduction, followed by coherent extensional exhumation of the pelitic and mafic lithologies, is suggested.

Chapter 6

Chapter 6 is in review in Geology as: Tamblyn, R., Hasterok, D., Hand, M. and Gard, M. "Mantle heating at ca. 2 Ga driven by crustal growth: evidence from granites and eclogites".

Chapter 6 steps back to look at a broader view of the record of HP–LT rocks throughout geological history. Subduction-related eclogites emerged in the geological record from ca. 2.1–1.8 Ga, suggesting the mantle was sufficiently cooled to allow the preservation of eclogites, and that modern-style subduction was operating on Earth at this time. However, eclogites disappear again until ca. 1.1 Ga. Coincident with the emergence and subsequent disappearance of eclogites, an investigation into the global record of granite chemistry shows that granites record step-changes in trace element chemistry, notably Sr, Eu, Y and HREE concentrations. These changes are explained by warming of the thermal gradient associated with granite genesis in the crust. We suggest warming of the mantle was achieved by continental insulation, during a significant crustal growth event around 2–1.8 Ga, aided by the assembly of the supercontinent Nuna. This thermal insulation of the mantle then prohibited the preservation of eclogites and caused the changes in granite chemistry world-wide. Eventually, secular cooling overcame the continental insulation effect, allowing eclogites to be preserved in the recent geological record.

Chapter 7

Chapter 7 provides a summary of the findings of this thesis. *P–T–t* evolutions from HP–LT rocks

studied are briefly compared and discussed to comment on the geodynamic and tectonic implications they pose. The findings and ideas put forward in this thesis are also discussed in a broader context and tied to the evolution of the crust and mantle through time, as well as other datasets from the geological record. Finally, limitations encountered and future directions for further research are suggested.

References:

Agard, P., Plunder, A., Angiboust, S., Bonnet, G., & Ruh, J. (2018). The subduction plate interface: Rock record and mechanical coupling (from long to short time scales). Lithos.

Agard, P., Yamato, P., Jolivet, L., & Burov, E. (2009). Exhumation of oceanic blueschists and eclogites in subduction zones: timing and mechanisms. Earth-Science Reviews, 92(1), 53-79.

Anczkiewicz, R., Platt, J. P., Thirlwall, M. F., & Wakabayashi, J. (2004). Franciscan subduction off to a slow start: evidence from high-precision Lu–Hf garnet ages on high grade-blocks. Earth and Planetary Science Letters, 225(1), 147-161.

Angiboust, S., Agard, P., Glodny, J., Omrani, J., & Oncken, O. (2016). Zagros blueschists: Episodic underplating and long-lived cooling of a subduction zone. Earth and Planetary Science Letters, 443, 48-58.

Angiboust, S., Pettke, T., De Hoog, J. C., Caron, B., & Oncken, O. (2014). Channelized fluid flow and eclogite-facies metasomatism along the subduction shear zone. Journal of Petrology, 55(5), 883-916.

Aulbach, S., Gerdes, A., & Viljoen, K. (2016). Formation of diamondiferous kyanite–eclogite in a subduction mélange. Geochimica et Cosmochimica Acta, 179, 156-176.

Baldwin, J. A., Bowring, S. A., Williams, M. L., & Williams, I. S. (2004). Eclogites of the Snowbird tectonic zone: petrological and U-Pb geochronological evidence for Paleoproterozoic high-pressure metamorphism in the western Canadian Shield. Contributions to Mineralogy and Petrology, 147(5), 528-548.

Blanco-Quintero, I. F., García-Casco, A., & Gerya, T. V. (2011). Tectonic blocks in serpentinite mélange (eastern Cuba) reveal large-scale convective flow of the subduction channel. Geology, 39(1), 79-82.

Boniface, N., Schenk, V., & Appel, P. (2012). Paleoproterozoic eclogites of MORB-type chemistry and three Proterozoic orogenic cycles in the Ubendian Belt (Tanzania): Evidence from monazite and zircon geochronology, and geochemistry. Precambrian Research, 192, 16-33.

Brown, D. A., Tamblyn, R., Hand, M., & Mor-

rissey, L. J. (2020). Thermobarometric constraints on burial and exhumation of 2-billion-year-old eclogites and their metapelitic hosts. Precambrian Research, 105833.

Brown, M. (2006). Duality of thermal regimes is the distinctive characteristic of plate tectonics since the Neoarchean. Geology, 34(11), 961-964.

Brown, M. (2007). Metamorphic conditions in orogenic belts: a record of secular change. International Geology Review, 49(3), 193-234.

Brown, M. (2010). Paired metamorphic belts revisited. Gondwana Research, 18(1), 46-59.

Brown, M., & Johnson, T. (2018). Secular change in metamorphism and the onset of global plate tectonics. American Mineralogist, 103(2), 181-196.

Brown, M., Johnson, T., & Gardiner, N. J. (2020). Plate tectonics and the Archean Earth. Annual Review of Earth and Planetary Sciences, 48.

Brown, M., Kirkland, C., & Johnson, T. (2020). Evolution of geodynamics since the Archean: Significant change at the dawn of the Phanerozoic. Geology, 48(5), 488-492.

Chapman, T., & Clarke, G. L. (2020). Cryptic evidence for the former presence of lawsonite in blueschist and eclogite. Journal of metamorphic Geology.

Cloos, M., & Shreve, R. L. (1988). Subduction-channel model of prism accretion, melange formation, sediment subduction, and subduction erosion at convergent plate margins: 1. Background and description. Pure and Applied Geophysics, 128(3), 455-500.

Cloos, M., & Shreve, R. L. (1988). Subduction-channel model of prism accretion, melange formation, sediment subduction, and subduction erosion at convergent plate margins: 2. Implications and discussion. Pure and Applied Geophysics, 128(3), 501-545.

Collins, A. S., Reddy, S. M., Buchan, C., & Mruma, A. (2004). Temporal constraints on Palaeoproterozoic eclogite formation and exhumation (Usagaran Orogen, Tanzania). Earth and Planetary Science Letters, 224(1-2), 175-192.

Condie, K. C., & Pease, V. (2008). When did plate tectonics begin on planet Earth? (Vol. 440): Geological Society of America.

Dallmeyer, R., & Gibbons, W. (1987). The age of blueschist metamorphism in Anglesey, North Wales: evidence from 40Ar/39Ar mineral dates of the Penmynydd schists. Journal of the Geological Society, 144(6), 843-850.

dos Santos, T. J. S., da Silva Amaral, W., Ancelmi, M. F., Pitarello, M. Z., Fuck, R. A.,

& Dantas, E. L. (2015). U–Pb age of the coesite-bearing eclogite from NW Borborema Province, NE Brazil: Implications for western Gondwana assembly. Gondwana Research, 28(3), 1183-1196.

Ernst, W. (1972). Occurrence and mineralogic evolution of blueschist belts with time. American Journal of Science, 272(7), 657-668.

Ernst, W., & Liou, J. (2008). High-and ultra-high-pressure metamorphism: Past results and future prospects. American Mineralogist, 93(11-12), 1771-1786.

Evans, T. (2004). A method for calculating effective bulk composition modification due to crystal fractionation in garnet-bearing schist: implications for isopleth thermobarometry. Journal of metamorphic Geology, 22(6), 547-557.

Ferry, J., & Watson, E. (2007). New thermodynamic models and revised calibrations for the Ti-in-zircon and Zr-in-rutile thermometers. Contributions to Mineralogy and Petrology, 154(4), 429-437.

Festa, A., Ogata, K., & Pini, G. A. (2020). Polygenetic mélanges: a glimpse on tectonic, sedimentary and diapiric recycling in convergent margins. Journal of the Geological Society, 177(3), 551-561.

Fornash, K. F., Cosca, M. A., & Whitney, D. L. (2016). Tracking the timing of subduction and exhumation using 40 Ar/39 Ar phengite ages in blueschist-and eclogite-facies rocks (Sivrihisar, Turkey). Contributions to Mineralogy and Petrology, 171(7), 67.

François, C., Debaille, V., Paquette, J.-L., Baudet, D., & Javaux, E. J. (2018). The earliest evidence for modern-style plate tectonics recorded by HP–LT metamorphism in the Paleoproterozoic of the Democratic Republic of the Congo. Scientific reports, 8(1), 1-10.

García-Casco, A., Torres-Roldán, R., Millán, G., Monié, P., & Schneider, J. (2002). Oscillatory zoning in eclogitic garnet and amphibole, Northern Serpentinite Melange, Cuba: a record of tectonic instability during subduction? Journal of metamorphic Geology, 20(6), 581-598.

Gerya, T. (2011). Future directions in subduction modeling. Journal of Geodynamics, 52(5), 344-378.

Gerya, T. V., Stöckhert, B., & Perchuk, A. L. (2002). Exhumation of high-pressure metamorphic rocks in a subduction channel: A numerical simulation. Tectonics, 21(6).

Gilotti, J. A. (2013). The realm of ultrahigh-pressure metamorphism. Elements, 9(4), 255-260.

Glassley, W. E., Korstgård, J. A., Sørensen, K., & Platou, S. W. (2014). A new UHP metamorphic complex in the~ 1.8 Ga Nags-

sugtoqidian Orogen of West Greenland. American Mineralogist, 99(7), 1315-1334.

Grambling, J. A. (1981). Pressures and temperatures in Precambrian metamorphic rocks. Earth and Planetary Science Letters, 53(1), 63-68.

Guillot, S., Hattori, K., Agard, P., Schwartz, S., & Vidal, O. (2009). Exhumation processes in oceanic and continental subduction contexts: a review Subduction zone geodynamics (pp. 175-205): Springer.

Hacker, B., Andersen, T., Root, D., Mehl, L., Mattinson, J., & Wooden, J. (2003). Exhumation of high-pressure rocks beneath the Solund Basin, western gneiss region of Norway. Journal of metamorphic Geology, 21(6), 613-629.

Hefferan, K. P., Admou, H., Hilal, R., Karson, J. A., Saquaque, A., Juteau, T., . . . Kornprobst, J. M. (2002). Proterozoic blueschist-bearing mélange in the Anti-Atlas Mountains, Morocco. Precambrian Research, 118(3-4), 179-194.

Hermann, J., Spandler, C., Hack, A., & Korsakov, A. V. (2006). Aqueous fluids and hydrous melts in high-pressure and ultra-high pressure rocks: Implications for element transfer in subduction zones. Lithos, 92(3-4), 399-417.

Herwartz, D., Skublov, S., Berezin, A., & Mel'Nik, A. (2012). First Lu-Hf garnet ages of eclogites from the Belomorian mobile belt (Baltic shield, Russia). Paper presented at the Doklady Earth Sciences.

Hogmalm, K. J., Zack, T., Karlsson, A. K.-O., Sjöqvist, A. S., & Garbe-Schönberg, D. (2017). In situ Rb–Sr and K–Ca dating by LA-ICP-MS/MS: an evaluation of N 2 O and SF 6 as reaction gases. Journal of Analytical Atomic Spectrometry, 32(2), 305-313.

Holder, R. M., Viete, D. R., Brown, M., & Johnson, T. E. (2019). Metamorphism and the evolution of plate tectonics. Nature, 572(7769), 378-381.

Hyppolito, T., Cambeses, A., Angiboust, S., Raimondo, T., García-Casco, A., & Juliani, C. (2019). Rehydration of eclogites and garnet-replacement processes during exhumation in the amphibolite facies. Geological Society, London, Special Publications, 478(1), 217-239.

Jahn, B.-m., Caby, R., & Monie, P. (2001). The oldest UHP eclogites of the World: age of UHP metamorphism, nature of protoliths and tectonic implications. Chemical Geology, 178(1-4), 143-158.

Johnson, T. E., Brown, M., Gardiner, N. J., Kirkland, C. L., & Smithies, R. H. (2017). Earth's first stable continents did not form by subduction. Nature, 543(7644), 239-242.

Kabir, M., & Takasu, A. (2010). Evidence for

multiple burial–partial exhumation cycles from the Onodani eclogites in the Sambagawa metamorphic belt, central Shikoku, Japan. Journal of metamorphic Geology, 28(8), 873-893.

Krebs, M., Maresch, W., Schertl, H.-P., Münker, C., Baumann, A., Draper, G., . . . Trapp, E. (2008). The dynamics of intra-oceanic subduction zones: a direct comparison between fossil petrological evidence (Rio San Juan Complex, Dominican Republic) and numerical simulation. Lithos, 103(1), 106-137.

Lanari, P., & Engi, M. (2017). Local bulk composition effects on metamorphic mineral assemblages. Reviews in mineralogy and geochemistry, 83(1), 55-102.

Lázaro, C., García-Casco, A., Rojas Agramonte, Y., Kröner, A., Neubauer, F., & Iturralde-Vinent, M. (2009). Fifty-five-million-year history of oceanic subduction and exhumation at the northern edge of the Caribbean plate (Sierra del Convento mélange, Cuba). Journal of metamorphic Geology, 27(1), 19-40.

Leng, W., & Huang, L. (2018). Progress in numerical modeling of subducting plate dynamics. Science China Earth Sciences, 61(12), 1761-1774.

Leng, W., & Mao, W. (2015). Geodynamic modeling of thermal structure of subduction zones. Science China Earth Sciences, 58(7), 1070-1083.

Li, J. (2020). Blueschist: A window into high-pressure/low-temperature metamorphism and subduction zone dynamics. Science China Earth Sciences, 1-16.

Li, Z. (2014). A review on the numerical geodynamic modeling of continental subduction, collision and exhumation. Science China Earth Sciences, 57(1), 47-69.

Liati, A., Theye, T., Fanning, C. M., Gebauer, D., & Rayner, N. (2016). Multiple subduction cycles in the Alpine orogeny, as recorded in single zircon crystals (Rhodope zone, Greece). Gondwana Research, 29(1), 199-207.

Liou, J., Maruyama, S., Wang, X., & Graham, S. (1990). Precambrian blueschist terranes of the world. Tectonophysics, 181(1-4), 97-111.

Loose, D., & Schenk, V. (2018). 2.09 Ga old eclogites in the Eburnian-Transamazonian orogen of southern Cameroon: Significance for Palaeoproterozoic plate tectonics. Precambrian Research, 304, 1-11.

Marmo, B., Clarke, G., & Powell, R. (2002). Fractionation of bulk rock composition due to porphyroblast growth: effects on eclogite facies mineral equilibria, Pam Peninsula, New Caledonia. Journal of metamorphic Geology, 20(1), 151-165.

Maruyama, S., Liou, J., & Terabayashi, M. (1996). Blueschists and eclogites of the world and

their exhumation. International Geology Review, 38(6), 485-594.

Maruyama, S., Santosh, M., & Azuma, S. (2018). Initiation of plate tectonics in the Hadean: Eclogitization triggered by the ABEL Bombardment. Geoscience Frontiers, 9(4), 1033-1048.

Möller, A., Appel, P., Mezger, K., & Schenk, V. (1995). Evidence for a 2 Ga subduction zone: eclogites in the Usagaran belt of Tanzania. Geology, 23(12), 1067-1070.

Monie, P., & Agard, P. (2009). Coeval blueschist exhumation along thousands of kilometers: Implications for subduction channel processes. Geochemistry, Geophysics, Geosystems, 10(7).

Mulcahy, S., Vervoort, J., & Renne, P. (2014). Dating subduction-zone metamorphism with combined garnet and lawsonite Lu–Hf geochronology. Journal of metamorphic Geology, 32(5), 515-533.

Mulcahy, S. R., King, R. L., & Vervoort, J. D. (2009). Lawsonite Lu-Hf geochronology: A new geochronometer for subduction zone processes. Geology, 37(11), 987-990.

Müller, S., Dziggel, A., Kolb, J., & Sindern, S. (2018). Mineral textural evolution and PT-path of relict eclogite-facies rocks in the Paleoproterozoic Nagssugtoqidian Orogen, South-East Greenland. Lithos, 296, 212-232.

Palin, R. M., Santosh, M., Cao, W., Li, S.-S., Hernández-Uribe, D., & Parsons, A. (2020). Secular metamorphic change and the onset of plate tectonics. Earth-Science Reviews, 103172.

Palin, R. M., White, R. W., Green, E. C., Diener, J. F., Powell, R., & Holland, T. J. (2016). High-grade metamorphism and partial melting of basic and intermediate rocks. Journal of metamorphic Geology, 34(9), 871-892.

Peacock, S. M. (1996). Thermal and petrologic structure of subduction zones. Subduction: top to bottom, 96, 119-133.

Peacock, S. M. (2003). Thermal structure and metamorphic evolution of subducting slabs. Geophysical Monograph-American Geophysical Union, 138, 7-22.

Peacock, S. M. (2020). Advances in the thermal and petrologic modeling of subduction zones. Geosphere, 16(4), 936-952.

Pearce, M., White, A., & Gazley, M. (2015). TC-Investigator: automated calculation of mineral mode and composition contours for thermocalc pseudosections. Journal of metamorphic Geology, 33(4), 413-425.

Petersen, K. D., & Buck, W. R. (2015). Eduction, extension, and exhumation of ultra-high-pressure rocks in metamorphic core complexes due to subduction initiation. Geochemistry, Geophysics, Geosystems, 16(8), 2564-2581.

Pourteau, A., Scherer, E. E., Schorn, S., Bast, R., Schmidt, A., & Ebert, L. (2019). Thermal evolution of an ancient subduction interface revealed by Lu–Hf garnet geochronology, Halilbağı Complex (Anatolia). Geoscience Frontiers, 10(1), 127-148.

Proyer, A. (2003a). Metamorphism of pelites in NKFMASH–a new petrogenetic grid with implications for the preservation of high-pressure mineral assemblages during exhumation. Journal of metamorphic Geology, 21(5), 493-509.

Proyer, A. (2003b). The preservation of high-pressure rocks during exhumation: metagranites and metapelites. Lithos, 70(3-4), 183-194.

Rebay, G., Powell, R., & Diener, J. (2010). Calculated phase equilibria for a MORB composition in a P–T range, 450–650 C and 18–28 kbar: the stability of eclogite. Journal of metamorphic Geology, 28(6), 635-645.

Redaa, A., Farkaš, J., Gilbert, S., Collins, A. S., Wade, B., Löhr, S., ... & Garbe-Schönberg, D. (2021). Assessment of elemental fractionation and matrix effects during in situ Rb–Sr dating of phlogopite by LA-ICP-MS/MS: implications for the accuracy and precision of mineral ages. Journal of Analytical Atomic Spectrometry.

Rubatto, D., & Hermann, J. r. (2001). Exhumation as fast as subduction? Geology, 29(1), 3-6.

Ruh, J. B., Le Pourhiet, L., Agard, P., Burov, E., & Gerya, T. (2015). Tectonic slicing of subducting oceanic crust along plate interfaces: Numerical modeling. Geochemistry, Geophysics, Geosystems, 16(10), 3505-3531.

Rutte, D., Garber, J., Kylander-Clark, A., & Renne, P. R. (2020). An exhumation pulse from the nascent Franciscan subduction zone (California, USA). Tectonics, 39(10), e2020TC006305.

Schertl, H.-P., & O'Brien, P. J. (2013). Continental crust at mantle depths: key minerals and microstructures. Elements, 9(4), 261-266.

Schertl, H.-P., & Sobolev, N. (2013). The Kokchetav Massif, Kazakhstan:"Type locality" of diamond-bearing UHP metamorphic rocks. Journal of Asian Earth Sciences, 63, 5-38.

Sizova, E., Gerya, T., & Brown, M. (2014). Contrasting styles of Phanerozoic and Precambrian continental collision. Gondwana Research, 25(2), 522-545.

Sizova, E., Gerya, T., Brown, M., & Perchuk, L. (2010). Subduction styles in the Precambrian: insight from numerical experiments. Lithos, 116(3-4), 209-229.

Smit, M. A., Scherer, E. E., & Mezger, K. (2013). Lu–Hf and Sm–Nd garnet geochronology: chronometric closure and implications for dating petrological processes.

Earth and Planetary Science Letters, 381, 222-233.

Sonin, V., Leech, M., Chepurov, A., Zhimulev, E., & Chepurov, A. (2019). Why are diamonds preserved in UHP metamorphic complexes? Experimental evidence for the effect of pressure on diamond graphitization. International Geology Review, 61(4), 504-519.

Spandler, C., Hermann, J., Arculus, R., & Mavrogenes, J. (2003). Redistribution of trace elements during prograde metamorphism from lawsonite blueschist to eclogite facies; implications for deep subduction-zone processes. Contributions to Mineralogy and Petrology, 146(2), 205-222.

Stern, R. J. (2002). Subduction zones. Reviews of Geophysics, 40(4), 3-1-3-38.

Stern, R. J. (2005). Evidence from ophiolites, blueschists, and ultrahigh-pressure metamorphic terranes that the modern episode of subduction tectonics began in Neoproterozoic time. Geology, 33(7), 557-560.

Stern, R. J. (2018). The evolution of plate tectonics. Philosophical Transactions of the Royal Society A: Mathematical, Physical and Engineering Sciences, 376(2132), 20170406.

Tamblyn, R., Brown, D., Hand, M., Morrissey, L., Clark, C., & Anczkiewicz, R. (2021). The 2 Ga eclogites of Central Tanzania: Directly linking age and metamorphism. Lithos, 380, 105890.

Tamblyn, R., Hand, M., Kelsey, D., Anczkiewicz, R., & Och, D. (2020). Subduction and accumulation of lawsonite eclogite and garnet blueschist in eastern Australia. Journal of metamorphic Geology, 38(2), 157-182.

Tamblyn, R., Zack, T., Schmitt, A., Hand, M., Kelsey, D., Morrissey, L., . . . Savov, I. (2019). Blueschist from the Mariana forearc records long-lived residence of material in the subduction channel. Earth and Planetary Science Letters, 519, 171-181.

Tomkins, H., Powell, R., & Ellis, D. (2007). The pressure dependence of the zirconium-in-rutile thermometer. Journal of metamorphic Geology, 25(6), 703-713.

Tsujimori, T., & Ernst, W. (2014). Lawsonite blueschists and lawsonite eclogites as proxies for palaeo-subduction zone processes: a review. Journal of metamorphic Geology, 32(5), 437-454.

Tsujimori, T., Sisson, V. B., Liou, J. G., Harlow, G. E., & Sorensen, S. S. (2006). Very-low-temperature record of the subduction process: A review of worldwide lawsonite eclogites. Lithos, 92(3), 609-624.

van Keken, P. E., Currie, C., King, S. D., Behn, M.

D., Cagnioncle, A., He, J., . . . Spiegelman, M. (2008). A community benchmark for subduction zone modeling. Physics of the Earth and Planetary Interiors, 171(1-4), 187-197.

van Keken, P. E., Wada, I., Abers, G. A., Hacker, B. R., & Wang, K. (2018). Mafic high-pressure rocks are preferentially exhumed from warm subduction settings. Geochemistry, Geophysics, Geosystems, 19(9), 2934-2961.

Vervoort, J. (2015). Lu-Hf dating: the Lu-Hf isotope system Encyclopedia of scientific dating methods (pp. 379-390): Springer Netherlands.

Viete, D. R., Hacker, B. R., Allen, M. B., Seward, G. G., Tobin, M. J., Kelley, C. S., . . . Duckworth, A. R. (2018). Metamorphic records of multiple seismic cycles during subduction. Science advances, 4(3), eaaq0234.

Warren, C. (2013). Exhumation of (ultra-) high-pressure terranes: concepts and mechanisms. Solid Earth, 4(1), 75-92.

Warren, C., Beaumont, C., & Jamieson, R. A. (2008). Modelling tectonic styles and ultra-high pressure (UHP) rock exhumation during the transition from oceanic subduction to continental collision. Earth and Planetary Science Letters, 267(1-2), 129-145.

Warren, C. J., Beaumont, C., & Jamieson, R. A. (2008). Deep subduction and rapid exhumation: Role of crustal strength and strain weakening in continental subduction and ultrahigh-pressure rock exhumation. Tectonics, 27(6).

Watson, E., Wark, D., & Thomas, J. (2006). Crystallization thermometers for zircon and rutile. Contributions to Mineralogy and Petrology, 151(4), 413.

Wei, C., & Clarke, G. (2011). Calculated phase equilibria for MORB compositions: a reappraisal of the metamorphic evolution of lawsonite eclogite. Journal of metamorphic Geology, 29(9), 939-952.

Weller, O., & St-Onge, M. (2017). Record of modern-style plate tectonics in the Palaeoproterozoic Trans-Hudson orogen. Nature Geoscience, 10(4), 305-311.

Whitney, D. L., Fornash, K. F., Kang, P., Ghent, E. D., Martin, L., Okay, A. I., & Brovarone, A. V. (2020). Lawsonite composition and zoning as tracers of subduction processes: A global review. Lithos, 105636.

Xia, B., Zhang, L., Du, Z., & Xu, B. (2019). Petrology and age of Precambrian Aksu blueschist, NW China. Precambrian Research, 326, 295-311.

Xu, C., Kynický, J., Song, W., Tao, R., Lü, Z., Li, Y., . . . Zhang, L. (2018). Cold deep subduction recorded by remnants of a Paleoproterozoic carbonated slab. Nature communications, 9(1), 1-8.

Yakymchuk, C., Clark, C., & White, R. W. (2017). Phase relations, reaction sequences and petrochronology. Reviews in mineralogy and geochemistry, 83(1), 13-53.

Yamato, P., Agard, P., Burov, E., Le Pourhiet, L., Jolivet, L., & Tiberi, C. (2007). Burial and exhumation in a subduction wedge: Mutual constraints from thermomechanical modeling and natural P-T-t data (Schistes Lustrés, western Alps). Journal of Geophysical Research: Solid Earth, 112(B7).

Yu, H., Zhang, L., Lanari, P., Rubatto, D., & Li, X. (2019). Garnet LuHf geochronology and PT path of the Gridino-type eclogite in the Belomorian Province, Russia. Lithos, 326, 313-326.

Zack, T., & Hogmalm, K. J. (2016). Laser ablation Rb/Sr dating by online chemical separation of Rb and Sr in an oxygen-filled reaction cell. Chemical Geology, 437, 120-133.

Zhang, J. (2020). The study of subduction channels: Progress, controversies, and challenges. Science China Earth Sciences, 1-21.

Zhao, G., Sun, M., Wilde, S. A., & Li, S. (2004). A Paleo-Mesoproterozoic supercontinent: assembly, growth and breakup. Earth-Science Reviews, 67(1-2), 91-123.

Zhu, W., Zheng, B., Shu, L., Ma, D., Wu, H., Li, Y., . . . Yu, J. (2011). Neoproterozoic tectonic evolution of the Precambrian Aksu blueschist terrane, northwestern Tarim, China: insights from LA-ICP-MS zircon U–Pb ages and geochemical data. Precambrian Research, 185(3-4), 215-230.

Chapter 2:

Blueschist from the Mariana forearc records long-lived residence of material in the subduction channel

This chapter is published as:

Blueschist from the Mariana forearc records long-lived residence of material in the subduction channel (2019). R. Tamblyn, T. Zack, A.K. Schmitt, M. Hand, D. Kelsey, L. Morrissey, S. Pabst, I. Savov. *Earth and Planetary Science Letters*, 519, 171-181

The supplementary materials for this chapter can be found in Appendix 2

Statement of Authorship

Title of Paper	Blueschist from the Mariana forearc records long-lived residence of material in the subduction channel
Publication Status	[x] Published [ ] Accepted for Publication [ ] Submitted for Publication [ ] Unpublished and Unsubmitted w ork w ritten in manuscript style
Publication Details	Tamblyn, R., Zack, T., Schmitt, A. K., Hand, M., Kelsey, D., Morrissey, L., ... & Savov, I. P. (2019). Blueschist from the Mariana forearc records long-lived residence of material in the subduction channel. Earth and Planetary Science Letters, 519, 171-181..

Principal Author

Name of Principal Author (Candidate)	Renee Tamblyn		
Contribution to the Paper	Completed compositional data collection/mapping Completed mineral equilibria modelling Wrote the manuscript		
Overall percentage (%)	60		
Certification:	This paper reports on original research I conducted during the period of my Higher Degree by Research candidature and is not subject to any obligations or contractual agreements with a third party that would constrain its inclusion in this thesis. I am the primary author of this paper.		
Signature		Date	30/04/2020

Co-Author Contributions

By signing the Statement of Authorship, each author certifies that:

i. the candidate's stated contribution to the publication is accurate (as detailed above);

ii. permission is granted for the candidate in include the publication in the thesis; and

iii. the sum of all co-author contributions is equal to 100% less the candidate's stated contribution.

Name of Co-Author	Thomas Zack		
Contribution to the Paper	Provided the sample, collected the U-Pb data, reviewed the manuscript		
Signature		Date	08/10/2020

Name of Co-Author	Axel Schmitt		
Contribution to the Paper	Collected the U-Pb data, reviewed the manuscript		
Signature		Date	08/10/2020

Please cut and paste additional co-author panels here as required.

Name of Co-Author	Martin Hand		
Contribution to the Paper	Design of manuscript, assisted with mineral equilibria modelling, reviewed the manuscript		10%
Signature		Date	03/03/2021

Name of Co-Author	David Kelsey		
Contribution to the Paper	Assisted with mineral equilibria modelling and mapping of the sample		5%
Signature		Date	17/02/2021

Name of Co-Author	Laura Morrissey		
Contribution to the Paper	Design of manuscript, assisted with mineral equilibria modelling, reviewed the manuscript		5%
Signature		Date	02/03/2021

Name of Co-Author	Sonja Pabst		
Contribution to the Paper	Collected mineral chemical data		2.5%
Signature		Date	17/10/2020

Name of Co-Author	Ivan Savov		
Contribution to the Paper	Provided the sample, reviewed the manuscript		2.5%
Signature		Date	9/10/2020

Highlights

- Blueschist from serpentine mud volcano in Mariana forearc is ca. 50 Ma old
- The mineral assemblage records warm metamorphic conditions during IBM subduction initiation
- Blueschist rocks have resided in the subduction channel for at least 46 Ma

Abstract

From ca. 50 Ma to present, the western Pacific plate has been subducting under the Philippine Sea plate, forming the oceanic Izu-Bonin-Mariana (IBM) subduction system. It is the only known location where subduction zone products are presently being transported to the surface by serpentinite-mud volcanoes. A large serpentine mud "volcano" forms the South Chamorro Seamount and was successfully drilled by ODP during Leg 195. This returned mostly partially serpentinized harzburgites enclosed in serpentinite muds. In addition, limited numbers of small (1 mm–1 cm) fragments of rare blueschists were also discovered. U–Pb dating of zircon and rutile from one of these blueschist clasts give ages of 51.1 ± 1.2 Ma and 47.5 ± 2.0 Ma, respectively. These are interpreted to date prograde high-pressure metamorphism. Mineral equilibria modelling of the blueschist clast suggests the mineral assemblage formed at conditions of ~1.6 GPa and ~590 °C. We interpret that this high-pressure assemblage formed at a depth of ~50 km within the subduction channel and was subsequently exhumed and entrained into the South Chamorro serpentinite volcano system at depths of ~27 km. Consequently, we propose that the material erupted from the South Chamarro Seamount may be sampling far greater depths within the Mariana subduction system than previously thought. The apparent thermal gradient implied by the pressure–temperature modelling (~370 °C/GPa) is slightly warmer than that predicted by typical subduction channel numerical models and other blueschists worldwide. The age of the blueschist suggests it formed during the arc initiation stages of the proto-Izu-Bonin-Mariana arc, with the *P–T* conditions recording thermally elevated conditions during initial stages of western Pacific plate subduction. This indicates the blueschist had prolonged residence time in the stable forearc as the system underwent east-directed rollback. The Mariana blueschist shows that subduction products can remain entrained in subduction channels for many millions of years prior to exhumation.

1. Introduction

From ca. 50 Ma until present, the Western Pacific plate has been subducting under the Philippine Sea plate, forming the oceanic Izu-Bonin-Mariana (IBM) arc-basin system (Figure 1; Stern and Bloomer, 1992; Ishizuka et al., 2011, 2018). This

system provides an opportunity to study active processes within convergent intra-oceanic settings such as magmatism, seismicity, element recycling and hydrothermal transport. It is also the only known location on Earth where subduction zone products are actively transported to the surface by serpentinite-mud volcanoes (e.g. Fryer, 2012; Pabst et al., 2012). These serpentinite-mud volcanoes occur up to 90 km away from the trench axis in the forearc region (Figure 1; Fryer et al., 2006). In the southern Mariana segment, these volcanoes are interpreted to currently sample slab-generated fluids from a depth of up to 27 km (Fryer, 2012), offering a unique window into processes operating at shallow depths during subduction and in the mantle wedge above.

Previous studies on the variety of hard rock clasts "erupted" from these serpentinite-mud volcanoes have used them to infer the chemical and physical conditions of the subducting slab surface at shallow depths under the Mariana forearc (Savov et al., 2005; Fryer et al., 2006; Pabst et al., 2012). A major assumption from all previous studies is that the clasts and muds are derived from recently subducted products and hence are representative of the modern subduction system, however this assumption has never been tested. Additionally,

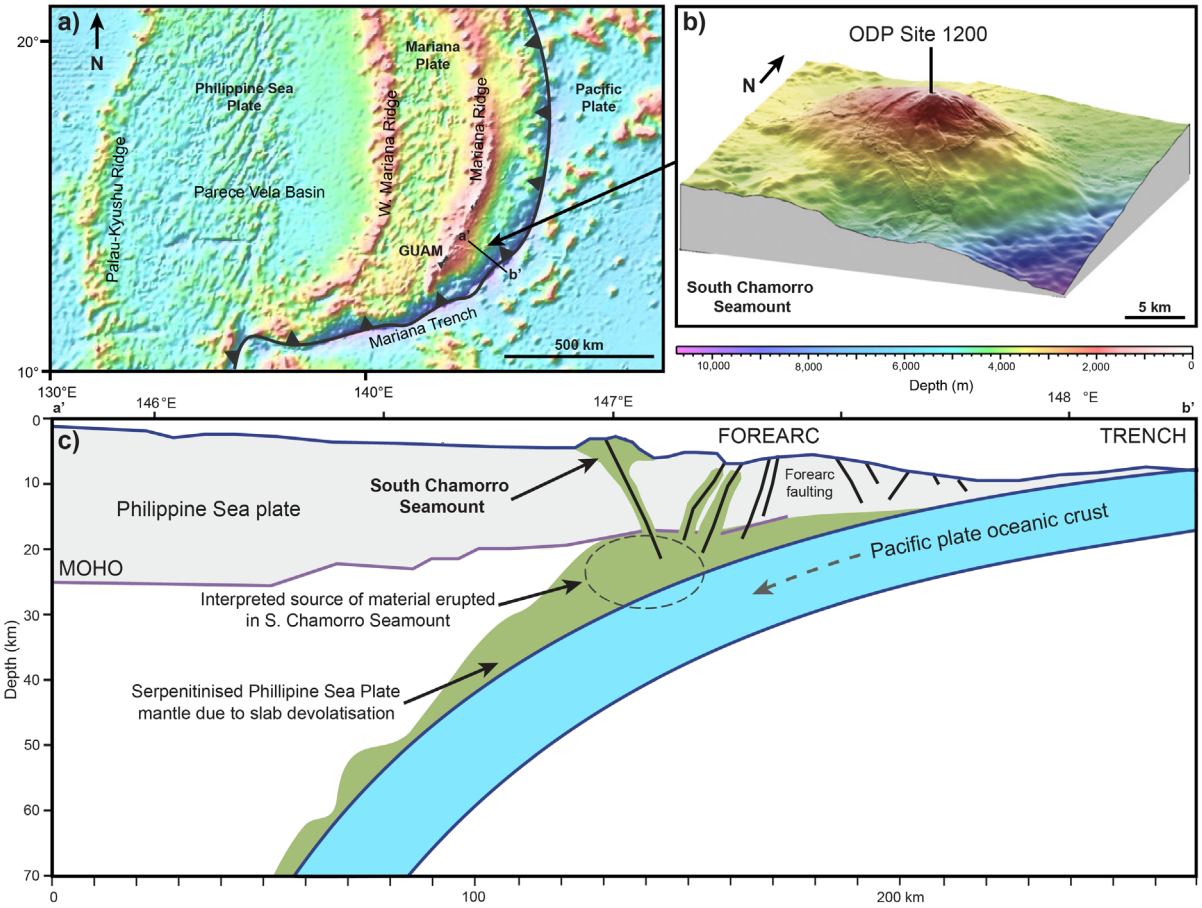


Figure 1. a) Bathymetric map of the Philippine Sea and Western Pacific, showing the major ridges, plates and trenches. Grey box indicates map b. b) Small scale bathymetric map of the Mariana forearc, indicating the locations of seamounts where blueschist chips have been recovered. Both after Fryer et al., (2002).

there has been no in-depth and detailed metamorphic work done on the clasts to constrain the metamorphic conditions of formation and therefore the depth they sample within the subduction system. A high-pressure origin for blueschist clasts from the Mariana serpentinite-mud volcanoes has been suggested before, but never quantified (Maekawa et al., 1993; Fryer et al., 2006; Yamamoto et al., 1995). Because these metamorphic clasts contain a wealth of information about the thermal conditions within the slab, as well as potentially providing avenues to determine the age of metamorphic recrystallization, they can provide unique insights into the residence times of material within subduction channels formed by ocean-ocean plate convergence.

This study is focused on one mafic clast (195-1200E-1H-3-4b), recovered from serpentinite mud drilled during ODP Leg 195 at Site 1200 at the summit of the active South Chamorro Seamount (Figure 1; see Pabst et al. (2012) for further description on this sample). Clasts recovered from the drilling were predominately serpentinite fragments, however rare blueschist-facies metamafic fragments were also recovered. While multiple clasts contained blueschist-facies mineral assemblages (including amphibole, chlorite, epidote and phengite), one rare sample contained rutile and zircon which could be targeted for geochronology. We derive constraints on the thermobarometric conditions recorded by this sample, and the age of metamorphism. The results provide insight into the depth of material return to the surface, and the subduction channel *P–T* conditions during the very beginning of Mariana subduction.

2. Background

2.2 Geology and geometry of the IBM system

The IBM system is generated by the westward directed subduction of the Pacific oceanic plate under the Philippine Sea, which initiated at ca. 51 Ma (Figure 1; Reagan et al., 2010; Ishizuka et al., 2018). The northern IBM trench segment (Izu-Bonin) shows an increasing dip of the Wadati-Benioff zone from ~40° in the north to ~80° in the south, with intermediate-depth seismicity occurring between depths of ~150 to ~300 km (Gvirtzman and Stern, 2004). In contrast, the southern IBM segment (Mariana) has a subvertical Wadati-Benioff zone, with deep (>300 km) seismic events (Gvirtzman and Stern, 2004). As such, the width of the subduction zone interface between the overriding and subducting plates increases along the IBM from north to south (Gvirtzman and Stern, 2004). While this only delineates the current subduction zone structure under the IBM, it is useful for interpretations of subduction channel dynamics which presently operate. Currently, the slab in the Mariana segment is in a state of roll-

back, as the Pacific and Philippine plates are both advancing westwards, with the latter at a slightly faster rate (Gvirtzman and Stern, 2004). Complex geometries involving slab tearing and steepening in the southern segment of the IBM have led to the extreme dip and hence depth of the trench in this area (Gvirtzman and Stern, 2004). The Mariana forearc is extensively faulted, due to oblique convergence as well as the curvature produced by back-arc extension, resulting in it being dominated by sinistral shear (Stern et al., 2003). This structural architecture is probably a crucial factor in allowing serpentinized mantle to exhume and rise to the surface, driving serpentinite-mud volcanism. The Mariana forearc is the only place on modern Earth where this occurs (Fryer et al., 1992, 1999, 2000, 2006; Fryer, 2012;).

The recent history of the IBM is well studied. However, the cause for subduction inception in the IBM is the source of much debate, due to lack of access to the earliest subduction-generated rocks (e.g. Arculus et al., 2015; 2016). However, the Jurassic oceanic crust to the east formed a west-dipping subduction zone under the Philippine Sea or Pacific crust. The timing of this is estimated to be ca. 51–47 Ma (Ishizuka et al, 2011, 2018). Ar–Ar whole rock ages for initial construction of the Mariana arc match those for the Izu-Bonin arc at ca. 49–47 Ma, while forearc basement from the IBM has been dated by Ar–Ar to have formed by at least ca. 47–45 Ma (Cosca et al., 1998). More recently, the basement of the IBM arc was dated by Ar–Ar geochronology at 48.7 ± 0.3 Ma (Ishizuka et al., 2018). This age is further supported by nano and microfossils in the overlying volcaniclastic sediments (Arculus et al., 2015). A ca. 51 Ma age is reported based on stratigraphic relationships for tholeiitic fore-arc basalts interpreted to be the first lavas to erupt when the Pacific plate initially sunk under the Philippine plate (Reagan et al., 2010; 2017). This has been further supported by a U–Pb zircon age of 51.1 ± 1.5 from gabbro underlying the fore-arc basalts (Ishizuka et al., 2011). Regardless of the exact timing of initiation, it seems that subduction initiation along the 2800 km IBM system occurred over 51–47 Ma (Stern et al., 2003; Arculus et al., 2015). The Kyushu-Palau Ridge (Figure 1) was active from ca. 48 Ma to ca. 25 Ma, and is the result of a stable magmatic arc during which the IBM subduction system was essentially immobile (Ishizuka et al., 2011). Spreading in the mid-southern Parece Vela Basin began after this (Figure 1a), and further spreading in the northern Izu-Bonin segment commenced at ca. 25 Ma with both terminating around 15 Ma due to collision of the northern IBM with Honshu (Stern et al., 2003). In the southern segment, eastwards rollback resulted in extension to form the Mariana Trough (~6 Ma back-arc basin), with the onset of seafloor spreading at ca. 3–4 Ma (Yamazaki and Stern, 1997). As such, the inception of the currently active Mariana Arc (Figure 1a; the West Mariana Ridge) is interpreted to be 3–4 Ma

old (Stern et al., 2003), and the remnant arc was left behind. Over this Eocene–Pleistocene evolution, the relative slab rollback to the east has resulted in two former oceanic arcs younging from the Palau-Kyushu Ridge (active from the onset of subduction to ca. 25 Ma), to the current Mariana Ridge (Figure 1a).

2.2 Previous studies of blueschists from the Mariana forearc drill sites

A series of active mud volcanoes occur on the upper plate between the arc (the Mariana Ridge) and the Mariana Trough (current trench; Figure 1a). The two most intensely studied active seamounts are the South Chamorro Seamount and the Conical Seamount, which occur 85 and 90 km from the trench respectively (Fryer et al., 1999; Savov et al., 2005). Deep sea drilling of these serpentinite seamounts (ODP Legs 125 and 195) returned predominantly serpentinized harzburgite and dunite clasts, but also rare metabasic blueschist clasts (~5% of clasts) in a matrix of fine serpentinite muds (Savov et al., 2004; Fryer and Salisbury, 2006; Fryer et al., 2006). These clasts have been divided into amphibole-talc-chlorite-schists, chlorite-epidote-schists, amphibole-chlorite-phengite-schists and mono-mineralic aggregates of talc or amphibole (Pabst et al., 2012).

A variety of metamafic clasts as well as matrix serpentinite muds have been studied to make inferences about the pressure–temperature (*P–T*) conditions within and below the Conical and South Chamorro seamounts. Blueschist clasts were discovered during drilling of the Conical Seamount in the northern Mariana forearc (east of Asuncion; Figure 1b) by Maekawa et al. (1993), who reported the first direct evidence for low temperature and relatively high-pressure metamorphism in a subduction zone. These blueschists were estimated to have formed at temperatures of 150–250 °C and pressures of 5–6 kbar (potentially corresponding to depths of 16–20 km), based on the presence of aragonite, the compositions of sodic pyroxenes and temperature dependence of inferred metamorphic reactions (Maekawa et al., 1993). Maekawa et al. (1995) also noted the existence of lawsonite-bearing blueschist clasts, and indicated that higher grade metamorphic rocks may be sourced from below the seamount. Numerous blueschist clasts were recovered from Conical Seamount drilled during ODP Leg 125. These were analysed for their whole rock geochemistry by Yamamato et al. (1995), who concluded the volcano was returning clasts derived from a MORB source.

Blueschist clasts drilled from the summit of the South Chamorro Seamount to the east of Guam were recovered only recently (Figure 1b; Shipboard Scientific Party, 2000). Due to similar jadeitic (Jd) compositions of their pyroxenes, Pabst et al. (2012) estimated that blueschists from the South Chamorro Seamount had reached similar

P–T conditions as those from Conical Seamount, studied by Maekawa et al. (1993; 1995). Further comparisons of the metamorphic mineral assemblages of the blueschists from South Chamorro Seamount with those of the Franciscan Complex have been used to infer conditions of 250–300 °C and 7 kbar for the late-stage blueschist facies assemblage (Pabst et al., 2012). Fryer et al. (2006) estimated conditions of ~250–300 °C and 4–5 kbar based on assumed equilibrium of epidote with magnesioriebeckite/barroisite from a different metabasite schist from South Chamorro Seamount. Higher grade conditions for metamorphic products have also been suggested by Murata et al. (2009) from the existence of antigorite in serpentinized peridotites. Antigorite coexisting with clinopyroxene and olivine indicates high-temperature serpentinization between ~450–550 °C, leading Murata et al., (2009) to suggest possible tectonic cycling of mantle wedge material. Additionally, temperatures and pressures of 350 °C and 8 kbar have been estimated for the source of serpentinite muds of the South Chamorro Seamount (Fryer et al., 2000), corresponding to depths of ~25–27 km. Fryer (1992) and Fryer et al. (2006) suggested that blueschists record higher grade conditions than those of the slab interface directly below the seamount, however no quantitative *P–T* estimates have been made. Geochemical and seismic studies, as well as earthquake locations on the subducting Pacific plate, have been used to suggest the mud volcanoes are sampling the slab interface at depth of 27–29 km (Oakley et al., 2008; Savov et al., 2005; Fryer et al., 2000). This is also generally supported by temperatures of ~200–300 °C estimated from chrysolite, lizardite and brucite-bearing serpentinized peridotites (D'Antonio and Kristensen, 2004). Fryer et al. (2006) suggested that MORB and OIB samples must have been derived from subducted oceanic plate buried to a depth of up to 30 km. This would suggest that the variety of clasts erupted from the South Chamorro Seamount and by inference other serpentinite volcanos in the Marianas forearc are being sampled from the slab interface beneath the volcano. While some of the geochemical signature of the fluid released from the South Chamorro Seamount appears to be originating from the currently subducting Pacific slab surface at a depth of ~27 km (Mottl et al., 2004), studies on the metamorphic conditions of the blueschist fragments span a range of *P–T* conditions.

In addition to the only limited constraints on the *P–T* conditions recorded by the metamorphic clasts, there is also lack of age data. While not overtly stated, existing studies on the mud hosted clasts assume they record modern conditions on the slab interface. However studies (Krebs et al., 2008; Lázaro et al., 2009; Blanco-Quintero et al., 2011) from high-pressure rocks in ancient serpentinite mélanges show that they may contain a range of metamorphic ages, indicating that material can reside within subduction zone channels

for potentially tens of millions of years.

3. Methods

The ~ 2×2 mm blueschist clast recovered from ODP Site 1200 was mounted in epoxy resin and polished. It was primarily mapped in BSE using a Quanta 600 SEM at Adelaide Microscopy, University of Adelaide, using Mineral Liberation Analysis software, to determine petrological relationships and mineral modal proportions in the clast.

Quantitative Electron probe microanalysis (EPMA) elemental mapping used a CAMECA SXFive equipped with 5 wavelength-dispersive spectrometers (WDS) and X-Ray detectors, running the PeakSite software. Beam conditions were set at an accelerating voltage of 15 kV and 100 nA, utilising a focussed beam. Compositional mapping was done at a 4 μm pixel resolution. Pixel dwell time in all maps was set to 40 ms. Calibration and quantitative data reduction of maps was carried out with the "Probe for EPMA" software, distributed by Probe Software Inc. Calibration was performed on certified natural and synthetic standards from Astimex Ltd and PandH Associates. The clast was mapped for 10 elements using their Kα lines, thus requiring two mapping passes on the five spectrometers (Pass 1: Ca, Na, P, Mg, Fe; Pass 2: Ti, Si, Al, Mn, K). Potentially mobile elements were analysed in the first pass. The average minimum detection limits (at the 99% confidence interval) in wt.% for the quantitative maps were: Ca (0.06), Na (0.12), Ti (0.07), Mg (0.08), Fe (0.17), K (0.06), Si (0.01), P (0.08), Al (0.08), Mn (0.16).

The X-ray maps were then used to identify the metamorphic mineral assemblages and mineral modal proportions were determined by pixel counting using image analysis software. Although the blueschist clast contains some coarse-grained minerals, is generally medium-grained. As such, these modal proportions are reasonably representative of the local equilibrium volume. The modal proportion and electron microprobe compositions of mineral assemblages was used to compute a bulk chemical composition for petrological modelling (Supplementary Data Table 1). We chose this approach to determine a bulk composition as the sample was considered too valuable to be consumed for conventional-style geochemical analysis. Ti-magnetite was omitted from the bulk rock chemistry calculations, based on textural evidence it is magmatic. Allanite and zircon were also omitted as they contain elements that cannot be modelled. Results of pixel counting and associated calculations to construct the bulk composition are shown in Supplementary Data Table 2.

Mineral equilibria forward modelling was undertaken using THERMOCALC v 3.4 in the NCFMASHTO system, using the internally consistent thermodynamic dataset 'ds55' (filename

tc-ds55.txt; November 2003 updated version of the Holland and Powell 1998 dataset) and activity–composition models in Diener et al. (2012) and references within. The calculated K and Mn concentrations in the calculated bulk rock composition are near zero, therefore K and Mn were excluded from the model system. Pumpellyite was not predicted in the modelling, possibly due to lack of a pumpellyite activity–composition model that allows solid solution. Calculations to test the sensitivity of modelled mineral equilibria to H_2O content using P–M_{H2O} models demonstrated the mineral assemblage, modal proportions and compositions recorded by the sample are stable over a large range of H_2O contents (from 9 mol% to more than 13 mol %, Supplementary Figure 1). As a specific value could not be pinpointed, and the sample evidently formed under water-rich conditions as indicated by abundant chlorite, amphibole and epidote, modelling was done with water in excess, i.e. defining H_2O as a saturating phase. Oxidation state (Fe_2O_3, or O in the bulk rock chemistry) was constrained from a P–M_O model (Supplementary Figure 2), where mineral modal proportions and compositions overlapped in the interpreted peak field at approximately M(O) = 0.55, or O = 1.97 mol%. This value directly overlaps with recalculated mineral microprobe chemical analyses used to calculate the bulk rock chemistry by assuming perfect mineral stoichiometry in the calculation of cations from the wt% oxide data (Droop, 1987; Leake et al., 1997). Contouring of the mineral equilibria models was calculated using the software TCInvestigator (Pearce et al., 2015). This produces contoured diagrams of normalised abundances (modes) of minerals, as well as mineral compositional contours, which can then be matched with measured EPMA data and calculated mineral modes of the sample to further constrain the pressure–temperature conditions experienced.

Secondary ionization mass spectrometry (SIMS) U-Pb geochronology was carried out using a CAMECA ims 1270 ion microprobe at the University of California of Los Angeles (Supplementary Data Table 3). In-situ analyses targeted zircon in the polished blueschist block using methods for analysis of small grains in their matrix as described in Schmitt et al. (2010). Rutile analyses were also performed in situ on the same mount, but due to the larger grain size of rutile compared to zircon, nearly full transmission was reached in the ion microprobe's field aperture. Instrumental set-up for rutile analysis is summarized in Schmitt and Zack (2012); all ages are reported relative to AS3 reference zircon (1099 Ma; Paces and Miller, 1993) and R10b reference rutile (1090 Ma; Luvizotto et al., 2009).

4. Results

4.1 Petrography

The blueschist clast (E1H3-4b) is dominated by an amphibole and chlorite-bearing matrix, with less

abundant epidote, rutile, titanite and allanite, and very rare pumpellyite, phengite and clinopyroxene (Figure 2). Amphibole is typically ~10–>200 µm in size and zoned (Figure 3; 4), with patchy magnesio-hornblende cores, surrounded by volumetrically dominant edenite/pargasite, and then a sharply-defined thin rim of magnesiokatophorite (Figure 5a, nomenclature follows Leake et al., 1997). This zonation can be seen in element maps (Figure 4a), with a marked increase in Na and Fe from core to rim, a decrease in Mg and Ca from core to rim, and high SiO_2 cores and rims and corresponding low alumina cores and rims. Small needle-like grains of actinolite also occur within the amphibole. Chlorite is commonly usually less than 50 µm, but rare grains are up to 300 µm in size. It is weakly zoned with thin rims that are comparatively poor in Fe and Al but rich in Si and Mg (Figure 3b, Figure 5b). It forms irregular grains intergrown with amphibole and epidote as well as narrow veins which cross-cut or occur along amphibole cleavage planes. Epidote occurs as smaller (occasionally up to ~250 µm) grains within amphibole or chlorite. It regularly overgrows texturally early allanite (Figure 2), and is unzoned, except for a thin rim of elevated Fe

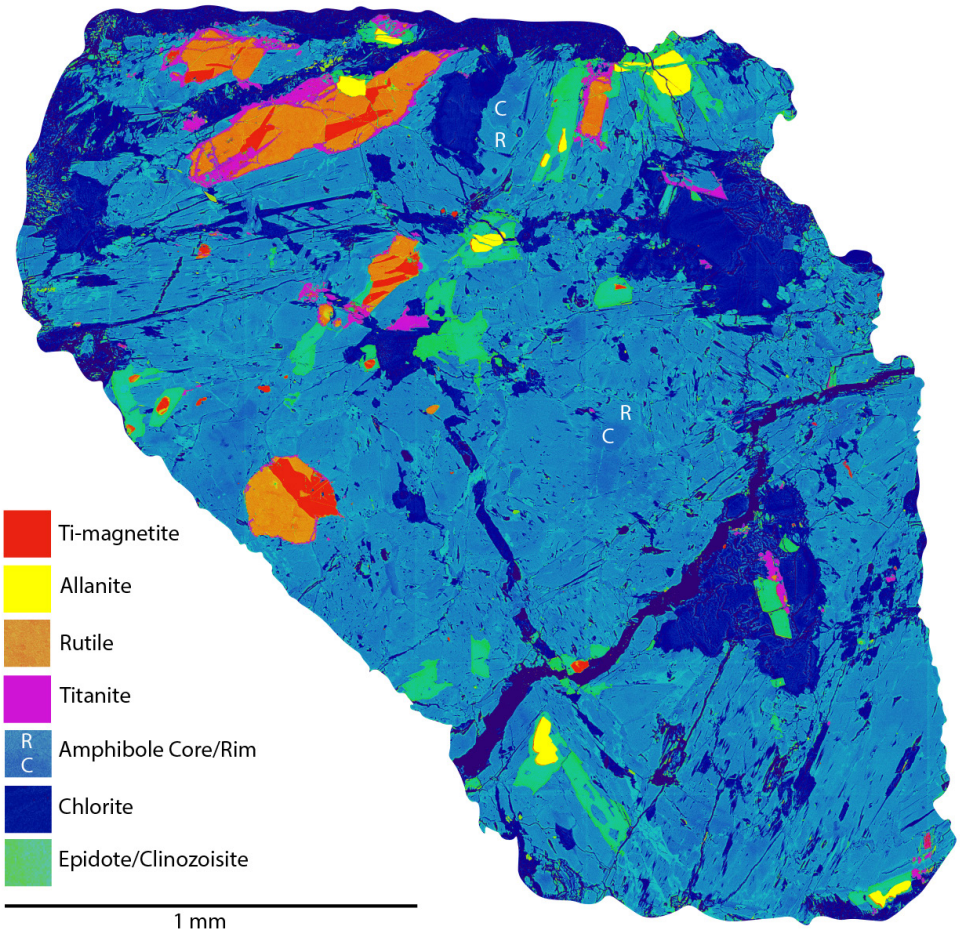


Figure 2: Mineralogical map of blueschist chip sample E1H3-4b, based on BSE imaging and X-ray derived elemental maps. C and R correspond to examples of amphibole cores and rims. Fine-grained minerals such as pumpellyite, clinopyroxene and zircon are not visible at this scale.

(Figure 5c, increase of ~1.65 wt% Fe_2O_3; Supplementary Data Table 1). Allanite is up to 80 μm in size and oscillatory zoned in rare earth elements (Figure 2), consistent with metamorphic allanite grown in the presence of fluid. Ti-magnetite (~10–100 μm) is overgrown by rims of rutile (up to ~100 μm across). Titanite forms discontinuous overgrowths on the rutile and Ti-magnetite which are up to 40 μm wide (Figure 2), and also occurs as euhedral crystals with amphibole and chlorite. Minor (<1%) fine-grained (5–20 μm) pumpellyite is associated with retrograde titanite and chlorite. Rare fine-grained clinopyroxene (<10 μm) occurs in the chlorite-amphibole matrix, and contains 7–26 mol% jadeite (Figure 5d, Pabst et al., 2012). Very fine-grained rare phengite occurs as needles in amphibole, and fine-grained zircon up to 10 μm also occurs in amphibole and epidote. The main mineral assemblages are: 1) early Na-rich amphibole core, chlorite, epidote, clinopyroxene and rutile, and 2) late Na-Fe rich amphibole rims, actinolite, titanite, and pumpellyite. Quartz is absent, and is typically absent from most blueschists from South Chamorro (Pabst et al., 2012).

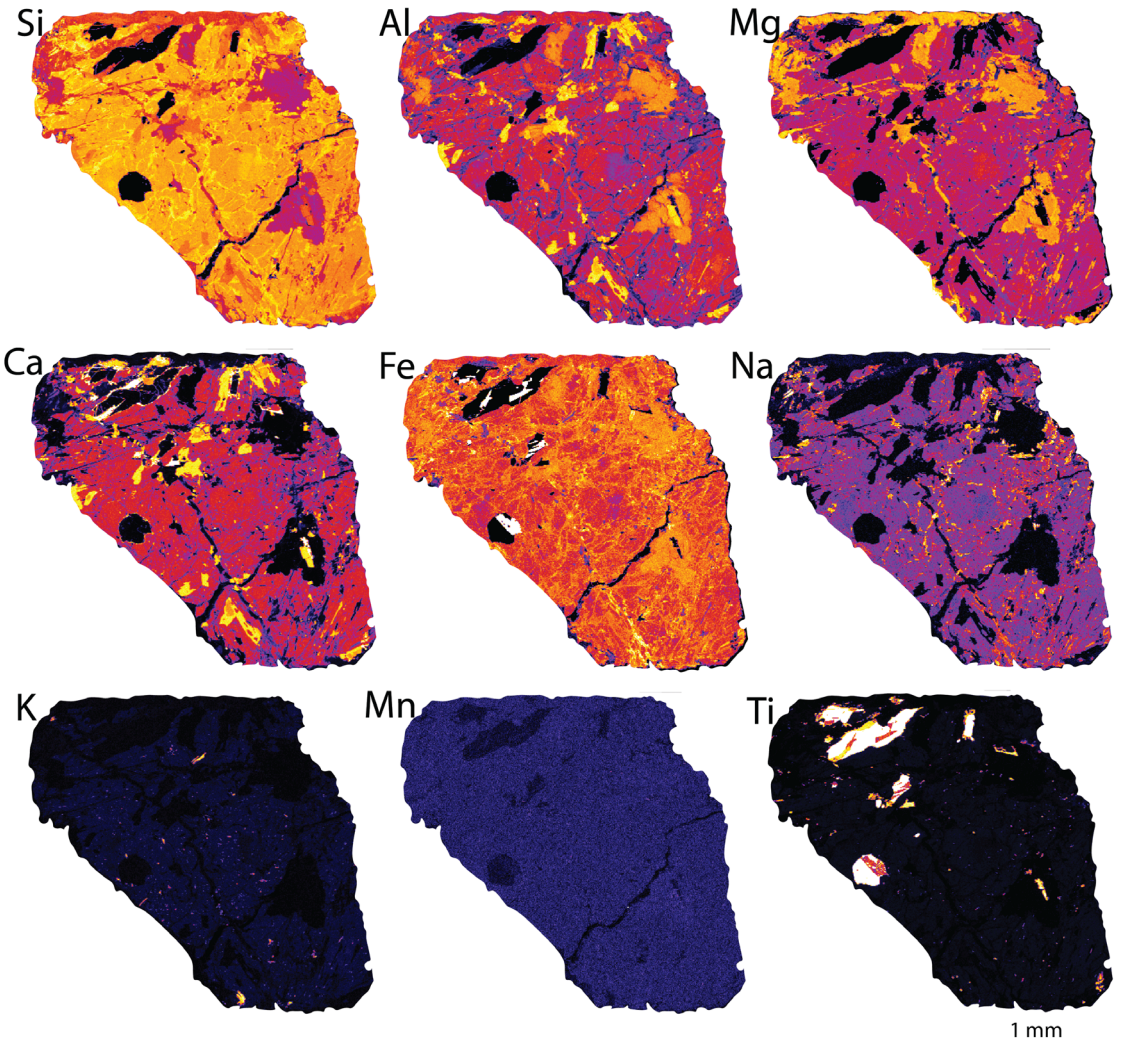


Figure 3: Electron microprobe X-ray element maps of blueschist chip E1H3-4b. Black and cooler colours indicate lower concentrations, whereas warmer colours indicates higher concentrations. The maps are not quantitative and the colours scales from different maps do not indicate the same numerical concentrations.

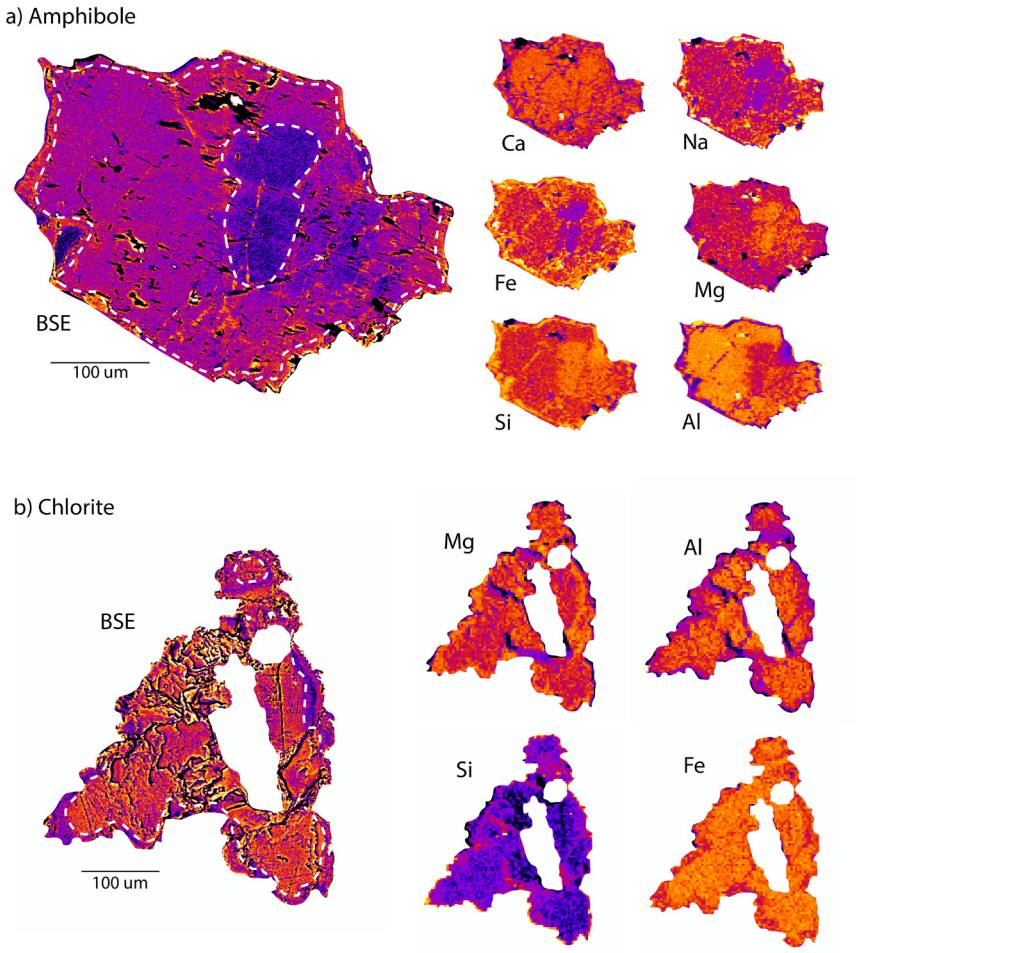


Figure 4: a) BSE and X-ray elemental maps of an amphibole grain from the blueschist clast. Dotted white lines indicate the boundary of the core, main grain volume and sharp rim. b) BSE and X-ray elemental maps of a chlorite grain that includes epidote (white core). Dotted line indicates thin outer rim. The maps are not quantitative and the colours scales from different maps do not indicate the same numerical concentrations.

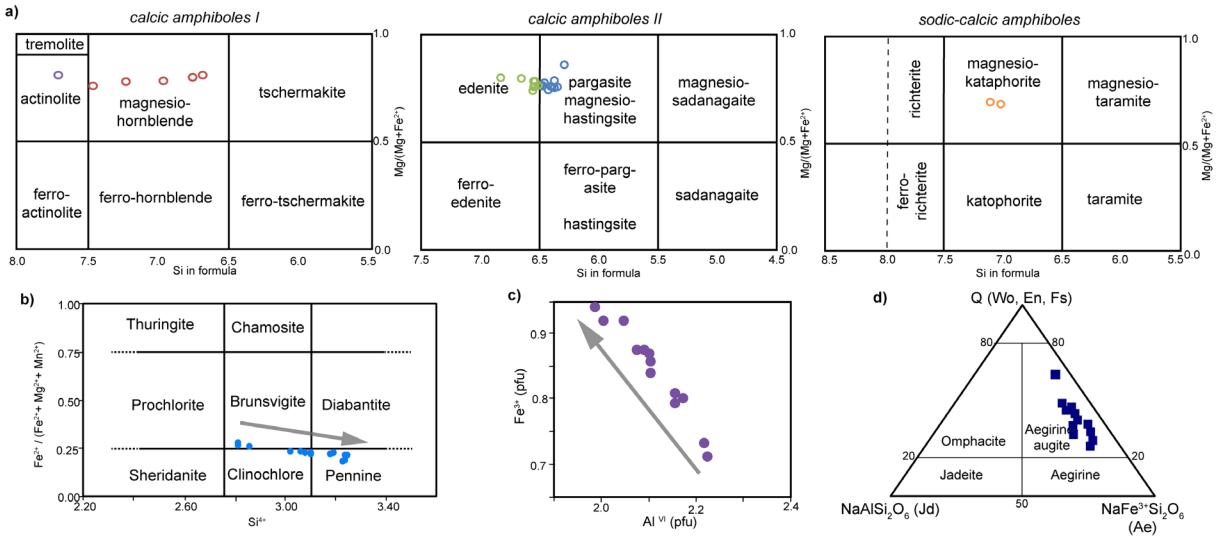


Figure 5: Mineral composition plots. a) Amphibole compositions. b) Chlorite compositions. c) Epidote compositions. d) Clinopyroxene compositions.

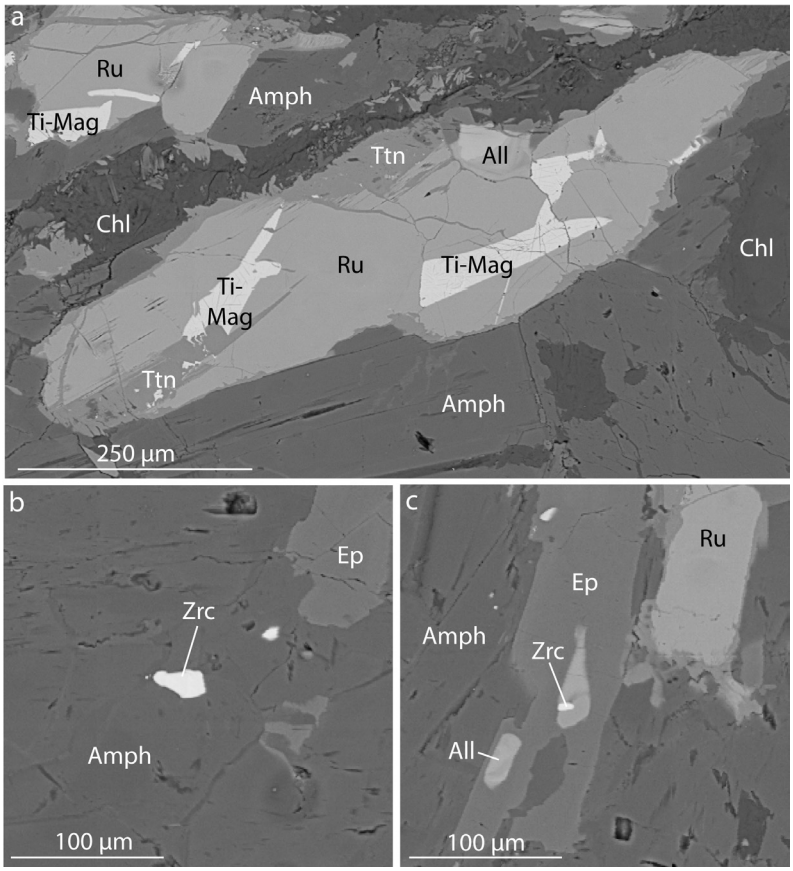


Figure 6: BSE images of locations of rutile and zircon targeted for U–Pb dating by Zack et al. (2013). a) Metamorphic rutile rimming Ti-magnetite, further rimmed by retrograde titanite. b) Zircon in the amphibole matrix. c) Zircon associated with metamorphic allanite/epidote. Ti-mag: Ti-magnetite, Ru: Rutile, Ttn: Titanite, Ep: Epidote, Chl: Chlorite, Amph: Amphibole, Zrc: Zircon, All: Allanite.

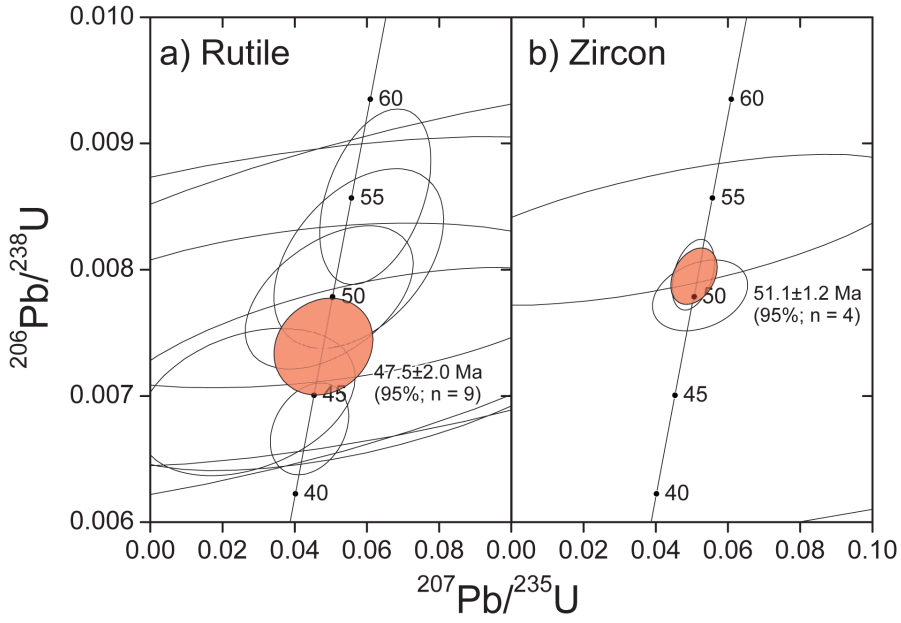


Figure 7: U–Pb Concordia for a) rutile and b) zircon analyses conducted on blueschist clast sample E1H3-4b. Individual error ellipses (open) and error-weighted averages (filled) are plotted at 95% confidence. Ages are calculated as concordia ages with probabilities of concordance of 0.98 (rutile) and 0.69 (zircon) using Isoplot v.4.15 (Ludwig, 2012).

4.2 Zircon and rutile geochronology

Textually resolved in-situ SIMS U–Pb geochronology (Figure 6) yields concordia ages of 47.5 ± 2.0 Ma (mean square of weighted deviates MSWD of concordance = 0.00052; n = 9) for rutile, and 51.1 ± 1.2 Ma (MSWD = 0.16; n = 4) for zircon (Figure 7; Supplementary Data Table 3). U abundances in rutile range between 11 and 30 ppm, and corresponding radiogenic ^{206}Pb yields are between 42 and 95%. U abundances in zircon range from ~180 to ~1300 ppm, with high radiogenic ^{206}Pb yields of >97% in favourable cases. Zirconium in rutile has on average 380 ppm, which corresponds in the presence of zircon and absence of quartz to a maximum temperature of 650 °C using the Tomkins et al. (2007) calibration at pressures 1.5 GPa derived from mineral equilibria modelling (see below).

4.3 Mineral equilibria modelling

A peak to retrograde P–T evolution can be inferred from the compositional isopleths of amphibole as well as the modal proportions of metamorphic minerals for the modelled mineral equilibria.

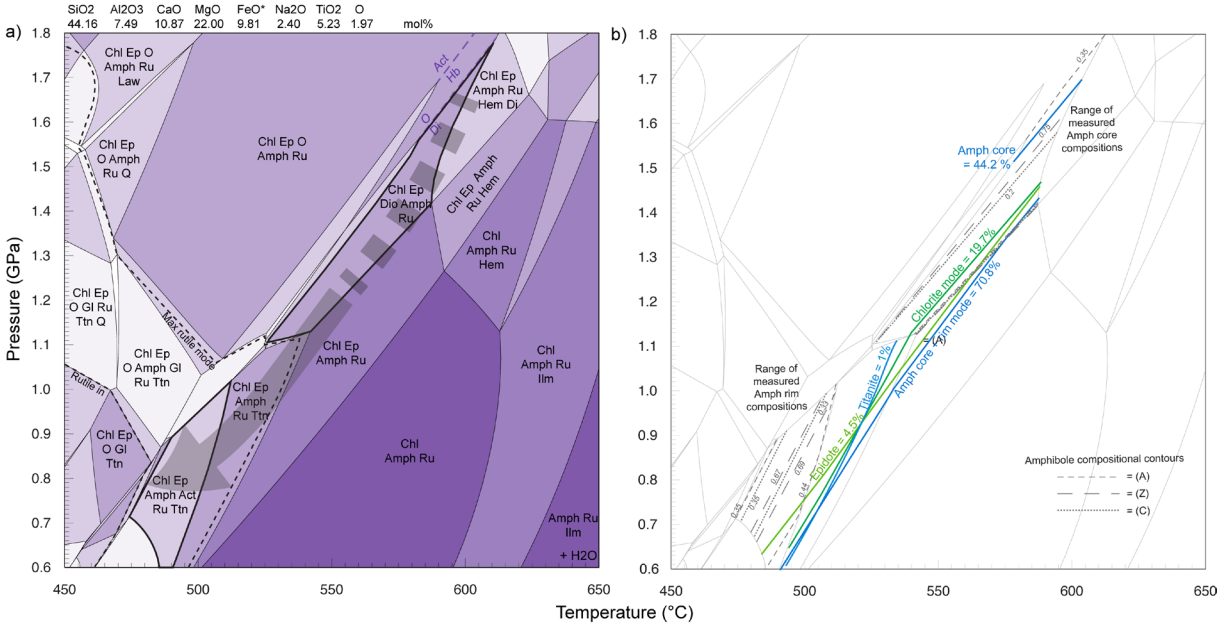


Figure 8: P–T mineral equilibria model for the blueschist chip, bulk composition used is in upper left corner in mol %. a) Mineral equilibria model with inferred P–T path as a grey arrow, dashed line represents unconstrained evolution. Fine black dotted line indicates rutile in and maximum rutile modes. Variance is coloured where v = 6 is the darkest shade and variance decreases as the shade lightens. Purple dashed lines indicate the locations of the omphacite-diopside and actinolite-hornblende solvi. b) Mineral equilibria model with EPMA measured ranges of amphibole compositions A (xNa on the A site), C (xCa on the M4 site) and Z (xNa on the M4 sites, where the minimum and maximum values for each measured composition are shown in grey dashed lines. Measured mineral modes (Supplementary Data Table 2) from the sample are shown as solid coloured lines. Chl: chlorite, Amph: Amphibole, O: Omphacite, Di: Diopside, Ep: Epidote, Ru: Rutile, Ttn: Titanite, Act: Actinolite, Gl: Glaucophane, Q: Quartz, Ilm: Ilmenite, Hem: Hematite, Law: Lawsonite, G: Garnet.

Compositions of amphibole cores are taken from EPMA analyses of magnesio-hornblende, magnesio-hastingsite and pargasite, and amphibole rim compositions from analyses of magnesio-katophorite (Figure 5; Supplementary Data Table 1; Pabst et al, 2012). Modal proportions of minerals are converted from volume % as measured by pixel counting, to one-oxide-normalized %, compliant with the modes computed by THERMOCALC (Supplementary Data Table 2; Figure 8). Uncertainties on the calculations in the mineral equilibria model are 2 sigma and are shown in Supplementary Figure 3. The peak assemblage consists of chlorite + amphibole + epidote + clinopyroxene (diopside) + rutile, and is bound by the disappearance of clinopyroxene and the addition of hematite to higher temperatures, and the solid-solution transition of diopside to omphacite (across the clinopyroxene solvus) at lower temperatures and higher pressures. The peak assemblage occurs over a large range of conditions, from 1.1 ± 0.07 GPa and 515 ± 9 °C to 1.8 ± 0.06 GPa and 600 ± 21 °C (Figure 8a). The retrograde evolution is characterized by the formation of titanite and calcic amphibole, evidenced by the presence of titanite coronas on rutile and small, late actinolite needles within amphibole. Clinopyroxene is interpreted to be relict from the peak assemblage, and therefore the retrograde path also involves the loss of clinopyroxene. The *P–T* path can be further constrained using amphibole compositional isopleths. Compositional parameters A (xNa on the A site), C (xCa on the M4 site) and Z (xNa on the M4 sites) were calculated from amphibole microprobe data and plotted on the mineral equilibria model (grey fields with dashed lines). Compositional isopleths of the amphibole cores plot over a wide range of pressures and temperatures, from 1.2–1.7 GPa and 540–600 °C, with average errors on each compositional range of ± 0.07 GPa and 12 °C (Figure 8b). Corresponding model proportions of the amphibole cores from 1.5–1.7 (± 0.06) GPa and 575–600 (± 12) °C (Figure 8b). Although not definitive, it is likely the compositions and modal proportions of the magnesio-hornblende cores point to a high-pressure history that predated the formation of the texturally dominant assemblage in the rock. Modal proportion isopleths of chlorite, total amphibole and epidote within the modelled peak field span from 1.1–1.45 GPa and 540–590 °C with average errors of 0.07 GPa and 10 °C, and also occur in retrograde *P–T* space with the addition of titanite (Figure 8b). The compositions of amphibole rims (magnesiokatophorite) plot within the field of the retrograde mineral assemblage from 0.7–0.9 GPa and 470–495 °C, with average errors of 0.06 GPa and 9 °C (Figure 8b).

4.4 Protolith constraints

The investigated sample has an unusual whole rock composition, with 44.2 mol% SiO2 and 22 mol% MgO (Supplementary Data Table 2). Technically it can be labelled a picrite, which is not typ-

ically observed in likely protoliths such as MORB, OIB or former arc basement. A more realistic scenario to explain the bulk rock composition is the formation of a hybrid rock composition derived from MORB with a metasomatic imprint from surrounding hydrated mantle, similar to that observed on Catalina Island (e.g. Bebout and Barton 2002; Pabst et al., 2012). The implication is that the investigated sample was not part of a coherent subducting slab at the time of zircon and rutile formation. Another likely protolith could be an already metasomatized and/or metamorphosed fragment, as have been reported from the Mariana forearc (Fryer et al., 2006; Pabst et al., 2012).

5. Discussion

Texturally, rutile in blueschist clast E1H3-4b forms part of a typical high-pressure metamorphic assemblage (Zack and Kooijman, 2017). Furthermore rutile is extremely rare as an igneous mineral in mafic rocks, and the chance that the erupted clast sampled a metamorphosed mafic rock with relic igneous rutile would appear negligible. Zircon is relatively common in mafic subvolcanic and plutonic rocks as a late-crystallizing igneous mineral, however in general it is not abundant in MORB. A magmatic zircon age from crystallisation of the subducting slab for the zircon can probably be dismissed as the age of oceanic crust being subducted into the IBM system is Jurassic (Stern et al., 2003). Moreover, the similarity in age to the rutile also strongly implies a metamorphic origin. Hence, the U–Pb ages from rutile and zircon are interpreted to record the high-pressure metamorphism.

Texturally, rutile rims early magmatic Ti-magnetite (Figure 6a). Regardless of the *P*–*T* path taken by the clast, rutile growth would have occurred on the prograde path (Figure 8), and continued to be stable to the peak conditions. To demonstrate this, black dashed lines on the mineral equilibria model indicate the stabilization of rutile (rutile in) and the maximum rutile mode reached (Figure 8a), after this mode line rutile abundance is unchanging as it does not continue to grow. As the closure temperature of U–Pb diffusion in rutile is estimated to be ca. 600–640 °C (Zack and Kooijman 2017), the age of ca. 47.5 Ma most likely represents the growth of rutile during prograde metamorphism.

The mechanism of metamorphic zircon formation in low-temperature metamorphic rocks is still not well understood. Zircon occurs in the clast as small (5–50 μm) euhedral grains within matrix amphibole and epidote/allanite (Figure 6b,c). Metamorphic zircon in blueschist-facies mafic rocks is thought to grow as a result of either dissolution-precipitation of inherited zircon, or release of zirconium through the breakdown of higher temperature minerals such as magmatic pyroxene (e.g. Rubatto and Hermann, 2007) and granulite-facies rutile (Zack and Kooijman 2017).

There is no evidence for relic inherited zircon or textural features suggesting dissolution-precipitation (Rubatto and Hermann, 2007; Rubatto et al., 2008). Possible mechanisms of zircon growth in the sample are the breakdown of Zr-bearing magmatic minerals which persisted to high pressures (Rubatto and Hermann, 2007). Breakdown of Ti-magnetite to form zircon (+ rutile + Fe-phase) on the prograde path would result in both minerals producing similar ages as they were formed in the same reaction. Alternatively, breakdown of magmatic clinopyroxene to amphibole also may release zirconium, and may have been the source during prograde metamorphism (Rubatto et al., 2008). While the exact prograde reaction that formed zircon is unclear, the closure temperature of U–Pb diffusion in zircon is estimated to be >900 °C (Cherniak and Watson, 2001). Therefore, the Eocene age is interpreted to record growth of zircon during metamorphism that occurred very soon after subduction initiation.

The mineral equilibria modelling results indicate a peak to retrograde evolution from ~ 1.6 GPa to 0.8 GPa. Although the exact *P–T* points are poorly constrained, the path is strongly supported by textural relationships within the sample, measured mineral modal proportions, and the compositions of zoned amphibole. It is possible to suggest a higher-pressure peak assemblage at approximately 1.6 ± 0.2 GPa and 585 ± 20 °C, followed by a retrograde evolution towards ~ 0.8 ± 0.15 GPa and 485 ± 30 °C. These conditions range in approximate apparent thermal gradients from ~ 370 °C/GPa at peak, and ~ 600 °C/GPa during the retrograde evolution, with an average of around 470 °C/GPa. These approximations could be within error of uncertainties within the mineral equilibria model (Supplementary Figure 1), and the geochronology from the clast only constrains the prograde part of this evolution. However, if it is not within error of the mineral equilibria model uncertainties, the change in thermal gradient may reflect changes in subducting slab geometry, as the slab becomes steeper at greater depth, resulting in lower thermal gradients at depth (Peacock, 2003; Syracuse et al, 2010; Penninston-Dorland et al., 2015). Alternatively, the change in thermal gradient could be due to the advection of heat within the rising serpentinite melange that carried the blueschist clast to comparatively shallow depths within the subduction channel (Gerya et al., 2002). These pressure-temperature conditions are in line with measured global subduction zone data (Figure 9a,b,c; Penniston-Dorland et al., 2015; Brown and Johnson, 2017; Agard et al., 2018). When compared to numerical models (Figure 9d; Gerya et al., 2002; Syracuse et al., 2010; van Keken et al., 2011; Ruh et al., 2018), the pressure-conditions are slightly above average, all though this may be due to the exclusion of shear heating as a model parameter (e.g. Kohn et al., 2018). Combined with the U–Pb rutile and zircon geochronology, the *P–T* data suggests the blueschist clast records ini-

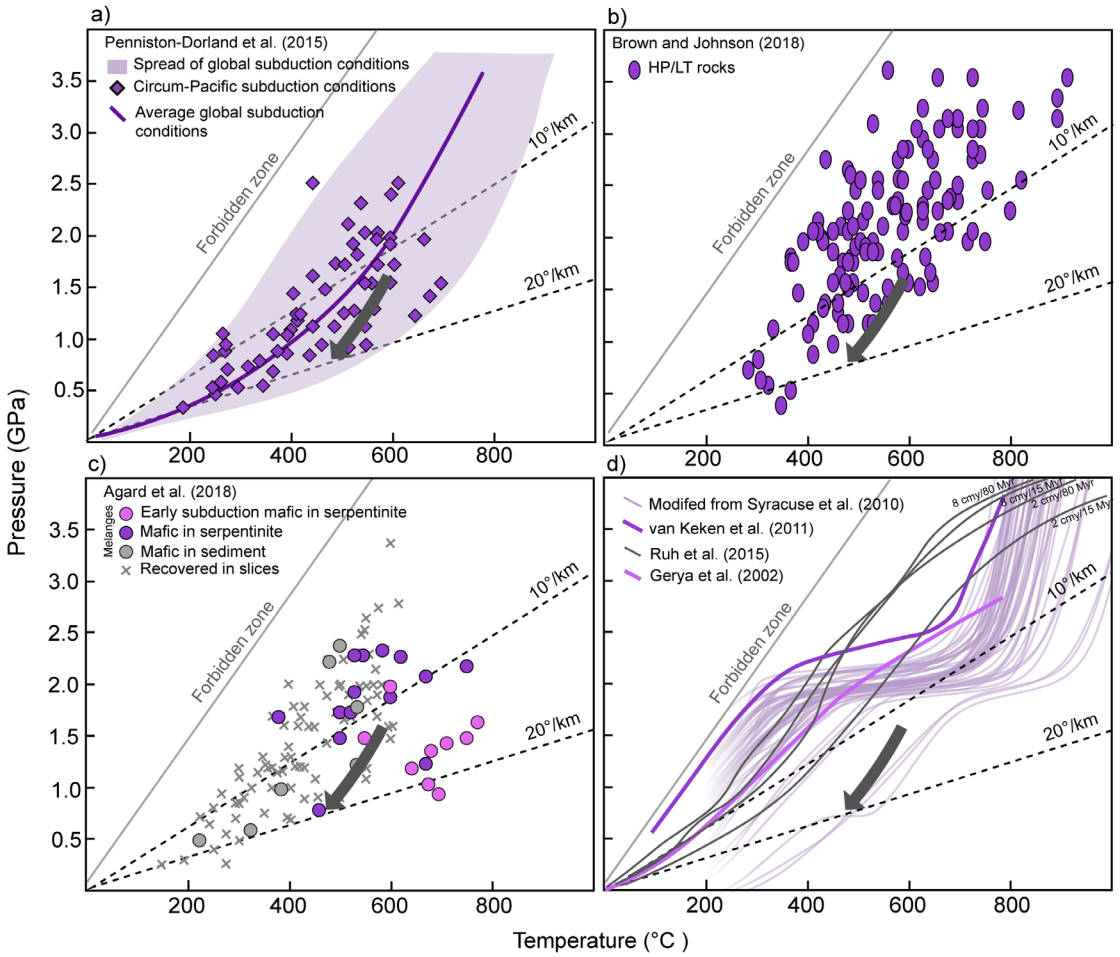


Figure 9: Pressure–temperature estimates from real subducted rocks and numerical models. Grey arrow indicates the P–T path of this study. a) Real rock dataset of Penniston-Dorland et al. (2015). b) Real rock dataset of Brown and Johnson (2018), including all low temperature-high pressure datasets. c) Real rock dataset of Agard et al. (2018), data from mélanges is indicated as circles. d) Prograde pressure-temperature paths taken from the top of subducting slabs from numerical models of Gerya et al. (2002), Syracuse et al. (2010), van Keken et al. (2011) and Ruh et al (2015).

tially warm conditions relative to numerical models during the early initiation of subduction of the Pacific plate (ca. 52 Ma; Ishizuka et al., 2011; 2018; Agard et al., 2018). During the early stages of subduction, conditions are generally warmer, as the plate subducts at a shallower angle, and the 'dragging down' of geotherms at the base of the overlying mantle wedge has not yet been significantly achieved (Gerya et al., 2002). This is in line with 'warm' pressure-temperature estimates from newly initiated subduction zones that have also been recorded by high-pressure mafic rocks (Figure 9c; Agard et al., 2018).

Forearc and rearc basalts mark the initiation of subduction in the Mariana system, and are immediately followed by forearc boninite magmatism from 48.2–45.1 Ma (Reagan et al., 2008; Ishuzuka et al., 2011; Arculus et al., 2015; Reagan et al., 2017). The eruption of these boninites necessitates the interaction of very depleted mantle wedge with slab-derived fluids at shallow depths during

subduction, and was coeval with blueschist metamorphism (this study). The similarity between the metamorphic ages obtained in this study and the age of boninitic magmatism, as well as the higher than usual thermal gradients recorded by the mineral assemblage, supports the existence of a hot mantle wedge above a warm subduction channel during early stages of subduction initiation in the Marianas.

If only lithostatic pressure is assumed, then the pressure estimates correspond to depths ranging from ~46 km to ~25 km. Therefore, it appears the retrograde *P–T* path essentially ends at conditions corresponding to the slab depth below the South Chamorro Seamount (~27 km; Pabst et al., 2012; Fryer et al., 2006). ODP Site 1200 is on the summit of the seamount (Figure 1b; Shipboard Scientific Party, 2000), and therefore it can be assumed that the drill core represents most recent mud extrusions from the serpentinite-mud volcano (Fryer et al., 2006). The oldest magmatic volcanism in the current Mariana arc (or Mariana ridge, Figure 1b) is interpreted to be ca. 3–4 Ma (Stern et al., 2003), and as such the position of the subduction zone and the maximum age of the serpentinite volcanoes is reasonably inferred as being similar. However, the rutile and zircon ages record metamorphism at ca. 50 Ma. This suggests that the clast was trapped somewhere within the subduction channel for at least ca. 46 Ma. The preservation of mineral assemblages that record 'warm' peak metamorphic conditions, as well as metamorphic rutile and zircon with Eocene ages, can be explained by either residence at peak depths for a significant portion of the metamorphic history of the clast, or that this clast was exhumed to shallower depths under the forearc and resided at cool conditions where recrystallization of minerals to lower pressure-temperature assemblages was not achieved. Unfortunately, there are no geochronologic constraints on when the blueschist was exhumed from depth to distinguish between these possibilities. The lack of retrograde recrystallisation may suggest that the small clast was protected from fluids and may have been armoured within a larger blueschist boudin or 'knocker', as commonly occur in high-pressure metamorphic and serpentinite mélanges such as the Franciscan Complex and Carribean (cf. Becker and Cloos, 1985; Lázaro et al., 2009; Blanco-Quintero et al., 2011). While the lack of geochronology on the retrograde history of the rock precludes definite explanation, it seems likely that the clast was exhumed to a shallow refrigerated region under the forearc in the Mariana subduction channel some time between ca 49 and 3 Ma, prior to its eruption in the mud volcano (Figure 10). However, the exact mechanism of this exhumation from ca. 50 km deep remains unknown. It could have occurred as return flow of the hydrated serpentinite mantle wedge cycled high-pressure material as the Mariana subduction system matured and steepened (Gerya et al., 2002). Alternatively, detachment

and slicing of oceanic crust within the subduction channel could have allowed partial exhumation of the blueschist-facies material (Ruh et al., 2015; Agard et al., 2018). Regardless, given that the clast is erupted in a serpentinite-mud volcano, serpentinite-driven buoyancy appears to have been an important part of the exhumation mechanism.

Implicit in the above scenario is that the blueschist must have formed during the early stages of subduction under the proto-IBM arc. A number of workers (e.g. Cosca et al., 1988; Reagan et al., 2008; 2010; Ishizuka et al., 2018), have argued that subduction initiated at around 51–47 Ma ago. High-pressure metamorphism at ca. 50 Ma supports the upper scale of those scenarios. The current location of the trench is ~ 1300 km to the east of the ridge (Figure 1a), as slab rollback has resulted in extension of the Philippine Sea Plate. This means that the forearc not only entrapped and preserved the blueschist clast, but it also survived at least partly intact in its ~1300 km long eastward journey transported by slab rollback. A similar scenario has been suggested for long-lived (>40 Ma) entrapment of high-pressure metamorphic rocks in serpentinite mélange in other oceanic subduction systems such as the Caribbean and the Franciscan Complex (Krebs et al., 2008; Lázaro et al., 2009; Blanco-Quintero et al., 2011).

The age and source region of the blueschist clast sampled from the South Chamorro seamount has implications for interpretations and future models regarding subduction zone conditions inferred

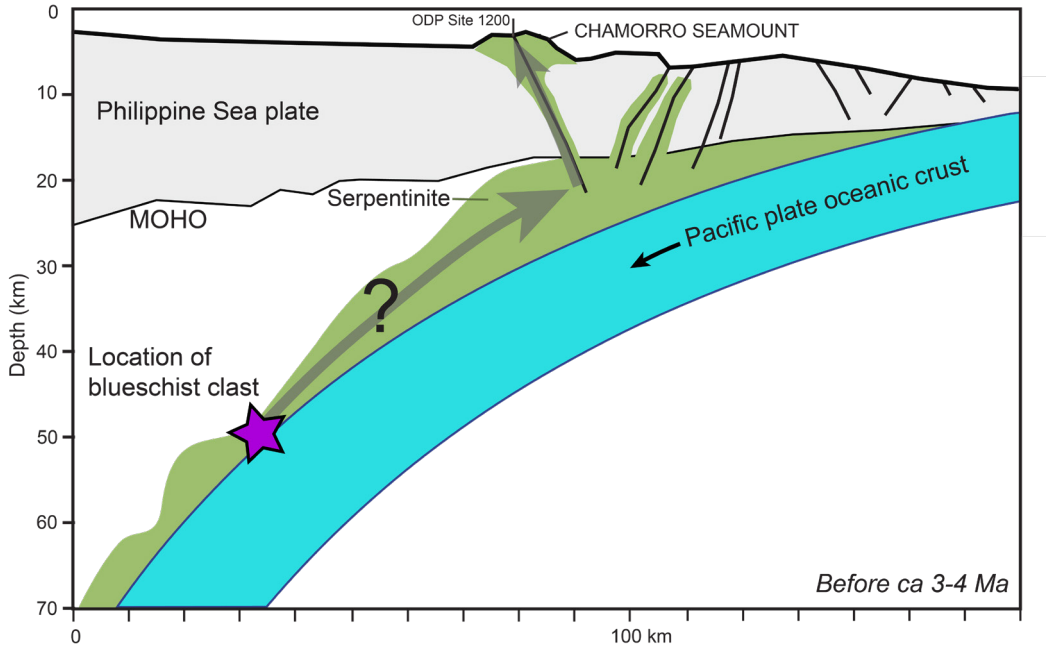


Figure 10: Schematic model for formation and exhumation of the blueschist chip. Structure of subduction zone after Fryer et al. (1999), Oakley et al. (2008) and Pabst et al. (2012). Schematic serpentinisation after Ruh et al (2015). Blueschist clast indicated as purple star. The mechanism of exhumation of the blueschist clast from ca. 50 km ca. 49 Ma ago to the shallow region under the forearc before the last 3 Ma is unknown.

from past studies on erupted clasts and muds from these seamounts. Some authors (Fryer et al., 1992; Savov et al., 2005; Fryer et al., 2006; Murato et al., 2009), have indicated that subduction products from serpentinite volcanoes may be sampled from greater depths than the slab immediately below the mud volcano and therefore have more complex source regions. However, they have been unable to quantify those depths. These authors have also assumed that the material exhumed in the mud volcanism was recently subducted. As such, the data has been used to describe ongoing Mariana trench subduction systematics, when in fact the subduction zone retains an integration of material from its inception until recently. The inferred depth from the modelled metamorphic assemblage in the blueschist clast indicates that the 'plumbing system' of the Marianas mud volcanoes is much more temporally and spatially complex than previously thought, meaning the metamorphic clasts in the IBM mud volcanoes capture a long history of the chemical and thermal evolution of the western Pacific slab. This temporally and spatially complex range of sources for material from the mud volcanoes means that caution should be exercised when interpreting data from clasts or muds erupted from seamounts in the Mariana forearc.

6. Conclusions

Detailed petrographic analyses and mineral equilibria forward modelling of a blueschist clast from the South Chamorro Seamount in the Mariana forearc indicates the mud volcano samples material from depths of ca. 50 km, which is well below the current depth of the slab directly below the volcano. The modelled *P–T* conditions (ca. 1.6 GPa and 590 °C) of the blueschist clast indicate the thermal regime was warmer than typical oceanic subduction, suggesting the modelled mineral assemblage formed in the initial stages of the IBM subduction system. This is consistent with concordant U–Pb ages of ca. 50 Ma from rutile and zircon within the blueschist assemblage, confirming the mineral assemblage formed soon after the Pacific plate began subducting under the Philippine Sea plate. Maturation of the subduction zone and formation of serpentinite within the subduction channel then facilitated return flow, driving exhumation of the blueschist clast to a refrigerated region under the forearc for at least ca. 46 Ma, before it was erupted in the South Chamorro mud volcano in the Mariana forearc. During this period of time there was ~1300 km of east-directed slab rollback, which transported the blueschist and other early subduction products with it. Therefore the South Chamorro Seamount, and by inference other volcanoes in the Mariana forearc, are probably sampling a temporally and spatially diverse range of lithologies and *P–T–t* histories that document the thermal evolution of the surface of the subducting plate over time. The data from the Mariana system suggests that potential serpentinite hosted

blueschist and eclogite blocks in ancient subduction product complexes (e.g. Franciscan and Caribbean) may hold extensive records of the thermal evolution of subducting slabs.

Acknowledgements

We would like to thank Ben Wade of Adelaide Microscopy for his assistance running element maps. We also thank E. Baxter and P. Agard for their thoughtful reviews, and M. Bickle for his editorial handling. This work was supported by ARC grant DP160104637 and DFG grant Za285/4. The ion microprobe facility at UCLA is partly supported by a grant from the Instrumentation and Facilities Program, Division of Earth Sciences, National Science Foundation.

References

Agard, P., Plunder, A., Angiboust, S., Bonnet, G., and Ruh, J. (2018). The subduction plate interface: Rock record and mechanical coupling (from long to short time scales). *Lithos*.

Arculus, R. J., Ishizuka, O., Bogus, K. A., Gurnis, M., Hickey-Vargas, R., Aljahdali, M. H., . . . Drab, L. (2015). A record of spontaneous subduction initiation in the Izu-Bonin-Mariana arc. *Nature Geoscience, 8*(9), 728-733.

Arculus, R. J., Ishizuka, O., Bogus, K. A., Gurnis, M., Hickey-Vargas, R., Aljahdali, M. H., . . . Drab, L. (2016). Reply to'Unclear causes for subduction'. *Nature Geoscience, 9*(5), 338.

Bebout, G. E., and Barton, M. D. (1993). Metasomatism during subduction: products and possible paths in the Catalina Schist, California. *Chemical Geology, 108*(1-4), 61-92.

Becker, D. G., and Cloos, M. (1985). Mélange diapirs into the Cambria Slab: A Franciscan trench slope basin near Cambria, California. *The Journal of Geology, 93*(2), 101-110.

Blanco-Quintero, I. F., García-Casco, A., and Gerya, T. V. (2011). Tectonic blocks in serpentinite mélange (eastern Cuba) reveal large-scale convective flow of the subduction channel. *Geology, 39*(1), 79-82.

Brown, M., and Johnson, T. (2018). Secular change in metamorphism and the onset of global plate tectonics. *American Mineralogist, 103*(2), 181-196.

Cherniak, D., and Watson, E. (2001). Pb diffusion in zircon. *Chemical Geology, 172*(1), 5-24.

Cosca, M., Arculus, R. J., Perace, J., and Mitchell, J. G. (1998). 40Ar/39Ar and K–Ar geochronological age constraints for the inception and early evolution of the Izu–Bonin–Mariana arc system. *Island Arc, 7*(3), 579-595.

D'antonio, M., and Kristensen, M. (2004). Serpen-

tine and brucite of ultramafic clasts from the South Chamorro Seamount (Ocean Drilling Program Leg 195, Site 1200): inferences for the serpentinization of the Mariana forearc mantle.

Diener, J., and Powell, R. (2012). Revised activity–composition models for clinopyroxene and amphibole. *Journal of metamorphic Geology, 30*(2), 131-142.

Droop, G. (1987). A general equation for estimating Fe3+ concentrations in ferromagnesian silicates and oxides from microprobe analyses, using stoichiometric criteria. *Mineralogical Magazine, 51*(361), 431-435.

Fryer, P. (2012). Serpentinite mud volcanism: observations, processes, and implications. *Annual review of marine science, 4*, 345-373.

Fryer, P., Gharib, J., Ross, K., Savov, I., and Mottl, M. (2006). Variability in serpentinite mudflow mechanisms and sources: ODP drilling results on Mariana forearc seamounts. *Geochemistry, Geophysics, Geosystems, 7*(8).

Fryer, P., Lockwood, J. P., Becker, N., Phipps, S., and Todd, C. S. (2000). Significance of serpentine mud volcanism in convergent margins. *Special Papers-Geological Society Of America*, 35-52.

Fryer, P., Pearce, J., and Stokking, L. (1992). *36. A synthesis of Leg 125 drilling of serpentine seamounts on the Mariana and Izu–Bonin forearcs.* Paper presented at the Proceedings of the Ocean Drilling Program, Scientific Results.

Fryer, P., and Salisbury, M. (2006). *Leg 195 synthesis: Site 1200-Serpentinite seamounts of the Izu-Bonin/Mariana convergent plate margin (ODP Leg 125 and 195 drilling results).* Paper presented at the Proc. ODP, Sci. Results.

Fryer, P., Wheat, C., and Mottl, M. (1999). Mariana blueschist mud volcanism: Implications for conditions within the subduction zone. *Geology, 27*(2), 103-106.

Gerya, T. V., Stöckhert, B., and Perchuk, A. L. (2002). Exhumation of high-pressure metamorphic rocks in a subduction channel: A numerical simulation. *Tectonics, 21*(6).

Gvirtzman, Z., and Stern, R. J. (2004). Bathymetry of Mariana trench-arc system and formation of the Challenger Deep as a consequence of weak plate coupling. *Tectonics, 23*(2).

Holland, T., and Powell, R. (1998). An internally consistent thermodynamic data set for phases of petrological interest. *Journal of metamorphic Geology, 16*(3), 309-343.

Ishizuka, O., Hickey-Vargas, R., Arculus, R. J., Yogodzinski, G. M., Savov, I. P., Kusano, Y., . . . Sudo, M. (2018). Age of Izu–Bonin–Mariana arc basement. *Earth and Plan-*

etary Science Letters, 481(Supplement C), 80-90. doi: https://doi.org/10.1016/j.epsl.2017.10.023

Ishizuka, O., Tani, K., Reagan, M. K., Kanayama, K., Umino, S., Harigane, Y., . . . Dunkley, D. J. (2011). The timescales of subduction initiation and subsequent evolution of an oceanic island arc. *Earth and Planetary Science Letters, 306*(3), 229-240.

Kohn, M. J., Castro, A. E., Kerswell, B. C., Ranero, C. R., & Spear, F. S. (2018). Shear heating reconciles thermal models with the metamorphic rock record of subduction. *Proceedings of the National Academy of Sciences*, 115(46), 11706-11711.

Krebs, M., Maresch, W., Schertl, H.-P., Münker, C., Baumann, A., Draper, G., . . . Trapp, E. (2008). The dynamics of intra-oceanic subduction zones: a direct comparison between fossil petrological evidence (Rio San Juan Complex, Dominican Republic) and numerical simulation. *Lithos, 103*(1), 106-137.

Lázaro, C., García-Casco, A., Rojas Agramonte, Y., Kröner, A., Neubauer, F., and ITURRALDE-VINENT, M. (2009). Fifty-five-million-year history of oceanic subduction and exhumation at the northern edge of the Caribbean plate (Sierra del Convento mélange, Cuba). *Journal of metamorphic Geology, 27*(1), 19-40.

Leake, B. E., Woolley, A. R., Arps, C. E., Birch, W. D., Gilbert, M. C., Grice, J. D., . . . Krivovichev, V. G. (1997). Report. Nomenclature of amphiboles: report of the subcommittee on amphiboles of the international mineralogical association commission on new minerals and mineral names. *Mineralogical Magazine, 61*(2), 295-321.

Ludwig, K. (2003). User's manual for Isoplot 3.00: a geochronological toolkit for Microsoft Excel: Kenneth R. Ludwig.

Luvizotto, G., Zack, T., Meyer, H., Ludwig, T., Triebold, S., Kronz, A., . . . Klemme, S. (2009). Rutile crystals as potential trace element and isotope mineral standards for microanalysis. *Chemical Geology, 261*(3-4), 346-369.

Maekawa, H., Fryer, P., and Ozaki, A. (1995). Incipient Blueschist-Facies Metamorphism in the Active Subduction Zone Beneath the Mariana Forearc. *Active margins and marginal Basins of the Western pacific*, 281-289.

Maekawa, H., Shozul, M., Ishll, T., Fryer, P., and Pearce, J. A. (1993). Blueschist metamorphism in an active subduction zone. *Nature, 364*(6437), 520-523.

Mottl, M. J., Wheat, C. G., Fryer, P., Gharib, J., and Martin, J. B. (2004). Chemistry of springs across the Mariana forearc shows progressive devolatilization of the subducting plate. *Geochimica et Cosmochimica Acta, 68*(23), 4915-4933.

Murata, K., Maekawa, H., Yokose, H., Yamamoto, K., Fujioka, K., Ishii, T., . . . Wada, Y. (2009). Significance of serpentinization of wedge mantle peridotites beneath Mariana forearc, western Pacific. *Geosphere, 5*(2), 90-104.

Oakley, A., Taylor, B., and Moore, G. (2008). Pacific Plate subduction beneath the central Mariana and Izu-Bonin fore arcs: New insights from an old margin. *Geochemistry, Geophysics, Geosystems, 9*(6).

Pabst, S., Zack, T., Savov, I. P., Ludwig, T., Rost, D., Tonarini, S., and Vicenzi, E. P. (2012). The fate of subducted oceanic slabs in the shallow mantle: insights from boron isotopes and light element composition of metasomatized blueschists from the Mariana forearc. *Lithos, 132*, 162-179.

Paces, J. B., and Miller, J. D. (1993). Precise U-Pb ages of Duluth complex and related mafic intrusions, northeastern Minnesota: Geochronological insights to physical, petrogenetic, paleomagnetic, and tectonomagmatic processes associated with the 1.1 Ga midcontinent rift system. *Journal of Geophysical Research: Solid Earth, 98*(B8), 13997-14013.

Peacock, S. M. (2003). Thermal structure and metamorphic evolution of subducting slabs. *Inside the subduction factory*, 7-22.

Pearce, M., White, A., and Gazley, M. (2015). TC-Investigator: automated calculation of mineral mode and composition contours for thermocalc pseudosections. *Journal of metamorphic Geology, 33*(4), 413-425.

Penniston-Dorland, S. C., Kohn, M. J., and Manning, C. E. (2015). The global range of subduction zone thermal structures from exhumed blueschists and eclogites: Rocks are hotter than models. *Earth and Planetary Science Letters, 428*, 243-254.

Reagan, M. K., Hanan, B. B., Heizler, M. T., Hartman, B. S., and Hickey-Vargas, R. (2008). Petrogenesis of volcanic rocks from Saipan and Rota, Mariana Islands, and implications for the evolution of nascent island arcs. *Journal of Petrology, 49*(3), 441-464.

Reagan, M. K., Ishizuka, O., Stern, R. J., Kelley, K. A., Ohara, Y., Blichert-Toft, J., . . . Hanan, B. B. (2010). Fore-arc basalts and subduction initiation in the Izu-Bonin-Mariana system. *Geochemistry, Geophysics, Geosystems, 11*(3).

Reagan, M. K., Pearce, J. A., Petronotis, K., Almeev, R. R., Avery, A. J., Carvallo, C., . . . Godard, M. (2017). Subduction initiation and ophiolite crust: new insights from IODP drilling. *International Geology Review, 59*(11), 1439-1450.

Rubatto, D., and Hermann, J. r. (2007). Zircon behaviour in deeply subducted rocks. *Elements, 3*(1), 31-35.

Rubatto, D., Müntener, O., Barnhoorn, A., and

Gregory, C. (2008). Dissolution-reprecipitation of zircon at low-temperature, high-pressure conditions (Lanzo Massif, Italy). *American Mineralogist, 93*(10), 1519-1529.

Ruh, J. B., Le Pourhiet, L., Agard, P., Burov, E., and Gerya, T. (2015). Tectonic slicing of subducting oceanic crust along plate interfaces: Numerical modeling. *Geochemistry, Geophysics, Geosystems, 16*(10), 3505-3531.

Savov, I., Tonarini, S., Ryan, J., and Mottl, M. (2004). *Boron isotope geochemistry of serpentinites and porefluids from Leg 195, Site 1200, S. Chamorro Seamount, Mariana forearc region.* Paper presented at the International Geological Congress (IGC), Florence, Italy.

Savov, I. P., Ryan, J. G., D'Antonio, M., Kelley, K., and Mattie, P. (2005). Geochemistry of serpentinized peridotites from the Mariana Forearc Conical Seamount, ODP Leg 125: Implications for the elemental recycling at subduction zones. *Geochemistry, Geophysics, Geosystems, 6*(4).

Schmitt, A. K., Stockli, D. F., Lindsay, J. M., Robertson, R., Lovera, O. M., and Kislitsyn, R. (2010). Episodic growth and homogenization of plutonic roots in arc volcanoes from combined U–Th and (U–Th)/He zircon dating. *Earth and Planetary Science Letters, 295*(1-2), 91-103.

Schmitt, A. K., and Zack, T. (2012). High-sensitivity U–Pb rutile dating by secondary ion mass spectrometry (SIMS) with an O2+ primary beam. *Chemical Geology, 332*, 65-73.

Stern, R. J., and Bloomer, S. H. (1992). Subduction zone infancy: examples from the Eocene Izu-Bonin-Mariana and Jurassic California arcs. *Geological Society of America Bulletin, 104*(12), 1621-1636.

Stern, R. J., Fouch, M. J., and Klemperer, S. L. (2003). An overview of the Izu-Bonin-Mariana subduction factory. *Inside the subduction factory*, 175-222.

Syracuse, E. M., van Keken, P. E., and Abers, G. A. (2010). The global range of subduction zone thermal models. *Physics of the Earth and Planetary Interiors, 183*(1-2), 73-90.

Tomkins, H., Powell, R., and Ellis, D. (2007). The pressure dependence of the zirconium-in-rutile thermometer. *Journal of metamorphic Geology, 25*(6), 703-713.

van Keken, P. E., Hacker, B. R., Syracuse, E. M., and Abers, G. A. (2011). Subduction factory: 4. Depth-dependent flux of H2O from subducting slabs worldwide. *Journal of Geophysical Research: Solid Earth, 116*(B1).

Yamamoto, K., Asahara, Y., Maekawa, H., and Sugitani, K. (1995). Origin of blueschist-facies clasts in the Mariana forearc, Western Pacific. *Geochemical Journal, 29*(4), 259-

275.

Yamazaki, T., and Stern, R. J. (1997). Topography and magnetic vector anomalies in the Mariana Trough. *JAMSTEC J. Deep Sea Res, 13*, 31-45.

Zack, T., and Kooijman, E. (2017). Petrology and geochronology of rutile. *Reviews in mineralogy and geochemistry, 83*(1), 443-467.

Chapter 3:

Subduction and accumulation of lawsonite eclogite and garnet blueschist in eastern Australia

This chapter is published as:

Subduction and accumulation of lawsonite eclogite and garnet blueschist in eastern Australia (2020). R. Tamblyn, M. Hand, D. Kelsey, R. Anczkiewicz, D. Och. *Journal of Metamorphic Geology*, 38(2), 157-182.

The supplementary materials for this chapter can be found in Appendix 3

Statement of Authorship

Title of Paper	Subduction and accumulation of lawsonite eclogite and garnet blueschist in eastern Australia.
Publication Status	[x] Published [ ] Accepted for Publication [ ] Submitted for Publication [ ] Unpublished and Unsubmitted w ork w ritten in manuscript style
Publication Details	Tamblyn, R., Hand, M., Kelsey, D., Anczkiewicz, R., & Och, D. (2020). Subduction and accumulation of lawsonite eclogite and garnet blueschist in eastern Australia. Journal of Metamorphic Geology, 38(2), 157-182.

Principal Author

Name of Principal Author (Candidate)	Renee Tamblyn		
Contribution to the Paper	Collected zircon U-Pb data Completed mineral separation Completed mineral equilibria modelling Collected mineral chemical data Wrote the manuscript		
Overall percentage (%)	75		
Certification:	This paper reports on original research I conducted during the period of my Higher Degree by Research candidature and is not subject to any obligations or contractual agreements with a third party that would constrain its inclusion in this thesis. I am the primary author of this paper.		
Signature		Date	04/03/2021

Co-Author Contributions

By signing the Statement of Authorship, each author certifies that:

i. the candidate's stated contribution to the publication is accurate (as detailed above);

ii. permission is granted for the candidate in include the publication in the thesis; and

iii. the sum of all co-author contributions is equal to 100% less the candidate's stated contribution.

Name of Co-Author	Martin Hand		
Contribution to the Paper	Interpretations of data, reviewed the manuscript 10%		
Signature		Date	03/03/2021

Name of Co-Author	David Kelsey		
Contribution to the Paper	Interpretations of data, assisted with mineral equilibria modelling, reviewed the manuscript 5%		
Signature		Date	17/02/2021

Please cut and paste additional co-author panels here as required.

Name of Co-Author	Robert Anczkiewicz
Contribution to the Paper	Collected Lu-Hf and Sm-Nd data 5%
Signature	Date 04/12/2020

Name of Co-Author	David Och
Contribution to the Paper	Introduced us to the study location, reviewed the manuscript 5%
Signature	Date 16/02/2021

Highlights

- Lawsonite eclogite and garnet blueschist were subducted seperately.
- Both record different *P–T–t* evolutions.
- HP–LT rocks were accumulated in mélange and transported approximately 1000 km east by slab rollback .

Abstract

Lawsonite eclogite and garnet blueschist occur as metre-scale blocks within serpentinite mélange in the southern New England Orogen in eastern Australia. These high-pressure fragments are the products of early Palaeozoic subduction of the palaeo-Pacific plate beneath East Gondwana. Lu–Hf, Sm–Nd and U–Pb geochronological data from Port Macquarie shows that eclogite mineral assemblages formed between ca. 500–470 Ma ago and became mixed together within a serpentinite-filled subduction channel. Age data and *P–T* modelling indicates lawsonite eclogite formed at around 2.7 GPa and 590 °C at ca. 490 Ma, whereas peak garnet in blueschist formed at around 2.0 GPa and 550 °C at ca. 470 Ma. The post-peak evolution of lawsonite eclogite was associated with preservation of pristine lawsonite-bearing assemblages and the formation of glaucophane. In contrast, the garnet blueschist was derived from a precursor garnet-omphacite assemblage. The geochronological data from these different aged high-pressure assemblages indicates the high-pressure rocks were formed during subduction on the margin of cratonic Australia during the Cambro-Ordovician. The rocks however now reside in the Devonian-Carboniferous southern New England Orogen, which forms the youngest and most outboard of the eastern Gondwanan Australian orogenic belts. Geodynamic modelling suggests that over the time scales that subduction products accumulated, the high-pressure rocks migrated large distances (ca. > 1000km) during slab retreat. Consequently, high-pressure rocks that are trapped in subduction channels may also migrate large distances prior to exhumation, potentially becoming incorporated into younger orogenic belts whose evolution is not directly related to the formation of the exhumed high-pressure rocks.

1. Introduction

High-pressure rocks which preserve eclogite and blueschist facies mineral assemblages are important recorders of subduction. Pressure–temperature–time (*P–T–t*) histories from high-pressure low-temperature rocks document the timing and physical conditions of subduction, as well as the potential durations that material resides within subduction channels prior to exhumation. These *P–T–t* histories provide important companionship to numerical models (e.g. Gerya et al., 2002; Stöckhert and Gerya, 2005; Peacock, 2003; Ruh et al.,, 2015) that seek to explain the burial and exhu-

mation of material entrained within subduction channels.

High-pressure mélanges, which often contain eclogite and blueschist facies blocks encased within serpentinite and/or weakly metamorphosed sediments, are generally interpreted to reflect the subduction and subsequent mixing of lithologies within oceanic subduction channels (Bebout and Barton, 2002; Federico et al., 2007). High-precision geochronology and well-constrained pressure-temperature estimates are beginning to reveal the complex histories contained within these mélanges (e.g. Wakabayashi and Dumitru, 2007; Krebs et al., 2008; Krebs et al., 2011). A recurring finding is that subducted oceanic rocks now found mixed in mélange can record different *P*–*T*–*t* histories, implying they experienced different evolutions within the subduction channel before becoming exhumed together (Federico et al., 2007; Krebs et al., 2008; Porteau et al., 2019). These samples can also record long-lived metamorphism within oceanic subduction channels, often coupled with generally slow exhumation rates (Guillot et al., 2009; Agard et al., 2009; Lázaro et al., 2009; Angiboust et al., 2016; Tamblyn et al., 2019). In order to preserve deeply buried, long-lived, refrigerated mineral assemblages, these oceanic-derived high-pressure rocks must reside for extended timescales within the subduction channel (Gerya et al., 2002). Numerical models show that subduction systems are unlikely to stay stationary for the apparent durations of cooling that have been recorded from high-pressure rocks (e.g. Baitsch-Ghiradello et al., 2014; Moresi et al., 2014). Logically, in order to continually exist in a low-temperature metamorphic environment, slowly exhuming material within the subduction channel must migrate with the trench. For the high-pressure exhumation durations implied by geochronology from the Caribbean (ca. 55 m.y.; Krebs et al., 2008; Lázaro et al., 2009) and Zagros (ca. 30 m.y.; Angiboust et al., 2016), trench migrations in excess of 1000 km appear realistic (Gerya, 2011; Baitsch-Ghiradello et al., 2014).

Arguably the thermobarometrically most sensitive high-pressure mineral assemblages that record low-temperature exhumation conditions are lawsonite-bearing eclogites, whose preservation appears to require cold, hydrous conditions be maintained during exhumation. Globally such assemblages are rare (Tsujimori and Ernst, 2014), despite the range of bulk compositions that should be able to stabilize lawsonite-garnet-omphacite bearing assemblages (Wei and Clarke, 2011). Well-preserved lawsonite strongly supports the concept that subducted oceanic material is exhumed via active subduction channels (Tsujimori and Ernst, 2014).

Lawsonite eclogite and garnet blueschist occur within serpentinite mélange in the Southern New England Orogen (SNEO) in eastern Australia. The

SNEO is the youngest of three orogenic belts that formed on the margin of East Gondwana during the early to late Palaeozoic (Figure 1; Kemp et al., 2009; Glen, 2013; Rawlinson et al., 2014; Phillips et al., 2015). In this paper we present garnet Lu–Hf, Sm–Nd and zircon U–Pb data coupled with calculated phase equilibria forward models that constrain the timing of high-pressure metamorphism, as well as physical conditions of metamorphism. The results indicate early Palaeozoic lawsonite eclogite was subducted and tectonically mixed with younger high-pressure rocks within serpentinite-filled subduction channel.

2. Geological setting

The Tasmanides of eastern Australia consist of the Delamerian (515–490 Ma), Lachlan (484–340 Ma), and New England (305–230 Ma) orogens (Figure 1a; Kemp et al.,, 2009; Glen, 2013). The orogens are interpreted to have formed in response to subduction on the East Gondwanan margin. The SNEO is divided into three components: a Devonian–Carboniferous volcanic arc in the west, a forearc basin, and an accretionary wedge to the east (Jenkins et al., 2002). In the SNEO, the Tamworth Belt represents a Late Devonian–Carboniferous forearc basin and the Tablelands Complex represents a Silurian–Carboniferous accretionary complex. These are separated by the serpentinite-bearing Peel Manning Fault System (PMFS; Figure 1b; Aitchison and Ireland, 1995; Jenkins et al, 2002).

Rare, high-pressure low-temperature metamorphic blocks occur in the SNEO within serpentinite at Attunga, Gleneden, Glenrock, Pigna Barney and Port Macquarie (Figure 1b). Eclogite facies metamorphism at Attunga has been constrained to the mid to late Cambrian by zircon U–Pb geochronology (Phillips et al., 2015; Manton et al.,, 2017). Cooling or peak blueschist metamorphism has been constrained by $^{40}Ar/^{39}Ar$ and K–Ar geochronology to the Ordovician–Silurian (Fukui et al.,, 1995; Sano et al., 2004; Och et al., 2003; Phillips, 2010; Phillips and Offler, 2011; Phillips et al., 2015).

Within the SNEO, the Port Macquarie mélange is unique in the abundance and lithological range of the high-pressure metamorphic blocks (Barron et al., 1976, Och et al., 2003; Och, 2007; and Och et al., 2007). The mélange consists of two lenses of chlorite-actinolite schist separated by a domain of serpentinite (Figure 1c). The metamorphic blocks consist of variably foliated high-pressure rocks mostly of probable mafic igneous origin. Blocks comprise blueschist facies conglomerate, marble and other sedimentary rocks (Figure 2a). The high-pressure metamorphic blocks make up about 20% of the mélange. Rounded eclogite blocks range up to 2 m across and are characterised by abundant euhedral garnet up to 1 cm, but more commonly 2–5 mm, set in either an ompha-

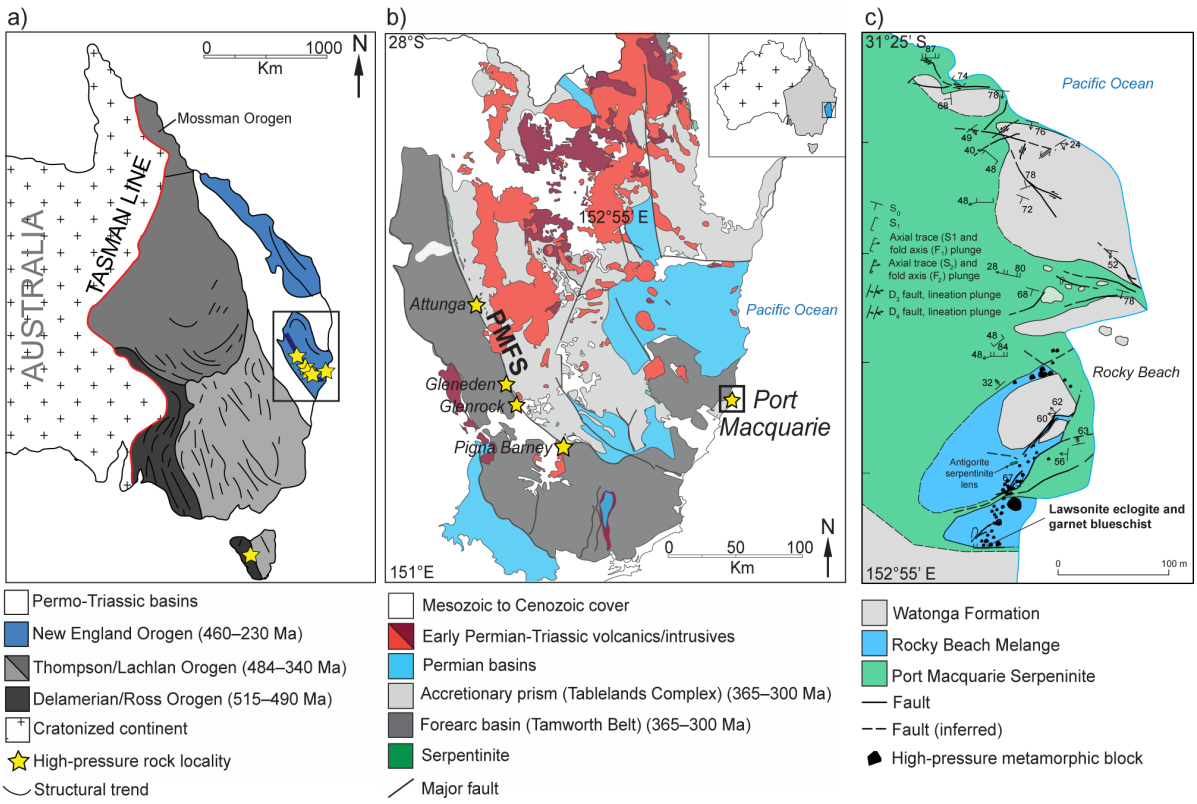


Figure 1: a) Simplified tectonic map of Eastern Australia showing the main eastwards-younging orogens and high-pressure localities. Study area is indicated in black box. b) Geological map of the Southern New England Fold Belt, indicating the Port Macquarie locality in black box. Yellow stars indicate other high-pressure rock localities (e.g. Phillips et al., 2015). PMFS: Peel Manning Fault System. c) The Port Macquarie mélange showing the high-pressure metamorphic blocks encased in serpentinite, modified from Och et al. (2003).

cite rich matrix or together with euhedral lawsonite porphyrobasts, set in a phengite rich matrix (Figure 2b). In some instances, blocks consist of essentially monomineralic unfoliated omphacite, with less abundant lawsonite (Och et al., 2003). In several of the eclogite blocks, the eclogite assemblages have been partially replaced by glaucophane schist. Blueschist blocks range up to at least 6 m in their longest dimension, and usually have a strong foliation that ranges from planar to intensely folded. Some of the blueschist was clearly derived from a conglomerate protolith, and contains highly deformed prolate clasts up to 20 cm long of probable volcanic origin. There are two varieties of garnet-bearing blueschist. One is intensely foliated with porphyroblasts of garnet and lawsonite enclosed by a glaucophane dominated matrix. The other variety is weakly foliated with garnet porphyroblasts commonly occurring in clump like aggregates (Figure 2c).

Ordovician (ca. 470 Ma) K–Ar ages have been obtained from late-stage phengite in blueschist, which have been interpreted to provide a lower age limit on the timing of the high-pressure metamorphism (Fukui et al., 1995). In contrast,

Nutman et al. (2013) dated zircons interpreted to be detrital in origin within eclogite, to provide an apparent maximum possible age for eclogite metamorphism of 251 ± 6 Ma and attributed the older K–Ar ages to excess argon. Och et al. (2003) obtained *P–T* conditions for the eclogite assemblages of ~1.8 GPa and 560 °C using conventional thermobarometry and rudimentary *P–T* grids, and lower-temperature conditions of ~360–450 °C for the blueschist facies conditions. Conversely, Nutman et al. (2013) suggested the eclogite and blueschist experienced the same *P–T* history, with maximum conditions less than 450 °C and 1.0 GPa, arguing the blueschist and eclogite assemblages reflect variations in bulk composition.

3. Samples

The samples used in this study come from: (1) a 2 by 1.5 m block of garnet-lawsonite-omphacite-phengite at the southern end of the Port Macquarie mélange that contains domains of retrograde blueschist that were avoided during sampling (Figure 2b) and (2) a weakly foliated garnet-bearing blueschist from a 2 by 1 metre block, approximately 3 meters away from the garnet-lawsonite-omphacite-phengite block (Figure 2c; 31°26'14.02" S, 152°55'31.54" E). Both blocks have broken free of the chlorite-actinolite matrix (Figure 1c, 2a), and their current proximity may simply reflect the vigorous wave action on the beach. In both samples, proportions of minerals were determined by mapping with a scanning electron microscope (SEM) with mineral liberation analysis (MLA) software.

RB11: lawsonite eclogite

The abundant phengite in sample RB11 means it mineralogically does not represent a true eclogite *sensu stricto*, rather it is an eclogite-facies rock. For simplicity, the term lawsonite eclogite will be used, to encompass the thermobarometrically important mineralogy and conditions reached by the sample. The sample contains porphyroblastic euhedral lawsonite (up to 3 mm), garnet (up to 7 mm) and omphacite (up to 1 mm) in a phengite-dominated matrix (Figure 3a,b). The phengite (48% of the rock; determined by mineral liberation analysis (MLA) mapping) contains minor but well distributed fine-grained titanite trails that parallel the phengite foliation. Garnet comprises 20% of the rock and contains inclusions of lawsonite, titanite, omphacite, chlorite, glaucophane, phengite, epidote, quartz, stilpnomelane and zircon (Figure 3c). Lawsonite comprises 7% of the assemblage and contains inclusions of titanite, glaucophane, garnet, epidote and phengite (Figure 3d). In both garnet and lawsonite, fine-grained titanite defines sigmodal inclusion trails that are sometimes truncated within near rim locations within the porphyroblasts by inclusions trails of a younger titanite defined foliation. Chlorite and stilpnomelane inclusions are predominantly in the

garnet cores (Figure 3c). Garnet is locally replaced by chlorite (Figure 3b,c). Omphacite (5% of the rock) forms small porphyroblasts with garnet and lawsonite, which are partially replaced by chlorite and glaucophane (Figure 3a,b). Elsewhere, glaucophane occurs with chlorite within micro-boudin necks in deformed aggregates of garnet-omphacite-lawsonite (Figure 3b). Retrograde glaucophane and chlorite comprise 9% each of the rock.

RB12: garnet blueschist

RB12 contains garnet porphyroblasts up to 6mm in diameter, which are transected by aragonite-quartz veins and partially pseudomorphed by chlorite (Figure 2c, Figure 3e). Aragonite was opti-

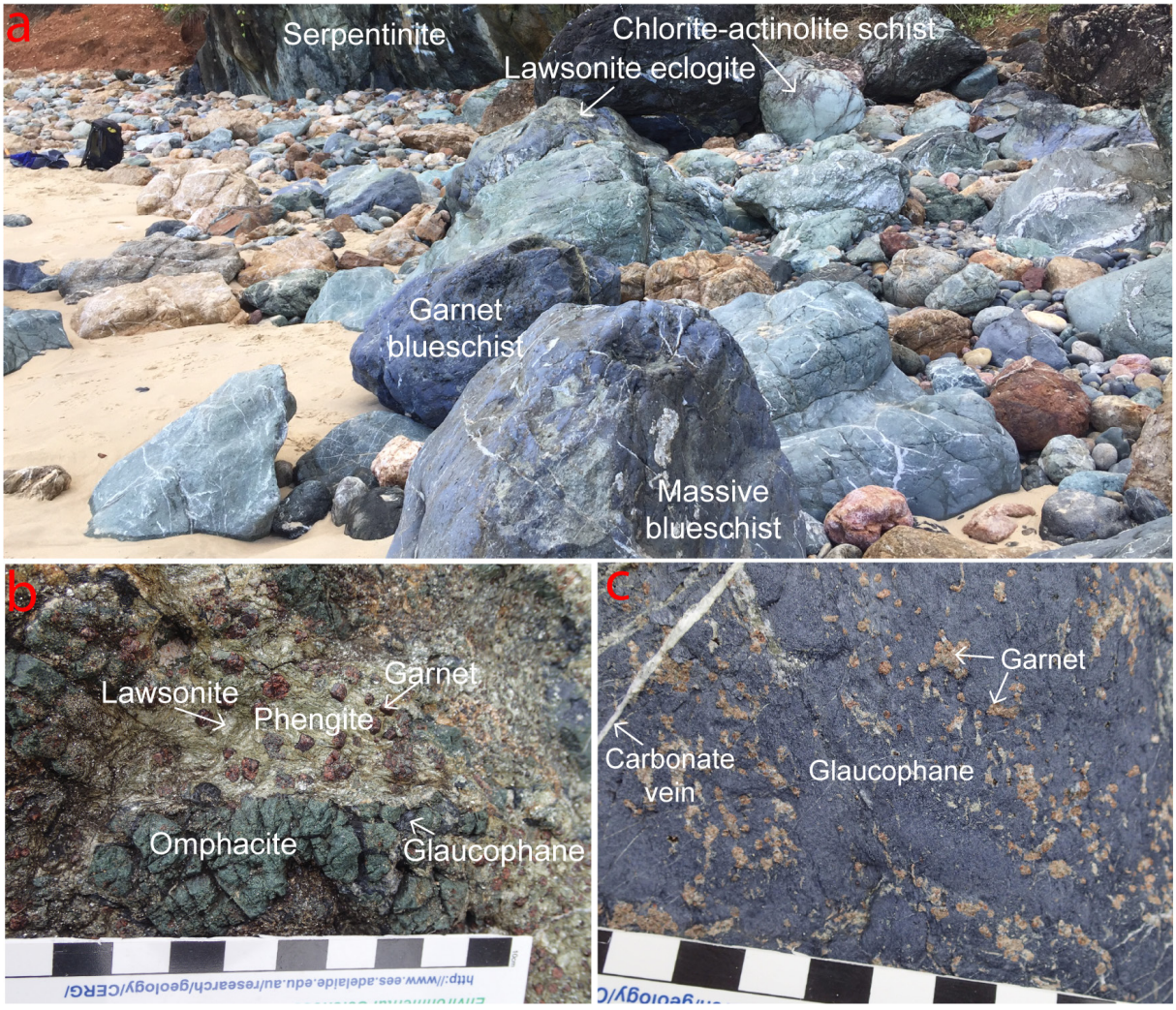


Figure 2: Field photographs of high-pressure rocks from Port Macquarie. a) High-pressure rocks eroded from mélange, showing locations of lawsonite eclogite and garnet blueschist. b) Lawsonite-garnet bearing eclogite with matrix phengite and coarse grained omphacite. c) Garnet blueschist derived from eclogite. The garnet porphyroblasts are partially replaced by chlorite.

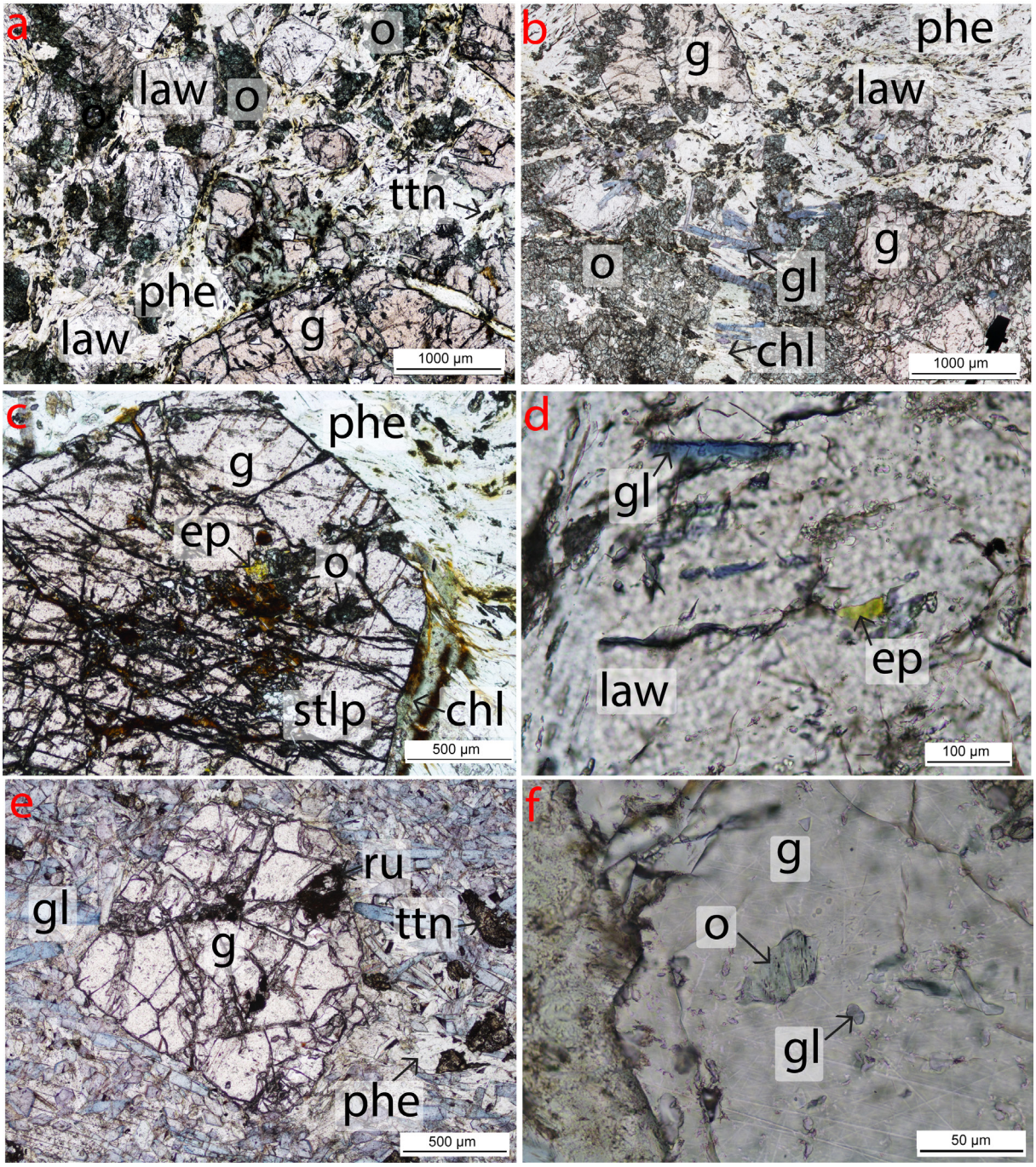


Figure 3: Photomicrographs of the samples taken in plane polarised light. a) Lawsonite eclogite showing porphyroblastic lawsonite, omphacite and garnet, with fine grained titanite in phengite-rich matrix. b) Retrograde chlorite and glaucophane in lawsonite eclogite. c) Omphacite, epidote and stilpnomelane inclusions in garnet in the lawsonite eclogite. d) Inclusions of glaucophane and epidote in porphyroblastic lawsonite in the lawsonite eclogite. e) Porphyroblastic garnet in glaucophane-phengite matrix in garnet blueschist. f) Omphacite and glaucophane inclusions within a garnet rim from garnet blueschist. Abbreviations: Chl: Chlorite, Ep: Epidote, G: Garnet, Gl: Glaucophane, Law: Lawsonite, O: Omphacite, Phe: Phengite, Ru: Rutile, Ttn: Titanite.

cally identified as carbonate with a low 2V biaxial negative interference figure. The relic garnet now comprises 5% of the assemblage. However, the original outlines of garnet are still easily discernible, and prior to its partial replacement, it comprised 13% of the rock. Garnet contains inclusions of omphacite, with lesser amounts of glaucophane, quartz, rutile and phengite (Figure 3f). Omphacite is abundant in some garnets, forming a myriad of small irregular grains that occur throughout the garnet (Figure 3f). The rock matrix consists of glaucophane (80%), phengite (6%) and quartz (3%), lawsonite (<1 %) and titanite that mantles rutile. The abundance of glaucophane in the matrix and its existence as inclusions within garnet suggests it was present throughout the development of peak to retrograde conditions. There is no omphacite in the matrix, but its presence as inclusions in garnet suggests that it was present prior to retrograde conditions, possibly at eclogite facies.

4. ANALYTICAL METHODS

4.1 Electron Probe Micro Analyses and X-Ray mapping

Spot analyses were obtained using a Cameca SX-5 WDS electron microprobe with a beam current of 20 nA and an accelerating voltage of 15 kV, with an andradite crystal analysed for calibration. Zr maps used a 200 nA beam current and an accelerating voltage of 15 kV, and Zr was mapped using Wavelength Dispersive Spectrometers (WDS).

4.2 LA–ICP–MS mapping

Rare earth elements were mapped in garnet and lawsonite to aid in the interpretation of Sm–Nd and Lu–Hf ages. This was done using an ASI m50 LA–ICP–MS with an Agilent 7900 MS. Mapping targeted Lu and Sm to determine elemental concentrations. The data was processed in Iolite (Paton et al., 2011), using Ca as the index element. Quantitative maps were processed using the Matlab script XMapTools (Lanari et al., 2014).

4.3 Lu–Hf and Sm–Nd geochronology

Garnet and lawsonite were separated using crushing, magnetic separations, heavy liquid procedures and hand-picking to obtain pure (>99%) mineral samples. Whole rock samples were obtained by pulverising a representative part of the rock. Lu–Hf and Sm–Nd analyses were collected at the Kraków Research Centre, Institute of Geological Sciences, Polish Academy of Sciences. Analyses followed the methods of Anczkiewicz and Thirlwall (2003) with modifications for the Lu–Hf method from Anczkiewicz et al. (2004). JMC475 measured over the course of analyses yielded $^{176}Hf/^{177}Hf$ = 0.282161 ± 8, and $^{143}Nd/^{144}Nd$ = 0.51209697 ± 8 for JNd-1 standard over the course of analyses. For age calculations internal errors were used. Isochron plots were done using Isoplot (Ludwig,

2003). All uncertainties are reported as 2 sigma.

4.4 U–Pb geochronology

Zircon geochronology was undertaken in-situ on zircons from the lawsonite eclogite. Zircons from the eclogite were identified and imaged within polished rock blocks using a Quanta 600 Scanning Electron Microscope. Attempts to image zircons using cathodoluminescence (FEI, Quanta 600) were unsuccessful. The zircons showed a bland low intensity response that likely resulted from their fine-grain size (< 15 μm) and hosting within silicate minerals. Isotopic compositions of ^{204}Pb, ^{206}Pb, ^{207}Pb, ^{208}U, ^{232}Th and ^{238}U were measured using a New Wave 213 nm Nd–YAG laser, coupled with an Agilent 7500cs/7500s ICP–MS. Given the small size of the in-situ zircons a spot size of 10 μm was used. Due to the small spot size and resulting low counts during acquisition, trace element compositions of the zircons were not collected. A frequency of 5 Hz was used with an acquisition time of 60 seconds, including 30 seconds of background measurement and 30 seconds of ablation. Data analyses and correction for mass bias and elemental fractionation utilizing the program Glitter (Griffin et al., 2004), and the primary zircon standard GJ. Instrument drift was accounted for using a linear correction and standard bracketing every 5 zircon analyses. Age calculations were done using Isoplot (Ludwig, 2003). All uncertainties on U–Pb ages are reported as 1 sigma. Over the course of the analyses, the primary standard GJ returned a $^{206}Pb/^{238}U$ weighted mean age of 596.9 ± 4.3 Ma (n = 48, MSWD = 1.8) and a $^{207}Pb/^{235}U$ weighted mean age of 596.7 ± 6.4 Ma (n = 48, MSWD = 0.88). The secondary standard Plesovice returned a $^{206}Pb/^{238}U$ weighted mean age of 329.8 ± 5.3 Ma (n = 12, MSWD – 1.9) and a $^{207}Pb/^{235}U$ weighted mean age of 340.1 ± 7.7 Ma (n = 12, MSWD = 0.54).

4.5 Phase equilibria forward modelling

Metamorphic geochemistry was determined for the eclogite and blueschist by combining determined modal proportions of each mineral with their measured composition (Table 1; Supplementary Table 1; 2). This was done as both samples contain retrograde carbonate and quartz veins that may have been derived from beyond the effective metamorphic bulk composition and would have been incorporated into any XRF bulk rock analysis. Thin sections were mapped using a scanning electron microscope (SEM) with mineral liberation analysis software (MLA) to identify and calculate the modal proportions of metamorphic minerals. The mineral volumes were then converted to weight percent estimates by applying densities based on their average compositions. These modal proportions where then integrated to create a bulk composition for modelling.

Phase equilibria modelling was undertaken us-

ing THERMOCALC (Powell and Holland, 1988; Holland and Powell, 2011) employing the internally-consistent thermodynamic dataset 'ds5' (filename tc-ds55.txt; November 2003 updated version of the Holland and Powell, 1998 data set) and activity–composition models (Powell and Holland, 1988; Holland and Powell, 2003; White et al., 2007; Green et al., 2007; Holland and Powell, 2011; Diener and Powell, 2012). The latest thermodynamic dataset 'ds62' (Green et al., 2016) was not used, as calculations could not solve for equilibria with multiple amphibole or clinopyroxene end-members.

Mn was incorporated in the whole rock bulk compositional calculations to predict the stability of garnet on the prograde path. Further, calculations for the lawsonite eclogite in the MnNCKFMASHTO system predicted the stable coexistence of rutile–garnet–lawsonite–omphacite–phengite ± glaucophane ± chlorite in the modelled bulk composition, whereas the rock contains the assemblage titanite–garnet–lawsonite–omphacite–phengite, with retrograde glaucophane and chlorite. The presence of titanite rather than rutile may reflect the role of Fe^{3+} and Al substitution as well as the presence of a H_2O-rich fluid , which expands the stability of titanite up pressure (Enami et al.,, 1993; Carswell et al., 1996; Brovarone et al., 2001; Castelli and Rubatto, 2002). In the modelling presented below, we did not investigate the dependency of titanite verse rutile stability as a function of XCO_2 at high pressures. However we note that titanite-lawsonite bearing eclogites have been reported previously (e.g. Brovarone et al., 2001; Ravna et al., 2010; Brovarone et al., 2011; Lü et al., 2019), confirming that titanite rather than rutile can be stable at high pressures. Additionally, the currently available activity–composition model for titanite does not incorporate Fe^{3+} and Al. Con-

Table 1: Modal proportion estimates for lawsonite eclogite and garnet blueschist, obtained from MLA mapping and then used to calculate bulk rock chemistries for phase equilibria forward models.

		Volume %	Density	Weight %
	Garnet	20	4.07	26
	Lawsonite	7	3.08	7
RB11	Omphacite	5	3.38	2
Lawsonite eclogite	Glaucophane	10	3.07	9
	Chlorite	10	3.03	9
	Phengite	48	2.93	46
	Garnet	5	4.07	7
RB12	Glaucophane	80	3.07	78
Garnet blueschist	Phengite	6	2.94	6
	Chlorite	4	2.81	3
	Quartz	3	2.7	2
	Omphacite	1	3.38	1

sequently, phase equilibria calculations do not appear to correctly predict the stability of titanite in our samples. Therefore, modelling of the eclogite was undertaken in the MnNCKFMASHO system. To maintain consistency, the garnet blueschist was also modelled in the same system.

Modelling in a Ti-free system probably does not significantly affect the modelled phase relations as titanite accounts for <1% of the assemblage for the lawsonite eclogite, and <2% for the retrogressed garnet blueschist. Titanite and rutile were not used in the bulk composition calculations that underpin the modelling. Stilpnomelane is restricted to inclusions in garnet and was not included in the modelling.

Aside from limiting the model system to Ti-free, uncertainties in modelling the *P–T* conditions of rocks from bulk rock chemistry are the oxidation state (Fe_2O_3), and water content (H_2O) during the formation of the mineral assemblage. As the eclogite and blueschist are interpreted to be hydrous (as suggested by the presence of abundant phengite, and lawsonite or glaucophane), and probably formed in a water-rich subduction environment (e.g. Martin et al., 2014), they were modelled with water in excess. Oxidation state was constrained from the microprobe chemical analyses used to calculate the metamorphic rock chemistry by assuming mineral stoichiometry in the calculation of cations from raw weight % oxide data (Droop, 1987).

5. Results

5.1 Electron Probe Micro Analyses

Representative mineral compositions from electron probe analysis are shown in Supplementary Table 1, garnet traverses are in Figure 4. Garnets in both the lawsonite eclogite and retrogressed garnet blueschist have Mn-rich (25-30%) cores and Mn depleted rims, consistent with preservation of prograde zoning (Figure 4). In both samples, X_{Mg} decreases from the core (0.55) to a value of around 0.35. In the lawsonite eclogite grossular increases slightly from core to rim (from 0.23 to 0.3), whereas in the garnet blueschist, grossular decreases slightly from core (0.3) to the rim (0.27). In both samples pyrope contents are low (0-02–0.03) in the garnet core and show a step to 0.05 within 250 μm from the rim in the lawsonite eclogite, and a step to 0.09–0.1 toward the rim of garnet in the blueschist. On average omphacite in the lawsonite eclogite has 39% and 42% jadeite and diopside components respectively, with 11% hedenbergite and 8% aegirine. In the garnet blueschist, omphacite inclusions in garnet contain 36% jadeite, 42% diopside, 3% hedenbergite and 25% aegerine. Phengite in the lawsonite eclogite shows anti-tschermaks zoning with cores enriched in Al and depleted in Si relative to the rims. Phengite has an average Si content of 3.57 p.f.u.

and 3.76 p.f.u. in the lawsonite eclogite and garnet blueschist respectively. There is no major detectable compositional zonation in lawsonite, with Fe and Ti contents less than 1%. In the lawsonite eclogite, retrograde chlorite has an X_{Mg} of 0.62, and retrograde glaucophane has an X_{Mg} of 0.4 and X_{Al}^{iv} of 0.31. In contrast, in the garnet blueschist, glaucophane is consistently zoned with Mg rich-$_{Al-}$ ^{vi} –rich cores (X_{Mg} = 0.62; X_{Al}^{vi} = 0.35) and comparatively depleted rims (X_{Mg} = 0.57; X_{Al}^{vi} = 0.33).

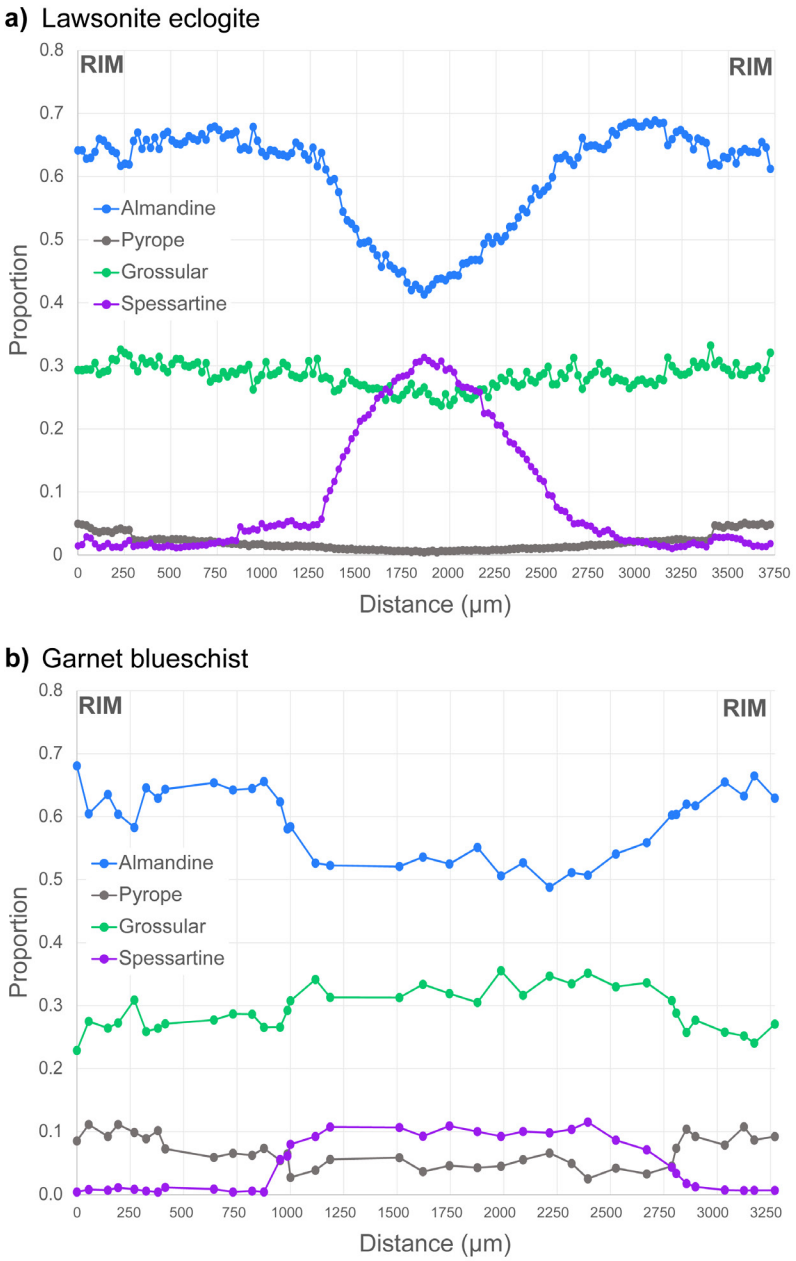


Figure 4: EPMA profiles across garnet. a) Zoning profile across garnet from lawsonite eclogite RB11, showing prograde zoning in spessartine and almandine. b) Zoning profile across garnet from garnet blueschist RB12, demonstrating less obvious prograde zoning. Garnets are more fractured in this sample hence the sparsity of data.

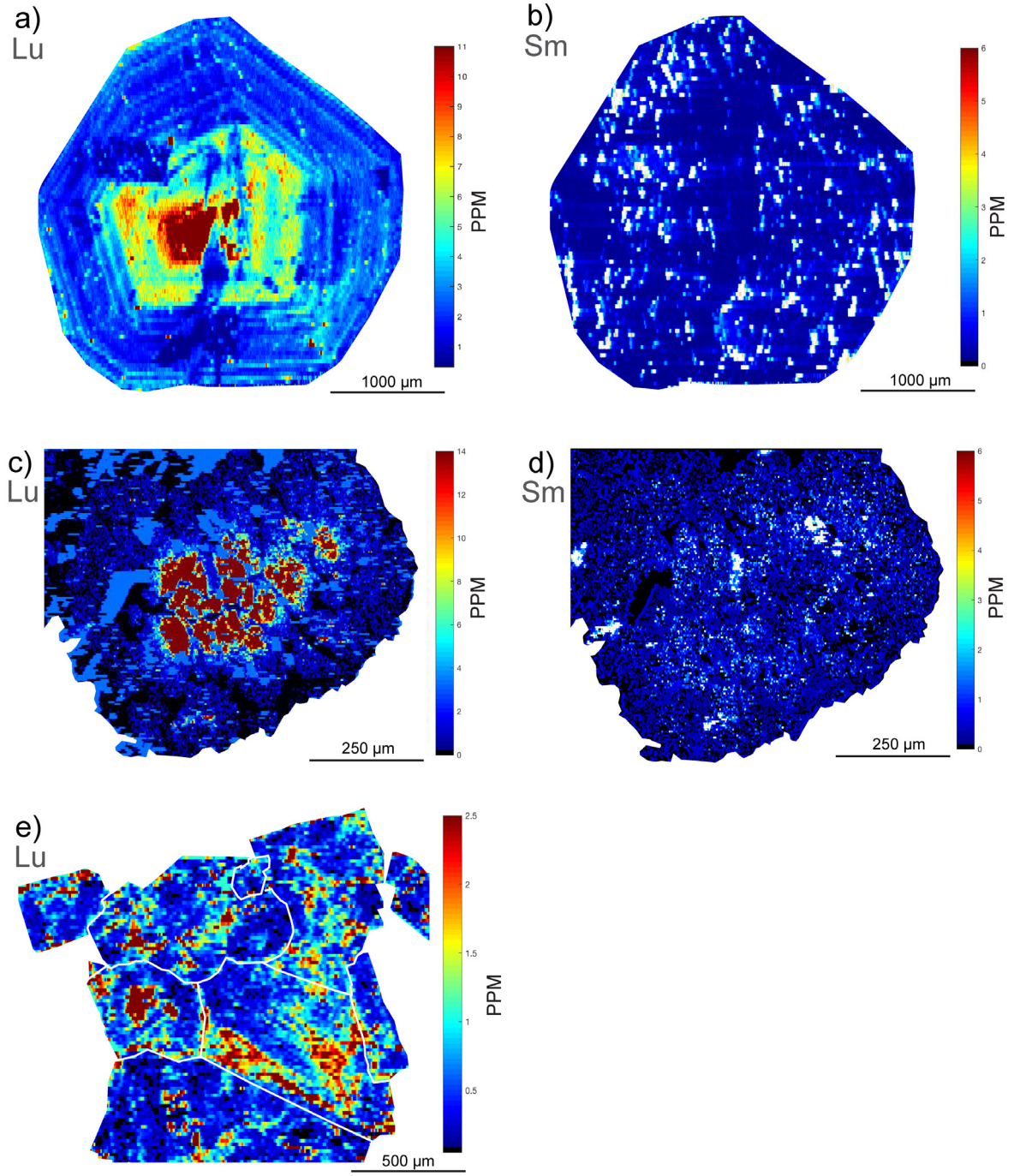


Figure 5: LA-ICP-MS element maps of metamorphic minerals targeted for geochronology. Inclusions are masked in white, parts of the grain below LOD are black. a) Lu map of a garnet from lawsonite eclogite showing a pronounced enrichment of Lu in the core. b) Sm map of the same garnet from the lawsonite eclogite, showing no discernible zoning. c) Lu map of a garnet from garnet blueschist, showing enrichment in the core. d) Sm map of the same garnet from the garnet blueschist, showing no discernible zoning. e) Lu map of several lawsonite crystals in lawsonite eclogite sample.

In the garnet blueschist the chlorite X_{Mg} is 0.55.

5.1 LA–ICP–MS mapping

The results of quantitative LA–IC–PMS mapping of lawsonite and garnet are shown in Figure 5. Mapping was done to assist interpretation of Lu–Hf and Sm–Nd geochronology, and the largest grain of lawsonite, or garnet, from each sample was mapped. Inclusions are masked in white, and parts of the grains below the limit of detection (LOD) are shown in black. Garnet has highly Lu enriched cores with respect to rims in both the lawsonite eclogite and the garnet blueschist, consistent with Mn compositional patterns that reflect prograde zoning. In contrast to Lu, Sm concentrations in the lawsonite eclogite do not vary significantly across garnet. In the garnet blueschist there is a suggestion of a slight Sm enrichment in the core. Lu concentrations in lawsonite range between < 0.5–2.5 ppm. In some instances, grains have a distinctly Lu-enriched core, suggesting that Lu may have concentrated into lawsonite prior to the availability of a garnet reservoir. In other grains, the domains of Lu enrichment less obviously coinciding with the cores of the grains.

5.2 Lu–Hf and Sm–Nd geochronology

Lu–Hf and Sm–Nd analyses of garnet, whole rock and lawsonite yield various ages, dependant on the isotopic system used or the mineral separates selected (Figure 6; Supplementary Table 3). The Sm–Nd garnet–whole rock two point isochron from the lawsonite eclogite gives an age of 533.0 ± 9.8 Ma. Three Lu–Hf isochrons can be compared for the lawsonite eclogite: garnet–lawsonite–whole rock, lawsonite–whole rock and garnet–whole rock, yielding ages of 487 ± 11 Ma, 506 ± 15 Ma and 489.7 ± 5.5 Ma respectively. One lawsonite fraction was excluded due to a high $^{176}Lu/^{177}Lu$ ratio (Supplementary Table 3).

The Sm–Nd garnet–whole rock isochron from the garnet blueschist yields an Sm–Nd age of 464.0 ± 3.9 Ma, with the two garnet fractions representing different garnets in the sample. One garnet fraction was excluded from the analyses due to high (7.239 ppm) Nd concentrations resulting in low $^{147}Sm/^{144}Nd$ ratios (Supplementary Table 3), that probably reflects contamination by titanite. The Lu–Hf garnet–whole rock isochron for the garnet blueschist gives an age of 472.4 ± 1.7 Ma. One garnet fraction was excluded due to high Lu and Hf concentrations, which resulted in a low $^{167}Lu/^{177}Hf$ ratio (Supplementary Table 3).

5.3 U–Pb geochronology

In-situ U–Pb dating of zircons was undertaken on the lawsonite eclogite. U–Pb results are in Supplementary Table 4. This rock contains a remarkable number of zircons. They occur as ~1–10 μm inclusions in garnet where they define inclusions

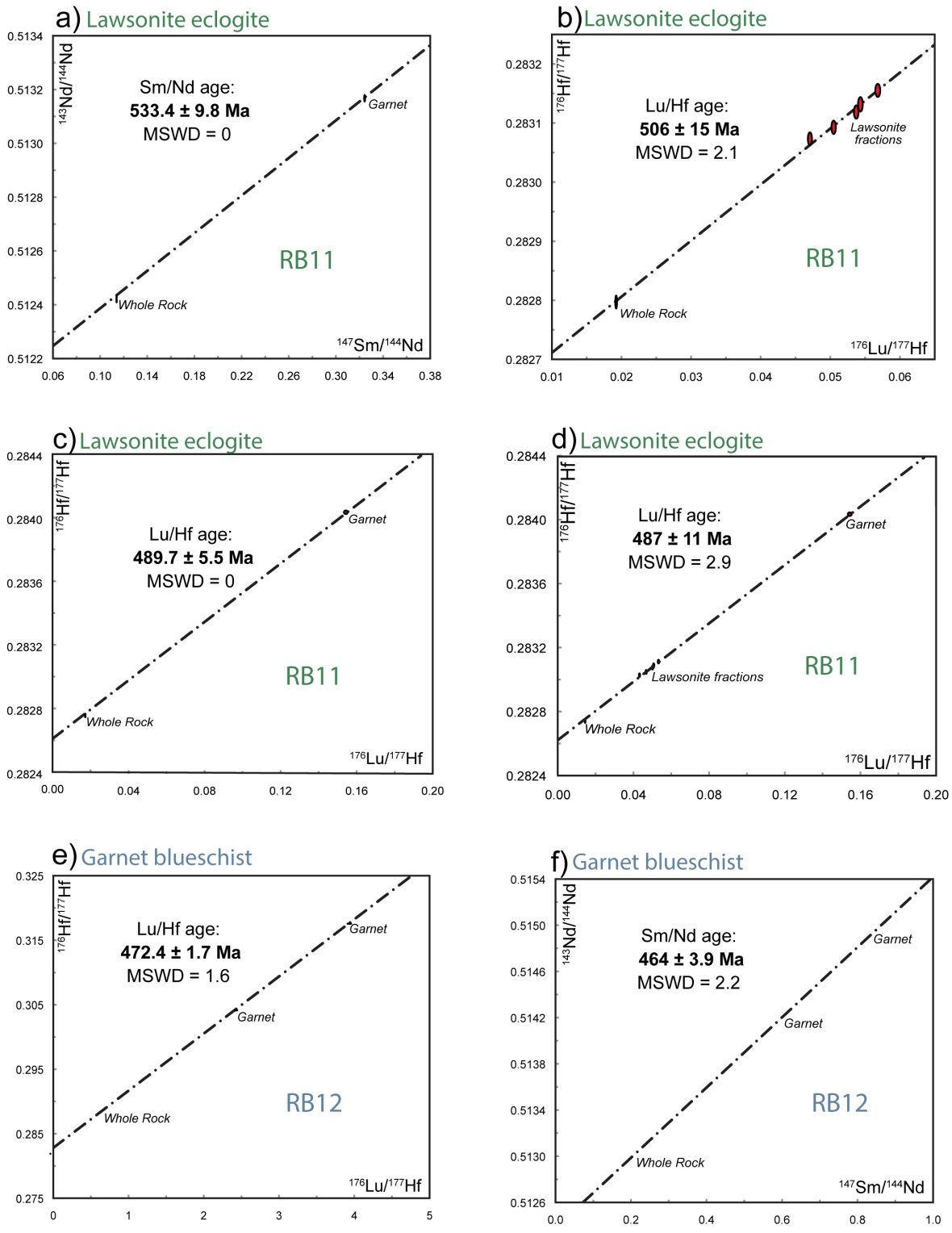


Figure 6: Lu-Hf and Sm-Nd isochrons for lawsonite eclogite and garnet blueschist. a) Sm–Nd isochron for lawsonite eclogite. b) Lu–Hf isochron for lawsonite and whole rock points from lawsonite eclogite. c) Lu–Hf isochron for the garnet and whole rock points for lawsonite eclogite. d) Lu–Hf isochron for all lawsonite, garnet and whole rock points for lawsonite eclogite. e) Lu–Hf isochron for garnet blueschist. f) Sm–Nd isochron for garnet blueschist.

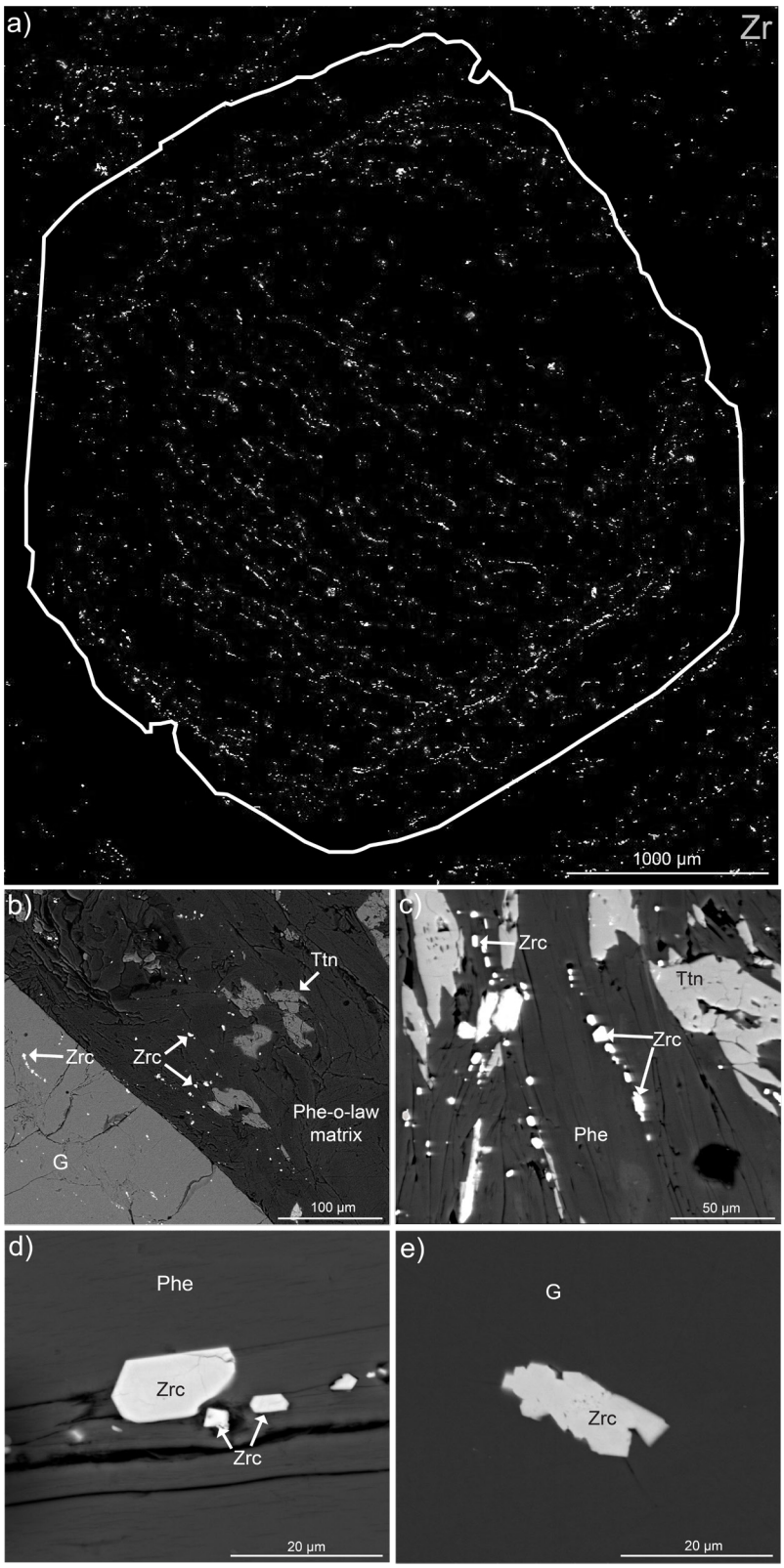


Figure 7: BSE images and Zr map of metamorphic micro-zircons target for U–Pb geochronology. a) WDS electron microprobe Zr map of a garnet and surrounding matrix with Zr hotspots shown in white, white line indicates the outline of the garnet crystal. The identity of the Zr hotspots as zircon has been confirmed with EDS. Inclusion trails of zircon within garnet and within the external foliation wrapping garnet can be seen. The X-ray map may somewhat over emphasize the size of the zircons, as zircon is vastly richer in Zr compared to host garnet. Nonetheless the image depicts the foliated distribution of the zircon grains. (b) Zircon in garnet rim and surround phengite rich matrix. (c) Zircon inclusion in garnet. (d) Trail of zircon forming in phengite and with titanite. (e) Euhedral zircons forming in a phengite cleavage plane. Abbreviations: G: Garnet, O: Omphacite, Phe: Phengite, Ttn: Titanite, Zrc: Zircon.

trails with titanite (Figure 7a-c). Zircons of 1-10 μm size also occur in the phengite-bearing matrix surrounding the garnet (Figure 7d-e). The zircons are commonly euhedral, showing well developed simple tetragonal forms (Figure 7e). However, despite the large number of zircons in the sample, only a small number were large enough to be analysed. Low U contents and the small size of the zircons made zircon U–Pb dating challenging. Twenty-two analyses of the fifty-five in total were excluded due to high concentrations of ^{204}Pb, that probably reflect incorporation of adjoining minerals and grain boundaries in the analysis, and ten analyses were excluded due to significant discordance. The thirty-three remaining concordant analyses span a range of ages from ca. 560 ± 40 to 440 ± 10 Ma (Figure 8). There is no statistical age difference between zircons that occur as inclusions in garnet and zircons in the matrix, although the comparison is hampered by the generally large individual errors on each analysis. The spread of data points along concordia presents no overt case for Pb loss, as all presented data is concordant. However concordance may be due to large the individual data point errors. Therefore, the spread of ages along concordia could reflect minor Pb-loss.

5.4 Phase equilibria forward modelling

The lawsonite eclogite RB11 contains the interpreted peak assemblage phengite–garnet– omphacite– lawsonite–quartz (+ titanite). The modelled bulk composition incorporates the entire garnet. Because the garnet is prograde zoned, this bulk composition is useful to estimate garnet nucleation and growth on the prograde path. However, this means it is an approximation for the effective composition at the metamorphic peak and during the formation of the retrograde assemblages. Aside from core enrichment in MnO, the major compositional components in garnet are FeO and CaO. Garnet compositional zoning (Figure

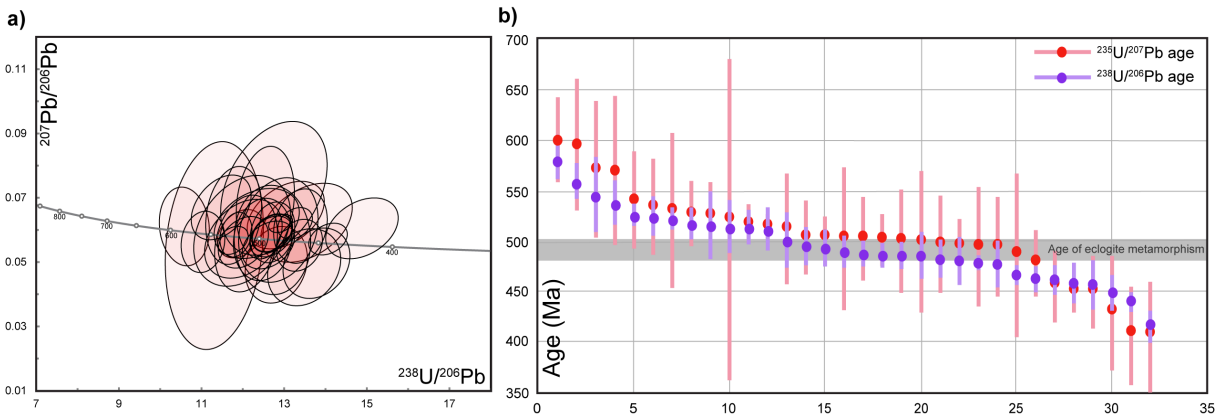


Figure 8: a) Terra-Wasserburg plot of U–Pb data from microzircons in lawsonite eclogite. b) Range of zircon U–Pb ages. The horizontal shaded rectangle is the age of peak high-pressure metamorphism of the lawsonite eclogite, inferred in the study from garnet and lawsonite Lu–Hf geochronology.

4) shows the outer parts of garnet are comparatively homogeneous in FeO and CaO, and volumetrically this outer domain comprises more than 80% of the garnet volume. Since garnet comprises approximately 15–20% of each sample, the core regions of garnet comprise only a small fraction of the rock volume. Therefore, while modelling the peak assemblage using a composition that includes the garnet cores is obviously an approximation, it is unlikely to negate the general predictions for the peak *P*–*T* estimation.

The peak assemblage is modelled to occur at ~2.7 GPa and ~590 °C (Figure 9a). The peak field is bound by the conversion of quartz to coesite as well as the conversion of omphacite to jadeite, the lower temperature appearance of talc, and the loss of lawsonite at higher temperature (Figure 9a).

The inferred prograde evolution is marked by the grey dashed arrow. This evolution is based on the inclusions in garnet, which comprise lawsonite, omphacite, glaucophane, epidote, chlorite and quartz. The generalised retrograde evolution is defined by the appearance of glaucophane and chlorite. The retrograde trajectory tracks approximately parallel to lawsonite modal abundance contours, depicted by the grey arrow. This trajectory is based on the appearance of chlorite and glaucophane, while maintaining a lawsonite–garnet–omphacite–quartz assemblage. The *P*–*T* path passes through talc stability, however the modelled talc modal proportions in this part of *P*–*T* space are less than 1%, therefore if it formed, it could have easily been removed by continued retrogression and/or be difficult to detect in the presence of the abundant phengite in the sample.

The garnet blueschist RB12 contains the assemblage garnet–glaucophane–phengite–quartz (+rutile) with retrograde chlorite, lawsonite and titanite. The garnets contain abundant omphacite, quartz, glaucophane and phengite inclusions, suggesting omphacite and glaucophane coexisted with garnet during the prograde to peak evolution. There is no omphacite in the glaucophane-rich matrix, suggesting the matrix assemblage may in part be retrograde. The peak mineral assemblage is interpreted as existing in the large garnet–phengite–glaucophane–quartz–jadeite field (Figure 9c). The clinopyroxene inclusions in garnet are omphacitic, however their J value (Na/Na+Ca in the DS5 THERMOCALC model) is 0.61, indicating they are close to the jadeite/omphacite solvus. The modal proportion of garnet and the grossular content of garnet (g(Z)) can also be used as a guide to the potential *P*–*T* conditions. Prior to partial replacement by chlorite, garnet comprised ca. 12% of the sample when converted to one cation normalised proportions to accord with computed modes in DS5, and average grossular (z value in the DS5 THERMOCALC model) content in the outer part of the garnet is 0.24. These plot at approximate *P*–*T* conditions of 2.0 GPa and 550

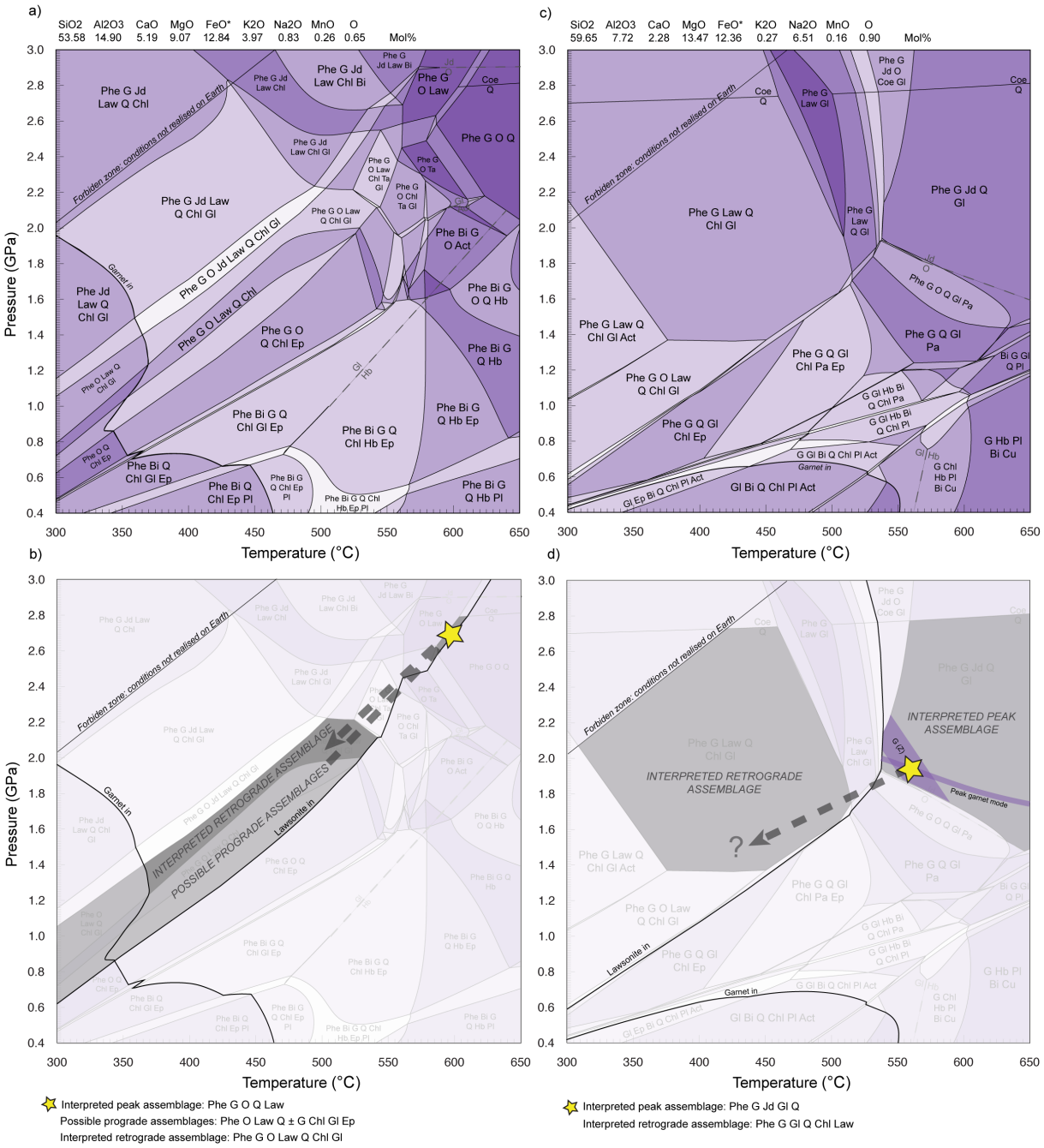


Figure 9: Phase equilibria forward models calculated with THERMOCALC DS5. Important mineral stabilities are indicated in thicker black lines (garnet-in and lawsonite-in). Grey dashed line indicated the location of a solvus. Yellow star marks the interpreted peak P–T conditions reached by each sample, while grey dashed arrows indicate a tentative prograde P–T evolution. a) Model for lawsonite eclogite. b) Simplified version of the lawsonite eclogite model, showing interpreted prograde, and peak fields. c) Model for garnet blueschist. d) Simplified version of the garnet blueschist model, showing P–T location of interpreted peak and assemblage. Transparent purple fields indicate estimated peak garnet modal proportion and range of measured grossular contents of garnet rims (G(Z)), used to constrain the peak P–T conditions. Act: Actinolite, Bi: Biotite, Chl: Chlorite, Coe: Coesite, Cu: Cummingtonite, Ep: Epidote, G: Garnet, Gl: Glaucophane, Hb: Hornblende, Jd: Jadeite, Law: Lawsonite, O: Omphacite, Pa: Paragonite, Phe: Phengite, Pl: Plagioclase, Q: Quartz, Ta: Talc.

°C (Figure 9d).

The retrograde evolution is defined by the partial replacement of garnet by chlorite, the loss of omphacite from the matrix, and the appearance of minor lawsonite, with the caveat we have modelled a rock composition that includes the garnet cores. Where retrograde chlorite is in contact with the matrix glaucophane, glaucophane crystals are euhedral, and there is no textural evidence for replacement of the glaucophane, suggesting glaucophane and chlorite were stable on the retrograde path. Therefore, the retrograde evolution probably passed into the garnet–glaucophane–phengite–quartz–chlorite–lawsonite field. This field covers a large range of *P–T* conditions, from 1.4–2.8 GPa and 310–510 °C, and it is difficult to pinpoint the exact retrograde P–T trajectory.

6. Discussion

6.1 Timing of high-pressure metamorphism at Port Macquarie

In garnet-bearing low-temperature high-pressure rocks, the Lu–Hf system has proved a reliable geochronomoter, as Lu fractionates into lawsonite and fractionates strongly into garnet, and is less influenced by inclusions than the Sm–Nd system, particularly in mafic rocks which are poor in or devoid of inherited zircons, (Becker et al., 2000; Martin et al., 2009, Mulcahy et al., 2014). In the lawsonite eclogite sample RB11, the whole rock and 4 lawsonite fractions give a Lu–Hf age of 506 ± 15 Ma, and the garnet–whole rock gives 489.7 ± 5.5 Ma (Figure 6). Although these are within error of each other, phase equilibria modelling suggests that lawsonite would have nucleated before garnet on the prograde path (Figure 9a), consistent with inclusions of lawsonite in garnet, and the formation of Lu-rich domains within lawsonite. However, the presence of abundant porphyroblasts of both minerals suggest they grew at the same time for a least a part of the metamorphic history. The larger error on the lawsonite-whole rock isochron is due to low $^{176}Lu/^{177}Hf$ ratios of the lawsonite fractions. The garnet–lawsonite–whole rock isochron gives an age of 487 ± 11 Ma (Figure 6c). However, this is controlled by the garnet–whole rock pair, and hence is similar to the garnet–whole rock isochron (489.7 ± 5.5 Ma).

The garnet–whole rock Lu–Hf age is interpreted to record garnet growth, based on the preservation of Lu-rich garnet cores in RB11 (Figure 5a), consistent with prograde growth. The pronounced concentration of Lu in the garnet cores (Figure 5a), indicates that the garnet Lu–Hf age is strongly biased toward the early stage of garnet formation, and therefore better constrains prograde, rather than peak metamorphism. The garnet contains micro-zircon inclusions that span an age range that encompasses the garnet Lu–Hf age. Although the sample preparation method for garnet Lu–Hf

analysis involved bench top dissolution rather than high pressure dissolution specifically to minimise inadvertant incorporation of zircon, it is possible that some zircon was incorporated into the TIMS analysis, and could have contributed to the measured Lu–Hf ratios of the garnet. However, quantitative laser ablation maps (Figure 5), show that Lu concentrations in garnet range between 1–11 ppm and Hf concentrations are ca. < 2 ppm across garnet grains. Lu and Hf ppms measured by TIMS are 2.83 and 2.58 respectively (Supplementary Table 3), close to a volumetrically weighted average of Lu–Hf concentrations derived from LA–ICP–MS analysis of garnet grains. Microprobe analyses of zircon from the same sample shows that zircons contain on average 1.08 wt% Hf (Supplementary Table 5). Therefore, while it is possible that some zircon was incoporated into the analysed garnet Lu–Hf aliqouts, it is evident the vast bulk of the analysed Lu and Hf isotopes come from garnet. Similarly, mapped concentrations of Lu in lawsonite show they have on average less than 1.5 ppm Lu, consistent with the TIMS data.

Figure 4 shows the distribution of Lu, Hf, Sm and Nd in examples of garnet and lawsonite from the dated samples. In the lawsonite eclogite, garnets have Lu rich cores whereas Sm is unzoned. However the Sm–Nd age of 533.4 ± 9.8 Ma is significantly older than the ca. 490 Ma Lu–Hf ages (Figure 6). Although great effort was taken to obtain pure mineral seperates, fine-grained inclusions of titanite contain high concentrations of Sm and Nd, and are difficult to remove completely during mineral separation. Furthermore, Sm/Nd ratios in titanite are typically lower than in garnet (Spandler et al., 2003), and contamination is therefore likely to lower the $^{147}Sm/^{144}Nd$ ratio of the analysed garnet aliquot, which may explain the comparatively low $^{147}Sm/^{144}Nd$ ratio of the analysed garnet compared to typical ratios in garnet (Anczkiewicz et al.,, 2004; Anczkiewicz et al., 2007). Therefore it is conceivable the Sm–Nd age of 533.4 ± 9.8 Ma reflects to some extent the age of an earlier titanite-bearing mineral assemblage. However, an assumption in isochron geochronology is that analysed materials were initially in isotopic equilibrium at t=0. Therefore, an alternative explanation for the Sm–Nd garnet age that is significantly older than the Lu–Hf age could be that the garnet and whole rock had different $^{143}Nd/^{144}Nd$ ratios at t=0. This could have occurred via the infiltration of isotopically evolved fluids affecting the eclogite matrix after garnet growth, creating isotopic disequilibrium between garnet and matrix minerals (e.g. Blichert-Toft and Frei, 2011). Depending on the repsective $^{143}Nd/^{144}Nd$ ratios, this effect could have resulted in a positive slope on the zero-age garnet-whole rock isochron, producing an invalid age that is older than the Lu–Hf garnet growth age. Therefore, for sample RB11, we conclude that garnet growth occurred at 487 ± 11 Ma.

Garnet in the garnet blueschist gives an Sm–Nd

age of 464.0 ± 3.9 Ma and a Lu–Hf age of 472.4 ± 1.7 Ma (Figure 6). The Lu–Hf and Sm–Nd ages are not in error of each other. Lu–Hf closure temperatures are generally considered to be higher than that of the Sm–Nd system (Sm–Nd: ~700°C, Lu–Hf: ~750°C; e.g. Scherer et al., 2000; Ganguly et al., 1988). However the phase equilibria modelling (Figure 9) suggests peak metamorphic temperatures were lower than closure for both these systems. Hence the difference in ages cannot simply be attributed to differences in closure systematics. The age difference could reflect non-zero t=0 slopes for either isochron. Alternatively, the difference in ages could arise from internal zonation patterns in the garnet (Figure 5). Garnet in RB12 shows enrichment of Lu (14 ppm) in the core, consistent with Rayleigh fractionation during growth (Otamendi et al.,, 2004). However there is no disernable zonation in Sm. The Lu zoning suggests the Lu–Hf age should be biased towards the early stages of garnet growth, whereas the Sm–Nd age is biased toward the outer parts of the garnet simply because of the spherical volumetric relationship (e.g. Lapen et al., 2003; Skora et al., 2006). This notion is consistent with the relative difference between the Lu–Hf and Sm–Nd ages, and if correct, provides some indication of the likely duration over which garnet grew. Therefore, garnet growth in RB12 probably occurred over the period 472.4 ± 1.7 Ma to 464 ± 3.9 Ma.

Although the matrix of the garnet blueschist is interpreted to be largely retrograde in origin due to the presence of omphacite inclusions in garnet and their absence in the matrix, the preservation of prograde zoning in the garnet indicates the Lu–Hf and Sm–Nd ages are not retrograde in origin. Instead, they clearly date prograde metamorphism up to and including the formation of an omphacite-garnet-bearing assemblage.

Comparing the garnet Lu–Hf ages of both samples, it is evident the lawsonite eclogite sample is older than the garnet blueschist. This age difference could reflect that the samples underwent subduction-driven burial at different times, or that the samples shared the same burial history, but that garnet formed at different times due to differences in bulk composition between the samples. Figure 9 shows the garnet-in line (i.e. the first nucleation point of garnet) for the lawsonite eclogite and garnet blueschist. The generalised prograde path for the lawsonite eclogite can be interpereted as having seen garnet nucleation at ca. 0.8–1.4 GPa and ca. 350 °C. The prograde history of the blueschist is unknown, and as such, the *P–T* conditions of garnet nucleation cannot be deduced. However, regardless of the prograde path taken by each rock, the garnet in line calculated for the garnet blueschist occurs at similar pressures and temperatures to the lawsonite eclogite (Figure 9c,d). As such, assuming garnet growth was not radically over stepped in the blueschist compared to the lawsonite eclogite, garnet growth

should have occurred at approximately the same conditions, and therefore time if both protoliths were subducted together. Therefore we interprete the difference in garnet Lu–Hf ages between the two samples reflects that the protoliths were subducted at different times. A similar scenario has been documented elsewhere, where high-pressure rocks have been dated with Lu–Hf geochronology and span an age range between ca. 105 to 86 Ma, leading to the interpretation they were subducted at different times (Mulcahy et al., 2014; Porteau et al., 2018).

The U–Pb data collected from micro-zircons in the lawsonite eclogite spread along concordia (Figure 8), with $^{206}Pb/^{238}U$ ages ranging between ca. 560 ± 40 Ma and 440 ± 10 Ma, suggesting they do not define a single age population. The analysed zircons are euhedral (Figure 7). Texturally the analysed zircons occur in garnet and in the surrounding phengite-rich matrix (Figure 7). Inclusion trails in garnet are defined by zircon and titanite (Figure 7) and form 2D microstructral trends that are discordant to titanite and zircon trails in the surrounding schistose matrix. This implies that zircon formed either in stages or progressively during the metamorphic evolution of the rock. Texturally zircon defining garnet-hosted inclusion trails predates zircon in the matrix. However there is no statistical age difference between the different zircon textural populations. In part this probably reflects the large uncertainties on individual analyses. But it also probably reflects that at least some of the zircons in the matrix formed at the same time as zircons located as inclusions in garnet. The microstructural distrubution is impossible to explain unless the zircon is metamorphic in origin. Therefore it is highly unlikely they were inherited from the eclogite protolith either as igneous or detrital grains. The interpretation that the zircons are metamorphic is consistent with numerous other studies showing zircon can form in eclogite with similar *P–T* conditions to those recorded at Port Macquarie (e.g. Tomaschek et al., 2003; Warren et al., 2005; Rubatto et al., 2008).

The span in concordant ages from the micro-zircons may reflect low temperature alteration and dissolution-precipitation processes (e.g. Rubatto and Hermann, 2007; Hermann and Rubatto, 2014). Potentially the oldest zircons formed during low-temperature hydrothermal alteration close to the sea floor (Spandler et al., 2004; Pagu et al., 2005; Grimes et al., 2009; Aranovich et al., 2017). The source of zirconium for low-temperature zircon growth can be the breakdown of high-temperature Zr-bearing magmatic minerals such as clinopyroxene (Rubatto et al., 2008), and in this scenario the oldest zircons would pre-date subduction. The zircons close to the age of prograde eclogite metamorphism at ca. 490 Ma could also be attributed to prograde low-temperature dissolution-precipitation during subduction (Tomaschek et al., 2003; Tamblyn et al., 2019). Zirco-

nium solubility is increased in silicon rich alkaline fluids, which form with increasing pressure, allowing zirconium to be dissolved and precipitaed from the fluid (Ayers et al., 2012; Hermann and Rubatto, 2014). The post ca. 490 Ma zircons may have formed by continued dissolution-precipitation during metamorphic mineral reactions and fluid chemistry changes (e.g. Rubatto et al., 2008), resulting in the continued (re)crystalization of zircon on the retrograde path. Alternatively the post ca. 490 Ma zircons ages may reflect minor Pb-loss.

Nothwithstanding the generalised uncertainties associated with interpretation of the age data discussed above, it is apparent that high-pressure metamorphism is late Cambrian to early Ordovician in age. Therfore the above age data indicate the ca. 251 Ma maximum age for eclogite metamorphism at Port Macquarie suggested by Nutman et al. (2013) is incorrect. Notwithstanding the geological implausibility of this early Triassic age maxima (e.g. Phillips et al., 2015), it was argued by Nutman et al. (2013) that the abraded nature of the zircons they analysed from a sample of eclogite indicated a detrital origin, thereby placing an upper age limit on the timing of eclogite metamorphism. However the similarity between the ages obtained by Nutman et al. (2013), and ages of zircons from modern beach sands in the SNEO (Sircombe, 1999), suggests the sample analysed by Nutman et al. (2013) was contaminated with modern beach sand, and therefore does not place an upper age constraint on the timing of high-pressure metamorphism. To test this hypothesis, we analysed zircons separated from the beach sand at the eclogite location and from a beach ~ 1 km to north (Supplementary File 1, Supplementary Table 6). The beach sand zircons are rounded, with abraided morphologies (Supplementary Figure 1) similar to those described by Nutman et al. (2013). Figure 10 shows the distribution of ages obtained from the beach sand at the eclogite location and from a beach 1 km to the north. Also shown is the distribution of beach sand zircons from elsewhere in the SNEO (Sircombe, 1999). For reference, our intepreted age of high-pressure metamorphism is also shown. It is evident the beach sand zircon populations contain significant age groups < 400 Ma, including grains as young as ca. 250 Ma. It is also evident the beach sand zircon age distribution from the eclogite location shares most of the age peaks analysed by Nutman et al. (2013; Figure 10). It could be argued that the beach sand zircons at the eclogite locality could be sourced from the eclogite itself. However the eclogite block is only approximately 8 m^3 in size, and its unlikely it could provide enough zircon to consitute the beach sand zircon population, or provide the beach zircons 1 km and more regionally within the SNEO. Therefore we conclude the maximum age of ca. 250 Ma for high-pressure metamorphism inferred by Nutman et al. (2013) is incorrect, and was based on analysis of a contaminated sample.

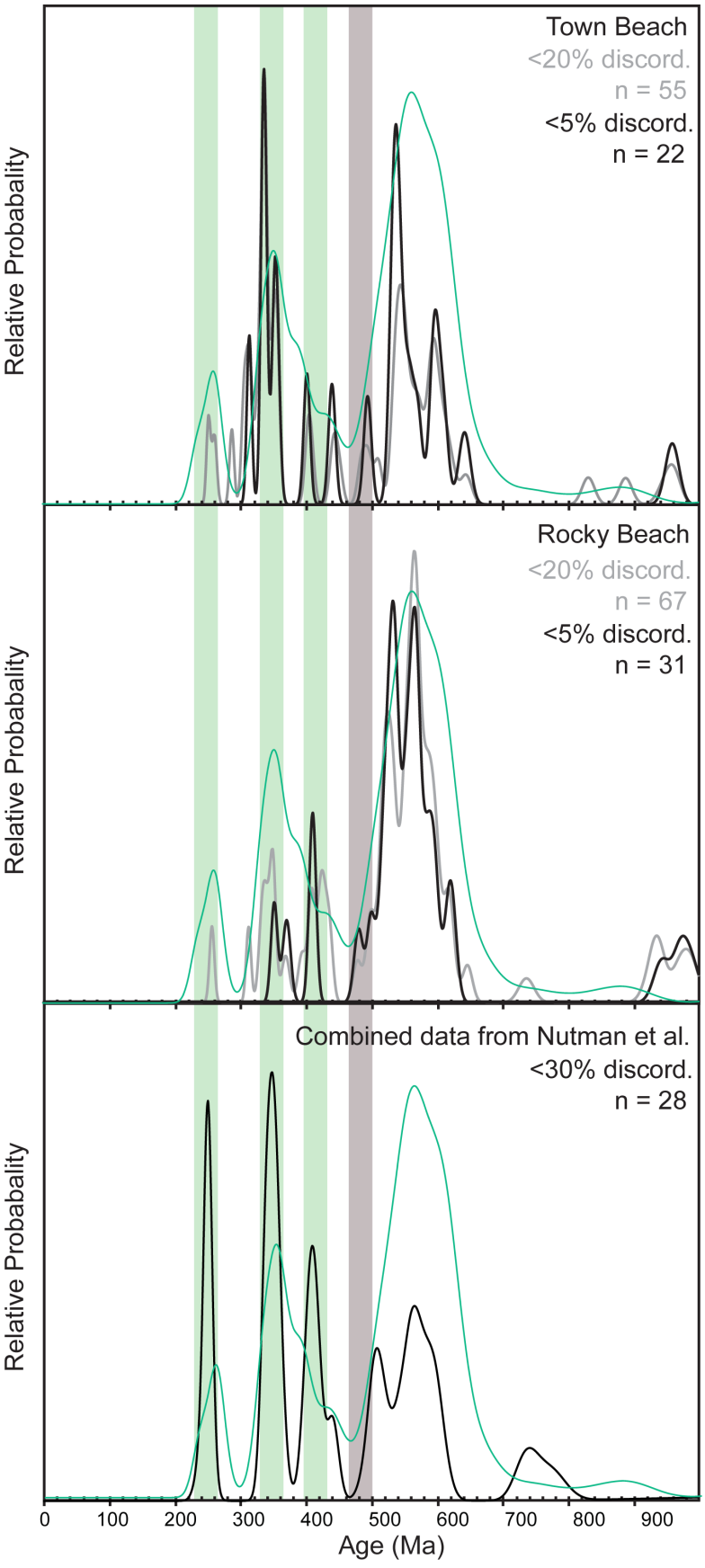


Figure 10: Comparisons between modern beach sand zircon ages at Port Macquarie and the zircon ages interpreted by Nutman et al. (2013) to be detrital in origin, derived from the eclogite at Port Macquarie. Also shown for reference (in dark green) are modern beach sand zircon ages at Coffs Harbour within the SNEO, 150 km north of Port Macquarie (Sircombe, 1999). a) Modern beach sand zircons from Town Beach ca. 1 km north of the eclogite location. b) Modern beach sand zircons from the eclogite locality. c) The zircon age distribution reported by Nutman et al. (2013). Shown in pale green are common zircon age peaks between modern beach sand zircons and the zircon ages reported by Nutman et al. (2013). Shown in grey is the age of eclogite metamorphism determined from this study.

Nutman et al. (2013) also obtained a poorly constrained U–Pb age from combined rutile and titanite from an undescribed retrogressed high-pressure rock at Port Macquarie. The upper uncertainty on this age (332 ± 140 Ma) overlaps with the garnet Lu–Hf and Sm–Nd ages (ca. 464–472 Ma) obtained from the garnet blueschist . Therefore this poorly defined age bracket records Ordovician high-pressure metamorphism.

The interpretation that high-pressure metamorphism at Port Macquarie is ca. 500–470 Ma is consistent with the Ordovician (ca. 470 Ma) K–Ar age obtained from phengite in blueschist (Fukui et al., 1995). It is also consistent with the range of ages obtained from high-pressure rocks elsewhere in the SNEO, which are all Cambro-Ordovician in age. U–Pb zircon geochronology from eclogite at Attunga (Figure 1) gives an age of ca. 490 Ma (Figure 11; Phillips et al., 2015; Manton et al., 2017). K–Ar and $^{40}Ar/^{39}Ar$ from blueschist at Pigna Barney and Glenrock (Figure 1) gives ages between ca. 470 and 480 Ma (Figure 11; Fukui et al., 1995; Phillips et al., 2015).

6.2 Pressure-temperature conditions during metamorphism

Phase equilibria forward modelling (Figure 9) suggests the peak assemblage in the lawsonite eclogite formed at ca. 2.7 GPa and 590 °C, and in the garnet blueschist at slightly lower *P*–*T* conditions of ca. 2.0 GPa and 550 °C. The peak eclogite conditions are slightly warmer, however broadly similar, to those suggested by Och et al. (2003), who obtained temperatures of 560 ± 40 °C and

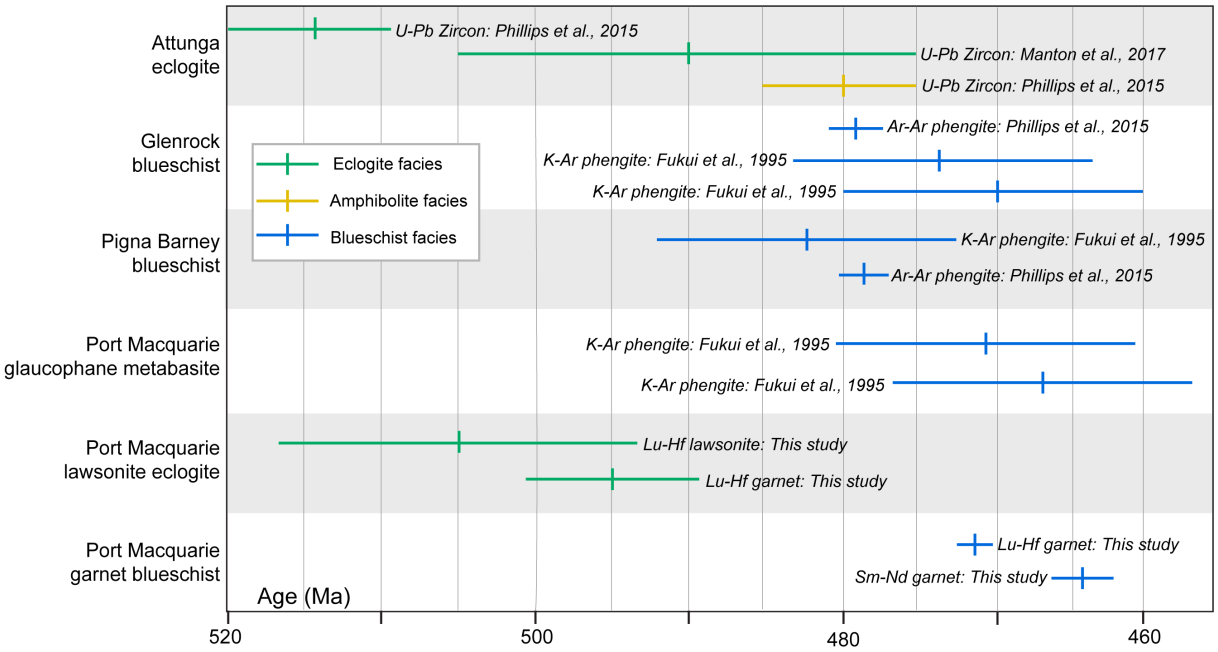


Figure 11: Summary of geochronology on high-pressure rocks exhumed via the Peel Manning Fault System in the SNEO.

pressures between 1.8–2.6 GPa, with subsequent cooling to temperatures between 300–500 °C. Although the use of inclusion assemblages to constrain prograde paths needs to be taken with caution, the garnets in the lawsonite eclogite contain a plethora of inclusions that include lawsonite, glaucophane, clinopyroxene, chlorite, epidote and quartz. These minerals have not all been observed in a single garnet, but nonetheless occur in garnets within a single thin section. Taken in their entirety, this group of inclusions suggests a prograde path that crossed the epidote-lawsonite field, leading initially to loss of epidote from the assemblage, and then at higher *P*–*T*, the loss of chlorite and followed by glaucophane.

The retrograde evolution of the lawsonite-eclogite is characterised by the formation of glaucophane and chlorite at the expense of garnet and omphacite. There is no textural evidence for the breakdown of lawsonite, suggesting the retrograde evolution approximately followed modal proportion contours of lawsonite. As such, the prograde and retrograde evolution of the lawsonite eclogite tracks along the same *P*–*T* path. In the garnet blueschist, there is less mineralogical diversity, and the prograde path is poorly constrained. However, inclusions of clinopyroxene and glaucophane and a lack of epidote and paragonite in garnet tentatively point to a prograde path that tracks above 1.4 GPa, although a lack of lawsonite inclusions makes this suggestion speculative. The retrograde evolution involved the stability of glaucophane, lawsonite and chlorite, and loss of omphacite and reduction in garnet abundance. This inferred *P*–*T* evolution tracks through the same field as the prograde path, remaining above pressures of 1.4 GPa while temperature decreases.

Using a reasoned interpretation of the *P*–*T* path of the lawsonite eclogite and the garnet blueschist, it appears their prograde evolution tracked through a similar path as their retrograde evolution. These inferred 'hair-pin' style *P*–*T* loops are similar to previously inferred metamorphic evolutions experienced by rocks within subduction channels (Ernst et al., 1988; Porteau et al., 2019). The geothermal gradients recorded by the lawsonite eclogite and garnet blueschist are approximately 245 °C/GPa and 275 °C/GPa and respectively. While the exact retrograde evolutions of the high-pressure rocks are tentative, both must have tracked within the lawsonite stability field in their respective bulk compositions. Preservation of pristine lawsonite-bearing assemblages has been previously interpreted to reflect rapid burial and exhumation (Whitney and Davis, 2006; Tsujimori et al., 2006; Tsujimori and Ernst, 2014). However, it has also been suggested that slow exhumation along cool geothermal gradients (such as within the subduction channel), also aids in the preservation of lawsonite (Tsujimori et al., 2006; Tsujimori and Ernst, 2014).

At Port Macquarie, maintenance of cold geothermal conditions during exhumation are supported by the preservation of pristine lawsonite and the formation of stage late aragonite veins that cross-cut the metamorphic mineral assemblages. The timing and depth at which the different-aged lawsonite eclogite and garnet blueschist became juxtaposed is uncertain and there are no direct constraints on the timing of their passage through their inferred retrograde conditions.

6.3 Tectonic framework for high-pressure metamorphism in East Gondwana

There are essentially two models for the development of the Gondwanan orogens in eastern Australia. One model is that formation of the orogens was controlled by a long-lived west-dipping subduction system that progressively migrated oceanward (eastwards) during the Palaeozoic (e.g. Collins, 2002; Phillips and Offler, 2011; Moresi et al., 2014; Phillips et al., 2015). This proto-Pacific system created a back-arc regime in which sedimentary sequences accumulated in extensional basins (Collins, 2002; Kemp et al., 2009; Moresi et al., 2014). This geodynamically extensional regime was punctuated by transient shortening events that reflected changing dynamics on the subductive margin (e.g. Collins, 2002). Metamorphism accompanying these shortening events was high thermal gradient in character, consistent with thinned back arc lithosphere, and was characterised by voluminous S and I-type magmatism (Collins and Richards, 2008).

The physio-mechanical plausibility of this model has been underpinned by 3D numerical geodynamic experiments. Modelling by Moresi et al. (2014) explored the consequence of partial pinning of the East Gondwana margin by the arrival of a small continental collider (Figure 12). Where the margin was not pinned by the collider, slab rollback was associated with arc migration and infilling of an extending back-arc environment. Between ca. 500 Ma and 460 Ma, up to 1500 km of dynamically predicted rollback (Moresi et al., 2014), recreates the complex macroscopic tectonic architecture of Australia's eastern margin remarkably well, and validates the plausibility of a single long-lived subduction system controlling the geodynamic development of the east Gondwanan margin.

The second model for the development of the east Australian orogens is more complex and involves formation of numerous subduction systems and subduction polarity reversals, coupled with accretion of exotic terrains inferred to comprise parts of the New England Orogen which forms the most outboard of the east Australian orogens (Aitchison and Buckman, 2012; Buckman et al., 2015; Manton et al., 2017). An element of these tectonic models is that the high-pressure metamorphism at Port Macquarie occurred in the early Triassic

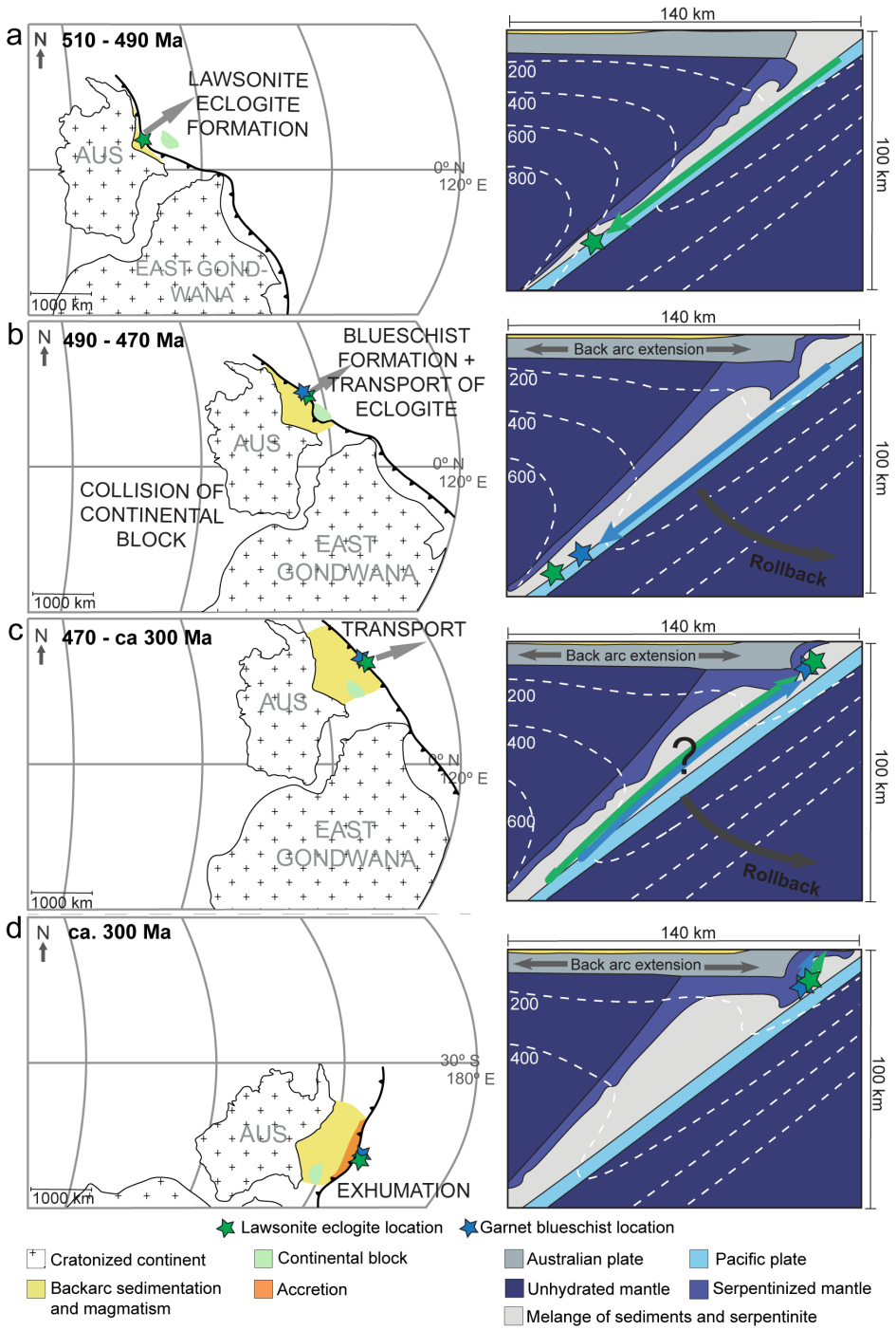


Figure 12: Simplified geodynamic model for the evolution of the east Gondwanan margin throughout the Palaeozoic. Left hand panels show the location and style of crust-building, with the collision of a continental block after Moresi, Betts, Miller, and Cayley (2014). Right hand panels show a cross-section through a model subduction zone with the location of the lawsonite eclogite and garnet blueschist adapted from numerical models by Gerya, Stöckhert, and Perchuk (2002). a) During the Ross/Delamerian Orogen, the lawsonite eclogite is formed. b) Slab rollback followed the termination of the Ross/Delamerian Orogen. The garnet blueschist is subducted, and the collision of a continental block affects the southern margin. c) Rollback continues, the eclogites are trapped within the subduction channel however their depth is unknown. d) The New England Orogen initiates ca. 160 Ma later, the high-pressure rocks are exhumed within their hosting serpentinite, at least ca. 1500 km from the location of their initial subduction.

(Nutman et al., 2013) in response to terrain accretion. However, the age data presented in this paper shows that high-pressure metamorphism at Port Macquarie is Cambro-Ordovician in age, and not Triassic. Furthermore, recent work (Glen et al., 2011; Li et al., 2015; Hoy and Rosenbaum, 2017), has shown the supposed exotic terrains in this second model are likely to have been derived from cratonic Australia. Given these constraints, the simplest and most geodynamically plausible interpretation is the Australian margin of east Gondwana developed in response to a long-lived west-dipping subduction system that bordered the palaeo-Pacific Ocean and whose locus migrated eastward during the Palaeozoic.

6.4 Accumulation of high-pressure products and spatial translation during slab rollback

The geochronological data from Port Macquarie suggests that high-pressure rocks accumulated in a subduction channel over an interval of at least ca. 20 m.y., as demonstrated by the age difference between garnet in the lawsonite eclogite and the garnet blueschist (Figure 11). Timescales from ca. 515–480 Ma have been suggested for subduction and exhumation of eclogite at Attunga in the SNEO (Phillips et al., 2015; Manton et al., 2017). K–Ar and $^{40}Ar/^{39}Ar$ geochronology on blueschist facies rocks at Glenrock, Pigna Barney and Port Macquarie (Figure 1) gives ages between 483–470 Ma (Fukui et al., 1995; Phillips et al., 2015). These periods between eclogite formation at Attunga and blueschist formation elsewhere in the SNEO have been used to suggest extended durations of subduction metamorphism, albeit the time scale has been derived from across widely separated samples (Figure 11; Phillips et al., 2015).

Timeframes of the order determined for the record of high-pressure metamorphism in the Port Macquarie mélange have been suggested for durations of high-pressure metamorphism and accumulation in serpentinite or sediment filled oceanic-hosted subduction systems elsewhere. Examples of long-lived accumulation have been documented in the Carribean (Tsujimori et al., 2006; Krebs et al., 2008; Krebs et al.,, 2011; Schertl et al., 2012). In the Dominican Republic, blocks of eclogite, jadiete blueschist and omphacite blueschist in serpentinite mélange record subduction over ca. 40 m.y., constrained by Lu–Hf, Rb–Sr and $^{40}Ar/^{39}Ar$ age data (Krebs et al., 2008). Within the same system in eastern Cuba, ca. 55 m.y. of subduction and exhumation is recorded from U–Pb zircon and $^{40}Ar/^{39}Ar$ data obtained from six blocks of migmatized amphibolite (Lázaro et al., 2009). White mica and amphibole $^{40}Ar/^{39}Ar$ ages from several high-pressure blocks within the Franciscan Complex suggest that subduction and high-pressure metamorphism spanned at least 80 m.y. (Wakabayashi and Dumitru, 2007). Franciscan eclogites also record ca. 7 m.y. between eclogite and overprinting lawsonite-blueschist metamorphism

in the same sample (Anczkiewicz et al.,, 2004; Mulcahy et al., 2009). In Zagros, blueschists (some containing lawsonite) record cooling from ca. 90 to 65 Ma from Rb–Sr data (Angiboust et al., 2016), or ca. 105 to 85 Ma from in-situ $^{40}Ar/^{39}Ar$ geochronology (Agard et al., 2006; Monie and Agard, 2009). However in contrast to serpentinite-hosted tectonic blocks, the Zagros high-pressure rocks were exhumed as coherent 'slices'. In another non-mélange example, lawsonite and non-lawsonite bearing high-pressure rocks in Turkey were dated by Lu–Hf techniques, and show a span of prograde ages between ca. 105 and 86 Ma (Mulcahy et al., 2014; Pourteau et al., 2018). This is further supported by $^{40}Ar/^{39}Ar$ data which points to retrograde and prograde high-pressure metamorphism from ca. 100 Ma to ca. 75 Ma (Fornash et al., 2016). Finally, in the currently active Mariana subduction system, blueschist from recently erupted serpentinite-mud volcanism on forearc trench slope formed in the Eoecene, pointing to ca. 48 m.y. of residence time in the subduction channel (Tamblyn et al., 2019).

Based on the examples above, and the difference in age and *P–T* conditions recorded by the lawsonite eclogite and garnet blueschist in this study, it seems likely the Port Macquarie mélange records accumulation and mixing of newly subducted material with material that had already been subducted. This accumulation of subduction products is consistent with 2D modelling of serpentinised subduction channels (e.g. Gerya et al., 2002). These models predict mélange can accumulate rocks with different *P–T–t* histories that effectively record different points and times in the evolution of the subduction channel. A further prediction of these models is that widening of the subduction channel and return flow from mantle depths (ca. 80 km) requires timeframes of at least ca. 25 m.y. after the initiation of subduction (Gerya et al., 2002). This may provide some explanation for long timeframes between subduction of material and either its accumulation and/or exhumation.

The ages of the Port Macquarie eclogite and blueschist are similar to the age of serperninite hosted eclogite and blueschist eslewehere in the Southern New England Orogen (SNEO; Fukui et al., 1995; Sano et al., 2004; Och et al.,, 2003; Phillips, 2010; Phillips and Offler, 2011; Phillips et al., 2015; Manton et al.,, 2017). These Cambro-Orodvician high-pressure rocks now reside within the forearc system of a Devonian-Carboniferous orogen. Logically, these high-pressure rocks must have been metamorphosed during an older phase of subduction to that which created the younger SNEO. This is aligned with the long-lived west-dipping subduction model for eastern Palaeozoic Australia (e.g. Collins, 2002; Kemp et al., 2009; Moresi et al., 2014). Palaeotectonic models sugget late Cambrian-early Ordovician subduction was located much closer to the ancient craton margin (Figure 12). If

this is correct, it suggests the high pressure rocks in the SNEO were transported over ca. 1500 km from their initial position of subduction. Moresi et al. (2014) also showed it was thermomechanically feasible for more than 1000 km of eastward trench retreat during the Ordovician and into the early Silurian. Logically this transport occurred during slab roll back while the subduction material was entrained within the subduction channel.

A simplified geodynamic evolution of the Australian margin during the formation and accumulation of the high-pressure rocks in the Port Macquarie mélange is shown in Figure 12. It provides a geodynamic context for the subduction and accumulation of the lawsonite eclogite and garnet blueschist with the tectonic evolution of the upper plate. It also provides a mechanism for translocation of high-pressure rocks now located in the SNEO from their probable formation nearer the margin of cratonic of Australia, to their current position in the forearc system of the youngest and most outboard of the eastern Australian Gondwanan orogens.

The formation of the lawsonite eclogite coincides with the latter stages of the Ross-Delamerian Orogeny (514–490 Ma), which flanks cratonic Australia and forms the oldest and most inboard of the eastern Australian Palaeozoic orogens (Figure 12a; Phillips and Offler, 2011; Phillips et al., 2015). Pinning of part of this system by accretion of a continental block led to subsequent eastward slab retreat (Moresi et al., 2014), which allowed opening of a large back arc basin and accumulation of sediments and magmatic rocks on the upper plate (Figure 12b; Glen et al., 2011; Phillips et al., 2015). On-going subduction is recorded by the garnet blueschist at Port Macquarie (Figure 12b). Unfortunately, subsequent to ca. 470 Ma and prior to final exhumation of the serpentinite mélange in the early Permian (Aitchison et al., 1994), there is no record of the location of the high-pressure material now located at Port Macquarie within the SNEO. However, given the absence of serpentinite detritus in sequences in the SNEO until the Permian (Aitchison et al., 1994), we suggest the high-pressure rocks remained buried in a low temperature environment that allowed the preservation of lawsonite and aragonite-bearing assemblages. The incorporation of the high-pressure rocks into the Devonian–Carboniferous accretionary complex in the SNEO suggests the Cambro–Ordovician subduction products were able to continue their migration outboard until at least the Carboniferous, more than 200 m.y. after they formed (Figure 12d).

7. Conclusions

Serpentinite mélange at Port Macquarie in the southern New England Fold Belt, eastern Australia, contains blocks of eclogite and blueschist that formed during early Palaeozoic subduction

of the Protopacific plate beneath east Gondwana. Lawsonite eclogite formed at around 590 °C and 2.7 GPa, and eclogite now retrogressed to garnet blueschist formed at around 2.0 GPa and 550 °C. Despite their current proximity to each other, garnet Lu–Hf and Sm–Nd dating indicates the high-pressure rocks formed at different times. Lawsonite eclogite formed at ca. 490 Ma, whereas the garnet-omphacite bearing precursor to blueschist formed at ca. 470 Ma. The different ages of eclogite metamorphism indicates progressively created subduction products accumulated within the subduction channel and experienced different *P–T–t* evolutions. This is consistent with numerical modeling that predicts mixing of subduction products within serpentinite-filled subduction channels. The interval over which metamorphism of the high-pressure rocks occurred coincides with subduction rollback on the Australian segment of the east Gondwanan margin. Rollback and migration of the subduction channel appears to have transported the high-pressure rocks more than ca. 1500 km oceanward, where they underwent final exhumation within a younger orogen whose development, while geodynamically associated, was not responsible for the formation of the high-pressure rocks. Thermal durations recorded by oceanic hosted high-pressure low-temperature rocks may encompass tens of millions of years, recording long residence times within subduction channels. Over these timescales, subduction zone migration is likely to occur, potentially transporting subducted rocks large distances prior to their exhumation. The *P–T–t* records of accumulated tectonic blocks in serpentinite mélange provide an avenue to interrogate the thermal histories of palaeosubduction systems as they evolve.

Acknowledgements

We are grateful to Laura Morrissey for assistance with the phase equilibria modelling and to Justin Payne for his assistance with the U–Pb geochronology. Kiara Alessio and Mark Pearce are thanked for discussions regarding post processing of petrological modelling data. Ben Wade at Adelaide Microscopy is also thanked for his technical assistance with data collection. Diana Zivak is thanked for assisting with acquisition of WDS Zr mapping and BSE imaging of zircon. C. L. Friend and two anonymous reviewers are thanked for their contributions to the manuscript, and Bernardo Cesare is thanked for his editorial handing. This research was in part supported by Australian Research Council grant DP160104637.

References

Agard, P., Monié, P., Gerber, W., Omrani, J., Molinaro, M., Meyer, B., . . . Yamato, P. (2006). Transient, synobduction exhumation of Zagros blueschists inferred from P-T, deformation, time, and kinematic constraints: Implications for Neotethyan

wedge dynamics. *Journal of Geophysical Research: Solid Earth*, 111(B11).

Agard, P., Yamato, P., Jolivet, L., and Burov, E. (2009). Exhumation of oceanic blueschists and eclogites in subduction zones: timing and mechanisms. *Earth-Science Reviews, 92*(1), 53-79.

Aitchison, J. C., Blake, M. C., Flood, P. G., & Jayko, A. S. (1994). Paleozoic ophiolitic assemblages within the southern New England orogen of eastern Australia: Implications for growth of the Gondwana margin. *Tectonics*, 13(5), 1135-1149. doi: 10.1029/93TC03550

Aitchison, J. C., & Buckman, S. (2012). Accordion vs. quantum tectonics: Insights into continental growth processes from the Paleozoic of eastern Gondwana. *Gondwana Research*, 22(2), 674-680.

Aitchison, J., and Ireland, T. (1995). Age profile of ophiolitic rocks across the Late Palaeozoic New England Orogen, New South Wales: implications for tectonic models. *Australian Journal of Earth Sciences, 42*(1), 11-23.

Anczkiewicz, R., Platt, J. P., Thirlwall, M. F., and Wakabayashi, J. (2004). Franciscan subduction off to a slow start: evidence from high-precision Lu–Hf garnet ages on high grade-blocks. *Earth and Planetary Science Letters, 225*(1), 147-161.

Anczkiewicz, R., Szczepański, J., Mazur, S., Storey, C., Crowley, Q., Villa, I. M., Thirlwall, M. F., and Jeffries, T. E. (2007). Lu–Hf geochronology and trace element distribution in garnet: implications for uplift and exhumation of ultra-high pressure granulites in the Sudetes, SW Poland. *Lithos, 95*(3-4), 363-380.

Anczkiewicz, R., and Thirlwall, M. F. (2003). Improving precision of Sm-Nd garnet dating by H2SO4 leaching: a simple solution to the phosphate inclusion problem. *Geological Society, London, Special Publications, 220*(1), 83-91.

Angiboust, S., Agard, P., Glodny, J., Omrani, J., and Oncken, O. (2016). Zagros blueschists: Episodic underplating and long-lived cooling of a subduction zone. *Earth and Planetary Science Letters, 443*, 48-58.

Aranovich, L. Y., Bortnikov, N., Zinger, T., Borisovskiy, S., Matrenichev, V., Pertsev, A., Sharkov, E., and Skolotnev, S. (2017). Morphology and impurity elements of zircon in the oceanic lithosphere at the Mid-Atlantic ridge axial zone (6°–13° N): Evidence of specifics of magmatic crystallization and postmagmatic transformations. *Petrology, 25*(4), 339-364.

Ayers, J. C., Zhang, L., Luo, Y., and Peters, T. (2012). Zircon solubility in alkaline aqueous fluids at upper crustal conditions. *Geochimica et Cosmochimica Acta, 96*, 18-28.

Baitsch-Ghirardello, B., Gerya, T. V., and Burg, J.-P. (2014). Geodynamic regimes of intra-oceanic subduction: Implications for arc extension vs. shortening processes. *Gondwana Research, 25*(2), 546-560.

Barron, B., Scheibner, E., and Slanskīī, E. N. (1976). *A dismembered ophiolite suite at Port Macquarie, New South Wales*: New South Wales Department of Mines.

Bebout, G. E., and Barton, M. D. (2002). Tectonic and metasomatic mixing in a high-T, subduction-zone mélange—insights into the geochemical evolution of the slab–mantle interface. *Chemical Geology, 187*(1-2), 79-106.

Becker, H., Jochum, K. P., and Carlson, R. W. (2000). Trace element fractionation during dehydration of eclogites from high-pressure terranes and the implications for element fluxes in subduction zones. *Chemical Geology, 163*(1), 65-99.

Blichert-Toft, J., and Frei, R. (2001). Complex Sm-Nd and Lu-Hf isotope systematics in metamorphic garnets from the Isua supracrustal belt, West Greenland. *Geochimica et Cosmochimica Acta, 65*(18), 3177-3189.

Brovarone, A. V., Groppo, C., Hetényi, G., Compagnoni, R., and Malavieille, J. (2011). Coexistence of lawsonite-bearing eclogite and blueschist: phase equilibria modelling of Alpine Corsica metabasalts and petrological evolution of subducting slabs. *Journal of Metamorphic Geology, 29*(5), 583-600.

Buckman, S., Nutman, A. P., Aitchison, J. C., Parker, J., Bembrick, S., Line, T., Hidaka, H., and Kamiichi, T. (2015). The Watonga Formation and Tacking Point Gabbro, Port Macquarie, Australia: insights into crustal growth mechanisms on the eastern margin of Gondwana. *Gondwana Research, 28*(1), 133-151.

Carswell, D., Wilson, R., and Zhai, M. (1996). Ultra-high pressure aluminous titanites in carbonate-bearing eclogites at Shuanghe in Dabieshan, central China. *Mineralogical Magazine, 60*(3), 461-471.

Castelli, D., and Rubatto, D. (2002). Stability of Al-and F-rich titanite in metacarbonate: petrologic and isotopic constraints from a polymetamorphic eclogitic marble of the internal Sesia Zone (Western Alps). *Contributions to Mineralogy and Petrology, 142*(6), 627-639.

Collins, W., and Richards, S. (2008). Geodynamic significance of S-type granites in circum-Pacific orogens. *Geology, 36*(7), 559-562.

Collins, W. J. (2002). Nature of extensional accretionary orogens. *Tectonics, 21*(4).

Diener, J., and Powell, R. (2012). Revised activity–composition models for clinopyroxene and amphibole. *Journal of Metamorphic Geology, 30*(2), 131-142.

Droop, G. (1987). A general equation for estimating Fe3+ concentrations in ferromagnesian silicates and oxides from microprobe analyses, using stoichiometric criteria. *Mineralogical Magazine, 51*(361), 431-435.

Enami, M., Suzuki, K., Liou, J., and Bird, D. K. (1993). Al-Fe3+ and F-OH substitutions in titanite and constraints on their PT dependence. *European Journal of Mineralogy, 5*(2), 219-231.

Ernst, W. (1988). Tectonic history of subduction zones inferred from retrograde blueschist PT paths. *Geology*, 16(12), 1081-1084.

Federico, L., Crispini, L., Scambelluri, M., and Capponi, G. (2007). Ophiolite mélange zone records exhumation in a fossil subduction channel. *Geology, 35*(6), 499-502.

Fornash, K. F., Cosca, M. A., and Whitney, D. L. (2016). Tracking the timing of subduction and exhumation using 40 Ar/39 Ar phengite ages in blueschist-and eclogite-facies rocks (Sivrihisar, Turkey). *Contributions to Mineralogy and Petrology, 171*(7), 67.

Fukui, S., Watanabe, T., Itaya, T., and Leitch, E. C. (1995). Middle Ordovician high PT metamorphic rocks in eastern Australia: Evidence from K-Ar ages. *Tectonics, 14*(4), 1014-1020.

Ganguly, J., Tirone, M., and Hervig, R. (1998). Diffusion kinetics of samarium and neodymium in garnet, and a method for determining cooling rates of rocks. *Science, 281*(5378), 805-807.

Gerya, T. (2011). Future directions in subduction modeling. *Journal of Geodynamics, 52*(5), 344-378.

Gerya, T. V., Stöckhert, B., and Perchuk, A. L. (2002). Exhumation of high-pressure metamorphic rocks in a subduction channel: A numerical simulation. *Tectonics, 21*(6).

Glen, R. (2013). Refining accretionary orogen models for the Tasmanides of eastern Australia. *Australian Journal of Earth Sciences, 60*(3), 315-370.

Glen, R., Saeed, A., Quinn, C., and Griffin, W. (2011). U–Pb and Hf isotope data from zircons in the Macquarie Arc, Lachlan Orogen: Implications for arc evolution and Ordovician palaeogeography along part of the east Gondwana margin. *Gondwana Research, 19*(3), 670-685.

Green, E., Holland, T., and Powell, R. (2007). An order-disorder model for omphacitic pyroxenes in the system jadeite-diopside-hedenbergite-acmite, with applications to eclogitic rocks. *American Mineralogist, 92*(7), 1181-1189.

Green, E., White, R., Diener, J., Powell, R., Holland, T., and Palin, R. (2016). Activity–composition relations for the calculation of partial melting equilibria in metabasic

rocks. *Journal of Metamorphic Geology, 34*(9), 845-869.

Griffin, W., Belousova, E., Shee, S., Pearson, N., and O'reilly, S. (2004). Archean crustal evolution in the northern Yilgarn Craton: U–Pb and Hf-isotope evidence from detrital zircons. *Precambrian Research, 131*(3-4), 231-282.

Grimes, C. B., John, B. E., Cheadle, M. J., Mazdab, F. K., Wooden, J. L., Swapp, S., and Schwartz, J. J. (2009). On the occurrence, trace element geochemistry, and crystallization history of zircon from in situ ocean lithosphere. *Contributions to Mineralogy and Petrology, 158*(6), 757.

Guillot, S., Hattori, K., Agard, P., Schwartz, S., and Vidal, O. (2009). Exhumation processes in oceanic and continental subduction contexts: a review *Subduction zone geodynamics* (pp. 175-205): Springer.

Hermann, J., and Rubatto, D. (2014). Subduction of continental crust to mantle depth: geochemistry of ultrahigh-pressure rocks *Treatise on Geochemistry, 2nd Edition*: Elsevier.

Holland, T., and Powell, R. (1998). An internally consistent thermodynamic data set for phases of petrological interest. *Journal of Metamorphic Geology, 16*(3), 309-343.

Holland, T., & Powell, R. (2003). Activity–composition relations for phases in petrological calculations: an asymmetric multicomponent formulation. *Contributions to Mineralogy and Petrology*, 145(4), 492-501.

Holland, T., and Powell, R. (2011). An improved and extended internally consistent thermodynamic dataset for phases of petrological interest, involving a new equation of state for solids. *Journal of Metamorphic Geology, 29*(3), 333-383.

Hoy, D., and Rosenbaum, G. (2017). Episodic behavior of Gondwanide deformation in eastern Australia: Insights from the Gympie Terrane. *Tectonics*.

Jenkins, R., Landenberger, B., and Collins, W. (2002). Late Palaeozoic retreating and advancing subduction boundary in the New England fold belt, New South Wales. *Australian Journal of Earth Sciences, 49*(3), 467-489.

Kemp, A., Hawkesworth, C., Collins, W., Gray, C., and Blevin, P. (2009). Isotopic evidence for rapid continental growth in an extensional accretionary orogen: The Tasmanides, eastern Australia. *Earth and Planetary Science Letters, 284*(3), 455-466.

Krebs, M., Maresch, W., Schertl, H.-P., Münker, C., Baumann, A., Draper, G., Idleman, B., and Trapp, E. (2008). The dynamics of intra-oceanic subduction zones: a direct comparison between fossil petrological evidence (Rio San Juan Complex, Dominican Republic) and numerical simulation. *Lithos, 103*(1), 106-137.

Krebs, M., Schertl, H.-P., Maresch, W., and Draper, G. (2011). Mass flow in serpentinite-hosted subduction channels: P–T–t path patterns of metamorphic blocks in the Rio San Juan mélange (Dominican Republic). *Journal of Asian Earth Sciences, 42*(4), 569-595.

Lanari, P., Vidal, O., De Andrade, V., Dubacq, B., Lewin, E., Grosch, E. G., and Schwartz, S. (2014). XMapTools: A MATLAB©-based program for electron microprobe X-ray image processing and geothermobarometry. *Computers and Geosciences, 62*, 227-240.

Lapen, T. J., Johnson, C. M., Baumgartner, L. P., Mahlen, N. J., Beard, B. L., and Amato, J. M. (2003). Burial rates during prograde metamorphism of an ultra-high-pressure terrane: an example from Lago di Cignana, western Alps, Italy. *Earth and Planetary Science Letters, 215*(1), 57-72.

Lázaro, C., García-Casco, A., Rojas Agramonte, Y., Kröner, A., Neubauer, F., and Iturralde-Vinent, M. (2009). Fifty-five-million-year history of oceanic subduction and exhumation at the northern edge of the Caribbean plate (Sierra del Convento mélange, Cuba). *Journal of Metamorphic Geology, 27*(1), 19-40.

Li, P., Rosenbaum, G., Yang, J. H., and Hoy, D. (2015). Australian-derived detrital zircons in the Permian-Triassic Gympie terrane (eastern Australia): Evidence for an autochthonous origin. *Tectonics, 34*(5), 858-874.

Lü, Z., Lifei, Z., Yue, J., and Li, X. Ultrahigh-pressure and high-pressure lawsonite eclogites in Muzhaerte, Chinese western Tianshan. *Journal of Metamorphic Geology*.

Ludwig, K. (2003). *User's manual for Isoplot 3.00: a geochronological toolkit for Microsoft Excel*: Kenneth R. Ludwig.

Manton, R. J., Buckman, S., Nutman, A. P., and Bennett, V. C. (2017). Exotic island arc Paleozoic terranes on the eastern margin of Gondwana: Geochemical whole rock and zircon U–Pb–Hf isotope evidence from Barry Station, New South Wales, Australia. *Lithos, 286*, 125-150.

Martin, L., Hermann, J., Gauthiez-Putallaz, L., Whitney, D., Vitale Brovarone, A., Fornash, K., and Evans, N. J. (2014). Lawsonite geochemistry and stability–implication for trace element and water cycles in subduction zones. *Journal of Metamorphic Geology, 32*(5), 455-478.

Monie, P., & Agard, P. (2009). Coeval blueschist exhumation along thousands of kilometers: Implications for subduction channel processes. *Geochemistry, Geophysics, Geosystems*, 10(7).

Moresi, L., Betts, P., Miller, M., and Cayley, R. (2014). Dynamics of continental accretion. *Nature, 508*(7495), 245-248.

Mulcahy, S., Vervoort, J., and Renne, P. (2014). Dating subduction-zone metamorphism with combined garnet and lawsonite Lu–Hf geochronology. *Journal of Metamorphic Geology, 32*(5), 515-533.

Mulcahy, S. R., King, R. L., and Vervoort, J. D. (2009). Lawsonite Lu-Hf geochronology: A new geochronometer for subduction zone processes. *Geology, 37*(11), 987-990.

Nutman, A. P., Buckman, S., Hidaka, H., Kamiichi, T., Belousova, E., and Aitchison, J. (2013). Middle Carboniferous-Early Triassic eclogite–blueschist blocks within a serpentinite mélange at Port Macquarie, eastern Australia: Implications for the evolution of Gondwana's eastern margin. *Gondwana Research, 24*(3-4), 1038-1050.

Och, D., Leitch, E., Caprarelli, G., and Watanabe, T. (2003). Blueschist and eclogite in tectonic melange, port macquarie, new south wales, australia. *Mineralogical Magazine, 67*(4), 609-624.

Och, D., Leitch, E., & Caprarelli, G. (2007). Geological units of the Port Macquarie-Tacking Point tract, north-eastern Port Macquarie Block, Mid North Coast region of NSW. *Quarterly Notes Geological Survey of New South Wales*.

Och, D. J. (2007). *Eclogite, serpentinite, mélange and mafic intrusive rocks: manifestation of long-lived Palaeozoic convergent margin activity, Port Macquarie, eastern Australia*. Doctoral dissertation.

Otamendi, J. E., de La Rosa, J. D., Douce, A. E. P. o., and Castro, A. (2002). Rayleigh fractionation of heavy rare earths and yttrium during metamorphic garnet growth. *Geology, 30*(2), 159-162.

Paton, C., Hellstrom, J., Paul, B., Woodhead, J., & Hergt, J. (2011). Iolite: Freeware for the visualisation and processing of mass spectrometric data. *Journal of Analytical Atomic Spectrometry*, 26(12), 2508-2518.

Peacock, S. M. (2003). Thermal structure and metamorphic evolution of subducting slabs. *Geophysical Monograph-American Geophysical Union, 138*, 7-22.

Phillips, G. (2010). Discontinuous or slow exhumation after subduction-evidence from high-pressure rocks in the Peel Manning Fault system. *New England Orogen 2010*, 267.

Phillips, G., and Offler, R. (2011). Contrasting modes of eclogite and blueschist exhumation in a retreating subduction system: The Tasmanides, Australia. *Gondwana Research, 19*(3), 800-811.

Phillips, G., Offler, R., Rubatto, D., and Phillips, D. (2015). High-pressure metamorphism in the southern New England Orogen: Implications for long-lived accretionary orogenesis in eastern Australia. *Tectonics, 34*(9), 1979-2010.

Pourteau, A., Scherer, E. E., Schorn, S., Bast, R.,

Schmidt, A., and Ebert, L. (2019). Thermal evolution of an ancient subduction interface revealed by Lu–Hf garnet geochronology, Halilbağı Complex (Anatolia). *Geoscience Frontiers, 10*(1), 127-148.

Powell, R., and Holland, T. (1988). An internally consistent dataset with uncertainties and correlations: 3. Applications to geobarometry, worked examples and a computer program. *Journal of Metamorphic Geology, 6*(2), 173-204.

Puga, E., Fanning, C. M., Nieto, J. M., and De Federico, A. D. (2005). Recrystallization textures in zircon generated by ocean-floor and eclogite-facies metamorphism: a cathodoluminescence and U–Pb SHRIMP study, with constraints from REE elements. *The Canadian Mineralogist, 43*(1), 183-202.

Ravna, E., Andersen, T. B., Jolivet, L., & De Capitani, C. (2010). Cold subduction and the formation of lawsonite eclogite–constraints from prograde evolution of eclogitized pillow lava from Corsica. *Journal of metamorphic Geology*, 28(4), 381-395.

Rawlinson, N., Arroucau, P., Musgrave, R., Cayley, R., Young, M., and Salmon, M. (2014). Complex continental growth along the proto-Pacific margin of East Gondwana. *Geology, 42*(9), 783-786.

Rubatto, D., and Hermann, J. r. (2007). Zircon behaviour in deeply subducted rocks. *Elements, 3*(1), 31-35.

Rubatto, D., Müntener, O., Barnhoorn, A., and Gregory, C. (2008). Dissolution-reprecipitation of zircon at low-temperature, high-pressure conditions (Lanzo Massif, Italy). *American Mineralogist, 93*(10), 1519-1529.

Ruh, J. B., Le Pourhiet, L., Agard, P., Burov, E., and Gerya, T. (2015). Tectonic slicing of subducting oceanic crust along plate interfaces: Numerical modeling. *Geochemistry, Geophysics, Geosystems, 16*(10), 3505-3531.

Sano, S., Offler, R., Hyodo, H., and Watanabe, T. (2004). Geochemistry and chronology of tectonic blocks in serpentinite mélange of the southern New England Fold Belt, NSW, Australia. *Gondwana Research, 7*(3), 817-831.

Scherer, E. E., Cameron, K. L., and Blichert-Toft, J. (2000). Lu–Hf garnet geochronology: closure temperature relative to the Sm–Nd system and the effects of trace mineral inclusions. *Geochimica et Cosmochimica Acta, 64*(19), 3413-3432.

Schertl, H.-P., Maresch, W. V., Stanek, K. P., Hertwig, A., Krebs, M., Baese, R., & Sergeev, S. S. (2012). New occurrences of jadeitite, jadeite quartzite and jadeite-lawsonite quartzite in the Dominican Republic, Hispaniola: petrological and geochronological overview. *European Journal of*

Mineralogy, 24(2), 199-216.

Sircombe, K. N. (1999). Tracing provenance through the isotope ages of littoral and sedimentary detrital zircon, eastern Australia. *Sedimentary Geology, 124*(1-4), 47-67.

Skora, S., Baumgartner, L. P., Mahlen, N. J., Johnson, C. M., Pilet, S., and Hellebrand, E. (2006). Diffusion-limited REE uptake by eclogite garnets and its consequences for Lu–Hf and Sm–Nd geochronology. *Contributions to Mineralogy and Petrology, 152*(6), 703-720.

Spandler, C., Hermann, J., Arculus, R., and Mavrogenes, J. (2003). Redistribution of trace elements during prograde metamorphism from lawsonite blueschist to eclogite facies; implications for deep subduction-zone processes. *Contributions to Mineralogy and Petrology, 146*(2), 205-222.

Spandler, C., Hermann, J. r., and Rubatto, D. (2004). Exsolution of thortveitite, yttrialite, and xenotime during low-temperature recrystallization of zircon from New Caledonia, and their significance for trace element incorporation in zircon. *American Mineralogist, 89*(11-12), 1795-1806.

Stöckhert, B., and Gerya, T. V. (2005). Pre-collisional high pressure metamorphism and nappe tectonics at active continental margins: A numerical simulation. *Terra Nova, 17*(2), 102-110.

Tamblyn, R., Zack, T., Schmitt, A., Hand, M., Kelsey, D., Morrissey, L., Pabst, S., and Savov, I. (2019). Blueschist from the Mariana forearc records long-lived residence of material in the subduction channel. *Earth and Planetary Science Letters, 519*, 171-181.

Tomaschek, F., Kennedy, A. K., Villa, I. M., Lagos, M., and Ballhaus, C. (2003). Zircons from Syros, Cyclades, Greece—recrystallization and mobilization of zircon during high-pressure metamorphism. *Journal of Petrology, 44*(11), 1977-2002.

Tsujimori, T., and Ernst, W. (2014). Lawsonite blueschists and lawsonite eclogites as proxies for palaeo-subduction zone processes: a review. *Journal of Metamorphic Geology, 32*(5), 437-454.

Tsujimori, T., Sisson, V. B., Liou, J. G., Harlow, G. E., and Sorensen, S. S. (2006). Very-low-temperature record of the subduction process: A review of worldwide lawsonite eclogites. *Lithos, 92*(3), 609-624.

Wakabayashi, J., & Dumitru, T. A. (2007). 40Ar/39Ar ages from coherent, high-pressure metamorphic rocks of the Franciscan Complex, California: Revisiting the timing of metamorphism of the world's type subduction complex. *International Geology Review*, 49(10), 873-906.

Warren, C. J., Parrish, R. R., Waters, D. J., and

Searle, M. P. (2005). Dating the geologic history of Oman's Semail ophiolite: Insights from U-Pb geochronology. *Contributions to Mineralogy and Petrology, 150*(4), 403-422.

Wei, C., and Clarke, G. (2011). Calculated phase equilibria for MORB compositions: a reappraisal of the metamorphic evolution of lawsonite eclogite. *Journal of Metamorphic Geology, 29*(9), 939-952.

White, R., Powell, R., and Holland, T. (2007). Progress relating to calculation of partial melting equilibria for metapelites. *Journal of Metamorphic Geology, 25*(5), 511-527.

Whitney, D. L., and Davis, P. B. (2006). Why is lawsonite eclogite so rare? Metamorphism and preservation of lawsonite eclogite, Sivrihisar, Turkey. *Geology, 34*(6), 473-476.

Chapter 4:

Resubduction of lawsonite eclogite within a serpentinite-filled subduction channel

This chapter is published as:

Resubduction of lawsonite eclogite in serpentinite-filled subduction channel (2020). R. Tamblyn, M. Hand, L. Morrissey, T. Zack, G. Phillips, D. Och. *Contributions to Mineralogy and Petrology*, 175 (8), 1-22

The supplementary materials for this chapter can be found in Appendix 4

Statement of Authorship

Title of Paper	Resubduction of lawsonite eclogite within a serpentinite-filled subduction channel
Publication Status	[x] Published [ ] Accepted for Publication [ ] Submitted for Publication [ ] Unpublished and Unsubmitted w ork w ritten in manuscript style
Publication Details	Tamblyn, R., Hand, M., Morrissey, L., Zack, T., Phillips, G., & Och, D. (2020). Resubduction of lawsonite eclogite within a serpentinite-filled subduction channel. Contributions to Mineralogy and Petrology, 175(8), 1-22.

Principal Author

Name of Principal Author (Candidate)	Renée Tamblyn
Contribution to the Paper	Collected the Rb-Sr and U-Pb data Completed the mineral equilibria modelling Collected the mineral chemistry data Wrote the manuscript
Overall percentage (%)	80
Certification:	This paper reports on original research I conducted during the period of my Higher Degree by Research candidature and is not subject to any obligations or contractual agreements with a third party that would constrain its inclusion in this thesis. I am the primary author of this paper.
Signature	Date 04/03/2021

Co-Author Contributions

By signing the Statement of Authorship, each author certifies that:

i. the candidate's stated contribution to the publication is accurate (as detailed above);

ii. permission is granted for the candidate in include the publication in the thesis; and

iii. the sum of all co-author contributions is equal to 100% less the candidate's stated contribution.

Name of Co-Author	Martin Hand
Contribution to the Paper	Assisted with interpretations, reviewed the manuscript 5%
Signature	Date 03/03/2021

Name of Co-Author	Laura Morrissey
Contribution to the Paper	Assisted with interpretations, reviewed the manuscript 5%
Signature	Date 02/03/2021

Please cut and paste additional co-author panels here as required.

Name of Co-Author	Thomas Zack			
Contribution to the Paper	Assisted with Rb-Sr data collection, reviewed the manuscript			5%
Signature			Date	08/10/2020

Name of Co-Author	Glen Phillips			
Contribution to the Paper	Collected the Ar-Ar geochronological data			3%
Signature			Date	12/10/2020

Name of Co-Author	David Och			
Contribution to the Paper	Introduced us to the study area, reviewed the manuscript			2%
Signature			Date	16/02/2021

Highlights

- A second burial event is recognised in eclogite lawsonite
- Two hairpin-loop *P–T* paths occured within the subduction channel over ca. 50 My.
- The petrological record of recycling of HP–LT rocks in serpentinite may be cryptic

Abstract

Translating burial and exhumation histories from the petrological and geochronological record of high-pressure assemblages in subduction channels is key to understanding subduction channel processes. Convective return flow, either serpentinite or sediment hosted, has been suggested as a potential mechanism to retrieve rocks from significant depths and exhume them. Numerical modelling predicts that during convective flow, subducted material can be cycled within a serpentinite-filled subduction channel. Geochronological and petrological evidence for such cycling during subduction is preserved in lawsonite eclogite from serpentinite mélange in the Southern New England Orogen, eastern Australia. Ar–Ar, Rb–Sr phengite and U–Pb titanite geochronology, supported by phase equilibrium forward modelling and mineral zoning, suggest Cambro-Ordovician eclogite underwent two stages of burial separated by a stage of partial exhumation. The initial subduction of the eclogite at ca. 490 Ma formed porphyroblastic prograde-zoned garnet and lawsonite at approximate *P–T* conditions of at least 2.9 GPa and 600 °C. Partial exhumation to at least 2.0 GPa and 500 °C is recorded by garnet dissolution. Reburial of the eclogite resulted in growth of new Mg-rich garnet rims, growth of new prograde-zoned phengite and recrystallization of titanite at *P–T* conditions of approximately 2.7 GPa and 590 °C. U–Pb titanite, and Ar–Ar and Rb–Sr phengite ages constrain the timing of reburial to ca. 450 Ma. This was followed by a second exhumation event at approximately 1.9 GPa and 520 °C. These conditions fall along a cold approximate geotherm of 230 °C/GPa. The inferred changes in pressure suggest the lawsonite eclogite underwent depth cycling within the subduction channel. Geochronological data indicates that partial exhumation and reburial occurred over ca. 50 M.y., providing some estimation on the timescales of material convective cycling in the subduction channel.

1. Introduction

Metamorphism along cool geothermal gradients in subduction zones produces eclogite-facies mineral assemblages. These assemblages often preserve an abundance of prograde, peak and retrograde petrological relationships. For example, elemental zoning in garnet and micas can be preserved due to slow rates of diffusion, and temperature-sensitive minerals such as lawsonite can also be preserved (Tsujimori et al., 2006; Tsuji-

mori and Ernst, 2014). Given this potential to preserve extensive petrological relationship histories, methods such as phase equilibrium modelling coupled with new and emerging geochronological techniques open avenues to explore the pressure–temperature–time (*P–T–t*) histories of these high-pressure low-temperature assemblages, and make inferences about the behaviour of the subduction systems that host them.

The application of sophisticated petrological techniques to eclogite and blueschist assemblages has highlighted the potential for complex *P–T–t* histories. This is particularly apparent in serpentinite mélanges. Mixing, accumulation, long-lived residence and intrachannel circulation of high-pressure lithologies have started to emerge as common phenomena within subduction channels (e.g. Krebs et al., 2008; Lázaro et al., 2009). Numerical modelling has sought to explain the dynamics of material within subduction channels, and has demonstrated that complex *P–T–t* histories are possible, arising from cycling and corner flow within the channel (Gerya et al, 2002, Stöckhert and Gerya, 2005; Roda et al., 2019). Examples of high-pressure rocks that have seen two or more cycles of burial have been recognised through geochronological and mineralogical evidence, for example, dating zones within metamorphic zircon (e.g. Liati et al., 2016). However, in lieu of such useful petrochronological methods, recognising multiple burial cycles can prove difficult.

Lawsonite eclogite is globally rare, despite the range of bulk compositions that support the formation of lawsonite-garnet-omphacite (Wei and Clarke, 2011). Therefore, their occurrence probably reflects unusually good preservation of deeply buried, cold subducted material. Consequently, lawsonite eclogites potentially preserve comprehensive records of the physical conditions of subduction channels. This study presents detailed petrological results from eclogite in the Southern New England Orogen (SNEO), that supports partial exhumation and reburial of a single block of lawsonite eclogite during on-going subduction. Phase diagrams constrain the approximate pressure–temperature (*P–T*) conditions of partial exhumation and reburial within the subduction channel, which is supported by U–Pb titanite, and Rb–Sr and Ar–Ar phengite geochronological data. The cycle of exhumation and reburial records an approximate total pressure and temperature fluctuation of at least 1.6 GPa and 190 °C and is constrained to have occurred over ca. 50 M.y.. If the pressure fluctuations recorded by high-pressure mineral assemblages reflect oscillations in burial depths, such records support the notion of convective flow within the subduction channel.

2. Geological setting

2.1 The Southern New England Orogen

The Southern New England Orogen (SNEO) in

eastern Australia is the youngest and most outboard orogen of the Tasmanides (Fig. 1a; Kemp et al., 2009; Glen, 2013; Phillips et al., 2015). The Tasmanides are interpreted to have formed as a result of long-lived subduction on the East Gondwanan margin during the Cambrian–Triassic, which resulted in a series of eastwards-younging orogens. The oldest and most westerly of these is the Delamerian Orogen, which formed at ca. 515–490 Ma on the margin of cratonic Australia, and was post-dated by the Lachlan-Thompson Orogen at ca. 484–340 Ma (Fig. 1a). The SNEO formed between the upper Devonian-Triassic, and consists of a volcanic arc, forearc basin and accretionary complex (Fig. 1b; Jenkins et al., 2002; Jessop et al., 2019). The Devonian-Carboniferous volcanic arc outcrops, but is generally obscured under the younger Permian-Triassic Sydney-Gunnedah basin (Jenkins et al., 2002). The Tamworth Belt contains a forearc basin, consisting of felsic volcanic rocks and volcaniclastics (Roberts and James, 2010). The Tablelands Complex consists of deformed sediments and oceanic basalt that accumulated within an accretionary complex. These are separated by the serpentinite-bearing Peel Manning Fault System (Fig. 1b). The SNEO also contains numerous felsic magmatic rocks of the Permian-Triassic New England Batholith, which intrude the Tablelands Complex and the Early Permian basins (Leitch, 1975; Shaw and Flood, 1981; Phillips et al., 2011). These are interpreted to have formed as the orogen evolved from an accretionary system to a back-arc position (Jenkins et al., 2002; Phillips et al., 2011).

2.2 Tectonic framework of the high-pressure rocks and the Tasmanides

There has been significant debate surrounding the evolution of the Tasmanides, including the tectonic significance of the high-pressure rocks. Notably, all the geochronology reported from serpentinite-hosted high-pressure exotic blocks in the SNEO is significantly older than the enclosing geology (Fig. 1b; e.g. Fukui et al., 1995, Sano et al., 2004; Phillips et al., 2015; Manton et al., 2017; Tamblyn et al., 2019a). The most coherent views about the evolution of the Tasmanides involve eastward retreat of a subduction system that formed close to the cratonic margin during the mid-late Cambrian (e.g. Collins, 2002; Phillips and Offler, 2011; Moresi et al., 2014; Phillips et al., 2015). The general consensus is the high-pressure rocks found in the SNEO were formed in a subduction channel on the cratonic margin of Australia during the Delamerian Orogen in the Cambrian–Ordovician. Subsequent cooling and transport of the high-pressure rocks occurred during eastward-directed slab rollback, until the high-pressure rocks were exhumed in their current location in the Permian-Triassic SNEO (Phillips and Offler, 2011; Phillips et al., 2015; Tamblyn et al., 2019a). During this rollback, the Lachlan/Thompson Orogens developed in a backarc setting on the

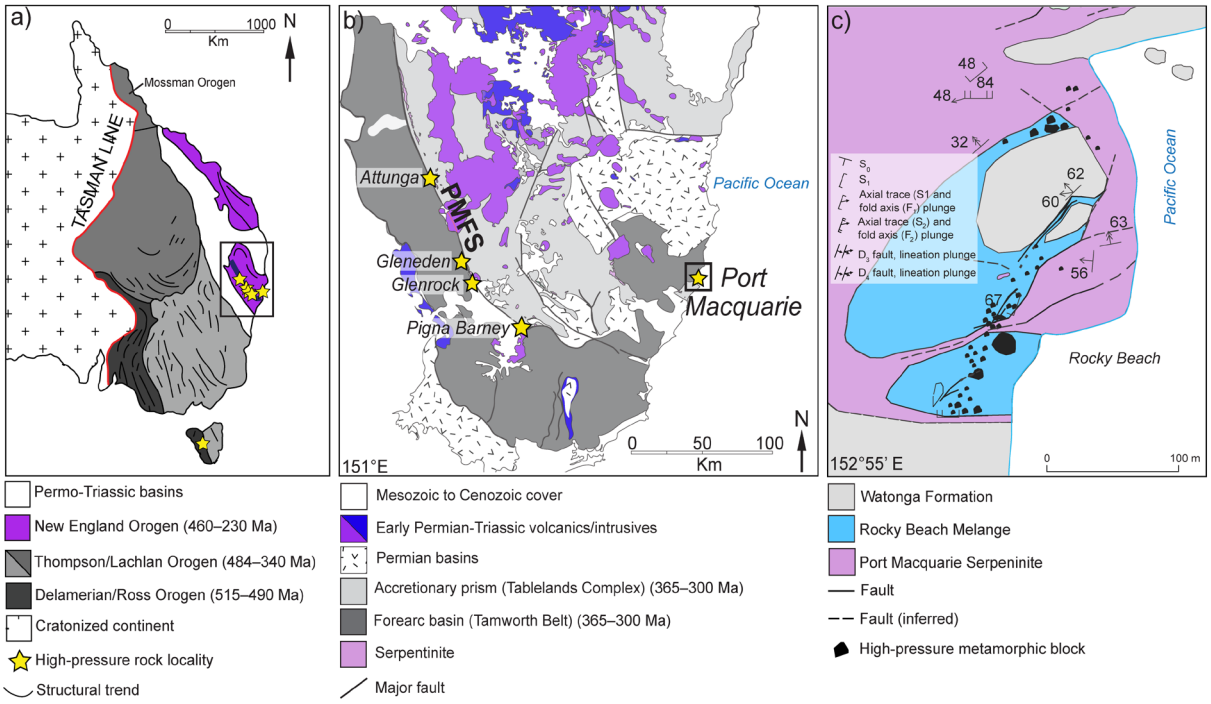


Figure 1: a) Simplified map of eastern Australia (east of the Tasman line) showing the main eastward-younging orogens. The SNEO is indicated in the black box. b) Geological map of the SNEO, showing other high-pressure rock localities and indicating the location of Port Macquarie in the black box. PMFS: Peel Manning Fault System. c) Geological map of Rocky Beach at Port Macquarie, showing the high-pressure mélange encased in serpentinite, modified from Och et al. (2003).

upper plate (e.g. Collins, 2002; Kemp et al., 2009; Moresi et al., 2014). Eastward younging arcs track the rollback of the subduction zone, accompanied by voluminous I and S-type magmatism formed from arc and back-arc rifting processes (Collins, 2002; Collins and Richards, 2008). This eastward migration is also revealed in ε_{Nd} isotopes of magmatic rocks, which demonstrate an increasingly juvenile signature as the subduction zone migrated away from the cratonic margin (Kemp et al., 2009).

2.3 High-pressure metamorphism and mélange formation in the SNEO

High-pressure metamorphic rocks hosted in serpentinite occur throughout the SNEO at Attunga, Gleneden, Glenrock, Pigna Barney and Port Macquarie (Fig. 1b; Phillips et al., 2015). The Port Macquarie mélange contains by far the largest lithological variety of high pressure-rocks, which are described in detail by Och et al. (2003; 2007) and Tamblyn et al. (2019a). The mélange consists of exotic high-pressure blocks encased in chlorite-actinolite schist, which is in turn encased within serpentinite (Fig. 1c). These exotic blocks consist of variably metamorphosed omphacitite, low-grade basaltic rocks, sedimentary rocks, marble, blueschist facies rocks, retrogressed eclogite and lawsonite-bearing eclogite. In-situ

U–Pb geochronology on micro-zircon from the lawsonite eclogite returned a range of ages from ca. 560–440 Ma (Tamblyn et al., 2019a). The zircons occur as inclusions in garnet and also occur in the surrounding matrix. Lu–Hf geochronology on lawsonite porphyroblasts gives an age of 506 ± 15 Ma, and a Lu–Hf garnet-whole rock isochron gives an age of 489.7 ± 5 Ma. These ages are interpreted to date prograde metamorphism, as garnet cores are enriched in Lu compared to rims, biasing the age to early garnet growth. Pressure-temperature conditions obtained from phase equilibrium modelling are approximately 2.7 GPa and 590 °C for the lawsonite eclogite, and 2.0 GPa and 550 °C for a garnet-omphacite-bearing blueschist block within the same mélange. Lu–Hf, Sm–Nd, K–Ar and Ar–Ar ages from adjacent blueschist blocks and fuchsite in serpentinite give ages between ca. 472 and 420 Ma (Fukui et al., 1995; Och et al., 2010; Tamblyn et al., 2019a). This geochronology, along with the presence of low-grade sedimentary blocks, confirms the accumulation of rocks with different *P*–*T* histories in the mélange.

3. Petrography

Mineralogy of the lawsonite eclogite block (sample RB11) has been described in detail by Tamblyn et al. (2019a) and Och et al. (2003; 2007). The eclogite contains porphyroblastic garnet, lawsonite and omphacite, in a well-foliated matrix dominated by phengite and containing minor titanite (Fig. 2). However, it is clear from optical petrography and elemental mapping that there are two distinct mineral assemblages recorded in the sample, summarized in Table 1, which are referred to as stage 1 and stage 2. Garnet is euhedral and forms crystals up to 7 mm in diameter, which have red-coloured cores and paler rims, referred to as garnet 1 and garnet 2 respectively (Fig. 2a-d). The inclusion relationships in garnet are summarised in Supplementary Figure 1. Garnet 1 has inclusion-rich cores which contain lawsonite, titanite, omphacite, phengite, glaucophane, chlorite, epidote, stilpnomelane, quartz and zircon (Supp. Fig. 1). Very rarely, quartz inclusions in the outermost part of garnet 1 are surrounded by prominent radial fractures, suggesting the possibility that they were once coesite (Fig. 2e). Garnet 2 forms as ~ 400 μm wide rims on garnet 1 that contain chlorite, glaucophane, titanite, omphacite, lawsonite, quartz and zircon (Fig. 2d), and in some instances overgrow matrix phengite. Enclosed inclusions of chlorite, phengite, omphacite, quartz, titanite and pyrite occur at the boundary between garnet 1 and 2 (Supp. Fig. 1). Sigmoidal inclusion trails of titanite are also commonly truncated at the boundary between garnet 1 and garnet 2, with the trails forming at a high angle to the matrix foliation (Supp. Fig. 1). Titanite included in garnet 2 is coarser-grained than in garnet 1. Lawsonite forms euhedral crystals up to 3 mm (Fig. 2b,f). It has darker sections containing abundant fine-grained inclusions and clearer sections with

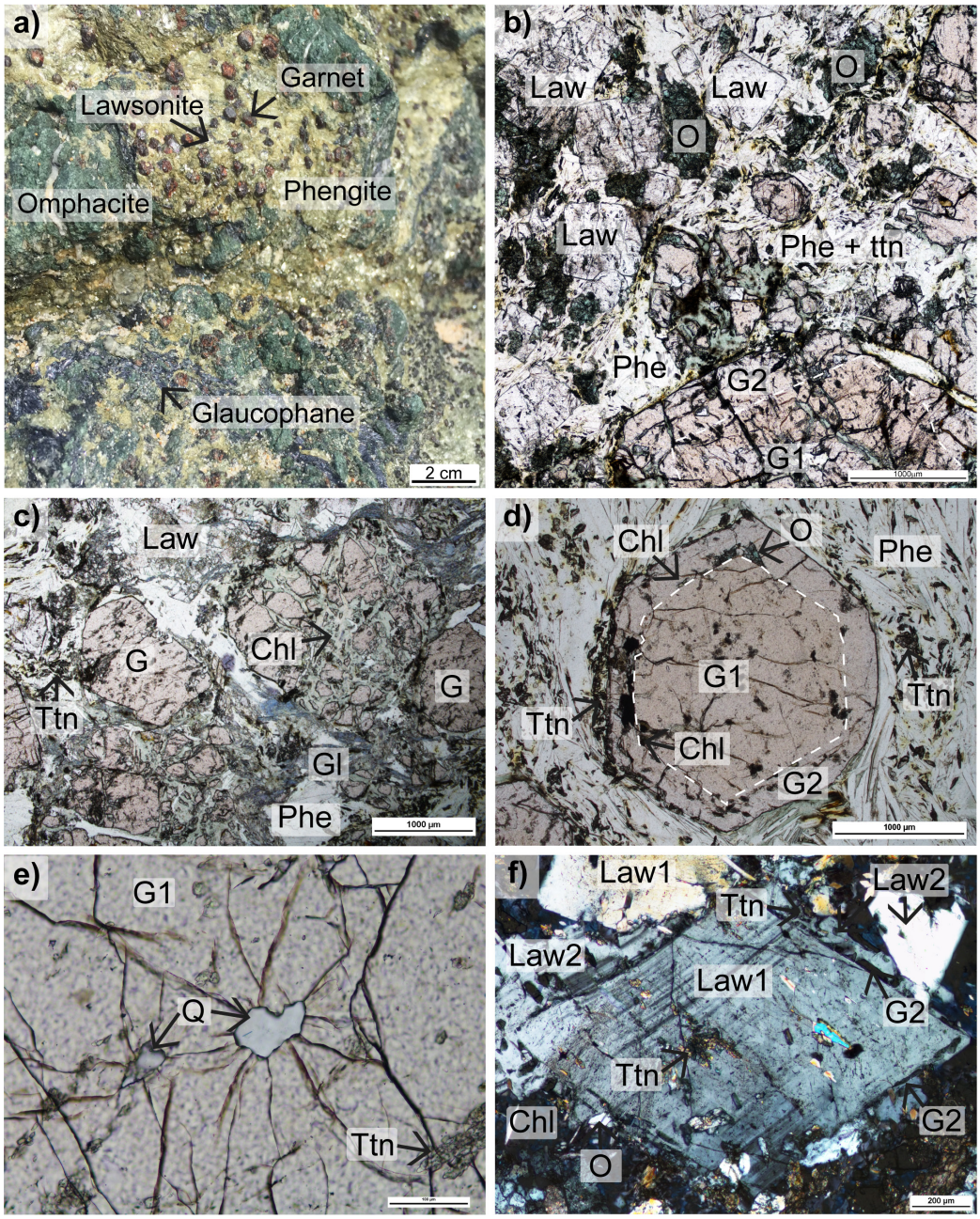


Figure 2: Mineral textural relationships in the Port Macquarie eclogite. a) Eclogite in outcrop, showing coarse-grained garnet, phengite and lawsonite with patches of omphacite, which is partially retrogressed by glaucophane. b) Photomicrograph showing the porphyroblastic nature of garnet, lawsonite and omphacite, in a finer-grained phengite and titanite matrix. c) Stage 2 retrograde features of the eclogite, showing chlorite replacement of garnet and glaucophane replacement of omphacite. d) Garnet 2 enclosing a pre-existing garnet 1 porphyroblast. Boundary between the stage 1 garnet and stage 2 garnet is shown by a white dashed line. The boundary between the two garnet domains contains entrapped chlorite and omphacite inclusions. This boundary also marks the truncation of titanite inclusion trails. e) Radial fractures surrounding a quartz inclusion in the outermost part garnet 1. f) Large lawsonite porphyroblast, with an inclusion-rich euhedral crystal (lawsonite 1) which is overgrown by a rim (lawsonite 2). The new lawsonite growth contains inclusions of garnet 2 that developed on the margin of the older lawsonite, as well as stage 2 glaucophane and titanite. Abbreviations: O: Omphacite; Law: Lawsonite; Phe: Phengite; Ttn: Titanite; G: Garnet; Chl: Chlorite; Gl: Glaucophane; Stlp: Stilpnomelane; Q: Quartz.

coarser-grained inclusions. The inclusions are predominately titanite, epidote, glaucophane and phengite. In places the lawsonite grain boundaries are mantled by small garnet grains, which have been overgrown by a second generation of lawsonite. In other places the clearer lawsonite occurs as an overgrowth on darker lawsonite crystals (Fig. 2f). The darker, older lawsonite is referred to as lawsonite 1 and the clearer overgrowths are referred to as lawsonite 2. The foliated matrix is part of the stage 2 mineral assemblage, and is defined by coarse phengite (up to 1 mm but commonly ~ 300 μm) and pervasive but modally minor titanite (< 100 μm; Fig. 2b,d). The latter is associated with fine grained allanite and zircon (< 20 μm). Titanite and phengite are coarser in the matrix relative to the inclusions in garnet cores, and in places titanite forms aggregates of grains that rim phengite grains. Omphacite forms monominerallic patches up to 10 mm which are partially replaced by glaucophane and chlorite, as well as relic fractured porphyroblasts up to ~ 500 μm in size (Fig. 2a,b). Omphacite is partially replaced by chlorite and glaucophane. Garnet is partially replaced by chlorite along its grain boundaries or along fractures which cross-cut the garnet (Fig. 2c; Supp. Fig. 1). Where retrograde chlorite occurs with lawsonite, lawsonite is euhedral and unretrogressed, suggesting it was stable during the retrogression of the eclogite. In the matrix, glaucophane also forms foliated euhedral crystals (Fig. 2c). These crystals, as well as coarse titanite crystals, are overgrown by stage 2 lawsonite rims. These petrological observations denote two distinct stages of peak metamorphism in the eclogite, separated by a period of retrogression. A schematic representation of the petrologic observations made from optical petrography, phase mapping and elemental mapping can be found in Figure 3.

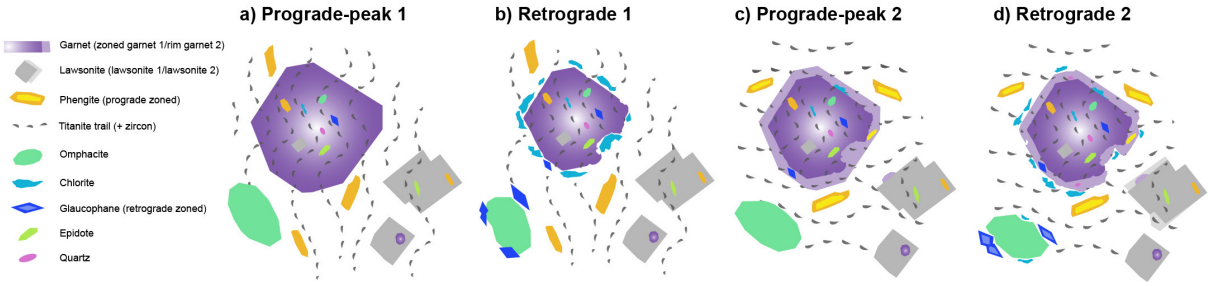


Figure 3: Schematic interpretation of the petrologic evolution of the lawsonite eclogite. a) Prograde–peak stage 1 burial: garnet cores nucleate and as garnet 1 grows it entraps prograde mineralogy and inclusion trails. Lawsonite porphyroblasts grow and entrap prograde minerals. b) Retrograde 1: garnet is partially consumed by chlorite, and glaucophane forms at the expense of omphacite. c) Prograde–peak 2: garnet forms new rims (garnet 2). In rare instances stage 2 garnet overgrows stage 1 lawsonite. Phengite recrystallises in the matrix with coarse-grained titanite during deformation. d) Stage 2 retrograde: garnet is partially replaced by chlorite and omphacite is partially replaced by glaucophane. There is minor growth of lawsonite.

	Stage 1			Stage 2		
	Prograde	**Peak**	**Retrograde**	**Prograde**	**Peak**	**Retrograde**
Garnet	Mn-rich core formed	Stable as large prograde-zoned porphyroblasts	Partially consumed by chlorite	Grew XMg and Mn-rich rims	Stable	Partially consumed by chlorite
Lawsonite	Formed inclusion-rich domains, and captured in garnet 1	Stable	Stable	Stable	Stable	Grew clean rims which captured garnet 2, titanite
Phengite	Captured in garnet 1 and lawsonite	High Si/low Al grains captured in outer part of garnet 1	Stable	Recrystallized, forming prograde zoning, low Si/high Al grains captured in garnet 2	Stable as prograde zoned grains	Stable throughout matrix
Titanite	Fine-grained, captured in garnet 1	Stable	Stable	Recrystallized to a slightly coarser size, captured in garnet 2	Stable throughout matrix	Stable throughout matrix
Omphacite	Captured in garnet 1	Stable	Partially consumed by glaucophane	Captured in garnet 2	Stable, formed large prograde-zoned porphyroblasts	Partially consumed by glaucophane
Quartz	Captured in garnet 1	Converts to coesite, captured within garnet 1	Reverts to quartz within garnet 1	Stable	Stable	Stable
Chlorite	Captured in garnet 1	-	Grew during breakdown of garnet 1, XMg = 0.46	Captured in garnet 2	-	Consumed garnet along fractures and grain boundaries, varied chemistry
Glaucophane	Captured in garnet 1	-	Consumed omphacite	Broke down during omphacite growth, captured in garnet 2 rims	-	Partially consumed omphacite, formed retrograde zoning
Epidote	Captured as inclusions in garnet 1 and lawsonite 1	-	-	-	-	-

Table 1: Interpreted petrology and related mineral chemistry, denoting two stages of metamorphism. A dash signifies that the mineral was absent

4. Methods

4.1 Electron Probe Micro Analyses and mapping

Spot analyses on minerals were obtained using a Cameca SX-5 microprobe at Adelaide Microscopy, using an accelerating voltage of 15 kV and a beam current of 20 nA. Element maps used an accelerating voltage of 15 kV and a 200 nA beam current, Ca, Fe, Mn and Mg were mapped using Wavelength Dispersive Spectrometers (WDS), whereas Al, Si, Ti, K and Na were mapped using Energy Dispersive Spectrometry (EDS). Maps were colour scaled in ImageJ.

4.2 Phase equilibrium forward modelling

Full phase equilibrium modelling methods are in Supplementary File 1. The rock composition was calculated for the lawsonite eclogite by combining modal proportions of each mineral with its measured chemical composition (Supplementary Table 1; 3). Thin sections were mapped with a Quanta600 scanning electron microscope (SEM) with mineral liberation analysis (MLA) software to calculate modal proportions of minerals.

The phase equilibrium models were calculated using THERMOCALC (TC340i) using the internally-consistent thermodynamic dataset 'ds5' (filename tc-ds55.txt; November 2003 updated version of the Holland and Powell, 1998 data set) and activity–composition (a–x) models (Supplementary Table 3; Holland and Powell, 1988; Holland and Powell, 2003; White et al., 2007; Green et al., 2007; Holland and Powell, 2011; Diener et al., 2012) in the chemical system NCKFMASHO. A model for the local rock composition was calculated with water in excess, and a model for the local rock composition was calculated with a set water content, derived from the abundance of hydrous minerals (Supplementary Table 1; 2).

4.3 U–Pb titanite geochronology

Titanite grains were analysed in-situ for U–Pb isotopes using an ASI m50 LA–ICP with an attached 7700 MS at Adelaide Microscopy. Grains were ablated using a spot size of 51 μm, a frequency of 5 Hz, and a surface energy density of 3.5 Jcm^{-2}, with an acquisition time of 80 s for each analysis including 30 s of background measurement and 50 s of ablation. The primary reference titanite MKED-1 was used to correct for elemental fractionation, mass bias and instrument drift over the courses of analyses (Spandler et al., 2016), and a titanite grain from Mt Painter with an age of 442.6 ± 1.8 Ma (Elburg et al., 2003) was used as the secondary standard. Corrections were done using the software Iolite (Paton et al., 2011) and age calculations were done using IsoplotR (Vermeesch, 2018). The secondary standard from Mt Painter returned a weighted mean $^{206}Pb/^{238}U$ age of 440.3± 2.5 Ma

(MSWD = 1.5, n = 22) throughout the course of the analyses.

4.4 Ar–Ar phengite geochronology

Phengite $^{40}Ar/^{39}Ar$ isotope analyses utilized conventional furnace step-heating techniques at the University of Melbourne, after the analytical procedures of Phillips et al. (2007). Phengite grains were selected from mineral separates. Due to the possibility of contamination by excess argon in high-pressure rocks (Kelley, 2002), a two-increment step-heating laser approach was employed on single grains of phengite. The laser analyses were conducted at The University of Melbourne, employing the analytical procedures described by Phillips and Harris (2008). This approach was used to screen for any significant intrasample inconsistency in argon content that could be an artefact of (i) multiple generations of phengite growth or (ii) varied amounts of isotopic resetting or excess argon contamination within single grains. Using the single-grain laser approach, spurious isotopic results from a single-grain analysis can be removed from the mean age calculations, using Isoplot software (Ludwig, 2003).

4.5 Rb–Sr phengite geochronology

Phengite was analysed in-situ for Rb and Sr isotopes and major and trace elements using an ESI 213 NWR (TwoVol2) laser ablation system with an attached Agilent 8800QQQ ICP-MS/MS in the Microgeochemistry Laboratory at the University of Gothenburg, Sweden, following the methods of Zack and Hogmalm (2016) and Hogmalm et al. (2017). Full methods are in Supplementary File 1. Laser parameters were a fluence of ~ 6 Jcm^{-2} and a frequency of 10 Hz. Phengite was analysed with a spot size of 40 μm, both perpendicular and parallel to cleavage. Titanite was also analysed to obtain initial $^{87}Sr/^{86}Sr$ ratios, with a spot size of 50 μm. The primary standard for $^{87}Rb/^{86}Sr$ calibration was a pressed nanopowder MicaMg ($^{87}Rb/^{86}Sr$ ratio of 154.6; Hogmalm et al., 2017). Other primary standards for $^{87}Sr/^{86}Sr$ ratios were the synthetic glass NIST610 ($^{87}Sr/^{86}Sr$ ratio: 0.709699; Woodhead and Hergt, 2001) and the natural basaltic glass BCR2G ($^{87}Sr/^{86}Sr$ ratio: 0.705003; Elburg et al., 2005). Secondary standards included La Posta biotite grains, with Rb–Sr isochron age of 91.6 ± 1.2 Ma and an initial $^{87}Sr/^{86}Sr$ ratio of 0.7049 ± 5 (Zack and Hogmalm, 2016), and MDC biotite grains with an isochron age of 519.4 ± 6.5 Ma and an initial $^{87}Sr/^{86}Sr$ ratio of 0.72 ± 0.002 (unpublished data). Over the course of the analyses, La Posta grains returned an isochron age of 90.5 ± 4.2 Ma, and MDC grains returned an isochron age of 501.2 ± 7.2 Ma.

4.6 LA–ICP–QQQ isotope mapping

Phengite was mapped in-situ for Rb and Sr using an ASI m50 LA–ICP–MS with attached Agilent 8800 triple quadropole MS at Adelaide Microscopy, Australia. The reaction gas used was O_2, with

laser parameters of a fluence of 7 Jcm^{-2} and a frequency of 10 Hz. The primary standard used was a pressed nanopowder MicaMg, and NIST610 was used as a secondary glass standard. The maps were processed in Iolite (Paton et al., 2011). Results of the mapping are semi-quantitative, and are presented in counts per second (CPS).

5. Results

5.1 Electron Probe Micro Analyses and mapping

Mineral compositions and end member proportions are reported in Supplementary Table 1 and Tamblyn et al. (2019a), additional phengite, chlorite, omphacite and glaucophane compositional data is in Supplementary Table 4.

EPMA traverses and mapping of whole garnet grains (Fig. 4; 5; Supp. Fig. 2) show complex zoning in the major elements. In garnet 1, cores show a bell-shaped Mn enrichment, consistent with prograde zoning (Fig. 4a; 5a). In the outer part of garnet 1 and prominently in garnet 2 there is a series of thin concentric Mn-rich rings or oscillations (Fig. 5b-c). These narrow Mn-rich zones are often regular, forming hexagonal garnet crystal shapes (Fig. 5c), but can also be highly irregular, appearing to form on embayments in the garnet crystal (Fig. 5b). There is an overall average increase in Mn content from the outer part of garnet 1 to the garnet 2 rim (Fig. 4b). The grossular content of the entire garnet increases slightly from core to rim, from 0.23 to 0.3, and also shows slight enrichments in thin concentric rings in the outer garnet that are correlated with the patterns exhibited by Mn (Fig. 5). Garnet 1 has almandine-poor cores (0.45) increasing to higher almandine content in the outer garnet (0.65; Fig. 4a), with the exception of slight almandine-poor concentric rings which correlate with the Mn-rich rings. Garnet 2 is slightly depleted in almandine (Fig. 4b). Pyrope contents are low in garnet 1, ~0.03, with the innermost core showing a very slight depletion compared to the rest of the garnet (Fig. 5a). Garnet 2 shows distinct step increase in pyrope (0.06) that defines an outer rim ~ 200 μm in width (Fig. 4b).

High resolution EPMA maps (Fig. 5b-c) reveal that garnet 2 forms on a regular to irregular-shaped original surface of the garnet, as indicated by the white dashed line. The growth of garnet 2 is marked by a sharp increase in Mn, followed by several variations in Mn, and a final Mn-poor rim which has been partially replaced by chlorite. Notably, these Mn zoning patterns only correspond to slight changes in MnO (<0.5 wt%). Fe is slightly depleted in garnet 2. This outer-rim transition is also marked by a sharp increase in Mg. The oscillations in Mn commonly correlate with slight increases in Ca.

EPMA X-ray maps were also obtained from

phengite grains in the matrix and in garnet (Fig. 6; Supp. Fig. 3). Matrix phengites display cores that are depleted in Fe, enriched in Al and slightly enriched in Na, surrounded by a rim enriched in Si, with enriched Fe and slight enrichment in Mg (Fig. 6). Phengite grains in garnet show phengite included in garnet 1 is enriched in Si, Mg and Fe, and depleted in Al and Na (Fig. 6). Phengite included in garnet 2 is enriched in Al and Na, and depleted in Si and Fe with a slight depletion in Mg,

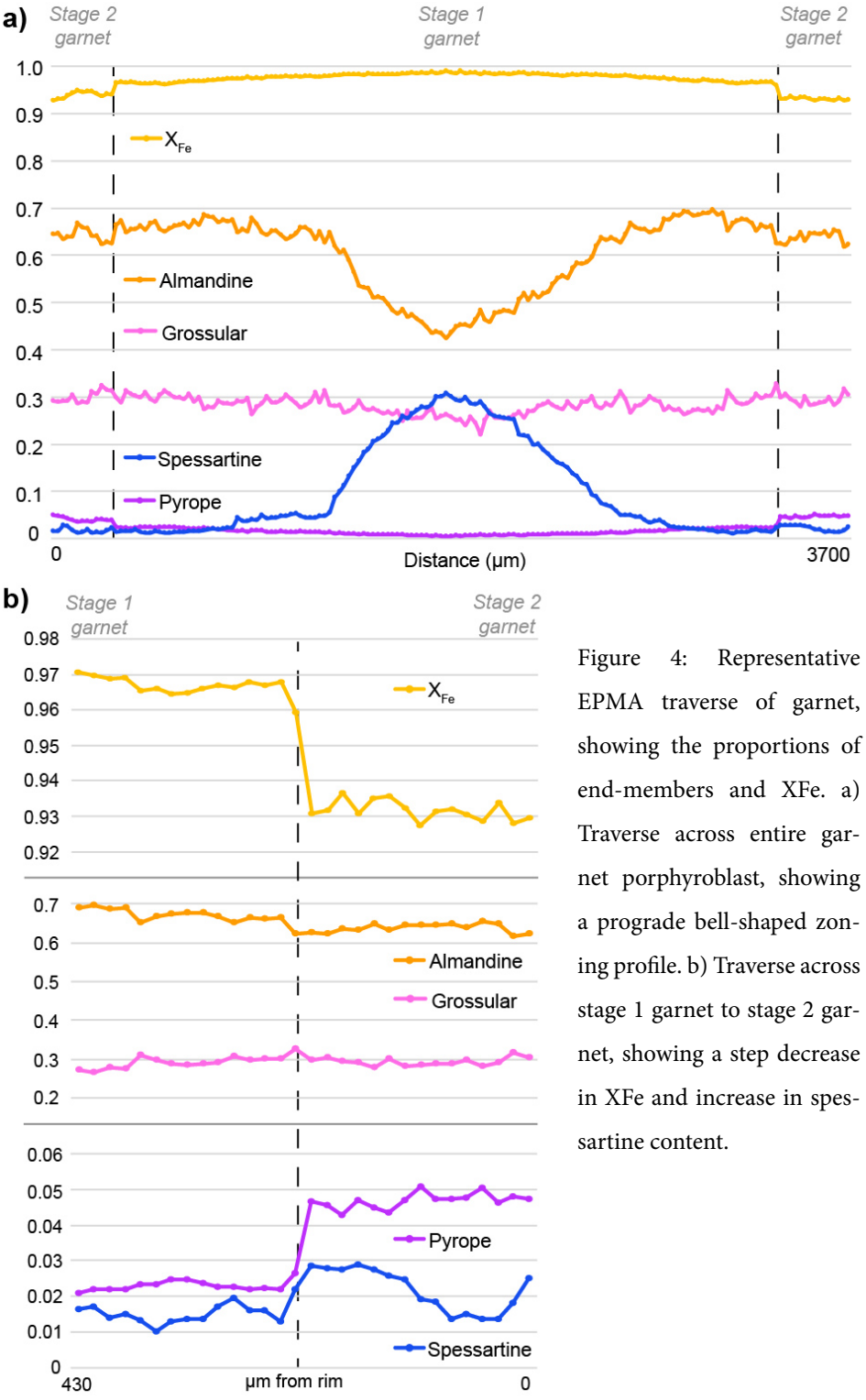


Figure 4: Representative EPMA traverse of garnet, showing the proportions of end-members and XFe. a) Traverse across entire garnet porphyroblast, showing a prograde bell-shaped zoning profile. b) Traverse across stage 1 garnet to stage 2 garnet, showing a step decrease in XFe and increase in spessartine content.

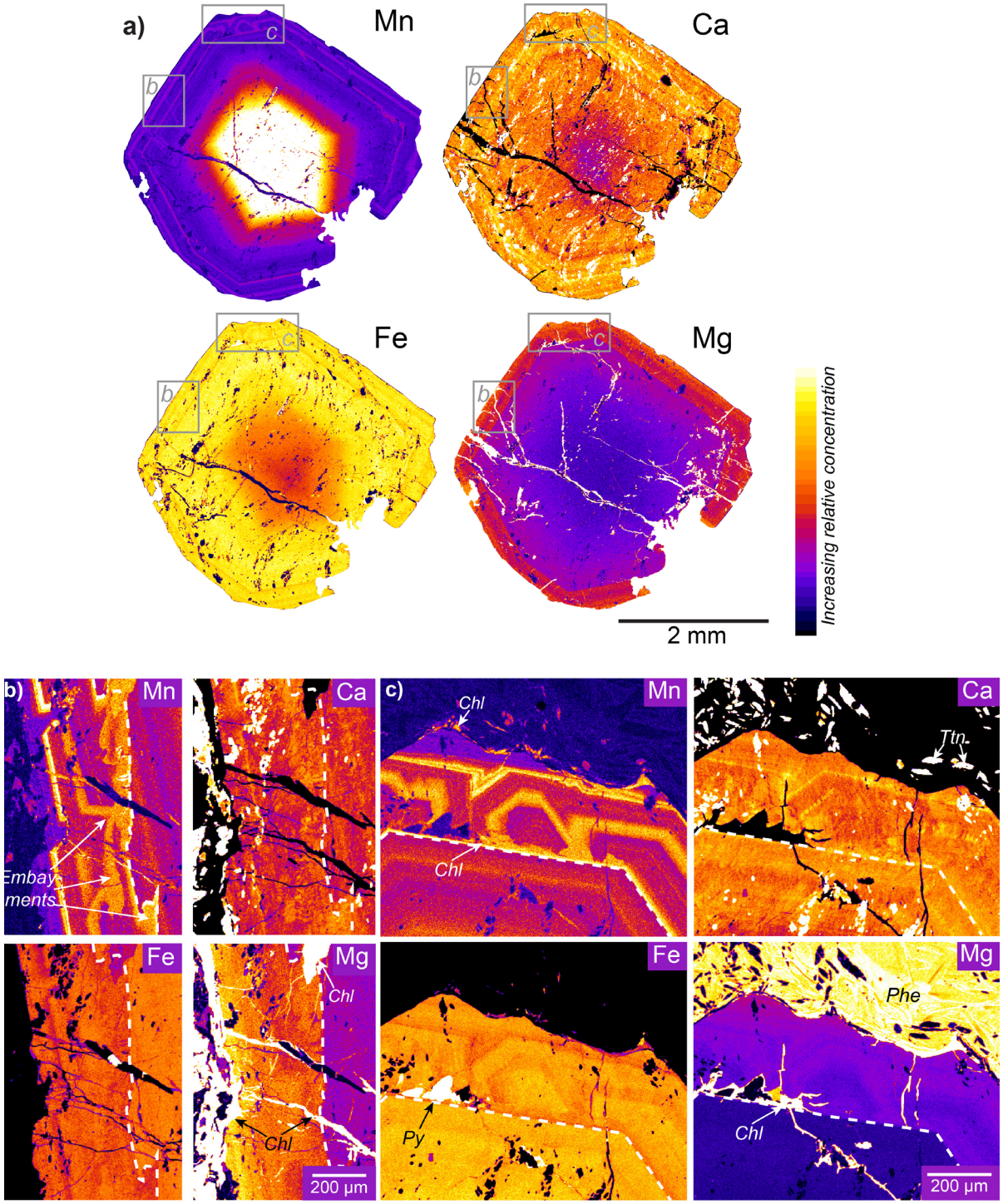


Figure 5: EPMA element maps of garnet, the white dashed line shows the interpreted boundary between garnet 1 and garnet 2. a) Garnet porphyroblasts with prograde zoning in Mn, along with several oscillatory rings in the stage 2 rim. Zoning in Fe and Mg show garnet 2 as a marked outer ring with elevated XMg. Subset maps are marked in grey boxes. b) Compositional oscillations in the garnet 2 which define smaller hexagonal garnet crystals that nucleated on the older garnet 1 rim. c) Complex Mn zoning patterns and a marked XMg increase in the outer garnet rim. Embayments and subsequent overgrowths are highlighted in the Mn oscillations, with correlate with Ca oscillations. Late chlorite replaces garnet. The boundary between garnet 1 and garnet 2 contains Mn-rich chlorite inclusions.

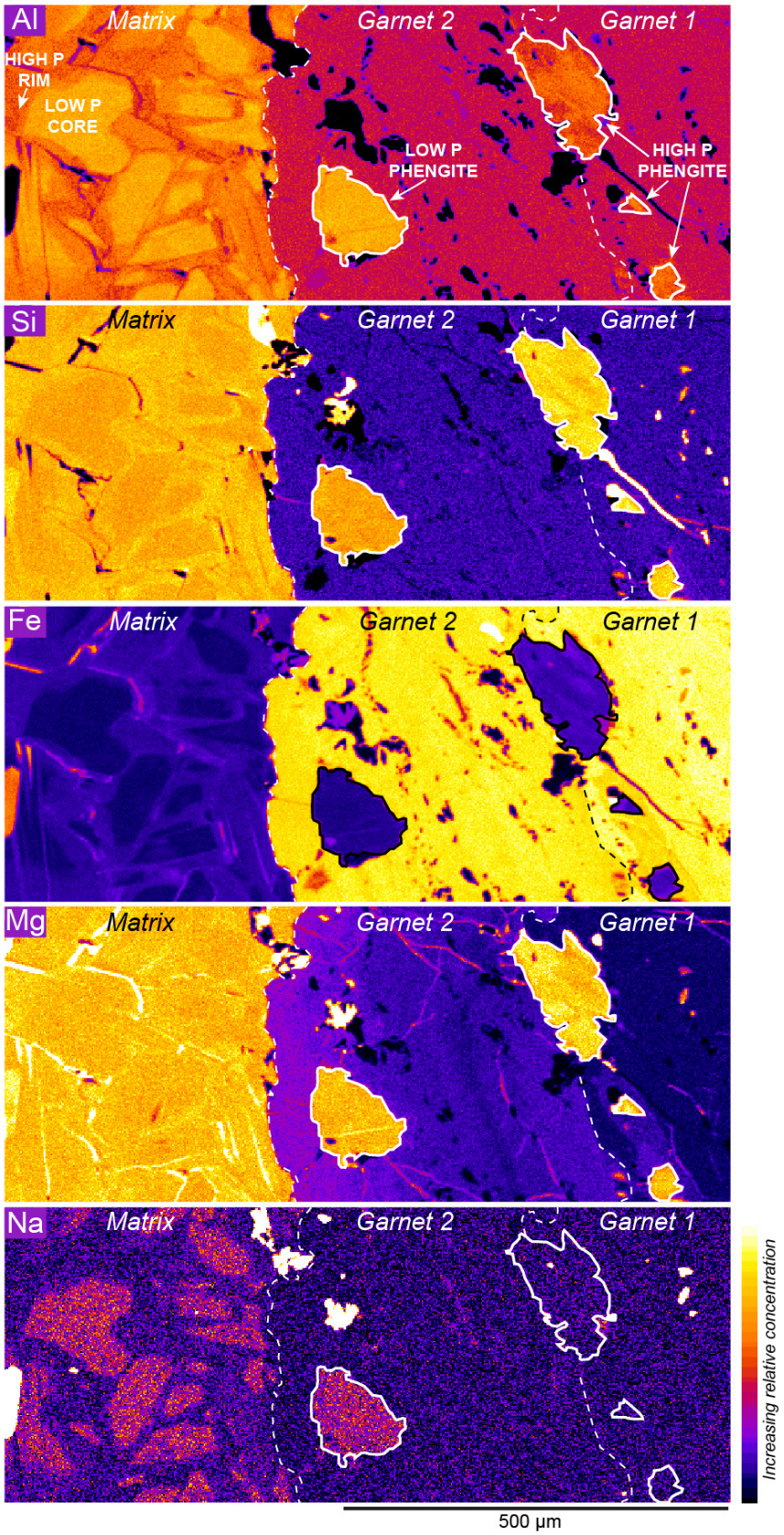


Figure 6: EPMA maps across transition from garnet 1 to garnet 2 and into matrix phengite. White/black dashed line indicates the boundaries of garnet 1 and garnet 2. Solid white/black line indicates the boundaries of phengite included in garnet.

similar to cores of phengite grains in the matrix (Fig. 6). Compositional zoning in the phengite is sharp and well defined. Overall, the phengite zoning is defined by an increase in celadonite proportion from core (40%) to outer rim (45%), accompanied by a decrease in X_{Mg} (0.71–0.63) and an increase in Si (3.43–3.56 p.f.u.; Fig. 7).

Omphacite occurs as inclusions in garnet 1 and garnet 2, and as coarser grains in the matrix, which show subtle differences in composition (Fig. 7). Omphacite in the matrix and as inclusions in garnet 1 is generally 0.37–0.44 proportion jadeite, 0.36–0.43 proportion diopside, 0.08–0.19 proportion hedenbergite with a minor acmite component. Omphacite as inclusions in garnet 2 is similar in composition, with the exception of occasional diopsodic grains, which are 0.15–0.23 proportion jadeite, 0.47–0.50 proportion diopside, and 0.19–0.26 proportion hedenbergite. Coarse grains in the matrix and as inclusions in garnet 2 are subtly zoned in X_{Fe}, from ~ 0.27 in the core to ~ 0.23 in the rim (Supp. Fig. 4). Inclusions in garnet 1 have an average X_{Fe} of 0.28, and inclusions in garnet 2 have an average X_{Fe} of 0.3.

Chlorite forms grains in the matrix that break down garnet and omphacite, along fractures which cross-cut garnet, and as inclusions at the boundary between garnet 1 and garnet 2 (Supp. Fig. 1). Chlorite as inclusions between garnet 1 and garnet 2 has an average X_{Mg} of 0.46 (Supplementary Table 4). It shows elevated MnO contents compared to the adjacent garnet (0.54–0.73 wt%). Chlorite throughout the matrix has an average X_{Mg} of 0.38. EPMA X-ray maps show that chlorite is often zoned or patchy in composition (Supp. Fig. 5).

Retrograde amphibole is ferro-glaucophane in composition after the nomenclature of Leake et al. (1997), and also shows sharply defined compositional zonation (Supp. Fig. 6). X_{Mg} increases from core to rim, accompanied by a slight decrease in Al (1.72–1.39 p.f.u.). There is a slight enrichment of Ca in the cores of the glaucophane (0.17 p.f.u.), however, the grains are dominantly sodic. Some grains have thin outer rims with slight enrichment in MnO (0.14–0.27 wt%, Supp. Fig. 6).

Titanite differs slightly from ideal formula, with incorporation of Al_2O_3 (up to 2.27 wt%), FeO (up to 0.66 wt%) and F (up to 0.6 wt%) into its crystal structure (Supplementary Table 4). Al_2O_3, FeO and F contents show positive correlations (Fig. 7).

5.2 Phase equilibrium forward modelling

The results of the phase equilibrium forward modelling and corresponding mineral modal and compositional isopleths are shown in Figures 8, 9 and 10. Figure 8 shows the phase equilibrium model for the total bulk rock composition after Tamblyn et al. (2019a). Figure 9 shows the phase

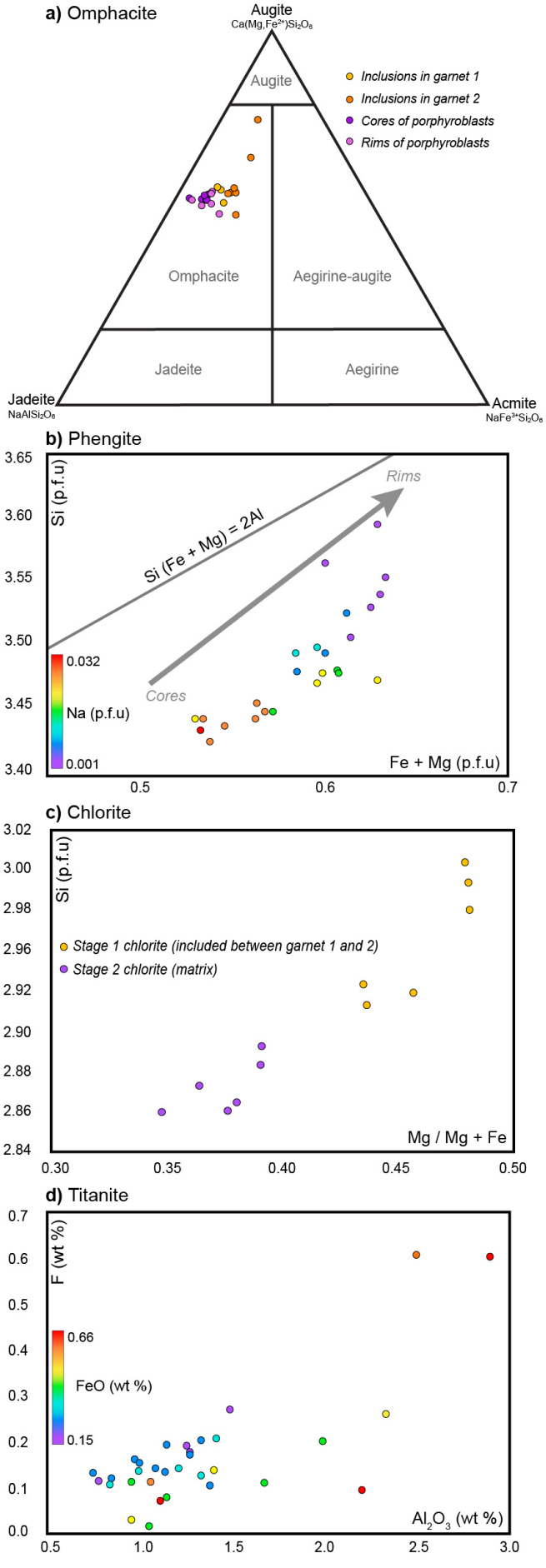


Figure 7: Mineral compositions of omphacite, phengite, chlorite and titanite measured by EPMA. a) Omphacite analyses from inclusions in garnet and omphacite porphyroblasts in the matrix. b) Phengite analyses showing increasing Si, Fe and Mg component from core to rim, and decreasing Na content. c) Chlorite analyses from stage 1 chlorite, from the boundary between garnet 1 and garnet 2, and stage 2 chlorite, from the matrix. d) Titanite analyses showing elevated Al2O3, FeO and F contents with a positive correlation, suggesting increasing pressure during crystallization (e.g. Castelli and Rubatto, 2002).

equilibrium model for the local rock composition with water in excess, and garnet 1 and lawsonite 1 removed. This was done to simulate the effective local composition for the stage 2 mineral assemblage, as garnet 1 and lawsonite 1 were chemically isolated from the reactive rock composition (e.g. Spear, 1988; Marmo et al., 2002; Evans, 2004; Gaides et al., 2008; Konrad-Schmolke et al., 2008; Lanari and Engi, 2017). Figure 10 shows the phase equilibrium model with garnet 1 and lawsonite 1 removed, but with a set water content, calculated from the modes of hydrous minerals (H_2O = 4.65 wt%). This was done as the current water content in the rock is most likely a measure of the minimum amount of water available in the local rock composition. Figures 11 and 12 can only be used for the mineral relations during the secondary assemblage formation after garnet 1 and lawsonite 1 have been formed. It is likely that the local rock composition had a water content between that which is measured in the rock currently, and water in excess. Therefore, the *P*–*T* points during retrograde 1, prograde 2 and peak 2 have been interpreted from both of the models. A summary of the phase equilibrium models used for each stage of the metamorphic evolution is in Supplementary Table 5. The interpreted stages of the *P*–*T* path are indicated as grey arrows.

5.2.1 Stage 1

The prograde path and peak conditions for the formation of the first mineral assemblage are shown on Figure 8b, after Tamblyn et al. (2019a). Garnet 1 nucleated at the 'garnet cores in' line at ~ 0.8–1.1 GPa and approximately 350 °C, based on the core inclusion assemblage of phengite + omphacite + lawsonite + quartz + chlorite + epidote. The path is then interpreted to track up-pressure into the + glaucophane field to satisfy the inclusion relationship of glaucophane in lawsonite and in the core domains of garnet 1 porphyroblasts.

The peak conditions of stage 1 metamorphism are determined from inclusions in the outer part of garnet 1 crystals. We acknowledge that the record of peak 1 has been obliterated by subsequent mineral growth, and as such the interpreted *P*–*T* conditions are tentative. We interpret that the lawsonite eclogite reached the phengite + garnet + lawsonite + omphacite + coesite field (based on radial fractures around quartz inclusions), at around 2.9 GPa and 600 °C. This field is bound up-pressure by the conversion of omphacite to jadeite, bound up-temperature by the destabilization of lawsonite, and is bound down-temperature and down-pressure by the loss of coesite or the conversion of coesite to quartz. No inclusions of jadeite were detected, supporting that clinopyroxene remained omphacitic during the metamorphic evolution. Lawsonite is interpreted to have been stable during stage 1 burial as lawsonite preserves ages synchronous with garnet growth (ca. 500 Ma; Tamblyn et al., 2019a), and is ubiquitously found

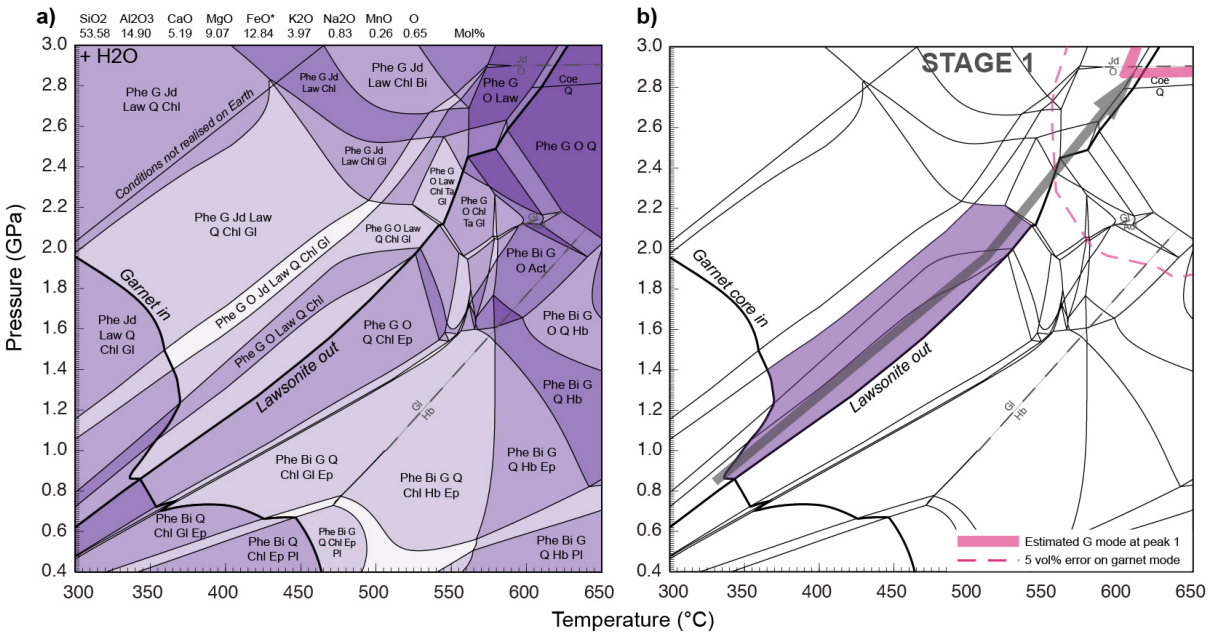


Figure 8: a) Phase equilibrium model calculated with THERMOCALC, modified from Tamblyn et al. (2019a), calculated with garnet 1 and lawsonite 2 included in the bulk rock chemistry. Dashed thin grey lines indicate the position of solvi. Colour changes indicate changes in variance across fields. b) Model (a) showing the prograde assemblage and estimated garnet mode at stage 1 peak. Thick grey arrow indicates the interpreted P–T path of stage 1 prograde-peak. Abbreviations: Act: Actinolite, Bi: Biotite, Chl: Chlorite, Coe: Coesite, Ep: Epidote, G: Garnet, Gl: Glaucophane, Hb: Hornblende, Jd: Jadeite, Law: Lawsonite, O: Omphacite, Pa: Paragonite, Phe: Phengite, Pl: Plagioclase, Q: Quartz, Ta: Talc.

as inclusions in garnet 1. Rare examples of radial fractures around quartz in the outer parts of garnet 1 (Fig. 2e) could indicate the former presence of coesite, further supporting these inferred *P–T* conditions.

These interpreted peak conditions are supported by the modal proportion of garnet 1. The interface between garnet 1 and 2 is marked by a step increase in X_{Mg} and a prominent increase in X_{Mn} (Fig. 4; 6), together with truncation of core-hosted inclusion trails. The microstructural relationships and change in X_{Mn} and X_{Mg} between the core and the rim strongly imply there was a hiatus in garnet growth. The overall average MnO of the garnet rim is higher than the MnO content of the outer garnet core (Fig. 4), suggesting that there was a period of garnet 1 breakdown prior to the formation of garnet 2. Making the assumption that garnet growth effectively sequesters all available MnO in the rock, particularly at high *P–T* conditions when chlorite is no longer stable, the higher average MnO concentrations in garnet 2 compared to the outer part of garnet 1 suggests that it originally occupied a larger modal proportion of the rock (Fig. 3a). The original size of the garnets during stage 1 can be calculated using the amount of MnO stored in the MnO dissolution rings in garnet 2. If the outer part of the garnet that formed during stage 1 is assumed to have had a flat MnO profile whose

MnO is now incorporated into garnet 2, stage 1 garnet at one point occupied ~ 1.05 times its current modal volume, equivalent to approximately 25 mol% (1-oxide-normalised; Fig. 4a). This is a minimum estimate, as the Mn-rich garnet 2 has been partially broken down and replaced by stage 2 Mn-rich chlorite. The calculated modal proportion of stage 1 garnet porphyroblasts plots at *P–T* conditions of ~ 2.9 GPa and 600 °C (Fig. 8c), within lawsonite stability. The modal proportion of garnet at this stage of the rock's evolution may be overestimated in the phase equilibrium model, by perhaps up to 5 vol % (e.g. Lanari and Engi, 2017), as garnet growth fractionates major elements. This uncertainty in the garnet mode estimate is presented on the phase equilibrium model (Fig. 8b). The calculated modal proportion of garnet passes through the phengite + lawsonite + omphacite + coesite field. The *P–T* path linking the interpreted prograde assemblages with the peak *P–T* point passes through talc-bearing *P–T* space, however the calculated modal proportion of talc is low (< 1 vol%), and as such it is unlikely that talc would have been preserved in the eclogite.

The retrograde conditions following peak 1 must be interpreted from the phase equilibrium models calculated from the local bulk rock composition, where garnet 1 and lawsonite 1 cores are not part of the chemical system. However, the *P–T* conditions are difficult to assess, as the water content in the rock at this stage in the lawsonite eclogite's evolution is unknown. Figure 9 shows the phase equilibrium model for the local rock composition with water set to excess (i.e. water saturation), and Figure 10 shows the same composition but with a water content defined by the current mineralogy in the rock. The amount of water currently in the rock is relevant to the assemblages formed during stage 2 retrogression, however its relation to the assemblages formed during stage 1 retrogression is unknown. Water content affects the stable mineral assemblages at lower pressures and temperatures, particularly the stability of garnet. The primary mineralogical evidence for stage 1 retrogression is the addition of chlorite + glaucophane to the mineral assemblage (as found as inclusions in garnet and lawsonite rims), and the consumption of garnet 1 rims. As such, the 'garnet-in' line is an important indicator of stage 1 retrograde *P–T* conditions, as it represents the modal volume of garnet in the rock before new stage 2 rims formed. In Figure 9, the garnet-in line occurs in the retrograde assemblage at ~ 1.8–2.1 GPa and 490–500 °C. However, it is unknown if the mineral assemblage was water saturated during retrogression. If the water content was below saturation, we would expect the garnet-in line to move further down pressure and temperature. This can be seen in Figure 10. The difference in position of the garnet-in line is due to water content limiting the formation of chlorite at the expense of garnet. Essentially, this means the garnet-in line in Figure 9 represents the *maximum* pressures and temperatures

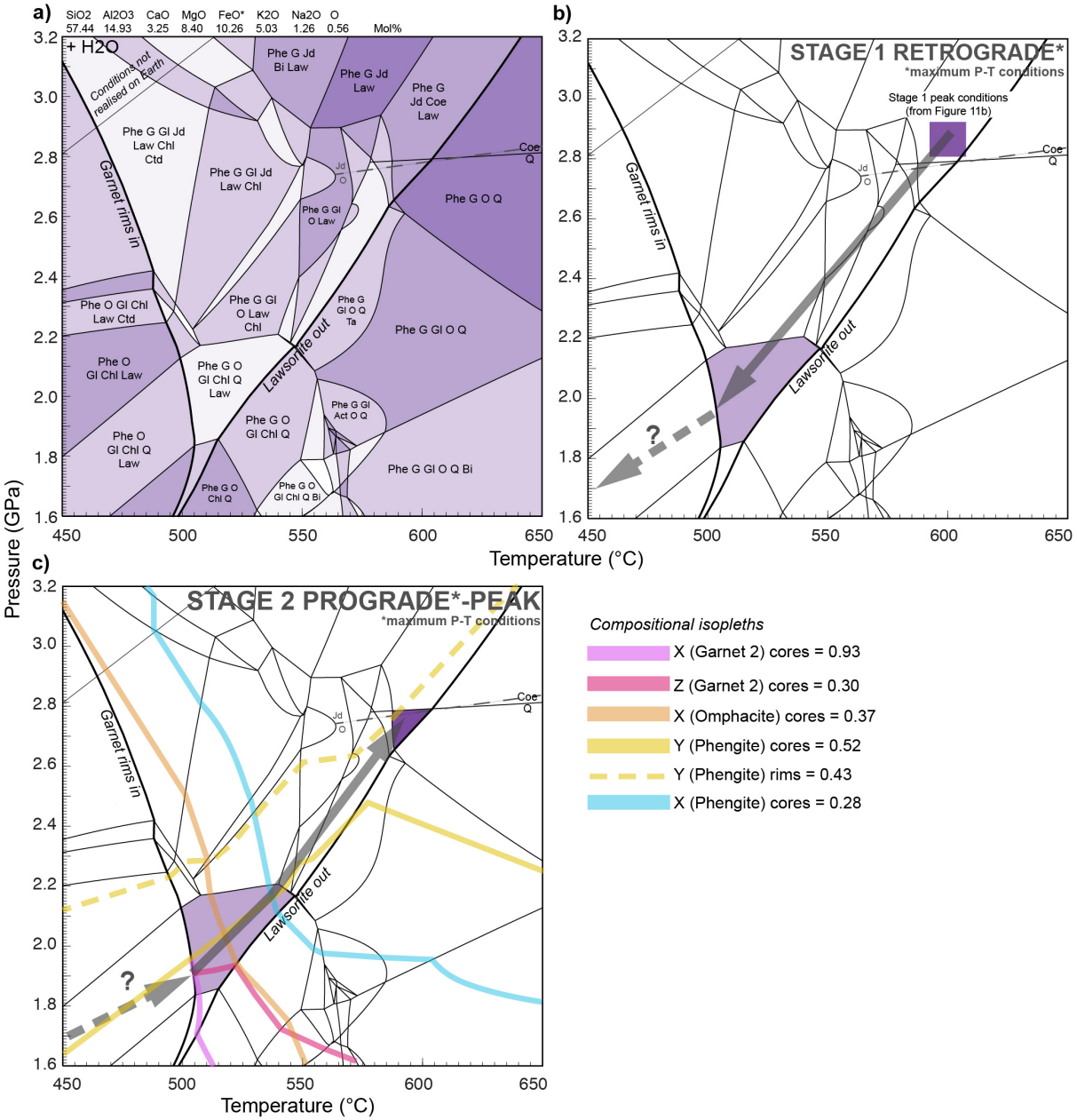


Figure 9: a) Phase equilibrium model calculated with THERMOCALC for the local rock composition with garnet 1 and lawsonite 1 removed, and water in excess. Dashed thin grey lines indicate the position of solvi. Colour changes indicate changes in variance across fields. Note the scale change from Figure 8. b) Model (a) showing the interpreted peak conditions of stage 1 peak from Figure 8b, and the interpreted stage 1 retrograde path in the thick grey arrow. Note these retrograde P–T conditions are considered the maximum possible pressures and temperatures obtained during retrogression. c) Model (a) showing the interpreted stage 2 prograde and peak assemblages, and mineral compositional isopleths. Thick grey arrow indicates the interpreted P–T path during stage 2 prograde to peak. Abbreviations are listed in Figure 8.

the rock could have reached during stage 1 retrogression. As water saturation during retrogression seems unlikely, it appears the lawsonite eclogite may have been exhumed to lower pressures and temperatures than can be constrained. In Figure 9, the amount of water in the local bulk composition

necessary to destabilize garnet is approximately 6 wt%, 1.35 wt% more than is currently held in hydrous minerals in the rock.

5.3.2 Stage 2

Renewed burial leading to the growth of the new garnet rims (garnet 2) is interpreted to start at the 'garnet rims in' line (Fig. 9). This is notably only an estimate of the maximum *P–T* conditions for the start of the prograde path for stage 2, as the water content in the eclogite was unknown as this time, and it may have been exhumed to shallower conditions within the subduction channel but failed to record it. The early stages of the prograde path can be determined using compositions of the cores of stage 2 minerals. Useful compositional parameters are x(g), z(g) and y(phe), where x(g) is the X_{Fe} in garnet, z(g) is the grossular component of garnet, and y(phe) is the proportion of Al on the M2 site in phengite (i.e. dioctahedral Al), a pressure-sensitive parameter. In the *P–T* model with water in excess, the x(g) and z(g) parameters from the interior of garnet 2 plot at approximately 1.9 GPa and 500–510 °C within the prograde field. Notably, the x(phe) and y(phe) parameters from the cores of phengite intersect at approximately 2.2 GPa and 540°C, possibly indicating the initiation of recrystallisation of phengite at this *P–T* point. The x(o) parameter from cores of omphacite grains, which reflects the X_{Fe}, also plots close to these conditions, however as the textural timing of omphacite growth in this sample is not well known, it is not clear if its compositions reflect stage 1 burial or stage 2 burial. In the *P–T* model with set water content, these same compositional parameters plot over a larger range of *P–T* conditions, however converge towards 1.95 GPa and 450 °C. The x(phe) and y(phe) parameters from the cores of phengite intersect at the same point as Figure 9: 2.2 GPa and 540°C. As such, an alternative prograde 2 *P–T* path may have begun at lower pressures and temperatures and tracked up towards ~ 2.2 GPa and 540 °C.

The peak assemblage during stage 2 is interpreted to have been phengite + garnet + omphacite + lawsonite + quartz, which is modelled to occur at conditions of ~ 2.7 GPa and 590 °C. This field exists identically on both Figure 9 and Figure 10, and is bound up-temperature by the loss of lawsonite, down-temperature by the presence of talc and/or glaucophane, and up-pressure by the conversion of quartz to coesite and/or omphacite to jadeite.

Stage 2 retrograde *P–T* conditions are constrained from Figure 10. It is characterised by the growth of chlorite and retrograde-zoned glaucophane at the expense of garnet and omphacite. It also includes a modal proportion increase in lawsonite (lawsonite 2), which overgrows garnet 2 (Fig. 2f). The current modal proportions of all stage 2 minerals – minus the garnet 1 and lawsonite 1 cores which are not included in the modelling – intersect in

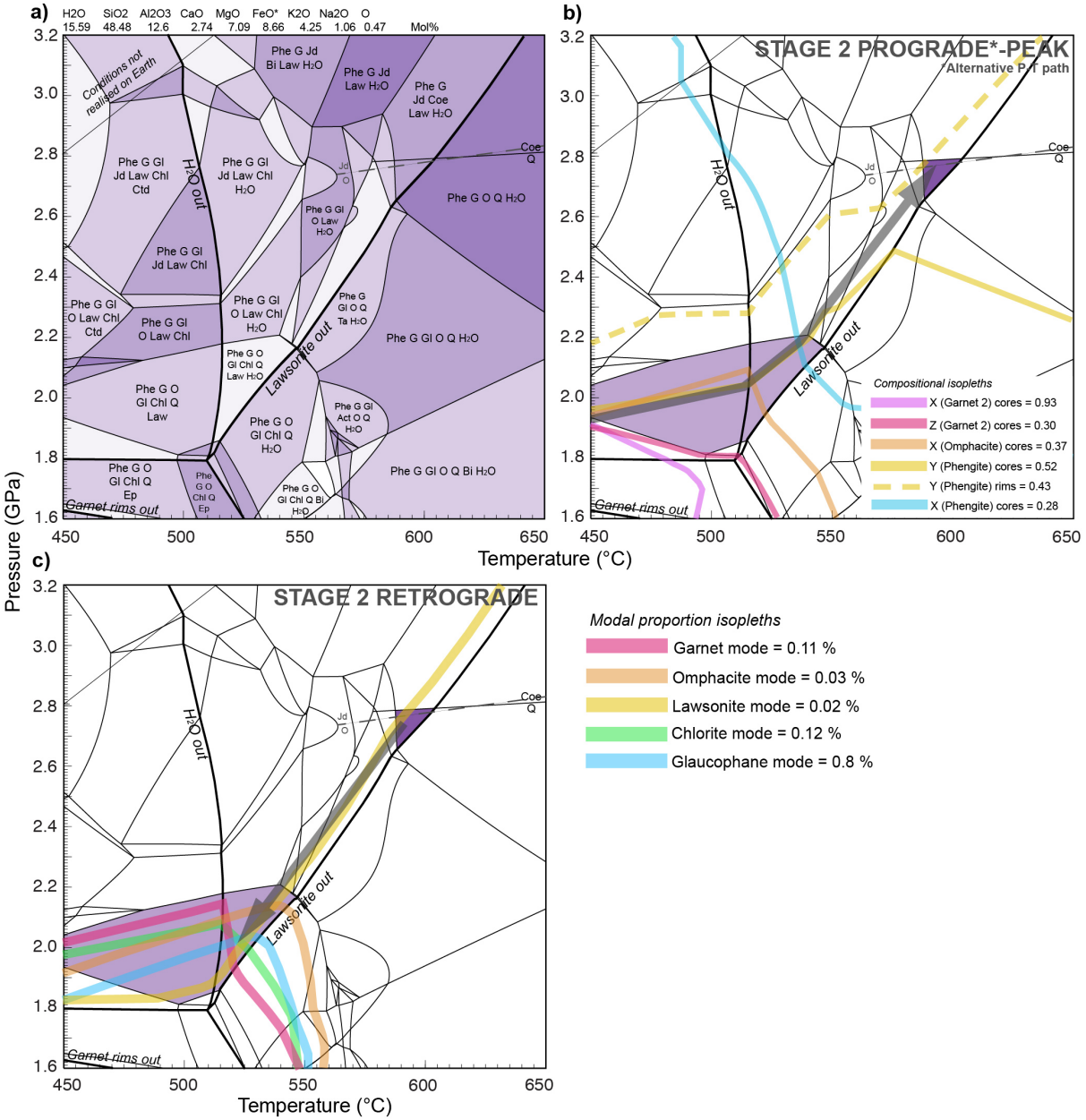


Figure 10: a) Phase equilibrium model calculated with THERMOCALC for the local rock composition with garnet 1 and lawsonite 1 removed, and set water content. Dashed thin grey lines indicate the position of solvi. Colour changes indicate changes in variance across fields. Note the scale change from Figure 8. b) Model (a) showing a possible alternative path for stage 2 prograde, based on compositional isopleths from garnet 1, omphacite and phengite cores. Peak conditions remain the same. c) Model (a) showing the final stage 2 retrograde conditions reached, based on modal proportion isopleths. Abbreviations are listed in Figure 8.

the phengite + garnet + lawsonite + omphacite + quartz + chlorite + glaucophane + H_2O field (Fig. 10c). The modelled isopleths track parallel to each other down temperature in the H_2O absent field, spanning between 1.8–2.1 GPa (Fig. 10c). Final recorded retrogression is therefore interpreted to occur down to ~ 2.0 GPa and 520 °C.

5.3 U–Pb titanite geochronology

In-situ U–Pb isotopic analyses of titanite in the matrix and in the garnet 2 rims define a common lead trend with a lower intercept of 455.1 ± 9.6 Ma (MSWD = 3.3, n = 163, Fig. 11a). The upper intercept has a $^{206}Pb/^{207}Pb$ ratio of 0.8166 ± 0.0096. During data processing, 16 analyses were discarded due to low or no signal, and a further 23 analyses were discarded due to contamination from detectable or visible micro-zircons. Incidental ablation of these zircons was visible in the signals as large Zr spikes. U–Pb geochronological data can be found in Supplementary Table 6

5.4 Ar–Ar phengite geochronology

Step-heating results of two aliquots of phengite from the lawsonite eclogite taken from ~ 50 cm apart are shown in Figure 12. The mineral grains come from the rock matrix. Ar–Ar data can be found in Supplementary Table 7. For aliquot 1, an age of 458.4 ± 3.7 Ma was obtained from 72.4% of released ^{39}Ar. Aliquot 2 shows a rise in age with

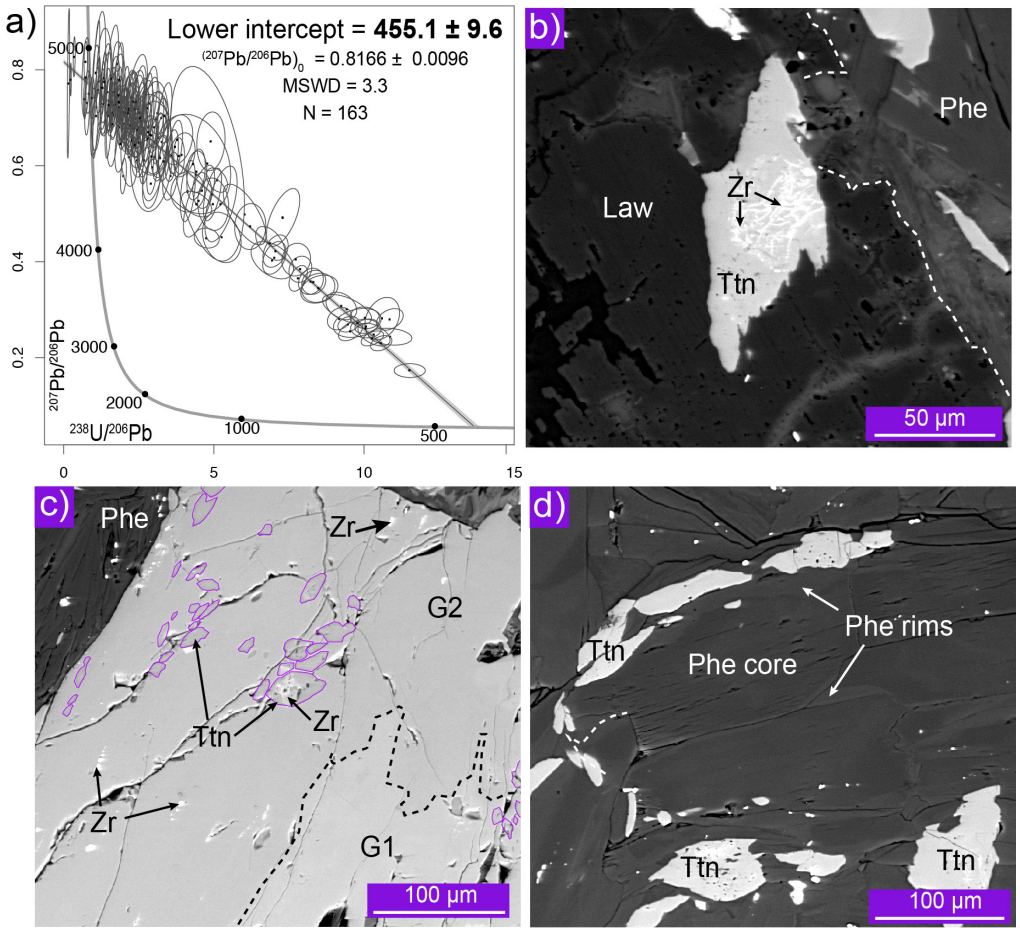


Figure 11: Results of LA–ICP–MS U–Pb titanite geochronology and representative BSE images of analysed titanite grains. a) Terra-Wasserburg plot . b) Coarse-grained titanite in the rim of a stage 2 lawsonite crystal (outlined in white dotted line) displaying a well-formed mesh-like intergrowth of exsolved zircon. c) Coarse titanite trails outlined in purple in the rims of stage 2 garnet, which is distinguished from the stage 1 garnet core by the black dotted line. d) Titanite grains rim a prograde zoned phengite, which has darker cores and brighter rims.

increasing temperature steps. An age of 462.6 ± 3.6 Ma was calculated from 61.9% of released ^{39}Ar.

5.5 Rb–Sr phengite geochronology

In-situ LA–ICP–MS Rb–Sr analyses of phengite cores and rims produce almost identical isochrons (Fig. 13). Phengite rims have a wide range of ^{87}Rb/^{86}Sr ratios and produce an age of 448 ± 13 Ma (MSWD = 0.61, *n* = 18, Fig. 13a), in many cases with favourably high ^{87}Rb/^{86}Sr ratios (up to 2000). Phengite cores generally have lower ^{87}Rb/^{86}Sr ratios and produce an age of 437 ± 37 Ma (MSWD = 0.84, *n* = 16, Fig. 13b). When combined, all phengite data give an isochron age of 449 ± 19 Ma (MSWD = 0.55, *n* = 34, Fig. 13c). Based on textural evidence that titanite occurs as inclusions in phengite, as matrix grains and locally as grains rimming phengite (Fig. 11), it was assumed to have grown synchronously with matrix phengite. Therefore, titanite was analysed to obtain an initial ^{87}Sr/^{86}Sr ratio to anchor the isochron, producing an average ^{87}Sr/^{86}Sr ratio of 0.70986 (*n* = 6, Fig. 13d). The rims are interpreted to form during peak metamorphism and thus were used in the final age calculations. When the phengite rims are anchored with the titanite analyses, the isochron age produced is 450 ± 11 Ma (MSWD = 1.09, *n* = 26, Fig. 13e). Rb–Sr geochronological data can be found in Supplementary Table 8.

5.6 LA–ICP–QQQ isotope mapping

Phengite was mapped for ^{85}Rb and ^{87}Sr (Fig. 14). The qualitative results reveal the phengites are zoned, showing enrichments in Sr in the cores of the grains with slight Rb depletion, and Rb enrichments in the rims which correlates to comparatively low levels of Sr. The boundary between these cores and rims is sharp, and in larger grains is aligned along cleavage (Fig. 14). This zoning correlates to zoning seen in the major elements; Sr enriched cores correspond to low Si/high Al cores, and Rb enriched rims correspond to high Si/low

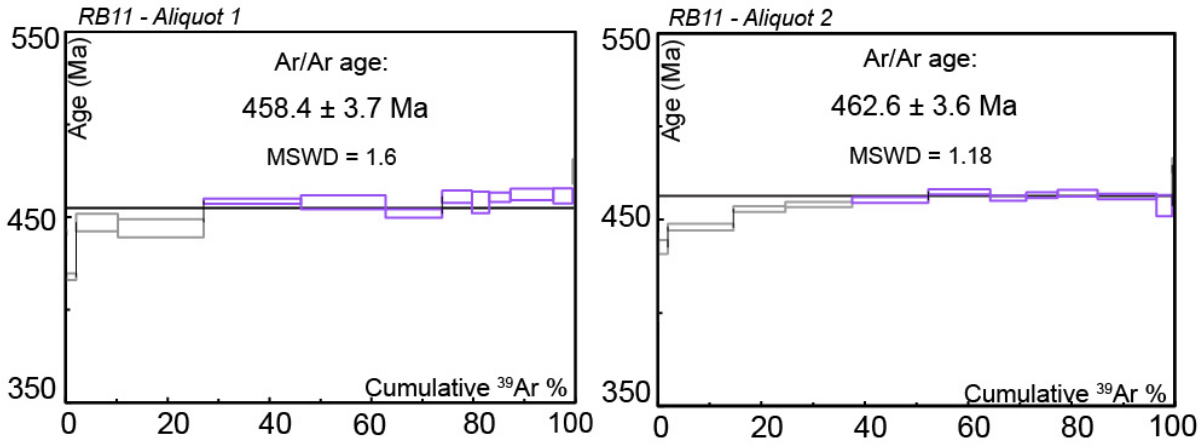


Figure 12: Step-heating Ar–Ar results from two phengite grains in the lawsonite eclogite.

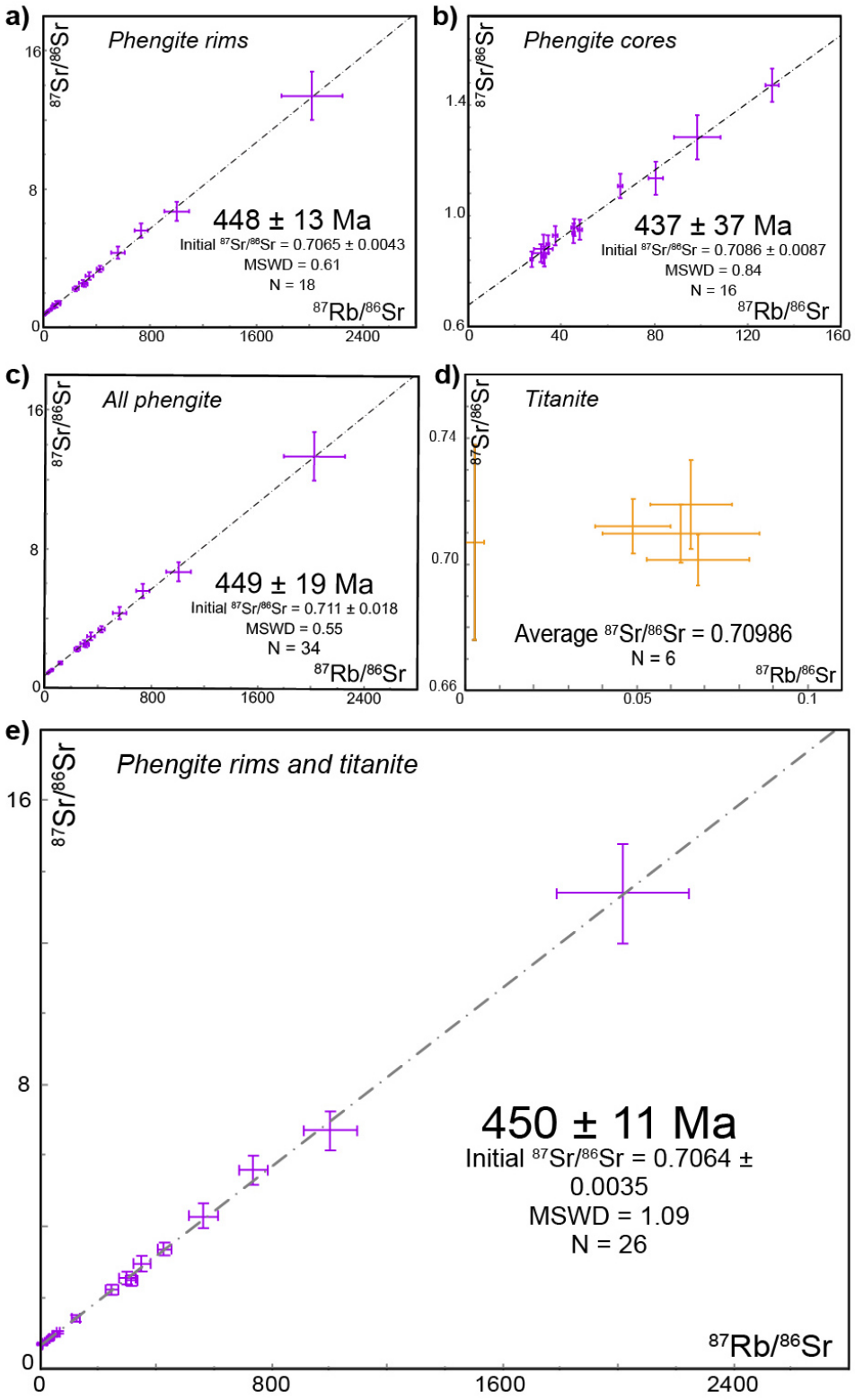


Figure 13: In-situ LA–ICP–MS Rb–Sr geochronological results. a) Isochron constructed from analyses of phengite rims. b) Isochron constructed from analyses of phengite cores. c) Isochron using both phengite cores and rims. The isochrons produce similar ages within the uncertainties. d) Isotopic analyses of texturally intergrown titanite, which records the initial 87Sr/86Sr isotopic ratio. e) Isochron constructed from phengite rims and anchored with titanite analyses.

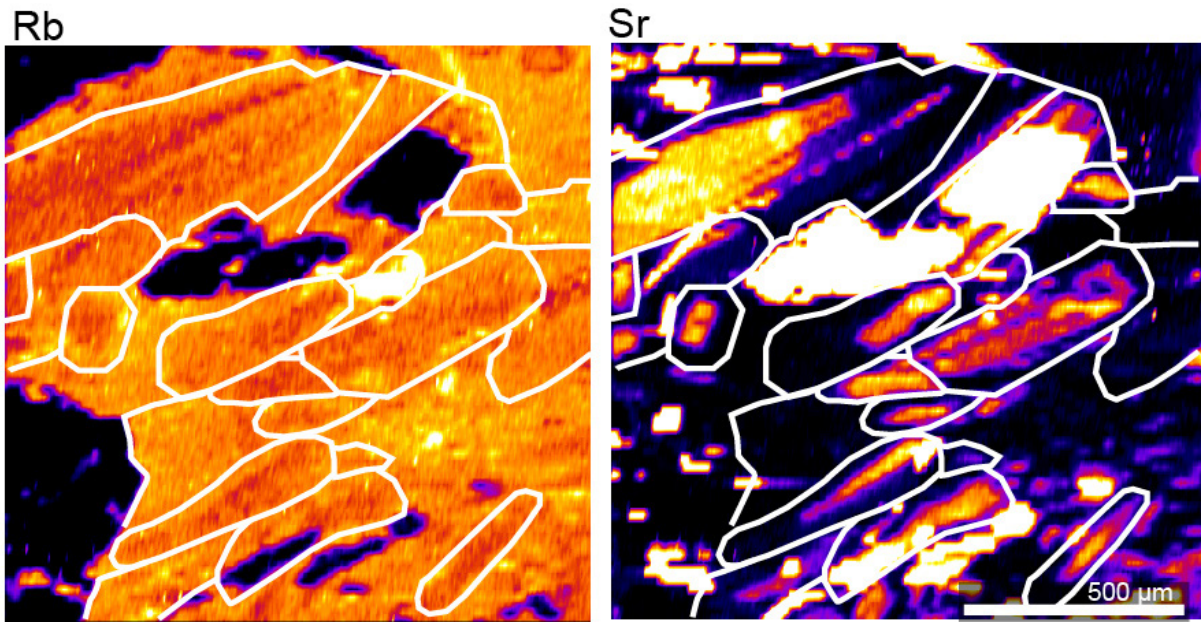


Figure 14: LA–ICP–MS Rb and Sr maps of phengite from the lawsonite eclogite. Maps are semi-quantitative. Phengites show Sr enrichments of all isotopes in their cores, and sometimes a slight Rb enrichment in their rims. These enrichments follow along cleavage planes of the phengite. The boundaries between these rims and cores are extremely sharp and well-defined. The Sr-rich mineral is titanite. The outline of phengite grains is shown in white. Rb-rich material without obvious grain boundaries traced is fine-grained phengite.

Al rims. High Sr grains are titanite. The outline of phengite grains is shown in white.

6. DISCUSSION

6.1 Petrological evidence for reburial of the lawsonite eclogite

Petrographical observations from the block of lawsonite eclogite in the Port Macquarie serpentinite mélange denote at least two interpretable burial events, summarized in Table 1 and schematically outlined in Figure 3.

Evidence for stage 1 prograde (or burial 1) is preserved in the cores of garnet porphyroblasts, which are prograde-zoned, showing bell-shaped Mn profiles. Lawsonite porphyroblasts grew in equilibrium with garnet, as evidenced by their ca. 500 Ma age, synchronous with garnet growth (Tamblyn et al., 2019a). Stage 1 burial is also recorded by phengite inclusions in the outer part of garnet 1, which are high in Si and low in Al, consistent with crystallization at high pressure. It is possible that rare coesite was formed and captured in the outer parts of garnet 1, interpreted from the presence of radial fractures around quartz.

The petrologic evidence for a second burial event after partial exhumation is recorded as inclusions within garnet rims, lawsonite rims, and the compositions of matrix minerals. The step increase in

X_{Mg} and a Mn oscillation marks the boundary of new garnet 2 growth, and the general increased Mn throughout the new garnet rim suggests that it was formed from the breakdown of previously larger garnet porphyroblasts. The presence of chlorite on the boundary between garnet 1 and garnet 2 is key evidence that lower temperatures and pressures were reached before the growth of garnet 2. Omphacite grains in the matrix are prograde zoned (Supp. Fig. 4), and possibly grew from the breakdown of glaucophane during the second burial event, however, may also be relic from stage 1. Phengite and titanite (which make up the strongly foliated rock matrix) underwent recrystallization during prograde 2 deformation (e.g. Spencer et al., 2013; de Meyer, 2014; Itaya and Tsujimori, 2015). This interpretation is supported by petrological observation that the pervasive foliation in the matrix is at an oblique angle to the foliation preserved as inclusion trails in garnet 1 (Fig. 3c). The prograde zoning in the phengite is consistent with recrystallization with increasing pressure and temperature, however the sharp boundary between zones could either be interpreted as i) progressive prograde zoning during total recrystallization of the phengite grains or ii) partial recrystallization of the phengite rims at higher pressure, preserving an older low-pressure core. Phengite with low Si/high Al, identical to the cores of phengite in the matrix, is preserved in the garnet 2 rims (Fig. 6), providing further evidence that garnet 2 rims grew at lower *P–T* conditions than the outer parts of garnet 1. Evidence for stage 2 retrograde includes partial replacement of garnet by chlorite, and partial replacement of omphacite by glaucophane and chlorite (Fig. 3d). Retrograde zoning in glaucophane (Supp. Fig. 6) supports that it grew during decreasing pressure and temperature. New lawsonite growth on existing crystals captured coarse titanite, garnet and glaucophane, suggesting that lawsonite increased its modal proportion during retrograde 2 (Fig. 3d).

6.2 The origin of oscillatory garnet zoning and the possible role of fluids

Garnets from the lawsonite eclogite show oscillatory zoning in Ca, Mn, Fe and Mg (Fig. 5; Supp. Fig. 2), which is subtle in the outer parts of stage 1 garnet but marked throughout the stage 2 garnet rims. Narrow annuli enriched in Mn and Ca are depleted in Fe and Mg, and vice versa. The oscillations are sharp; they occasionally form epitaxial hexagonal crystal shapes on pre-existing garnet (Fig. 5c), or form on irregular-shaped embayed surfaces of pre-existing garnet (Fig. 5b). These features suggest that garnet was resorbed and regrown several times during the metamorphic history of the lawsonite eclogite (aside from the major garnet resorption event between burial 1 and burial 2).

Garnet resorption and regrowth have been suggested to occur via changes in pressure and tem-

perature which influence garnet stability (e.g. García-Casco et al., 2002; Kohn, 2004). This mechanism has been interpreted as the cause of oscillatory garnet zoning from high-pressure rocks in subduction systems, where seismic instability and/or serpentinite hosted channel circulation cause cyclic *P–T* changes (García-Casco et al., 2002; Li et al., 2016, Viete et al., 2018). However, garnet resorption has also been suggested to be a result of external fluid influx, which dissolves and reprecipitates garnet in equilibrium with the fluid (Angiboust et al., 2011; Hyppolito et al, 2018). Additionally, the influx of fluids may enrich or deplete cations incorporated into the garnet during its growth (e.g. Martin et al., 2011; Angiboust et al., 2014; Park et al., 2017). Such fluid influxes may not be easy to trace, however the lack of oscillatory zoning in the major elements of other minerals (e.g. phengite, omphacite) suggests that fluid influxes did not occur on a major scale, or at least were only recorded in garnet. As there is no petrologic evidence supporting either case, the major element oscillatory zoning in garnet is interpreted to have formed by subtle fluctuations in *P–T* and/or influxes of fluid.

6.3 *P–T* conditions of reburial

The record of the *P–T* conditions during the first burial event is contained as inclusions in lawsonite and garnet, while the record of the second burial event is found in garnet and lawsonite rims and the matrix mineralogy. The *P–T* path proposed is summarised in Figure 15, the interpreted conditions are summarised in Supplementary Table 5. The proposed *P–T* path is tentative, due to the difficulty in reconstructing the mineralogical evolution of the sample.

The *P–T* path during stage 1 burial is recorded from 0.8–1.1 GPa at approximately 350 °C, and then tracks up to peak conditions of at least 2.9 GPa and 600 °C based on lawsonite stability, inclusion assemblages in lawsonite and garnet and the estimated modal proportion of garnet (Fig. 8). The potential former presence of coesite, now recorded by radial fractures around quartz inclusions in the outer parts of garnet 1, supports these peak conditions. High Si/low Al phengite inclusions in the outer parts of garnet 1 also support that high-pressures were reached during this stage (Fig. 6). Subsequent retrogression to maximum conditions of ~ 2.0 GPa and 500 °C is recorded by the consumption of garnet, and growth of chlorite and glaucophane (Fig. 9; 10). It is likely the lawsonite eclogite reached lower pressures and temperatures than this during retrogression, however this part of its evolution is difficult to reconstruct.

Stage 2 reburial began at maximum conditions of ~ 2.0 GPa and 500 °C. Growth of new garnet rims with elevated Mn and X_{Mg} captured the stage 1 chlorite and glaucophane. Stage 2 peak conditions of 2.7 GPa and 590 °C were reached, based

on the preserved peak mineral assemblage. Retrogression to approximately 1.9 GPa and 520 °C is based on the current modal mineralogy of the rock (Fig. 10c), and is supported by the formation of retrograde-zoned glaucophane and the partial break down of garnet to form chlorite.

If these tentative estimates are taken at face value, the earliest stages of the prograde evolution of the rock occurred on a geothermal gradient of approximately 370 °C/GPa, while the peak and retrograde stages of both stage 1 and 2 occurred on a cooler geothermal gradient of approximately 210–265 °C/GPa. These gradients are in line with a subduction channel which is cooling over time, potentially in response to the refrigeration effects of on-going subduction (Gerya, 2002; Agard et al., 2018). If this is correct, it suggests the eclogite records the transition from subduction initiation (e.g. Tamblyn et al., 2019a) to subduction maturity. These inferred geothermal estimates are comparable to the geothermal gradient experienced by garnet blueschist from the same mélange that hosts the lawsonite eclogite at Port Macquarie (~ 275 °C/GPa; Tamblyn et al., 2019a). The complete *P–T* path suggested in Figure 15 is two hair-pin loops, which are constrained by the presence of lawsonite throughout the recorded history. Such *P–T* evolutions have been previously suggested for high-pressure rocks in oceanic subduction systems (e.g. Gerya et al, 2002; Krebs et al., 2011; Pourteau et al., 2019).

6.4 Timing of reburial

Tamblyn et al. (2019a) obtained Lu–Hf ages of 489.7 ± 5 Ma for garnet–whole rock and 505 ± 15 Ma for lawsonite–whole rock from the eclogite. The cores of stage 1 garnet are highly enriched in Lu compared to the stage 2 garnet, indicating the garnet Lu–Hf age is essentially the age of stage 1 garnet growth. The lawsonite Lu–Hf age is less precise but within uncertainty of the garnet age, suggesting that stage 1 garnet and stage 1 lawsonite grew within a single isotopic reservoir at ca. 500–490 Ma. The lawsonite grains contain patches that are enriched in Lu (Tamblyn et al., 2019a), and in places are overgrown by volumetrically minor second generation lawsonite (Fig. 2f). The Lu-rich domains in stage 1 lawsonite formed prior to garnet nucleation. The *P–T* path during the stage 1 burial tracks up to tentative peak conditions of at least 2.9 GPa and 600 °C (section 6.3). This occurred at ca. 505–490 Ma as dated by garnet and lawsonite Lu–Hf (Tamblyn et al., 2019a; Fig. 15).

Matrix phengite that encloses garnet, lawsonite and omphacite porphyroblasts shows an increasing Si and celadonite content from core to rim (Fig. 6; Carswell et al., 2000). This compositional component is consistent with increasing pressure, which in the absence of information about changes in non-lithostatic stress, equates to increasing burial depth. The plateau ages obtained

from Ar–Ar geochronology from phengite from the rock matrix give ages of ca. 458 and ca. 462 Ma. The suggested closure temperature of argon diffusion in phengite is variable (e.g. Warren et al., 2011; Fornash et al., 2016), and is dependent on grain size and fluid availability (e.g. Glodny et al., 2002). Numerical diffusion modelling suggests that phengite grown at blueschist to eclogite facies (up to 550 °C) can retain argon from its prograde history (Warren et al., 2011). This has been supported by step-heating experiments which suggest phengite can be highly retentive of argon (Forster and Lister, 2014). These findings are in line with samples from high-pressure terranes where Ar–Ar ages are similar to peak metamorphic ages obtained from zircon or garnet geochronology (Fornash et al., 2016), or can be texturally related to mineral growth during sequential phases of deformation (Putlitz et al., 2005).

In-situ LA–ICP–MS Rb–Sr dating of mica is still in its infancy as a geochronological technique. However, it has the potential to rapidly constrain ages of metamorphism and deformation in metamorphic rocks. Rb–Sr analyses of phengite rims, coupled with an initial $^{87}Sr/^{86}Sr$ value from texturally intergrown titanite, give an isochron age of ca. 450 Ma. The rims of phengite were selected for the final age calculation, as they are interpreted to grow at peak conditions of stage 2.

Rb and Sr maps also support that the geochronologic results are growth ages (Fig. 14); the zoning is sharply defined, suggesting minimal post-growth diffusion within the grains (e.g. Konrad-Schmolke et al., 2011). Rb–Sr maps show Sr enrichments in the low-Si cores of phengite, and Rb enrichments in the high-Si rims, a pattern that has been noted in high-pressure rocks (Di Vincenzo et al., 2006). The incorporation of Sr into phengite may therefore be related to the breakdown of another Sr-bearing mineral in the system at lower pressures, or, a preference for Sr in low-Si less-phengitic white mica, which declines with increasing phengitic component up-pressure. The Rb–Sr age of the phengite rims is within uncertainty of the age obtained from phengite Ar–Ar analyses and titanite U–Pb age of ca. 455 Ma (below). This interpretation is in line with similar high-pressure terranes, where Rb–Sr dates record crystallization of phengite on the prograde-peak path during metamorphism (e.g. Hetzel and Romer, 2000; Glodny et al., 2002; Bosse et al., 2005; Di Vincenzo et al., 2006). In some of these examples, Rb–Sr phengite growth ages are synchronous with Ar–Ar phengite ages (Anczkiewicz et al., 2000; Hetzel and Romer, 2000; Glodny et al., 2002; Rodríguez et al., 2003). Rb–Sr has also been shown to date continuous recrystallization of white mica during retrograde deformation in polymetamorphic terranes, at peak temperatures of ~ 500–550 °C (Bröcker et al., 2013), demonstrating the ability for the Rb–Sr white mica ages to record recrystallization events.

The U–Pb data from titanite in the matrix and as inclusions in the stage 2 garnet gives an age of ca. 455 Ma. Although there is some dispersion in the data, it is evident the matrix titanites are significantly younger than the ca. 490 Ma age for stage 1 lawsonite and garnet. Phase equilibrium modelling suggests the rock experienced *P–T* conditions below the closure temperature of titanite (~600–800 °C; Hartnady et al., 2019). Additionally, there is no evidence of a rutile-bearing assemblage in the lawsonite eclogite. Therefore, it is unlikely the titanite formed from breakdown of rutile on the retrograde path. Consequently, we interpret the titanite U–Pb data to reflect the timing of titanite recrystallisation.

Titanite occurs throughout the matrix and forms around the edges of prograde-zoned phengite (Fig. 11b-d). It occurs as fine-grained inclusion trails in garnet cores and lawsonite, and as coarse-grained inclusions in stage 2 garnet and lawsonite rims (Fig. 11b-c). These textural relationships indicate that titanite was stable during the entire metamorphic evolution of the eclogite, first growing during the stage 1 burial event, and recrystallizing during the prograde evolution of the stage 2 burial event to form coarser-grained titanite. This recrystallization was possibly tracked by increasing F, Al_2O_3 and FeO content in the titanite (Fig. 7).

The inclusions in titanite are limited to fine-grained apatite, phengite and zircon (< 10 μm). Zircon is either euhedral and 5–10 μm in size, or occurs as fine-grained clusters or web-like intergrowths which are 2 μm or less (Fig. 11b,c). The 5–10 μm sized apatite, phengite and zircon inclusions are interpreted to predate the crystallization of titanite, and were avoided during analyses. However, the extremely fine-grained web-like micro-zircon was difficult to avoid, and was possibly incorporated into analyses. This is suggested by Zr concentrations in the titanite analyses of up to ~ 18800 ppm (Supplementary Table 6). Texturally, these extremely fine-grained zircon dustings only occur in sections of titanite grains, and are absent in phengite, garnet, lawsonite and omphacite. This suggests they are probably exsolution of Zr from the titanite, rather than inclusions (Fig. 11b,c). Titanite can substitute Zr^{4+} for Ti^{4+} in its crystal lattice, as evidenced by development of the Zr-in-titanite thermobarometer (Hayden et al., 2008). However, in quartz-absent rocks, titanite can take in significant amounts of ZrO_2 (up to 15 wt%; Della Ventura et al., 1999; Seifert and Kramer, 2003; Seifert; 2005; Vuorinen and Hålenius, 2005; Liferovich and Mitchell, 2005; Chakhmouradian, 2004). While these studies are from igneous rocks, they demonstrate the ability for significant Zr to substitute into titanite.

The phase equilibrium modelling of the stage 2 effective bulk composition suggests the prograde-peak path taken by the lawsonite eclogite during reburial was quartz-free until absolute

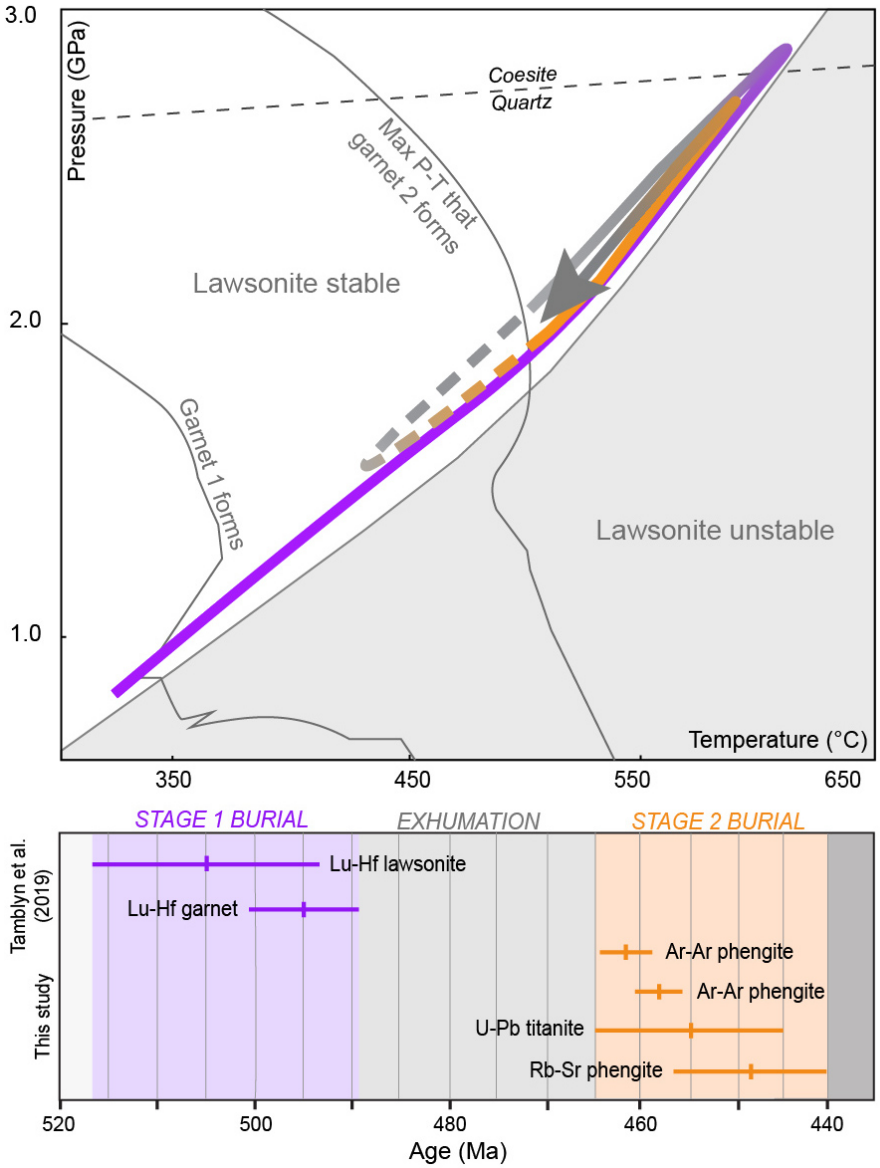


Figure 15: Summary of the P–T–t path of the lawsonite eclogite. Lu–Hf geochronology from lawsonite and garnet dates an earlier event during burial 1. Ar–Ar and Rb–Sr data from phengite, and U–Pb data from titanite, date a younger recrystallization event associated with reburial of the lawsonite eclogite within the subduction channel. This results in two hairpin P–T loops. While the exact timing of exhumation and P–T conditions reached between these two burial events is unknown, it must have occurred between approximately 485–465 Ma.

peak conditions were obtained (590 °C, 2.7 GPa). Zircon exsolution from titanite has not been directly reported before, but in lieu of other explanations, we suggest these fine-grained clusters of zircon within titanite represent high-Zr titanite which formed in a quartz absent matrix assemblage, which then exsolved zircon after crystallization of the parent mineral. As such, while we tried to avoid areas of obvious weblike zircon in titanite, we suggest that if small amounts of fine-grained zircon exsolution were incorporated into the titanite U–Pb analyses, we are dating U–Pb isotopic ratios related to titanite recrystallization at ca. 455 Ma.

The above interpretations suggest recrystallization of phengite and titanite at ca. 450 Ma dates the timing of burial 2, which reached peak *P–T* conditions of 2.7 GPa and 590 °C. The two burial events were separated by a period of exhumation to maximum conditions of approximately 2.0 GPa and 500 °C, however the lawsonite eclogite may have been exhumed further up the subduction channel. The two stages of metamorphism and burial in the lawsonite eclogite occurred over a period of at least ca. 50 M.y. (Fig. 15). The timing of final exhumation after burial 2 is unknown, but had occurred by the Permian, based on serpentinite detritus in nearby early Permian basins in the SNEO (Aitchison et al., 1994).

6.5 Examples of other burial cycles

The suggestion that the block of lawsonite eclogite at Port Macquarie underwent two stages of burial, each marked by garnet growth and separated by a stage of garnet breakdown, is similar to *P–T* histories proposed from other studies on subducted rocks in oceanic settings, and is supported by results of numerical modelling (e.g. Gerya et al., 2002). Despite the difficulties in recognizing and constraining multiple cycles of burial and exhumation within single high-pressure samples, workers have had success using various geochronological and mineralogical tools. Dating zones within metamorphic zircon, combined with REE chemistry and inclusion assemblages, have allowed two or more subduction cycles to be identified in Rhodope, Greece (Liati et al., 2016) and the Italian Alps (Rubatto et al., 2011), however the latter was within a continental subduction system. Three burial cycles in the Sambagawa belt in Japan have been identified from mineral assemblages and mineral chemistry of garnet and amphibole in eclogite by Kabir and Takasu (2010). Two burial cycles are recorded in eclogite from the Akeyazi terrane in Tianshan, China, interpreted from petrological and mineral zoning evidence, with *P–T* paths constrained from psuedosections (Li et al., 2016). García-Casco et al. (2002) modelled oscillatory zoning in garnet and amphibole chemistry from serpentinite mélange in Cuba, concluding that they formed in near-equilibrium and record fluctuations in *P–T* conditions during subduction. Blanco-Quintero et al. (2011) also reported reburial during interpreted large-scale convective flow from this mélange, interpreted from garnet zoning and *P–T* pseudosection modelling. Geochronological constraints on the development of the mineral assemblages in the Port Macquarie eclogite point to a long history of high-pressure metamorphism, with a significant age difference between the formation of stage 1 and stage 2 assemblages (Fig. 15). Based on time scales of material movement in subduction systems from numerical modelling (Gerya et al., 2002), the geochronological data from the eclogite supports the likelihood that multiple burial and partial exhu-

mation paths may have occurred.

6.6 Subduction channel dynamics

A corner or return flow model of material within the subduction channel (e.g. Shreve and Cloos, 1986, Gerya et al., 2002; Agard et al., 2009; Roda et al., 2019), is suggested for repeated burial and exhumation of the lawsonite eclogite at Port Macquarie. Numerical modelling predicts that during oceanic subduction, hydration of the mantle wedge creates a buoyant low viscosity serpentinite-filled subduction channel which can pluck high-pressure rocks from the subducting slab and circulate them within the channel (e.g. Gerya et al., 2002). In these models, the high-pressure fragments can become deeply subducted, but can also experience partial exhumation and reburial, resulting in *P–T* loops (Gerya et al., 2002). Rocks with different *P–T–t* histories can also accumulate within the channel and be exhumed together to form mélanges that contain a variety of subducted products (e.g. Krebs et al., 2008). At Port Macquarie, this behaviour is confirmed by the presence of garnet blueschist, which is ca. 470 Ma in age, and has a different *P–T* path to the eclogite, yet is found as a tectonic block less than 10 meters away from the lawsonite eclogite (Och et al., 2003; Tamblyn et al., 2019a).

The geochronological data presented above also supports the notion of long-lived residence of high-pressure materials within oceanic subduction channels. The minimum duration spent in the subduction channel by the lawsonite eclogite at Port Macquarie is ca. 50 M.y. (Fig. 15). Analogous durations of high-pressure metamorphism and accumulation have been reported from oceanic subduction systems. Exotic high-pressure rocks hosted in serpentinite, which have been interpreted to have been buried and exhumed by convective flow processes, span an age range of ca. 55 M.y. in Cuba (Lázaro et al., 2009), and ca. 40 M.y. in the Dominican Republic (Krebs et al., 2008). High-pressure rocks exhumed in Turkey with different *P–T–t* histories span an age range of ca. 20 M.y. (Pourteau et al., 2019), supported by in-situ Ar–Ar data (Fornash et al., 2016). In the Mariana subdution system, the residence time for blueschist within the subduction channel is ca. 48 M.y. (Tamblyn et al., 2019b).

With the caveat that the *P–T* conditions suggested from the phase equilibrium modelling of the eclogite at Port Macquarie are taken as approximations, a *P–T–t* path can be constructed for the lawsonite eclogite, and the rate of exhumation to reburial estimated. If the maximum possible *P–T* conditions of stage 1 exhumation are taken as 2.0 GPa and 500 °C, the total pressure and temperature change from peak stage 1 to peak stage 2 equates to ~ 1.6 GPa and 190 °C. If an average lithostatic pressure of 3.2 km/kbar with no non-lithostatic loads is assumed, this pressure change is equivalent to approximately 50 km of vertical depth

change. Depending on subduction angle, the total travel distance of the lawsonite eclogite within the channel may have been more than 100 km during the looping *P–T* history.

7. Conclusions

Lawsonite eclogite in serpentinite mélange at Port Macquarie in the Southern New England Orogen records *P–T* conditions of ~ 2.9 GPa and 600 °C, attained at ca. 500–490 Ma. The mineral assemblages that define these *P–T* conditions were overprinted by a second high-pressure assemblage that formed at ca. 450 Ma. Compositional zoning in phengite, and growth of a second generation of garnet, indicate the overprinting mineral assemblage formed during up-pressure metamorphism to ~ 2.7 GPa and 590 °C. Between these two stages of burial, partial exhumation occurred to at least 2.0 GPa, but probably to lower *P–T* conditions. The *P–T* evolution defines hair-pin looping *P–T* paths that developed along a similar geothermal gradient, suggesting the lawsonite eclogite was cycled within a serpentinite-filled subduction channel during return flow of subducted material. This cycling occurred over a minimum timeframe of ca 50 M.y., implying long-lived residence of the eclogite within the subduction system. A number of studies are beginning to discover that subducted material may undergo complex *P–T–t* evolutions that record multiple episodes of burial and exhumation during prolonged residence within subduction systems. These cyclic *P–T* evolutions support predictions from numerical models which suggest material can follow convective flow paths within evolving serpentinite filled subduction channels.

Acknowledgements

The authors would like to thank Ben Wade and Sarah Gilbert of Adelaide Microscopy, for their assistance with EPMA and LA–ICP–MS data collection. David Kelsey is thanked for helpful discussions and his ongoing support with phase equilibria modelling. Jack Gillespie of Curtin University is thanked for collecting the phase and EDS maps. Mitchell Bockmann of the University of Adelaide is thanked for setting up the titanite U–Pb method. We thank Pierre Lanari and an anonymous reviewer for their comments, which greatly strengthened the manuscript. This research in part was supported by Australian Research Council grant DP160104637. Renée Tamblyn acknowledges support from the University of Adelaide in the form of the Aldermann Kleeman travel scholarship and an Australian Postgraduate Award.

References

Agard, P., Plunder, A., Angiboust, S., Bonnet, G., and Ruh, J. (2018). The subduction plate interface: Rock record and mechanical

coupling (from long to short time scales). *Lithos*.

Agard, P., Yamato, P., Jolivet, L., and Burov, E. (2009). Exhumation of oceanic blueschists and eclogites in subduction zones: timing and mechanisms. *Earth-Science Reviews, 92*(1), 53-79.

Aitchison, J. C., Blake, M. C., Flood, P. G., and Jayko, A. S. (1994). Paleozoic ophiolitic assemblages within the southern New England orogen of eastern Australia: Implications for growth of the Gondwana margin. *Tectonics, 13*(5), 1135-1149. doi: 10.1029/93TC03550

Anczkiewicz, R., Burg, J., Villa, I. M., and Meier, M. (2000). Late Cretaceous blueschist metamorphism in the Indus suture zone, Shangla region, Pakistan Himalaya. *Tectonophysics, 324*(1-2), 111-134.

Angiboust, S., Agard, P., Raimbourg, H., Yamato, P., and Huet, B. (2011). Subduction interface processes recorded by eclogite-facies shear zones (Monviso, W. Alps). *Lithos, 127*(1-2), 222-238.

Angiboust, S., Pettke, T., De Hoog, J. C., Caron, B., and Oncken, O. (2014). Channelized fluid flow and eclogite-facies metasomatism along the subduction shear zone. *Journal of Petrology, 55*(5), 883-916.

Blanco-Quintero, I. F., García-Casco, A., and Gerya, T. V. (2011). Tectonic blocks in serpentinite mélange (eastern Cuba) reveal large-scale convective flow of the subduction channel. *Geology, 39*(1), 79-82.

Bosse, V., Féraud, G., Ballevre, M., Peucat, J.-J., and Corsini, M. (2005). Rb–Sr and 40Ar/39Ar ages in blueschists from the Ile de Groix (Armorican Massif, France): implications for closure mechanisms in isotopic systems. *Chemical Geology, 220*(1-2), 21-45.

Bröcker, M., Baldwin, S., and Arkudas, R. (2013). The geological significance of 40Ar/39Ar and Rb–Sr white mica ages from S yros and S ifnos, G reece: a record of continuous (re) crystallization during exhumation? *Journal of metamorphic Geology, 31*(6), 629-646.

Carswell, D., Wilson, R., and Zhai, M.-g. (2000). Metamorphic evolution, mineral chemistry and thermobarometry of schists and orthogneisses hosting ultra-high pressure eclogites in the Dabieshan of central China. *Lithos, 52*(1-4), 121-155.

Castelli, D., and Rubatto, D. (2002). Stability of Al-and F-rich titanite in metacarbonate: petrologic and isotopic constraints from a polymetamorphic eclogitic marble of the internal Sesia Zone (Western Alps). *Contributions to Mineralogy and Petrology, 142*(6), 627-639.

Chakhmouradian, A. R. (2004). Crystal chemistry and paragenesis of compositionally unique (Al-, Fe-, Nb-, and Zr-rich) titanite from Afrikanda, Russia. *American*

Mineralogist, 89(11-12), 1752-1762.

Cherniak, D. (2006). Zr diffusion in titanite. *Contributions to Mineralogy and Petrology, 152*(5), 639-647.

Collins, W., and Richards, S. (2008). Geodynamic significance of S-type granites in circum-Pacific orogens. *Geology, 36*(7), 559-562.

Collins, W. J. (2002). Nature of extensional accretionary orogens. *Tectonics, 21*(4).

de Meyer, C. M., Baumgartner, L. P., Beard, B. L., and Johnson, C. M. (2014). Rb–Sr ages from phengite inclusions in garnets from high pressure rocks of the Swiss Western Alps. *Earth and Planetary Science Letters, 395*, 205-216.

Della Ventura, G., Bellatreccia, F., and Williams, C. (1999). Zr-and LREE-rich titanite from Tre Croci, Vico volcanic complex (Latium, Italy). *Mineralogical Magazine, 63*(1), 123-130.

Di Vincenzo, G., Tonarini, S., Lombardo, B., Castelli, D., and Ottolini, L. (2006). Comparison of 40Ar–39Ar and Rb–Sr data on phengites from the UHP Brossasco–Isasca Unit (Dora Maira Massif, Italy): implications for dating white mica. *Journal of Petrology, 47*(7), 1439-1465.

Diener, J., and Powell, R. (2012). Revised activity–composition models for clinopyroxene and amphibole. *Journal of metamorphic Geology, 30*(2), 131-142.

Elburg, M., Bons, P., Foden, J., and Brugger, J. (2003). A newly defined Late Ordovician magmatic-thermal event in the Mt Painter Province, northern Flinders Ranges, South Australia. *Australian Journal of Earth Sciences, 50*(4), 611-631.

Elburg, M., Vroon, P., van der Wagt, B., and Tchalikian, A. (2005). Sr and Pb isotopic composition of five USGS glasses (BHVO-2G, BIR-1G, BCR-2G, TB-1G, NKT-1G). *Chemical Geology, 223*(4), 196-207.

Evans, T. (2004). A method for calculating effective bulk composition modification due to crystal fractionation in garnet-bearing schist: implications for isopleth thermobarometry. *Journal of metamorphic Geology, 22*(6), 547-557.

Fornash, K. F., Cosca, M. A., and Whitney, D. L. (2016). Tracking the timing of subduction and exhumation using 40 Ar/39 Ar phengite ages in blueschist-and eclogite-facies rocks (Sivrihisar, Turkey). *Contributions to Mineralogy and Petrology, 171*(7), 67.

Forster, M. A., and Lister, G. S. (2014). 40Ar/39Ar geochronology and the diffusion of 39Ar in phengite–muscovite intergrowths during step-heating experiments in vacuo. *Geological Society, London, Special Publications, 378*(1), 117-135.

Fukui, S., Watanabe, T., Itaya, T., and Leitch, E. C. (1995). Middle Ordovician high PT met-

amorphic rocks in eastern Australia: Evidence from K-Ar ages. *Tectonics, 14*(4), 1014-1020.

Gaidies, F., De Capitani, C., and Abart, R. (2008). THERIA_G: a software program to numerically model prograde garnet growth. *Contributions to Mineralogy and Petrology, 155*(5), 657-671.

García-Casco, A., Torres-Roldán, R., Millán, G., Monié, P., and Schneider, J. (2002). Oscillatory zoning in eclogitic garnet and amphibole, Northern Serpentinite Melange, Cuba: a record of tectonic instability during subduction? *Journal of metamorphic Geology, 20*(6), 581-598.

Gerya, T. V., Stöckhert, B., and Perchuk, A. L. (2002). Exhumation of high-pressure metamorphic rocks in a subduction channel: A numerical simulation. *Tectonics, 21*(6).

Glen, R. (2013). Refining accretionary orogen models for the Tasmanides of eastern Australia. *Australian Journal of Earth Sciences, 60*(3), 315-370.

Glodny, J., Bingen, B., Austrheim, H., Molina, J. F., and Rusin, A. (2002). Precise eclogitization ages deduced from Rb/Sr mineral systematics: the Maksyutov complex, Southern Urals, Russia. *Geochimica et Cosmochimica Acta, 66*(7), 1221-1235.

Green, E., Holland, T., and Powell, R. (2007). An order-disorder model for omphacitic pyroxenes in the system jadeite-diopside-hedenbergite-acmite, with applications to eclogitic rocks. *American Mineralogist, 92*(7), 1181-1189.

Hartnady, M. I., Kirkland, C. L., Clark, C., Spaggiari, C. V., Smithies, R. H., Evans, N. J., and McDonald, B. J. (2019). Titanite dates crystallization: Slow Pb diffusion during super-solidus re-equilibration. *Journal of metamorphic Geology, 37*(6), 823-838.

Hayden, L. A., Watson, E. B., and Wark, D. A. (2008). A thermobarometer for sphene (titanite). *Contributions to Mineralogy and Petrology, 155*(4), 529-540.

Hetzel, R., and Romer, R. L. (2000). A moderate exhumation rate for the high-pressure Maksyutov Complex, southern Urals, Russia. *Geological Journal, 35*(3-4), 327-344.

Hogmalm, K. J., Zack, T., Karlsson, A. K.-O., Sjöqvist, A. S., and Garbe-Schönberg, D. (2017). In situ Rb–Sr and K–Ca dating by LA-ICP-MS/MS: an evaluation of N 2 O and SF 6 as reaction gases. *Journal of Analytical Atomic Spectrometry, 32*(2), 305-313.

Holland, T., and Powell, R. (1998). An internally consistent thermodynamic data set for phases of petrological interest. *Journal of metamorphic Geology, 16*(3), 309-343.

Holland, T., and Powell, R. (2003). Activity–composition relations for phases in petrolog-

ical calculations: an asymmetric multi-component formulation. *Contributions to Mineralogy and Petrology, 145*(4), 492-501.

Holland, T., and Powell, R. (2011). An improved and extended internally consistent thermodynamic dataset for phases of petrological interest, involving a new equation of state for solids. *Journal of metamorphic Geology, 29*(3), 333-383.

Hyppolito, T., Cambeses, A., Angiboust, S., Raimondo, T., García-Casco, A., & Juliani, C. (2019). Rehydration of eclogites and garnet-replacement processes during exhumation in the amphibolite facies. *Geological Society, London, Special Publications*, 478(1), 217-239.

Itaya, T., and Tsujimori, T. (2015). White mica K–Ar geochronology of Sanbagawa eclogites from Southwest Japan: implications for deformation-controlled K–Ar closure temperature. *International Geology Review, 57*(5-8), 1014-1022.

Jenkins, R., Landenberger, B., and Collins, W. (2002). Late Palaeozoic retreating and advancing subduction boundary in the New England fold belt, New South Wales. *Australian Journal of Earth Sciences, 49*(3), 467-489.

Jessop, K., Daczko, N., and Piazolo, S. (2019). Tectonic cycles of the New England Orogen, eastern Australia: A review. *Australian Journal of Earth Sciences, 66*(4), 459-496.

Kabir, M., and Takasu, A. (2010). Evidence for multiple burial–partial exhumation cycles from the Onodani eclogites in the Sambagawa metamorphic belt, central Shikoku, Japan. *Journal of metamorphic Geology, 28*(8), 873-893.

Kelley, S. (2002). Excess argon in K–Ar and Ar–Ar geochronology. *Chemical Geology, 188*(1), 1-22.

Kemp, A., Hawkesworth, C., Collins, W., Gray, C., and Blevin, P. (2009). Isotopic evidence for rapid continental growth in an extensional accretionary orogen: The Tasmanides, eastern Australia. *Earth and Planetary Science Letters, 284*(3), 455-466.

Kohn, M. J. (2004). Oscillatory-and sector-zoned garnets record cyclic (?) rapid thrusting in central Nepal. *Geochemistry, Geophysics, Geosystems, 5*(12).

Konrad-Schmolke, M., O'Brien, P. J., de Capitani, C., and Carswell, D. A. (2008). Garnet growth at high-and ultra-high pressure conditions and the effect of element fractionation on mineral modes and composition. *Lithos, 103*(3-4), 309-332.

Krebs, M., Maresch, W., Schertl, H.-P., Münker, C., Baumann, A., Draper, G., Idleman, B., and Trapp, E. (2008). The dynamics of intra-oceanic subduction zones: a direct comparison between fossil petrological evidence (Rio San Juan Complex, Domin-

ican Republic) and numerical simulation. *Lithos, 103*(1), 106-137.

Krebs, M., Schertl, H.-P., Maresch, W., and Draper, G. (2011). Mass flow in serpentinite-hosted subduction channels: P–T–t path patterns of metamorphic blocks in the Rio San Juan mélange (Dominican Republic). *Journal of Asian Earth Sciences, 42*(4), 569-595.

Lanari, P., and Engi, M. (2017). Local bulk composition effects on metamorphic mineral assemblages. *Reviews in mineralogy and geochemistry, 83*(1), 55-102.

Lázaro, C., García-Casco, A., Rojas Agramonte, Y., Kröner, A., Neubauer, F., and Iturralde-Vinent, M. (2009). Fifty-five-million-year history of oceanic subduction and exhumation at the northern edge of the Caribbean plate (Sierra del Convento mélange, Cuba). *Journal of metamorphic Geology, 27*(1), 19-40.

Leake, B. E., Woolley, A. R., Arps, C. E., Birch, W. D., Gilbert, M. C., Grice, J. D., Hawthorne, F. C., Kato, A., Kisch, H. J., and Krivovichev, V. G. (1997). Report. Nomenclature of amphiboles: report of the subcommittee on amphiboles of the international mineralogical association commission on new minerals and mineral names. *Mineralogical Magazine, 61*(2), 295-321.

Leitch, E. (1975). Plate tectonic interpretation of the Paleozoic history of the New England Fold Belt. *Geological Society of America Bulletin, 86*(1), 141-144.

Li, J.-L., Klemd, R., Gao, J., and John, T. (2016). Poly-cyclic metamorphic evolution of eclogite: evidence for multistage burial–exhumation cycling in a subduction channel. *Journal of Petrology, 57*(1), 119-146.

Liati, A., Theye, T., Fanning, C. M., Gebauer, D., and Rayner, N. (2016). Multiple subduction cycles in the Alpine orogeny, as recorded in single zircon crystals (Rhodope zone, Greece). *Gondwana Research, 29*(1), 199-207.

Liferovich, R. P., and Mitchell, R. H. (2005). Composition and paragenesis of Na-, Nb-and Zr-bearing titanite from Khibina, Russia, and crystal-structure data for synthetic analogues. *The Canadian Mineralogist, 43*(2), 795-812.

Ludwig, K. (2003). User's manual for Isoplot 3.00: a geochronological toolkit for Microsoft Excel: Kenneth R. Ludwig.

Manton, R. J., Buckman, S., Nutman, A. P., Bennett, V. C., and Belousova, E. A. (2017). U-Pb-Hf-REE-Ti zircon and REE garnet geochemistry of the Cambrian Attunga eclogite, New England Orogen, Australia: Implications for continental growth along eastern Gondwana. *Tectonics, 36*(8), 1580-1613.

Marmo, B., Clarke, G., and Powell, R. (2002). Fractionation of bulk rock composition due to

porphyroblast growth: effects on eclogite facies mineral equilibria, Pam Peninsula, New Caledonia. *Journal of metamorphic Geology, 20*(1), 151-165.

Martin, L. A., Rubatto, D., Brovarone, A. V., and Hermann, J. (2011). Late Eocene lawsonite-eclogite facies metasomatism of a granulite sliver associated to ophiolites in Alpine Corsica. *Lithos, 125*(1-2), 620-640.

Moresi, L., Betts, P., Miller, M., and Cayley, R. (2014). Dynamics of continental accretion. *Nature, 508*(7495), 245-248.

Och, D., Leitch, E., Caprarelli, G., and Watanabe, T. (2003). Blueschist and eclogite in tectonic melange, port macquarie, new south wales, australia.

Och, D., Zwingmann, H., Philips, G., and Leitch, E. (2010). K-Ar dating of serpentinisation using fuchsite mica: the Rocky Beach metamorphic melange, PORT MACQUARIE.

Och, D. J. (2007). *Eclogite, serpentinite, mélange and mafic intrusive rocks: manifestation of long-lived Palaeozoic convergent margin activity, Port Macquarie, eastern Australia.*

Park, C., Song, Y., Kang, I.-M., Shim, J., Chung, D., and Park, C.-S. (2017). Metasomatic changes during periodic fluid flux recorded in grandite garnet from the Weondong W-skarn deposit, South Korea. *Chemical Geology, 451*, 135-153.

Paton, C., Hellstrom, J., Paul, B., Woodhead, J., and Hergt, J. (2011). Iolite: Freeware for the visualisation and processing of mass spectrometric data. *Journal of Analytical Atomic Spectrometry, 26*(12), 2508-2518.

Phillips, D., and Harris, J. (2008). Provenance studies from 40 Ar/39 Ar dating of mineral inclusions in diamonds: Methodological tests on the Orapa kimberlite, Botswana. *Earth and Planetary Science Letters, 274*(1), 169-178.

Phillips, G., Landenberger, B., and Belousova, E. (2011). Building the New England Batholith, eastern Australia—Linking granite petrogenesis with geodynamic setting using Hf isotopes in zircon. *Lithos, 122*(1-2), 1-12.

Phillips, G., and Offler, R. (2011). Contrasting modes of eclogite and blueschist exhumation in a retreating subduction system: The Tasmanides, Australia. *Gondwana Research, 19*(3), 800-811.

Phillips, G., Offler, R., Rubatto, D., and Phillips, D. (2015). High-pressure metamorphism in the southern New England Orogen: Implications for long-lived accretionary orogenesis in eastern Australia. *Tectonics, 34*(9), 1979-2010.

Phillips, G., Wilson, C. J., Phillips, D., and Szczepanski, S. K. (2007). Thermochronological (40Ar/39Ar) evidence of Early Palaeozoic basin inversion within the southern Prince Charles Mountains, East Antarc-

tica: implications for East Gondwana. *Journal of the Geological Society, 164*(4), 771-784.

Pourteau, A., Scherer, E. E., Schorn, S., Bast, R., Schmidt, A., and Ebert, L. (2019). Thermal evolution of an ancient subduction interface revealed by Lu–Hf garnet geochronology, Halilbağı Complex (Anatolia). *Geoscience Frontiers, 10*(1), 127-148.

Powell, R., and Holland, T. (1988). An internally consistent dataset with uncertainties and correlations: 3. Applications to geobarometry, worked examples and a computer program. *Journal of metamorphic Geology, 6*(2), 173-204.

Putlitz, B., Cosca, M., and Schumacher, J. (2005). Prograde mica 40Ar/39Ar growth ages recorded in high pressure rocks (Syros, Cyclades, Greece). *Chemical Geology, 214*(1-2), 79-98.

Roberts, J., and James, L. (2010). Stratigraphic relationships of Carboniferous volcanogenic successions in the Clifton–Carroll block and Werrie syncline, northern Tamworth Belt, southern New England Orogen. *Australian Journal of Earth Sciences, 57*(2), 193-205.

Roda, M., Zucali, M., Regorda, A., and Iole Spalla, M. (2019). Formation and evolution of a subduction-related mélange: The example of the Rocca Canavese Thrust Sheets (Western Alps). *Geological Society of America Bulletin*.

Rodrıguez, J., Cosca, M., Ibarguchi, J. G., and Dallmeyer, R. (2003). Strain partitioning and preservation of 40Ar/39Ar ages during Variscan exhumation of a subducted crust (Malpica–Tui complex, NW Spain). *Lithos, 70*(3-4), 111-139.

Rubatto, D., Regis, D., Hermann, J., Boston, K., Engi, M., Beltrando, M., and McAlpine, S. R. (2011). Yo-yo subduction recorded by accessory minerals in the Italian Western Alps. *Nature Geoscience, 4*(5), 338.

Sano, S., Offler, R., Hyodo, H., and Watanabe, T. (2004). Geochemistry and chronology of tectonic blocks in serpentinite mélange of the southern New England Fold Belt, NSW, Australia. *Gondwana Research, 7*(3), 817-831.

Seifert, W. (2005). REE-, Zr-, and Th-rich titanite and associated accessory minerals from a kersantite in the Frankenwald, Germany. *Mineralogy and Petrology, 84*(3-4), 129-146.

Seifert, W., and Kramer, W. (2003). Accessory titanite: an important carrier of zirconium in lamprophyres. *Lithos, 71*(1), 81-98.

Shaw, S., and Flood, R. (1981). The New England Batholith, eastern Australia: geochemical variations in time and space. *Journal of Geophysical Research: Solid Earth, 86*(B11), 10530-10544.

Shreve, R. L., and Cloos, M. (1986). Dynamics

of sediment subduction, melange formation, and prism accretion. *Journal of Geophysical Research: Solid Earth, 91*(B10), 10229-10245.

Spandler, C., Hammerli, J., Sha, P., Hilbert-Wolf, H., Hu, Y., Roberts, E., and Schmitz, M. (2016). MKED1: a new titanite standard for in situ analysis of Sm–Nd isotopes and U–Pb geochronology. *Chemical Geology, 425*, 110-126.

Spear, F. S. (1988). Metamorphic fractional crystallization and internal metasomatism by diffusional homogenization of zoned garnets. *Contributions to Mineralogy and Petrology, 99*(4), 507-517.

Spencer, K., Hacker, B., Kylander-Clark, A., Andersen, T., Cottle, J., Stearns, M., Poletti, J., and Seward, G. (2013). Campaign-style titanite U–Pb dating by laser-ablation ICP: Implications for crustal flow, phase transformations and titanite closure. *Chemical Geology, 341*, 84-101.

Stöckhert, B., and Gerya, T. V. (2005). Pre-collisional high pressure metamorphism and nappe tectonics at active continental margins: A numerical simulation. *Terra Nova, 17*(2), 102-110.

Tamblyn, R., Hand, M., Kelsey, D., Anczkiewicz, R., and Och, D. (2019). Subduction and accumulation of lawsonite eclogite and garnet blueschist in eastern Australia. *Journal of metamorphic Geology*.

Tamblyn, R., Zack, T., Schmitt, A., Hand, M., Kelsey, D., Morrissey, L., Pabst, S., and Savov, I. (2019). Blueschist from the Mariana forearc records long-lived residence of material in the subduction channel. *Earth and Planetary Science Letters, 519*, 171-181.

Tsujimori, T., and Ernst, W. (2014). Lawsonite blueschists and lawsonite eclogites as proxies for palaeo-subduction zone processes: a review. *Journal of metamorphic Geology, 32*(5), 437-454.

Tsujimori, T., Sisson, V. B., Liou, J. G., Harlow, G. E., and Sorensen, S. S. (2006). Very-low-temperature record of the subduction process: A review of worldwide lawsonite eclogites. *Lithos, 92*(3), 609-624.

Vermeesch, P. (2018). IsoplotR: a free and open toolbox for geochronology. *Geoscience Frontiers, 9*(5), 1479-1493.

Viete, D. R., Hacker, B. R., Allen, M. B., Seward, G. G., Tobin, M. J., Kelley, C. S., Cinque, G., and Duckworth, A. R. (2018). Metamorphic records of multiple seismic cycles during subduction. *Science advances, 4*(3), eaaq0234.

Vuorinen, J. H., and Hålenius, U. (2005). Nb-, Zr- and LREE-rich titanite from the Alnö alkaline complex: crystal chemistry and its importance as a petrogenetic indicator. *Lithos, 83*(1-2), 128-142.

Warren, C., Sherlock, S., and Kelley, S. (2011).

Interpreting high-pressure phengite 40Ar/39Ar laserprobe ages: an example from Saih Hatat, NE Oman. *Contributions to Mineralogy and Petrology, 161*(6), 991-1009.

Wei, C., and Clarke, G. (2011). Calculated phase equilibria for MORB compositions: a reappraisal of the metamorphic evolution of lawsonite eclogite. *Journal of metamorphic Geology, 29*(9), 939-952.

White, R., Powell, R., and Holland, T. (2007). Progress relating to calculation of partial melting equilibria for metapelites. *Journal of metamorphic Geology, 25*(5), 511-527.

Woodhead, J. D., and Hergt, J. M. (2001). Strontium, neodymium and lead isotope analyses of NIST glass certified reference materials: SRM 610, 612, 614. *Geostandards Newsletter, 25*(2-3), 261-266.

Zack, T., and Hogmalm, K. J. (2016). Laser ablation Rb/Sr dating by online chemical separation of Rb and Sr in an oxygen-filled reaction cell. *Chemical Geology, 437*, 120-133.

Chapter 5:

The 2 Ga eclogites of central Tanzania: directly linking age and metamoprhism

This chapter is published as:

The 2 Ga eclogites of Central Tanzania: Directly linking age and metamorphism (2020). R. Tamblyn, D. Brown, M. Hand, L. Morrissey, C. Clark, R. Anczkiewicz. *Lithos*, 380–38, 105890

The supplementary materials for this chapter can be found in Appendix 5

Statement of Authorship

Title of Paper	The 2 Ga eclogites of Central Tanzania: Directly linking age and metamorphism
Publication Status	[x] Published [ ] Accepted for Publication [ ] Submitted for Publication [ ] Unpublished and Unsubmitted w ork w ritten in manuscript style
Publication Details	Tamblyn, R., Brown, D., Hand, M., Morrissey, L., Clark, C. & Anczkiewicz, R. (2020) The 2 Ga eclogites of Central Tanzania: Directly linking age and metamorphism Lithos, 105890

Principal Author

Name of Principal Author (Candidate)	Renée Tamblyn
Contribution to the Paper	Completed the mineral equilibria modelling Collected mineral compositional data and laser maps Collected the rutile and titanite trace element + U–Pb data Completed part of the Lu-Hf analysis Wrote the manuscript
Overall percentage (%)	70
Certification:	This paper reports on original research I conducted during the period of my Higher Degree by Research candidature and is not subject to any obligations or contractual agreements with a third party that would constrain its inclusion in this thesis. I am the primary author of this paper.
Signature	Date: 04/03/2021

Co-Author Contributions

By signing the Statement of Authorship, each author certifies that:

i. the candidate's stated contribution to the publication is accurate (as detailed above);

ii. permission is granted for the candidate in include the publication in the thesis; and

iii. the sum of all co-author contributions is equal to 100% less the candidate's stated contribution.

Name of Co-Author	Dillon Brown
Contribution to the Paper	Collected mineral compositional data Assisted with the mineral equilibria modelling Assisted with interpretations and reviewed the manuscript 10%
Signature	Date: 13/01/2021

Name of Co-Author	Martin Hand
Contribution to the Paper	Assisted with interpretations and reviewed the manuscript 6%
Signature	Date: 03/03/2021

Please cut and paste additional co-author panels here as required.

Name of Co-Author	Laura Morrissey		
Contribution to the Paper	Assisted with interpretations and reviewed the manuscript		6%
Signature		Date	02/03/2021

Name of Co-Author	Chris Clark		
Contribution to the Paper	Collected the zircon trace element + U–Pb data Reviewed the manuscript		5%
Signature		Date	15/2/2021

Name of Co-Author	Robert Anczkiewicz		
Contribution to the Paper	Collected the Lu–Hf TIMS data Hosted the primary author in the laboratories at the Polish Academy of Sciences		3%
Signature		Date	04/12/2020

Highlights

- Eclogite-facies metamorphism in the Usagaran Belt occurred at ca. 1994 Ma as dated by garnet Lu–Hf.
- Peak conditions were at least 18 kbar at approximately 800 °C, pointing to warm subduction thermal gradients in the Palaeoproterozoic.
- Possible tectonic scenarios for formation of the Usagaran eclogites involve east- or west-dipping subduction followed by buoyancy driven exhumation and emplacement into a back arc basin.

Abstract

The ca. 2 Ga retrogressed eclogites in the Usagaran Belt in central Tanzania are among the oldest documented eclogites in the world. As such, they have been used to pinpoint the thermal conditions of the onset of modern style subduction on Earth. Two samples of retrogressed mafic eclogite have been interrogated to reconstruct the metamorphic history of the subducted crust. The samples are several kilometres apart, separated by a mylonitic upper amphibolite-transitional granulite foliation. Lu–Hf garnet geochronology pinpoints eclogite metamorphism at 1994 ± 9 Ma, supported by rutile U–Pb geochronology. Zircon U–Pb geochronology supports subduction metamorphism at ca. 2000 Ma. Mineral equilibria modelling and Zr in rutile thermometry suggests the retrogressed eclogites reached a minimum pressure of 18 kbar at approximately 800 °C, consistent with a warm subduction thermal gradient. These conditions were followed by amphibolite-granulite-facies overprinting. Proposed tectonic models for the formation of the eclogites involve either east-dipping subduction of the Tanzanian Craton margin, or west-dipping subduction of oceanic crust under the Tanzanian Craton. The retrogressed eclogites were likely exhumed via slab breakoff driven buoyancy of the oceanic crust and transferred to shallow crustal levels in a back arc position. This data, combined with data from eclogites from the Eburnian-Transamazonian and Ubende orogens, demonstrate the possible existence of a large subduction system on the margin of west Africa from ca. 2.1–1.9 Ga. This system has led to the preservation of several eclogitic rocks, which suggests that modern style subduction was operating on significant geographic and temporal scales at this time.

1. Introduction

The appearance of eclogite-facies mineral assemblages in the geological record has long been used to pinpoint the emergence of subduction on Earth. While abundant in the Neoproterozoic and Palaeozoic, subduction related eclogite-facies rocks are scarce throughout the Archaean to Mesoproterozoic. The oldest subduction related eclogite-facies rocks appear in the geological record in the

Palaeoproterozoic suggesting the emergence of 'modern style' subduction at around 2 Ga (Brown and Johnson, 2018; Palin et al., 2020). This raises debate as to why subduction related rocks appear at this time. One argument is that thermal gradients on Earth were too warm to produce eclogite-facies rocks prior to the Palaeoproterozoic. Conversely, eclogite-facies rocks may have been produced before and during the Palaeoproterozoic, but not preserved in the geological record. Regardless, constraining the *P–T–t* evolutions of ancient eclogites enables the timing of subduction related metamorphism, the thermal state of the subduction system and possible exhumation mechanisms to be understood, permitting insight to ancient tectonic processes.

Palaeoproterozoic-aged eclogite-facies rocks have been described in few localities and are often retrogressed to amphibolite or granulite conditions. Some of the oldest subduction related eclogite-facies rocks are preserved in the Eburnian-Transamazonian Orogen in southern Cameroon (ca. 2090 Ma; Loose and Schenk, 2018), the Congo Craton in the Democratic Republic of Congo (ca. 2090 Ma; François et al., 2018), the Usagaran Orogen in Tanzania (ca. 1991 Ma; Möller et al., 1995; Collins et al., 2004), the Snowbird Tectonic Zone in Canada (ca. 1904 Ma; Baldwin et al., 2004), the Belomorian Province in Russia (ca. 1940–1890 Ma; Herwartz et al., 2012; Xu et al., 2018; Yu et al., 2019), the Ubendian Orogen in Tanzania (ca. 1886 Ma; Boniface et al., 2012) and in the Trans-Hudson Orogen in North America (ca. 1831 Ma; Weller and St-Onge, 2017). A significant volume of work has been dedicated to investigating these high-pressure rocks, however, only some have been studied with modern, integrated petrologic and geochronologic techniques (i.e. petrochronology).

The *P–T* conditions for Usagaran eclogite-facies metamorphism have been constrained from mineral equilibria models (Brown et al., 2020) and the eclogite-facies rocks in the Usagaran Belt have been dated using zircon at 1986 ± 29 Ma (Collins et al., 2004). However, the absence of data on the trace-element compositions of the zircons means this age cannot be directly linked to the formation of the eclogite-facies mineral assemblages. No study has integrated modern geochronology and mineral equilibria modelling. This study presents garnet Lu–Hf and zircon, rutile and titanite U–Pb geochronology tied to trace-element chemistry, trace-element thermometry and mineral equilibria modelling to constrain the precise timing and *P–T* conditions of eclogite-facies metamorphism in the Usagaran Belt.

2. Geological background

The Usagaran Belt in central Tanzania contains relic eclogite-facies mineral assemblages. Eclogite-facies metamorphism is interpreted to have

occured during subduction of the rifted margin of the Tanzanian Craton (Möller et al., 1995; Reddy et al., 2003; Collins et al., 2004). The Usagaran Belt is bordered to the north and west by the ca. 2700 Ma Tanzanian Craton, to the east by the ca. 640–610 Ma East-African Orogen, and to the south-west by the Ubendian Belt (Fig. 1a). The Ubendian Belt is interpreted to have experienced high-pressure metamorphism between ca. 1870–1865 Ma (Boniface et al., 2012), leading to the formation of now sparsely preserved eclogite.

The Usagaran Belt is divided into two lithotectonic units, the Konse Group and the Isimani Suite (Fig. 1b). The Konse Group formed at ca. 1895 Ma, and unconformably overlies the Isimani Suite and the Tanzanian Craton (Mruma, 1989; Reddy et al., 2003). It is comprised of volcanic and sedimentary successions metamorphosed to greenschist facies (Mruma, 1989). It also contains pillow basalts which have a T- to N-MORB composition (Boniface and Tsujimori, 2018). The Isimani Suite has been described in detail by Mruma (1989) and Brown et al. (2020). It is dominated by mafic and metapelitic amphibolite-facies gneisses, some of which are migmatitic. It also contains rare whiteschist assemblages (Mori et al., 2018). Coarse-grained metapelitic gneisses (~ 5 m thick) are interlayered with amphibolite-granulite-facies mafic rocks (~10–50 m thick), which are boudinaged. Comparatively low strain domains of these mafic rocks contain the mineral assemblage garnet + clinopyroxene + hornblende + plagioclase + quartz ± orthopyroxene. Omphacite included in garnet was found by Möller et al. (1995) in one of these domains, confirming a precursor eclogite-facies mineral assemblage.

SHRIMP U–Pb geochronology from zircons from the retrogressed eclogite assemblage returned an age of 1986 ± 29 Ma (Collins et al., 2004). However, in absence of trace-element compositions of the zircons, it is not clear if these zircons grew during eclogite-facies metamorphism. The metapelitic gneisses and migmatitic rocks returned similar ages, with SHRIMP U–Pb zircon ages of ca 1997–1989 Ma (Mruma, 1989; Collins et al., 2004). Monazites from metapelitic rocks give $^{207}Pb/^{206}Pb$ ages of 1999 ± 2 Ma and 2000 ± 2 Ma (Möller et al., 1995), however the relationship between the monazite and the bulk silicate mineral assemblages in the metapelites is not clear. Collins et al. (2004) inferred that these U–Pb ages in the Isimani Suite reflected eclogite-facies metamorphism of the entire unit, despite the vast bulk of the Isimani Suite not consisting of eclogite-facies rocks. This was confirmed by Brown et al. (2020), who proposed the mafic and metapelitic gneisses from Yalumba Hill and Ruaha River were coevally buried to high-pressure conditions. The relict eclogite assemblage had previously been interpreted to have formed at *P–T* conditions of ~ 18 kbar and 750 °C (Möller et al., 1995), or at least 15 kbar and 750–850 °C (Herms, 2002). These es-

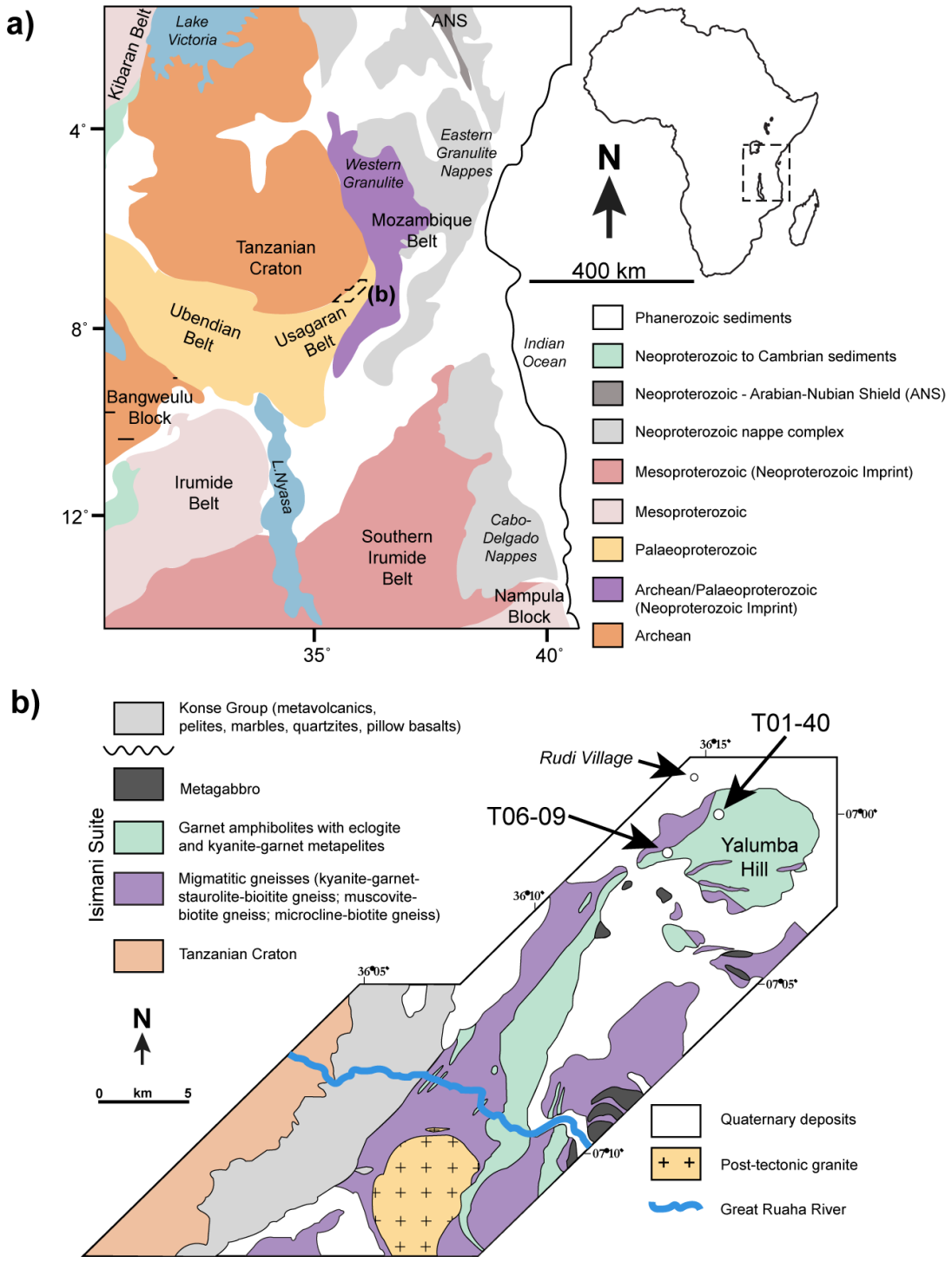


Figure 1: a) Geological map of central Tanzania, the Usagaran Belt is located on the eastern margin of the Tanzanian Craton. Location of map (b) is shown in dotted black line. b) Geological map of Yalumba Hill and the Ruaha River section in the Usagaran Belt, modified from Brown et al. (2020), Reddy et al. (2003) and Mruma (1989). Locations of samples T01-40 and T06-09 from this study are indicated.

timates were based in part on using the composition of demonstrably retrograde plagioclase and derived from a combination of texturally peak and retrograde minerals. Brown et al. (2020) calculated conditions of at least 18 kbar and 750 °C for relic eclogite, with the retrograde evolution passing through conditions of ~8 kbar and ~700 °C. The metapelitic garnet-kyanite-bearing gneisses formed at *P–T* conditions of at least ~17 kbar and 700 °C (Brown et al., 2020). Talc and kyanite bearing amphibolites 5 km south of Yalumba Hill in the Isimani Suite reached peak pressures of at least 10 kbar at 600–750 °C (Mori et al., 2018). After high-pressure metamorphism, the Isimani Suite is interpreted to have undergone a pressure decrease to amphibolite/granulite conditions, at conditions of 6–8 kbar and 520–600 °C as recorded by metapelitic assemblages (Brown et al., 2020).

The timing of retrograde metamorphism is constrained by a U–Pb titanite age of 1996 ± 2 Ma from amphibolite-facies mafic gneiss (Möller et al., 1995). This is supported by a SHRIMP U–Pb zircon age of 1992 ± 2 Ma from a pegmatite dyke that cross-cuts amphibolite-facies fabrics that overprint the eclogite assemblages (Collins et al., 2004). The unconformably overlying Konse Group contains post-tectonic granite with a SHRIMP U–Pb zircon age of 1877 ± 7 Ma (Reddy et al., 2003), suggesting that Isimani Suite metamorphism and deformation had concluded by this time. Furthermore, the Usagaran belt contains numerous I-type syn- to post-tectonic granitoids interpreted to be arc magmas, which intruded between ca. 1940–1877 Ma (Sommer et al., 2005a). The calc-alkaline volcanics of the Ndembera group also formed at this time (ca. 1920–1870 Ma; Sommer et al., 2005a; Bahame et al., 2016).

An early Palaeozoic greenschist facies overprint has been identified in the Usagaran Belt, attributed to the development of the East African Orogen (Möller et al., 1995; Reddy et al., 2003; Collins et al., 2004; Fritz et al., 2013). Discordant rutile U–Pb data from metapelitic rocks of the Isimani Suite has a lower intercept age of 501 ± 26 Ma (Möller et al., 1995). Muscovite from an Isimani Suite orthogneiss gave an $^{40}Ar/^{39}Ar$ plateau age of 535 ± 2 Ma (Reddy et al., 2003).

The interpreted tectonic evolution of the Usagaran Belt involves the subduction of the margin of the Tanzanian Craton (Reddy et al., 2003). Brown et al. (2020) suggested this convergence involved crustal thickening and shallow subduction of mafic lithologies and enclosing pelites. Following burial, slab breakoff induced buoyancy-driven exhumation, where the formation of an extensional system allowed the rock package to be exhumed within rapid timeframes (up to 20 Myr; Brown et al., 2020). It is clear the subducted margin comprised pelitic and mafic lithologies, now preserved as the kyanite-garnet gneisses and retrogressed eclogites of the Isimani Suite (Brown et al., 2020).

Geochemistry suggests the mafic eclogite was derived from a MORB-type source, although Sm–Nd and Hf isotopes suggest both the mafic and pelitic rocks of the Isimani Suite are evolved (Möller et al., 1998; Maboko, 2000; Brick, 2011). Furthermore, the pelitic rocks appear to be derived from the Tanzanian Craton, and an unidentified ca. 2600–2460 Ma source (Collins et al., 2004).

3. Samples

Two mafic samples from Yalumba Hill (Fig. 1b) were selected for this study based on their mineral assemblages and suitability for geochronology. Sample T01-40 is the same sample as that studied by Collins et al. (2004). T01-40 is granoblastic and is partially retrogressed to amphibolite-facies and T06-09 has a weak foliation and is partially retrogressed to granulite-facies. The two samples are several kilometres apart (Fig. 1b), and are separated by mylonitic shear fabrics. Taken together, both samples allow for investigation of the full *P–T–t* evolution of the mafic lithology at Yalumba Hill.

3.1 T01-40

T01-40 is granoblastic, and contains garnet, clinopyroxene, hornblende, plagioclase, quartz, rutile, ilmenite, magnetite, titanite, epidote, apatite and zircon. Garnet is euhedral-subhedral, up to 1500 μm in size and contains fine-grained inclusions of quartz, plagioclase, hornblende, rutile and titanite, and rare clinopyroxene, epidote, ilmenite, apatite and zircon (Fig. 2a,e,f). It is separated from the matrix by coronae of plagioclase, or by symplectic intergrowths of plagioclase and hornblende, or plagioclase, magnetite and ilmenite (Fig. 2a,b). Clinopyroxene forms coarse symplectites up to 1500 μm, where plagioclase forms elongate grains along clinopyroxene cleavage planes (Fig. 2d). Fine-grained magnetite also occurs in these symplectitic textures. Clinopyroxene is also replaced and rimmed by hornblende, which forms subhedral grains up to 200 μm (Fig. 2b,d). Quartz forms as euhedral grains throughout the matrix (up to 500 μm; Fig. 2a,b). Rutile grains occur only as inclusions in garnet, and often contain ilmenite exsolution lamellae (Fig. 2e). Ilmenite and magnetite are occasionally intergrown and form irregular grains throughout the matrix, which are up to 500 μm in size (Fig. 2c). Rare apatite and zircon grains (~ 50 μm) are present in the matrix. T01-40 contains a small 5 mm wide quartz vein, mantled by symplectitic clinopyroxene and garnet.

3.2 T06-09

T06-09 is weakly foliated, and generally finer grained than T01-40. It contains garnet, clinopyroxene, hornblende, plagioclase, orthopyroxene, quartz, rutile, ilmenite, magnetite, apatite and zircon. Garnet forms irregular grains (up to 1500 um, but generally smaller) which contain abundant fine-grained inclusions of quartz, plagioclase

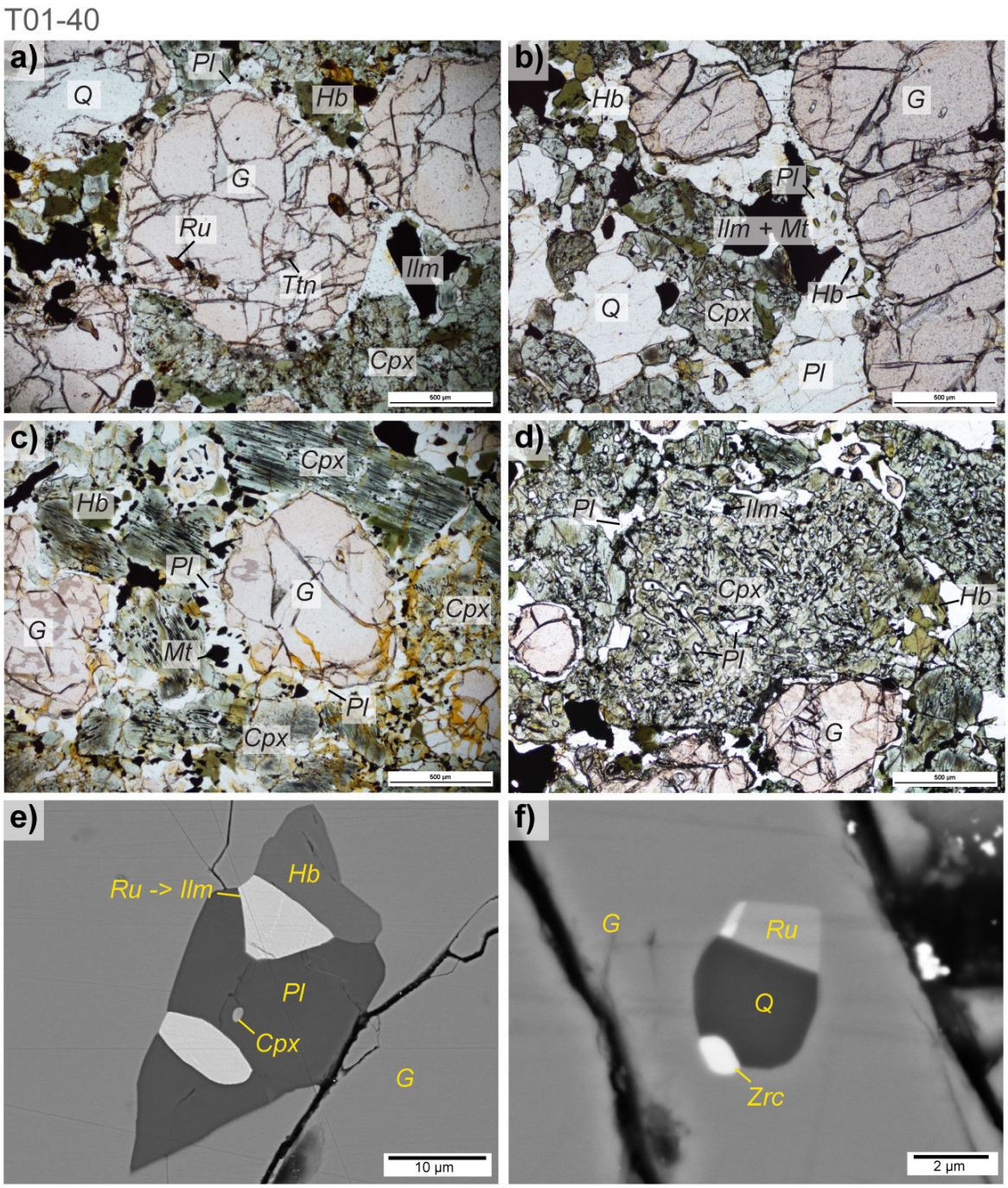


Figure 2: Photomicrographs and BSE images of retrogressed eclogites. a) Garnet in T01-40 with titanite and rutile inclusions. b). Coarse-grained garnet in T01-40 with plagioclase and hornblende symplectites forming coronae on its margin. c) Garnet in T01-40 with coronae of plagioclase and ilmenite/magnetite. Coarse-grained diopside grains with lamellae of plagioclase and opaques are separated from the garnet by coronae of plagioclase. Hornblende is interpreted to have replaced clinopyroxene along the grain margins. d) Symplectitic clinopyroxene in T01-40, the colourless inclusions in the clinopyroxene are plagioclase and opaque inclusions are magnetite, interpreted to have exsolved from a previous Na-rich clinopyroxene. Hornblende is interpreted to have replaced clinopyroxene on the grain margins. e) SEM image of a multiphase inclusion of hornblende, plagioclase, rutile and clinopyroxene in garnet from T01-40. The rutile has exsolved fine lamellae of ilmenite. f) SEM image of rutile, zircon and quartz included in garnet in T01-40.

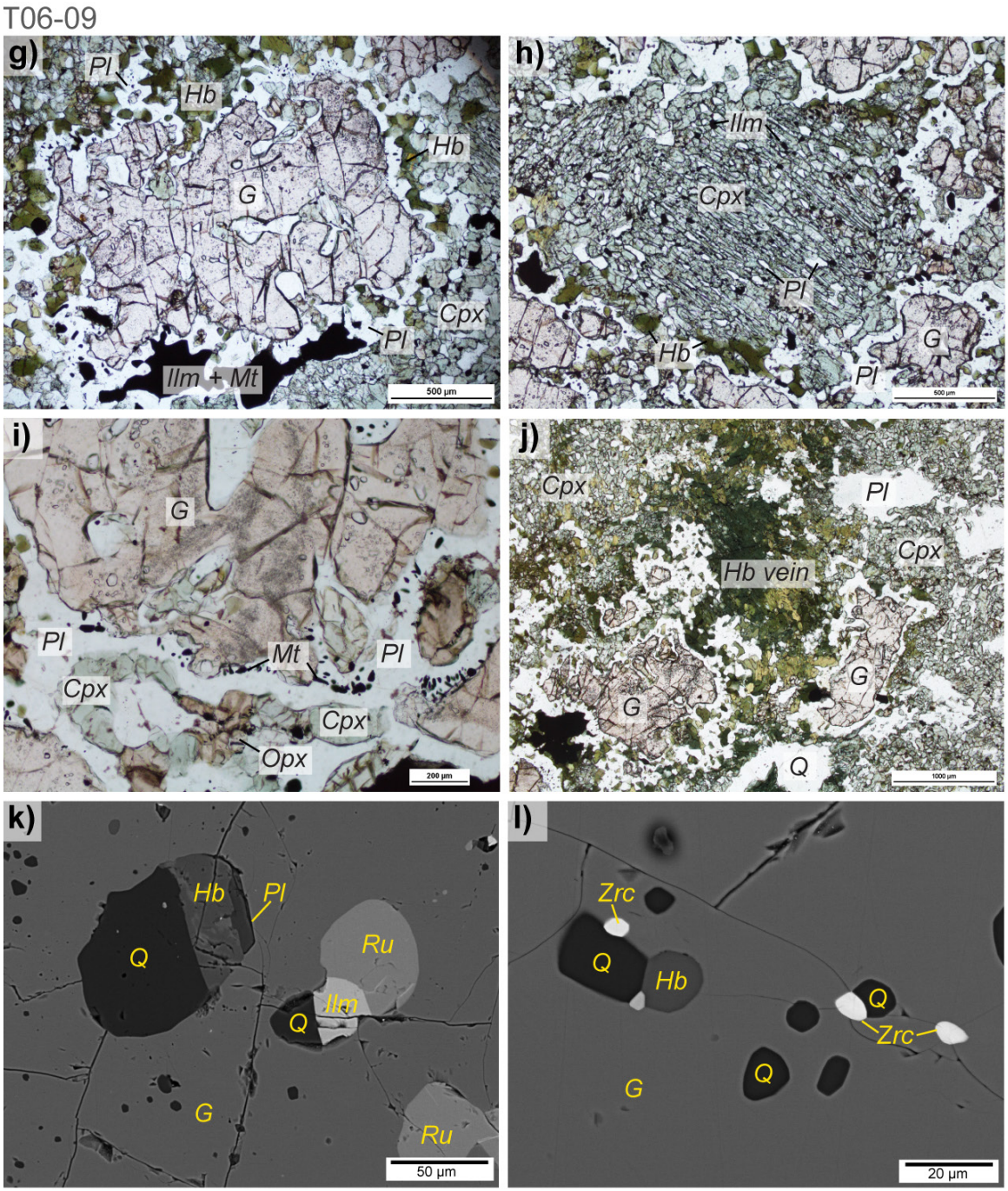


Figure 2 continued: g) Irregular-shaped garnet in T06-09, separated from clinopyroxene by double coronae of plagioclase and hornblende. h) Symplectitic clinopyroxene in T06-09, colourless inclusions in the clinopyroxene are plagioclase and opaque inclusions are ilmenite, interpreted to have exsolved from a previous Na-rich clinopyroxene. i) Garnet in T06-09, containing clouds of very fine-grained inclusions, which are primarily quartz. The garnet is surrounded by a corona of plagioclase with symplectic intergrowths of ilmenite and magnetite. Fine grained orthopyroxene has replaced clinopyroxene. j) A coarse hornblende grain cross-cutting the mineral assemblages in T06-09. The hornblende primarily replaced clinopyroxene. k) SEM images of rare hornblende, plagioclase, quartz, rutile and ilmenite inclusions in garnet from T06-09. l) Fine-grained zircon, quartz and hornblende inclusions in garnet from T06-09. Abbreviations: Cpx: Clinopyroxene, G: Garnet, Hb: Hornblende; Ilm: Ilmenite, Mt: Magnetite; Opx: Orthopyroxene, Pl: Plagioclase, Q: Quartz, Ru: Rutile; Ttn: Titanite, Zrc: Zircon.

and rutile, and rarer clinopyroxene, hornblende, zircon and chalcopyrite (Fig. 2g,k,l). Clinopyroxene in the matrix is sieve textured with plagioclase and magnetite inclusions (Fig. 2h), or extensively broken down to form fine-grained masses with plagioclase, hornblende and rare orthopyroxene (Fig. 2h,i). In some instances, these minerals form composite grains, and the original size of the clinopyroxene is up to 1000 μm. Garnet and clinopyroxene are separated by coronae of plagioclase with symplectic fine grained magnetite, or sometimes double coronae of plagioclase and hornblende, with hornblende on the clinopyroxene margin (Fig. 2g,i). Quartz forms euhedral grains up to 500 μm in size throughout the matrix (Fig. 2h). Ilmenite and magnetite form irregular grains up to 1000 μm long throughout the matrix (Fig. 2g). Rare apatite and zircon occur throughout the matrix. A thin hornblende vein 2 mm wide cross cuts the sample, encompassing and replacing clinopyroxene grains (Fig. 2j).

3.3 A previous eclogitic assemblage

Previous authors have argued for an eclogitic assemblage in the mafic rocks of Yalumba Hill (Möller et al., 1995; Herms, 2002; Collins et al., 2004; Brown et al., 2020). Originally, this argument was based on the existence of rare omphacite inclusions in garnet (Möller et al, 1995), but has since been supplemented with petrologic arguments and mineral equilibria modelling from Brown et al. (2020). No omphacite inclusions in garnet could be detected in this study, perhaps owing to the rarity of clinopyroxene inclusions in general. The existence of symplectitic intergrowths of Na-poor clinopyroxene and plagioclase has been used to argue for a previous Na-bearing clinopyroxene, namely omphacite, which has ejected its Na component to form albitic plagioclase during retrograde conversion to Na-poor clinopyroxene (e.g. Loose and Schenk, 2018). The abundance of well-developed symplectitic textures in both T01-40 and T06-09 would suggest that the previous clinopyroxene was Na-rich (Fig. 2). Reintegration of albitic plagioclase into the clinopyroxene shows that the precursor clinopyroxene was ferro-omphacite in composition (Brown et al., 2020). Additionally, the present garnet mode for each sample is ~ 25%, and prior to the development of retrograde plagioclase coronae, would have been up to ~ 40%. As such, samples T01-40 and T06-09 are referred to as retrogressed eclogites.

4. Methods

4.1 Q450 Scanning Electron Microscopy

Samples were imaged using a FEI Quanta 450 scanning electron microscope (SEM) with an attached Oxford Ultim Max Large Area energy dispersive X-Ray spectrometer (EDS) detector at Adelaide Microscopy, Australia. Images were acquired in back scattered electron (BSE) mode with

an accelerating voltage of 20 kV and a spot size of 4, at a working distance of 10 mm. Minerals were identified from EDS spectra and semi-quantitative compositional data, which were processed using Oxford Aztec EDS software.

4.2 Electron Probe Micro Analyses and X-Ray mapping

Mineral chemistries and garnet maps were obtained using a Cameca SX-5 WDS electron microprobe. Spot analyses used a beam current of 20 nA and an accelerating voltage of 15 kV, with an andradite crustal used for calibration. Element maps used a 200 nA beam current and an accelerating voltage of 15 kV. Ca, Fe, Mn and Mg were mapped using Wavelength Dispersive Spectrometers (WDS).

4.3 LA–ICP–MS garnet spot analyses and mapping

Major (Si, Al, Ca, Fe, Mg and Mn), trace (Ti, Cr, V, Y and Hf) and rare earth elements (La, Ce, Pr, Nd, Sm, Eu, Gd, Tb, Dy, Ho, Er, Tm, Yb and Lu) were analysed by single spots and mapping of garnet using an ASI m50 LA–ICP–MS with an Agilent 7900 MS at Adelaide Microscopy, Australia. The spot size was 30 μm, with a repetition rate of 5 Hz and a laser energy at the sample surface of 3.2 Jcm^{-2}. The primary reference material used for corrections was NIST612. The individual data spots and maps were processed in Iolite (Paton et al., 2011) using Ca as the internal reference element, as measured in the garnets by EPMA (Supplementary Table 2). Rare earth element (REE) plots were made using GCDkit (Janoušek et al., 2006).

4.4 Garnet Lu–Hf geochronology

Garnet was separated using conventional crushing, magnetic separation, and hand-picking to obtain pure mineral samples. Whole rock samples were obtained by hand-pulverising presentative parts of the rock in an agate mortar. Lu–Hf analyses were collected at the Kraków Research Centre, Institute of Geological Sciences, Polish Academy of Sciences. Methods followed Anczkiewicz and Thirlwall (2003) with modifications for the Lu–Hf method from Anczkiewicz et al. (2004). JMC475 measured over the course of the analyses yielded $^{176}Hf/^{177}Hf = 0.282158 \pm 8$ ($n = 7$; 2σ). Isochron ages were calculated using IsoplotR (Vermeesch, 2018), all certainties are reported as 2σ.

4.5 Zircon U–Pb geochronology and trace elements

Zircon grains were liberated from the samples using a SELFRAG electric pulse disaggregation system at Curtin University, and were separated using magnetic separation, heavy liquid and picking techniques. The grains were mounted in epoxy resin, polished to expose their cross section, and

then imaged in BSE and CL. This was done using a Quanta600 Scanning Electron Microscope (SEM) at Adelaide Microscopy. U–Pb and trace-element compositional data were collected using the laser ablation split stream (LASS) system at the Geo-History Facility in the John de Laeter Centre at Curtin University. Zircons were ablated using a Resonetics RESOlution M–50A–LR system, U–Pb isotopes were measured using a Nu Plasma II multi-collector inductivity coupled plasma mass spectrometer and trace-elements were measured using an Agilent 8900s quadrapole inductivity coupled plasma mass spectrometer. Samples were ablated using a spot size of 24 μm and a 5 Hz repetition rate, and a laser energy at the sample surface of 2.1 Jcm^{-2}. The acquisition time for each analysis was 115 s, including 40 s of background, 35 s of ablation, and a further 40 s of background. Time resolved mass spectra were reduced using Iolite (Paton et al., 2011) and in-house Microsoft Excel macros. Zircon standard GJ1 (Jackson et al., 2004) was used as a primary reference material. Zircon standards Pleśovice (337.13 ± 0.37 Ma; Sláma et al., 2008), 91500 (1065.3 ± 0.3 Ma; Wiedenbeck et al., 1995) and OGC (3465 ± 0.6 Ma; Stern et al., 2009) were used as secondary reference material. Over the course of the analyses all secondary reference materials yielded concordant U–Pb ages, Pleśovice yielded a weighted mean $^{206}Pb/^{238}Pb$ age of 339 ± 2 Ma (n = 11, MSWD = 1.8), 91500 yielded a weighted mean $^{207}Pb/^{206}Pb$ age of 1067 ± 2 Ma (n = 18, MSWD = 1.08), and OGC yielded a weighted mean $^{207}Pb/^{206}Pb$ age of 3460 ± 4 Ma (n = 19, MSWD = 1.3). Trace-element data were reduced using GJ1 as the primary standard (Zr = 3.55 ppm; Liu et al., 2010) and using ^{29}Si as the internal standard element (15.2 wt%). NIST glasses SRM610 and SRM612 were monitored to verify the accuracy of the trace-element data reduction, they returned Zr contents of 452 ppm (expected = 452 ppm) and 42 ppm (expected = 44 ppm) respectively. REE plots were made using GCDkit (Janoušek et al., 2006).

4.6 Rutile U–Pb geochronology and trace elements

Rutile grains were liberated from the samples using a SELFRAG electric pulse disaggregation system at Curtin University, and were separated using magnetitic separation, heavy liquid and picking techniques. The grains were mounted in epoxy resin and polished through to expose their cross section, and imaged using a Quanta600 Scanning Electron Microscope (SEM) to identify the presence of inclusions and/or exsolution. The rutile grains were analysed for U–Pb isotopes and trace element concentrations simultaneously using an ASI m50 LA–ICP–MS with an attached 7700 MS at Adelaide Microscopy, Australia. Grains were ablated using a spot size of 51 μm, a frequency of 5 Hz, and an intensity of 5 Jcm^{-2}. The acquisition time for each analysis was 80 s, including 30 s of background measurement of 50 s of ablation. The

primary reference standard R10 was used to correct for U–Pb elemental fractionation, mass bias and instrument drift over the course of the analyses (Luvizotto et al., 2009), and the R19 standard was used as a secondary reference (493 ± 10 Ma; Luvizotto et al., 2009; Zack et al., 2011). The synthetic glass standard NIST610 was used to correct for Zr and trace-element concentrations. Ti was used as the internal reference element for the trace-element analyses (unknowns were corrected to 59.94 wt % Ti). Corrections were done using the software Iolite (Paton et al., 2011) and age calculations were done using IsoplotR (Vermeesch, 2018). R19 was concordant and returned a weighted mean $^{206}Pb/^{238}U$ age of 496 ± 5.31 Ma (MSWD = 0.85, n = 20) over the course of the analyses. Temperature estimates were calculated from Zr concentrations (in ppm) using the pressure dependent calibration of Tomkins et al. (2007).

4.7 Mineral equilibria modelling

Mineral equilibria forward models were calculated using the code THERMOCALC (v. 345i), with the internally consistent thermodynamic dataset ds62 (Holland and Powell, 2011). The activity-composition (*a–x*) models of Green et al. (2016) were used, in the model chemical system MnNCFMASHTO. Potassium was omitted from the model chemical system as the amount measured by whole rock chemistry was negligible (< 0.3 wt%; Table. A. 1).

Whole rock geochemistry for the samples was acquired using X-ray fluorescence spectrometry at Franklin and Marshall College, Pennsylvania (Supplementary Table 1). The whole-rock compositions were adjusted for the presence of apatite, which is present in the samples in minor proportions and contains CaO, but cannot be modelled in the current chemical system. To assess the sensitivity of the mineral equilibria models to the oxidation state of each sample, pressure-molar oxygen (*P–M*o) models were calculated prior to *P–T* modelling (Supplementary Fig. 1). The constraints were compared with Fe_2O_3 values calculated from electron microprobe analyses of Fe^{3+} bearing minerals and their modal proportions (Supplementary Table 2; Droop, 1987). H_2O content in each sample was obtained by using the average composition of amphibole (the only hydrous metamorphic mineral in each rock) derived from electron microprobe analyses and its modal proportion in each sample (Supplementary Table 2). This was done as loss on ignition (LOI) values obtained from the whole rock geochemistry are likely to have been affected by minor low-temperature alteration.

Modal proportions of each mineral were determined by acquiring Mineral Liberation Analysis (MLA) images of each thin section. This was done using a FEI Quanta600 SEM at Adelaide Microscopy, Australia. Pixel counting using image analysis software was conducted on the resultant images and proportions were converted from volume

Table 1: Modal proportions of minerals in samples in 1-atom-normalised %, to comply with modes calculated in THERMOCALC.

	T01-40	**T06-09**
Hornblende	0.09	0.06
Garnet	0.23	0.23
Clinopyroxene	0.32	0.34
Quartz	0.04	0.06
Plagioclase	0.28	0.28
Magnetite	0.02	0.01
Ilmenite	0.02	0.02
Rutile	< 0.01	< 0.01
Epidote	< 0.01	-
Titanite	< 0.01	-
Orthopyroxene	-	0.01

% to atom-based mol % for direct comparison with THERMOCALC outputs (Table 1; Holland and Powell, 2011). Modelled mineral modal proportions and compositions were calculated using the software TCInvestigator (Pearce et al., 2015).

5. Results

5.1 Electron Probe Micro Analysis and mapping

Mineral compositions, end member proportions and THERMOCALC compositional variables are provided in Supplementary Table 2 and garnet maps and traverses are in Figure 3. Additional garnet maps are provided in Supplementary Figure 2. Garnet grains from T01-40 are dominantly almandine and show preservation of prograde zoning. Almandine contents decreases from 0.57 in the core to 0.52 in the rim. Spessartine also decreases from 0.06 in the core to 0.02 at the rims (Fig. 3a,c), whereas grossular and pyrope contents increase from 0.24 and 0.07 in the core to 0.25 and 0.1 in the rims, respectively. The very outer ~ 50 μm of the garnet shows a slight increase in spessartine content (Fig. 3a), accompanied by a slight increase in almandine and a slight decrease in pyrope. In contrast, garnet from T06-09 shows flat spessartine profiles despite being essentially the same size as the garnets in T01-40. The garnet cores in T06-09 contain X_{sps} of ~0.1 spessartine, increasing to 0.2 at the outermost ~ 50 μm of the garnet (Fig. 3b). The garnets are also dominantly almandine, the core is 0.46 almandine which increases to 0.54 towards the rim, corresponding to a core pyrope concentration of 0.14 which decreases slightly to 0.13 towards the rim (Fig. 3b,d). Grossular content is patchy throughout the grain, ranging from 0.24 to 0.26.

Clinopyroxene that occurs in symplectites with plagioclase in both samples is dominantly diop-

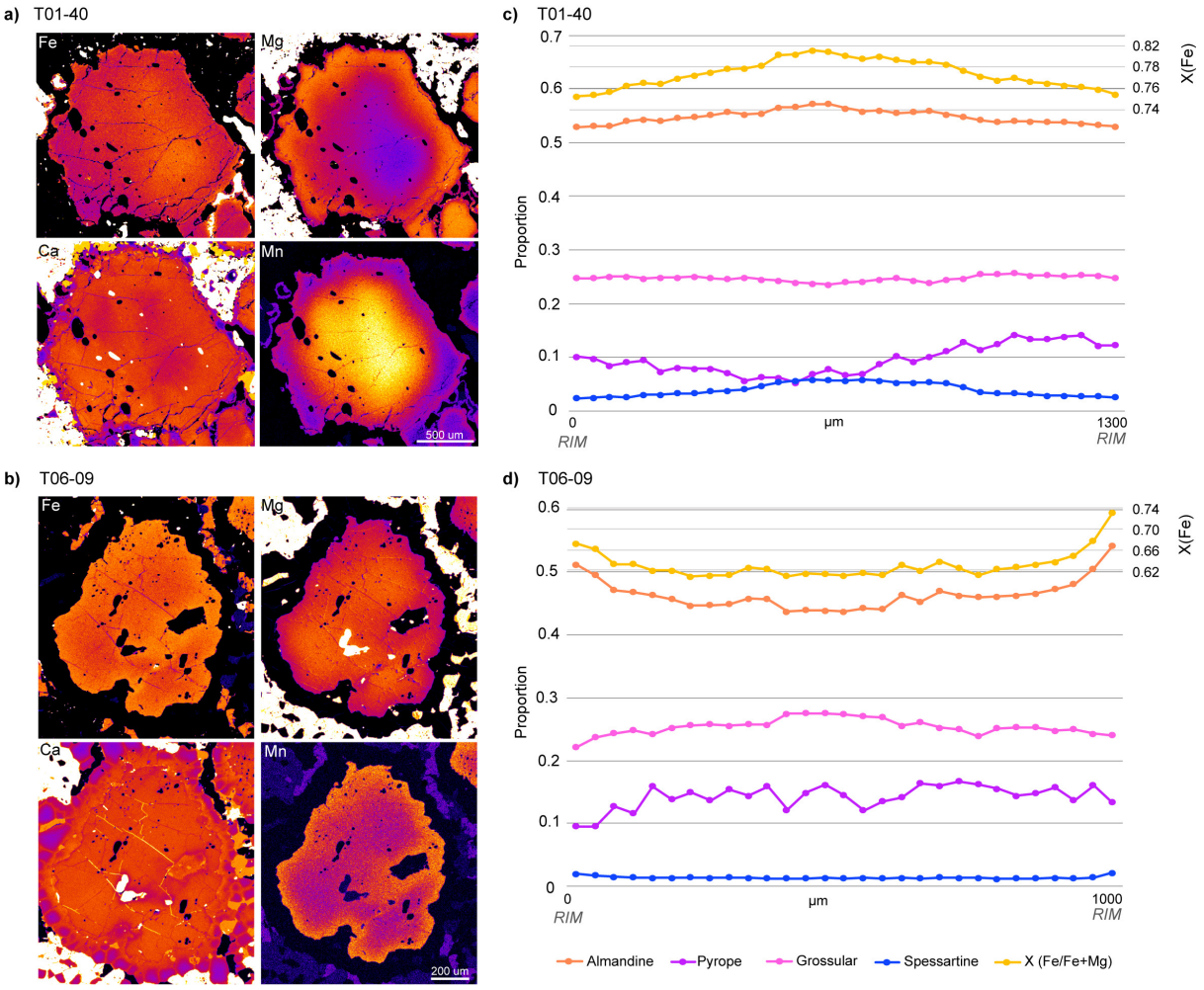


Figure 3: EPMA maps and traverses of representative garnets from the samples. Note that X(Fe) is plotted on a different axis and the scale changes between the two traverses. a) Maps of a garnet from T01-40, showing prograde zoning in the garnet core and 50–100 µm wide re-equilibrated rim. b) Maps of a garnet in T06-09, showing flat profiles in the garnet core and a 50–100 µm re-equilibrated rim. c) Traverse from garnet in T01-40. d) Traverse from garnet in T06-09.

sodic. Matrix clinopyroxene in T01-40 contains 72.8% diopside, 19.6% hedenbergite, 4.5% jadeite and 3.3% aegirine, with a X_J value of 0.08 and an X_{Fe} of 0.21 (X_J = Na/Na+Ca on the M4 site, X_{Fe} = Fe/Fe+Mg). Clinopyroxene included in the cores of garnet contains 63.2% diopside, 25.7% hedenbergite, 10% jadeite and 1% aegirine, with a slightly higher X_J value of 0.11 and an X_{Fe} value of 0.29. Clinopyroxene in T06-09 contains 80.3% diopside, 13.8% hedenbergite, 4.3% jadeite and 1.7% aegirine. It has a X_J of 0.0596 and an X_{Fe} of 0.15.

Amphibole in T01-40 and T06-09 is pargasite (following classification of Locock, 2014). In T01-40 amphibole has a X_{Fe} of 0.3, and a X_{Ti} of 0.07 (X_{Fe} = Fe/Fe+Mg, X_{Ti} = proportion of Ti on the M2 site as defined by the THERMOCALC *a–x* file). In T06-09 amphibole has a X_{Fe} of 0.33 and a X_{Ti} of 0.08.

Plagioclase is dominantly albitic in composition,

and is zoned when forming coronae around garnet grains, as can be seen in the Ca EPMA X-ray maps (Fig. 3). Plagioclase coronae that mantles garnet in T01-40 contain 81% albite and 19% anorthite, and plagioclase that mantles matrix minerals contain 73% albite and 27% anorthite. Plagioclase inclusions in the cores of garnets in T01-40 contain 74–75% albite and ~ 25% anorthite. In T06-09, cores of well-developed plagioclase coronae that mantles garnet contain 74% albite and 26% anorthite, and rims which mantle matrix minerals contain 66% albite and 34.1% anorthite. In all plagioclase, sanadine components are low (0.2–0.4%).

Orthopyroxene occurs in T06-09 and is 54–55% enstatite and 38–41% forsterite, the X_{Fe} (Fe/Fe+Mg) ranges from 0.39–0.42. Ilmenite in the samples has minor proportions of hematite (6–11%) but is dominantly ilmenite (89–94%). Magnetite in T06-09 and T01-40 is 99% magnetite and less than 1% other end members. Titanite in T01-40 contains up to 1.43 wt% Al_2O_3, 0.53 wt% FeO and 0.39 wt % F.

5.3 Garnet REE LA-ICP-MS maps

Garnets were mapped for trace and rare earth elements to assist with interpretation of Lu–Hf geochronology and mineral reactions during prograde growth. Garnets of comparable sizes were mapped in-situ from each sample. Quantitative spot analyses are in Supplementary Table 3. Semi-quantitative maps are in Figure 4 and Mn is shown for comparison. Additional maps are in Figure. B. 2. Garnets from T01-40 and T09-06 preserve distinctly different internal trace-element compositional patterns. Garnets from T01-40 (Fig. 4a-j) preserve Y (up to ~ 400 ppm) and Lu (up to ~ 6 ppm) enrichments in their cores, consistent with Rayleigh fractionation during prograde growth (e.g. Otamendi et al., 2002). These enriched cores can also be seen in much smaller garnets mapped in the images, which are only ~ 100 μm in diameter (e.g. Fig. 4b,c). They also contain a diffuse Y and Lu enriched ring (up to ~ 150 and 2 ppm in Y and Lu respectively; most evident in Fig. 4g-h), and a very narrow outer rim enrichment of Y and Lu, typical of garnets that have been partially resorbed (e.g. Carlson et al., 2012). Cr and V concentrations in the garnets from T01-40 are up to ~ 200 ppm, and show intriguing distributions. Cr is distributed as elongate enrichments throughout the garnet grains (indicated by white dashed lines; Fig. 4d,i), with a discontinuous Cr enrichment in the outermost rim (Fig. 4d,i). V shows a subtle enrichment in the garnet cores, and remains in low concentrations throughout the garnet grain until a slight enrichment in the outermost rim that is coincident with the discontinuous Cr enrichment (Fig. 4e,j). Additionally, there are small granular Cr and V enriched areas in the garnet indicated by white arrows, that occasionally correspond to discrete depletions in Y and Lu (Fig. 4). Quantitative spot analyses of garnets normalised to chondrite

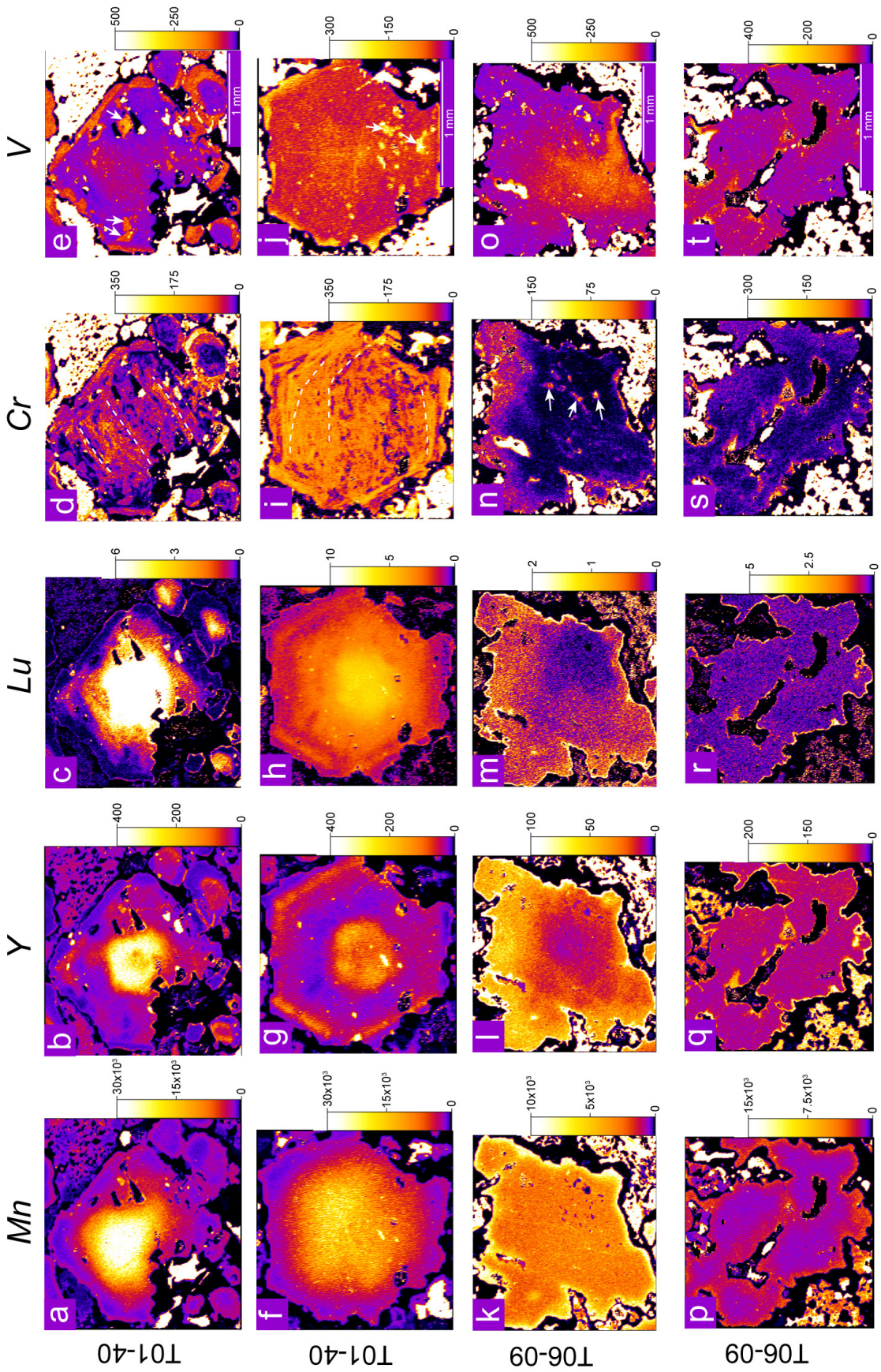


Figure 4: Selected major and trace-element maps for garnets in the retrogressed eclogites. Mn is shown for reference. White dashed lines represent trend of overgrown foliation. White arrows indicate locations of Cr and V rich overgrowths. a-j) Maps from two different sized garnets in T01-40. k-t) Maps from two different sized garnets in T06-09.

are in Figure 5. Garnet in T01-40 shows strong core-rim zoning, with cores enriched in Lu and the HREEs but comparatively depleted in Sm–Tb, and rims comparatively depleted in Lu and HREEs but showing a slight enrichment in Sm–Tb (Fig. 5a).

Compositional patterns in garnets from T06-09 (Fig. 4k-t) are more difficult to interpret, as it is unclear whether they are continuous large porphyroblasts or amalgamations of smaller garnet grains. Larger garnets (Fig. 4l,m) show Y and Lu depletions in their cores, with rimward enrichment of up to approximately 100 ppm Y and 2 ppm Lu. There is a narrow outer rim enriched in Y and Lu, consistent with partial resorption. Smaller garnets show flat Y and Lu (~ 10 and < 0.5 ppm respectively) profiles with very narrow outer enriched rims. Cr concentrations in garnets from T06-09 are low (close to detection limit), but show a diffuse and irregular enrichment towards the rims (Fig. 4n,s). V however shows an enrichment in the core of large garnets (up to 200 ppm; Fig. 4o), which does not correspond to the Y and Lu depleted core. Unlike the large garnet, the smaller garnet shows slight V enrichments close to its rims which correspond to Cr enrichments (Fig. 4t). In spot transects, garnets in T06-09 show a flat REE profile which is unchanging from core to rim (Fig. 5b).

5.3 Garnet Lu–Hf geochronology

Garnet and whole rock Lu–Hf concentrations and ratios can be found in Supplementary Table 4, and isochrons in Figure 6. Reported uncertainties are 2σ. The whole rock and garnet 1, 2, and 3 aliquots from T01-40 give an isochron age of 1994 ± 9 Ma (Fig. 6a; MSWD = 0.98; initial $^{176}Hf/^{177}Hf$ = 0.283227 ± 0.000010). Garnet aliquot 4 was omitted due to an anomalously low $^{176}Lu/^{177}Hf$ ratio. In sample T06-09, garnet aliquot 4 was also omitted from the age calculations, due to an anomalously

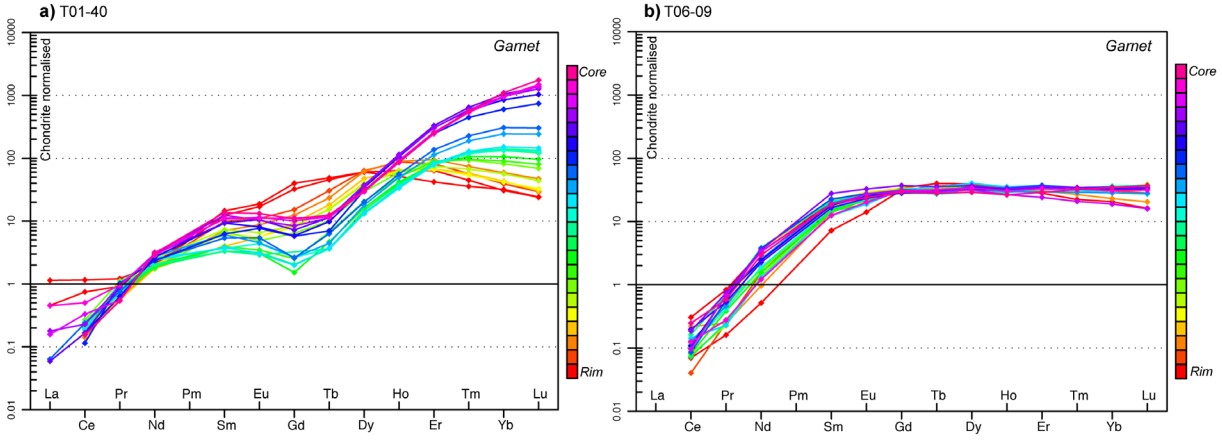


Figure 5: Chondrite normalised REE plots of single garnets. a) Garnet from T01-40, showing decreasing HREE and increasing MREE content from core to rim. b) Garnet from T06-09, showing a flat REE profile with only subtle change from core to rim.

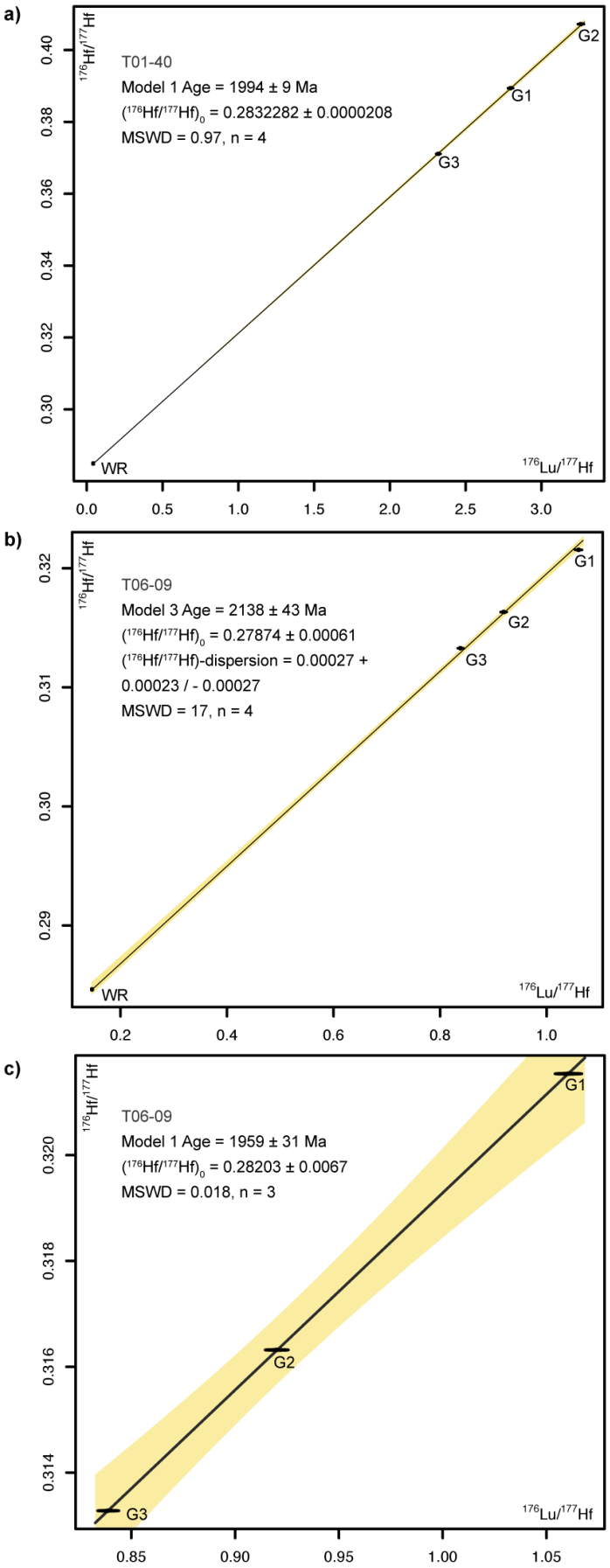


Figure 6: Lu–Hf isochrons, yellow shading represents the uncertainty on the isochron. a) Sample T01-40, showing the whole rock and three garnet aliquots that lie on an isochron. The Model 1 age is calculated as a maximum likelihood regression, taking into account the analytical uncertainties and error correlations, under the assumption that the error is caused by the analytical uncertainty. b) Sample T06-09, the Model 3 age is calculated as a maximum likelihood regression with overdispersion, which may be interpreted as analytical or geological, however the apparent age may not be meaningful. c) Garnet aliquots only from T06-09, there is a large uncertainty on the calculated Model 1 age due to the restricted range of 176Lu/177Hf ratios.

high $^{176}Lu/^{177}Hf$ ratio. The remaining three garnet aliquots in T06-09 have lower $^{176}Lu/^{177}Hf$ ratios than T01-40, and do not lie on an isochron with the whole rock analysis. When combined with the whole rock analysis, they give an age of 2138 ± 43 Ma (Fig. 6b; MSWD = 17; initial $^{176}Hf/^{177}Hf$ = 0.2787±0.0019). If the whole rock fraction is omitted the remaining three garnet aliquots give an isochron age of 1959 ± 31 Ma (Fig. 6c; MSWD = 0.018; initial $^{176}Hf/^{177}Hf$ = 0.28203 ± 0.0067).

5.4 Zircon U–Pb geochronology and trace elements

Isotopic and trace-element data for zircon can be found in Supplementary Table 5. Data for T01-40 and T09-09 are presented in Figure 7. Analyses with 100(1-α)% confidence ellipses that intersect concordia are defined as concordant and have been used in the age calculations, the errors on the ellipses are 2se.

In sample T01-40, zircons are rounded to sub-rounded and range from ~ 50–120 μm in their longest dimension (Fig. 7a). The CL responses often show irregular and patchy zoning and less common sector zoning (Fig. 7a). There is variation in CL response between grains, however no systematic core-rim relationships were observed. Seven analyses were excluded from age calculations as they were not concordant. The remaining seventy-seven analyses from T01-40 do not produce a concordia age. There is some dispersion in the age data, as can be seen in the $^{207}Pb/^{206}Pb$ age weighted mean plot (Fig. 7c). The individual spot ages produce a weighted mean $^{207}Pb/^{206}Pb$ age of 2023.7 ± 9.4 Ma (MSWD = 1.84; n = 77; all reported uncertainties on ages reflect the approximate 100(1-α)% confidence interval with overdispersion). By comparison, concordant analyses produce a weighted mean $^{207}Pb/^{235}U$ age of 2007 ± 5.3 Ma. (MSWD = 0.92) and a weighted mean $^{206}Pb/^{238}U$ age of 1993.4 ± 8.4 Ma (MSWD = 0.90). Individual spot age variation is not correlated to trace-element composition, Th/U ratio or CL response (Fig. 7c).

Zircons from T06-09 are rounded to sub-rounded and ~ 50–200 μm in diameter. The zircons display variation in CL response between grains and complex internal structures (Fig. 7b). They commonly show irregular and discontinuous zoning, as well as rarer fir-tree zoning and sector zoning typical of metamorphic zircons in mafic rocks (Corfu et al., 2003). The grains commonly show a thin (~ 5 μm) rim that has a dark CL response. However, these rims were too thin to be targeted for geochronology. The data show a possible lead loss trend. Fourteen analyses were excluded from age calculations as they were not concordant. The remaining thirteen analyses from T06-09 produce a concordia age of 2010.1 ± 7.3 Ma (MSWD = 1.7; Fig. 7b), a weighted mean $^{207}Pb/^{206}Pb$ age of 2010.6 ± 10.3 Ma (MSWD = 2.02; Fig. 7d), a weighted mean

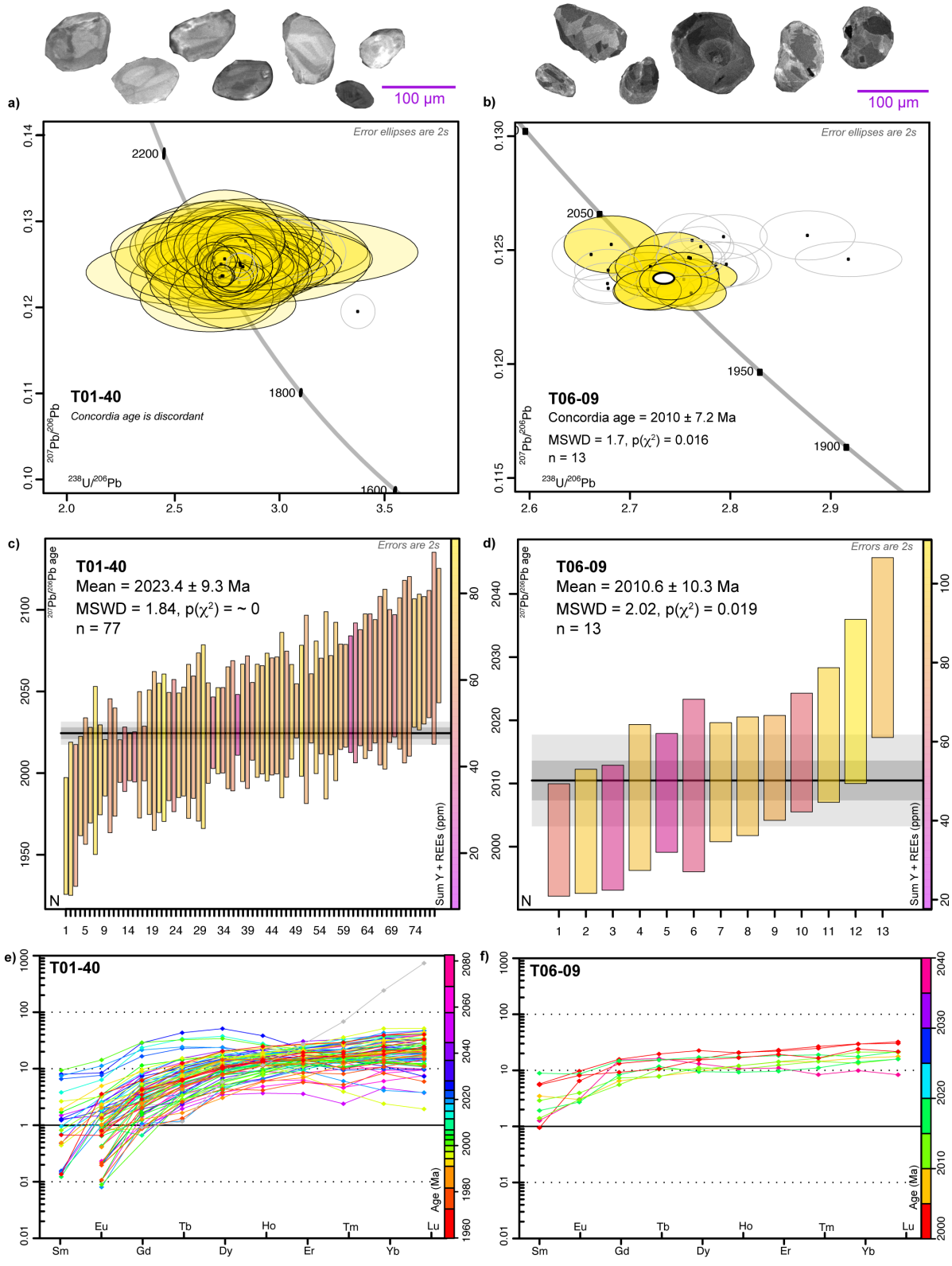


Figure 7: U–Pb and REE results and representative CL images of zircons from the retrogressed eclogites. Empty ellipses are discordant and were omitted from the age calculations. a) Concordia plot of data from T01-40. b) Concordia plot of data from T06-09. c) 207Pb/206Pb weighted mean plot of concordant data from T01-40. d) 207Pb/206Pb weighted mean plot of concordant data from T06-09. e) REE of zircons normalised to chondrite in T01-40. f) REE of zircons normalised to chondrite in T06-09.

$^{207}Pb/^{235}U$ age of 2009.7 ± 6.9 Ma (MSWD = 2.32) and a weighted mean $^{206}Pb/^{238}U$ age of 2008 ± 7.9. Ma (MSWD = 1.52). Similar to T01-40, individual spot ages are not correlated to trace-element composition, Th/U ratio or CL response (Fig. 7d).

The REE compositions of concordant zircons are shown in Figure 7. Zircons in T01-40 show slightly positively sloped REE profiles with slightly negative Eu anomalies (Fig. 7e). Some zircons show enrichments in Sm to Dy, and there is some minor variation in Lu, however these subtle variations in REE content show no relationship to age. Zircons in T06-09 show flat REE profiles with no Eu anomaly (Fig. 7f).

5.5 Rutile U–Pb geochronology

Isotopic and trace-element data for rutile are in Supplementary Table 6. Analysed rutile grains in both samples were typically 60–100 μm. When imaged in BSE some rutile grains contained fine exsolution of ilmenite, these were avoided. The rutile was analysed in grain mounts, however, in both samples rutile was only observed as inclusions in garnet. Rutile inclusions in garnet were observed in contact with ilmenite, zircon and quartz (Fig. 2). The U–Pb results for T01-40 are shown in Figure 8a (error ellipses are 2σ). Five analyses were omitted due to inclusions being incorporated in the ablation, and six analyses were omitted due to high concentrations of ^{208}Pb (> 0.2 ppm; Supplementary Fig. 3). These high ^{208}Pb analyses define a common lead trend (Supplementary Fig. 3). The remaining 80 analyses define a discordia array, with intercepts at 472.5 ± 15.5 and 1994 ± 57 Ma (MSWD = 2.3). Zr concentrations in the rutile analyses are not correlated to their position on the discordia (Fig. 8a). The rutile U–Pb data from T06-09 are discordant, but due to the low number of analyses (n = 10), a discordia and intercept ages cannot be well constrained (Fig. 8b). One analyses from T06-09 was omitted due to contamination. Zr concentrations are not correlated to discordance of the analyses.

5.6 Ti in zircon and Zr in rutile thermometry

In both samples, rutile, quartz and zircon all occur as inclusions within garnet porphyroblasts, and in T01-40 they occur together as multi-mineral inclusions (Fig. 2). As such, it is assumed that these phases were in equilibrium during rutile growth. The results of the thermometry are shown in Figure 9 and summarised in Table 2, Ti contents in zircon and Zr contents in rutile are in Supplementary Tables 5 and 6 respectively. Only concordant analyses were used in Ti in zircon calculations, and temperatures were calculated using the Watson and Ferry (2007) calibration. Zircons in T01-40 have Ti contents of 1.1 ± 2 to 17.2 ± 5.2 ppm, with an average of 6.5 ± 2.8 ppm (n = 78; 2σ). These Ti contents correspond to temperatures of 573 ± 127

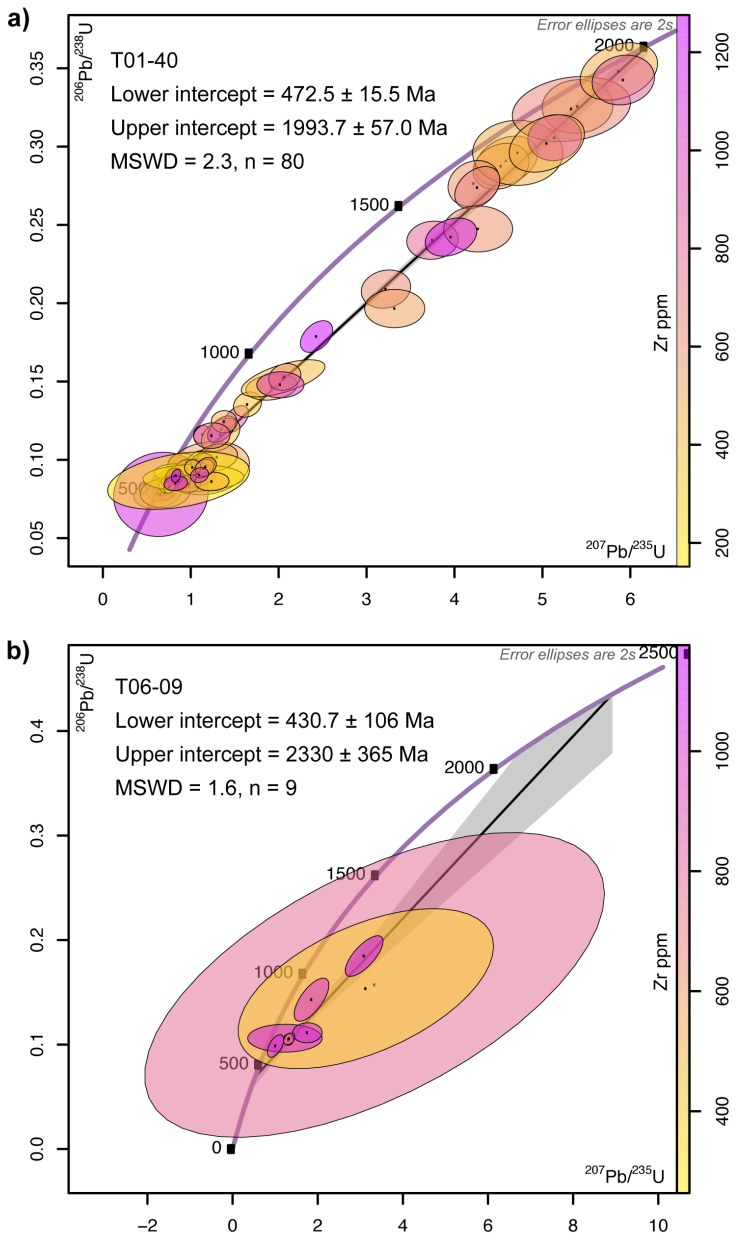


Figure 8: Rutile U–Pb results. Ellipses are colour-coded for Zr content. Omitted analyses are in Figure. B. 3. Error ellipses are 2σ. a) Rutile from T01-40, defining a discordia between ca. 1994 and 473 Ma. Zr content is not correlated with the resetting of rutile grains. b) Rutile from T06-09, lack of data means a meaningful discordia cannot be calculated, all though generally the analyses are defining a trend similar to that in T01-40. Zr content is not correlated with the resetting of the rutile grains.

°C to 799 ± 54 °C, with a mean of 705 ± 9°C (Fig. 9a; 2σ; MSWD = 2.01). Ti contents do not show a relationship with U–Pb date or core/rim location of analysis on zircon (Supplementary Fig. 4). Zircons in T06-09 have Ti contents of 3.4 ± 1.7 to 14.2 ± 3.5 ppm, with an average of 8.6 ± 2.7 ppm (*n* = 13; 2σ). This corresponds to temperatures of 653 ± 59 °C to 779 ± 51 °C, with a mean of 729 ± 25 °C (Fig. 9b; 2σ; MSWD = 2.33). Ti content, U–Pb date and location of analysis on zircon grain show no relationship (Supplementary Fig. 4).

Temperatures were calculated from Zr contents in rutile using the pressure-dependant calibration of Tomkins et al. (2007). Results are reported at pressures of 10 kbar and 18 kbar, this is done as 10 kbar is the minimum pressure at which rutile is stabilized, and 18 kbar is the interpreted peak pressure from mineral equilibria modelling (see below). Uncertainties on the temperatures were ~5.7 % on average, and were calculated using the quadrature summation of relative errors inherent in the calculations, including 2σ errors on the Zr content (± 1–1.2%), the error associated with the pressure (± 1 kbar), and the error associated with calibration of the thermometer. This was assigned at ± 3% after Watson et al. (2006), as no error is provided in the Tomkins et al. (2007) calibration. In T01-40, all rutile data have Si contents below 3000 ppm, within acceptable limits for eclogitic rutile (Zack et al., 2002), suggesting no incorporation of zircon and/or silicate inclusions. The rutile

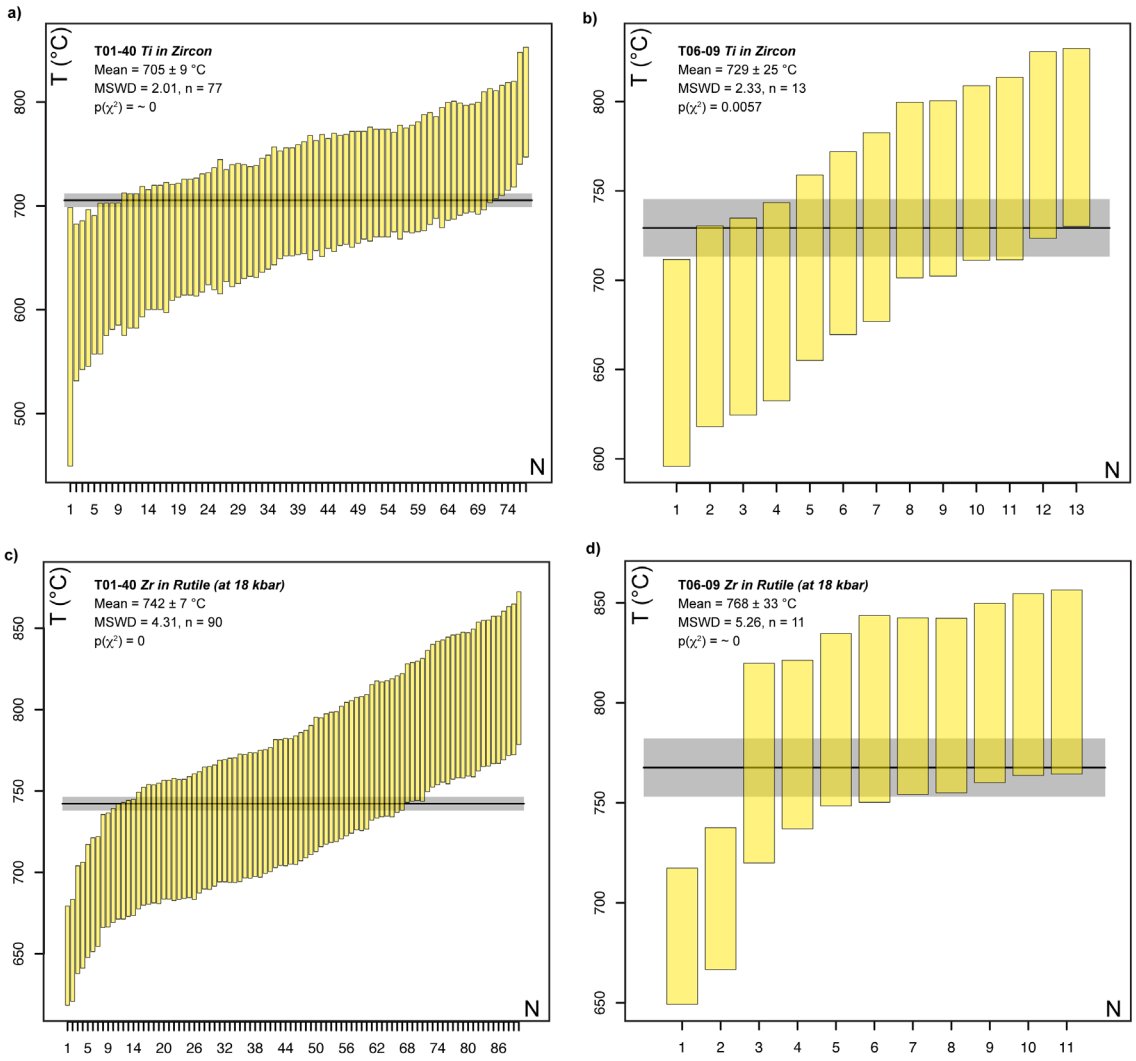


Figure 9: Calculated temperatures from Ti in zircon and Zr in rutile thermometry. Only analyses included in U–Pb age calculations were used in thermometry. Black line and grey bar indicate the calculated mean and uncertainty. a) Ti in zircon temperatures from T01-40. b) Ti in zircon temperatures from T06-09. c) Zr in rutile temperatures from T01-40 at 18 kbar. d) Zr in rutile temperatures from T06-09 at 18 kbar.

Table 2: Summary of temperatures calculated from Ti in zircon and Zr in rutile thermometry. Zr in rutile temperatures are reported at both 10 and 18 kbar. This is done as 10 kbar is the minimum pressure at which rutile is stabilized, and 18 kbar is the interpreted peak pressure from mineral equilibria modelling.

Method		**T01-40**	**T06-09**
Ti in zircon	Min	573 ± 127 °C	653 ± 59 °C
	Max	799 ± 54 °C	779 ± 51 °C
	Average	698 ± 59 °C	725 ± 53 °C
Zr in rutile	Min	616 ± 29 °C	648 ± 33 °C
At 10 kbar	Max	786 ± 45 °C	771 ± 44 °C
	Average	713 ± 38 °C	739 ± 42 °C
Zr in rutile	Min	649 ± 31 °C	683 ± 35 °C
At 18 kbar	Max	826 ± 48 °C	810 ± 47 °C
	Average	750 ± 40 °C	777 ± 44 °C

yields a range of Zr concentrations from 194 ± 2 to 1234 ± 16 ppm (n = 84), corresponding to temperatures of 649 ± 31 °C to 826 ± 48 °C at 18 kbar, with a mean value of 742 ± 7 °C (Fig. 9c; MSWD = 4.31). In T06-09, one rutile analysis was removed due to Si contents of ~ 20,000 ppm. The remaining ten analyses range from 297 ± 5 to 1143 ± 18 ppm Zr, corresponding to temperatures of 683 ± 35 °C to 810 ± 47 °C at 18 kbar, with a mean value of 768 ± 33 °C (Fig. 9d; MSWD = 5.26).

5.7 Mineral equilibria modelling

T01-40 was modelled with H_2O in excess to investigate the stabilised mineral assemblages on the prograde path (Fig. 10a-b). Since dry mafic rocks are notoriously unreactive, the formation of an interpreted peak eclogite-facies mineral assemblage suggests the rock contained adequate free water to promote reactivity until peak conditions. The mineral inclusions in garnet cores from T01-40 include quartz + titanite + plagioclase, which transitions to quartz + rutile + clinopyroxene closer towards the garnet rims, with hornblende and rare epidote inclusions throughout. Plagioclase is stable in the model to ~ 9 kbar, the titanite to rutile transition occurs at ~ 13.5 kbar, epidote is stable from ~7–21 kbar, and hornblende to ~ 18 kbar, and quartz is stable throughout (Fig. 10a). The inclusion assemblage in garnet suggests the sample evolved through this pressure history, however, there are only very broad temperature constraints from the mineral assemblages themselves. The range of compositions of plagioclase inclusions in garnet are outlined in Figure 10b, and are used to constrain the early prograde path to between 550–650 °C at 6–9 kbar. Additionally, the minimum Zr in rutile temperatures are used to constrain the prograde path. This is done as the minimum Zr in rutile temperatures are interpreted to represent

the first crystallization of rutile when rutile stability is reached, at approximately 670° C at 13.5 kbar. The prograde path is then interpreted to evolve up pressure and temperature, traversing the range of Zr in rutile temperatures.

Based on the interpreted former presence of omphacite, the peak assemblage is garnet + omphacite + rutile + quartz ± epidote ± H_2O or melt. This assemblage occurs in the same location in both the model calculated with excess water (Fig. 10) and the model calculated with a set water content (Fig. 11). This field is bound down pressure by the appearance of hornblende, at approximately 18 kbar, thus this is a minimum pressure constraint on the peak conditions. The peak temperatures are estimated from maximum Zr in rutile temperatures at approximately 800 °C, which plot in a melt-bearing field (Fig. 11b). There is no mesoscopic evidence that the rock underwent partial melting. However, melt modes in the peak field are low (< 4 %) and as such may not have left any

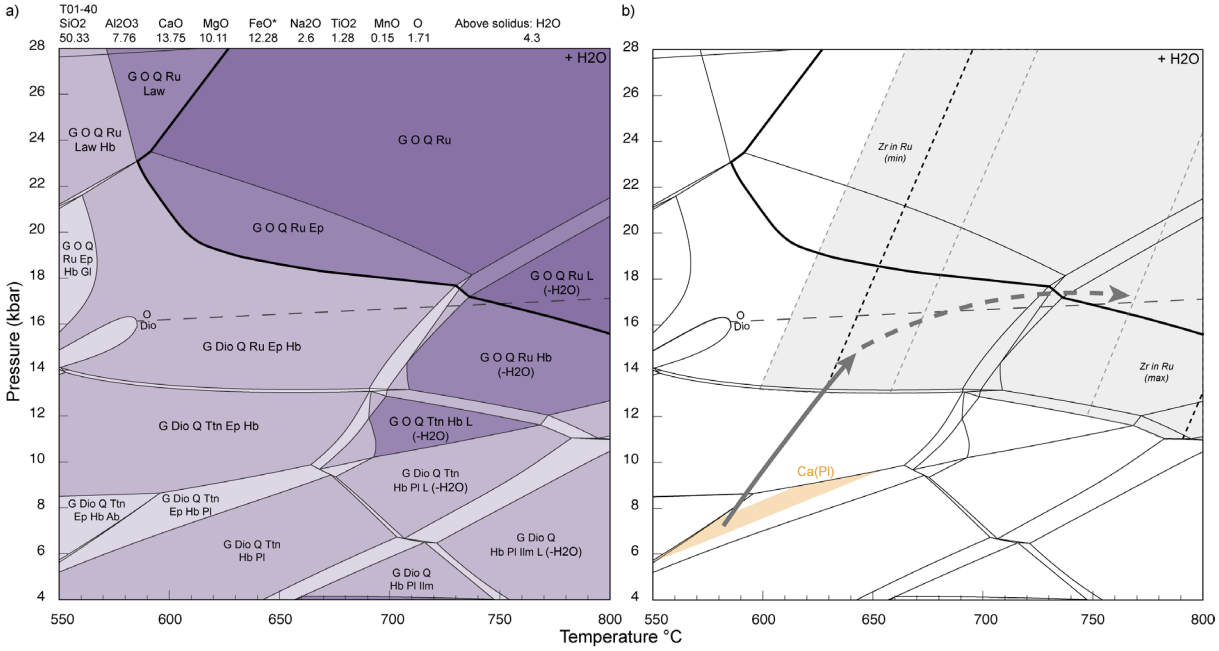


Figure 10: a) Mineral equilibria model calculated for T01-40 with water in excess, to model assemblages on the prograde path. Assemblages above the solidus were modelled with water set to 4.3 mol%. This was done as 4.3 mol% is the amount of water calculated to stabilise a water saturated solidus. Fields of interest are outlined in black bold line. The location of the omphacite-diopside solvus is marked in a thin grey dotted line. Colour of fields corresponds to variance in that field. b) Same mineral equilibria model showing the range of compositions of plagioclase included in garnet in orange. The minimum and maximum Zr in rutile temperatures are plotted in black dashed line, with the individual uncertainties outlined in grey dashed lines. The grey shaded area represents the total range of Zr in rutile temperatures. Thick grey arrows indicate interpreted prograde P–T path. Abbreviations: Ab: Albite, Act: Actinolite, Coe: Coesite, Dio: Diopside, Ep: Epidote, G: Garnet, Gl: Glaucophane, Hb: Hornblende, Ilm: Ilmenite, L: Liquid (melt), Law: Lawsonite, Mt: Magnetite, O: Omphacite, Opx: Orthopyroxene, Pl: Plagioclase, Q: Quartz, Ru: Rutile, Ttn: Titanite.

petrological evidence. Thus, the peak conditions are interpreted to be 800 °C at a minimum of 18 kbar.

The peak to retrograde evolution of T01-40 is interpreted using a mineral equilibria model calculated with a set water content (Fig. 11). This water content was determined from the modal proportion of hornblende in the rock, the only water-bearing mineral in the assemblage. The rock is interpreted to track into the garnet + diopside + quartz + hornblende + plagioclase + ilmenite field, which spans a wide range of temperatures (Fig. 11a). The conditions reached in this field are approximately 750 °C and 7 kbar, constrained by titanium in hornblende (*Hb(T)*), and the current modal proportion of garnet (Fig. 11b). The rock may have continued to evolve to conditions of ~ 500 °C and 6 kbar, as recorded by the addition of magnetite to the retrograde assemblage. This is supported by the X_{Fe} composition of garnet rims, labelled as *G(X)R*, which overlap with the range of

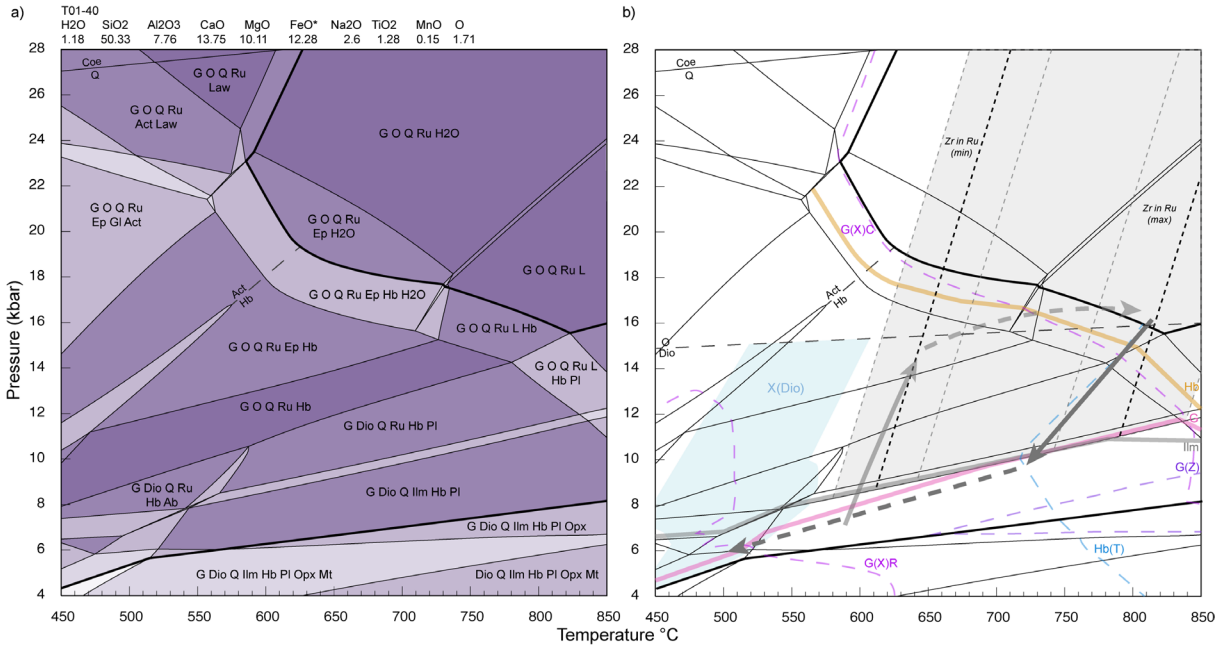


Figure 11: a) Mineral equilibria model calculated for T01-40 with a set water content, used to model the peak to retrograde path. Fields of interest are outlined in black bold line. The location of the actinolite-hornblende solvus is marked in a thin grey dotted line. Colour of fields corresponds to variance in that field. b) Same mineral equilibria model with compositions and modal proportions of minerals of interest. The minimum and maximum Zr in rutile temperatures are plotted in black dashed line, with the individual uncertainties outlined in grey dashed lines. The grey shaded area represents the total range of Zr in rutile temperatures. Coloured thick lines indicate the modal proportion of labelled minerals, dashed coloured lines indicate the composition of labelled minerals. The transparent blue field covers the range of retrograde diopside X(Fe) compositions. Thick grey arrows indicate interpreted P–T path, the transparent grey arrow indicates the P–T path from Figure 10. Abbreviations: Ab: Albite, Act: Actinolite, Coe: Coesite, Dio: Diopside, Ep: Epidote, G: Garnet, Gl: Glaucophane, Hb: Hornblende, Ilm: Ilmenite, L: Liquid (melt), Law: Lawsonite, Mt: Magnetite, O: Omphacite, Opx: Orthopyroxene, Pl: Plagioclase, Q: Quartz, Ru: Rutile, Ttn: Titanite.

retrograde diopside $X_{(Fe)}$ compositions. This may reflect re-equilibration of garnet rims with diopside at retrograde conditions (Fig. 11b).

The prograde history of T06-09 is difficult to reconstruct, as the rock does not contain a diverse range of inclusions inside garnet. As such, we present the peak-retrograde evolution of T06-09, as this is well recorded by the retrograde mineralogy. Similar to T01-40, the maximum Zr in rutile temperature plots above the solidus in the garnet + omphacite + rutile + quartz + melt field, which is bound down-pressure by the hornblende-in line (Fig. 12a). There is no overt evidence for partial melting. However, like sample T01-40, melt modes in this field are low (< 3 %) and may not have left any petrological evidence. As such, the peak conditions are interpreted to be 800 °C at a minimum of 18 kbar. The interpreted retrograde field is garnet + diopside + quartz + hornblende + plagioclase + orthopyroxene + ilmenite, which spans a large *P–T* range. The retrograde path is interpreted to reach approximately 750 °C and 8 kbar, where Ti in hornblende (*Hb(T)*) and garnet

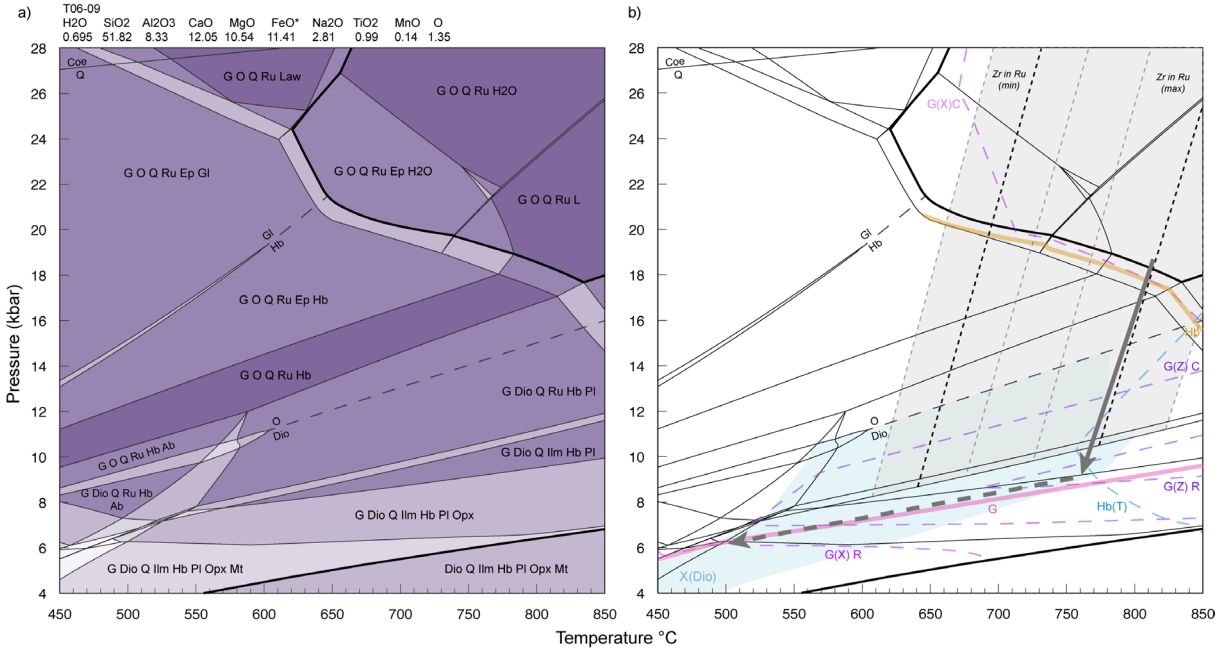


Figure 12: a) Mineral equilibria model calculated for T06-09 with a set water content, used to model the peak to retrograde path. Fields of interest are outlined in black bold line. Thin grey dotted lines mark the position of solvi. Colour of fields corresponds to variance in that field. b) Same mineral equilibria model with compositions and modal proportions of minerals of interest. The minimum and maximum Zr in rutile temperatures are plotted in black dashed line, with the individual uncertainties outlined in grey dashed lines. The grey shaded area represents the total range of Zr in rutile temperatures. Coloured thick lines indicate the modal proportion of labelled minerals, dashed coloured lines indicate the composition of labelled minerals. The transparent blue field covers the range of retrograde diopside X(Fe) compositions. Thick grey arrows indicate interpreted P–T path. Abbreviations: Ab: Albite, Act: Actinolite, Coe: Coesite, Dio: Diopside, Ep: Epidote, G: Garnet, Gl: Glaucophane, Hb: Hornblende, Ilm: Ilmenite, L: Liquid (melt), Law: Lawsonite, Mt: Magnetite, O: Omphacite, Opx: Orthopyroxene, Pl: Plagioclase, Q: Quartz, Ru: Rutile, Ttn: Titanite.

modes intersect in this field (Fig. 12b). The retrograde evolution may have continued to 500–650 °C and 4–6 kbar, as recorded by the addition of magnetite. This is supported by the X_{Fe} composition of garnet rims (*G(X)R*), which overlap with the range of retrograde diopside $X_{(Fe)}$ compositions, and may record conditions at which garnet rims re-equilibrated with diopside (Fig. 12b)

6. Discussion

6.1. Timing of eclogite-facies metamorphism

Geochronology collected from the two retrogressed eclogite samples suggests that metamorphism took place at ca. 2 Ga, in agreement with previous work (Möller et al., 1995; Collins et al., 2004).

Garnet Lu–Hf geochronology, the first of its kind collected from the Tanzanian retrogressed eclogites, pinpoints the timing of garnet formation in T01-40 to 1994 ± 9 Ma (Fig. 6a). Lu zoning in the garnet is diffuse but slightly elevated in the core, meaning this age probably reflects the average timing of garnet growth (Fig. 4; 5). In T06-09 however, the whole rock analysis does not fall on an isochron with the garnet aliquots. It is possible that the whole rock Lu–Hf ratio has been disturbed or altered by a later event, possibly related to the fine-grained hornblende veins that cross-cut the sample (Fig. 2). As such, the apparent whole rock-garnet Lu–Hf age may be geologically meaningless. When only the garnet aliquots are included in the isochron age calculation, they give an isochron age of 1959 ± 31 (Fig. 6c). All though this calculated age has a large error, the upper limit of the uncertainty is close to the T01-40 whole rock-garnet isochron age, suggesting the garnets in T06-09 may have grown at a similar time.

Zircon U–Pb geochronology from the retrogressed eclogite samples gives ages dispersed around ca. 2000 Ma for T01-40, and ca. 2010 Ma for T06-09 (Fig. 7). In T01-40, the weighted mean $^{207}Pb/^{206}Pb$ age is ca. 2023 Ma, older than the weighted mean $^{207}Pb/^{235}U$ age of ca. 2007 Ma and the weighted mean $^{206}Pb/^{238}U$ age of ca. 1994 Ma. This disagreement may possibly reflect a subtle combination of common lead and lead loss in the zircons. The lower limit of the weighted mean $^{207}Pb/^{235}U$ age uncertainty is within the garnet Lu–Hf age uncertainty, and the $^{206}Pb/^{238}U$ age is identical to the garnet age. Most zircons show flat to gently positively sloped REE profiles with slightly negative Eu anomalies, and some show humped MREE profiles, however individual age is not correlated with trace-element composition, making in-depth discussion of the zircon REE patterns difficult (Fig. 7). Garnet cores from this sample are enriched in HREEs, and garnet rims show flat or slightly humped REE profiles, similar to patterns in zircon. As such, we interpret the zircon

grew in the presence of garnet. Therefore, in T01-40 prograde-peak metamorphism occurred at ca. 1994 Ma as recorded by garnet and supported by zircon. In T06-09, the zircons generally show flat REE profiles with no Eu anomalies, similar to that of garnet in the sample, suggesting the zircons may have grown in the presence of garnet. However, the large uncertainty on the garnet Lu–Hf age means no definite relative age relationship between the zircon and garnet can be stated. Regardless, prograde-peak metamorphism occurred at ca. 2010 Ma in sample T06-09.

Results from rutile geochronology from T01-40 lie on a discordia array, with an upper intercept of 1994 ± 57 Ma (Fig. 8). Rutile texturally occurs as inclusions in garnet, and was likely entrapped during garnet growth. Despite the large uncertainty, it is evident this upper intercept is within uncertainty of the garnet Lu–Hf age, and reflects the timing of rutile growth during high-pressure metamorphism. The lower intercept of 473 ± 16 Ma most likely reflects resetting of the rutile during cooling in the Pan-African event, which affected the East African Orogen (Fritz et al., 2013) that borders and reworks part of the Isimani Suite (Fig. 1a). Rutile grains in T01-40 range from 50–200 mm but are generally ~ 100 mm in diameter. The closure temperature for rutile is proposed to be ~ 520–610 °C for a 100 mm diameter grain at cooling rate of 2–20 °C/Myr (Cherniak, 2000; Vry and Baker, 2006). As such, conditions in the Isimani Suite during the Pan-African event must have reached close to these temperatures. Unlike Pb, Zr concentrations appear comparatively undisturbed by the resetting event (Fig. 8).

6.3. P–T conditions during subduction

The Zr in rutile thermometer requires the assemblage zircon + rutile + quartz to be in equilibrium. This is likely for at least most of the metamorphic evolution, above approximately 10–13 kbar where rutile becomes stable (Fig. 10–12). In both samples, zircon, rutile and quartz occur as inclusions in garnet (Fig. 2), and in T01-40 all three occur as a polyphase inclusion in garnet (Fig. 2f), further supporting this interpretation. The results of the zircon U–Pb geochronology also indicate zircon grew during the metamorphic event that formed the garnet + rutile assemblage in the retrogressed eclogites.

In each sample, rutile is restricted to inclusions in garnet, suggesting the calculated rutile temperatures reflect temperatures during prograde to peak metamorphism. In both T01-40 and T06-09, the $p(\chi^2)$ values for each temperature mean are 0 (Fig. 9). This suggests the spread of temperatures are not within range of the analytical uncertainty. As such, the range of temperatures in each sample are interpreted to reflect the prograde to peak temperatures of rutile crystallization. This requires rutile to be recrystallising and updating its Zr con-

tent as it was captured in growing garnet during prograde metamorphism. Mineral equilibria modelling suggests the minimum pressure rutile stabilizes at is approximately 10–13 kbar, and peak pressures reached for each sample were 18 kbar (as a minimum; Fig. 10–12). In T01-40 the total range of temperatures calculated from 10 to 18 kbar are ~ 615–825 °C, in T06-09 the total range of temperatures calculated from 10 to 18 kbar are ~ 650–810 °C.

Similarly, the range of calculated Ti in zircon temperatures have low $p(\chi^2)$ values, indicating the range may reflect individual crystallization temperatures, and are generally in agreement with the results from Zr in rutile thermometry. In T01-40, the total range of temperatures are ~ 570–800 °C, however as there is no correlation with Ti content and age due to large uncertainties on each spot analysis, it is difficult to establish the relationship between the calculated temperatures and the *P–T* evolution of the retrogressed eclogite. However, it is likely the Ti in zircon temperatures reflect prograde-peak temperatures. In T06-09 the total range of Ti in zircon temperatures are 650–780 °C. As the timing of zircon vs garnet growth is difficult to assess, but zircons in T06-09 have flat REE profiles and appear to have grown with garnet, it is assumed that these temperatures reflect crystallization during prograde metamorphism of the eclogite.

The two samples experienced similar peak *P–T* conditions of approximately 18 kbar and 800 °C, however the pressure estimate is a minimum. The peak mineral assemblage in both samples is interpreted to be hornblende-free, and the peak field is constrained by a hornblende-in line at approximately 18 kbar. It is therefore possible that the retrogressed eclogites reached higher pressures above this line. This may have been preserved in the composition of garnet rims, but these have been resorbed by subsequent retrogression. It may have also been preserved by matrix mineralogy in the form of peak epidote (or its absence), however the matrix has also been significantly reworked. As such, the exact pressures reached by the samples remains unknown, but must have been at least 18 kbar. The retrogressed eclogites experienced similar retrograde conditions of approximately 7–8 kbar and 750 °C, as recorded by the development of retrograde Na-poor clinopyroxene-hornblende and/or orthopyroxene-bearing assemblages. This was possibly followed by cooling to 500 °C at ~ 5 kbar, recorded by the X_{Fe} compositions of the outermost garnet rims and the X_{Fe} of diopside, interpreted to have re-equilibrated at retrograde conditions, and the formation of late-stage magnetite.

The calculated peak conditions recorded by the retrogressed eclogites are similar to published results of approximately 18 kbar and 750 °C (Möller et al., 1995; Brown et al., 2020), although Möller et al. combined texturally retrograde plagioclase

with texturally peak metamorphic minerals. The *P–T* paths are also similar to those of Brown et al. (2020). The peak *P–T* conditions correspond to thermal gradients of 45 °C/kbar, consistent with warm conditions during subduction (e.g. Brown and Johnson, 2018; Agard et al., 2018). These conditions may be a result of warmer ambient mantle temperatures in the Palaeoproterozoic. However, as shown by Ganne and Feng (2017), ambient mantle temperatures at ca. 2000 Ma were probably only marginally warmer than in the late Neoproterozoic when eclogite emerged in the geological record. Therefore, the warm thermal conditions recorded by the Usagaran high-pressure rocks could also potentially reflect slow burial either due to slow subduction rates and/or a shallow subduction angle

6.4. Garnet zoning and thermal histories of the retrogressed eclogites

Despite the similarities in the mineralogy between the two samples, garnets in T01-40 and T06-09 show distinctly different zoning patterns in both major and trace-elements. There is no immediate explanation for why this is the case, as the garnets have experienced similar *P–T–t* histories and have grown in similar bulk compositions, and hence interacted with similar mineral assemblages. Garnets in all samples show a narrow, resorbed rim, enriched in Y and Lu. Y and Lu zoning in T01-40 show enrichments in the garnet cores, consistent with Rayleigh fractionation during porphyroblast growth (Otamendi et al., 2002), and an enriched annulus close to the rim, probably correlated with breakdown of an accessory mineral during prograde metamorphism (possibly allanite, e.g. Hyppolito et al., 2019). This core enrichment can be seen in garnets of all sizes (~200–1500 mm). Garnets in T06-09 however show either flat Y and Lu profiles in smaller garnets (~ 400 mm across), or depleted Y and Lu cores and progressive enrichments towards the rims in larger garnets (~ 1500 mm across), the inverse of what is seen in garnets of T01-40. Garnets in T06-09 are generally smaller than in T01-40, however small garnets mapped on the edge of the larger garnet in T01-40 show similar patterns to the largest garnets of T01-40 (Fig. 4), negating size as the explanation for these differing patterns across the two samples.

Reverse Rayleigh zoning in HREE elements has been noted, largely in high-pressure rocks (Hickmott and Spear, 1992; Skora et al., 2006; Moore et al., 2013; Maldonado et al., 2018; Hyppolito et al., 2019). This reverse zoning could have been formed during prograde growth, or during diffusional modification of originally Rayleigh-fractionated garnets. The latter would require T06-09 to have resided at high temperatures (> 650 °C) for an extended period of time, resulting in garnets with relatively flat core profiles and enriched resorption rims (e.g. Kelly et al., 2011). However, garnets in T01-09 show a depletion of Y and

Lu in their cores, which would require uphill diffusion of these elements towards the edge of the garnet. As this seems unlikely, we postulate the reverse Rayleigh zoning formed as a result of diffusion-limited REE uptake during garnet growth (Skora et al., 2006; Moore et al., 2013). This may have occurred if T06-09 had a lower water content than T01-40, limiting diffusivity of the REE elements through the matrix to the site of garnet growth. The current mineral assemblages in the retrogressed eclogites do not record the amount of water available during prograde metamorphism, however T06-09 currently has 0.2 wt% mineral bound H_2O, compared to T01-40 which currently has 0.35 wt% mineral bound H_2O (Supplementary Table 2). Even though the samples are now retrogressed, it appears likely that T01-40 contained more H_2O than T06-09.

The Cr and V distributions in garnets from the samples show patterns which are not correlated with major or rare earth elements (Fig. 4). Like the REEs, Cr and V have low rates of diffusivity, and their distributions in garnet are usually the result of breakdown of Cr and V bearing minerals, namely amphibole and epidote in mafic rocks (Spandler et al., 2003; Yang and Enami, 2003; Carlson, 2012; Volkova et al., 2014). Garnets in T01-40 and T06-09 have patchy Cr enrichments, in T01-40 these are abundant and elongate, and in T09-09 they are less abundant and equant. The enrichments probably formed due to overgrowth of a pre-existing hornblende foliation (e.g., Yang and Rivers, 2001). In V, small equant enrichments can be seen in garnet in T01-40, and large patchy enrichments can be seen in the garnet in T06-09, suggesting overgrowth of V rich crystals, such as epidote (Yang and Rivers, 2001). Garnets in T01-40 have a sharp rim enriched in both Cr and V, and in T06-09 garnets have a thin irregular rim enriched in Cr. These rims probably formed during final breakdown of hornblende on the prograde path (e.g., Fig. 11; 12).

Major element zoning in garnet has been widely used to infer the thermal histories of metamorphic rocks (e.g. Ganguly et al., 2000; Dachs and Proyer, 2002; Carlson, 2006; Caddick et al., 2010; Spear, 2014). However, this must be done with caution as it requires assumptions about the compositional zoning in garnet prior to diffusional modification. The compositional patterns in garnet in T01-40 and T06-09 during prograde to peak metamorphism are unknown. Currently, garnets in T01-40 have modified prograde zoning in the major elements, preserved as diffuse bell-shaped Mn profiles and Fe and Mg zoning, however garnets in T06-09 preserve flat major element profiles (Fig. 3). Garnets in both samples preserve ~ 50 μm wide rims that are enriched in Mn. These observations hold true in garnets with similar sizes (~1000 μm) across the two samples (Supplementary Fig. 2). If the assumption is made that garnets in T06-09 developed prograde growth zoning similar to

garnets in T01-40, this zoning must have been homogenised or flattened by post-growth diffusional relaxation (e.g., Caddick et al., 2010; Carlson, 2012). We note that this may not have been the case. Trace-elements in garnets in T06-09 show diffusion-limited zoning, which may suggest that major elements in T06-09 did not prograde zone in a similar way to T01-40. If diffusional relaxation of any prograde zoning in T06-09 did occur, it must have occurred prior to retrogression and consumption of garnet rims, as the Mn-rich rims in T06-09 are still preserved.

Using Figure 2 of Caddick et al. (2010), the timescale at which diffusion becomes significant can be estimated if the temperature and diffusion length-scale are known. Maximum peak temperatures are estimated to be ~ 800 °C for both of the samples. The average preserved diameter of garnets T06-09 is ~1000 mm. Thus, for T06-09 to flatten any major element zoning, it must have remained at 800 °C for at least 6 Myr. Garnets ~ 1000 μm in diameter in T01-40 retain a vestige of their major element zoning, but record similar peak temperatures to T06-09 (Fig. 3, Supplementary Fig. 2). T01-40 also is likely to have undergone diffusion of major elements, as the zonation patterns in Mn, Fe and Mg are diffuse. However, it has experienced less homogenisation than T06-09.

If the above is true, sample T01-40 and T06-09 may have recorded different thermal histories. The simplest explanation is that T06-09 may have been stalled at depth above the closure temperature for major element diffusion in garnet during peak metamorphism for at least 6 Myr, while T01-40 was immediately exhumed to depths below the closure temperature of major element diffusion in garnet. T01-40 and T06-09 are sampled from ~ 5 km of each other (Fig. 1b), however are separated by > 100 meters of amphibolite-facies shear zones. It is possible that T01-40 was exhumed immediately to shallower crustal levels and thus lower temperatures and pressures than T06-09 following peak metamorphism via these shear zones.

6.5. Tectonic model for formation of the Usagaran retrogressed eclogites

The current tectonic model for metamorphism of the Usagaran retrogressed eclogites and the Isimani Suite involves subduction of the Tanzanian margin (Möller et al., 1995; Ring et al., 1997; Reddy et al., 2003; Collins et al., 2004). The MORB-like composition of the retrogressed eclogites has led authors to suggest subduction of either oceanic crust or mafic intrusions in a marginal basin (Möller et al., 1995; Reddy et al., 2003). The existence of Archean and Palaeoproterozoic crust immediately adjacent to the Usagaran Belt in the reworked Mozambique Belt, as well as the abundance of continental and felsic material in the Isimani Suite, has led to the suggestion that a small microcontinent or continental ribbon was

rifted off the Tanzanian Craton prior to formation of the Usagaran eclogites (Maboko et al., 2000; Muhongo et al., 2001; Reddy et al., 2003; Sommer et al., 2005b). Subduction has been interpreted as east-dipping, based on the presence of Palaeoproterozoic amphibolite-facies east-dipping fabrics in the Isimani Suite (Reddy et al., 2003). This basin was then subducted under the continental ribbon at ca. 2000 Ma, and then exhumed in a transpressional regime during docking of the ribbon on the margin of the craton. Brown et al. (2020) suggested the retrogressed eclogites were exhumed in an extensional regime after slab breakoff and buoyancy driven exhumation, a more likely driver of exhumation of high-pressure rocks from mantle depths (e.g. Sizova et al., 2014; Petersen and Buck, 2015). This was supported by the fact that the east-dipping fabrics in the Isimani Suite are shallowly dipping, a feature often indicative of extension or transtention (Reddy et al., 2003; Brown et al., 2020). I-type granitoids and volcanics which intruded the Usagaran Belt between ca. 1940 and 1870 Ma are interpreted to be subduction related, calling for continued subduction of oceanic crust for up to ca. 130 Myr after metamorphism of the Usagaran retrogressed eclogites (Maboko and Nakamura, 1996; Reddy et al., 2003; Sommer et al., 2005a; Bahame et al., 2016).

We postulate two likely tectonic scenarios for subduction and exhumation of the Usagaran retrogressed eclogites and the Isimani Suite (Fig. 13). The primary difference between the models is the polarity of subduction during eclogite-facies metamorphism. The first scenario is similar to that of previous workers (Möller et al., 1995; Ring et al., 1997; Reddy et al., 2003; Collins et al., 2004). It involves east-dipping subduction of oceanic crust on the margin of the Tanzanian Craton under a possible continental ribbon (Fig. 13a). The Isimani Suite metapelitic and felsic gneisses formed in an accretionary wedge, which is sourced from both the Tanzanian Craton and possibly the ribbon (Collins et al., 2004). Metamorphism of the retrogressed eclogites occurred from ca. 2010–1994 Ma, and they reached pressures of at least 18 kbar. Within at least 6 Myr, slab breakoff resulted in buoyancy-driven exhumation of the mafic eclogites, which were incorporated into the metapelitic gneisses (Fig. 13b; e.g. Petersen and Buck, 2015). Following this, subduction polarity was flipped, and oceanic crust began to subduct under the ribbon (Reddy et al., 2003). The exhumed oceanic crust and accretionary material of the Isimani Suite then became part of an extensional back arc system (Fig. 13e). At this point, the retrogressed eclogites were feasibly at shallow crustal levels, and had been exhumed by further extension and formation of shallowly east-dipping fabrics in the Isimani Suite (Reddy et al., 2003; Brown et al., 2020).

The above model accounts for the geology of the Usagaran Belt, however, there is another tectonic

scenario which is also possible for formation and exhumation of the Usagaran eclogites (Fig. 13c-d). This scenario involves west-dipping subduction of oceanic crust under the margin of the Tanzanian Craton, where the mafic eclogites and encasing Isimani gneisses were metamorphosed from ca. 2010–1994 Ma (Fig. 13c). While west-dipping subduction under the Tanzanian Craton has not been suggested for formation of the eclogites before, it does align with ca. 2 Ga metasomatic mantle enrichments under the craton in the northern Usagaran Belt, which were probably formed from subduction related fluids (Konreef et al., 2009; Aulbach et al., 2011). Buoyancy-driven exhumation of the retrogressed eclogites occurred immediately (within ca. 6 Myr) after peak conditions,

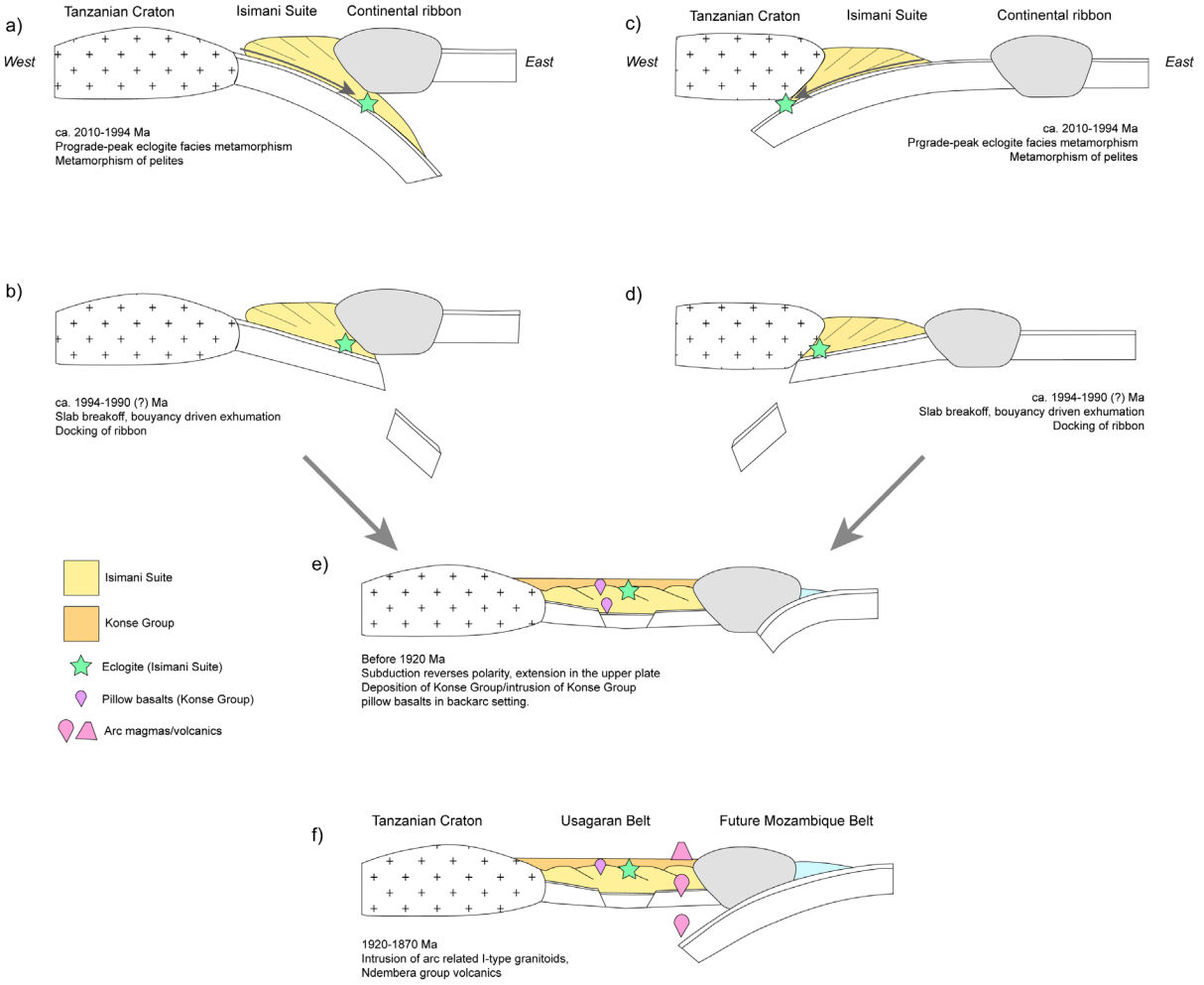


Figure 13: Two possible tectonic scenarios for subduction and exhumation of the Usagaran retrogressed eclogites. a-b) Scenario involving east-dipping subduction of oceanic crust on the margin of the Tanzanian Craton under a continental ribbon previously rifted off the cratonic margin. After slab breakoff and docking of the ribbon, subduction polarity is reversed, placing the Isimani Suite in a back arc position. c-d) Scenario involving west-dipping subduction of oceanic crust under the Tanzanian Craton. After slab breakoff and docking of the rifted continental ribbon, subduction steps back, and the Isimani Suite is placed into a back arc position. e-f) Exhumation of the retrogressed eclogites in the back arc, and continued evolution of the Usagaran belt, including deposition and intrusion of the Konse Group and intrusion of arc-like granitoids and associated volcanics.

and the continental ribbon was docked onto the margin of the Isimani Suite (Fig. 13d). This resulted in stepping back of the subduction zone, which placed the Isimani Suite into an extensional back arc basin, possibly aiding in exhuming the retrogressed eclogites to shallow crustal levels (Fig. 13e).

After exhumation of the eclogites, the tectonic evolution of the Usagaran Belt above a west-dipping subduction zone is the same in both models (Fig. 13e-f). Thinning of the basement oceanic crust in the back arc basin led to the deposition of the Konse Group sediments, and the extrusion of pillow basalts with back arc affinities into these sediments (Fig. 13e; Boniface and Tsujimori, 2018). This occurred between ca. 1990–1920 Ma. Continued west-dipping subduction of oceanic crust resulted in intrusion of post-tectonic granitoids and the Ndembera group volcanics, interpreted to be arc related, into the Usagaran Belt from ca. 1940–1870 Ma (Fig. 13f; Sommer et al., 2005a; Bahame et al., 2016).

The newly suggested scenario for formation and exhumation of the high-pressure rocks is similar to that of the Ordovician–Silurian Western Gneiss Complex in Norway (Hacker et al., 2003; Kylander-Clark et al., 2008; Hacker et al., 2010). Following high pressure metamorphism and slab breakoff, the subducted crust buoyantly exhumed into the upper plate (Hacker et al., 2010). As the subduction zone stepped back, further exhumation occurred along extensional detachments in a back arc system. *P–T* paths during exhumation of the Western Gneiss Complex eclogites were isothermal, resulting in amphibolite-facies overprinting of the mafic eclogites, similar to that recorded by the Usagaran retrogressed eclogites (Walsh and Hacker, 2004). While it is not possible to distinguish between the two tectonic models that led to the formation of the high-pressure rocks and evolution of the Usagaran Belt, it is evident that slab breakoff, buoyant rise of the underlying plate and its conversion to a back arc system were integral in exhuming the eclogites of the Isimani Suite.

7. Conclusions

Retrogressed eclogites from Yalumba Hill in the Usagaran Belt preserve evidence for subduction related eclogite-facies metamorphism. Garnet growth is dated by Lu–Hf at ca. 1994 Ma in one of the samples, and is supported by zircon U–Pb geochronology dispersed around ca. 2000 Ma. Rutile U–Pb geochronology from the same sample yields an upper intercept of ca. 1994 Ma, supporting eclogite-facies metamorphism at this time. Zr in rutile thermometry and mineral equilibria modelling suggest the eclogites reached 800 °C and at least 18 kbar, and were retrogressed to conditions of approximately 7–8 kbar and 750 °C. This corresponds to thermal gradients of ~ 45 °C/kbar, consistent with warm conditions during

subduction. These warm conditions may have been the result of a warmer mantle temperature in the Palaeoproterozoic, and shallow, low-angle subduction. Tectonic models for formation and exhumation of the retrogressed eclogites involve either east-dipping subduction of oceanic crust on the Tanzanian Craton margin, or, west-dipping subduction of oceanic crust under the Tanzanian Craton. Buoyancy driven exhumation of the retrogressed eclogites occurred after slab breakoff, followed by a subduction polarity switch or a step back in the subduction zone, which placed the eclogites and Isimani Suite into a back-arc position. The similarity in age and *P–T* conditions of the Usagaran retrogressed eclogites with eclogites from the Eburnian-Transamazonian and Ubende orogens demonstrates that a large subduction system may have been stable on the margin of the Tanzanian Craton from ca. 2.1–1.9 Ga. This suggests that modern style subduction was operating on significant geographic and temporal scales by this time in Earth's history.

Acknowledgements

We are grateful to Sarah Gilbert, Ben Wade and Aoife McFadden of Adelaide Microscopy for their assistance with data collection. Alan Collins is thanked for providing sample T01-40. We thank Dariusz Sala, Milena Matyszczak, Martyna Rogozik and Maria Repczyńska for their assistance with Lu–Hf data collection. David Kelsey and Jack Gillespie are thanked for helpful discussions. We thank Andrew Kylander-Clark and an anonymous reviewer for their helpful comments on the manuscript, and Marco Scambelluri for his editorial handling. The authors acknowledge financial support from the Australian Research Council (ARC) grant 180104074. Renée Tamblyn acknowledges financial support from the Aldermann Kleeman travel scholarship from the University of Adelaide.

References:

Agard, P., Plunder, A., Angiboust, S., Bonnet, G., and Ruh, J. (2018). The subduction plate interface: Rock record and mechanical coupling (from long to short time scales). *Lithos*.

Anczkiewicz, R., Platt, J. P., Thirlwall, M. F., and Wakabayashi, J. (2004). Franciscan subduction off to a slow start: evidence from high-precision Lu–Hf garnet ages on high grade-blocks. *Earth and Planetary Science Letters, 225*(1), 147-161.

Anczkiewicz, R., and Thirlwall, M. F. (2003). Improving precision of Sm-Nd garnet dating by H2SO4 leaching: a simple solution to the phosphate inclusion problem. *Geological Society, London, Special Publications, 220*(1), 83-91.

Aulbach, S., Rudnick, R. L., and McDonough, W. F. (2011). Evolution of the lithospheric mantle beneath the East African Rift in

Tanzania and its potential signatures in rift magmas. *Geological Society of America Bulletin, 478*, 105-125.

Bahame, G., Manya, S., and Maboko, M. A. (2016). Age and geochemistry of coeval felsic volcanism and plutonism in the Palaeoproterozoic Ndembera Group of southwestern Tanzania: Constraints from SHRIMP U–Pb zircon and Sm–Nd data. *Precambrian Research, 272*, 115-132.

Baldwin, J. A., Bowring, S. A., Williams, M. L., and Williams, I. S. (2004). Eclogites of the Snowbird tectonic zone: petrological and U-Pb geochronological evidence for Paleoproterozoic high-pressure metamorphism in the western Canadian Shield. *Contributions to Mineralogy and Petrology, 147*(5), 528-548.

Boniface, N., Schenk, V., and Appel, P. (2012). Paleoproterozoic eclogites of MORB-type chemistry and three Proterozoic orogenic cycles in the Ubendian Belt (Tanzania): Evidence from monazite and zircon geochronology, and geochemistry. *Precambrian Research, 192*, 16-33.

Boniface, N., and Tsujimori, T. (2019). Pillow lava basalts with back-arc MORB affinity from the Usagaran Belt, Tanzania: relics of Orosirian ophiolites. *Journal of the Geological Society, 176*(5), 1007-1021.

Brick, R. A. (2011). *Palaeoproterozoic eclogite formation in Tanzania: a structural, geochronological, thermochronological and metamorphic study of the Usagaran and Ubende orogenic belts.* Doctoral dissertation.

Brown, D. A., Tamblyn, R., Hand, M., and Morrissey, L. J. (2020). Thermobarometric constraints on burial and exhumation of 2-billion-year-old eclogites and their metapelitic hosts. *Precambrian Research*, 105833.

Brown, M., and Johnson, T. (2018). Secular change in metamorphism and the onset of global plate tectonics. *American Mineralogist, 103*(2), 181-196.

Caddick, M. J., Konopásek, J., and Thompson, A. B. (2010). Preservation of garnet growth zoning and the duration of prograde metamorphism. *Journal of Petrology, 51*(11), 2327-2347.

Carlson, W. D. (2006). Rates of Fe, Mg, Mn, and Ca diffusion in garnet. *American Mineralogist*, 91(1), 1-11.

Carlson, W. D. (2012). Rates and mechanism of Y, REE, and Cr diffusion in garnet. *American Mineralogist, 97*(10), 1598-1618.

Cherniak, D. (2000). Pb diffusion in rutile. *Contributions to Mineralogy and Petrology, 139*(2), 198-207.

Collins, A. S., Reddy, S. M., Buchan, C., and Mruma, A. (2004). Temporal constraints on Palaeoproterozoic eclogite formation and exhumation (Usagaran Orogen, Tanza-

nia). *Earth and Planetary Science Letters, 224*(1-2), 175-192.

Corfu, F., Hanchar, J. M., Hoskin, P. W., and Kinny, P. (2003). Atlas of zircon textures. *Reviews in mineralogy and geochemistry, 53*(1), 469-500.

Dachs, E., and Proyer, A. (2002). Constraints on the duration of high-pressure metamorphism in the Tauern Window from diffusion modelling of discontinuous growth zones in eclogite garnet. *Journal of metamorphic Geology, 20*(8), 769-780.

Droop, G. (1987). A general equation for estimating Fe3+ concentrations in ferromagnesian silicates and oxides from microprobe analyses, using stoichiometric criteria. *Mineralogical Magazine, 51*(361), 431-435.

Ferry, J., and Watson, E. (2007). New thermodynamic models and revised calibrations for the Ti-in-zircon and Zr-in-rutile thermometers. *Contributions to Mineralogy and Petrology, 154*(4), 429-437.

François, C., Debaille, V., Paquette, J.-L., Baudet, D., and Javaux, E. J. (2018). The earliest evidence for modern-style plate tectonics recorded by HP–LT metamorphism in the Paleoproterozoic of the Democratic Republic of the Congo. *Scientific reports, 8*(1), 1-10.

Fritz, H., Abdelsalam, M., Ali, K., Bingen, B., Collins, A., Fowler, A., Ghebreab, W., Hauzenberger, C., Johnson, P., and Kusky, T. (2013). Orogen styles in the East African Orogen: A review of the Neoproterozoic to Cambrian tectonic evolution. *Journal of African Earth Sciences, 86*, 65-106.

Ganguly, J., Dasgupta, S., Cheng, W., and Neogi, S. (2000). Exhumation history of a section of the Sikkim Himalayas, India: records in the metamorphic mineral equilibria and compositional zoning of garnet. *Earth and Planetary Science Letters, 183*(3-4), 471-486.

Ganne, J., and Feng, X. (2017). Primary magmas and mantle temperatures through time. *Geochemistry, Geophysics, Geosystems, 18*(3), 872-888.

Green, E., White, R., Diener, J., Powell, R., Holland, T., and Palin, R. (2016). Activity–composition relations for the calculation of partial melting equilibria in metabasic rocks. *Journal of metamorphic Geology, 34*(9), 845-869.

Hacker, B., Andersen, T., Root, D., Mehl, L., Mattinson, J., and Wooden, J. (2003). Exhumation of high-pressure rocks beneath the Solund Basin, western gneiss region of Norway. *Journal of metamorphic Geology, 21*(6), 613-629.

Hacker, B. R., Andersen, T. B., Johnston, S., Kylander-Clark, A. R., Peterman, E. M., Walsh, E. O., and Young, D. (2010). High-tem-

perature deformation during continental-margin subduction and exhumation: The ultrahigh-pressure Western Gneiss Region of Norway. *Tectonophysics, 480*(1-4), 149-171.

Herms, P. (2002). Fluids in a 2 Ga old subduction zone—deduced from eclogite-facies rocks of the Usagaran belt, Tanzania. *European Journal of Mineralogy, 14*(2), 361-373.

Herwartz, D., Skublov, S., Berezin, A., and Mel'Nik, A. (2012). *First Lu-Hf garnet ages of eclogites from the Belomorian mobile belt (Baltic shield, Russia).* Paper presented at the Doklady Earth Sciences.

Hickmott, D., and Spear, F. S. (1992). Major-and trace-element zoning in garnets from calcareous pelites in the NW Shelburne Falls Quadrangle, Massachusetts: garnet growth histories in retrograded rocks. *Journal of Petrology, 33*(5), 965-1005.

Holland, T., and Powell, R. (2011). An improved and extended internally consistent thermodynamic dataset for phases of petrological interest, involving a new equation of state for solids. *Journal of metamorphic Geology, 29*(3), 333-383.

Hyppolito, T., Cambeses, A., Angiboust, S., Raimondo, T., García-Casco, A., and Juliani, C. (2019). Rehydration of eclogites and garnet-replacement processes during exhumation in the amphibolite-facies. *Geological Society, London, Special Publications, 478*(1), 217-239.

Jackson, S. E., Pearson, N. J., Griffin, W. L., and Belousova, E. A. (2004). The application of laser ablation-inductively coupled plasma-mass spectrometry to in situ U–Pb zircon geochronology. *Chemical geology*, *211*(1-2), 47-69.

Jochum, K. P., Weis, U., Stoll, B., Kuzmin, D., Yang, Q., Raczek, I., Jacob, D. E., Stracke, A., Birbaum, K., and Frick, D. A. (2011). Determination of reference values for NIST SRM 610–617 glasses following ISO guidelines. *Geostandards and Geoanalytical Research, 35*(4), 397-429.

Janoušek, V., Farrow, C. M., and Erban, V. (2006). Interpretation of whole-rock geochemical data in igneous geochemistry: introducing Geochemical Data Toolkit (GCDkit). *Journal of Petrology*, *47*(6), 1255-1259.

Kelly, E., Carlson, W. D., and Connelly, J. (2011). Implications of garnet resorption for the Lu–Hf garnet geochronometer: an example from the contact aureole of the Makhavinekh Lake Pluton, Labrador. *Journal of metamorphic Geology, 29*(8), 901-916.

Koornneef, J. M., Davies, G. R., Döpp, S. P., Vukmanovic, Z., Nikogosian, I. K., and Mason, P. R. (2009). Nature and timing of multiple metasomatic events in the sub-cratonic lithosphere beneath Labait,

Tanzania. *Lithos, 112*, 896-912.

Kylander-Clark, A., Hacker, B., and Mattinson, J. (2008). Slow exhumation of UHP terranes: titanite and rutile ages of the Western Gneiss Region, Norway. *Earth and Planetary Science Letters, 272*(3-4), 531-540.

Liu, Y., Hu, Z., Zong, K., Gao, C., Gao, S., Xu, J., and Chen, H. (2010). Reappraisement and refinement of zircon U-Pb isotope and trace element analyses by LA-ICP-MS. *Chinese Science Bulletin*, *55*(15), 1535-1546.

Liu, F., Zhang, L., Li, X., Slabunov, A. I., Wei, C., and Bader, T. (2017). The metamorphic evolution of Paleoproterozoic eclogites in Kuru-Vaara, northern Belomorian Province, Russia: Constraints from PT pseudosections and zircon dating. *Precambrian Research, 289*, 31-47.

Locock, A. J. (2014). An Excel spreadsheet to classify chemical analyses of amphiboles following the IMA 2012 recommendations. *Computers and Geosciences, 62*, 1-11.

Loose, D., and Schenk, V. (2018). 2.09 Ga old eclogites in the Eburnian-Transamazonian orogen of southern Cameroon: Significance for Palaeoproterozoic plate tectonics. *Precambrian Research, 304*, 1-11.

Luvizotto, G., Zack, T., Meyer, H., Ludwig, T., Triebold, S., Kronz, A., Münker, C., Stockli, D., Prowatke, S., and Klemme, S. (2009). Rutile crystals as potential trace-element and isotope mineral standards for microanalysis. *Chemical Geology, 261*(3-4), 346-369.

Maboko, M. A. (2000). Nd and Sr isotopic investigation of the Archean–Proterozoic boundary in north eastern Tanzania: constraints on the nature of Neoproterozoic tectonism in the Mozambique Belt. *Precambrian Research, 102*(1-2), 87-98.

Maboko, M. A., and Nakamura, E. (1996). Nd and Sr isotopic mapping of the Archaean-Proterozoic boundary in southeastern Tanzania using granites as probes for crustal growth. *Precambrian Research, 77*(1-2), 105-115.

Maldonado, R., Weber, B., Ortega-Gutiérrez, F., and Solari, L. A. (2018). High-pressure metamorphic evolution of eclogite and associated metapelite from the Chuacús complex (Guatemala Suture Zone): Constraints from phase equilibria modelling coupled with Lu-Hf and U-Pb geochronology. *Journal of metamorphic Geology, 36*(1), 95-124.

Möller, A., Appel, P., Mezger, K., and Schenk, V. (1995). Evidence for a 2 Ga subduction zone: eclogites in the Usagaran belt of Tanzania. *Geology, 23*(12), 1067-1070.

Moore, S., Carlson, W. D., and Hesse, M. A. (2013). Origins of yttrium and rare earth element distributions in metamorphic garnet. *Journal of metamorphic Geology,*

31(6), 663-689.

Mori, K., Tsujimori, T., and Boniface, N. (2018). Finding of talc–and kyanite–bearing amphibolite from the Paleoproterozoic Usagaran Belt, Tanzania. *Journal of Mineralogical and Petrological Sciences, 113*(6), 316-321.

Mruma, A. (1989). *Stratigraphy, Metamorphism and Tectonic Evolution of the Early Proterozoic Usagaran Belt, Tanzania.* (Ph.D), University of Oulu, Finland.

Muhongo, S., Kröner, A., and Nemchin, A. (2001). Single zircon evaporation and SHRIMP ages for granulite-facies rocks in the Mozambique Belt of Tanzania. *The Journal of Geology, 109*(2), 171-189.

Müller, S., Dziggel, A., Sindern, S., Kokfelt, T. F., Gerdes, A., and Kolb, J. (2018). Age and temperature-time evolution of retrogressed eclogite-facies rocks in the Paleoproterozoic Nagssugtoqidian Orogen, South-East Greenland: Constrained from U-Pb dating of zircon, monazite, titanite and rutile. *Precambrian Research, 314*, 468-486.

Otamendi, J. E., de La Rosa, J. D., Douce, A. E. P. o., and Castro, A. (2002). Rayleigh fractionation of heavy rare earths and yttrium during metamorphic garnet growth. *Geology, 30*(2), 159-162.

Paton, C., Hellstrom, J., Paul, B., Woodhead, J., and Hergt, J. (2011). Iolite: Freeware for the visualisation and processing of mass spectrometric data. *Journal of Analytical Atomic Spectrometry, 26*(12), 2508-2518.

Pearce, M., White, A., & Gazley, M. (2015). TC-Investigator: automated calculation of mineral mode and composition contours for thermocalc pseudosections. *Journal of metamorphic Geology*, 33(4), 413-425.

Petersen, K. D., and Buck, W. R. (2015). Eduction, extension, and exhumation of ultrahigh-pressure rocks in metamorphic core complexes due to subduction initiation. *Geochemistry, Geophysics, Geosystems, 16*(8), 2564-2581.

Reddy, S. M., Collins, A. S., and Mruma, A. (2003). Complex high-strain deformation in the Usagaran Orogen, Tanzania: structural setting of Palaeoproterozoic eclogites. *Tectonophysics, 375*(1-4), 101-123.

Ring, U., Kröner, A., and Toulkeridis, T. (1997). Palaeoproterozoic granulite-facies metamorphism and granitoid intrusions in the Ubendian-Usagaran Orogen of northern Malawi, east-central Africa. *Precambrian Research, 85*(1-2), 27-51.

Rubatto, D. (2002). Zircon trace-element geochemistry: partitioning with garnet and the link between U–Pb ages and metamorphism. *Chemical Geology, 184*(1-2), 123-138.

Sizova, E., Gerya, T., and Brown, M. (2014). Contrasting styles of Phanerozoic and Pre-

cambrian continental collision. *Gondwana Research, 25*(2), 522-545.

Skora, S., Baumgartner, L. P., Mahlen, N. J., Johnson, C. M., Pilet, S., and Hellebrand, E. (2006). Diffusion-limited REE uptake by eclogite garnets and its consequences for Lu–Hf and Sm–Nd geochronology. *Contributions to Mineralogy and Petrology, 152*(6), 703-720.

Sláma, J., Košler, J., Condon, D. J., Crowley, J. L., Gerdes, A., Hanchar, J. M., ... and Schaltegger, U. (2008). Plešovice zircon—a new natural reference material for U–Pb and Hf isotopic microanalysis. *Chemical Geology*, *249*(1-2), 1-35.

Sommer, H., Kröner, A., Hauzenberger, C., and Muhongo, S. (2005). Reworking of Archaean and Palaeoproterozoic crust in the Mozambique belt of central Tanzania as documented by SHRIMP zircon geochronology. *Journal of African Earth Sciences, 43*(4), 447-463.

Sommer, H., Kröner, A., Muhongo, S., and Hauzenberger, C. (2005). SHRIMP zircon ages for post-Usagaran granitoid and rhyolitic rocks from the Palaeoproterozoic terrain of southwestern Tanzania. *South African Journal of Geology, 108*(2), 247-256.

Spandler, C., Hammerli, J., Sha, P., Hilbert-Wolf, H., Hu, Y., Roberts, E., and Schmitz, M. (2016). MKED1: a new titanite standard for in situ analysis of Sm–Nd isotopes and U–Pb geochronology. *Chemical Geology, 425*, 110-126.

Spear, F. (2014). The duration of near-peak metamorphism from diffusion modelling of garnet zoning. *Journal of metamorphic Geology, 32*(8), 903-914.

Stern, R. A., Bodorkos, S., Kamo, S. L., Hickman, A. H., and Corfu, F. (2009). Measurement of SIMS instrumental mass fractionation of Pb isotopes during zircon dating. *Geostandards and Geoanalytical Research*, *33*(2), 145-168.

Tomkins, H., Powell, R., and Ellis, D. (2007). The pressure dependence of the zirconium-in-rutile thermometer. *Journal of metamorphic Geology, 25*(6), 703-713.

Vermeesch, P. (2018). IsoplotR: a free and open toolbox for geochronology. *Geoscience Frontiers, 9*(5), 1479-1493.

Volkova, N. I., Kovyazin, S. V., Stupakov, S. I., Simonov, V. A., & Sakiev, K. S. (2014). Trace element distribution in mineral inclusions in zoned garnets from eclogites of the atbashi range (south tianshan). *Geochemistry International*, 52(11), 939-961.

Vry, J. K., and Baker, J. A. (2006). LA-MC-ICPMS Pb–Pb dating of rutile from slowly cooled granulites: confirmation of the high closure temperature for Pb diffusion in rutile. *Geochimica et Cosmochimica Acta, 70*(7), 1807-1820.

Walsh, E. O., & Hacker, B. R. (2004). The fate of subducted continental margins: Two-stage exhumation of the high-pressure to ultrahigh-pressure western gneiss region, norway. Journal of Metamorphic Geology, 22(7), 671-687.

Watson, E., Wark, D., and Thomas, J. (2006). Crystallization thermometers for zircon and rutile. *Contributions to Mineralogy and Petrology, 151*(4), 413.

Weller, O., and St-Onge, M. (2017). Record of modern-style plate tectonics in the Palaeoproterozoic Trans-Hudson orogen. *Nature Geoscience, 10*(4), 305-311.

Wiedenbeck, M. A. P. C., Alle, P., Corfu, F., Griffin, W. L., Meier, M., Oberli, F. V., ... and Spiegel, W. (1995). Three natural zircon standards for U-Th-Pb, Lu-Hf, trace-element and REE analyses. *Geostandards newsletter*, *19*(1), 1-23.

Xu, C., Kynický, J., Song, W., Tao, R., Lü, Z., Li, Y., ... and Fei, Y. (2018). Cold deep subduction recorded by remnants of a Paleoproterozoic carbonated slab. *Nature communications*, *9*(1), 1-8.

Yang, J.-J., and Enami, M. (2003). Chromian dissakisite-(Ce) in a garnet lherzolite from the Chinese Su-Lu UHP metamorphic terrane: Implications for Cr incorporation in epidote-group minerals and recycling of REE into the Earth's mantle. *American Mineralogist, 88*(4), 604-610.

Yang, P., and Rivers, T. (2001). Chromium and manganese zoning in pelitic garnet and kyanite: Spiral, overprint, and oscillatory (?) zoning patterns and the role of growth rate. *Journal of metamorphic Geology, 19*(4), 455-474.

Yu, H., Zhang, L., Lanari, P., Rubatto, D., and Li, X. (2019). Garnet LuHf geochronology and PT path of the Gridino-type eclogite in the Belomorian Province, Russia. *Lithos, 326*, 313-326.

Zack, T., Stockli, D. F., Luvizotto, G. L., Barth, M. G., Belousova, E., Wolfe, M. R., and Hinton, R. W. (2011). In situ U–Pb rutile dating by LA-ICP-MS: 208 Pb correction and prospects for geological applications. *Contributions to Mineralogy and Petrology, 162*(3), 515-530.

Chapter 6:

Mantle heating at ca. 2 Ga driven by crustal growth: evidence from granites and eclogites

This chapter is in review as:

Mantle heating at ca. 2 Ga driven by crustal growth: Evidence from granites and eclogites (in review). R. Tamblyn, D. Hasterok, M. Hand, M. Gard. *Geology*

The supplementary materials for this chapter can be found in Appendix 6

Statement of Authorship

Title of Paper	Mantle heating at ca. 2 Ga driven by crustal growth: evidence from granites and eclogites
Publication Status	☐ Published ☐ Accepted for Publication ☒ Submitted for Publication ☐ Unpublished and Unsubmitted w ork w ritten in manuscript style
Publication Details	In review with Geology as: Tamblyn, R., Hasterok, D., Hand, M., and Gard, M. Mantle heating at ca. 2 Ga driven by crustal growth: evidence from granites and eclogites

Principal Author

Name of Principal Author (Candidate)	Renée Tamblyn		
Contribution to the Paper	Completed the mineral equilibria modelling Interpreted the data Wrote the manuscript		
Overall percentage (%)	65%		
Certification:	This paper reports on original research I conducted during the period of my Higher Degree by Research candidature and is not subject to any obligations or contractual agreements with a third party that would constrain its inclusion in this thesis. I am the primary author of this paper.		
Signature		Date	04/03/2021

Co-Author Contributions

By signing the Statement of Authorship, each author certifies that:

i. the candidate's stated contribution to the publication is accurate (as detailed above);

ii. permission is granted for the candidate in include the publication in the thesis; and

iii. the sum of all co-author contributions is equal to 100% less the candidate's stated contribution.

Name of Co-Author	Derrick Hasterok		
Contribution to the Paper	Compiled the database Completed the database analysis Interpreted the data Reviewed the manuscript		20%
Signature		Date	18/02/2021

Name of Co-Author	Martin Hand		
Contribution to the Paper	Interpreted the data Reviewed the manuscript		10%
Signature		Date	03/03/2021

Please cut and paste additional co-author panels here as required.

Name of Co-Author	Matthew Gard			
Contribution to the Paper	Compiled the database			5%
Signature			Date	15/02/2021

Highlights

- The emergence of eclogites is linked to a global change in granite chemistry at ca. 2 Ga.
- Warming of the mantle by continental insulation is suggested as the trigger for these changes.
- In the past, eclogite preservation and mantle temperature were sensitive to changes in the spatial extent and distribution of continental crust on Earth.

Abstract

The thermal state of the Earth is recorded in the mineralogical and geochemical record of thermally-driven processes. The generally accepted thermal budget of the mantle indicates a steady cooling trend from ca. 3 Ga to present. The geological record, however, indicates this simple cooling model may not hold true. Subduction-related eclogites substantially emerge in the rock record from 2.1–1.8 Ga, indicating mantle thermal conditions cooled below a critical threshold for widespread eclogite preservation. Following this brief period, eclogite disappeared again until ca. 1.1 Ga. Coincident with the transient emergence of eclogite, global granite chemistry recorded a decrease in Sr and Eu and increases Y and HREE concentrations. These changes are most simply explained by warming of the thermal regime associated with granite genesis. We suggest warming was caused by increased continental insulation of the mantle, driven by an acceleration of crustal growth between 2 to 1.8 Ga, which inhibited continued preservation of eclogite in the geological record. Ultimately, secular cooling of the mantle overcame insulation, allowing the second emergence and widespread preservation of eclogite from ca. 1.1 Ga until present.

Introduction

Investigating the record of igneous and metamorphic rocks allow us to understand the thermal regimes effective on Earth through time. For example, subduction-related metamorphism has long been used to probe the secular change in the thermal state of the mantle (Brown and Johnson, 2018; Brown et al., 2020b; Holder et al., 2019). Subduction-related eclogites unambiguously emerged in the geological record in the Palaeoproterozoic (ca. 2.1–1.8 Ga; Fig. 1a), leading to the conclusion that modern-style subduction along cool thermal gradients was operating on Earth by this time (Brown and Johnson, 2018; Brown et al., 2020a; Brown et al., 2020b; Holder et al., 2019). The paucity of eclogites in the record before ca. 2.1 Ga has been explained by two arguments: (1) The mantle was too warm to allow eclogite-facies mineral assemblages to form during subduction, or (2) Eclogites formed throughout history, but were exhumed and reworked, or lost to the mantle, and therefore not preserved. However, if the mantle has cooled

since the Neoarchean (Condie et al., 2016; Ganne and Feng, 2017; Herzberg et al., 2010), these arguments do not explain the lack of eclogites in the geological record from ca. 1.8 to 1.1 Ga (Fig. 1b).

While metamorphic rocks record their formative pressure-temperature (*P–T*) conditions in their mineralogy, igneous rocks record their formative *P–T* conditions in their trace element geochemistry. Concentrations of Sr, Eu, Y and heavy rare earth elements (HREEs) in igneous systems are controlled by the stability of plagioclase, garnet and hornblende, whose stability is depth and temperature dependant, allowing geochemists to investigate the crustal thickness and thermal regime associated with magmatism (Chapman et al., 2015; Ducea et al., 2015; Lieu and Stern, 2019; Profeta et al., 2015). By combining this geochemical understanding with large geochemical databases across the history of the Earth (Gard et al., 2019; Hasterok et al., 2019), secular variations in chemistry can be explored.

Methods

Geochemical analyses and filtering

The geochemical database by Gard et al. (Gard et al., 2019) used in this study is a whole-rock database of major and trace elements and age. For normalization of Eu* and Sr* and the trace element compatibility diagram (Supp. Fig. 1) we use NMORB by Gale et al. (Gale et al., 2013). For full database analysis see Supplementary File 1.

Mineral equilibria forward modelling

An average basaltic composition was calculated from the global dataset of continental basalts (n = 3581), using only basalts with measured Fe^{2+}/Fe^{3+} ratios. The average LOI was used as the H_2O content. This composition was modelled using the code THERMOCALC (v. 345i), using the internally consistent thermodynamic dataset ds62 (Holland and Powell, 2011) and mafic activity-composition models (Green et al., 2016), in the model chemical system NCKFMASHTO. The composition and full model are in Supplementary Fig. 4.

Province age-area analysis

A set of geological province polygons by Hasterok et al. (in prep) were used for the age-area analysis. For full methods see Supplementary File 1.

The P–T sensitive geochemistry of granites

For the majority of crustal magmatic systems, Sr and Eu behaviour is controlled by plagioclase, and Y and HREEs are controlled by garnet and/or amphibole (Chapman et al., 2015; Davidson et al., 2007; Ducea et al., 2015; Lieu and Stern, 2019; Profeta et al., 2015). A negative Sr and Eu anom-

aly (<1) indicates formation of plagioclase, either by crystal fractionation or its stability in the magmatic source, removing Sr and Eu from the melt. Depletions in Y and HREEs indicates production of melt in the garnet stability field, where Y and HREEs are strongly fractionated into garnet (Chapman et al., 2015; Ducea et al., 2015) (Fig. 1). A coeval decrease in the Gd/Y ratio suggests that a depletion in Y and HREE is driven by garnet rather than hornblende, as garnet fractionates more Y than Gd, but hornblende prefers Gd over Y (Nandedkar et al., 2016). Across a broad range of igneous rock compositions, the stability of these minerals is controlled primarily by pressure and temperature (Ducea et al., 2015). Therefore, Sr/Y or Sr/HREE ratios and Sr and Eu anomalies encode the *P–T* conditions of granite genesis (Chapman et al., 2015; Ducea et al., 2015; Lee and Anderson, 2015; Lee et al., 2006; Lieu and Stern, 2019; Profeta et al., 2015). We recognise the complexity of magma generation processes means Sr, Eu, Y and HREE concentrations are not always simple functions of plagioclase verse garnet stability. Nonetheless, in large datasets, statistically-recognised variations in granite compositions are likely to reflect first-order changes in granite genesis.

Compositions of granites *sensu stricto* were extracted from the geochemical database of Gard et al. (Gard et al., 2019) (Supp. Fig. 1), using the TAS classification of granite (n = 29931; Supp. Fig. 2). We make the assumption that a large portion of this record was formed in continental arcs. When plotted by age (Fig. 1), it is evident there are long-term compositional changes in granite chemistry separated by step changes at the scales of the age-binning. These step changes are identified by Pettitt's tests with statistically significant P-values of 0.0016–0.0018 (Fig. 1c-f). There is an overall step decrease in the Sr/Y and Sr/HREE ratio of granites at 2 Ga (Fig. 1c,d). Coincident with these changes are associated steps to more negative Eu and Sr anomalies (Fig. 1d) and a step increase in Y and HREE concentrations at ca. 2 Ga (Fig. 1e). Therefore, the step decrease in Sr/Y ratios of granite is controlled by an overall depletion in Sr and an enrichment in Y. There is a step decrease in Gd/Y ratio at ca. 1.8 Ga, possibly coeval with the ca. 2 Ga changes within the uncertainty of the age binning (Fig. 1f). There are general long-term trends of Y and HREE enrichment and more subtle Sr and Eu depletion in granites over time, resulting in an overall Sr/Y or Sr/HREE decrease from 4 Ga until present (Fig 1). The corresponding basaltic record (Supp. Fig. 3; n = 24940) shows no step changes in Sr, Eu, Y or HREEs at 2 Ga, indicating the changes in the granite record are not a function of change in basalt compositions in arcs. Therefore, the formation of average granite shifted from source regions with significant amount of garnet to source regions dominated by plagioclase at ca. 2 Ga.

A difficulty in interpreting the *P–T* conditions

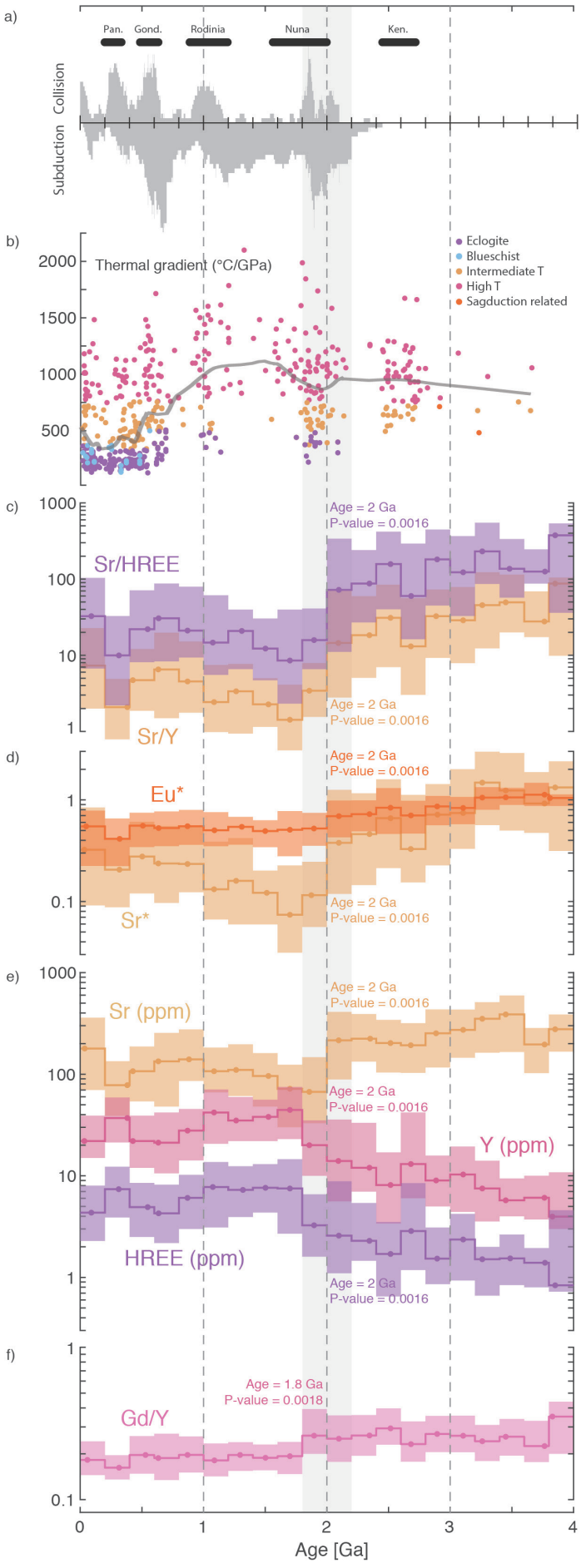


Figure 1: Comparison of selected records over the past 4 Ga. Grey bar indicates the widespread emergence of eclogites in the geological record. a) Periods of collision and subduction after Condie and Aster (Condie and Aster, 2010). b) The thermal gradients of metamorphic rocks, updated from Brown and Johnson (Brown and Johnson, 2018). The grey line indicates the LOWESS curve of Brown et al. (Brown et al., 2020a). c-f) Chemical trends in granites. The heavy centre line represents the median value, and the transparent field the interquartile range (25th to 75th quantiles). The point shows the median age of each 0.2 Ga bin. The age and P-value of the change points identified by Pettitt's tests are noted for each series.

of plagioclase and garnet stability is they can reflect two non-independent parameters. Usually, the thickness of the crust (or P) is thought to be the dominant control on plagioclase verses garnet stability (Chapman et al., 2015; Ducea et al., 2015; Lieu and Stern, 2019; Profeta et al., 2015). However, the thermal gradient in the crust (or T/P) also strongly controls plagioclase and garnet stability. This control is illustrated in a simplified mineral equilibria forward model in Fig. 2a, showing plagioclase and garnet stability above the solidus in a basaltic composition, calculated as the average of continental basalts in the geochemical dataset (*n* = 3581, for full model see Supp. Fig. 4). A basaltic composition is chosen to represent the deep crust, from which granites are generated (Ducea et al., 2015; Lee and Anderson, 2015; Lee et al., 2006). Along a cooler thermal gradient (e.g. < 900 °C/GPa), garnet is stabilised at ~ 0.8 GPa and above. However, along warmer thermal gradients (e.g. >1150 °C/GPa), garnet is not stabilised at all, regardless of the pressures reached (Fig. 2a). Therefore, melt in a basaltic system at cooler conditions of 950 °C at ~ 35 km deep in the crust should have a higher Sr/Y ratio compared to melt at warmer conditions at the same depth (Fig. 2b). While the above is only for one composition, the stability field of garnet above the solidus is similar across many compositions. Therefore, thermal gradient, as well as crustal thickness, is important in determining the Sr/Y ratios of granites (Fig. 2c,d).

The simplest, global control on the thermal gradient experienced by melts produced in the crust is the mantle temperature (Lenardic and Kaula, 1995). While a significant decrease in the depth of granite generation could also control the decrease in Sr/Y ratios, it is difficult to envisage a global-scale and on-going process that would lead to such a radical step change in arc thickness. Therefore, we suggest the mantle experienced a large-scale heating event, beginning at ca. 2–1.8 Ga.

Thermal insulation of the mantle by continental crust

The areal extent of continental crust, its thickness and distribution thermally insulate the mantle on a large scale (Coltice et al., 2009; Cooper et al., 2006; Lenardic et al., 2011). To explain mantle heating at ca. 2–1.8 Ga, we suggest there was a significant increase in the amount of continental crust. This growth is demonstrated by the ages and distributions of preserved igneous rocks (Gard et al., 2019; Puetz et al., 2018)(Fig. 3). By viewing the age spectra of igneous crystallization ages for a set of continental geologic provinces, we can estimate the creation age of crust in each province as the oldest significant age peak. Notably, the oldest significant age peak is most often the maximum probability peak in each province (Fig. 3b), suggesting the highest volume of magmatic activity occurred during the creation of the province. Additionally, metamorphic ages rarely

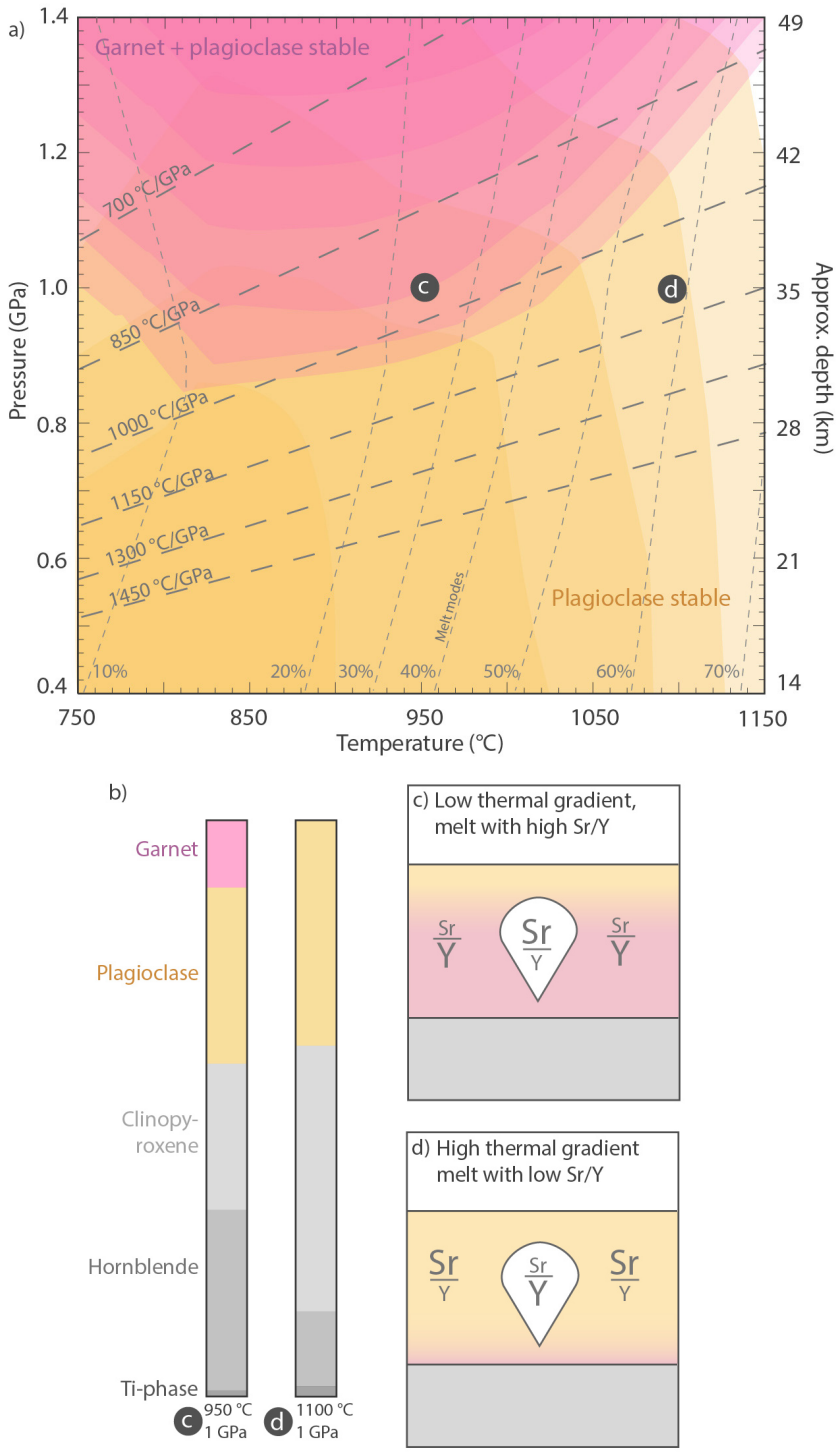


Figure 2: Plagioclase and garnet stability during granite genesis and the origin of Sr/Y changes. a) Simplified mineral equilibria model for an average basaltic composition. Modelled garnet and plagioclase stability fields and abundances are shown in pink and orange respectively, with each transparency interval representing a 5 % increase in modal abundance. Lettered circles correspond to hypothetical crustal P–T scenarios in (c,d). b) Examples of modal abundances of solid phases at two temperatures at the same depth. c,d) Schematic cross-sections showing melting in crustal scenarios.

exceed the oldest igneous dates in each province, supporting this interpretation. When combined with information about the currently preserved size of that province, the rate of generation of new crust through time can be estimated (Fig. 3c). We acknowledge the size of the province and the crystallisation ages recorded within it are only what is currently preserved at the surface and does not incorporate crust lost from the geological record (Condie, 2014). Nonetheless, it is evident that from ca. 2–1.8 Ga there was an increased period of igneous rock production (Fig. 3a,b), which we interpret as an increase in the rate of crustal generation (Fig. 3c). Approximately 8% of currently preserved continental crust may have been created in this time period (Fig. 3). A major pulse of new juvenile crust generation between 2–1.8 Ga was previously identified from Nd isotopes of igneous rocks and Hf isotopes of detrital zircons (Condie and Aster, 2010; Condie et al., 2005; Kemp et al., 2006). This pulse corresponds to a significant peak in detrital zircon U–Pb ages, suggesting a period of increased magmatism (Belousova et al., 2010). As such, we suggest an increase in the areal extent of continental crust between ca. 2–1.8 Ga was the likely source of increased mantle insulation. Another way to thermally insulate the mantle is underneath an aggregated supercontinent (Brandl et al., 2013; Lenardic et al., 2011). Therefore, we suggest the progressive amalgamation of the supercontinent Nuna acted to further insulate the mantle (Brandl et al., 2013; Brown and Johnson, 2018; Brown et al., 2020b; Lenardic et al., 2011).

The proposed mantle heating event between ca. 2–1.8 Ga correlates well with the overall *P–T* trend of metamorphic rocks in the geological record, which indicate warmer thermal gradients in the continental crust from ca. 1.8–1.1 Ga (Brown et al., 2020b) (Fig. 1b). However, the suggestion of a global mantle heating event at ca. 2–1.8 Ga is at odds with current models of mantle temperature evolution through time (Condie et al., 2016; Ganne and Feng, 2017; Herzberg et al., 2010). These estimates are derived from the composition of primary mantle melts throughout Earth's history. However, the data are sparse, particularly between 2–1.5 Ga, and temperature estimates are highly dependent on assumed source redox and sample filtering (Condie et al., 2016; Ganne and Feng, 2017; Herzberg et al., 2010). We suggest that a departure at ca. 2 Ga from a general mantle cooling trend is probably within error of the scarce number of temperature estimates or impossible to constrain within the current mantle temperature models.

Preservation of subduction-related eclogites

Subduction-related eclogites globally emerge in the geological record from 2.1–1.8 Ga and disappear until 1.1 Ga (Brown and Johnson, 2018; Brown et al., 2020a; Brown et al., 2020b; Holder et al., 2019). We suggest that warming of the mantle,

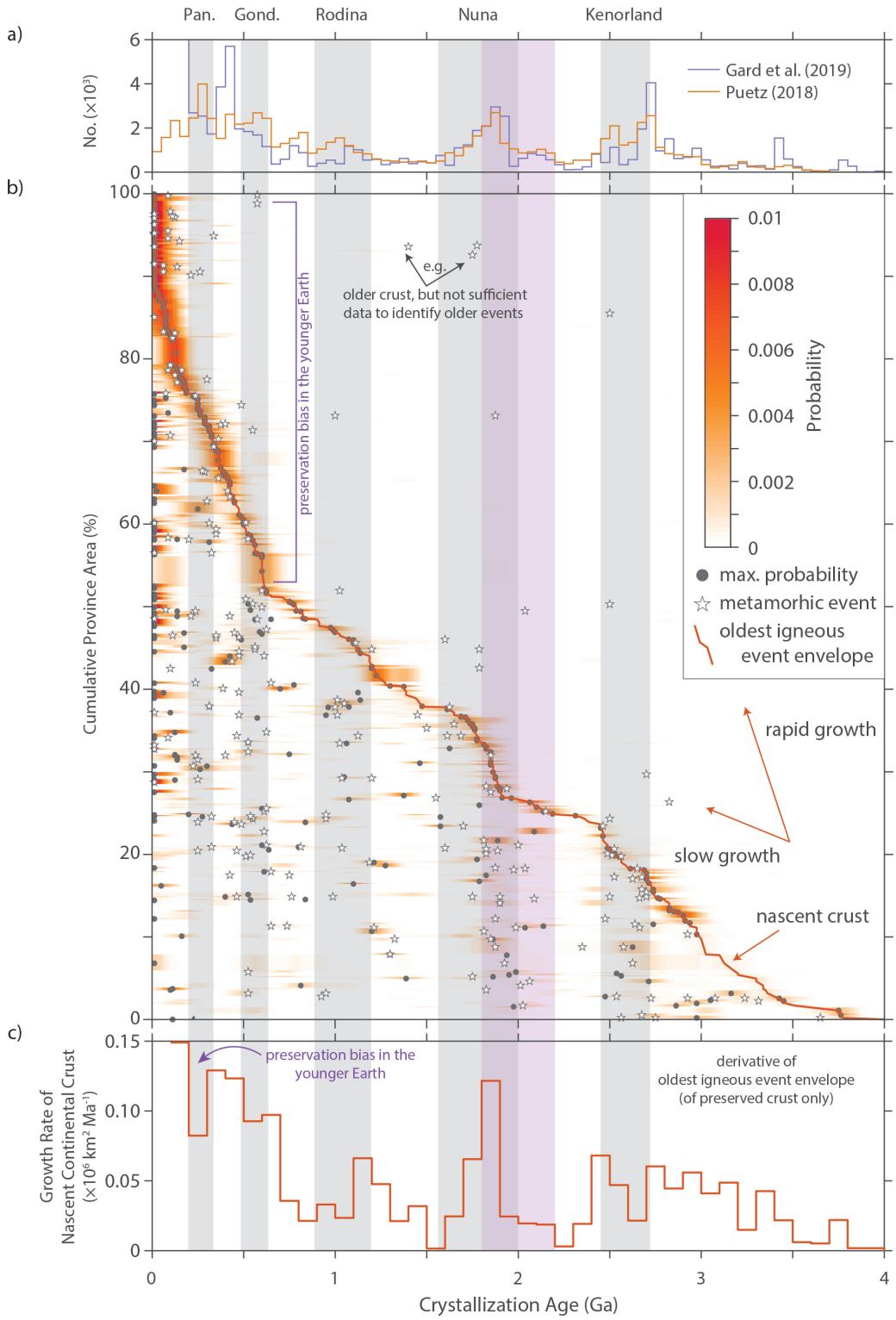


Figure 3: A 4 Ga record of crustal growth. a) Global crystallization age spectra for igneous protoliths within the global geochemical database (Gard et al., 2019) and the global zircon U–Pb age database (Puetz et al., 2018). b) Cumulative area and crystallization age spectra of igneous rocks for a global set of geologic provinces. The area of each province is signified by the y-axis width of the age spectra bands. The oldest peak of each province is often the maximum probability peak and may identify the formation of nascent crust. There are 467 provinces with sufficient geochronologic data used for this model, which accounts for 66.4% of the total continental area. For full list of provinces see Supp. File 2. c) Calculated growth rate of currently preserved continental crust through time.

driven by continental insulation, prohibited the preservation of eclogites in the geological record from 1.8–1.1 Ga. Sizova et al. (Sizova et al., 2010) demonstrate that a potential mantle temperature of at least ~180 °C above present temperatures can significantly reduce the strength of the downgoing oceanic plate. In turn, the plate is not able to sustain the stresses arising from deep subduction, and a subduction channel reaching high-pressure conditions cannot form (Sizova et al., 2010). Thus, the proposed mantle insulation event would have needed to increase mantle temperatures by at least 180 °C at ca. 2 Ga to prevent exhumation of eclogite, depending upon the model considered for mantle temperature through time. As such, we suggest the mantle was heated to at least 180 °C above present day values. Models for continental insulation vary, however ~180 °C of mantle heating is easily attainable by increasing continental coverage by around 12–15 % (Coltice et al., 2009; Lenardic et al., 2011), close to our estimations of crustal growth between 2–1.8 Ga (Fig. 3). By ca. 1.1 Ga, overall cooling of the mantle finally overcame the continental insulation effect, reviving preservation of subduction-related eclogites. High-pressure low-temperature rocks then persisted in the geological record until present day.

The balance of crustal growth and mantle temperature

Did growth of new continental crust drive other mantle heating events in Earth's history? Estimates for rates of continental crustal growth over Earth's history are varied. However, a key feature shared across the different models is that at ca. 1 Ga, at least 50–80 % of the present-day continental crust was present on Earth (Belousova et al., 2010; Condie and Aster, 2010; Dhuime et al., 2012; Pujol et al., 2013). Therefore, in the last billion years there may not have been significant contributions of continental crust which could further insulate the mantle to the point of making eclogite preservation unlikely (Cawood and Hawkesworth, 2019). In Earth's earlier history, mantle temperature and the preservation of eclogites in the geological record existed in a delicate balance, sensitive to changes in continental crustal growth and consequent mantle heating.

Acknowledgements

The authors thank Laura Morrissey, Carl Spandler and Lucy McGee for discussions which greatly improved the manuscript. R.T. acknowledges the University of Adelaide for a postgraduate research scholarship. D.H. and M.H. acknowledge ARC DP DP180104074.

References

Belousova, E., Kostitsyn, Y., Griffin, W. L., Begg, G. C., O'Reilly, S. Y., and Pearson, N. J., 2010, The growth of the continental crust:

constraints from zircon Hf-isotope data: Lithos, v. 119, no. 3-4, p. 457-466.

Brandl, P. A., Regelous, M., Beier, C., and Haase, K. M., 2013, High mantle temperatures following rifting caused by continental insulation: Nature Geoscience, v. 6, no. 5, p. 391-394.

Brown, M., and Johnson, T., 2018, Secular change in metamorphism and the onset of global plate tectonics: American Mineralogist, v. 103, no. 2, p. 181-196.

Brown, M., Johnson, T., and Gardiner, N. J., 2020a, Plate tectonics and the Archean Earth: Annual Review of Earth and Planetary Sciences, v. 48.

Brown, M., Kirkland, C., and Johnson, T., 2020b, Evolution of geodynamics since the Archean: Significant change at the dawn of the Phanerozoic: Geology, v. 48, no. 5, p. 488-492.

Cawood, P. A., and Hawkesworth, C. J., 2019, Continental crustal volume, thickness and area, and their geodynamic implications: Gondwana Research, v. 66, p. 116-125.

Chapman, J. B., Ducea, M. N., DeCelles, P. G., and Profeta, L., 2015, Tracking changes in crustal thickness during orogenic evolution with Sr/Y: An example from the North American Cordillera: Geology, v. 43, no. 10, p. 919-922.

Coltice, N., Bertrand, H., Rey, P., Jourdan, F., Phillips, B. R., and Ricard, Y., 2009, Global warming of the mantle beneath continents back to the Archaean: Gondwana Research, v. 15, no. 3-4, p. 254-266.

Condie, K., 2014, Growth of continental crust: a balance between preservation and recycling: Mineralogical Magazine, v. 78, no. 3, p. 623-637.

Condie, K. C., and Aster, R. C., 2010, Episodic zircon age spectra of orogenic granitoids: the supercontinent connection and continental growth: Precambrian Research, v. 180, no. 3-4, p. 227-236.

Condie, K. C., Aster, R. C., and Van Hunen, J., 2016, A great thermal divergence in the mantle beginning 2.5 Ga: Geochemical constraints from greenstone basalts and komatiites: Geoscience Frontiers, v. 7, no. 4, p. 543-553.

Condie, K. C., Beyer, E., Belousova, E., Griffin, W., and O'Reilly, S. Y., 2005, U–Pb isotopic ages and Hf isotopic composition of single zircons: the search for juvenile Precambrian continental crust: Precambrian Research, v. 139, no. 1-2, p. 42-100.

Cooper, C. M., Lenardic, A., and Moresi, L., 2006, Effects of continental insulation and the partitioning of heat producing elements on the Earth's heat loss: Geophysical Research Letters, v. 33, no. 13.

Davidson, J., Turner, S., Handley, H., Macpherson, C., and Dosseto, A., 2007, Amphibole "sponge" in arc crust?: Geology, v. 35, no.

9, p. 787-790.

Dhuime, B., Hawkesworth, C. J., Cawood, P. A., and Storey, C. D., 2012, A change in the geodynamics of continental growth 3 billion years ago: Science, v. 335, no. 6074, p. 1334-1336.

Ducea, M. N., Saleeby, J. B., and Bergantz, G., 2015, The architecture, chemistry, and evolution of continental magmatic arcs: Annual Review of Earth and Planetary Sciences, v. 43, p. 299-331.

Gale, A., Dalton, C. A., Langmuir, C. H., Su, Y., and Schilling, J. G., 2013, The mean composition of ocean ridge basalts: Geochemistry, Geophysics, Geosystems, v. 14, no. 3, p. 489-518.

Ganne, J., and Feng, X., 2017, Primary magmas and mantle temperatures through time: Geochemistry, Geophysics, Geosystems, v. 18, no. 3, p. 872-888.

Gard, M., Hasterok, D., and Halpin, J. A., 2019, Global whole-rock geochemical database compilation.

Green, E., White, R., Diener, J., Powell, R., Holland, T., and Palin, R., 2016, Activity–composition relations for the calculation of partial melting equilibria in metabasic rocks: Journal of Metamorphic Geology, v. 34, no. 9, p. 845-869.

Hasterok, D., Gard, M., Cox, G., and Hand, M., 2019, A 4 Ga record of granitic heat production: Implications for geodynamic evolution and crustal composition of the early Earth: Precambrian Research, v. 331, p. 105375.

Herzberg, C., Condie, K., and Korenaga, J., 2010, Thermal history of the Earth and its petrological expression: Earth and Planetary Science Letters, v. 292, no. 1-2, p. 79-88.

Holder, R. M., Viete, D. R., Brown, M., and Johnson, T. E., 2019, Metamorphism and the evolution of plate tectonics: Nature, v. 572, no. 7769, p. 378-381.

Holland, T., and Powell, R., 2011, An improved and extended internally consistent thermodynamic dataset for phases of petrological interest, involving a new equation of state for solids: Journal of Metamorphic Geology, v. 29, no. 3, p. 333-383.

Kemp, A., Hawkesworth, C., Paterson, B., and Kinny, P., 2006, Episodic growth of the Gondwana supercontinent from hafnium and oxygen isotopes in zircon: Nature, v. 439, no. 7076, p. 580-583.

Lee, C.-T. A., and Anderson, D. L., 2015, Continental crust formation at arcs, the arclogite "delamination" cycle, and one origin for fertile melting anomalies in the mantle: Science Bulletin, v. 60, no. 13, p. 1141-1156.

Lee, C.-T. A., Cheng, X., and Horodyskyj, U., 2006, The development and refinement of continental arcs by primary basaltic magmatism, garnet pyroxenite accumulation, ba-

saltic recharge and delamination: insights from the Sierra Nevada, California: Contributions to Mineralogy and Petrology, v. 151, no. 2, p. 222-242.

Lenardic, A., and Kaula, W., 1995, Mantle dynamics and the heat flow into the Earth's continents: Nature, v. 378, no. 6558, p. 709-711.

Lenardic, A., Moresi, L., Jellinek, A., O'neill, C., Cooper, C., and Lee, C., 2011, Continents, supercontinents, mantle thermal mixing, and mantle thermal isolation: Theory, numerical simulations, and laboratory experiments: Geochemistry, Geophysics, Geosystems, v. 12, no. 10.

Lieu, W. K., and Stern, R. J., 2019, The robustness of Sr/Y and La/Yb as proxies for crust thickness in modern arcs: Geosphere, v. 15, no. 3, p. 621-641.

Nandedkar, R. H., Hürlimann, N., Ulmer, P., and Müntener, O., 2016, Amphibole–melt trace element partitioning of fractionating calc-alkaline magmas in the lower crust: an experimental study: Contributions to Mineralogy and Petrology, v. 171, no. 8-9, p. 71.

Profeta, L., Ducea, M. N., Chapman, J. B., Paterson, S. R., Gonzales, S. M. H., Kirsch, M., Petrescu, L., and DeCelles, P. G., 2015, Quantifying crustal thickness over time in magmatic arcs: Scientific reports, v. 5, p. 17786.

Puetz, S. J., Ganade, C. E., Zimmermann, U., and Borchardt, G., 2018, Statistical analyses of global U-Pb database 2017: Geoscience Frontiers, v. 9, no. 1, p. 121-145.

Pujol, M., Marty, B., Burgess, R., Turner, G., and Philippot, P., 2013, Argon isotopic composition of Archaean atmosphere probes early Earth geodynamics: Nature, v. 498, no. 7452, p. 87-90.

Sizova, E., Gerya, T., Brown, M., and Perchuk, L., 2010, Subduction styles in the Precambrian: insight from numerical experiments: Lithos, v. 116, no. 3-4, p. 209-229.

Chapter 7:
Discussion and conclusions

1. Discussion and conclusions

The studies contained in this thesis have examined the *P–T–t* histories of eclogites and blueschists from different stages throughout the evolution of modern-style subduction on Earth. As outlined in Chapter 1, this thesis set out to unravel the complex behaviour of HP–LT rocks in the subduction channel, including the timescales of subduction, accumulation and exhumation, using multi-method geochronology and mineral equilibria modelling. This thesis also endeavours to investigate the emergence of eclogites on Earth and their distribution in the geological record, by tying the metamorphic record to other time-integrated datasets. The findings have implications for: i) the durations that material can stay entrapped within subduction zones; and ii) the distribution of eclogites in the geological record, which exist in a sensitive balance with the thermal state of the mantle.

1.2 Complex behaviour of HP–LT rocks in the subduction channel

A primary finding of the studies in this thesis is that HP–LT rocks can experience long-lived and complex *P–T–t* evolutions while inside the subduction channel, supporting predictions from numerical models of subduction systems (e.g. Gerya et al., 2002; Ruh et al., 2015). The low viscosity and high buoyancy of serpentinite, cycled by the continuously subducting slab, allows for effective entrapment and exhumation of eclogite and blueschist facies rocks from the oceanic crust (e.g. Gerya et al., 2002). The timeframes of this process may be long, with HP–LT rocks from the Mariana Trench and Port Macquarie residing within the subduction channel for at least ca. 50 My. Furthermore, over such timescales subduction systems tend to migrate, especially during slab rollback (e.g. Baitsch-Ghiradello et al., 2012). Therefore, trapped HP–LT rocks can be laterally relocated thousands of kilometers and exhumed into younger orogens associated with the migrating subduction system. Chapter 3 gives an example of this at Port Macquarie, where Cambrian–Ordovician HP–LT rocks were exhumed in a Permian-Triassic orogen. An additional finding in Chapter 4 is that during this entrapment, rocks can experience multiple burial cycles (Fig. 1). An interesting note to this is that even during multiple retrogression events, pristine lawsonite crystals can be preserved (e.g. Port Macquarie eclogite), due to the extremely cool conditions that are maintained by on-going subduction (Fig. 1). Therefore, rapid exhumation is not necessary for the preservation of lawsonite (e.g., Tsujimori et al., 2006). The mineralogical record of multiple burial cycles may be cryptic, but can be unravelled with detailed petrology and modern geochronological methods. As petrochronological methods continue to improve, complex cycling of subducted materials may become routinely recognised, which in turn may complement predictions from

numerical modelling (e.g. Gerya et al., 2002; Yamato et al., 2007; Ruh et al., 2015). Moreover, studies on HP–LT rocks must take into account that these lithologies may have been subducted significantly earlier than the geology that they currently reside within, and that subduction channels have the capacity to entrap and accumulate HP–LT rocks with diverse *P*–*T*–*t* histories.

1.3 The emergence of modern-style subduction in the Earth

Subduction is suggested to have been operating on Earth as early as the Archean (Turner et al., 2014; Kusky et al., 2018), but the exact style of tectonism and the thermal gradients involved are unknown. Modern-style subduction is referred to in this thesis as 'rigid-lid', one-sided subduction. Numerical modelling suggests subduction systems could form in the Earth in the Palaeo- and Mesoarchean (Sizova et al., 2014; Fischer and Gerya, 2016; Brown et al., 2020). Evidence of early subduction derived from the presence of arc magmatism in the geological record, which is interpreted from their chemistry, is controversial (e.g. Moyan and Laurent, 2018, and references within). Additionally, this possible geochemical evidence of arc magmatism may be considered indirect, as igne-

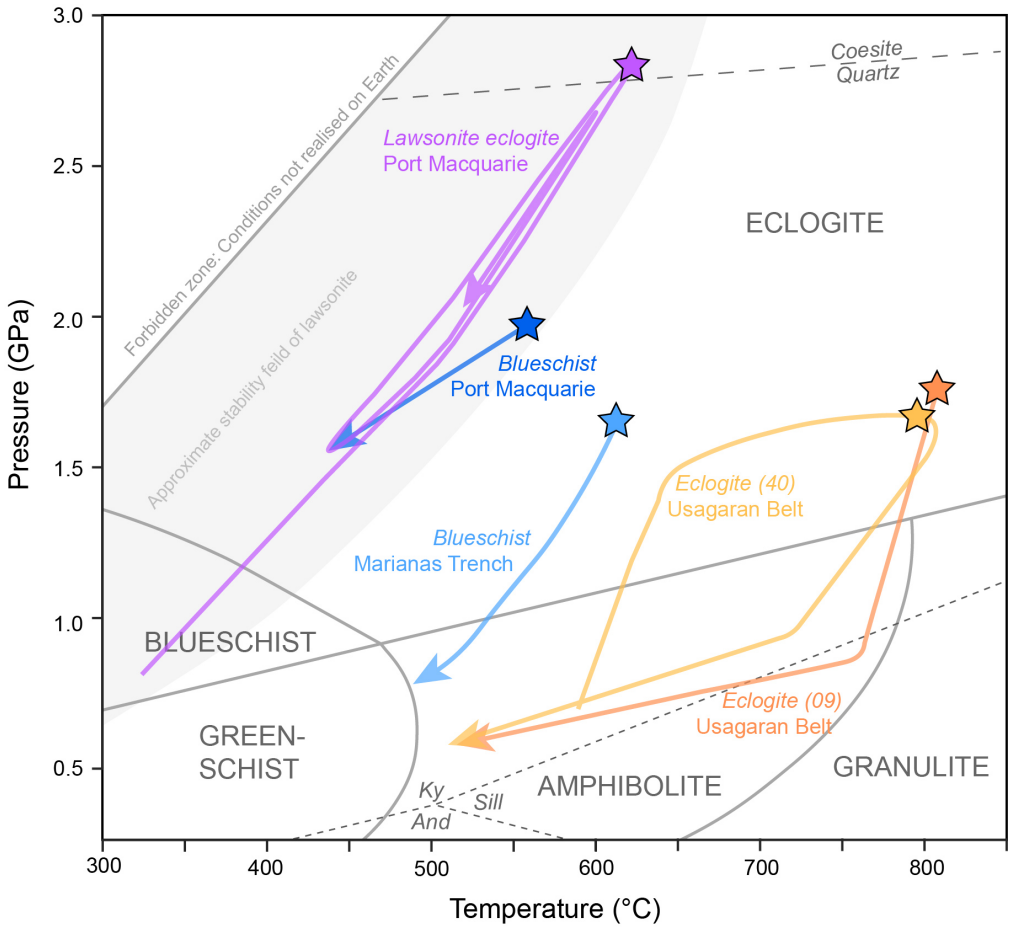


Figure 1: Summary of *P*–*T* paths investigated in this thesis. Star indicates the peak *P*–*T* conditions. Dashed grey lines indicate the approximate phase transitions.

ous rocks themselves do not form in subduction zones, but rather are a product of them. On the other hand, HP–LT assemblages form within the subduction channel, and may be considered direct petrological evidence of subduction (e.g. Brown and Johnson, 2018). It is important to note that it is most likely that modern-style subduction did not appear on Earth abruptly, but rather slowly emerged during a transition from 'soft' to 'rigid' lid plate tectonics (Ernst, 2017; Moyan and Laurent, 2018; Bédard, 2018; Condie, 2018).

Some of the earliest petrological examples of subduction-related metamorphism are found in central Tanzania. Unlike the Cambrian and Eocene examples, the Palaeoproterozoic eclogites in the Usagaran Orogen of Tanzania appeared to have experienced short-lived, warm subduction and

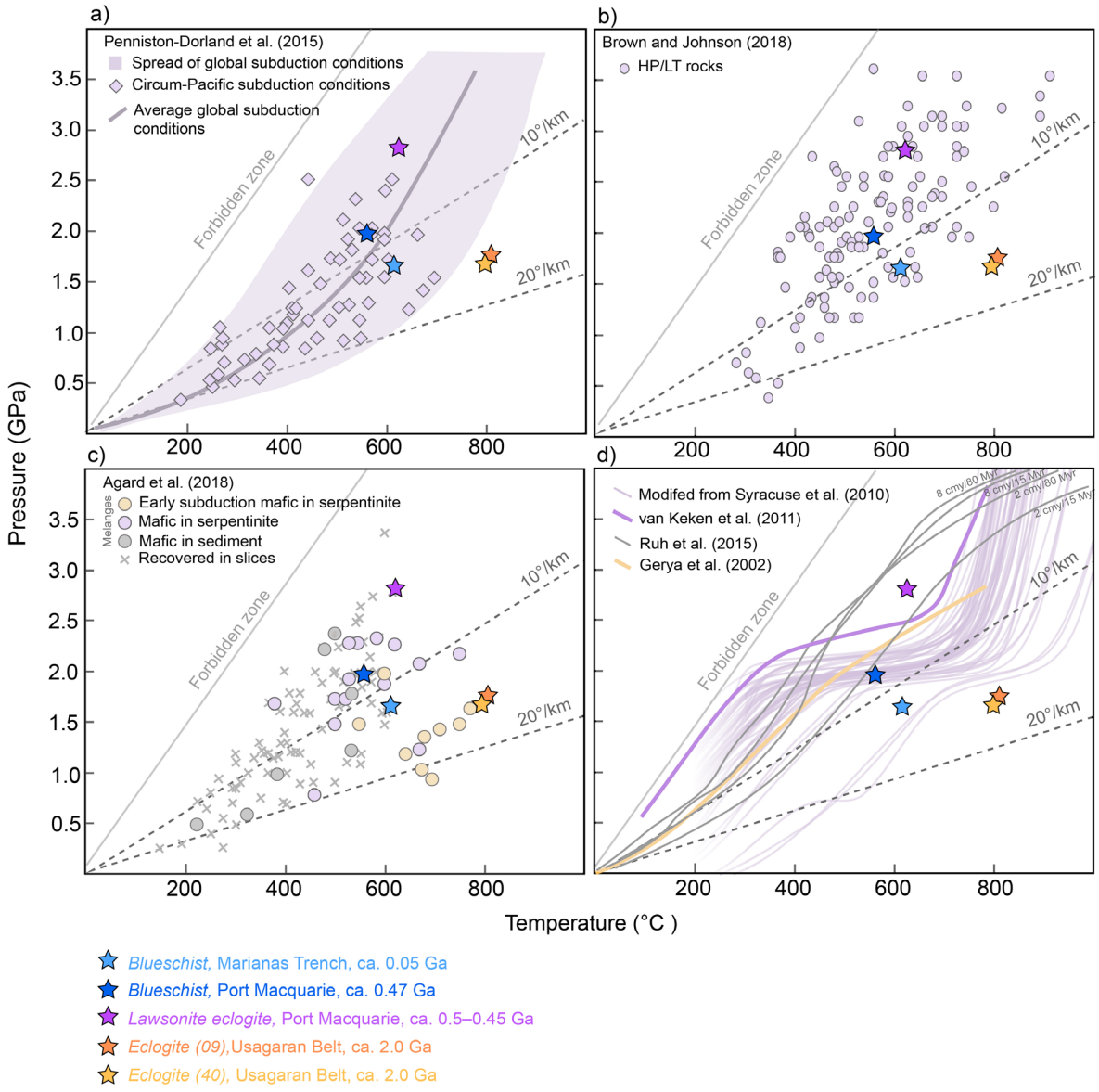


Figure 2: *P–T* conditions of rocks from this thesis compared to other subduction-related HP–LT rock datasets (Penniston-Dorland et al., 2015; Brown and Johnson, 2018; Agard et al., 2018) and numerical models. There are some discrepancies between real-world samples and *P–T* conditions modelled for the top of the subducting slab (d).

exhumation (Fig 1; Fig 2). This may potentially be for two reasons, either i) warmer mantle conditions in the Palaeoproterozoic; or ii) that continental material rather than purely oceanic material was being subducted, evidenced by the fact that the mafic eclogites are encased in metapelitic lithologies. Regardless, the existence of several other Palaeoproterozoic subduction-related eclogites along the margin of the Tanzania and Congo cratons may indicate the existence of a large subduction system operating at this time (Fig. 3). Intriguingly, these eclogites span a large age range between ca. 2093–1886 Ma, and a large range of *P–T* conditions with thermal gradients that vary between 240–465 °C/GPa (Fig. 3; Collins et al., 2004; Boniface et al., 2012; Loose and Schenk, 2018; François et al., 2018; Brown et al., 2020b; Tamblyn et al., 2020). The eclogites have been investigated using a variety of methods to obtain the timing and *P–T* conditions of their formation, for example, conventional thermobarometry and several methods of mineral equilibria modelling have been using to obtain their metamorphic evolutions. While it is feasible the apparent variation in the age and *P–T* conditions of metamorphism may have a meaningful geological explanation, it possibly also highlights the necessity to investigate and compare metamorphic rocks using consistent methodologies. For example, U–Pb zircon ages and Lu–Hf garnet ages may not be analogous, as zircon and garnet may grow during different parts of the rock's metamorphic evolution. Additionally, *P–T* estimates derived from different approaches may not be directly comparable. Given the potential geodynamic importance of these eclogites, using consistent methodology to determine thermal regimes and timescales of metamorphism is essential in order to reveal if secular variations in metamorphic styles exist. The companion study (Appendix 1) of this thesis also highlights the usefulness in targeting metapelitic compositions for metamorphic investigation of subduction systems, as they may be useful in delineating prograde and retrograde paths during subduction, as well as exhumation mechanisms, that may not be recorded by mafic lithologies.

Despite the non-uniformity of approaches used to estimate *P–T* conditions of eclogites, it is well

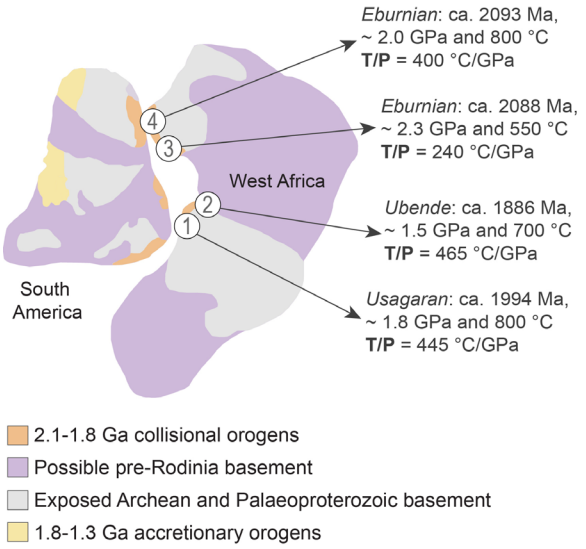


Figure 3: Proposed palaeosubduction system on the margin of West Africa. This may be the first petrological example of large-scale modern subduction in the geological record. Ages and *P–T* estimates are from: Boniface et al., 2012; Loose and Schenk, 2018; François et al., 2018; Brown et al., 2020b; Tamblyn et al., 2020.

noted that in the Palaeoproterozoic, the average thermal gradients experienced by subduction-related eclogites are warmer when compared to modern day (Fig. 2; Boniface et al., 2012; Loose and Schenk, 2018; François et al., 2018; Holder et al., 2018; Brown and Johnson, 2018; Tamblyn et al., 2020; Brown et al., 2020; Brown et al., 2020b). The simplest explanation is that mantle temperatures, and therefore also crustal temperatures, were higher in the Palaeoproterozoic than in the modern Earth (Condie et al., 2016; Ganne and Feng, 2017; Herzberg et al., 2010). This may be reflected in the LOWESS (locally weighted scatterplot smoothing) curve through all metamorphic *P–T* data from Brown et al. (2020), which shows a general cooling trend over time (Fig. 4). When looking at these old subduction-related rocks, the primary mineral assemblage recognised is eclogite (i.e., garnet + omphacite), which then retrogressed through the amphibolite or granulite facies (e.g., Fig. 1). Therefore, it appears omphacite is the key mineral in recognising subduction zone thermal gradients in the Palaeo- to Mesoproterozoic, as blueschist facies mineral assemblages are absent during this time. This raises the question — if ancient subduction zone thermal gradients did not pass through blueschist facies, is there an equivalent amphibolite facies assemblage that might represent subduction zone metamorphism? The likely answer seems to be high-pressure to medium-pressure amphibolite facies, as recorded by the prograde and retrograde path of the Tanzanian eclogites (Fig. 1). Discerning this from amphibolite-grade metamorphic rocks formed via other tectonic processes may prove difficult, but nonetheless could be a previously unidentified marker of modern-style subduction in the geological record.

Collectively, data from central Tanzania, Eastern Australia and the Mariana Trench provide snapshots of subduction zone thermal gradients through time. The *P–T–t* evolutions of these HP–LT rocks support that subduction zone thermal gradients were warmer in the Palaeoproterozoic, and can be warmer during subduction initiation in the modern Earth. The *P–T–t* evolutions also support that in long-lived oceanic subduction systems in the Cambrian and younger, thermal gradients can be very cool, allowing serpentinization of the mantle wedge and material cycling within the subduction channel.

2. Reconciling the records

This thesis not only investigates specific locations of HP–LT metamorphism, but also explores temporal variations in global datasets of metamorphism and magmatism, to tie this into the distribution of eclogites in the geological record. While somewhat unconventional, the following discusses how the union of complex datasets can be used to unravel secular changes in the Earth.

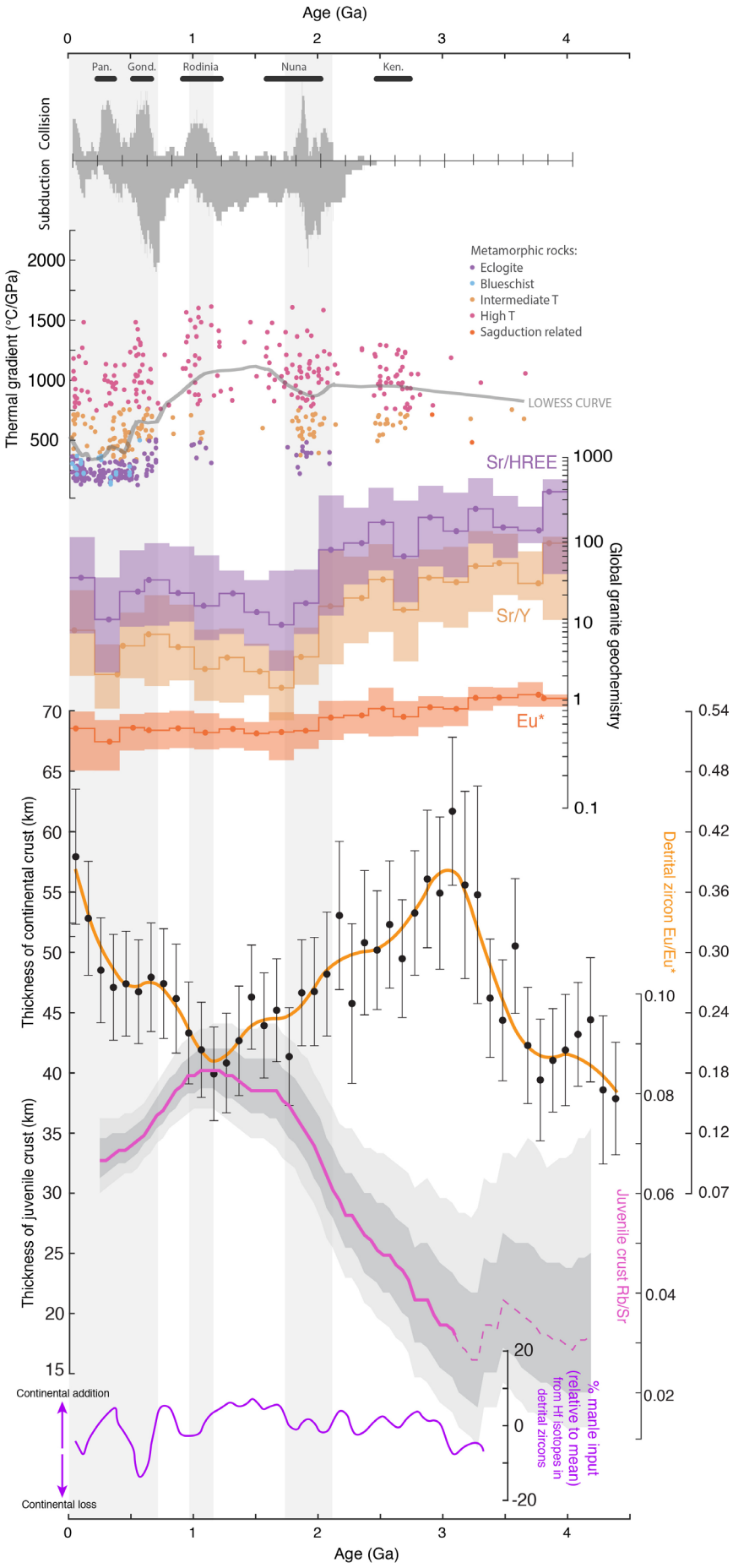


Figure 4: Various time-integrated datasets from the geological record. Pale grey bars indicate significant occurrences of eclogite. Subduction versus collision is from Condie and Aster (2013). Thermal gradients of metamorphic rocks are after Brown and Johnson (2018), LOWESS curve is from Brown et al. (2020). Sr/HREE, Sr/Y and Eu anomaly in the global granite geochemistry database are from Chapter 6 of this thesis. Detrital zircon Eu/Eu* and corresponding continental crustal thickness is after Tang et al. (2021a). Juvenile crustal Rb/Sr and corresponding juvenile crustal thickness is after Dhuime et al. (2015). Even though juvenile crust may usually be thinner than overall continental crust, there is a significant mismatch between the models. Calculated mantle input from Hf isotopes in detrital zircons is after Roberts (2012).

2.1 The power of datasets

Chapter 5 reconciles several apparently disconnected datasets to provide a perspective on the long-term thermal evolution of the mantle and crust. HP–LT rocks and granites are both formed by thermally-driven processes which leave a petrological or geochemical imprint. HP–LT rocks record the *P–T* conditions of their formation in their mineralogy. In contrast, granites can record the thermal conditions of their genesis in their trace element chemistry. During granite genesis, elements like Sr and Eu are sequestered from the melt by plagioclase, and Y and HREEs are sequestered from the melt by garnet (Ducea et al., 2015; Profeta et al., 2015; Lieu & Stern, 2019). The time-resolved ratios of these thermally-sensitive trace elements from a global dataset of granites shows step-changes around ca. 2 Ga, which suggest global heating of the conditions associated with granite genesis (Fig. 4). This is close to the timing of when eclogite preservation was temporarily halted, a process which is strongly controlled by mantle temperature (Sizova et al., 2010). Thus, it appears the mantle may have been heated for a significant period of time in the Palaeo- to Mesoproterozoic. The likely cause of this heating is continental insulation, possibly driven by a high rate of crustal growth and the assembly of the supercontinent Nuna at this time (e.g. Coltice et al., 2009; Lenardic et al,. 2011; Brown et al., 2020). At ca. 1.1 Ga, eclogites re-emerge in the geological record during the assembly of Rodinia, disappear for a short timeframe and re-emerge at ca. 0.75 Ga with blueschists, and then are ubiquitous to present day (Fig. 4). The mantle has become more effectively cooled than it was at ca. 2 Ga by the continued loss of heat producing elements through time. The Earth possibly reached a point in the Neoproterozoic where even with potential periods of increased crustal growth and resultant continental insulation, mantle temperatures remained cool enough to allow the preservation of subduction-related eclogites.

A critical question in understanding the temporal patterns in the metamorphic *P–T* record is assessing preservation bias. The lack of eclogites in the geological record between ca. 1.8–1.1 Ga is interpreted to reflect warmed mantle conditions which supressed the formation of a deep subduction channel and forced the slab to break off at shallower depths in the mantle (Fig. 4; Sizova et al., 2010; Sizova et al., 2015). While it is difficult to tell from numerical models if eclogite-facies mineral assemblages are formed within a warmer mantle (see discussion below), it is probable that deep subduction rocks are not exhumed, and therefore preserved, in warmer mantle scenarios (Sizova et al., 2010; Sizova et al., 2015). However, it could be possible that eclogite-facies rocks were formed between ca. 1.8–1.1 Ga but were overprinted or recycled, or were not exhumed into continental systems which would aid in their preservation in

the geological record. This point is difficult to address directly, however there is evidence for subduction throughout that period of Earth's history in the form of widespread arc magmatism and collisional orogenesis (Fig. 4; Condie and Aster, 2013; Cawood et al., 2013), and there are plenty of amphibolite and granulite facies metamorphic rocks preserved in the crust (Fig. 4; Brown & Johnson, 2018). As such, it appears tectonic plates on Earth were undergoing subduction, but probably not into a cool enough mantle to exhume eclogite-facies rocks.

3. Future directions

The following points outline important limitations in our understanding of subduction zone metamorphism encountered in this thesis, and the future directions that could be followed to address them.

3.1 Limitations of collection of geochronological data in HP–LT assemblages

A difficulty frequently encountered while working on cold, mafic mineral assemblages is the lack of target minerals for geochronology, or the lack of quick and effective methods to analyse them. Improvements in laser-ablation mass spectrometry have allowed the analysis of low-U minerals such as rutile and titanite, common minerals in HP–LT rocks, as well as smaller spot analyses on high-U minerals such as zircon, which may be in low abundance and grain size in HP–LT rocks. High-precision TIMS analysis of Lu and Sm rich minerals, such as garnet, remains the most effective way to directly date the formation of blueschist and eclogite facies assemblages, but much of the textural and compositional information of the target mineral can be lost, and the process can be time consuming. A future direction in the geochronology of HP–LT rocks would be to develop and improve laser-ablation mass spectrometry and reaction cell techniques of dating metamorphic minerals, for example Rb–Sr geochronology of mica and Lu–Hf geochronology of garnet (Zack and Hogmalm, 2016; Simpson et al., in review). While precision of this type of data is still low, the benefits of this type of in-situ analyses are the ability to target specific textural and compositional domains within minerals, and the rapid and cost-effective acquisition of data.

3.2 Tying geodynamic modelling to petrochronological studies

A future direction in the understanding of material behaviour in subduction systems may be the tying together of petrological observation and numerical modelling (Fig. 2; Syracuse et al., 2010; Penniston-Dorland et al., 2015; Kohn et al., 2018; Hernàndez-Uribe et al., 2019; Peacock, 2020). While each are used to inform the other, there are few detailed studies which construct nu-

merical models to directly explain *P–T–t* evolutions translated from real-world rock samples or vice versa (e.g. Yamato et al., 2007; Yamato et al., 2008). Additionally, Gerya et al. (2002) presented a dynamic-kinematic numerical model for *P–T–t* paths of material during convective flow, but an update to this model is becoming necessary. More generally, there is a significant disconnect between *P–T* conditions predicted in the subducting slab by numerical models and *P–T* conditions recorded by real-world HP–LT rocks (Fig 2d; Gerya et al., 2002; Syracuse et al., 2010; Penniston-Dorland et al, 2015). Metamorphic rocks from subduction channels are up to 300 °C warmer than numerical models at their peak pressure (Penninston-Dorland et al., 2015), and may be up to 500 °C hotter at ~ 80 km depth (Kohn et al., 2018). Even when shear heating is included in the numerical models (Kohn et al., 2018; van Keken et al., 2018) there is still a discrepancy between modelled temperatures and those documented in the geological record (Fig. 2d; Peacock, 2020). As such, there may be fundamental parameters missing from modelled subduction systems. Detailed petrochronological studies of subducted HP–LT rocks may therefore be useful in informing the styles of chemical fluxes (e.g., fluid release), thermal conditions and material dynamics of modelled subduction systems throughout their evolution.

3.3 Interrogating combined datasets to fully understand the evolution of the solid Earth

As more extensive and detailed datasets of rocks are compiled, avenues are opened to explore secular changes in processes and fundamental changes within the Earth. Some datasets are often interrogated in tandem, such as U–Pb and Hf isotopic systematics of zircon. More recently, geoscientists are starting to combine more complex and unconventional time-integrated data as shown in Figure 4, such as U–Pb, Hf and O isotopes in zircon versus *P–T* conditions of metamorphic rocks to comment on the relationship between metamorphism, magmatism and tectonism (Brown et al., 2020), and U–Pb and trace element compositions in detrital zircons to infer past crustal thickness and geodynamics (e.g., Balica et al., 2019; Tang et al., 2021a, Tang et al., 2021b). While studies such as these can offer unique insights into processes and changes in the crust through time, they often utilise zircon and are therefore biased toward certain bulk rock compositions, e.g. felsic rocks, and to certain processes, e.g. melting and magmatism (Moecher et al., 2006; Keller et al., 2018). Expanding our interrogation of the geological record to include non-zircon bearing rock ages (e.g. Gard et al., 2019) and other detrital accessory mineral ages such as apatite and rutile (O'Sullivan et al., 2016; Chew et al., 2020; Guo et al., 2020) is one way to combat this bias. A secondary way to expand our understanding of the Earth through time is by utilising rock geochemical databases that include igneous, sedimentary and metamorphic lithologies. For example, the database of Gard et al.

(2019) contains the whole-rock geochemistry and age of over 1 million rock samples though Earth's history. These types of databases can be strengthened with more information, such as mineral or whole-rock isotopic compositions and detailed *P–T* work for metamorphic samples.

Sometimes, the various databases compiled by workers might fundamentally disagree, e.g. the geochemical proxies for crustal thickness through time of Dhuime et al. (2015) and Tang et al. (2021b) infer opposite patterns of crustal thicknesses throughout Earth's history (Fig. 4). Even though juvenile crust may usually be thinner than continental crust and continental arcs, there is still a significant mismatch between the overall trends in the models (Fig. 4; Dhuime et al., 2015; Tang et al., 2021b). The time-integrated pattern of Eu anomalies in granite geochemistry (Chapter 6) and detrital zircons (Tang et al., 2021b) are also not comparable, although arguably they should contain the same record (Fig. 4). The disconnects between these records may simply exist because we do not yet fully understand all the complex yet underlying geochemical and thermodynamic processes operating within the Earth. Undoubtedly, cross-examining and connecting these global datasets together will be the future of tackling large-scale questions in geoscience.

References

Simpson, A., Gilbert, S., Tamblyn, R., Hand, M., Spandler, C., Gillespie, J., Nixon, A., Glorie, S. (In review). In-situ Lu–Hf geochronology of garnet, apatite and xenotime by LA ICP MS/MS. *Chemical Geology*.

Baitsch-Ghirardello, B., Gerya, T. V., & Burg, J.-P. (2014). Geodynamic regimes of intra-oceanic subduction: Implications for arc extension vs. shortening processes. *Gondwana Research, 25*(2), 546-560.

Balica, C., Ducea, M., Gehrels, G., Kirk, J., Roban, R., Luffi, P., . . . Stoica, A. (2020). A zircon petrochronologic view on granitoids and continental evolution. *Earth and Planetary Science Letters, 531*, 116005.

Bédard, J. H. (2018). Stagnant lids and mantle overturns: Implications for Archaean tectonics, magmagenesis, crustal growth, mantle evolution, and the start of plate tectonics. *Geoscience Frontiers, 9*(1), 19-49.

Boniface, N., Schenk, V., & Appel, P. (2012). Paleoproterozoic eclogites of MORB-type chemistry and three Proterozoic orogenic cycles in the Ubendian Belt (Tanzania): Evidence from monazite and zircon geochronology, and geochemistry. *Precambrian Research, 192*, 16-33.

Brown, D. A., Tamblyn, R., Hand, M., & Morrissey, L. J. (2020). Thermobarometric constraints on burial and exhumation

of 2-billion-year-old eclogites and their metapelitic hosts. *Precambrian Research*, 105833.

Brown, M., & Johnson, T. (2018). Secular change in metamorphism and the onset of global plate tectonics. *American Mineralogist, 103*(2), 181-196.

Brown, M., Kirkland, C., & Johnson, T. (2020). Evolution of geodynamics since the Archean: Significant change at the dawn of the Phanerozoic. *Geology, 48*(5), 488-492.

Cawood, P. A., Hawkesworth, C., & Dhuime, B. (2013). The continental record and the generation of continental crust. *Bulletin, 125*(1-2), 14-32.

Chew, D., O'Sullivan, G., Caracciolo, L., Mark, C., & Tyrrell, S. (2020). Sourcing the sand: Accessory mineral fertility, analytical and other biases in detrital U-Pb provenance analysis. *Earth-Science Reviews, 202*, 103093.

Collins, A. S., Reddy, S. M., Buchan, C., & Mruma, A. (2004). Temporal constraints on Palaeoproterozoic eclogite formation and exhumation (Usagaran Orogen, Tanzania). *Earth and Planetary Science Letters, 224*(1-2), 175-192.

Coltice, N., Bertrand, H., Rey, P., Jourdan, F., Phillips, B. R., & Ricard, Y. (2009). Global warming of the mantle beneath continents back to the Archaean. *Gondwana Research, 15*(3-4), 254-266.

Condie, K. C. (2018). A planet in transition: the onset of plate tectonics on Earth between 3 and 2 Ga? *Geoscience Frontiers, 9*(1), 51-60.

Condie, K. C., & Aster, R. C. (2013). Refinement of the supercontinent cycle with Hf, Nd and Sr isotopes. *Geoscience Frontiers, 4*(6), 667-680.

Condie, K. C., Aster, R. C., & Van Hunen, J. (2016). A great thermal divergence in the mantle beginning 2.5 Ga: Geochemical constraints from greenstone basalts and komatiites. *Geoscience Frontiers, 7*(4), 543-553.

Dhuime, B., Hawkesworth, C. J., Cawood, P. A., & Storey, C. D. (2012). A change in the geodynamics of continental growth 3 billion years ago. *Science, 335*(6074), 1334-1336.

Ducea, M. N., Saleeby, J. B., & Bergantz, G. (2015). The architecture, chemistry, and evolution of continental magmatic arcs. *Annual Review of Earth and Planetary Sciences, 43*, 299-331.

Fischer, R., & Gerya, T. (2016a). Early Earth plume-lid tectonics: A high-resolution 3D numerical modelling approach. *Journal of Geodynamics, 100*, 198-214.

Fischer, R., & Gerya, T. (2016b). Regimes of subduction and lithospheric dynamics in the Precambrian: 3D thermomechanical modelling. *Gondwana Research, 37*, 53-70.

François, C., Debaille, V., Paquette, J.-L., Baudet, D., & Javaux, E. J. (2018). The earliest evidence for modern-style plate tectonics recorded by HP–LT metamorphism in the Paleoproterozoic of the Democratic Republic of the Congo. *Scientific reports, 8*(1), 1-10.

Ganne, J., & Feng, X. (2017). Primary magmas and mantle temperatures through time. *Geochemistry, Geophysics, Geosystems, 18*(3), 872-888.

Gard, M., Hasterok, D., Hand, M., & Cox, G. (2019). Variations in continental heat production from 4 Ga to the present: evidence from geochemical data. *Lithos, 342*, 391-406.

Gerya, T. V., Stöckhert, B., & Perchuk, A. L. (2002). Exhumation of high-pressure metamorphic rocks in a subduction channel: A numerical simulation. *Tectonics, 21*(6).

Guo, R., Hu, X., Garzanti, E., Lai, W., Yan, B., & Mark, C. (2020). How faithfully do the geochronological and geochemical signatures of detrital zircon, titanite, rutile and monazite record magmatic and metamorphic events? A case study from the Himalaya and Tibet. *Earth-Science Reviews, 201*, 103082.

Herzberg, C. (2011). Basalts as temperature probes of Earth's mantle. *Geology, 39*(12), 1179-1180.

Holder, R. M., Viete, D. R., Brown, M., & Johnson, T. E. (2019). Metamorphism and the evolution of plate tectonics. *Nature, 572*(7769), 378-381.

Keller, C. B., Boehnke, P., & Schoene, B. (2018). Temporal variation in relative zircon abundance throughout Earth history.

Kohn, M. J., Castro, A. E., Kerswell, B. C., Ranero, C. R., & Spear, F. S. (2018). Shear heating reconciles thermal models with the metamorphic rock record of subduction. *Proceedings of the National Academy of Sciences, 115*(46), 11706-11711.

Kusky, T. M., Windley, B. F., & Polat, A. (2018). Geological evidence for the operation of plate tectonics throughout the Archean: Records from Archean paleo-plate boundaries. *Journal of Earth Science*, 29(6), 1291-1303.

Lenardic, A., Moresi, L., Jellinek, A., O'neill, C., Cooper, C., & Lee, C. (2011). Continents, supercontinents, mantle thermal mixing, and mantle thermal isolation: Theory, numerical simulations, and laboratory experiments. *Geochemistry, Geophysics, Geosystems, 12*(10).

Lieu, W. K., & Stern, R. J. (2019). The robustness of Sr/Y and La/Yb as proxies for crust thickness in modern arcs. *Geosphere, 15*(3), 621-641.

Loose, D., & Schenk, V. (2018). 2.09 Ga old eclogites in the Eburnian-Transamazonian

orogen of southern Cameroon: Significance for Palaeoproterozoic plate tectonics. *Precambrian Research, 304*, 1-11.

Moecher, D. P., & Samson, S. D. (2006). Differential zircon fertility of source terranes and natural bias in the detrital zircon record: Implications for sedimentary provenance analysis. *Earth and Planetary Science Letters, 247*(3-4), 252-266.

Moyen, J.-F., & Laurent, O. (2018). Archaean tectonic systems: a view from igneous rocks. *Lithos, 302*, 99-125.

O'Sullivan, G., Chew, D., & Samson, S. (2016). Detecting magma-poor orogens in the detrital record. *Geology, 44*(10), 871-874.

Peacock, S. M. (2020). Advances in the thermal and petrologic modeling of subduction zones. *Geosphere, 16*(4), 936-952.

Penniston-Dorland, S. C., Kohn, M. J., & Manning, C. E. (2015). The global range of subduction zone thermal structures from exhumed blueschists and eclogites: Rocks are hotter than models. *Earth and Planetary Science Letters, 428*, 243-254.

Profeta, L., Ducea, M. N., Chapman, J. B., Paterson, S. R., Gonzales, S. M. H., Kirsch, M., . . . DeCelles, P. G. (2015). Quantifying crustal thickness over time in magmatic arcs. *Scientific reports, 5*, 17786.

Roberts, N. M. (2012). Increased loss of continental crust during supercontinent amalgamation. *Gondwana Research, 21*(4), 994-1000.

Ruh, J. B., Le Pourhiet, L., Agard, P., Burov, E., & Gerya, T. (2015). Tectonic slicing of subducting oceanic crust along plate interfaces: Numerical modeling. *Geochemistry, Geophysics, Geosystems, 16*(10), 3505-3531.

Sizova, E., Gerya, T., & Brown, M. (2014). Contrasting styles of Phanerozoic and Precambrian continental collision. *Gondwana Research, 25*(2), 522-545.

Sizova, E., Gerya, T., Brown, M., & Perchuk, L. (2010). Subduction styles in the Precambrian: insight from numerical experiments. *Lithos, 116*(3-4), 209-229.

Syracuse, E. M., van Keken, P. E., & Abers, G. A. (2010). The global range of subduction zone thermal models. *Physics of the Earth and Planetary Interiors, 183*(1-2), 73-90.

Tamblyn, R., Brown, D., Hand, M., Morrissey, L., Clark, C., & Anczkiewicz, R. (2021). The 2 Ga eclogites of Central Tanzania: Directly linking age and metamorphism. *Lithos, 380*, 105890.

Tang, M., Chu, X., Hao, J., & Shen, B. (2021). Orogenic quiescence in Earth's middle age. *Science, 371*(6530), 728-731.

Tang, M., Ji, W.-Q., Chu, X., Wu, A., & Chen, C. (2021). Reconstructing crustal thickness evolution from europium anomalies in detrital zircons. *Geology, 49*(1), 76-80.

Turner, S., Rushmer, T., Reagan, M., & Moyen, J. F. (2014). Heading down early on? Start of subduction on Earth. *Geology*, 42(2), 139-142.

van Keken, P. E., Wada, I., Abers, G. A., Hacker, B. R., & Wang, K. (2018). Mafic high-pressure rocks are preferentially exhumed from warm subduction settings. *Geochemistry, Geophysics, Geosystems, 19*(9), 2934-2961.

Yamato, P., Agard, P., Burov, E., Le Pourhiet, L., Jolivet, L., & Tiberi, C. (2007). Burial and exhumation in a subduction wedge: Mutual constraints from thermomechanical modeling and natural P-T-t data (Schistes Lustrés, western Alps). *Journal of Geophysical Research: Solid Earth, 112*(B7).

Yamato, P., Burov, E., Agard, P., Le Pourhiet, L., & Jolivet, L. (2008). HP-UHP exhumation during slow continental subduction: Self-consistent thermodynamically and thermomechanically coupled model with application to the Western Alps. *Earth and Planetary Science Letters, 271*(1-4), 63-74.

Zack, T., & Hogmalm, K. J. (2016). Laser ablation Rb/Sr dating by online chemical separation of Rb and Sr in an oxygen-filled reaction cell. *Chemical Geology, 437*, 120-133.

Appendix 1:
Companion study to Chapter 5

This chapter is published as: Brown, D.A., Tamblyn, R., Hand, M. and Morrissey, L.J. (2020). Thermobarometric constraints on burial and exhumation of 2-billion-year-old eclogites and their metapelitic hosts. Precambrian Research, 347, p.105833.

The supplementary materials for this appendix can be found online at:
https://doi.org/10.1016/j.precamres.2020.105833

Abstract

One of the first appearances of eclogite-facies mineral assemblages in the geological record occurs in the c. 2000 Ma Palaeoproterozoic Usagaran Belt in central Tanzania, where the extended margin of the Tanzanian Craton is interpreted to have been subducted. Mafic rocks are interpreted to have contained the mineral assemblage garnet + omphacite + rutile + quartz ± amphibole. This high-pressure assemblage has been overprinted by a secondary mineral assemblage containing clinopyroxene + plagioclase + hornblende + ilmenite ± orthopyroxene. Mineral equilibria forward modelling indicates that the eclogite-facies assemblages reached minimum peak pressure-temperature (*P–T*) conditions of ~17 kbar and ~700 °C. Inclusions in garnet document a prograde *P–T* history consistent with burial through upper amphibolite-facies conditions and possible partial melting. Petrological and compositional evidence from garnet suggests that following peak metamorphism, the eclogite-facies rocks were heated while stalled at approximate peak pressures. Temperature estimates derived from Zr concentrations in interpreted texturally retrograde rutile support a near-isothermal post-peak *P–T* evolution for the eclogite-facies rocks – an evolution that terminates at retrograde *P–T* conditions of approximately 7.6–8.2 kbar and 680–790 °C. The relict eclogite domains form part of a larger assemblage with enclosing migmatitic metapelitic lithologies (the Isimani Suite). The metapelitic gneisses contain garnet + kyanite + biotite + staurolite + hornblende + plagioclase + muscovite + rutile + quartz and preserve minimal evidence of a high-pressure history, conceivably due to post-peak mineralogical recrystallisation. *P–T* modelling, inclusion assemblages and compositional zonation patterns in porphyroblastic garnet suggests the metapelitic gneisses — similarly to the relict eclogites — experienced burial to minimum peak pressures of approximately 16.5–17 kbar. Compositional zoning patterns in eclogitic garnet suggest the Isimani system was buried, reached peak metamorphic conditions, and was subsequently exhumed within a timeframe of up to 20 Myr. A tectonic regime involving crustal thickening and subduction, followed by extensional exhumation of the entire Isimani Suite is our preferred model for the development of the c. 2000 Ma Usagaran Belt.

1. Introduction

Despite evidence that eclogitization can occur as a consequence of collisional-related processes in orogenic crustal roots (e.g. Leech, 2001; Foley *et al.*, 2003; Johnson *et al.*, 2013), eclogites are typically regarded as diagnostic markers of subduction, and are therefore inferred to indicate the operation of modern-style plate tectonic processes (e.g. Peacock, 1996; Brown, 2006; Brown, 2010; Brown and Johnson, 2018). Additionally, eclogites and associated high-pressure rocks are widely

interpreted to record the thermal state of palaeosubduction systems (e.g. Stern, 2005; Brown 2006). Although rocks older than c. 1500 Ma that preserve evidence of reaching eclogite-facies conditions are rare (O'Brien and Rötzler, 2003), the fact that some examples exist in the geological record (Fig. 1; Table 1) suggests that subduction processes were underway by this time. Subduction in the Palaeoproterozoic is thought to have occurred along warmer geothermal gradients than those documented for modern post-Neoproterozoic subduction systems (e.g. Brown and Johnson, 2018), given the comparatively high thermal gradients recorded in eclogite-facies rocks of this

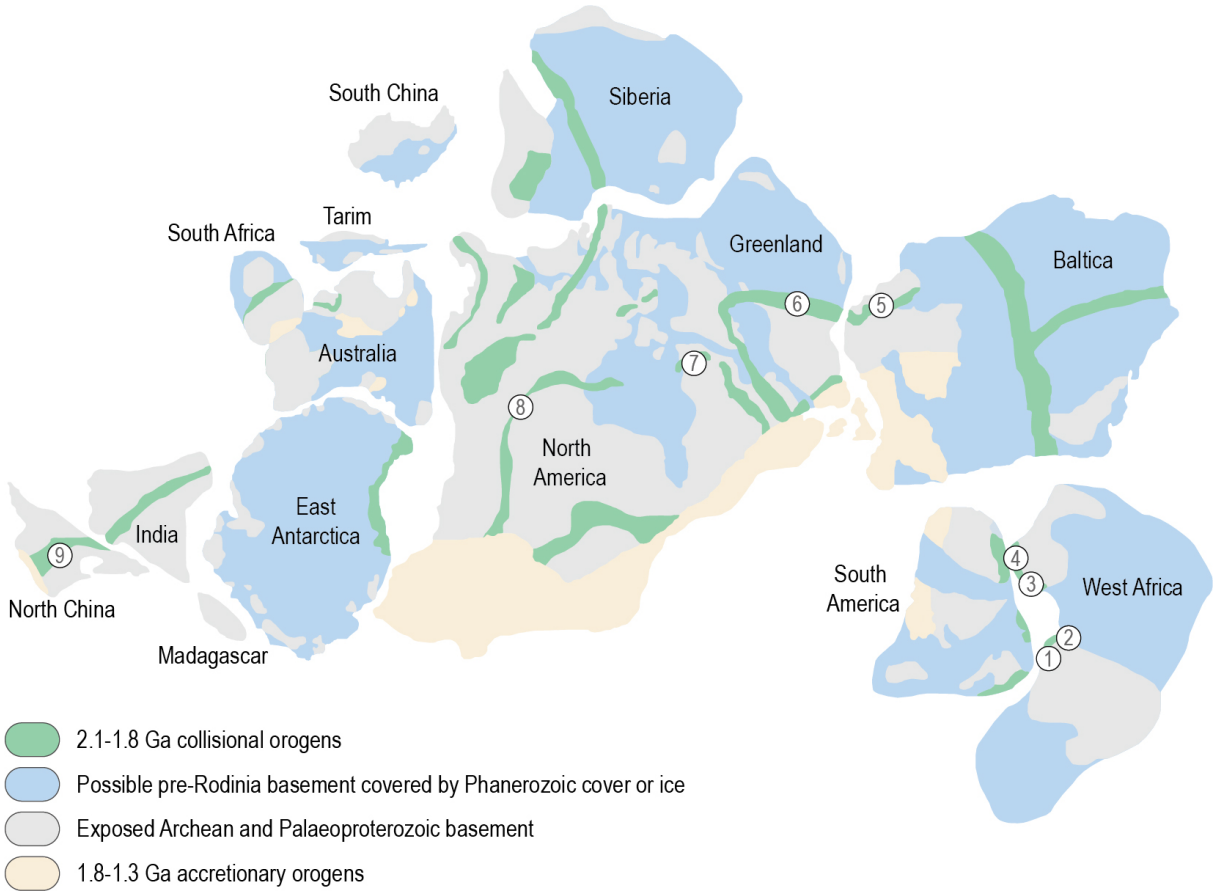


Fig. 1. Locations of documented Palaeoproterozoic eclogite-facies assemblages shown in the context of the supercontinent Columbia – the reconstruction depicted here is modified after Zhao et al. (2004). The numbered identifiers for each location correspond to the following: (1) Usagaran Orogen, Tanzania (Möller et al., 1995; Collins et al., 2004); (2) Ubendian Orogen, Tanzania (Boniface et al., 2012); (3) Eburnian-Transamazonian Orogen, the Democratic Republic of the Congo (François et al., 2018); (4) Eburnian-Transamazonian Orogen, Southern Cameroon (Loose and Schenk, 2018; Houketchang Bouyo et al., 2019); (5) Kola-Lapland Orogen, Belomorian Province, Russia (Skublov et al., 2010, 2014; Li et al., 2015, 2017, 2018; Liu et al., 2017; Yu et al., 2017, 2019); (6) Nagssugtoqidian Orogen, South-East Greenland (Nutman et al., 2008; Müller et al., 2018a; Müller et al., 2018b); (7) Trans-Hudson Orogen, North America (Weller and St-Onge, 2017); (8) Snowbird Tectonic Zone, Canada (Baldwin et al., 2003, 2004, 2007); (9) Trans-North China Orogen, Hengshan Complex, North China (Zhao et al., 2001; Kröner et al., 2006; Qian et al., 2017; Xu et al., 2018).

Terrane	Location	Sample	Peak age (Ma)	Retrograde age (Ma)	Peak P–T conditions (°C, GPa)	Retrograde P–T conditions (°C, GPa)	Thermal gradient (°C/GPa)	Method to constrain P–T
Eburnian-Transamazonian Orogen	Southern Cameroon	Eclogite (B)	2093 ± 45 U–Pb(Zrn) 1 U–Pb(Zrn) 1	-	800, 1.8–2.0 1 850, 2.5 2	700, 0.7 1 750, 1.2 2	445 1 340 2	Conventional thermobarometry 1 Conventional thermobarometry 2
	Democratic Republic of the Congo	Eclogite (outcrop association unknown)	2087 ± 45 U–Pb(Zrn) 3 2089 ± 13 U–Pb(Rt) 3	-	500–550, 1.7–2.3 3	450–575, 0.75–0.95 3	410 3	Perple_X (v.6.8.3, sm682) 3
Kola-Lapland Orogen, Belomorian Province	Russia	Uzkaya Salma Eclogite (B)	1870 ± 2 U–Pb(Ttn) 4 2000–1900 U–Pb(Zrn) 5	1830–1800 U–Pb(Zrn) 5	700–750, 1.7–1.8 5	800–850, 1.3–1.5 5	410 5	Theriak-Domino (v.03.01.2012, ds55) 5
		Gridino Eclogite (B)	1900 U–Pb(Ttn) 6 1900 U–Pb(Zrn) 7	1870–1880 U–Pb(Ttn) 6	710, 18.5 8 725–750, 1.9–2.2 9	760, 1.5 8 680–730, 9.0–1.0 9	380 8 380 9	THERMOCALC (v.333, ds55) 8, 9
		Kuru-Vaara Eclogite (B)	1897–1895 U–Pb(Zrn) 10 (prograde)	1885 ± 6 U–Pb(Zrn) 10	720–820, 1.8–2.0 10	870–915, 1.1–1.3 10	400 10	THERMOCALC (v.333, ds55) 10
		Shirokaya Salma Eclogite (B)	-	-	750–800, 1.6–1.8 11	820–850, 1.1–1.5 11	470 11	Theriak-Domino (v.03.01.2012, ds55) 11
Usagaran Belt	Tanzania	Eclogite (B)	1999.1 ± 1.1 U–Pb(Zrn) 12	1991 ± 2 U–Pb(Zrn) 12 1996 ± 2	750–800, 1.8 13	665–780, 0.9–10 13	415 13	Conventional thermobarometry 13

				U–Pb(Ttn) 13				
Snowbird Tectonic Zone	Canada	Eclogite (B)	1904 ± 0.3 U–Pb(Zrn) 14	1900–1895 U–Pb(Ttn) 15	750, 1.6 16	750, 0.7 16	470 16	THERMOCALC (v.325, ds55) 16
Ubendian Orogen	Tanzania	Eclogite (B)	1886 ± 16 U–Pb(Zrn) 17	1831 ± 11 U–Pb(Mnz) 17 1817 ± 26 U–Pb(Zrn) 17	700, 1.5 17	-	465 17	Conventional thermobarometry 17
Nagssugtoqidian Orogen	South-East Greenland	Eclogite (B)	1867 ± 28 U–Pb(Zrn) 18 1891–1882 U–Pb(Mnz-Ttn-Zrn) 19	1872–1773 U–Pb(Mnz-Ttn) 19	740–810 20	17–19 20	435 20	Conventional thermobarometry 20
Trans-North China Orogen	China	Eclogite (B)	1888–1848 U–Pb(Zrn) 21 1839 ± 26 U–Pb(Mnz) 22 1963–1769 U–Pb (Zrn) 23	1766 ± 7 U–Pb(Mnz) 22	650–670, 2.5–2.8 22 770–840, 1.34–1.55 24	750–830, 0.65–0.8 24	575 24	THERMOCALC (v.333, ds55) 22 THERMOCALC (v.275) 24
Trans-Hudson Orogen	North America	Eclogite (B)	1831 ± 4.7 U–Pb(Mnz) 25	-	700–770, 2.35–2.65 25	700, 0.7 25	300 25	THERMOCALC (v.340, ds55) 25

Table 1. Palaeoproterozoic eclogite occurrences. Thermal gradient ranges are calculated for minimum peak metamorphic conditions. (B) signifies that that eclogites are preserved as boudins and/or lenses at the outcrop scale. Superscripts correspond to the following references: (1) Loose and Schenk (2018); (2) Houketchang Bouyo et al. (2019); (3) François et al. (2018); (4) Skublov et al. (2010); (5) Li et al. (2017); (6) Skublov et al. (2014); (7) Yu et al. (2017); (8) Li et al. (2015); (9) Yu et al. (2019); (10) Liu et al. (2017); (11) Li et al. (2018); (12) Collins et al. (2004); (13) Möller et al. (1995); (14) Baldwin et al. (2004); (15) Baldwin et al. (2003); (16) Baldwin et al. (2007); (17) Boniface et al. (2012); (18) Nutman et al. (2008); (19) Müller et al. (2018b); (20) Müller et al. (2018a); (21) Kröner et al. (2006); (22) Xu et al. (2018); (23) Qian et al. (2017); (24) Zhao et al. (2001); (25) Weller and St-Onge (2017). Mineral abbreviations after Whitney and Evans, (2010): Zrn: zircon, Mnz: monazite, Ttn: titanite, Rt: rutile.

age (Table 1). Documented Palaeoproterozoic high-pressure rocks include those preserved in the Eburnian-Transamazonian Orogen in Southern Cameroon (Loose and Schenk, 2018; Houketchang Bouyo *et al.*, 2019), the Ubendian and Usagaran orogens, in Tanzania (Möller *et al.*, 1995; Collins *et al.*, 2004; Boniface *et al.*, 2012), the Kola-Lapland Orogen, Belomorian Province in Russia (Skublov *et al.*, 2010, 2014; Li *et al.*, 2015, 2017, 2018; Liu *et al.*, 2017; Yu *et al.*, 2017, 2019), and the Snowbird Tectonic Zone in Canada (Baldwin *et al.*, 2003, 2004, 2007).

The scarcity of pre-Palaeozoic rocks preserving eclogite-facies mineral assemblages (Brown and Johnson, 2018) has been argued to reflect either an issue of preservation (Möller *et al.*, 1995; Baldwin *et al.*, 2004; Collins *et al.*, 2004; Weller and St-Onge, 2017), or their lack of formation as a consequence of higher geothermal gradients in the Proterozoic Earth (Herzberg *et al.*, 2010; Bradley 2011; Anderson *et al.*, 2012; Condie *et al.*, 2016). Important in addressing questions of the thermal character of Palaeoproterozoic plate tectonic systems is an improved understanding of the absolute *P–T* conditions associated with the formation of Palaeoproterozoic high-pressure mineral assemblages. Of the recognised Palaeoproterozoic high-pressure rocks (Table 1), only those preserved in the Gridino and Kuru-Vaara Complexes of the Kola-Lapland Orogen (Liu *et al.*, 2017; Yu *et al.*, 2017), the Snowbird Tectonic Zone (Baldwin *et al.*, 2007), the Trans-North China Orogen (Xu *et al.*, 2018) and the Trans-Hudson Orogen (Weller and St-Onge, 2017), have been interrogated using robust mineral equilibria forward models to constrain their respective *P–T* conditions of formation. The inconsistencies between the methods used to constrain the respective *P–T* conditions of formation for the high-pressure rocks creates ambiguities when comparisons are drawn between the thermal gradients derived from these *P–T* conditions and the thermal gradients calculated using subduction zone thermal models (e.g. Syracuse *et al.*, 2010; Penniston-Dorland *et al.*, 2015; Brown and Johnson, 2018; van Keken *et al.*, 2018). Not only is there a necessity for improved *P–T* estimates for Palaeoproterozoic eclogitic assemblages, there remains uncertainty regarding the relationship between the *P–T* histories of Palaeoproterozoic eclogitic assemblages and their enclosing country rock hosts. Relic eclogitic mineral assemblages preserved as boudins or lenses are commonly found in association with host rocks at the outcrop scale (e.g. Table 1; Cuthbert *et al.*, 2000; Chopin, 2003; Reddy *et al.*, 2003; Collins *et al.*, 2004; Bousquet, 2008; Palmeri *et al.*, 2009). Notably, host rocks almost invariably lack eclogitic mineral assemblages. Rock associations of this sort are commonly interpreted to represent metamorphism of a single rock package, where the mineralogical variability between rocks — particularly with respect to barically-controlled mineral assemblages — is argued to reflect either

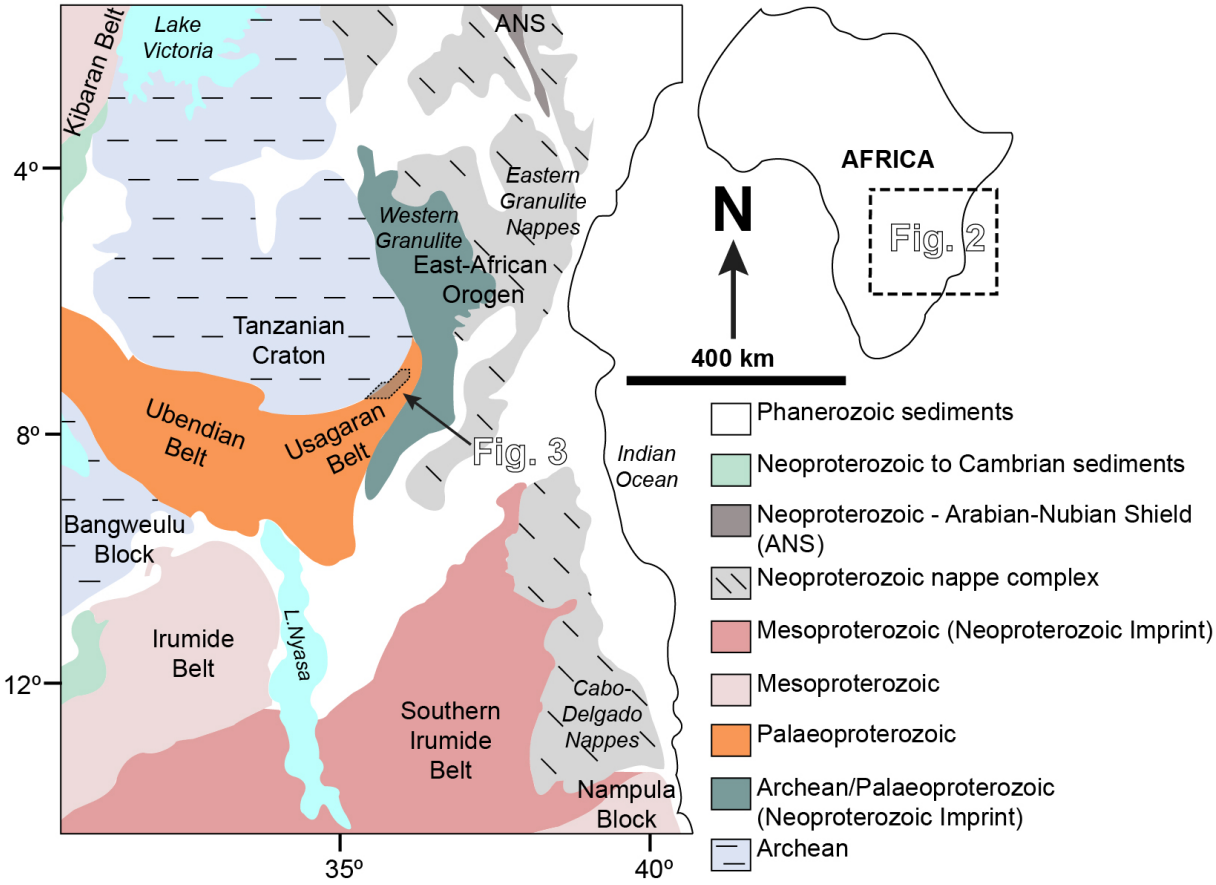


Fig. 2. Regional geological map of central-eastern Tanzania comprising the Tanzanian Craton, Ubendian Belt, Usagaran Belt and the East-African Orogen. The region bounded by the bold dashed black line labelled Fig. 3 is the locality of this study – the Usagaran Belt. Map modified from Fritz et al. (2005).

the partial or complete eradication of high-pressure mineral assemblages in the host rocks during exhumation (e.g. Meyre *et al.*, 1999; Chopin and Schertl, 1999; Yea *et al.*, 2000; Cuthbert *et al.*, 2000; Liu *et al.*, 2001; Janák *et al.*, 2009; Spencer *et al.*, 2013). Another common explanation is that the mineral assemblages do not transform during high-pressure metamorphism (e.g. Young and Kylander-Clark, 2015). Despite such explanations, it remains enigmatic whether high-pressure assemblages and their structural hosts record a contemporaneous subduction-related history or whether their association may be better explained by structural juxtaposition (e.g. Smith, 1988; Liu *et al.*, 2003; Štípská *et al.*, 2006; Bousquet, 2008; Hacker *et al.*, 2010).

In this study, we derive *P*–*T* constraints for the relict eclogite-facies assemblages in the c. 2000 Ma Usagaran Belt, and the metapelitic rocks that regionally enclose them through the implementation of mineral equilibria forward modelling. The overarching goal is to better understand (1) the thermal conditions associated with (i) the formation of the eclogite-facies assemblages and (ii) the burial of their protoliths, and (2) the tectonometamorphic relationship between the eclogites and their metapelitic hosts that evolved from burial to

exhumation.

2. Geological background

The Palaeoproterozoic Usagaran Belt in central Tanzania (Fig. 2) preserves some of the oldest known relict eclogite-facies mineral assemblages, with ages of c. 2000 Ma (Möller *et al.*, 1995; Collins *et al.*, 2004). The relict high-pressure assemblages are contained within a km-scale domain which is regionally enclosed by high-strain amphibolite-facies rocks (Fig. 3a; Möller *et al.*, 1995; Reddy *et al.*, 2003; Collins *et al.*, 2004). Rudimentary thermobarometric methods applied to the eclogitic mafic rocks have derived peak pressures of ~18 kbar and temperatures of ~750 °C. Geochemical arguments suggest the protoliths to the eclogites are MORB-like, adopting a slightly more evolved composition with respect to MORB (Möller *et al.*, 1995, 1998; Maboko, 2000; Brick, 2011). These findings are consistent with a subduction-related origin for the development of the Usagaran eclogites.

Regionally, the Usagaran Belt is bordered by the c. 2700 Ma Tanzanian Craton to the north-west and the c. 655–610 Ma East-African Orogen to the east (Fig. 2; Möller *et al.*, 2000; Muhongo *et al.*, 2001). Bordering the Tanzanian Craton on its south-west margin is the Palaeoproterozoic Ubendian Belt which also hosts relict eclogite domains (Sklyarov *et al.*, 1998). Boniface *et al.* (2012) demonstrated that the Ubendian eclogite-facies metamorphism occurred between c. 1870–1865 Ma, well after the c. 2000 Ma eclogite-facies metamorphism in the Usagaran Belt (Möller *et al.*, 1995; Collins *et al.*, 2004).

The Usagaran Belt contains two lithotectonic domains: the medium- to high-grade Isimani Suite and the lower grade Konse Group (Fig. 3a; Mruma, 1989). The c. 1895 Ma Konse Group (Collins *et al.*, 2004) consists of sedimentary and volcanic

Rock type	Sample	Mineral Assemblage	DMS Coordinates
Mafic Granofels	T01-39	garnet + clinopyroxene + plagioclase + quartz + amphibole + ilmenite + hematite + rutile + apatite + titanite + zircon	36° 16' 34"E, 06° 59' 00"S
Mafic Gneiss	T06-11	garnet + clinopyroxene + plagioclase + quartz + ilmenite + hematite + amphibole + rutile + orthopyroxene + titanite + apatite + zircon	36° 14' 31"E, 06° 59' 47"S
Migmatitic Metapelitic Gneiss	T06-20	garnet + kyanite + plagioclase + biotite + quartz + amphibole + rutile + staurolite + chlorite + apatite + muscovite + zircon	36° 09' 42"E, 07° 09' 09"S

Table 2. Sample locations and mineral descriptions.

units that unconformably overlie the highly metamorphosed Isimani Suite (Mruma, 1989; Collins *et al*., 2004). SHRIMP U–Pb zircon ages of c. 2700 Ma from Isimani gneisses are interpreted to reflect the crystallisation ages of igneous protoliths (Reddy *et al*., 2003; Collins *et al*., 2004). Moreover, Collins *et al*. (2004) inferred from detrital zircon ages that the protoliths to the Isimani metapelitic gneisses were derived from the Tanzanian Craton and likely comprise a cover sequence atop c. 2700 Ma granitoids of the Tanzanian Craton (Möller *et al*., 1998; Maboko, 2000).

Mruma (1989) described the Isimani Suite in detail. The most common rock types are mafic and metapelitic gneisses and amphibolites. Coarse-grained kyanite-garnet metapelitic gneisses occur as 5 m thick layers and are interlayered with garnet-clinopyroxene-hornblende-plagioclase-bearing amphibolites, which occur as layered and boudinaged 10–50 m thick domains (Fig. 3b). This gneiss-amphibolite association is regionally enclosed within migmatitic coarse-grained biotite-bearing gneisses containing kyanite, garnet, staurolite and muscovite (Fig. 3c, d). In the mafic rocks, Mruma (1989) identified mineral reaction textures consistent with garnet breakdown to fine-grained hornblende and plagioclase symplectites. Comparatively low-strain mafic domains enclosed by the amphibolite-metapelitic association (Fig. 3e) contain an assemblage of garnet, clinopyroxene, plagioclase, hornblende and quartz (Möller *et al*., 1995). Möller *et al*. (1995) inferred a former eclogitic mineralogy based on the occurrence of omphacite included within garnet. A SHRIMP U–Pb zircon age of 1986 ± 29 Ma was derived from a relict eclogite assemblage (Collins *et al*., 2004). Similar ages were obtained from an Isimani kyanite-garnet gneiss interlayered with migmatitic garnet-hornblende-bearing rocks (Mruma, 1989), which gave a SHRIMP U–Pb age of 1989 ± 10 Ma from zircon rims, and a mylonitic felsic gneiss, which returned a SHRIMP U–Pb age of 1997.6 ± 2.2 Ma (Collins *et al*., 2004). Monazite from metapelitic rocks enclosed within the highly deformed Isimani migmatitic metapelitic gneisses, which are interpreted to overprint the eclogite-facies assemblages (Reddy *et al*., 2003), give $^{207}Pb/^{206}Pb$ dates of 1999 ± 2 Ma and 2000 ± 2 Ma (Möller *et al*., 1995). According to Collins *et al*. (2004), the weighted mean of these four ages yielded an age of 1999.1 ± 1.1 Ma, and this was interpreted to represent the timing of the high-grade eclogite-facies metamorphism within the Isimani Suite. Due to the consistency between high-grade metamorphic ages throughout the Isimani Suite, Collins *et al*. (2004) inferred that the eclogite-facies metamorphic event affected all rock units in the region.

A garnet-clinopyroxene-plagioclase-hornblende-quartz-bearing mafic gneiss interlayered with garnet-bearing metapelitic gneisses returned a U–Pb titanite age of 1996 ± 2 Ma, which was in-

terpreted to date the timing of down-pressure retrogression (Möller *et al*., 1995). A pegmatite dyke that cross-cuts amphibolite-facies fabrics that overprint the eclogite-facies assemblages yields a SHRIMP U-Pb zircon age of 1991 ± 2 Ma (Collins *et al*., 2004), providing further constraints on the timing of retrogression. Moreover, post-tectonic granites intruding the unconformably overlying Konse Group record a SHRIMP U–Pb zircon age of 1877 ± 7 Ma (Reddy *et al*., 2003), further constraining the interval of Isimani gneiss deformation and metamorphism.

Additionally, an early Palaeozoic greenschist-facies overprint has been identified in the Usagaran rocks. Rb–Sr biotite-whole-rock data for both Isimani gneisses and post-tectonic granites return ages that vary from 1956 ± 53 Ma to 432 ± 5 Ma (Wendt *et al*., 1972). Furthermore, discordant U–Pb rutile ages from metapelitic rocks show a lower intercept of 501 ± 26 Ma (Möller *et al*., 1995), similar to an $^{40}Ar/^{39}Ar$ muscovite age of 535.4 ± 2.3 Ma from Isimani orthogneisses (Reddy *et al*., 2004). The greenschist-facies metamorphism is likely to be associated with the development of the East-African Orogen (Fig. 2a; Möller *et al*., 1995; Reddy *et al*., 2004; Collins *et al*., 2004).

Three phases of deformation have been identified in the Usagaran Belt. The first (D_1) is recorded by sub-parallel foliations associated with compositional layering, and has been correlated with the development of eclogite-facies mineral assemblages (Mruma, 1989; Reddy *et al*., 2003). A second deformation event (D_2) defined by amphibolite-facies assemblages is the most pervasive in the Isimani Suite, and is recorded by well-preserved mylonitic foliations that overprint D_1-related fabrics (Reddy *et al*., 2003). Foliation geometries associated with D_2 are inferred to have formed during a transpressional sinistral shear regime and interpreted to be associated with the exhumation of the Isimani Suite, because these fabrics are interpreted to post-date the eclogite-facies metamorphic event (Reddy *et al*., 2003; Collins *et al*., 2004). However, because the structural analysis of Reddy *et al*. (2003) was confined to a region where relict eclogite is absent (Fig. 2b), the inference that D_2 fabrics overprint eclogite-facies assemblages is indirect. Furthermore, the primary structural orientation of the ~2.5–3 km thick domain of D_2 mylonitic amphibolite-facies gneisses is not well constrained because the bedding in the unconformably overlying Konse Group is moderately to steeply dipping (10–80°; Mruma, 1989). The third deformation event (D_3) described by Reddy *et al*. (2003) is characterised by top-to-SE extensional greenschist-facies shear zones that cut earlier structural features.

Previous interpretations of the tectonic evolution of the Usagaran Belt suggest that burial of the Isimani Suite occurred in response to south-east dipping subduction (present orientation) of a rift-

ed marginal zone of the Tanzanian Craton (Ring *et al.*, 1997; Reddy *et al.*, 2003). This model describes a burial and exhumation history whereby all Isimani rock types are interpreted to form part of a coherent subducting slab system. However, in the absence of robust *P–T* constraints, it remains unclear whether the Usagaran eclogites and the high-strain foliated rocks described by Reddy *et al.* (2003) share a common *P–T* evolution as part of a coherently subducted and exhumed slab, or were juxtaposed during the exhumation of the eclogite-facies rocks. Therefore, the aim of this study is to determine if the Isimani Suite is a coherent metamorphic system or a system that contains fundamental tectonic boundaries that separate domains of contrasting *P–T* histories.

2.1 Sample selection and petrography

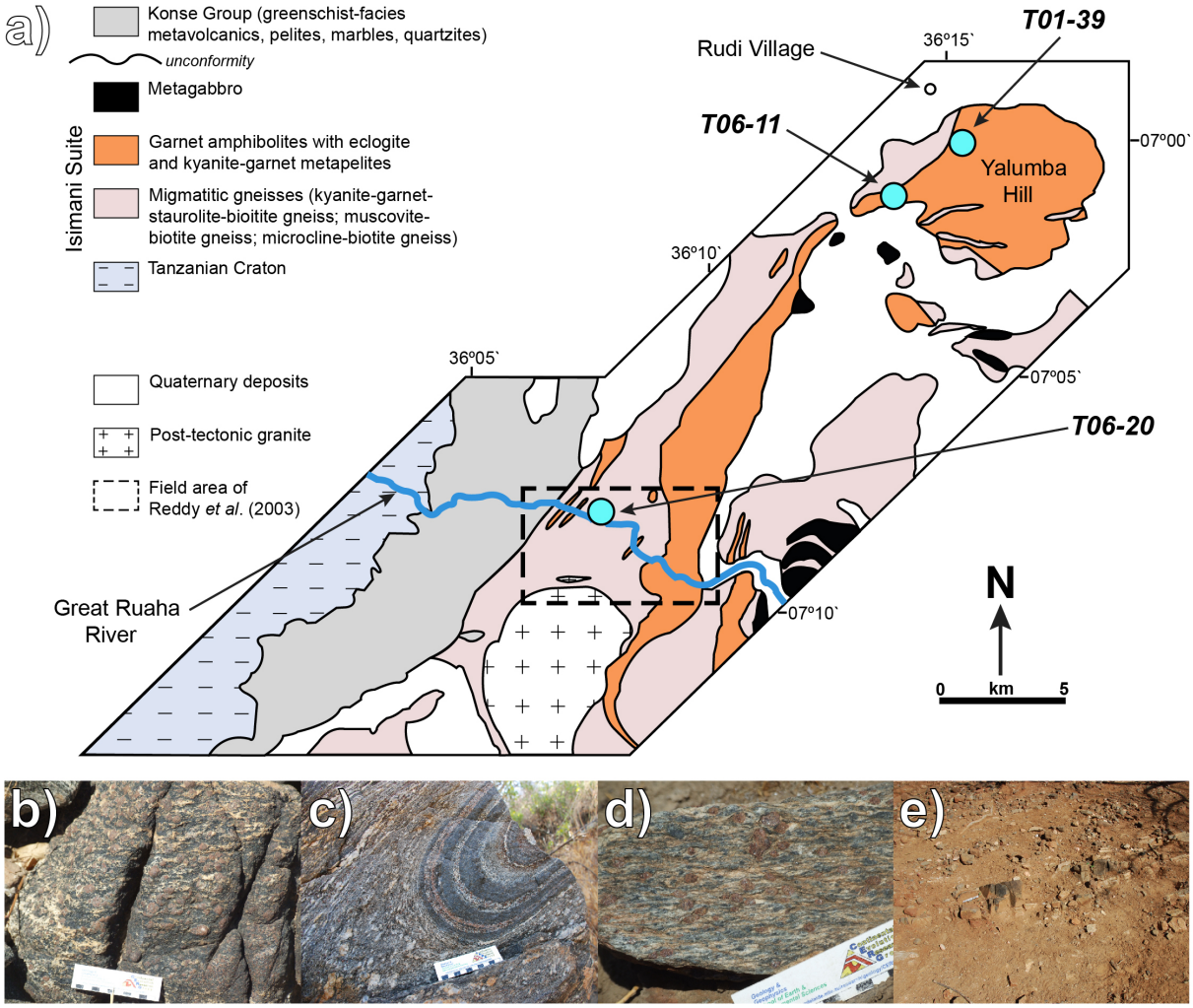


Fig. 3. (a) Geological map of the Usagaran Belt showing the sample localities (blue circles) at Yalumba Hill and the great Ruaha River. Modified from Reddy et al. (2003) and Mruma (1989). (b) Garnet-clinopyroxene-amphibole migmatitic mafic gneiss, Great Ruaha River. (c) Folded garnet-bearing metapelitic and mafic interlayered migmatitic gneisses, Great Ruaha River. (d) Foliated garnet-kyanite metapelitic gneiss with parallel-to-foliation quartzofeldspathic domains, Great Ruaha River – location of sample T06-20. (e) Mafic gneiss, Yalumba Hill – proximal to the location of sample T06-11.

Three rocks have been investigated in this study. Two mafic samples come from the inferred relict eclogite domain. The relict eclogite samples are T01-39 (mafic granofels) and T06-11 (mafic gneiss), and were collected from Yalumba Hill (Fig. 3a). A metapelitic sample comes from the system of highly deformed gneisses described by Reddy *et al.* (2003), which are interpreted to overprint the eclogite-facies assemblages and therefore record exhumation conditions (Reddy *et al.*, 2003; Collins *et al.*, 2004). Migmatitic metapelitic gneiss T06-20 was collected from an outcrop along the Great Ruaha River (Fig. 3a; Table 2).

Table 2. Sample locations and mineral descriptions.

Sample T01-39 mafic granofels

Sample T01-39 is unfoliated and contains the mineral assemblage listed in Table 2. Medium-grained (1–2.5 mm) garnet contains primary inclusions of quartz, plagioclase, rutile, amphibole and clinopyroxene (Fig. 4a-d). Rare titanite is also included within garnet porphyroblasts. Plagioclase coronae separate garnet porphyroblasts from matrix clinopyroxene (Fig. 4e). Clinopyroxene is fine- to coarse-grained (0.5–2 mm), is overprinted at its margins by subhedral to anhedral amphibole of variable grain size (0.1–0.5 mm) and commonly contains abundant inclusions of plagioclase, forming composite grains (Fig. 4f). Subhedral to euhedral amphibole of medium to coarse grain size (0.5–2.5 mm) also occurs in the sample (Fig 4g). In the matrix, veins 5–6 mm in width consist of quartz, rare plagioclase and fine-grained rutile, and have irregular boundaries with the garnet-bearing matrix (Fig. 4h). The remainder of the matrix comprises subhedral quartz (<0.5 mm), subhedral fine- to medium-grained plagioclase (0.2–0.5 mm), fine- to medium-grained ilmenite (<1 mm) — which preserves fine-grained exsolution of hematite (<0.5 mm) — and minor rutile, apatite, titanite and zircon. Despite the occurrence of rare zircon, there is insufficient sample material to undertake zircon geochronology.

Sample T06-11 mafic gneiss

Unlike T01-39, sample T06-11 has a strong gneissic foliation defined by medium-grained bands of garnet and quartz, which are interlayered with fine-grained clinopyroxene-rich domains that also contain fine-grained orthopyroxene (Fig. 5a). Subhedral, equigranular garnet porphyroblasts (<1–1.5 mm) contain quartz, plagioclase, clinopyroxene and less common rutile, amphibole and zircon. Garnet is separated from fine-grained (<0.5 mm), anhedral to subhedral clinopyroxene by plagioclase coronae. Matrix clinopyroxene hosts intergrowths of plagioclase (Fig. 5b), although these are typically poorly preserved due to the development of a strong orthopyroxene-bearing foliation. Veins parallel to the foliation contain

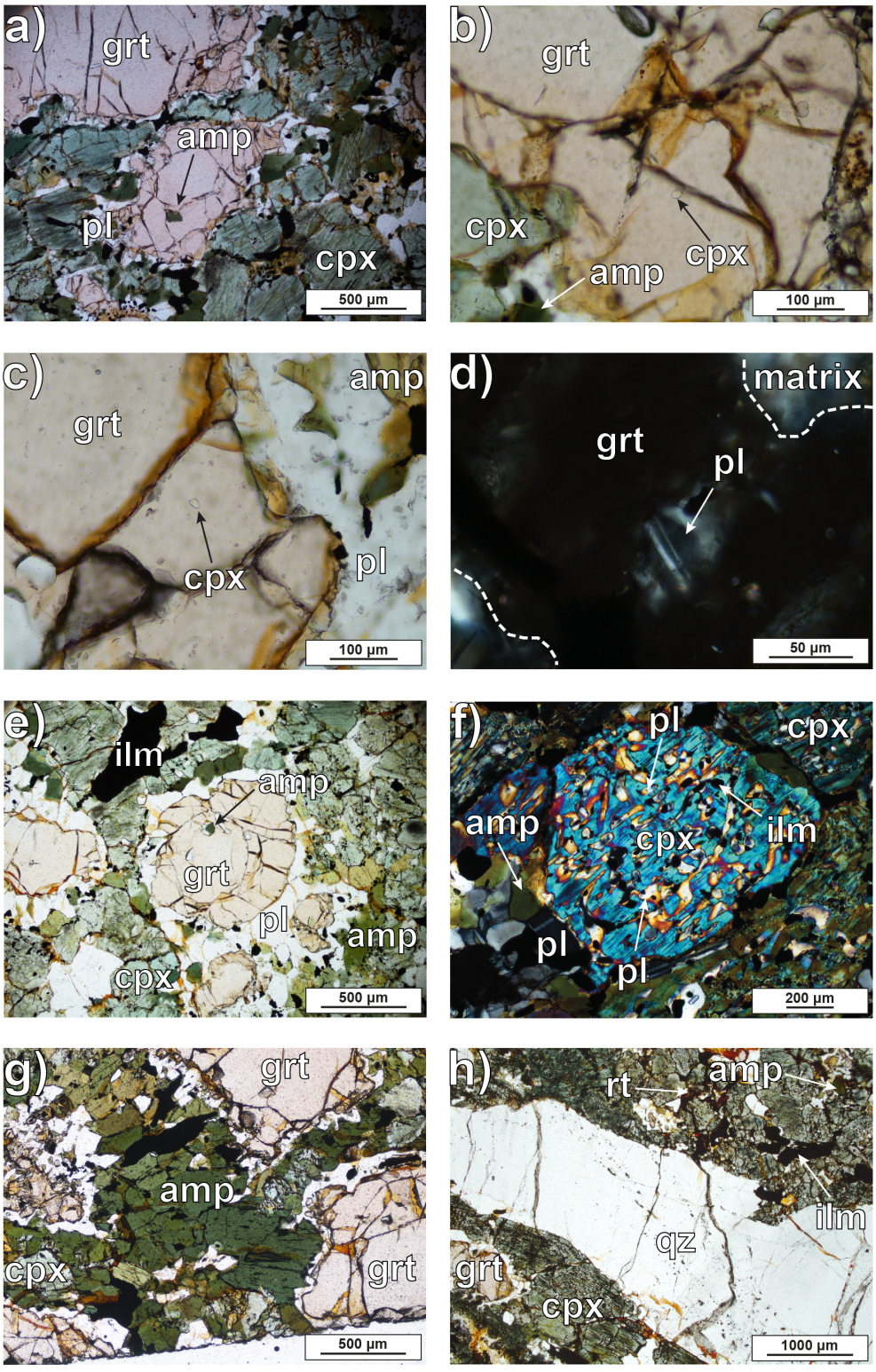


Fig. 4. Sample T01-39. (a-d) Inclusions of amphibole, clinopyroxene and plagioclase in garnet. (e) Garnet separated from clinopyroxene by a plagioclase coronae. Amphibole overprints matrix clinopyroxene. (f) Retrograde clinopyroxene with intergrowths of plagioclase in XPL. (g) Coarse-grained amphibole is separated from garnet by plagioclase. (h) Coarse-grained quartz vein. Mineral abbreviations after Whitney and Evans, (2010).

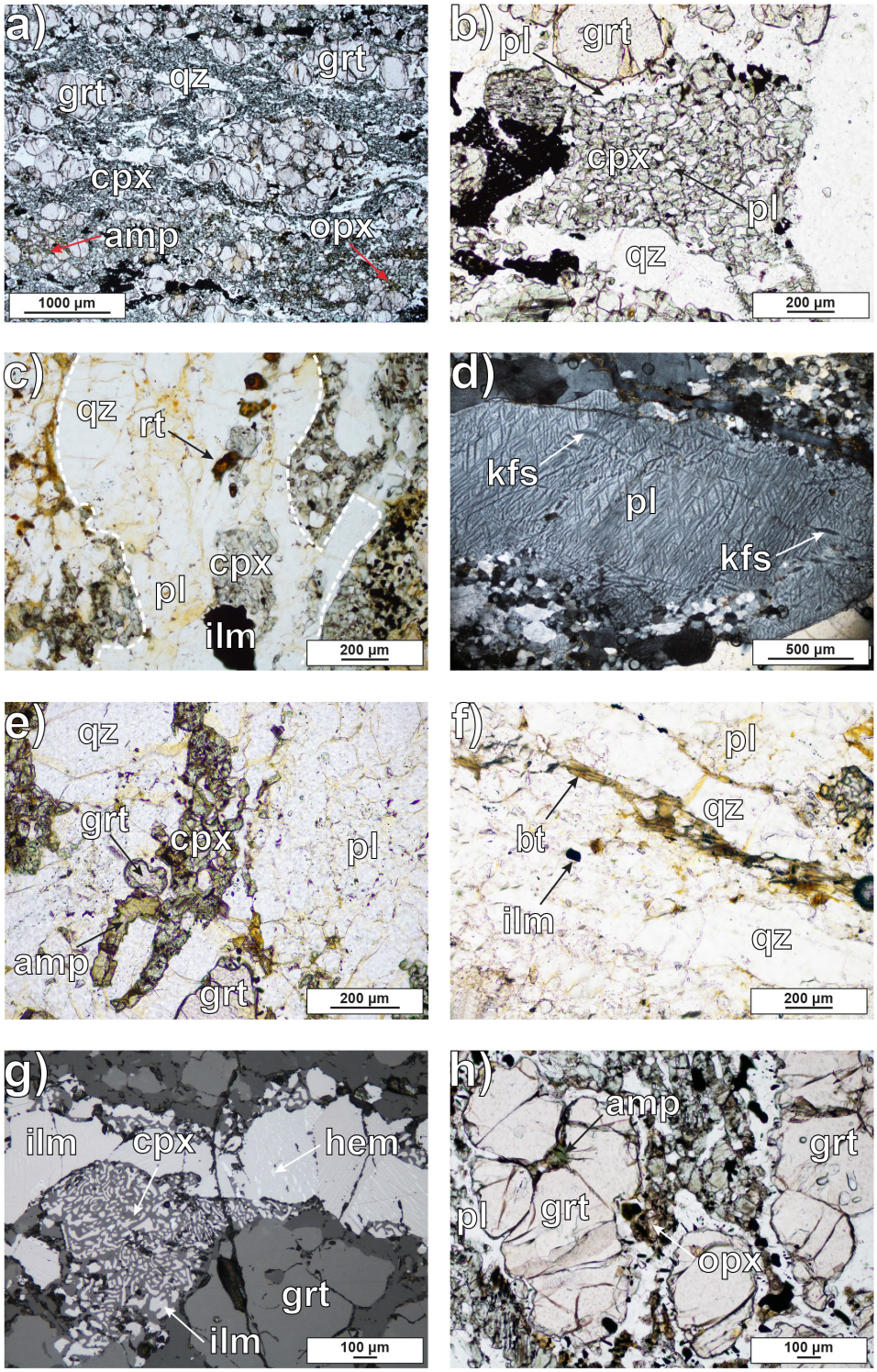


Fig. 5. Sample T06-11. (a) Coarse-grained domains comprising garnet and quartz alternating with fine-grained domains of clinopyroxene and minor orthopyroxene. (b) Retrograde clinopyroxene intergrown with plagioclase. (c-f) Quartz-feldspar-rutile-garnet-clinopyroxene-amphibole-biotite-bearing veins. The white dashed lines in (c) represent the boundary between the veins and the matrix. Included is an XPL image of antiperthitic plagioclase in a vein. (g) Reflected light image of ilmenite with hematite exsolution. Rimming ilmenite are intergrowths of clinopyroxene and ilmenite. (h) Orthopyroxene associated with clinopyroxene.

equal proportions of quartz (0.5–1.5 mm) and plagioclase (0.5–2.5 mm). They also contain rutile (which is commonly rimmed by ilmenite), garnet, clinopyroxene, and minor amphibole and biotite (Fig. 5c-f). The veins are thin (<4 mm) and sparse, comprising no more than ~2% of the sample. Plagioclase grains within the veins typically show antiperthite exsolution lamellae (Fig. 5d). Fine- to medium- grained ilmenite (0.2–1 mm) contains lamellae of hematite and in some instances, forms fine-grained (<0.1 mm) symplectite structures with clinopyroxene (Fig. 5g). The rest of the matrix is characterised by fine- to medium-grained quartz and plagioclase, fine-grained amphibole that overprints clinopyroxene, fine-grained orthopyroxene associated with clinopyroxene (Fig. 5h), and rare titanite, apatite and zircon.

Interpretation of mafic rock peak assemblages

Mafic samples T01-39 and T06-11 preserve mineral reaction microstructures which obscure their peak metamorphic assemblages. Interpretation of the petrological relationships is therefore required to determine the peak assemblages for the purposes of *P–T* mineral equilibria modelling.

Garnet is unambiguously a peak mineral in sample T01-39, though the garnet rims that were present at peak metamorphic conditions are no longer preserved as a result of the formation of plagioclase coronae (Fig. 4e). Inferred texturally peak amphibole also occurs in the sample, where the grains are coarse and separated from garnet by inferred retrograde plagioclase (Fig. 4g). However, the interpretation of peak rutile and omphacite is more ambiguous. In both T01-39 and T06-11, rutile inclusions are preserved within garnet and rare fine-grained relics of rutile occur throughout the rock matrix, suggesting the widespread occurrence of medium-grained matrix ilmenite may have developed at the expense of rutile. In T06-11, rutile also occurs at the margins of quartz-feldspar-bearing veins (Fig. 5c). These relationships strongly suggest that rutile was present at peak metamorphic conditions.

Na-poor clinopyroxene is commonly intergrown with fine-grained inclusions of plagioclase (Fig. 4f) and these textures strongly resemble those proposed by other workers to reflect the former presence of omphacite (e.g. Sklyarov *et al.*, 1998; Lombardo and Rolfo, 2000; Anderson and Moecher, 2007; Chu *et al.*, 2016; Li *et al.*, 2018; Loose and Schenk, 2018; Müller *et al.*, 2018). The interpretation that an omphacitic clinopyroxene was present at peak metamorphic conditions is supported by the reintegration of intergrown clinopyroxene and plagioclase compositions in T01-39 which yield an average ferric-sodic composition for precursor clinopyroxene (section 5.1.2). The record of the peak assemblage for mafic sample T06-11 has been significantly affected by the development of a pervasive post-peak orthopyroxene-bearing foliation (Fig. 5h). The mylonitic foliation has com-

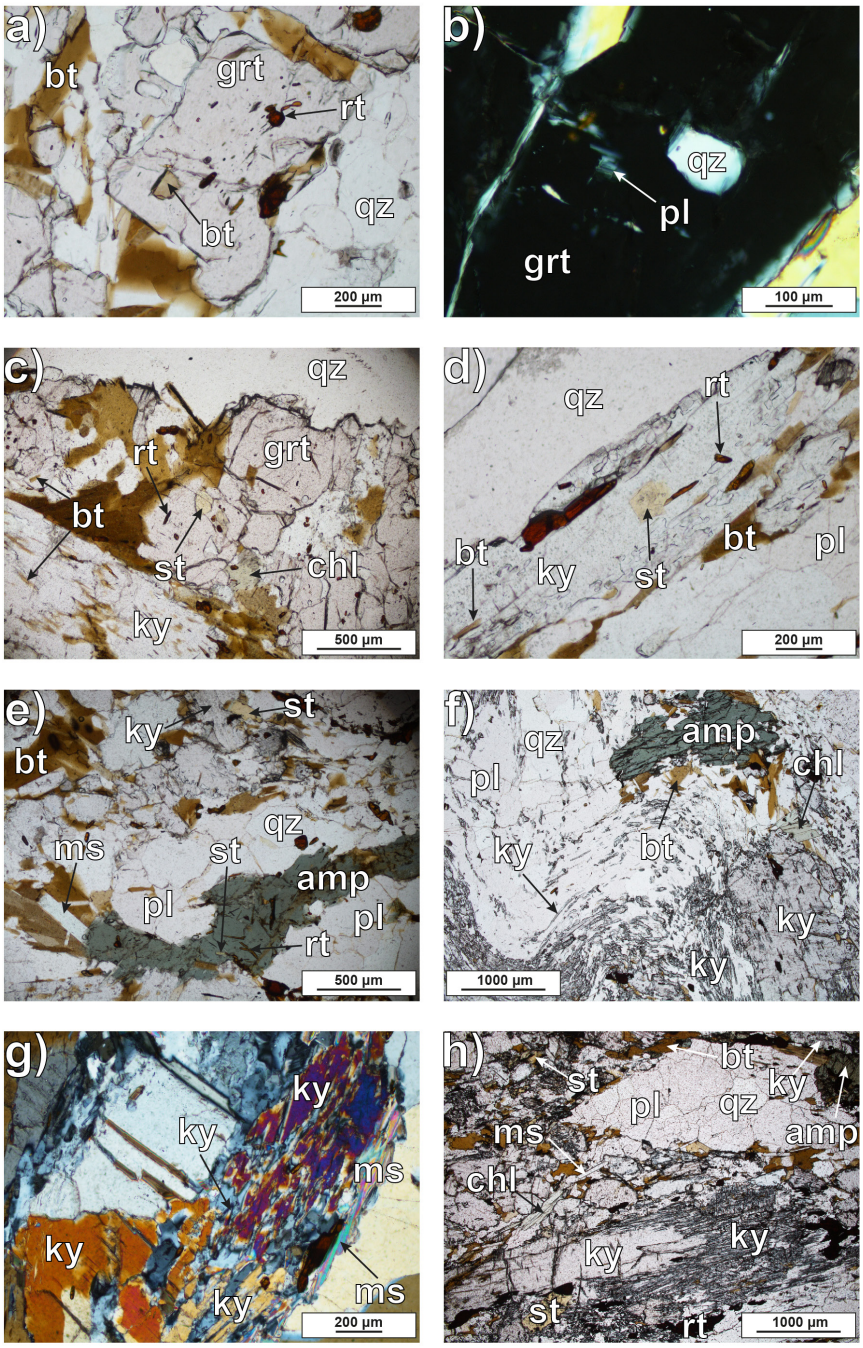


Fig. 6. Sample T06-20. (a) Anhedral garnet with inclusions of biotite and rutile. Biotite replaces garnet at its margin. (b) Plagioclase and quartz inclusions in garnet. (c) Staurolite and rutile hosted by garnet, biotite included in medium-grained kyanite, and chlorite and biotite replacing both garnet and kyanite. (d) Kyanite hosts inclusions of staurolite, rutile and biotite. (e) Coarse-grained amphibole hosts rutile and staurolite. Muscovite and biotite overprint amphibole, and staurolite overprints kyanite. Also shown is a domain of coarse-grained quartz and plagioclase. (f) Coarse-grained amphibole and kyanite – both defining a crenulated foliation. Kyanite needles are folded, and chlorite replaces kyanite. (g) Medium-grained kyanite replaced by fine-grained kyanite needles. Secondary muscovite overprints kyanite. (h) Porphyroblastic kyanite overprinted by staurolite, chlorite, muscovite and secondary kyanite. A coarse-grained domain of plagioclase and quartz is parallel to the foliation. Amphibole and biotite overprint kyanite at the top of the photomicrograph.

promised the preservation of clinopyroxene-plagioclase intergrowth textures making it difficult to infer a precursor clinopyroxene composition. However, relict matrix clinopyroxene with inclusions of plagioclase are still preserved in the sample in rare instances (Fig. 5b), suggesting the sample contained omphacite prior to its reworking by the orthopyroxene-bearing foliation. The interpretation of peak omphacite is additionally supported by the observation of omphacite included within garnet from a mafic eclogite in the same region (e.g. Möller, 1995).

Both mafic samples contain volumetrically minor (<5%) veins whose origin is ambiguous. The coarse-grained quartz veins in unfoliated sample T01-39 show irregular contact relationships with the surrounding matrix (Fig. 4h), suggesting they could either be a part of the matrix assemblage, or they may have predated it. A conservative interpretation is that these veins formed when amphibole grew at the expense of clinopyroxene. This interpretation is consistent with the observation of significant proportions of amphibole in the sample (~10 vol%; Table S1), and the observation of amphibole overprinting matrix clinopyroxene (Fig. 4f). Alternatively, the veins in T01-39 could either be externally derived or have formed during prograde eclogitization as the rock underwent dehydration (e.g. Spandler and Hermann, 2006; Gao *et al.*, 2007). The veins in T06-11 constitute a minor proportion of the rock (~2%) and are quartzofeldspathic with inclusions of garnet, clinopyroxene, rutile rimmed by ilmenite, amphibole, and biotite (Fig. 5c-f; section 3.2). These veins are parallel to the orthopyroxene-bearing fabric and contain a recrystallised quartz matrix (Fig. 5c-f). It is our tentative interpretation that these veins developed during the rock's post-peak *P–T* history before the development of the retrograde orthopyroxene-bearing mylonitic fabric. However, there is insufficient petrological evidence in this sample to determine whether the veins were sourced internally — possibly from the crystallisation of a small volume of partial melt or the liberation of mineral-bound fluids — or externally.

Sample T06-20 migmatitic metapelitic gneiss

Sample T06-20 has a well-developed foliation and contains the minerals listed in Table 2. Poikiloblastic garnet porphyroblasts (8–10 mm) are enclosed by a well-developed fabric dominated by kyanite, plagioclase, quartz, and biotite, with less common amphibole, staurolite, muscovite and chlorite. Garnet contains inclusions of staurolite, biotite, quartz, plagioclase and rutile (Fig. 6a-c). Coarse-grained kyanite hosts inclusions of staurolite, biotite, rutile and minor muscovite (Fig. 6d). Matrix amphibole is medium- to coarse-grained (0.5–1.5 mm), has inclusions of biotite, rutile and rare staurolite (Fig. 6e), and in some cases texturally overprints garnet and kyanite porphyroblasts. Matrix staurolite occurs as fine- to medium-

grained subhedral grains (0.2–0.8 mm) located at the margins of coarse-grained kyanite (1–4 mm) and garnet (Fig. 6e). Fine-grained, subhedral chlorite is associated with post-deformational kyanite needles at the margins of porphyroblastic kyanite (Fig. 6f). These kyanite needles are typically associated with fine-grained muscovite (Fig. 6g). Millimetre-scale domains comprising comparatively medium- to coarse-grained equigranular plagioclase and quartz form aggregates parallel to the foliation (Fig. 6h). The remainder of the matrix contains medium-grained rutile (0.5–1 mm), plagioclase (0.5–1.5 mm), quartz (0.5–2 mm), minor apatite and minor zircon. Zircon is also preserved as inclusions in coarse-grained kyanite porphyroblasts. T06-20 contains the inferred prograde assemblage, kyanite, garnet, plagioclase, biotite, quartz, amphibole, staurolite, muscovite and rutile. The inferred peak assemblage from the petrology is kyanite, garnet, plagioclase, biotite, quartz, amphibole and rutile. The retrograde assemblage comprises the peak assemblage with the addition of staurolite, muscovite and chlorite.

3. Analytical methods

3.1 Mineral chemistry

Major element mineral compositions were obtained using electron microprobe analysis (EPMA) undertaken using a CAMECA SXFive electron microprobe at the University of Adelaide. Mineral composition analyses were obtained using a beam current of 20 nA, a beam diameter of 2 μm and an accelerating voltage of 15 kV. Calibration procedures were undertaken on both synthetic and natural standards produced by Astimex Pty Ltd. and data reduction was performed in Probe for EPMA by Probe Software Inc.

3.2 Mineral equilibria forward modelling

Mineral equilibria forward models were calculated using the thermodynamic calculation program THERMOCALC v.340 and v.345, with the internally-consistent thermodynamic dataset ds62 of Holland and Powell (2011). Pressure–temperature (*P–T*) models for mafic samples were calculated using the model chemical system, MnNCFMASHTO ($MnO–Na_2O–CaO–FeO–MgO–Al_2O_3–SiO_2–H_2O–TiO_2–Fe_2O_3$) and the 'metabasite set' of activity-composition (*a–x)* relations outlined in (Green *et al.*, 2016). The metapelitic sample was modelled in the system MnNCKFMASHTO using the *a–x* models of White *et al.* (2014a, b), with the addition of clinoamphibole from Green *et al.* (2016). Mineral abbreviations in all pseudosections were used from THERMOCALC.

Mineral modal proportions in each sample were determined by first acquiring Mineral Liberation Analysis (MLA) images of each thin section using an FEI Quanta MLA–600 scanning electron microscope at the University of Adelaide. Given gar-

net in sample T06-20 is very coarse-grained, the modal proportion of garnet in this sample was estimated from two rock-blocks (~8 cm x 4cm), giving a more representative estimate than obtained from a smaller thin-section. Mn enrichment at the garnet rims in sample T06-20 (section 5.1.1) suggests the garnet rims may have undergone dissolution. Therefore, determination of the modal proportion of peak metamorphic garnet in sample T06-20 was undertaken following the method of Kohn and Spear (2000), which accounts for compositional net-transfer and dissolution at the garnet rim. EPMA semi-quantitative compositional maps for three garnet grains in sample T06-20 were used to determine the amount of garnet dissolution, and therefore, the precursor modal proportion of garnet (section 5.1.1). Image analysis software was utilised to perform pixel counting on the minerals identified in the MLA images, and the resultant proportions in vol% were converted to atom-based mol% using molar volume data from Holland and Powell (2011) for direct comparison with THERMOCALC. Mineral modal proportion data is provided in Table S1. Modelled mineral modal proportions and mineral compositions were contoured using the software TCInvestigator (Pearce *et al*., 2015).

The whole-rock geochemical compositions for all samples were acquired using X-ray fluorescence spectrometry, undertaken at Franklin and Marshall College, Pennsylvania. The results from whole-rock geochemical analysis are given in Table 3. The whole-rock compositions were adjusted to correct for components that influence mineral stability but cannot be modelled. For instance, apatite, which is present in all samples in minor proportions of ~1%, contains significant CaO, but cannot be modelled in the MnNCKFMASHTO chemical system. Thus, a CaO correction was applied to all bulk-rock compositions based on the amount of P_2O_5. Additionally, garnet core

	T01-39	T06-11	T06-20
SiO2	47.13	47.13	55.1
TiO2	1.80	1.51	2.06
Al2O3	13.3	16.26	30.5
Fe2O3	17.54	15.14	5.63
MnO	0.30	0.30	0.053
MgO	5.90	5.54	1.78
CaO	11.21	11.29	1.48
Na2O	2.92	2.32	1.065
K2O	0.07	0.08	0.848
P2O5	0.11	0.18	0.198
Total	100.32	99.75	98.714
H2O*	0.422	0.076	0.835

Table 3. Bulk rock geochemistries.

compositions in metapelitic sample T06-20 and mafic sample T06-11 were subtracted from their respective bulk-rock compositions to create matrix-dominated compositions prior to performing *P–T* calculations aimed at addressing the peak to retrograde *P–T* evolution of these samples. Due to the coarse-grained nature of the garnet porphyroblasts in this sample and the preservation of garnet growth zonation (section 5.1.1), it is reasonable to suspect that garnet core compositions were partially chemically isolated from the bulk-rock composition and did not form part of the peak metamorphic equilibrium bulk composition (Stüwe, 1997). Compositional information from T06-11 garnet (section 5.1.1) indicates that only the rims were likely in equilibrium with the retrograde mylonitic fabric, thereby supporting the approach used in mineral equilibria modelling. Garnet core compositions were retained in the bulk-rock composition for *P–T* calculations intended on interrogating the prograde history of sample T06-20.

To constrain the oxidation state of each sample, Fe_2O_3 values were calculated from electron microprobe analyses of Fe^{3+} bearing minerals following Droop (1987). To assess the sensitivity of mineral equilibria modelling calculations with respect to the oxidation state, pressure–composition (*P–Mo*) models, where 'Mo' denotes a proportion of Fe_2O_3, were calculated for all samples prior to *P–T* modelling (Fig. S1; Fig. S2; Fig. S3).

The loss of ignition (LOI) values obtained from whole-rock geochemical analyses were not considered an accurate measure of the mineral-bound H_2O content due to minor amounts of secondary alteration present in all samples. Instead, in cases where samples were not modelled with H_2O in excess (e.g. section 5.3), the H_2O content of each sample was constrained using the average composition of hydrous minerals (amphibole, biotite, staurolite and muscovite) derived from electron microprobe analyses and their modal proportions. Sample T01-39 is interpreted to contain three textural generations of amphibole (section 3.1) and the total amount of amphibole in the rock was used to determine its H_2O content. Therefore, a $P–M_{H2O}$ model was calculated to monitor how sensitive the inferred peak assemblage is to varying H_2O content (Fig. S4). Here, a 'dry' composition calculated from the proportion of inferred peak amphibole was treated as one end-member and a 'wet' composition calculated from the total amount of amphibole in the sample was treated as the second end-member composition. We also acknowledge the possibility that a small proportion of volatiles might reside in nominally anhydrous minerals (e.g. Sheng and Gong, 2017).

Table 3. Whole-rock geochemical analyses for all samples (in wt%). Note: the whole-rock H_2O values provided are those calculated from hydrous mineral electron microprobe analyses. More information regarding these calculations is provided

in the text.

3.3 Zr-in-rutile thermometry

Zr-in-rutile thermometry was undertaken using a RESOlution LR 193 nm Excimer laser system coupled with an Agilent 7900x ICP–MS at the University of Adelaide. The instrument conditions were: a 5 Hz laser repetition rate, a 5 J/cm^2 fluence, a 25 kV operating voltage and 70 seconds total acquisition time encompassing 30 seconds of background measurement and a further 40 seconds of ablation. The spot size was adjusted between 13 μm and 29 μm depending on the rutile grain size. Trace element concentrations were calibrated to the synthetic glass standard, NIST-610 (Zr = 448 ± 9 ppm) and accuracy was monitored using the glass standard, GSD-1G (42 ± 2 ppm; Jochum *et al.*, 2010; Jochum *et al.*, 2011). In this study, NIST-610 yielded an average Zr concentration of 448 ± 4.8 ppm (n = 24, 2σ) and GSD-1G yielded an average Zr concentration of 38.2 ± 0.7 ppm (n = 60, 2σ). Data processing was undertaken using Iolite (Hellstrom *et al.*, 2008; Woodhead *et al.*, 2008; Paton *et al.*, 2011), to correct for instrument drift and downhole fractionation effects. Ti was used as the internal reference element for all samples where the concentration of Ti in rutile (in wt%) was acquired from electron microprobe analyses of rutile. Temperature estimates were calculated from Zr concentrations (in ppm) using the calibration of Tomkins *et al.* (2007).

Zr-in-rutile temperature estimates were ascribed uncertainties of ~3.4% (T01-39), ~3.2% (T06-11) and ~4.2% (T06-20). Uncertainties were calculated through the quadrature summation of relative errors inherent in the calculations. Considered in the calculation: (1) the error associated with the pressure (± 1 kbar), (2) the 2σ errors associated with the measurement of Zr concentrations (± 1.6% for T01-39, ± 1.1% for T06-11 and ± 2.9% for T06-20), and (3) the error accompanying the analytical calibration of the Zr-in-rutile thermometer (assigned as ± 3% after Watson *et al.* (2006) given no error value is provided in the Tomkins *et al.* (2007) calibration).

Rutile grains (50–200 μm) hosted in thin-section as inclusions in garnet porphyroblasts were targeted in samples T01-39 and T06-20. Sample T06-11 lacks garnet-hosted rutile grains of sufficient size for LA–ICP–MS analysis, so instead, rutile grains (up to 300 μm) located at the margins of quartzofeldspathic veins were selected (Fig. 5c). Rutile grains in thin-section were imaged using a back-scattered electron (BSE) detector coupled with a FEI Quanta MLA–600 scanning electron microscope (SEM) to identity any evidence of zirconium exsolution.

4. Results

4.1 Mineral Chemistry

Representative electron microprobe analyses are provided in Tables 4–6. The ranges of measured compositional values for oxide species, element ratios and end-member proportions in selected minerals are shown in Table 7. The definitions of all notations quoted in the text are outlined in Table 7.

Garnet

Mafic samples T01-39 and T06-11 contain garnet dominant in almandine and grossular where their respective core proportions range from 0.574–0.591 (X_{alm}) and 0.227–0.242 (X_{grs}), and 0.462–0.470 (X_{alm}) and 0.299–0.310 (X_{grs}; Fig. 7a-d; Table 7). T01-39 shows core-rim compositional zoning in X_{alm}, X_{py} and X_{sps}. X_{alm} decreases from core to rim, X_{py} increases and X_{sps} decreases significantly (Table 7). All compositional variables remain approximately constant from core to rim in T06-11 with the exception of an increase in X_{sps} near the garnet rims, from 0.014–0.016 in the core to 0.015–0.023 at the rim. Garnet in metapelitic sample T06-20 is predominantly almandine and pyrope with core proportions of 0.659–0.665 (X_{alm}) and 0.166–0.177 (X_{py}; Table 7). In sample T06-20, X_{alm} slightly increases from core to rim, X_{py} increases from core to mantle, flattening at the rim, and X_{grs} decreases from core to rim (Fig. 8a-d; Table 7).

Three coarse-grained garnets from sample T06-20 show an increase in Mn at the rim (Fig. 8a-d), likely resulting from net-transfer reactions and garnet dissolution during the rock's retrograde evolution. Following the method of Kohn and Spear (2000) to determine the amount of garnet dissolution, it is estimated that ~30% of garnet was consumed as a consequence of net-transfer reactions. This method assumes garnet was the sole reservoir of Mn, the system was compositionally closed, and the Mn composition of the precursor garnet rim was similar to that of the interior of the garnet.

Pyroxene

In contrast to Möller *et al.* (1995), no omphacitic clinopyroxene was found in this study, despite extensive examination of clinopyroxene inclusions in garnet. Clinopyroxene in samples T01-39 and T06-11 is diopsidic and compositionally unzoned. X_{dio} values in matrix clinopyroxene range between 0.699–0.753 in T01-39 and 0.733–0.822 in T06-11 (Table 7). Matrix clinopyroxene X_{jd} proportions range from 0.027–0.066 in both mafic samples and there is no increase in X_{jd} values in clinopyroxene included within garnet with respect to matrix clinopyroxene (X_{jd} = 0.025–0.028). Clinopyroxene preserved in both mafic samples has been compositionally modified during retrogression and as such, is not representative of clinopyroxene present at peak metamorphic conditions. The composition for reintegrated clinopyroxene (Table 4) is ferric-omphacitic and gives an Na/(Na + Ca) val-

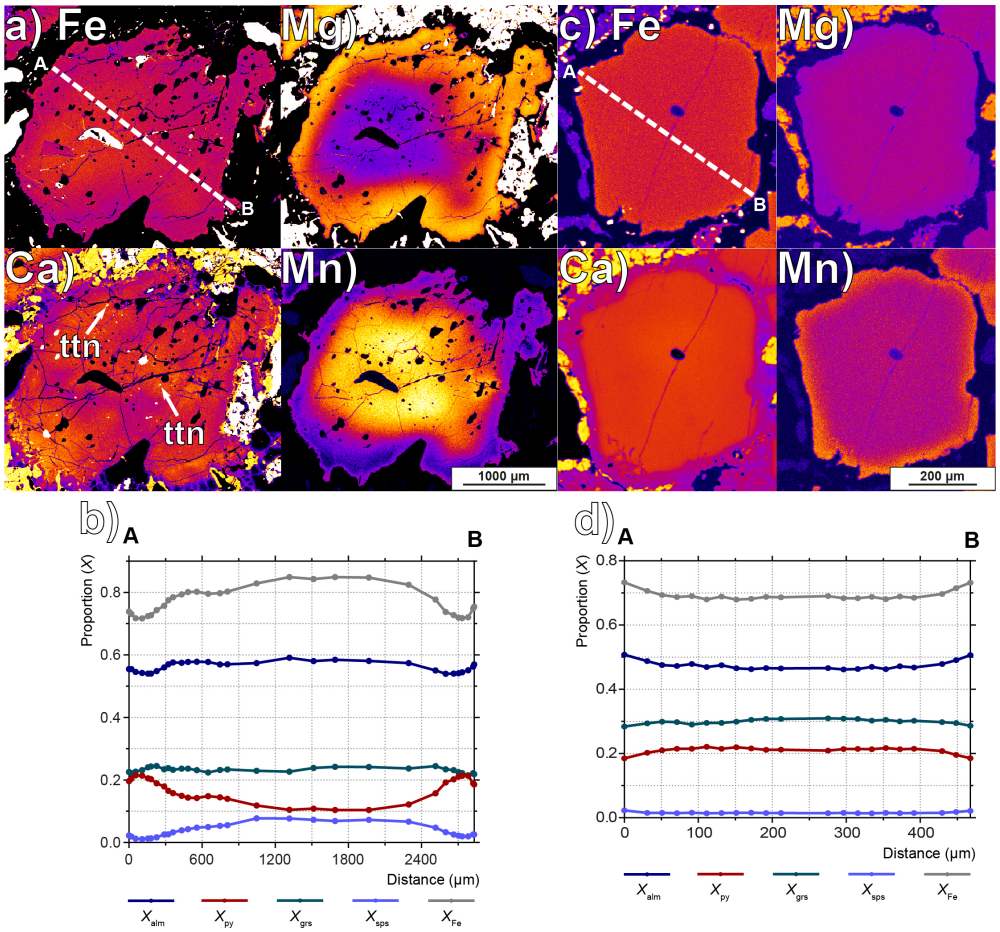


Fig. 7. EPMA semi-quantitative major element compositional maps and quantitative rim-to-rim traverses across garnets from mafic samples (a-b) T01-39 and (c-d) T06-11. In (a) and (c), warmer colours reflect greater relative major element concentrations. In (b) and (d), the colour-coded traverses correspond to the proportions of each garnet end-member (Table 7). In (a), titanite inclusions in garnet are annotated on the Ca composition map.

ue of 0.20, consistent with the accepted definition of an omphacitic clinopyroxene (Morimoto *et al.*, 1988). The reintegrated composition is the product of the summation of the wt% oxide compositions of clinopyroxene, plagioclase and titano-hematite (i.e. $SiO_{2(cpx)}$ + $SiO_{2(pl)}$ + $SiO_{2(hem)}$; + $TiO_{2(cpx)}$ + $TiO_{2(pl)}$ + $TiO_{2(hem)}$; …), all of which are the constituents of the clinopyroxene-plagioclase intergrowth textures preserved in T01-39 (Fig. 4f). The Na_2O content in minor amphibole overprinting symplectic clinopyroxene at its margin was not accounted for in the reintegration of the clinopyroxene composition and therefore, the Na/(Na + Ca) value quoted above is considered a minimum estimate. Unretrogressed orthopyroxene is rare in sample T06-11 with only one grain unaffected by secondary alteration. The composition of orthopyroxene is enstatitic-ferrosilitic (X_{en} = 0.554 and X_{fs} = 0.353) and X_{Fe} = 0.376 (Table 7).

Amphibole

Amphibole in T01-39 and T06-11 has a tschermakite-pargasite composition. In T01-39, amphi-

bole included within garnet has a composition dominant in pargasite, more so than in matrix amphibole. X_{Fe} values in T01-39 amphibole range from 0.277–0.387 with the largest values corresponding to amphibole included in garnet (Table 7) and X_{Fe} values in T06-11 amphibole range from 0.219–0.236. X_{Ti} values in matrix amphibole from T01-39 and T06-11 are comparable (0.063–0.086 and 0.060–0.083, respectively) and amphibole included in garnet in T01-39 shows a slightly smaller X_{Ti} range with respect to that in matrix amphibole (0.065–0.067). T06-20 amphibole has a tschermakite-pargasite composition with an X_{Fe} of 0.456–0.475 and an X_{Ti} of 0.022–0.025.

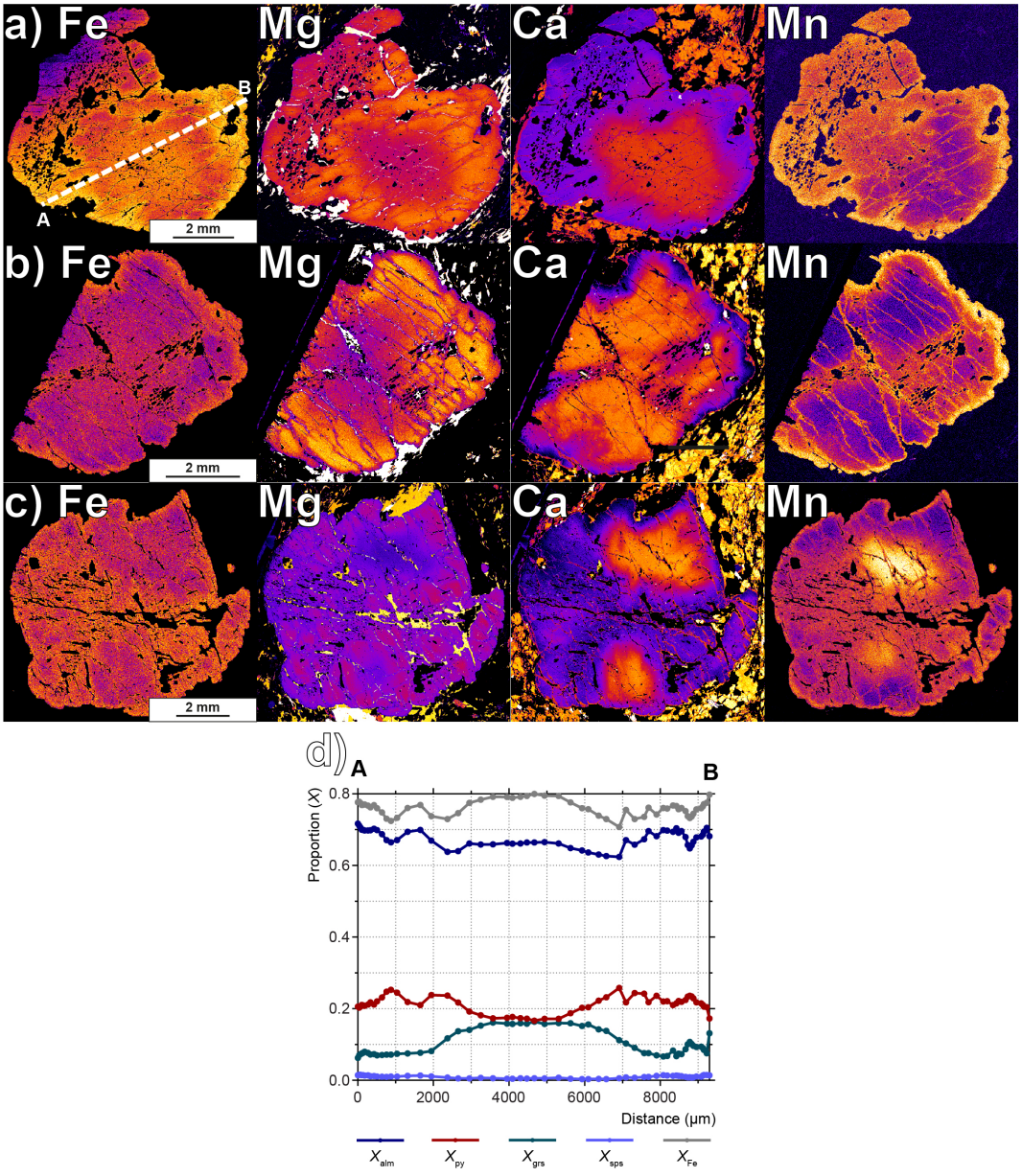


Fig. 8. (a, c, d) EPMA semi-quantitative major element compositional maps for three garnets from metapelitic gneiss sample T06-20. Warmer colours reflect greater relative major element concentrations. (b) Quantitative rim-to-rim traverses across the T06-20 garnet that was compositionally mapped in (a). The colour-coded traverses correspond to the proportions of each garnet end-member (Table 7).

Plagioclase

In all samples, plagioclase is albitic. Sample T01-39 has higher X_{ab} values in plagioclase included within garnet (0.760–0.834) than in matrix plagioclase (0.600–0.782; Table 7).

Staurolite

Matrix staurolite and staurolite included in both garnet and kyanite from sample T06-20 have comparable MgO (wt%) contents of 1.884% to 2.357% and 1.954% to 2.334%, respectively (Table 7). ZnO (wt%) content in staurolite ranges from 1.478% to 1.702% in matrix staurolite and 1.446% to 1.842% in staurolite inclusions, showing no difference between texturally distinct domains.

Mica

Biotite in sample T06-20 contains negligible contents of MnO (0–0.010 wt%) and minor quantities of TiO_2 (1.538–1.558 wt%; Table 7). X_{Mg} in biotite ranges from 0.620–0.627. X_{Mg} in muscovite ranges from 0.494–0.584, the MnO content ranges from 0.001–0.005 and TiO_2 content ranges from 0.445–0.467 wt% (Table 7).

4.2 Zr-in-rutile thermometry

Zr-in-rutile thermometry used in this study considers the textural setting of the rutile grains, their resultant Zr-in-rutile derived temperature estimates, and how these relate to the different stages of the *P–T* evolution for each sample. All samples contain matrix zircon, garnet- and/or kyanite-hosted zircon (e.g. Fig. 9c), and abundant quartz, suggesting that rutile could have grown in the presence of both zircon and quartz. However, given the small proportion of zircon and the apparent absence of zircon in direct contact with rutile grains in all samples, it is unclear whether equilibrium was established. Therefore, Zr-in-rutile derived temperatures are treated as minimum estimates (Zack *et al.*, 2004; Taylor-Jones and Powell, 2015). The presence of Zr micro-exsolution textures in rutile grains cannot be precluded, however, detailed inspection of rutile grains from all samples using SEM imaging shows no evidence of Zr exsolution or zircon growth at grain boundaries (Fig. 9a-d).

Sample T01-39

Sample T01-39 yields Zr-in-rutile concentrations ranging from 258–879 ppm (Table S2). Of the 14 analyses, four showed Si concentrations above 15,500 ppm which are significantly higher than typical Si concentrations in eclogitic rutile (e.g. Zack *et al.*, 2002), and likely reflect minor incorporation of the host garnet. Given the rutile grains are located within garnet porphyroblasts and they are texturally homogeneous (Fig. 9a), the

T01-39	grt core	grt rim	cpx	cpx (i)	cpx (r)	amp	amp (i)	pl	pl (i)	ttn	ilm	hem
SiO2	37.7	37.8	50.6	52.2	43.9	43.2	40.3	59.5	60.7	30.3	0.0	0.0
TiO2	0.0	0.0	0.4	0.0	4.4	1.1	1.2	0.0	0.0	37.3	42.6	23.1
Al2O3	21.0	21.4	3.7	1.4	9.7	11.4	13.3	24.7	23.6	1.2	0.1	0.1
Cr2O3	0.0	0.1	0.0	0.0	0.0	0.0	0.0	0.0	0.0	0.0	0.0	0.0
FeO	25.8	25.1	9.1	10.3	18.5	14.6	16.7	0.1	0.4	0.5	56.5	74.9
MnO	3.4	1.0	0.1	0.2	0.1	0.1	0.0	0.0	0.0	0.0	0.3	0.1
MgO	3.0	5.5	12.6	12.8	6.5	11.7	9.5	0.0	0.0	0.0	0.9	0.3
ZnO	0.0	0.0	0.0	0.0	0.0	0.0	0.0	0.0	0.0	0.0	0.0	0.0
CaO	8.0	8.2	21.3	21.5	13.0	11.4	10.5	6.0	5.4	27.1	0.1	0.0
Na2O	0.0	0.0	1.0	0.8	3.2	2.3	3.0	9.7	9.8	0.0	0.0	0.0
K2O	0.0	0.0	0.0	0.0	0.0	0.1	0.9	0.0	0.0	0.0	0.0	0.0
Cl	0.0	0.0	0.0	0.0	0.0	0.0	0.2	0.0	0.0	0.0	0.0	0.0
F	0.0	0.0	0.0	0.0	0.0	0.1	0.1	0.0	0.0	0.3	0.1	0.1
Total	99.07	99.07	98.84	99.31	99.31	95.95	95.62	100.08	99.88	96.7	100.41	98.74
Si	3.0	3.0	1.9	2.0	1.7	6.4	6.1	2.6	2.7	1.0	0.0	0.0
Ti	0.0	0.0	0.0	0.0	0.1	0.1	0.1	0.0	0.0	0.9	0.8	0.4
Al	2.0	2.0	0.2	0.1	0.4	2.0	2.4	1.3	1.2	0.1	0.0	0.0
Cr	0.0	0.0	0.0	0.0	0.0	0.0	0.0	0.0	0.0	0.0	0.0	0.0
Fe3+	0.0	0.1	0.1	0.1	0.2	0.8	0.8	0.0	0.0	0.0	0.4	1.1
Fe2+	1.7	1.6	0.2	0.3	0.4	1.0	1.4	0.0	0.0	0.0	0.8	0.4
Mn2+	0.2	0.1	0.0	0.0	0.0	0.0	0.0	0.0	0.0	0.0	0.0	0.0
Mg	0.4	0.6	0.7	0.7	0.4	2.6	2.2	0.0	0.0	0.0	0.0	0.0
Zn	0.0	0.0	0.0	0.0	0.0	0.0	0.0	0.0	0.0	0.0	0.0	0.0
Ca	0.7	0.7	0.9	0.9	0.5	1.8	1.7	0.3	0.3	1.0	0.0	0.0
Na	0.0	0.0	0.1	0.1	0.2	0.7	0.9	0.8	0.8	0.0	0.0	0.0
K	0.0	0.0	0.0	0.0	0.0	0.0	0.2	0.0	0.0	0.0	0.0	0.0
Cl	0.0	0.0	0.0	0.0	0.0	0.0	0.1	0.0	0.0	0.0	0.0	0.0
F	0.0	0.0	0.0	0.0	0.0	0.0	0.1	0.0	0.0	0.0	0.0	0.0
OH-	0.0	0.0	0.0	0.0	0.0	0.0	0.0	0.0	0.0	0.0	0.0	0.0
Cations	8	8	4	4	4	15.4	15.66	5	5	3	2	2

Tables 4–6. Representative mineral analyses derived from EPMA for samples T01-39, T06-11 and T06-20. (i) signifies that the given mineral is an inclusion in gt and (r) signifies that the given mineral is the product of a compositional reintegration. Note: the representative hematite analyses comprise a proportion of TiO2 that classifies them as titano-hematite. Mineral abbreviations after Whitney and Evans (2010).

T06-11	grt core	grt rim	cpx	opx	amp	pl	ttn	ilm	hem
SiO2	36.4	37.2	50.3	50.6	42.8	56.7	28.5	0.0	0.0
TiO2	0.1	0.1	0.6	0.0	1.1	0.0	37.9	47.2	21.7
Al2O3	21.7	21.7	4.4	1.4	12.5	27.0	1.6	0.0	0.1
Cr2O3	0.0	0.1	0.1	0.0	0.1	0.0	0.0	0.1	0.8
FeO	22.3	23.1	7.2	24.4	13.1	0.2	0.7	51.5	76.9
MnO	0.7	0.7	0.1	0.2	0.0	0.0	0.0	0.2	0.1
MgO	5.7	5.4	13.5	20.9	13.1	0.0	0.0	1.1	0.3
ZnO	0.1	0.0	0.1	0.1	0.1	0.0	0.0	0.1	0.0
CaO	11.5	10.9	22.8	0.3	11.6	8.7	27.6	0.1	0.0
Na2O	0.0	0.1	0.8	0.0	1.7	6.9	0.0	0.0	0.0
K2O	0.0	0.0	0.0	0.0	1.3	0.1	0.0	0.0	0.0
Cl	0.0	0.0	0.0	0.0	0.1	0.0	0.0	0.0	0.0
F	0.0	0.0	0.0	0.0	0.2	0.0	0.5	0.1	0.2
Total	98.55	99.28	99.66	97.95	97.48	99.61	96.6	100.21	100.07
Si	2.9	2.9	1.9	1.9	6.2	2.5	1.0	0.0	0.0
Ti	0.0	0.0	0.0	0.0	0.1	0.0	1.0	0.9	0.4
Al	2.0	2.0	0.2	0.1	2.2	1.4	0.1	0.0	0.0
Cr	0.0	0.0	0.0	0.0	0.0	0.0	0.0	0.0	0.0
Fe3+	0.3	0.2	0.1	0.1	0.8	0.1	0.0	0.2	1.2
Fe2+	1.2	1.3	0.1	0.7	0.8	0.0	0.0	0.8	0.4
Mn2+	0.1	0.1	0.0	0.0	0.0	0.0	0.0	0.0	0.0
Mg	0.7	0.6	0.7	1.2	2.8	0.0	0.0	0.0	0.0
Zn	0.0	0.0	0.0	0.0	0.0	0.0	0.0	0.0	0.0
Ca	1.0	0.9	0.9	0.0	1.8	0.4	1.0	0.0	0.0
Na	0.0	0.0	0.1	0.0	0.5	0.6	0.0	0.0	0.0
K	0.0	0.0	0.0	0.0	0.2	0.0	0.0	0.0	0.0
Cl	0.0	0.0	0.0	0.0	0.0	0.0	0.0	0.0	0.0
F	0.0	0.0	0.0	0.0	0.1	0.0	0.1	0.0	0.0
OH-	0.0	0.0	0.0	0.0	0.0	0.0	0.0	0.0	0.0
Cations	8	8	4	4	15.48	5	3	2	2

Tables 4–6. Representative mineral analyses derived from EPMA for samples T01-39, T06-11 and T06-20. (i) signifies that the given mineral is an inclusion in gt and (r) signifies that the given mineral is the product of a compositional reintegration. Note: the representative hematite analyses comprise a proportion of TiO2 that classifies them as titano-hematite. Mineral abbreviations after Whitney and Evans (2010).

T06-20	grt core	grt rim	amp	pl	st	st (i)	bt	ms	chl
SiO2	37.8	37.5	40.8	58.8	26.7	26.1	37.7	44.7	23.9
TiO2	0.0	0.0	0.4	0.0	0.6	0.6	1.6	0.5	0.1
Al2O3	21.4	21.5	18.4	26.3	53.5	54.4	18.1	34.9	22.9
Cr2O3	0.0	0.0	0.1	0.0	0.3	0.3	0.2	0.1	0.2
FeO	30.5	32.8	15.5	0.1	12.0	11.9	14.5	1.2	17.2
MnO	0.2	0.7	0.0	0.0	0.0	0.0	0.0	0.0	0.0
MgO	4.4	5.3	8.2	0.0	2.2	2.0	13.6	0.9	19.5
ZnO	0.1	0.0	0.0	0.0	1.6	1.8	0.0	0.0	0.0
CaO	5.7	2.2	10.7	7.7	0.0	0.0	0.0	0.0	0.0
Na2O	0.0	0.0	1.9	7.6	0.0	0.1	0.3	1.7	0.0
K2O	0.0	0.0	0.5	0.0	0.0	0.0	9.0	8.6	0.0
Cl	0.0	0.0	0.6	0.0	0.0	0.0	0.3	0.0	0.0
F	0.0	0.0	0.1	0.0	0.0	0.0	0.1	0.0	0.0
Total	100.08	99.99	97.01	100.56	96.83	97.17	95.27	92.51	83.68
Si	3.0	3.0	6.0	2.6	7.5	7.3	2.8	3.1	2.5
Ti	0.0	0.0	0.1	0.0	0.1	0.1	0.1	0.0	0.0
Al	2.0	2.0	3.2	1.4	17.7	18.0	1.6	2.8	2.9
Cr	0.0	0.0	0.0	0.0	0.1	0.1	0.0	0.0	0.0
Fe3+	0.1	0.1	0.4	0.0	0.0	0.1	0.0	0.0	0.1
Fe2+	2.0	2.1	1.5	0.0	2.8	2.7	0.9	0.1	1.5
Mn2+	0.0	0.0	0.0	0.0	0.0	0.0	0.0	0.0	0.0
Mg	0.5	0.6	1.8	0.0	0.9	0.8	1.5	0.1	3.1
Zn	0.0	0.0	0.0	0.0	0.3	0.4	0.0	0.0	0.0
Ca	0.5	0.2	1.7	0.4	0.0	0.0	0.0	0.0	0.0
Na	0.0	0.0	0.5	0.7	0.0	0.0	0.0	0.2	0.0
K	0.0	0.0	0.1	0.0	0.0	0.0	0.9	0.7	0.0
Cl	0.0	0.0	0.1	0.0	0.0	0.0	0.0	0.0	0.0
F	0.0	0.0	0.0	0.0	0.0	0.0	0.0	0.0	0.0
OH-	0.0	0.0	0.0	0.0	4.0	4.0	2.0	2.0	8.0
Cations	8	8	15.34	5	29.5	29.5	7.74	7	10

Table 7. Values for elements, element ratios and end-member proportions for selected minerals. (i) denotes an included mineral in gt and/or ky.

	T01-39	T06-11	T06-20
Garnet Core			
Xalm	0.580–0.591	0.462–0.470	0.659–0.665
Xpy	0.104–0.109	0.209–0.220	0.166–0.177
Xgrs	0.227–0.242	0.299–0.310	0.158–0.164
Xsps	0.069–0.077	0.014–0.016	0.004–0.007
XFe	0.842–0.849	0.679–0.690	0.789–0.800
Garnet Rim			
Xalm	0.541–0.543	0.476–0.508	0.624–0.717
Xpy	0.206–0.214	0.185–0.210	0.173–0.258
Xgrs	0.225–0.241	0.284–0.299	0.063–0.159
Xsps	0.011–0.022	0.015–0.023	0.003–0.016
XFe	0.717–0.724	0.694–0.733	0.707–0.798
Clinopyroxene			
Xjd	0.033–0.066	0.027–0.042	-
Xdio	0.699–0.753	0.733–0.822	-
Xhed	0.171–0.217	0.112–0.209	-
Xaeg	0.023–0.034	0.019–0.025	-
XFe	0.187–0.237	0.120–0.222	-
Clinopyroxene (i)			
Xjd	0.025–0.028	-	-
Xdio	0.695–0.715	-	-
Xhed	0.226–0.247	-	-
Xaeg	0.031–0.034	-	-
XFe	0.240–0.262	-	-
Orthopyroxene			
Xmgts	-	0.001	-
Xen	-	0.554	-
Xfs	-	0.353	-
Xfm	-	0.022	-
XFe	-	0.376	-
Amphibole			
XTi	0.063–0.086	0.060–0.083	0.022–0.025
XFe	0.277–0.325	0.219–0.236	0.456–0.475
XNa+K	0.396–0.486	0.475–0.518	0.292–0.355
Amphibole (i)			
XTi	0.065–0.067	-	-
XFe	0.380–0.387	-	-

XNa+K	0.628–0.666	-	-
Plagioclase			
Xab	0.600–0.782	0.584–0.680	0.619–0.638
Plagioclase (i)			
Xab	0.760–0.834	-	-
Staurolite			
ZnO (wt%)	-	-	1.478–1.702
MnO (wt%)	-	-	0.003–0.056
MgO (wt%)	-	-	1.884–2.357
Staurolite (i)			
ZnO (wt%)	-	-	1.446–1.842
MnO (wt%)	-	-	0.003–0.041
MgO (wt%)	-	-	1.954–2.334
Biotite			
XMg			0.620–0.627
MnO (wt%)	-	-	0.000–0.010
TiO2 (wt%)	-	-	1.538–1.558
Muscovite			
XMg			0.494–0.584
MnO (wt%)	-	-	0.001–0.005
TiO2 (wt%)	-	-	0.445–0.467

Xalm = Fe2+/(Fe2+ + Mg + Ca + Mn)	Xmgts = magnesio-tschermak	
Xpy = Mg/(Fe2+ + Mg + Ca + Mn)	Xen = enstatite	
Xgrs = Ca/(Fe2+ + Mg + Ca + Mn)	Xfs = ferrosilite	
Xsps = Mn/(Fe2+ + Mg + Ca + Mn)	Xfm = Fe–Mg ordered pyroxene	
XFe = Fe2+/(Fe2+ + Mg)	Xjd = jadeite	
XMg = Mg/(Mg + Fe2+)	Xdio = diopside	
Xab = Na/(Na + Ca)	Xhed = hedenbergite	
XTi = Ti	Xaeg = aegirine	
XNa+K = Na + K		

observed Zr concentration range is not inferred to be a consequence of post-peak processes, including diffusional exchange. In cases where rutile has been inferred to have been influenced by post-peak processes, previous workers have noted the preservation of exsolved zircon and zircon growth at rutile grain margins (e.g. Jiao *et al.*, 2011; Pape *et al.*, 2016). The entire range of Zr-in-rutile concentrations are therefore considered to be representative of the prograde to peak history of this sample, where the lowest Zr concentrations likely relate to the earliest part of the recorded prograde history. Because it is inferred that rutile grew during the prograde to peak evolution of sample T01-39, minimum, mean and maximum temperature estimates (and their associated 2σ errors) from the entire range of Zr concentrations have been plotted on the mineral equilibria forward model for sample T01-39 (section 5.3.1). Though it is acknowledged that the Zr-in-rutile temperature estimates are entirely independent of mineral equilibria modelling, the modelling results predict where in *P–T* space rutile-present assemblages are stabilised and they therefore enable temperature ranges to be calculated at specific pressures where rutile is interpreted to have grown.

The Zr concentrations from T01-39 rutile correspond to temperatures of 646–745 °C (at 12 kbar) and 668–778 °C (at 17 kbar), using the

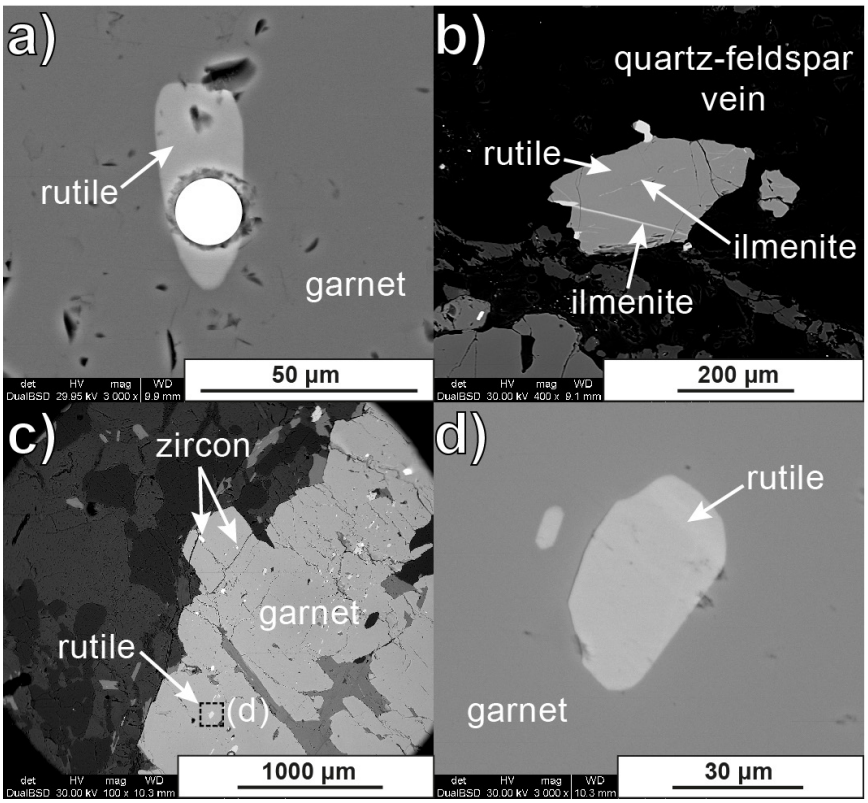


Fig. 9. Annotated back scattered electron (BSE) images of rutile. (a) Sample T01-39: the location of the ablation pit on the rutile grain is given by a white circle. (b) Sample T06-11: rutile preserved within a quartz-feldspar-bearing vein shows ilmenite exsolution textures. (c) Sample T06-20: garnet rim comprising inclusions of rutile and zircon. (d) Zoomed-in image of rutile hosted within garnet from (c).

pressure-dependent calibration of Tomkins *et al.* (2007). These temperature ranges are quoted at selected pressures because mineral equilibria modelling suggests the inferred prograde to peak *P–T* path traversed through pressures of 12–17 kbar in rutile-present assemblages (section 5.3.1). Therefore, it is likely that rutile grew at temperatures between the pressures of 12 and 17 kbar (Fig. 10a). Temperature estimates calculated at additional pressures where rutile is stable on the phase diagram (section 5.3.1) are given in Table S2.

Sample T06-11

Rutile grains preserved within quartz-feldspar-bearing veins (Fig. 9b) were analysed for their trace element concentrations in sample T06-11. Zr-in-rutile concentrations range from 399–1307 ppm. Of the 28 analyses, four analyses were omitted due contamination from the surrounding quartz matrix. As with sample T01-39, there is no evidence of Zr exsolution from rutile (Fig. 9b). It is therefore possible that the large spread of Zr concentrations could reflect rutile growth during the rock's prograde and peak evolution, with the lowest concentrations corresponding to the rock's earlier history. However, because the rutile grains are hosted within quartz-feldspar-bearing veins that are interpreted to have recrystallised during the rock's retrograde history (but before the development of the mylonitic fabric), the Zr concentrations are instead interpreted to relate to the retrograde *P–T* history. Moreover, the rutile grains are not compositionally homogenous as is evident by the occurrence of widespread ilmenite exsolution textures (Fig. 9b). They are also commonly rimmed by inferred retrograde ilmenite. These observations suggest at the very least that the rutile grains located in the quartzofeldspathic veins in sample T06-11 were compositionally affected by post-peak processes, however, the degree to which they were influenced is not known.

The calculated Zr-in-rutile temperatures for sample T06-11 range from 673–785 °C (at 10 kbar) and 704–820 °C (at 17 kbar; Table S2). Assuming the rutile grains developed during the rock's peak through retrograde *P–T* history, it is inferred that their Zr concentrations developed at temperatures between pressures of 10 kbar and 17 kbar (Fig. 10b), where 10 kbar represents the approximate pressure on the *P–T* phase diagram (section 5.3.2) below which rutile is not stable, and 17 kbar represents the approximate peak pressure as constrained from sample T01-39 (section 5.3.1). In considering the natural variation in Zr concentrations in the rutile grains, minimum, mean and maximum temperature estimates from the entire range of Zr concentrations have been plotted on the mineral equilibria forward model for sample T06-11 (section 5.3.2). Temperature estimates calculated at additional pressures where rutile is stable are provided in Table S2.

Sample T06-20

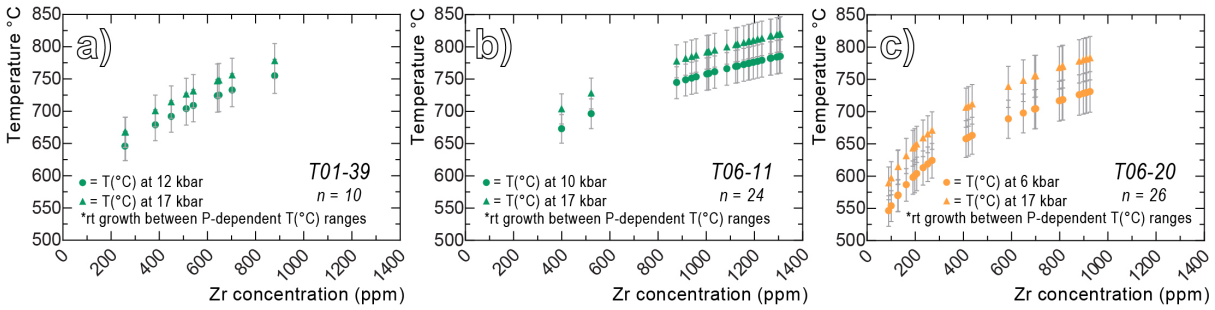


Fig. 10. Relationship between Zr concentration (in ppm) and temperature (calculated using the calibration of Tomkins et al., 2007) for rutile grains in samples (a) T01-39, (b) T06-11 and (c) T06-20. Each plot contains two sets of temperature ranges, corresponding to temperature estimates calculated at different pressures. Justification for the specific pressures selected is provided in the text.

30 analyses were obtained from rutile grains included within garnet (Fig. 9c, d). Four analyses recorded higher than typical Si concentrations in rutile (i.e. >10,000 ppm; Zack *et al.*, 2002) and were omitted. Zr concentrations range from 90–926 ppm and are interpreted to have developed along the rock's prograde to peak *P–T* evolution due to the location of rutile grains within coarse-grained garnet (Fig. 9c, d). Rutile analyses from T06-20 yield temperatures between 546–731 °C (at 6 kbar) and 589–784 °C (at 17 kbar; Table S2), where 6 kbar represents the approximate pressure in the *P–T* model below which rutile is not stable, and 17 kbar represents the approximate peak pressure calculated for sample T06-20 (section 5.3.3). Temperature estimates calculated at additional pressures where rutile is stable are provided in Table S2.

4.3 Mineral equilibria forward modelling

Mafic samples T01-39 and T06-11 form part of the same rock package (Fig. 3a) and contain similar mineral assemblages (section 3). However, they contain contrasting rock textures and so can be used in combination to investigate the collective *P–T* history of the mafic rock system. The prograde and peak *P–T* conditions are best constrained by sample T01-39, which is unfoliated and preserves early microstructures. The retrograde *P–T* conditions are constrained by mylonitic sample T06-11. The peak assemblage in metapelitic sample T06-20 is interpreted to have been recrystallised (section 6.2.1). However, inclusions in porphyroblastic garnet and kyanite, and compositional zonation patterns in garnet permit an investigation into the prograde to peak *P–T* history. Due to the well-developed retrograde mineral assemblage, sample T06-20 provides constraints on the retrograde *P–T* conditions.

Sample T01-39

Minerals included within garnet (clinopyroxene, amphibole, plagioclase, rutile, quartz and titanite)

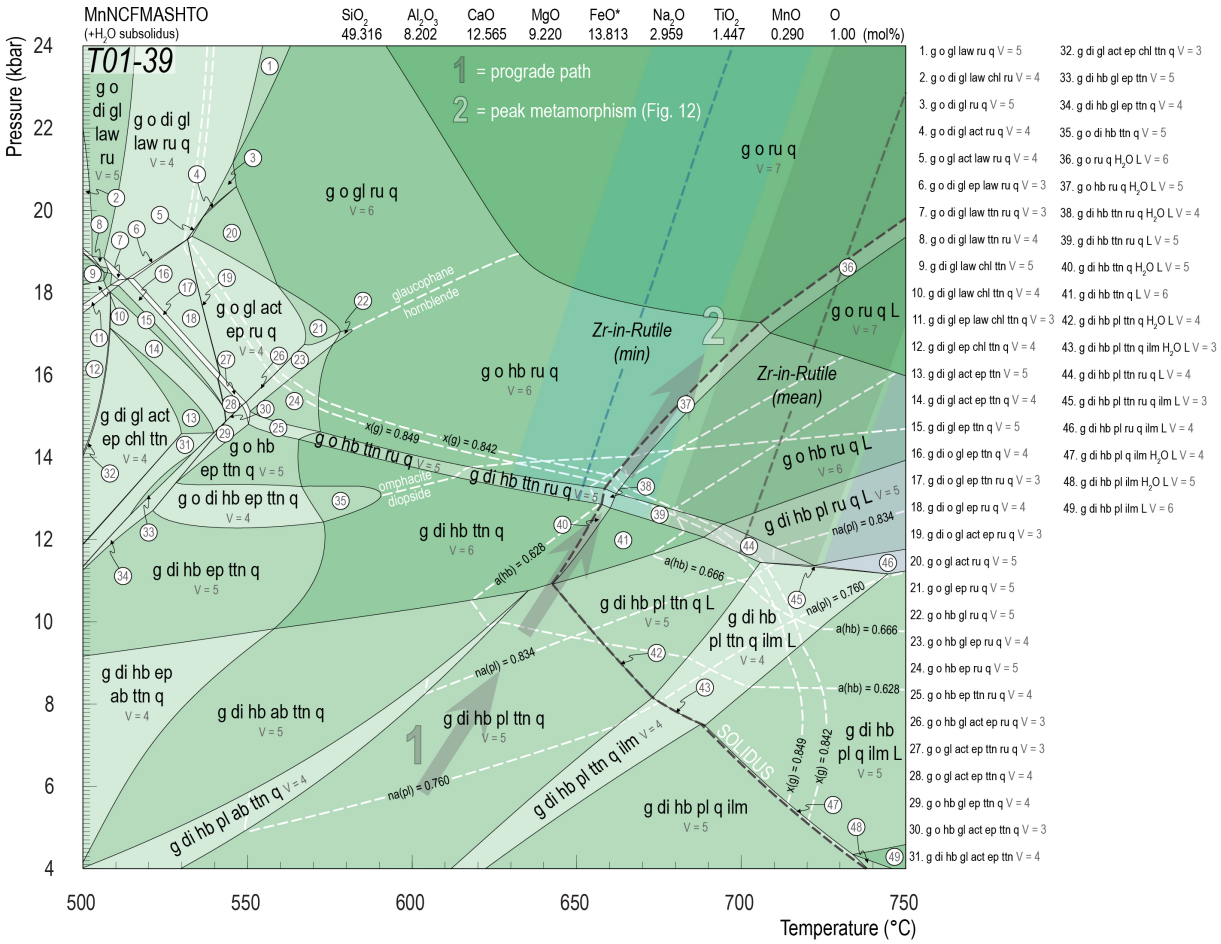


Fig. 11. Calculated prograde P–T pseudosection for the bulk-rock composition of sample T01-39. The solidus is represented with a dark grey dashed line. Zr-in-rutile derived temperature estimates are shown at different pressures in rutile-stable modelled fields with dashed contours (grey: average estimates, blue: minimum estimates). The shaded regions in P–T space enclosing the Zr-in-rutile temperature estimates signify the associated 2σ uncertainties. Composition contours are annotated on the pseudosection with white dashed lines. The grey arrow depicts the inferred prograde to peak P–T path (labelled as '1'). The peak P–T conditions constrained from the pseudosection in Figure 12 are represented with the label '2'. The modelled system and bulk-rock composition (in mol%) are provided above the pseudosection. The subsolidus equilibria are calculated with H2O in excess. Equilibria above the solidus are calculated with a H2O content of 4.33 mol% such that assemblages are H2O-saturated at the solidus. V signifies the variance for each mineral assemblage.

have been used in combination with the pseudosection presented in Figure 11 to address the prograde *P–T* history of sample T01-39. This pseudosection is calculated with H_2O in excess below the solidus and assumes that the rock has not undergone significant compositional modification throughout its *P–T* evolution, which is a reasonable assumption given there is no evidence for migmatization at the scale to promote melt loss. The prograde path is inferred to originate in the modelled field containing garnet, diopside, hornblende, plagioclase, titanite and quartz at comparatively low-pressure conditions of ~5 kbar and 600–650 °C (Fig. 11). The prograde *P–T* path is

based on the occurrence of titanite in garnet (Fig. 7a), the range of X_{Fe} values in garnet cores (0.842–0.849; Fig. S5a, b), the compositions of amphibole and plagioclase inclusions (X_{Na+K} in amphibole = 0.628–0.666; X_{ab} in plagioclase = 0.750–0.834; Fig. S5c, d; Fig. S5f, g), and the range of temperatures derived from Zr concentrations in rutile (section 5.2.1). Modelled titanite proportions are low (Fig. S5h, i), consistent with the observation that they only rarely occur within garnet porphyroblasts. The inferred prograde *P*–*T* path intersects the modelled solidus at ~10 kbar. Its trajectory above the solidus into rutile-present assemblages passes through modelled fields with low proportions of melt (Fig. S5e) and agrees with calculated temperatures from Zr concentrations in rutile hosted within garnet (Fig. 11; section 5.2.1). The prograde path terminates at the inferred peak metamorphic conditions constrained using the pseudosection presented in Figure 12, which models the peak to retrograde history of sample T01-39.

The peak to retrograde pseudosection in Figure 12 is modelled using the H_2O content currently contained in hydrous minerals (amphibole) in the rock. The inferred peak assemblage for sample T01-39 comprises garnet, omphacite, amphibole, rutile and quartz. This assemblage occurs in the *P*–*T* pseudosection, albeit with the addition of small amounts of H_2O, at *P*–*T* conditions of 15.5–19 kbar and 570–710 °C (Fig. 12). Plagioclase coronae rimming garnet (Fig. 4e) formed at the expense of garnet rims that were present at peak metamorphic conditions. The garnet grains show a rimward decrease in X_{Fe}, suggesting that the X_{Fe} values of the current garnet rims (Fig. 7b; Table 7) are likely to be an overestimation of the original rim composition. Thus, it is reasonable to hypothesise that this rock tracked through *P*–*T* space from a region corresponding to the current garnet rim X_{Fe} to a region along which (1) garnet X_{Fe} values decrease and (2) garnet modal proportions increase. A maximum X_{Fe} value (0.7245) from a near-rim location in garnet plots within the hornblende-bearing variant of the inferred peak field (Fig. 12). Additionally, the abundance of texturally peak amphibole (~0.9 mol%) corresponds to calculated proportions that plot within the inferred peak field and intersect minimum garnet X_{Fe} values (Fig. S5j). These factors define a temperature of ~700 °C and a minimum peak pressure of ~17 kbar (Fig. 12). From this approximate point in *P*–*T* space, the rock is interpreted to have followed an isobaric heating path into the suprasolidus region of *P*–*T* space as constrained by the observed decrease in garnet X_{Fe} and the observed increase in garnet modal proportions in modelled *P*–*T* space (Fig. S5k-m). The interpreted heating path is consistent with the range of inferred prograde to peak Zr-in-rutile temperature estimates calculated at a pressure of ~17 kbar (Fig. 12). Given that the hypothesised isobaric temperature increase is small and the uncertainties on the temperature are unknown, the notion that this rock traversed such a

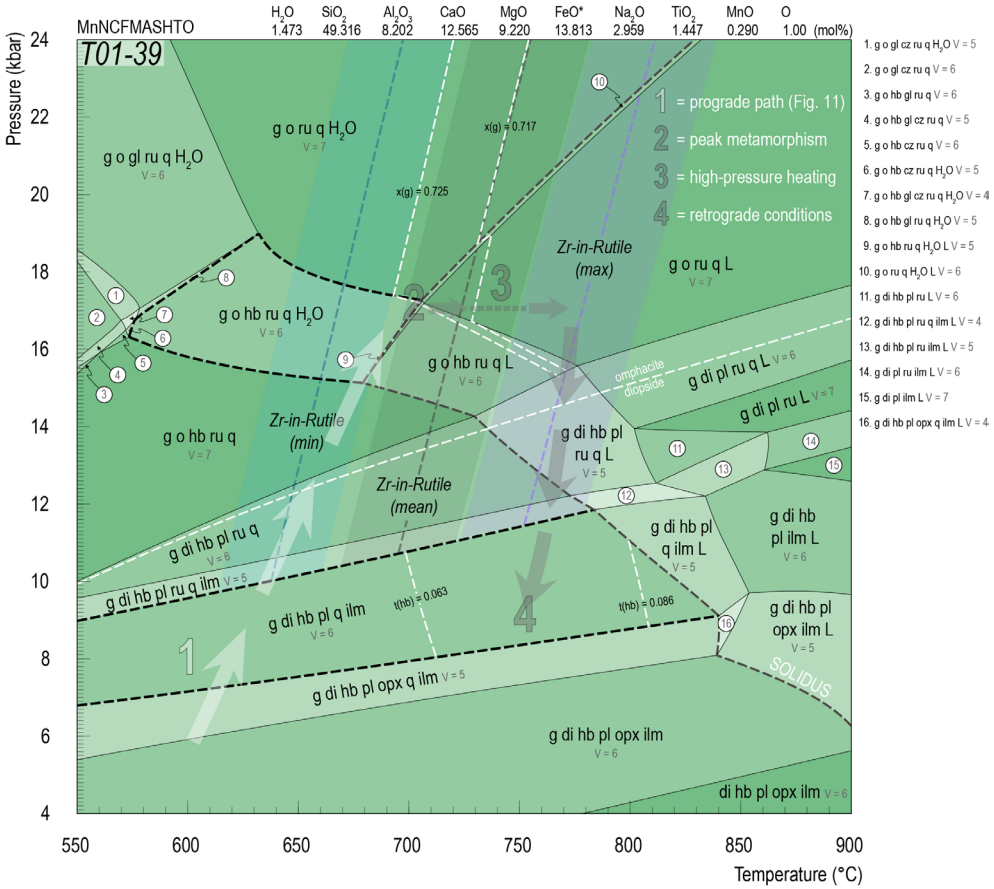


Fig. 12. Calculated peak to retrograde P–T pseudosection for the bulk-rock composition of sample T01-39. The solidus is represented with a dark grey dashed line. Zr-in-rutile derived temperature estimates are shown at different pressures in rutile-stable modelled fields with dashed contours (grey: average estimates, blue: minimum estimates, purple: maximum estimates). The shaded regions in P–T space enclosing the Zr-in-rutile temperature estimates signify the associated 2σ uncertainties. The peak and retrograde metamorphic assemblages inferred from the petrography are bordered by black dashed lines. Composition contours are annotated on the pseudosection with white dashed lines. The white arrow depicts the inferred prograde to peak P–T path (labelled as '1') from Figure 11. The peak P–T conditions are represented with the label '2'. The horizontal arrow represented by the label '3' attempts to signify the isobaric heating path at ~17 kbar. A dashed line is shown between the heating path to demonstrate that the magnitude of temperature increase is not well constrained. The grey arrow toward label '4' represents the post-peak P–T path. The modelled system and bulk-rock composition (in mol%) are provided above the pseudosection. All equilibria are calculated with a fixed H2O content. V signifies the variance for each mineral assemblage.

path is proposed tentatively.

The retrograde evolution of T01-39 involves the conversion of omphacite to Na-poor clinopyroxene and the appearance of plagioclase, amphibole and ilmenite, culminating in a retrograde assemblage consisting of residual garnet, low-Na clinopyroxene, hornblende, plagioclase, quartz and ilmenite (Fig. 12). Retrograde temperatures are constrained using minimum and maximum X_{Ti} values in matrix amphibole (0.063–0.086; Fig. S5n), yielding temperatures between 700–810 °C.

Considering the bounds of X_{Ti} values within the retrograde field, pressures are constrained between 8–12 kbar.

Sample T06-11

The strong mylonitic overprint in sample T06-11 complicates efforts to reasonably determine a peak metamorphic assemblage and therefore, no robust peak *P–T* constraints can be obtained for this sample. However, the retrograde *P–T* history may still be inferred from both mineral modal proportions and compositions in the *P–T* model (Fig. 13).

As outlined in sections 3.3 and 5.2.2, the quartzofeldspathic veins in sample T06-11 are conservatively interpreted to have developed during the rock's retrograde *P–T* history and prior to the formation of the orthopyroxene-bearing mylonitic fabric. The veins contain garnet, clinopyroxene, rutile rimmed by ilmenite, amphibole and rare biotite (Fig. 5c-f). Zr concentrations in rutile grains hosted within quartzofeldspathic veins (section 5.2.2) yield temperatures of 673–820 °C from 10–17 kbar within the modelled assemblage containing garnet + diopside + hornblende + plagioclase + rutile + quartz ± ilmenite (Fig. 13). This modelled assemblage is inferred to represent the retrograde vein assemblage. Though it is not completely clear what the precise pressure conditions were when the vein formed, we can infer from the *P–T* pseudosection that the rock conceivably tracked down-pressure along the temperatures derived from Zr-in-rutile thermometry (Fig. 13) from peak pressures of ~17 kbar (as constrained from sample T01-39) to ~10 kbar where rutile is destabilised.

The post-peak history for T06-11 is additionally recorded by the appearance of orthopyroxene (Fig. 13). Orthopyroxene modal proportions in the sample are ~1–2 vol%, and these proportions occur between pressures of 6.5–9.5 kbar within the modelled retrograde field containing garnet, diopside, hornblende, plagioclase, orthopyroxene, quartz and ilmenite (Fig. S6a). Modelled retrograde temperatures are constrained from minimum and maximum X_{Ti} values in matrix amphibole of 0.060 and 0.083 (Fig. S6b), thereby resulting in a retrograde pressure–temperature window constrained at 7.6–8.2 kbar and 680–790 °C. Constraints for the retrograde conditions of this sample are further supported by the range of X_{Fe} values from garnet rims (0.694–0.733) which plot within the orthopyroxene-bearing modelled retrograde field (Fig. S6c).

Sample T06-20

The *P–T* pseudosection presented in Figure 14 is calculated with H_2O in excess below the solidus and is used to constrain the prograde to peak evolution of sample T06-20. The inferred prograde as-

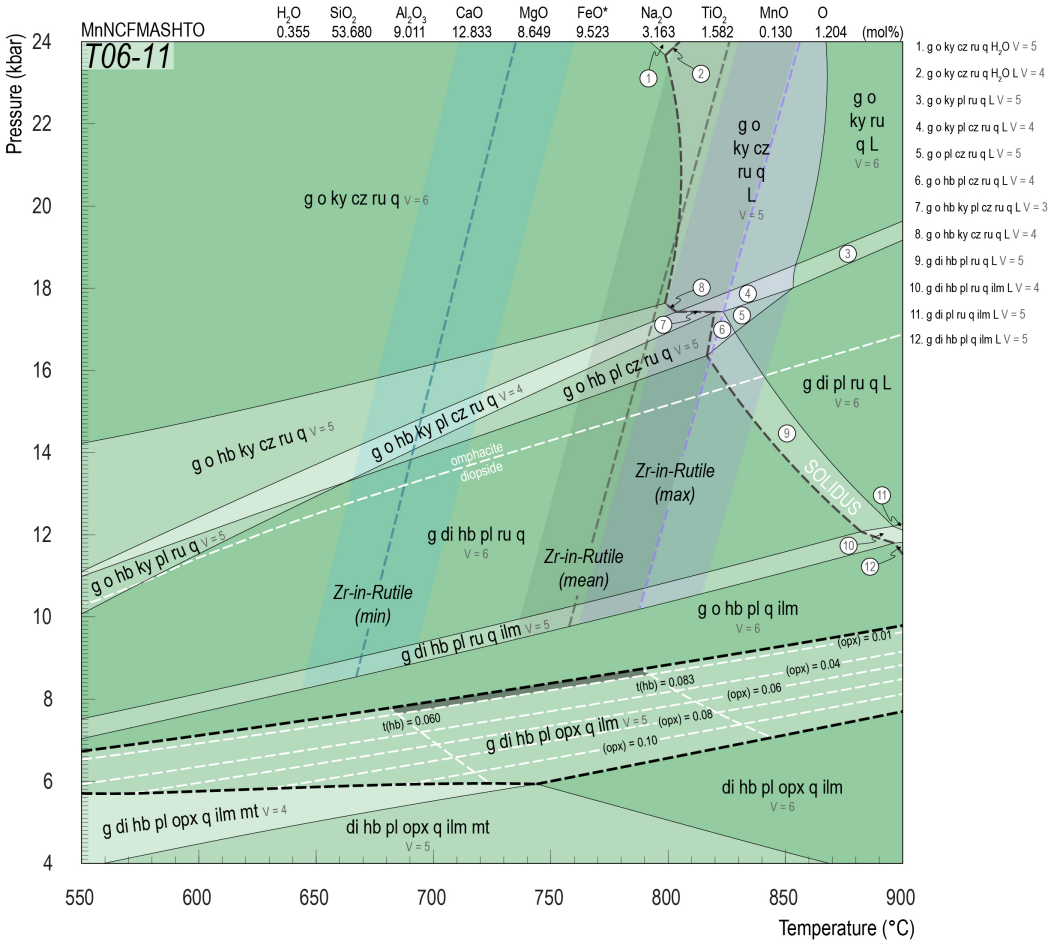


Fig. 13. Calculated retrograde P–T pseudosection for the bulk-rock composition of sample T06-11 (with garnet core compositions subtracted from the bulk-rock composition). The solidus is represented with a dark grey dashed line. Zr-in-rutile derived temperature estimates are shown at different pressures in rutile-stable modelled fields with dashed contours (grey: average estimates, blue: minimum estimates, purple: maximum estimates). The shaded regions in P–T space enclosing the Zr-in-rutile temperature estimates signify the associated 2σ uncertainties. The retrograde metamorphic assemblage inferred from the petrography is bordered by a black dashed line. Composition and modal proportion contours are annotated on the pseudosection with white dashed lines. The grey polygon within the inferred retrograde field containing g-di-hb-pl-opx-q-ilm defines the constrained retrograde conditions. The modelled system and bulk-rock composition (in mol%) are provided above the pseudosection. All equilibria are calculated with a fixed H2O content. V signifies the variance for each mineral assemblage.

semblage for this sample contains garnet, kyanite, amphibole, staurolite, plagioclase, biotite, muscovite, rutile and quartz. The inclusions in garnet, kyanite and amphibole occur at modelled *P–T* conditions of 5–6.3 kbar and 585–625 °C (Fig. 14). From these conditions, a prograde path is inferred to track along increasing pressures and temperatures to conditions of 7.5–9 kbar and 645–660 °C, as kyanite and hornblende proportions increase (Fig. S7a-d). These conditions represent those which stabilise both garnet and plagioclase at subsolidus conditions, and they agree with the range of X_{Fe} values in the garnet core (0.789–0.800; Fig. S7e, f; Table 7).

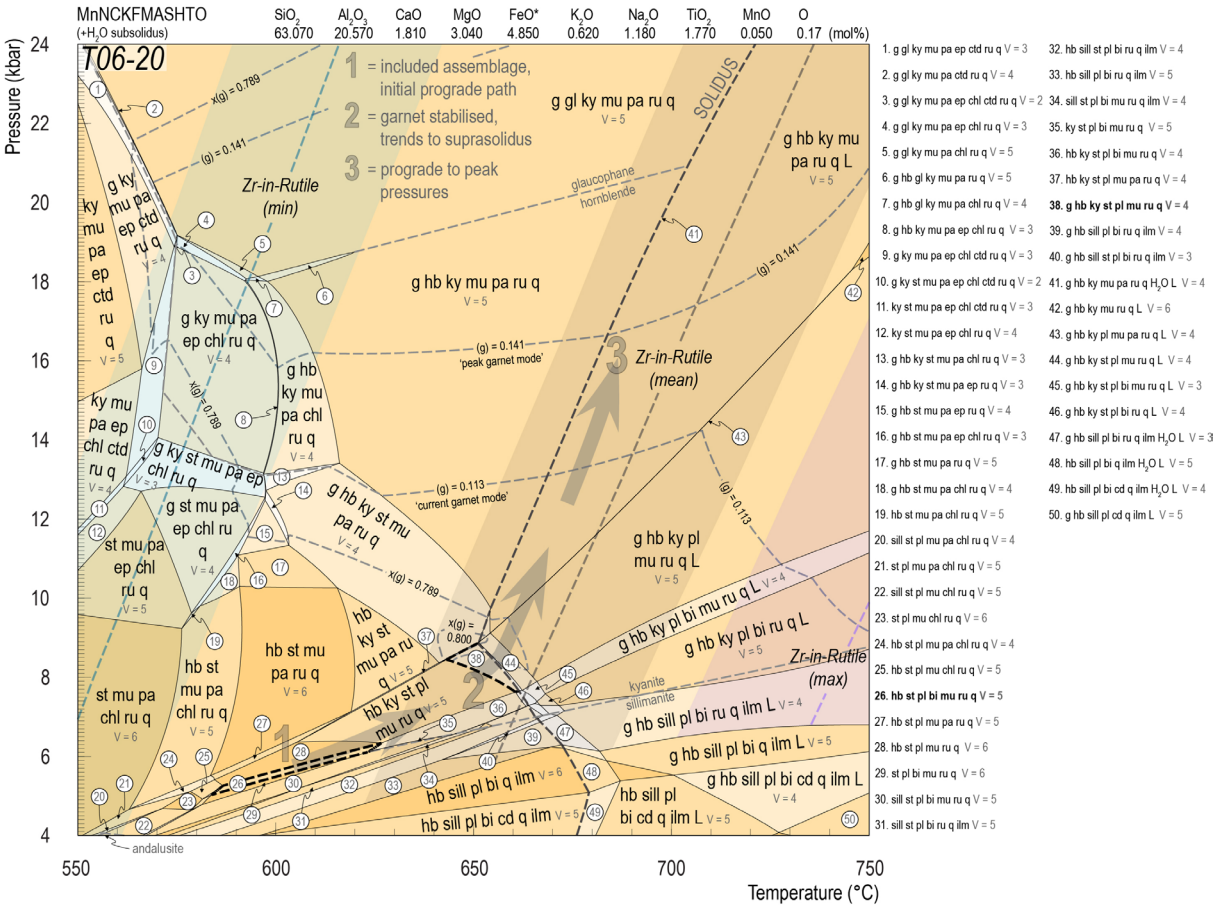


Fig. 14. Calculated prograde to peak P–T pseudosection for the bulk-rock composition of sample T06-20. The solidus is represented with a dark grey dashed line. Zr-in-rutile derived temperature estimates are shown at different pressures in rutile-stable modelled fields with dashed contours (grey: average estimates, blue: minimum estimates, purple: maximum estimates). The shaded regions in P–T space enclosing the Zr-in-rutile temperature estimates signify the associated 2σ uncertainties. The inferred inclusion assemblage (assemblage 26) is bordered by a black dashed line and labelled '1'. The modelled field with coexisting garnet and plagioclase (assemblage 38) is bordered by a black dashed line and labelled '2'. Composition and modal proportion contours are annotated on the pseudosection with grey dashed lines. The grey arrow depicts the inferred prograde to peak P–T path. The peak pressures are represented with the label '3'. The modelled system and bulk-rock composition (in mol%) are provided above the pseudosection. The subsolidus equilibria are calculated with H2O in excess. Equilibria above the solidus are calculated with a H2O content of 5.00 mol% such that assemblages are H2O-saturated at the solidus. V signifies the variance for each mineral assemblage.

Sample T06-20 does not record clear petrographic evidence of peak metamorphism. However, significant Mn enrichment at the rims of garnet grains suggest that the modal proportion of garnet has decreased by ~30% (Fig. 8; section 5.1.1). The determined modal proportion of peak metamorphic garnet is ~14 mol% – approximately 3 mol% greater than the proportion of garnet currently preserved in the sample (section 5.1.1). It is interpreted that the rock followed a *P–T* path consistent with increasing garnet modal proportions

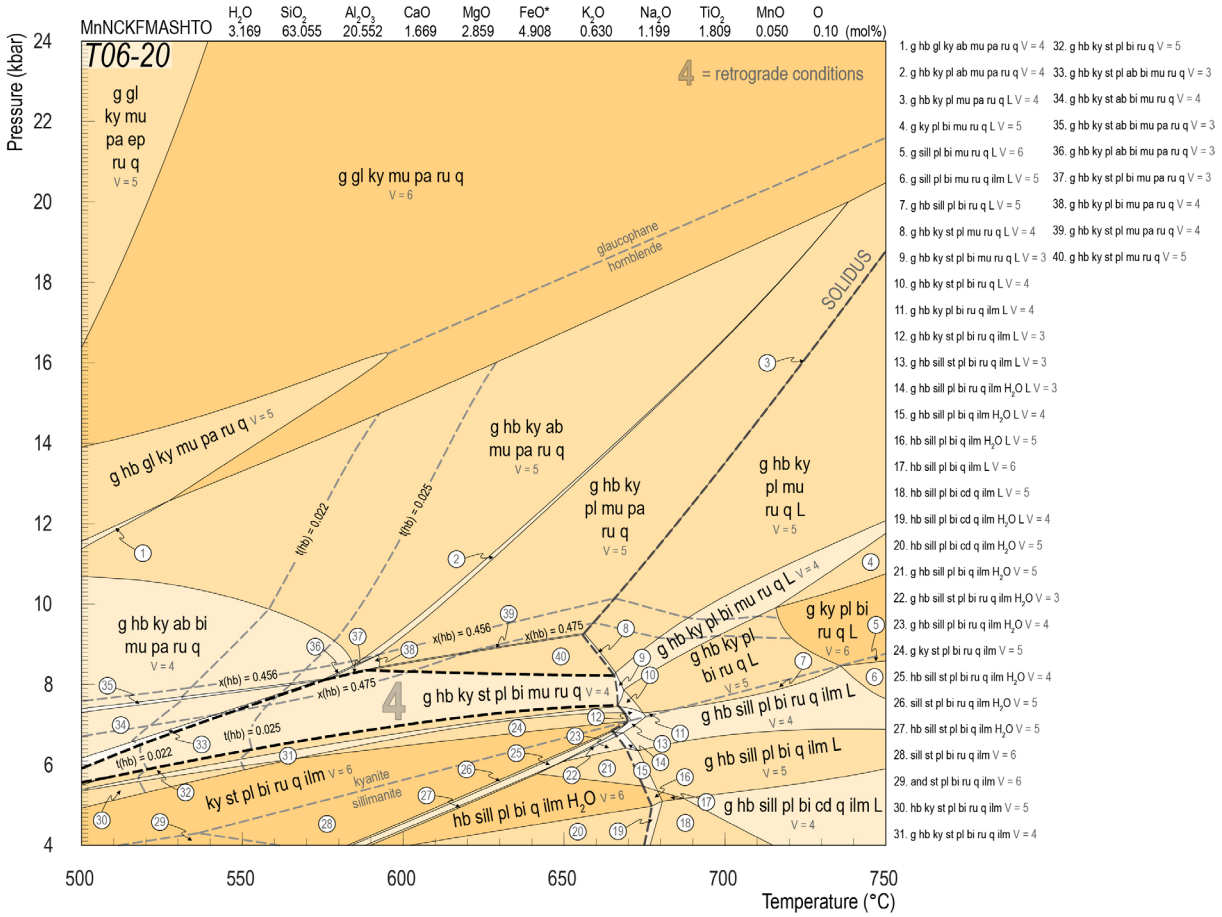


Fig. 15. Calculated retrograde P–T pseudosection for the bulk-rock composition of sample T06-20 (with garnet core compositions subtracted from the bulk-rock composition). The solidus is represented with a dark grey dashed line. Composition contours are annotated on the pseudosection with grey dashed lines. The modelled retrograde field is represented with the label '4' (numbering continues from Fig. 14). The modelled system and bulk-rock composition (in mol%) are provided above the pseudosection. The subsolidus equilibria are calculated with H2O in excess. All equilibria are calculated with a fixed H2O content. Garnet core compositions have been omitted from the P–T calculations. V signifies the variance for each mineral assemblage.

to peak pressures of at least 16.5–17 kbar (Fig. 14; Fig. S7g, h). Although this path crosses into suprasolidus conditions, melt volumes are low (Fig. S7i). A suprasolidus *P–T* path is consistent with average temperatures derived from Zr concentrations in rutile included within garnet (Fig. 14; section 5.2.3). We acknowledge that the spread of Zr-in-rutile temperatures is significant in this sample (Fig. 14; section 5.2.3). However, as outlined in section 5.2, it is clear the calculated temperatures may represent minimum estimates. Given the spread of Zr-in-rutile temperatures in this sample, it is conceivable that a path that agrees with average temperatures better represents the prograde history of the sample. This interpretation is based on the fact that such a path agrees with robust petrological information from the sample, such as the inferred prograde assemblage and garnet core compositions.

The retrograde evolution of sample T06-20 is modelled using a H_2O content determined from the proportions and compositions of hydrous minerals currently preserved in the rock. The retrograde evolution involves the development of muscovite and staurolite, culminating in an inferred retrograde assemblage containing garnet, hornblende, kyanite, staurolite, plagioclase, biotite, muscovite, rutile and quartz (Fig. 15). The retrograde conditions are constrained at approximately 6–8 kbar and 520–600 °C (Fig. 15) using the range of X_{Fe} and X_{Ti} values in matrix amphibole (X_{Fe} = 0.456–0.475; X_{Ti} = 0.022–0.025; Fig. S7j, k). More generally, modelled modal proportions of garnet, hornblende, staurolite, and biotite in the retrograde field broadly agree with those currently preserved in the sample (Fig. S7l-o).

5. Discussion

5.1 Metamorphic evolution of the Usagaran Belt

P–T evolution of the mafic rocks

The early history of the mafic samples is best recorded by sample T01-39. Evidence from (1) mineral equilibria forward modelling (Fig. 11; Fig. S5a-i), (2) Zr-in-rutile thermometry applied to rutile grains hosted within garnet (section 5.2.1), (3) X_{ab} values from garnet-hosted plagioclase, (4) X_{Na+K} values from garnet-hosted amphibole, and (5) X_{Fe} values from garnet cores, suggests the mafic rocks experienced a burial history trending toward upper amphibolite-facies *P–T* conditions, and then to peak eclogite-facies conditions. The evolution of the eclogite protoliths through upper amphibolite-facies conditions may have involved very minor amounts of partial melting according to the *P–T* modelling (Fig. 11). However, it is not clear if melting occurred because there is no compelling evidence at outcrop- or thin-section-scale that the mafic rocks had partially melted. Additionally, modelled melt proportions along the inferred prograde path are below ~3% (Fig. S5e), and are therefore likely too low to have enabled the rocks to preserve evidence of having melted (Rosenberg and Handy, 2005).

The interpretation by Möller *et al.* (1995) that the Usagaran mafic rocks reached eclogite-facies conditions was based on the observation of a sodic clinopyroxene inclusion within coarse-grained garnet. Quantitative compositional reintegration of clinopyroxene-plagioclase intergrowth textures in T01-39 strongly imply that clinopyroxene present at peak metamorphic conditions was omphacitic (section 5.1.2). Mineral equilibria forward modelling applied to sample T01-39 (Fig. 11; Fig. 12), combined with garnet modal proportions and compositions, suggests the eclogites reached *P–T* conditions of ~17 kbar and ~700 °C, correlating with a peak metamorphic assemblage consisting of garnet, omphacite, hornblende, rutile, quartz

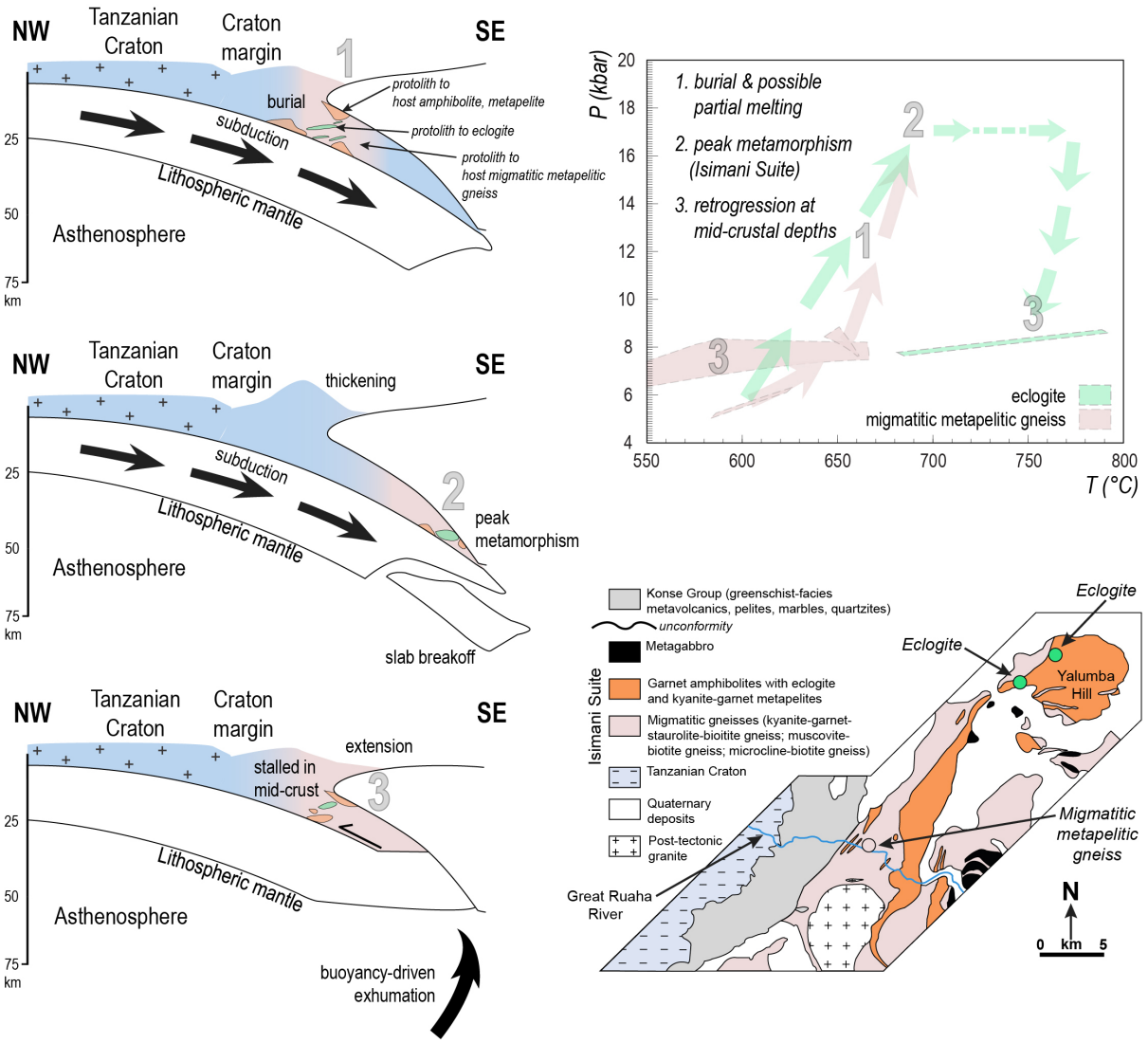


Fig. 16. Schematic illustration of the proposed geodynamic regime for the Isimani Suite in the Palaeoproterozoic. Cross section 1: the margin of the Tanzania Craton (blue), comprising primarily sedimentary and some mafic material, was subducted to the south-east. The sedimentary and mafic materials — which were the protoliths to the mafic eclogites (green) and garnet amphibolites (orange), metapelites (orange) and migmatitic metapelitic gneisses (pink) that hosted them — were buried coherently. During burial, the metapelitic gneisses underwent partial melting, though it is not clear if the mafic rocks melted. Cross section 2: the eclogites and high-strain migmatitic metapelitic gneisses underwent peak metamorphism to pressures of ~17 kbar as a response to warm subduction and crustal thickening. Slab breakoff may have been initiated at deeper crustal levels. Cross section 3: the tectonic regime conceivably became dominated by buoyancy-driven exhumation where rapid exhumation of the Isimani rock package was induced, resulting in a stalled rock system in the mid-crust. A simplified illustration of the P–T paths for the eclogites and the metapelitic gneisses is also shown and annotated. The simplification is based on pseudosections in the study (Fig. 11-15). Fields and arrows in green correspond to those constrained for the eclogites and those constrained for the metapelitic gneiss are given in pink. The numbers annotated on the simplified P–T diagram relate the P–T paths directly to the schematic illustration. Also included in the figure is a simplified version of the geological map in Figure 3a to show how the mapped units relate to the proposed schematic tectonic evolution.

and H_2O. In Figure 12, the occurrence of H_2O in the subsolidus region of modelled *P–T* space may reflect either the legitimate presence of free H_2O or the inability of mineral *a–x* models in THERMOCALC to incorporate mineral-bound H_2O into nominally anhydrous minerals such as omphacite (Green *et al.*, 2016). Several studies have addressed the importance of omphacite as a carrier of H_2O at high-pressure conditions (e.g. Smyth *et al.*, 1991; Katayama and Nakashima, 2003; Bromiley and Kepler, 2004; Sheng and Gong, 2017). The observation that amphibole overprints clinopyroxene-plagioclase intergrowths in T01-39 (Fig. 4f) demonstrates the possibility that H_2O was derived from a formerly stable mineral, potentially supporting a peak metamorphic regime characterised by the residence of a proportion of H_2O in omphacite. However, it is likely that the majority of H_2O was either contained within a hydrous phase, present as an interstitial fluid or introduced on the retrograde path. As a consequence of these uncertainties, the validity of the H_2O content used to calculate the *P–T* pseudosection for sample T01-39 was tested using a $P–M_{H2O}$ model (Fig. S4). Because the inferred peak metamorphic assemblage is relatively pressure insensitive with varying H_2O abundance, our interpretation is that the H_2O content determined for *P–T* calculations is reasonable.

The *P–T* evolution is additionally characterised by an up-temperature isobaric *P–T* path into the suprasolidus field containing garnet, omphacite, rutile, quartz and melt, subsequent to the establishment of conditions of ~17 kbar and ~700 °C. The interpretation that the eclogites were heated along an isobaric *P–T* path near peak pressures is based on the X_{Fe} zonation pattern in prograde zoned T01-39 garnet, which shows a decreasing trend to lower X_{Fe} values toward the garnet rim, and can reasonably be projected outward into the region now occupied by plagioclase coronae that replaced garnet rims (Fig. 7b). These projected X_{Fe} values plot at higher temperatures. Further supporting the notion of a prograde to peak isobaric *P–T* path for the mafic rocks are garnet modal proportions, which increase along the same isobaric *P–T* trajectory (Fig. S5k). The calculated peak metamorphic conditions of ~17 kbar and ~700 °C correspond to a geothermal gradient of ~410 °C/GPa, consistent with a geodynamic regime characterised by warm continental collision and subduction (section 6.2.3; Syracuse *et al.*, 2010; Penniston-Dorland *et al.*, 2015; Brown and Johnson, 2018; van Keken *et al.*, 2018). Peak metamorphic temperatures are warm with respect to modern oceanic and continental subduction systems (e.g. Gerya *et al.*, 2002; Sizova *et al.*, 2014; Penniston-Dorland *et al.*, 2015). This result can be plausibly attributed to the higher thermal gradients present in the Palaeoproterozoic Earth (e.g. Herzberg *et al.*, 2010; Bradley 2011; Anderson *et al.*, 2012; Condie *et al.*, 2016).

The retrograde evolution of the eclogites, constrained by sample T06-11, involved near-isothermal post-peak decompression to granulite-facies conditions of 7.6–8.2 kbar and 680–790 °C (Fig. 13). Sample T06-11 records lower retrograde pressures with respect to sample T01-39 (Fig. 12). We suggest this pressure difference may be explained by the influence of strain catalysing the formation of a strong post-peak foliation in sample T06-11. In contrast, unfoliated sample T01-39 likely represents a kinetically less reactive low-strain domain. The interpreted near-isothermal post-peak *P–T* evolution for the eclogites (constrained using the range of Zr-in-rutile temperature estimates from rutile grains within quartzofeldspathic veins in sample T06-11), agrees with the interpreted post-peak evolution for sample T01-39 (Fig. 12). This supports the notion that both mafic samples experienced a similar *P–T* history.

The calculated peak *P–T* conditions for the eclogites are in general agreement with published results of ~18 kbar and ~750 °C (Moller *et al.*, 1995). However, the peak pressure estimates derived by Moller *et al.* (1995) use plagioclase-bearing barometers and garnet core-rim compositions. Since plagioclase is unambiguously retrograde, the compositions used by Moller *et al.* (1995) are not representative of an equilibrium mineral assemblage. Mineral equilibria forward modelling in this study not only predicts the establishment of slightly lower peak pressures and temperatures than those derived by Moller *et al.* (1995), it also predicts a peak metamorphic history characterised by isobaric heating subsequent to the establishment of peak pressure conditions of ~17 kbar – a history that was not reflected in the previous attempt to derive *P–T* constraints on the Usagaran mafic rocks using conventional thermobarometric methods (Moller *et al.*, 1995). Importantly, this study presents the first interpretation of a burial history for the Usagaran mafic rocks.

P–T evolution of the metapelitic rocks

Metapelitic sample T06-20 is interpreted to record an upper amphibolite-facies prograde evolution characterised by increasing pressures and temperatures, consistent with a burial history (Fig. 14). The inclusion assemblage within garnet, kyanite and amphibole porphyroblasts (section 3.4) and the observation of the preservation of growth zonation in porphyroblastic garnet (Fig. 8d) suggests the metapelitic gneisses reached garnet-plagioclase-stable conditions of 7.5–9 kbar and 645–660 °C (Fig. 14). However, compositional zoning patterns in porphyroblastic garnet suggests that sample T06-20 likely reached higher pressures, while increasing its proportion of garnet and kyanite (Fig. S7a, b; Fig. S7g, h). Continued burial to higher pressures is also suggested by evidence for minor, outcrop- and thin-section-scale migmatization (Fig. 3c, d; Fig. 6e, h), and average temperatures derived from Zr concentrations in

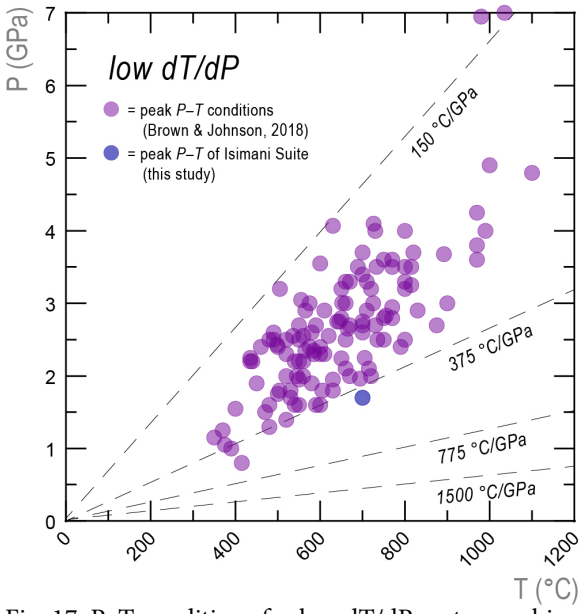


Fig. 17. P–T conditions for low dT/dP metamorphism in the literature (purple circles; after Brown and Johnson, 2018). P–T conditions for the Isimani rock system (blue circle; this study). The Isimani P–T point corresponds to one of the highest recorded thermal gradients among the examples on the P–T diagram. This indicates that the Isimani rock system was not metamorphosed under subduction conditions comparable to those operating post-Neoproterozoic time. Rather, comparatively thermally elevated subduction likely produced the Isimani Suite.

inferred prograde to peak rutile (Fig. 10c). Despite the potential for partial melting, modal proportions of melt along the interpreted suprasolidus burial path are consistently below ~4%. Therefore, the inferred burial *P–T* conditions are not conducive to melt loss (Fig. 14; Fig. S7i; Rosenberg and Handy, 2005).

Porphyroblastic garnets show evidence for Mn enrichment at their rims (Fig. 8), consistent with dissolution. Estimates for the amount of dissolution suggest the garnets were ~30% larger than as currently preserved (section 5.1.1). We infer this precursor garnet proportion to be representative of the garnet proportion at peak pressure conditions, implying that the burial history of the metapelitic rocks terminated at pressures of at least 16.5–17 kbar (Fig. 14; Fig. S7g, h). It is not clear which Zr-in-rutile-derived temperature estimates are representative of those recorded at the temperature peak given a significant proportion of the estimates reflect prograde temperatures (Fig. 10c). This factor, as well as the insufficient petrological data relating to the peak history of the rock, does not permit peak temperatures to be well constrained. At the pressures quoted above, and within the 2σ uncertainty on the average Zr-in-rutile temperatures, the modelled assemblage is garnet + hornblende + kyanite + muscovite + paragonite + rutile + quartz ± H_2O, melt. This modelled assemblage is not consistent with the petrologically inferred peak assemblage (section 3.4). However, given the significant degree of garnet dissolution inferred to have occurred during retrogression (section 5.1.1), it is possible that the inferred peak assemblage — including mineral proportions and compositions — is in no way representative of the assemblage present at peak pressure conditions. If this interpretation is correct, it means that the estimation of the precursor garnet mode is the only observable variable that may provide insight into the peak history of the metapelitic rocks. Conceivably, the disparity between the true peak assemblage and the inferred

peak assemblage in the metapelitic rocks may be a consequence of retrogression during the rock's post-peak evolution. Because the mafic rocks preserve petrological evidence of their high-pressure history, the implication for the metapelitic gneisses is that they were more easily retrogressed. This interpretation appears reasonable given the evidence of minor migmitization in the metapelitic rocks (Fig. 3c, d; Fig. 6e, h) – suggesting that the fluid retained in the rock at peak metamorphic conditions may have helped facilitate the conversion of peak minerals into the current assemblage observed in the rock.

Workers have also commonly presented two additional models used to explain the preserved petrological character of metapelitic rocks that host mafic domains in high-pressure terranes. (1) The metapelitic rocks were unable to transform their assemblage during their high-pressure history (e.g. Young and Kylander-Clark, 2015), or (2) they did not reach high-pressure conditions, but rather, they experienced a comparatively low-pressure *P–T* history to that of the mafic rocks the enclose (e.g. Bousquet, 2008; Hacker *et al.*, 2010). With respect to the metapelitic gneisses in question, both models appear possible, yet implausible – particularly the second model. Due to the reasoning outlined in the previous paragraph, we prefer a model whereby the metapelitic gneisses underwent high-pressure conditions and were subsequently re-equilibrated during post-peak retrogression.

The current assemblage in metapelitic sample T06-20 records amphibolite-facies retrograde *P–T* conditions of approximately 6–8 kbar and 520–600 °C (Fig. 15). It is difficult to interpret a precise post-peak *P–T* path for the metapelitic rocks due to the absence of petrological information relating to its immediate post-peak *P–T* history. The two calculated *P–T* models for metapelitic sample T06-20 are only valid for interpreting the prograde to peak history (Fig. 14) and the retrograde conditions (Fig. 15), due to the specific effective compositions used in the *P–T* calculations. Therefore, we cannot propose a reasonable interpretation regarding the character of the post-peak evolution based on the results from mineral equilibria modelling. The results from *P–T* modelling only permit us to conclude that the metapelitic rocks reached minimum peak pressures of approximately 16.5–17 kbar and evolved through unconstrained pressures and temperatures, until stalling at mid-crustal depths.

Burial and exhumation history of the Isimani Suite

Comparing the metamorphic evolution of the eclogites and metapelitic gneisses

Current consensus holds that all rock types of the Isimani Suite in the Usagaran Belt share a mutual tectonometamorphic history (Möller *et al.*, 1995; Ring *et al.*, 1997; Reddy *et al.*, 2003; Collins *et al.*, 2004). The interpretations in this study derived from mineral equilibria modelling, mineral compositions (particularly garnet compositions)

and the petrology, broadly agree with this model. The relict eclogites (represented by sample T01-39) preserve plagioclase coronae rimming garnet (Fig. 4e), and clinopyroxene-plagioclase intergrowths (Fig. 4f), both of which are consistent with high-pressure metamorphic conditions. Compositions of intergrown clinopyroxene, plagioclase and titano-hematite in mafic sample T01-39 reintegrate to a ferric-omphacitic clinopyroxene composition (Table 4), further supporting a former high-pressure regime. Additionally, mineral equilibria modelling of sample T01-39 (section 5.3.1) suggests the eclogites reached eclogite-facies conditions of ~17 kbar and ~700 °C. In contrast, evidence for a high-pressure history in the metapelitic gneiss is enigmatic. However, the interpretation that a significant proportion of garnet underwent dissolution at the rim suggests the metapelitic gneisses were buried to pressures of at least 16–17.5 kbar. These pressures are comparable to those experienced by the relict eclogites and therefore support a shared peak *P*–*T* history for the eclogites and metapelitic gneisses (Fig. 16). The metapelitic gneiss sample lacks evidence for heating at high-pressures, as recorded by mafic sample T01-39. However, this may be plausibly explained by the influence of post-peak recrystallisation and retrogression in the metapelitic gneiss.

Mineral equilibria modelling also demonstrates that the protoliths to the eclogites and metapelitic gneisses underwent a similar prograde to peak burial evolution that was characterised by partial melting in the metapelitic gneisses (Fig. 16). However, the nature of the partial melting process during burial of the mafic rocks is not well constrained and it is not clear if the mafic rocks underwent partial melting (Fig. 11; section 6.1.1). If these rocks did melt, mineral equilibria modelling shows they would have produced significantly less melt than the protoliths to the metapelitic gneisses (Fig. S5e; Fig. S7i). This difference can simply be attributed to the greater proportion of hydrous minerals in the metapelitic gneisses.

The retrograde *P*–*T* conditions constrained for the eclogitic rocks and metapelitic gneisses are barically similar but thermally distinct (Fig. 16). Both sets of retrograde conditions span large temperature ranges, suggesting that the temperature disparity may not be linked to an external geological factor, but instead be a consequence of the inability to precisely constrain retrograde temperatures using calculated compositions and mineral proportions. However, mafic sample T06-11 preserves an orthopyroxene-bearing mylonitic fabric (section 3.2), suggesting its retrograde evolution may have involved a degree of shear heating. The fabric in metapelitic sample T06-20 shows clear microstructural deformation features (Fig. 6f), but lacks minerals that typically grow at elevated temperatures and relatively low pressures. Therefore, the retrograde temperature disparity may also be accounted for by localised deformation as the Isimani rock system was being exhumed.

There is not enough information to distinguish between the two possibilities.

5.2 Timescales associated with burial and exhumation of the Isimani Suite

Collins *et al.* (2004) interpreted an age of c. 2000 Ma for the eclogite-facies metamorphic event based on a U–Pb zircon-monazite weighted average using three amphibolite-facies gneissic samples and one relict eclogite sample. Implicit in this approach is the assumption that the different rock types of the Isimani Suite underwent the same *P–T* history, and the mineral geochronometers in each rock type formed at the same time. The mineral equilibria modelling in this study demonstrates that the Isimani eclogites and metapelitic gneisses likely experienced a shared *P–T* history, therefore confirming the assumption by Collins *et al.* (2004). The age of the zircons in the relict eclogite (1986 ± 29 Ma; Collins *et al.*, 2004) is within error of the ages of the amphibolite-facies gneisses (1999 ± 2 Ma and 2000 ± 2 Ma; Möller *et al.*, 1995; 1989 ± 10 Ma and 1997.6 ± 2.2 Ma; Collins *et al.*, 2004), and therefore, it is possible that peak metamorphism in the respective thermobarometric domains occurred coevally. However, the uncertainty on the zircon age of the relict eclogite is large, making this interpretation difficult to evaluate. Furthermore, the regionally pervasive amphibolite-facies mylonitic fabric interpreted to have developed during the exhumation of the eclogite-facies rocks (Reddy *et al.*, 2003) has a minimum age of c. 1991 Ma, based on the age of a cross-cutting pegmatite (Collins *et al.*, 2004). This age was inferred by Collins *et al.* (2004) to mark the termination of the eclogite-facies regime, and was used to suggest that the eclogites were exhumed rapidly. However, the lack of precise age constraints on the eclogite facies metamorphism means that an interpretation of rapid exhumation cannot be based on geochronology alone.

The partial preservation of growth zonation in relict eclogite T01-39 garnet (Fig. 7a, b) provides an alternative method for assessing exhumation rates. The garnets in T01-39 show decreasing almandine and spessartine, and increasing pyrope from core to rim, typical in garnet interpreted to preserve growth zonation in high-pressure mafic rocks (O'Brien, 1997; Konrad-Schmolke *et al.*, 2008). Furthermore, the rimward decrease in X_{Fe} is consistent with an increase in temperature during garnet growth (Spear, 1995). Temperature–time–crystal-size diffusional gradients calculated by Caddick *et al.* (2010) show that the core composition of a 2.5 mm spherical garnet at ~750 °C will undergo significant re-equilibration if these thermal conditions are sustained for longer than ~2 Myr. If the diameter of garnet is increased by 0.5 mm (the width of plagioclase coronae in sample T01-39), re-equilibration of the garnet core composition occurs if peak temperatures are maintained for longer than ~3 Myr. The mineral equi-

libria models suggest that the greatest decrease in garnet X_{Fe} trending up-pressure (and thus most of the garnet growth) occurs at temperatures between 680 and 700 °C in the broad region of *P–T* space through which the rock is inferred to have traversed through during burial (Fig. 11; Fig. S5a, b). At these temperatures, growth zoning in a 3 mm garnet can be preserved for up to 20 Myr (Caddick *et al.*, 2010). Therefore, although it is not possible to exactly constrain the duration of eclogite-facies metamorphism, the partial preservation of growth zonation in T01-39 garnet requires that the prograde, peak and retrograde *P–T* evolution for the eclogites spanned up to 20 Myr (Caddick *et al.*, 2010), and that the rocks cooled rapidly after experiencing near-isothermal decompression (Fig. 16). The similar burial history of the protoliths to the metapelitic gneisses to that of eclogite protoliths as suggested by mineral equilibria modelling (Fig. 16), the conformable baric histories of the eclogites and the host metapelitic gneisses (Fig. 16), and the evidence for garnet growth zonation in the metapelitic gneiss (Fig. 8d), suggests the timescales based on eclogitic garnet quoted above also apply to the metapelitic rocks.

5.3 Thermal character of peak metamorphism and implications for Precambrian tectonics

The prograde, peak and retrograde *P–T* history of the eclogites and metapelitic gneisses of the Isimani Suite appears to have been short-lived. A short-lived *P–T* history is only conceivable in a tectonic system that promotes rapid burial and exhumation. Figure 16 shows that the protoliths to the eclogites and metapelitic gneisses saw similar burial and peak histories. As suggested in section 6.1.1, the warm peak thermal gradient interpreted for the Isimani system and the peak metamorphic isobaric heating path constrained for the mafic rocks may be a consequence of the higher thermal gradients present in the Palaeoproterozoic Earth (e.g. Herzberg *et al.*, 2010; Bradley 2011; Anderson *et al.*, 2012; Condie *et al.*, 2016). At elevated ambient upper mantle temperatures akin to those apparent in the Palaeoproterozoic, Sizova *et al.* (2014) demonstrates using 2-D thermomechanical numerical models that rocks may be buried to pressures of 20–30 kbar along similar geotherms as those described in this study. Moreover, such models predict that these rocks are buried and subsequently exhumed to mid-crustal levels in the space of ~10 Myr (e.g. Sizova *et al.*, 2014). Such collisional systems promote subduction and comprise strongly deformed and weak lower crustal keels. The continental crust undergoes partial melting at its base and does not reach mantle depths (e.g. Burov and Yamato, 2008; Sizova *et al.*, 2014). Instead, slab breakoff occurs beneath the orogenic keel, and substantial thickening of the continental crust occurs at the collision zone. These Palaeoproterozoic collisional systems typically produce clockwise *P–T* paths, as observed

for the metamorphic evolution of relict eclogite sample T01-39 in this study (Fig. 16). Granted, the overall *P–T* path for metapelitic gneiss T06-20 is partly unconstrained, with information about its post-peak history lacking. However, given the evidence presented in this study demonstrating a similar baric history for both the eclogites and metapelitic gneisses, it is unlikely that the metapelitic gneisses evolved through a counter-clockwise peak to post-peak *P–T* path.

The model described above may be a reasonable analogue for rocks of the Isimani Suite, where it is envisaged that the margin of the Tanzanian Craton was subducted during the Palaeoproterozoic (Reddy *et al*., 2003). This is supported by Sm–Nd isotopic data and Lu–Hf in zircon indicating that both the c. 2000 Ma Usagaran eclogitic domains and the Usagaran metapelitic gneisses are comparatively evolved (Möller *et al*., 1998; Maboko, 2000; Brick, 2011). The calculated apparent thermal gradient for eclogite-facies metamorphism (~410 °C/GPa; section 6.1.1) is consistent with a convergent regime involving crustal thickening and comparatively warm subduction (such as the regime proposed by Sizova *et al*., 2014), as opposed to one characterised by deep, cold, modern-style subduction (Fig. 17; Syracuse *et al*., 2010; Penniston-Dorland *et al*., 2015; Brown and Johnson, 2018; van Keken *et al*., 2018).

5.4 Exhumation of the Isimani Suite

Although Reddy *et al*. (2003) argued that transpression was responsible for the exhumation of the Isimani Suite, the lineation geometries of the rocks that form part of the same rock package as metapelitic sample T06-20 are shallowly plunging; a structural feature that is also common in extensional or transtentional systems (Krabbendam and Dewey, 1998; Dewey, 2002; Johnston *et al*., 2007; Hacker *et al*., 2010). Furthermore, most workers agree that thrust-related processes will not exhume rocks from mantle depths (e.g. Ernst and Liou, 2008; Gerya, 2014; Hacker and Gerya, 2013; Sizova *et al*., 2014). An alternative mechanism is buoyancy-driven exhumation that acts on its own or is augmented by upper plate extension (e.g. Anderson *et al*., 1991; Burov *et al*., 2001; Ernst *et al*., 2001; Kaneko *et al*., 2001; Hacker *et al*., 2003; Bousquet, 2008; Duretz *et al*., 2012; Petersen and Buck, 2015). Following high-pressure metamorphism, the eclogites and the metapelitic gneisses that enclosed them were exhumed to mid-crustal depths (~30 km depth) by 1991 ± 2 Ma (Fig. 16; Collins *et al*., 2004). The drivers for initial exhumation from eclogite-facies conditions are difficult to identify, however, it is conceivable — given the apparent short-lived *P–T* history for the Isimani system — that the continental host rocks, together with the eclogite-facies domains, were buoyantly exhumed following slab breakoff. It is possible that the buoyant rise of material created an effective wedge characterised by an upper

surface bounded by an extensional detachment, and a lower surface which was effectively a thrust (Fig. 16). Though speculative, such an exhumation mechanism has been interrogated using 2-D numerical thermomechanical models, similar to those presented by Sizova *et al.* (2014) for the burial and exhumation of Palaeoproterozoic continental crust (e.g. Duretz *et al.*, 2012; Duretz and Gerya, 2013; Petersen and Buck, 2015). Petersen and Buck (2015) demonstrate that, in a subduction-collision tectonic system, buoyancy-driven extensional to transtentional exhumation invariably occurs following crustal thickening and slab breakoff, and can exhume continental material within a time-span of 5 Myr.

In a similar context, the occurrence of high-pressure and ultrahigh-pressure rocks in the Western Gneiss Region (WGR) of Norway has been attributed to an exhumation mechanism that may be an analogue for the Isimani Suite (e.g. Andersen, 1998; Krabbendam and Dewey, 1998; Hacker *et al.*, 2003; Walsh and Hacker, 2004; Hacker, 2007; Johnston *et al.*, 2007; Hacker *et al.*, 2010). Hacker *et al.* (2010) describes a post-peak tectonic evolution for the high-pressure rocks of the WGR whereby the ultrahigh- to high-pressure section of the slab is exhumed coherently and along near-isothermal conditions by normal-sense motion along a major detachment (Fig. 8; e.g. Hacker *et al.*, 2003; Hacker *et al.*, 2007; Johnston *et al.*, 2007; Hacker *et al.*, 2010). Walsh and Hacker (2004) describe a similar exhumation mechanism for the WGR high-pressure terrane. They describe the exhumation of the WGR Upper Allochthon — containing mafic eclogite, hosted by garnet amphibolites, feldspathic gneisses and garnet-kyanite-staurolite-mica metapelites — from approximately Moho depths to mid-crustal depths. The high-pressure rock package is thought to have been driven to mid-crustal depths along large-scale extensional detachments, possibly partly as a response to ongoing crustal thickening. This exhumation event presented by Walsh and Hacker (2004) is inferred to precede an earlier stage of exhumation from ultrahigh pressures. Importantly, the workers demonstrate that the mafic rocks record aspects of their ultrahigh- and high-pressure histories, while their enclosing host gneisses show pervasive mineralogical recrystallisation – not unlike what is proposed for the rocks of the Isimani Suite in this study.

6. Conclusion

Rocks comprising the Palaeoproterozoic Isimani Suite in the Usagaran Belt of central Tanzania were buried and exhumed as a single, coherent rock package. Circa 2000 Ma eclogite-facies mafic rocks preserve clear evidence of their high-pressure history. In contrast, the migmatitic metapelitic gneisses preserve only enigmatic evidence of a high-pressure history. The protoliths to the eclogites and metapelitic gneisses were buried rapidly

in a warm continental collision and subduction system involving the rifted margin of the Tanzanian Craton. After reaching peak pressures of ~17 kbar, the Isimani rock package containing both the eclogites and metapelitic gneisses was likely exhumed rapidly to mid-crustal depths, conceivably as a consequence of extensional tectonics. The heightened thermal gradient and rapid exhumation recorded by the Isimani rocks suggests that subduction-driven geodynamic systems – operating at comparatively warmer thermal regimes with respect to the modern day – were well established by the mid-Palaeoproterozoic. Additionally, the use of modern modelling methods to derive the peak metamorphic conditions and thermal gradient for the mafic eclogite-facies rocks is an important addition to the emergent dataset of *P–T* conditions for Palaeoproterozoic eclogite-facies rocks, thereby ensuring that this dataset may be reasonably compared with Palaeoproterozoic subduction thermal models.

Acknowledgements

We acknowledge the financial support provided by the Australian Research Council (ARC) grant DP16010437 and the financial support provided by the University of Adelaide. The quality of the manuscript was greatly improved by helpful suggestions from Andrew Kylander-Clark and one anonymous reviewer. We thank the two reviewers. We also thank Eric Tohver and Guochun Zhao for their editorial handling. Lastly, we are grateful to Ben Wade and Sarah Gilbert of Adelaide Microscopy for their assistance in mineral analysis. Alan Collins is also thanked for providing sample T01-39.

For supplementary materials of this Appendix please see the published version at https://doi.org/10.1016/j.precamres.2020.105833.

References

Agard, P., Plunder, A., Angiboust, S., Bonnet, G., and Ruh, J. (2018). The subduction plate interface: rock record and mechanical coupling (from long to short timescales). *Lithos, 320-321*, 537-566. doi:10.1016/j.lithos.2018.09.029

Agard, P., Yamato, P., Jolivet, L., and Burov, E. (2009). Exhumation of oceanic blueschists and eclogites in subduction zones: Timing and mechanisms. *Earth-Science Reviews, 92*(1-2), 53-79. doi:10.1016/j.earscirev.2008.11.002

Andersen, T. B. (1991). Subduction and eduction of continental crust: major mechanisms during continent-continent collision and orogenic extensional collapse, a model based on the south Norwegian Caledonides. *Terra Nova, 3*(3), 303-310. doi:10.1111/j.1365-3121.1991.tb00148.x

Andersen, T. B. (1998). Extensional tectonics in

the Caledonides of southern Norway, an overview. *Tectonophysics, 285*(3-4), 333-351. doi:10.1016/S0040-1951(97)00277-1

Anderson, E. D., and Moecher, D. P. (2007). Omphacite breakdown reactions and relation to eclogite exhumation rates. *Contributions to Mineralogy and Petrology, 154*(3), 253-277. doi:10.1007/s00410-007-0192-x

Anderson, J. R., Payne, J. L., Kelsey, D. E., Hand, M., Collins, A. S., and Santosh, M. (2012). High-pressure granulites at the dawn of the Proterozoic. *Geology, 40*(5), 431-434. doi:10.1130/g32854.1

Baldwin, J. A., Bowring, S. A., and Williams, M. L. (2003). Petrological and geochronological constraints on high pressure, high temperature metamorphism in the Snowbird tectonic zone, Canada. *Journal of Metamorphic Geology, 21*(1), 81-98. doi:10.1046/j.1525-1314.2003.00413.x

Baldwin, J. A., Bowring, S. A., Williams, M. L., and Williams, I. S. (2004). Eclogites of the Snowbird tectonic zone: petrological and U-Pb geochronological evidence for Paleoproterozoic high-pressure metamorphism in the western Canadian Shield. *Contributions to Mineralogy and Petrology, 147*(5), 528-548. doi:10.1007/s00410-004-0572-4

Baldwin, J. A., Powell, R., Williams, M. L., and Goncalves, P. (2007). Formation of eclogite, and reaction during exhumation to mid-crustal levels, Snowbird tectonic zone, western Canadian Shield. *Journal of Metamorphic Geology, 25*(9), 953-974. doi:10.1111/j.1525-1314.2007.00737.x

Boniface, N., Schenk, V., and Appel, P. (2012). Paleoproterozoic eclogites of MORB-type chemistry and three Proterozoic orogenic cycles in the Ubendian Belt (Tanzania): Evidence from monazite and zircon geochronology, and geochemistry. *Precambrian Research, 192-195*, 16-33. doi:10.1016/j.precamres.2011.10.007

Bousquet, R. (2008). Metamorphic heterogeneities within a single HP unit: Overprint effect or metamorphic mix? *Lithos, 103*(1-2), 46-69. doi:10.1016/j.lithos.2007.09.010

Bradley, D. C. (2011). Secular trends in the geologic record and the supercontinent cycle. *Earth-Science Reviews, 108*(1-2), 16-33. doi:10.1016/j.earscirev.2011.05.00

Brick, R. A. (2011). *Palaeoproterozoic eclogite formation in Tanzania: a structural, geochronological, thermochronological and metamorphic study of the Usagaran and Ubende orogenic belts.* (Doctorate), University of Adelaide, Australia.

Bromiley, G. D., and Keppler, H. (2004). An experimental investigation of hydroxyl solubility in jadeite and Na-rich clinopyroxenes. *Contributions to Mineralogy and Petrology, 147*(2), 189-200. doi:10.1007/s00410-003-0551-1

Brown, M. (2006). Duality of thermal regimes is the distinctive characteristic of plate tectonics since the Neoarchean. *Geology, 34*(11), 961. doi:10.1130/g22853a.1

Brown, M. (2010). Paired metamorphic belts revisited. *Gondwana Research, 18*(1), 46-59. doi:10.1016/j.gr.2009.11.004

Brown, M., and Johnson, T. (2018). Secular change in metamorphism and the onset of global plate tectonics. *American Mineralogist, 103*(2), 181-196. doi:10.2138/am-2018-6166

Burov, E., Jolivet, L., Le Pourhiet, L., and Poliakov, A. (2001). A thermomechanical model of exhumation of high pressure (HP) and ultra-high pressure (UHP) metamorphic rocks in Alpine-type collision belts. *Tectonophysics, 342*(1-2), 113-136. doi:10.1016/S0040-1951(01)00158-5

Burov, E., and Yamato, P. (2008). Continental plate collision, P–T–t–z conditions and unstable vs. stable plate dynamics: Insights from thermo-mechanical modelling. *Lithos, 103*(1-2), 178-204. doi:10.1016/j.lithos.2007.09.014

Caddick, M. J., Konopásek, J., and Thompson, A. B. (2010). Preservation of Garnet Growth Zoning and the Duration of Prograde Metamorphism. *Journal of Petrology, 51*(11), 2327-2347. doi:10.1093/petrology/egq059

Chopin, C. (2003). Ultrahigh-pressure metamorphism: tracing continental crust into the mantle. *Earth and Planetary Science Letters, 212*(1-2), 1-14. doi:10.1016/s0012-821x(03)00261-9

Chopin, C., and Schertl, H.-P. (1999). The UHP Unit in the Dora-Maira Massif, Western Alps. *International Geology Review, 41*(9), 765-780. doi:10.1080/00206819909465168

Chu, X., Ague, J. J., Axler, J. A., and Tian, M. (2016). Taconian retrograde eclogite from northwest Connecticut, USA, and its petrotectonic implications. *Lithos, 240-243*, 276-294. doi:10.1016/j.lithos.2015.10.011

Collins, A. S., Reddy, S. M., Buchan, C., and Mruma, A. (2004). Temporal constraints on Palaeoproterozoic eclogite formation and exhumation (Usagaran Orogen, Tanzania). *Earth and Planetary Science Letters, 224*(1-2), 175-192. doi:10.1016/j.epsl.2004.04.027

Condie, K. C., Aster, R. C., and van Hunen, J. (2016). A great thermal divergence in the mantle beginning 2.5 Ga: Geochemical constraints from greenstone basalts and komatiites. *Geoscience Frontiers, 7*(4), 543-553. doi:10.1016/j.gsf.2016.01.006

Cuthbert, S. J., Carswell, D. A., Krogh-Ravna, E. J., and Wain, A. (2000). Eclogites and eclogites in the Western Gneiss Region, Norwegian Caledonides. *Lithos, 52*(1-4), 165-195. doi:10.1016/S0024-4937(99)00090-0

Dewey, J. F. (2010). Transtension in Arcs and Oro-

gens. *International Geology Review, 44*(5), 402-439. doi:10.2747/0020-6814.44.5.402

Droop, G. T. R. (1987). A general equation for estimating Fe3+ concentrations in ferromagnesian silicates and oxides from microprobe analyses, using stoichiometric criteria. *Mineralogical Society, 51*(361), 431-435. doi:10.1180/minmag.1987.051.361.10

Duretz, T., and Gerya, T. V. (2013). Slab detachment during continental collision: Influence of crustal rheology and interaction with lithospheric delamination. *Tectonophysics, 602*, 124-140. doi:10.1016/j.tecto.2012.12.024

Duretz, T., Gerya, T. V., Kaus, B. J. P., and Andersen, T. B. (2012). Thermomechanical modeling of slab eduction. *Journal of Geophysical Research: Solid Earth, 117*(8). doi:10.1029/2012jb009137

Ernst, W. G. (2001). Subduction, ultrahigh-pressure metamorphism, and regurgitation of buoyant crustal slices — implications for arcs and continental growth. *Physics of the Earth and Planetary Interiors, 127*(1-4), 253-275. doi:10.1016/S0031-9201(01)00231-X

Ernst, W. G., and Liou, J. G. (2008). High- and ultrahigh-pressure metamorphism: Past results and future prospects. *American Mineralogist, 93*(11-12), 1771-1786. doi:10.2138/am.2008.2940

Foley, S. F., Buhre, S., and Jacob, D. E. (2003). Evolution of the Archaean crust by delamination and shallow subduction. *Nature, 421*(6920), 249-252. doi:10.1038/nature01319

Francois, C., Debaille, V., Paquette, J. L., Baudet, D., and Javaux, E. J. (2018). The earliest evidence for modern-style plate tectonics recorded by HP-LT metamorphism in the Paleoproterozoic of the Democratic Republic of the Congo. *Sci Rep, 8*(1), 15452. doi:10.1038/s41598-018-33823-y

Fritz, H., Tenczer, V., Hauzenberger, C. A., Wallbrecher, E., Hoinkes, G., Muhongo, S., and Mogessie, A. (2005). Central Tanzanian tectonic map: A step forward to decipher Proterozoic structural events in the East African Orogen. *Tectonics, 24*(6), 1-26. doi:10.1029/2005tc001796

Gao, J., John, T., Klemd, R., and Xiong, X. (2007). Mobilization of Ti–Nb–Ta during subduction: Evidence from rutile-bearing dehydration segregations and veins hosted in eclogite, Tianshan, NW China. *Geochimica et Cosmochimica Acta, 71*(20), 4974-4996. doi:10.1016/j.gca.2007.07.027

Gerya, T. (2014). Precambrian geodynamics: Concepts and models. *Gondwana Research, 25*(2), 442-463. doi:10.1016/j.gr.2012.11.008

Gerya, T. V., Stöckhert, B., and Perchuk, A. L. (2002). Exhumation of high-pressure met-

amorphic rocks in a subduction channel: A numerical simulation. *Tectonics, 21*(6), 6-1-6-19. doi:10.1029/2002tc001406

Green, E. C. R., White, R. W., Diener, J. F. A., Powell, R., Holland, T. J. B., and Palin, R. M. (2016). Activity-composition relations for the calculation of partial melting equilibria in metabasic rocks. *Journal of Metamorphic Geology, 34*(9), 845-869. doi:10.1111/jmg.12211

Hacker, B. (2007). Ascent of the ultrahigh-pressure Western Gneiss Region, Norway, in Cloos, M., Carlson, W.D., Gilbert, M.C., Liou, J.G., and Sorensen, S.S., eds., Convergent Margin Terranes and Associated Regions: A Tribute to W.G. Ernst: *Geological Society of America Special Paper*, *(419)*, 171-184. doi: 10.1130/2006.2419(09)

Hacker, B. R., and Gerya, T. V. (2013). Paradigms, new and old, for ultrahigh-pressure tectonism. *Tectonophysics, 603*, 79-88. doi:10.1016/j.tecto.2013.05.026

Hacker, B. R., Andersen, T. B., Johnston, S., Kylander-Clark, A. R. C., Peterman, E. M., Walsh, E. O., and Young, D. (2010). High-temperature deformation during continental-margin subduction and exhumation: The ultrahigh-pressure Western Gneiss Region of Norway. *Tectonophysics, 480*(1-4), 149-171. doi:10.1016/j.tecto.2009.08.012

Hacker, B. R., Andersen, T. B., Root, D. B., Mehl, L., Mattinson, J. M., and Wooden, J. L. (2003). Exhumation of high-pressure rocks beneath the Solund Basin, Western Gneiss Region of Norway. *Journal of Metamorphic Geology, 21*(6), 613-629. doi:10.1046/j.1525-1314.2003.00468.x

Hand, M., and Dirks, P. H. G. M. (1992). The influence of deformation on the formation of axial-planar leucosomes and the segregation of small melt bodies within the migmatitic Napperby Gneiss, central Australia. *Journal of Structural Geology, 14*(5), 591-604. doi:10.1016/0191-8141(92)90159-T

Hellstrom, J., Paton, C., Woodhead, J. D., and Hergt, J. (2008). Iolite: Software for spatially resolved LA–(QUAD and MC)–ICP–MS Analysis. *Mineralogical Association of Canada, Short Course Series, 40*, 343-348.

Herzberg, C., Condie, K., and Korenaga, J. (2010). Thermal history of the Earth and its petrological expression. *Earth and Planetary Science Letters, 292*(1-2), 79-88. doi:10.1016/j.epsl.2010.01.022

Holland, T. J. B., and Powell, R. (2011). An improved and extended internally consistent thermodynamic dataset for phases of petrological interest, involving a new equation of state for solids. *Journal of Metamorphic Geology, 29*(3), 333-383. doi:10.1111/j.1525-1314.2010.00923.x

Houketchang Bouyo, M., Penaye, J., Mouri, H., and Toteu, S. F. (2019). Eclogite facies metabasites from the Paleoproterozoic Nyong Group, SW Cameroon: Mineralogical evidence and implications for a high-pressure metamorphism related to a subduction zone at the NW margin of the Archean Congo craton. *Journal of African Earth Sciences, 149*, 215-234. doi:10.1016/j.jafrearsci.2018.08.010

Janák, M., Cornell, D., Froitzheim, N., De Hoog, J. C. M., Broska, I., Vrabec, M., and Hurai, V. (2009). Eclogite-hosting metapelites from the Pohorje Mountains (Eastern Alps): P-T evolution, zircon geochronology and tectonic implications. *European Journal of Mineralogy, 21*(6), 1191-1212. doi:10.1127/0935-1221/2009/0021-1966

Jiao, S., Guo, J., Mao, Q., and Zhao, R. (2010). Application of Zr-in-rutile thermometry: a case study from ultrahigh-temperature granulites of the Khondalite belt, North China Craton. *Contributions to Mineralogy and Petrology, 162*(2), 379-393. doi:10.1007/s00410-010-0602-3

Jochum, K. P., Weis, U., Stoll, B., Kuzmin, D., Yang, Q., Raczek, I., . . . Enzweiler, J. (2011). Determination of Reference Values for NIST SRM 610-617 Glasses Following ISO Guidelines. *Geostandards and Geoanalytical Research, 35*(4), 397-429. doi:10.1111/j.1751-908X.2011.00120.x

Jochum, K. P., Wilson, S. A., Abouchami, W., Amini, M., Chmeleff, J., Eisenhauer, A., . . . Woodhead, J. D. (2010). GSD-1G and MPI-DING Reference Glasses for In Situ and Bulk Isotopic Determination. *Geostandards and Geoanalytical Research, 35*(2), 193-226. doi:10.1111/j.1751-908X.2010.00114.x

Johnson, T. E., Brown, M., Kaus, B. J. P., and VanTongeren, J. A. (2013). Delamination and recycling of Archaean crust caused by gravitational instabilities. *Nature Geoscience, 7*(1), 47-52. doi:10.1038/ngeo2019

Johnston, S. M., Hacker, B. R., and Andersen, T. B. (2007). Exhuming Norwegian ultrahigh-pressure rocks: Overprinting extensional structures and the role of the Nordfjord-Sogn Detachment Zone. *Tectonics, 26*(5). doi:10.1029/2005tc001933

Kaneko, Y., Maruyama, S., Terabayashi, M., Yamamoto, H., Ishikawa, M., Anma, R., . . . Yamauchi, K. (2001). Geology of the Kokchetav UHP-HP metamorphic belt, Northern Kazakhstan. *The Island Arc, 9*(3), 264-283. doi:10.1046/j.1440-1738.2000.00278.x

Katayama, I., and Nakashima, S. (2003). Hydroxyl in clinopyroxene from the deep subducted crust: Evidence for H_2O transport into the mantle. *American Mineralogist, 88*(1), 229-234. doi:10.2138/am-2003-0126

Kohn, M. J., and Spear, F. S. (2000). Retrograde

net transfer reaction insurance for pressure-temperature estimates. *Geology, 28*(12), 1127-1130. doi:10.1130/0091-7613(2000)028<1127:RNTRIF>2.3.CO;2

Konrad-Schmolke, M., Zack, T., O'Brien, P. J., and Jacob, D. E. (2008). Combined thermodynamic and rare earth element modelling of garnet growth during subduction: Examples from ultrahigh-pressure eclogite of the Western Gneiss Region, Norway. *Earth and Planetary Science Letters, 272*(1-2), 488-498. doi:10.1016/j.epsl.2008.05.018

Krabbendam, M., and Dewey, J. F. (1998). Exhumation of UHP rocks by transtension in the Western Gneiss Region, Scandinavian Caledonides. *Geological Society, London, Special Publications, 135*(1), 159-181. doi:10.1144/gsl.Sp.1998.135.01.11

Kröner, A., Wilde, S. A., Zhao, G. C., O'Brien, P. J., Sun, M., Liu, D. Y., . . . Guo, J. H. (2006). Zircon geochronology and metamorphic evolution of mafic dykes in the Hengshan Complex of northern China: Evidence for late Palaeoproterozoic extension and subsequent high-pressure metamorphism in the North China Craton. *Precambrian Research, 146*(1-2), 45-67. doi:10.1016/j.precamres.2006.01.008

Leech, M. L. (2001). Arrested orogenic development: eclogitization, delamination, and tectonic collapse. *Earth and Planetary Science Letters, 185*(1-2), 149-159. doi:10.1016/S0012-821X(00)00374-5

Li, X., Zhang, L., Wei, C., and Slabunov, A. I. (2015). Metamorphic PT path and zircon U–Pb dating of Archean eclogite association in Gridino complex, Belomorian province, Russia. *Precambrian Research, 268*, 74-96. doi:10.1016/j.precamres.2015.07.009

Li, X., Zhang, L., Wei, C., Slabunov, A. I., and Bader, T. (2017). Neoarchean-Paleoproterozoic granulite-facies metamorphism in Uzkaya Salma eclogite-bearing mélange, Belomorian Province (Russia). *Precambrian Research, 294*, 257-283. doi:10.1016/j.precamres.2017.03.031

Li, X., Zhang, L., Wei, C., Slabunov, A. I., and Bader, T. (2018). Quartz and orthopyroxene exsolution lamellae in clinopyroxene and the metamorphic P-T path of Belomorian eclogites. *Journal of Metamorphic Geology, 36*(1), 1-22. doi:10.1111/jmg.12280

Liu, F., Zhang, L., Li, X., Slabunov, A. I., Wei, C., and Bader, T. (2017). The metamorphic evolution of Paleoproterozoic eclogites in Kuru-Vaara, northern Belomorian Province, Russia: Constraints from P-T pseudosections and zircon dating. *Precambrian Research, 289*, 31-47. doi:10.1016/j.precamres.2016.11.011

Liu, J., Jahn, B., Dong, S., Li, H., and Oberhansli, R. (2003). Neoproterozoic Granitoid Did Not Record Ultrahigh-Pressure Meta-

morphism from the Southern Dabieshan of China. *The Journal of Geology, 111*(719-732). doi:10.1086/378336

Liu, J., Ye, K., Maruyama, S., Cong, B., and Fan, H. (2001). Mineral Inclusions in Zircon from Gneisses in the Ultrahigh-Pressure Zone of the Dabie Mountains, China. *The Journal of Geology, 109*(4), 523-535. doi:10.1086/320796

Lombardo, B., and Rolfo, F. (2000). Two contrasting eclogite types in the Himalayas: implications for the Himalayan orogeny. *Journal of Geodynamics, 30*(1-2), 37-60. doi:10.1016/S0264-3707(99)00026-5

Loose, D., and Schenk, V. (2018). 2.09 Ga old eclogites in the Eburnian-Transamazonian orogen of southern Cameroon: Significance for Palaeoproterozoic plate tectonics. *Precambrian Research, 304*, 1-11. doi:10.1016/j.precamres.2017.10.018

Maboko, M. A. H. (2000). Nd and Sr isotopic investigation of the Archean–Proterozoic boundary in north eastern Tanzania: constraints on the nature of Neoproterozoic tectonism in the Mozambique Belt. *Precambrian Research, 102*(1-2), 87-98. doi:10.1016/S0301-9268(00)00060-7

Meyre, C., De Capitani, C., Zack, T., and Frey, M. (1999). Petrology of High-Pressure Metapelites from the Adula Nappe (Central Alps, Switzerland). *Journal of Petrology, 40*(1), 199-213. doi:10.1093/petroj/40.1.199

Mints, M. V., Belousova, E. A., Konilov, A. N., Natapov, L. M., Shchipansky, A. A., Griffin, W. L., . . . Kaulina, T. V. (2010). Mesoarchean subduction processes: 2.87 Ga eclogites from the Kola Peninsula, Russia. *Geology, 38*(8), 739-742. doi:10.1130/g31219.1

Möller, A. (1995). *Eclogites and migmatitic gneisses in the Usagaran domain* (Doctorate), Universität Kiel, Mainz, Germany.

Möller, A., Appel, P., Mezger, K., and Schenk, V. (1995). Evidence for a 2Ga subduction zone: Eclogites in the Usagaran belt of Tanzania. *Geology, 23*(12), 1067-1070. doi:10.1130/0091-7613(1995)023<1067:EFAGSZ>2.3.CO;2

Morimoto, N., Fabries, J., Ferguson, A. K., Ginzburg, I. V., Ross, M., Seifert, F. A., . . . Gottardi, G. (1988). Nomenclature of pyroxenes. *American Mineralogist, 73*, 1123-1133.

Mruma, A. (1989). *Stratigraphy, Metamorphism and Tectonic Evolution of the Early Proterozoic Usagaran Belt, Tanzania*. University of Oulu, Finland.

Muhongo, S., Kröner, A., and Nemchin, A. A. (2001). Single Zircon Evaporation and SHRIMP Ages for Granulite-Facies Rocks in the Mozambique Belt of Tanzania *The Journal of Geology, 109*(2), 171-189. doi:10.1086/319240

Müller, S., Dziggel, A., Kolb, J., and Sindern, S. (2018a). Mineral textural evolution and PT-path of relict eclogite-facies rocks in the Paleoproterozoic Nagssugtoqidian Orogen, South-East Greenland. *Lithos, 296-299*, 212-232. doi:10.1016/j.lithos.2017.11.008

Müller, S., Dziggel, A., Sindern, S., Kokfelt, T. F., Gerdes, A., and Kolb, J. (2018b). Age and temperature-time evolution of retrogressed eclogite-facies rocks in the Paleoproterozoic Nagssugtoqidian Orogen, South-East Greenland: Constrained from U-Pb dating of zircon, monazite, titanite and rutile. *Precambrian Research, 314*, 468-486. doi:10.1016/j.precamres.2018.07.002

Nutman, A. P., Kalsbeek, F., and Friend, C. R. L. (2008). The Nagssugtoqidian Orogen in south-east Greenland: Evidence for Paleoproterozoic collision and plate assembly. *American Journal of Science, 308*, 529-572. doi:10.2475/04.2008.06

O'Brien, P. J. (1997). Garnet zoning and reaction textures in overprinted eclogites, Bohemian Massif, European Variscides: A record of their thermal history during exhumation. *Lithos, 41*(1-3), 119-133. doi:10.1016/S0024-4937(97)82008-7

O'Brien, P. J., and Rötzler, J. (2003). High-pressure granulites: formation, recovery of peak conditions and implications for tectonics. *Journal of Metamorphic Geology, 21*(1), 3-20. doi:10.1046/j.1525-1314.2003.00420.x

Palmeri, R., Chmielowski, R., Sandroni, S., Talarico, F., and Ricci, C. A. (2009). Petrology of the eclogites from western Tasmania: Insights into the Cambro-Ordovician evolution of the paleo-Pacific margin of Gondwana. *Lithos, 109*(3-4), 223-239. doi:10.1016/j.lithos.2008.06.016

Pape, J., Mezger, K., and Robyr, M. (2016). A systematic evaluation of the Zr-in-rutile thermometer in ultra-high temperature (UHT) rocks. *Contributions to Mineralogy and Petrology, 171*(5). doi:10.1007/s00410-016-1254-8

Paton, C., Hellstrom, J., Paul, B., Woodhead, J., and Hergt, J. (2011). Iolite: Freeware for the visualisation and processing of mass spectrometric data. *Journal of Analytical Atomic Spectrometry, 26*(12), 2508. doi:10.1039/c1ja10172b

Peacock, S. M. (1996). Thermal and Petrologic Structure of Subduction Zones. *Subduction: Top to Bottom* (Vol. 96, pp. 119-133).

Pearce, M. A., White, A. J. R., and Gazley, M. F. (2015). TCInvestigator: automated calculation of mineral mode and composition contours for thermocalc pseudosections. *Journal of Metamorphic Geology, 33*(4), 413-425. doi:10.1111/jmg.12126

Penniston-Dorland, S. C., Kohn, M. J., and Man-

ning, C. E. (2015). The global range of subduction zone thermal structures from exhumed blueschists and eclogites: Rocks are hotter than models. *Earth and Planetary Science Letters, 428*, 243-254. doi:10.1016/j.epsl.2015.07.031

Petersen, K. D., and Buck, W. R. (2015). Eduction, extension, and exhumation of ultrahigh-pressure rocks in metamorphic core complexes due to subduction initiation. *Geochemistry, Geophysics, Geosystems, 16*(8), 2564-2581. doi:10.1002/2015gc005847

Qian, J., Wei, C., and Yin, C. (2017). Paleoproterozoic P–T–t evolution in the Hengshan–Wutai–Fuping area, North China Craton: Evidence from petrological and geochronological data. *Precambrian Research*, 303, 91-104. doi:10.1016/j.precamres.2017.02.016

Reddy, S. M., Collins, A. S., and Mruma, A. (2003). Complex high-strain deformation in the Usagaran Orogen, Tanzania: structural setting of Palaeoproterozoic eclogites. *Tectonophysics, 375*(1-4), 101-123. doi:10.1016/s0040-1951(03)00335-4

Reddy, S. M., Collins, A. S., and Mruma, A. (2003). Complex high-strain deformation in the Usagaran Orogen, Tanzania: structural setting of Palaeoproterozoic eclogites. *Tectonophysics, 375*(1-4), 101-123. doi:10.1016/s0040-1951(03)00335-4

Ring, U., Kröner, A., and Toulkeridis, T. (1997). Palaeoproterozoic granulite-facies metamorphism and granitoid intrusions in the Ubendian-Usagaran Orogen of northern Malawi, east-central Africa. *Precambrian Research, 85*(1-2), 27-51. doi.org/10.1016/S0301-9268(97)00028-4

Rosenberg, C. L., and Handy, M. R. (2005). Experimental deformation of partially melted granite revisited: implications for the continental crust. *Journal of Metamorphic Geology, 23*(1), 19-28. doi:10.1111/j.1525-1314.2005.00555.x

Ruh, J. B., Le Pourhiet, L., Agard, P., Burov, E., and Gerya, T. (2015). Tectonic slicing of subducting oceanic crust along plate interfaces: Numerical modeling. *Geochemistry, Geophysics, Geosystems, 16*(10), 3505-3531. doi:10.1002/2015gc005998

Sheng, Y.-M., and Gong, B. (2017). Hydrous species in eclogitic omphacite: Implication for metamorphic dehydration during exhumation. *Journal of Asian Earth Sciences, 145*, 123-129. doi:10.1016/j.jseaes.2016.12.020

Sizova, E., Gerya, T., and Brown, M. (2014). Contrasting styles of Phanerozoic and Precambrian continental collision. *Gondwana Research, 25*(2), 522-545. doi:10.1016/j.gr.2012.12.011

Sklyarov, E. V., Theunissen, K., Melnikov, A. I., Klerkx, J., Gladkochub, D. P., and Mru-

ma, A. (1998). Paleoproterozoic eclogites and garnet pyroxenites of the Ubende belt (Tanzania). *Swiss Bulletin of Mineralogy and Petrology, 78*, 257-271. doi:10.5169/seals-59287

Skublov, S. G., Berezin, A. V., Marin, Y. B., Rizvanova, N. G., Bogomolov, E. S., Sergeeva, N. A., . . . Guseva, V. F. (2010). Complex isotopic-geochemical (Sm-Nd, U-Pb) study of Salma eclogites. *Doklady Earth Sciences, 434*(2), 1396-1400. doi:10.1134/s1028334x10100247

Skublov, S. G., Berezin, A. V., Marin, Y. B., Rizvanova, N. G., Bogomolov, E. S., Sergeeva, N. A., . . . Guseva, V. F. (2010). Complex isotopic-geochemical (Sm-Nd, U-Pb) study of Salma eclogites. *Doklady Earth Sciences, 434*(2), 1396-1400. doi:10.1134/s1028334x10100247

Skublov, S. G., Berezin, A. V., Rizvanova, N. G., Mel'nik, A. E., and Myskova, T. A. (2014). Multistage Svecofennian metamorphism: Evidence from the composition and U-Pb age of titanite from eclogites of the Belomorian Mobile Belt. *Petrology, 22*(4), 381-388. doi:10.1134/s0869591114040067

Smith, D. C. (1988). A review of the peculiar mineralogy of the Norwegian coesite-eclogite province with crystal-chemical, petrological, geochemical and geodynamical notes and an extensive bibliography. In D. C. Smith (Ed.), *Developments in Petrology* (Vol. 12, pp. 1-206). Amsterdam: Elsevier.

Smyth, J. R., Bell, D. R., and Rossman, G. R. (1991). Incorporation of hydroxyl in upper-mantle clinopyroxenes, *Nature, 351*(6329), 732-735.

Spandler, C., and Hermann, J. (2006). High-pressure veins in eclogite from New Caledonia and their significance for fluid migration in subduction zones. *Lithos, 89*(1-2), 135-153. doi:10.1016/j.lithos.2005.12.003

Spear, F. S. (1995). *Metamorphic Phase Equilibria And Pressure-Temperature-Time-Paths*. Washington, D.C.: Mineralogical Society of America.

Spencer, K. J., Hacker, B. R., Kylander-Clark, A. R. C., Andersen, T. B., Cottle, J. M., Stearns, M. A., . . . Seward, G. G. E. (2013). Campaign-style titanite U–Pb dating by laser-ablation ICP: Implications for crustal flow, phase transformations and titanite closure. *Chemical Geology*, 341, 84-101. doi:10.1016/j.chemgeo.2012.11.012

Stern, R. J. (2005). Evidence from ophiolites, blueschists, and ultrahigh-pressure metamorphic terranes that the modern episode of subduction tectonics began in Neoproterozoic time. *Geology, 33*(7), 557. doi:10.1130/g21365.1

Stipska, P., Pitra, P., and Powell, R. (2006). Separate or shared metamorphic histories of eclogites and surrounding rocks? An example from the Bohemian Massif. *Journal*

of Metamorphic Geology, 24(3), 219-240. doi:10.1111/j.1525-1314.2006.00634.x

Stüwe, K. (1997). Effective bulk composition changes due to cooling: a model predicting complexities in retrograde reaction textures. *Contributions to Mineralogy and Petrology, 129*(1), 43-52. doi:10.1007/s004100050322

Syracuse, E. M., van Keken, P. E., and Abers, G. A. (2010). The global range of subduction zone thermal models. *Physics of the Earth and Planetary Interiors, 183*(1-2), 73-90. doi:10.1016/j.pepi.2010.02.004

Taylor-Jones, K., and Powell, R. (2015). Interpreting zirconium-in-rutile thermometric results. *Journal of Metamorphic Geology, 33*(2), 115-122. doi:10.1111/jmg.12109

Tomkins, H. S., Powell, R., and Ellis, D. J. (2007). The pressure dependence of the zirconium-in-rutile thermometer. *Journal of Metamorphic Geology, 25*(6), 703-713. doi:10.1111/j.1525-1314.2007.00724.x

van Keken, P. E., Wada, I., Abers, G. A., Hacker, B. R., and Wang, K. (2018). Mafic High-Pressure Rocks Are Preferentially Exhumed From Warm Subduction Settings. *Geochemistry, Geophysics, Geosystems, 19*(9), 2934-2961. doi:10.1029/2018gc007624

Volodichev, O. I., Slabunov, A. I., Bibikova, E. V., Konilov, A. N., and Kuzenko, T. I. (2004). Archean eclogites in the Belomorian mobile belt, baltic shield. *Petrology, 12*(6), 540-560.

Walsh, A. K., Kelsey, D. E., Kirkland, C. L., Hand, M., Smithies, R. H., Clark, C., and Howard, H. M. (2015). P–T–t evolution of a large, long-lived, ultrahigh-temperature Grenvillian belt in central Australia. *Gondwana Research, 28*(2), 531-564. doi:10.1016/j.gr.2014.05.012'

Walsh, E. O., and Hacker, B. R. (2004). The fate of subducted continental margins: Two-stage exhumation of the high-pressure to ultrahigh-pressure Western Gneiss Region, Norway. *Journal of Metamorphic Geology, 22*(7), 671-687. doi:10.1111/j.1525-1314.2004.00541.x

Watson, E. B., Wark, D. A., and Thomas, J. B. (2006). Crystallization thermometers for zircon and rutile. *Contributions to Mineralogy and Petrology, 151*(4), 413-433. doi:10.1007/s00410-006-0068-5

Weller, O. M., and St-Onge, M. R. (2017). Record of modern-style plate tectonics in the Palaeoproterozoic Trans-Hudson orogen. *Nature Geoscience, 10*(4), 305-311. doi:10.1038/ngeo2904

Wendt, I., Besang, C., Harre, W., Kreuzer, H., Lenz, H., and Müller, P. (1972). *Age determinations of granitic intrusions and metamorphic events in the early Precambrian of Tanzania*. Paper presented at the 24th International Geological Congress, Montreal.

White, R. W., Powell, R., and Johnson, T. E. (2014b). The effect of Mn on mineral stability in metapelites revisited: new a-x relations for manganese-bearing minerals. *Journal of Metamorphic Geology, 32*(8), 809-828. doi:10.1111/jmg.12095

White, R. W., Powell, R., Holland, T. J. B., Johnson, T. E., and Green, E. C. R. (2014a). New mineral activity-composition relations for thermodynamic calculations in metapelitic systems. *Journal of Metamorphic Geology, 32*(3), 261-286. doi:10.1111/jmg.12071

Whitney, D. L., and Evans, B. W. (2010). Abbreviations for names of rock-forming minerals. *American Mineralogist, 95*(1), 185-187. doi:10.2138/am.2010.3371

Woodhead, J. D., Hellstrom, J., Paton, C., Hergt, J. M., Greig, A., and Mass, R. (2008). A guide to depth profiling and imaging applications of ICP-MS. *Mineralogical Association of Canada, Short Course Series, 40*, 135-145.

Xu, C., Kynicky, J., Song, W., Tao, R., Lu, Z., Li, Y., . . . Fei, Y. (2018). Cold deep subduction recorded by remnants of a Paleoproterozoic carbonated slab. *Nature Communications, 9*(1), 2790. doi:10.1038/s41467-018-05140-5

Yea, K., Yao, Y., Katayama, I., Cong, B., Wang, Q., and Maruyama, S. (2000). Sulu ultrahigh-pressure terrane of East China: new implications from coesite and omphacite inclusions in zircon of granitic gneiss. *Lithos, 52*(1-4), 157-164. doi:10.1016/S0024-4937(99)00089-4

Young, D. J., and Kylander-Clark, A. R. C. (2015). Does continental crust transform during eclogite facies metamorphism? *Journal of Metamorphic Geology, 33*(4), 331-357. doi:10.1111/jmg.12123

Yu, H. L., Zhang, L. F., Wei, C. J., Li, X. L., and Guo, J. H. (2017). Age and P-T conditions of the Gridino-type eclogite in the Belomorian Province, Russia. *Journal of Metamorphic Geology, 35*(8), 855-869. doi:10.1111/jmg.12258

Yu, H., Zhang, L., Lanari, P., Rubatto, D., and Li, X. (2019). Garnet Lu Hf geochronology and P-T path of the Gridino-type eclogite in the Belomorian Province, Russia. *Lithos, 326-327*, 313-326. doi:10.1016/j.lithos.2018.12.03

Zack, T., Kronz, A., Foley, S. F., and Rivers, T. (2002). Trace element abundances in rutiles from eclogites and associated garnet mica schists. *Chemical Geology, 184*(1-2), 97-122. doi:10.1016/S0009-2541(01)00357-6

Zack, T., Moraes, R., and Kronz, A. (2004). Temperature dependence of Zr in rutile: empirical calibration of a rutile thermometer. *Contributions to Mineralogy and Petrology, 148*(4), 471-488. doi:10.1007/

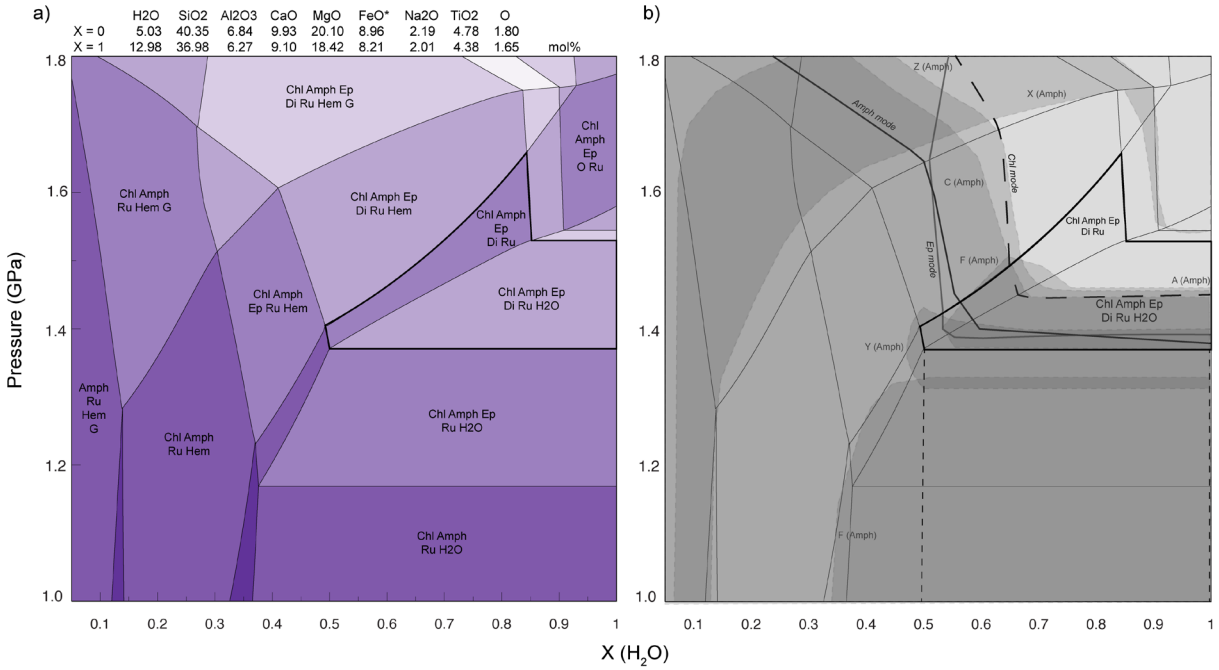
s00410-004-0617-8

Zhao, G. C., Cawood, P. A., Wilde, S. A., and Lu, L. (2001). High-Pressure Granulites (Retrograded Eclogites) from the Hengshan Complex, North China Craton: Petrology and Tectonic Implications. *Journal of Petrology, 42*(6), 1141-1170. doi:10.1093/petrology/42.6.1141

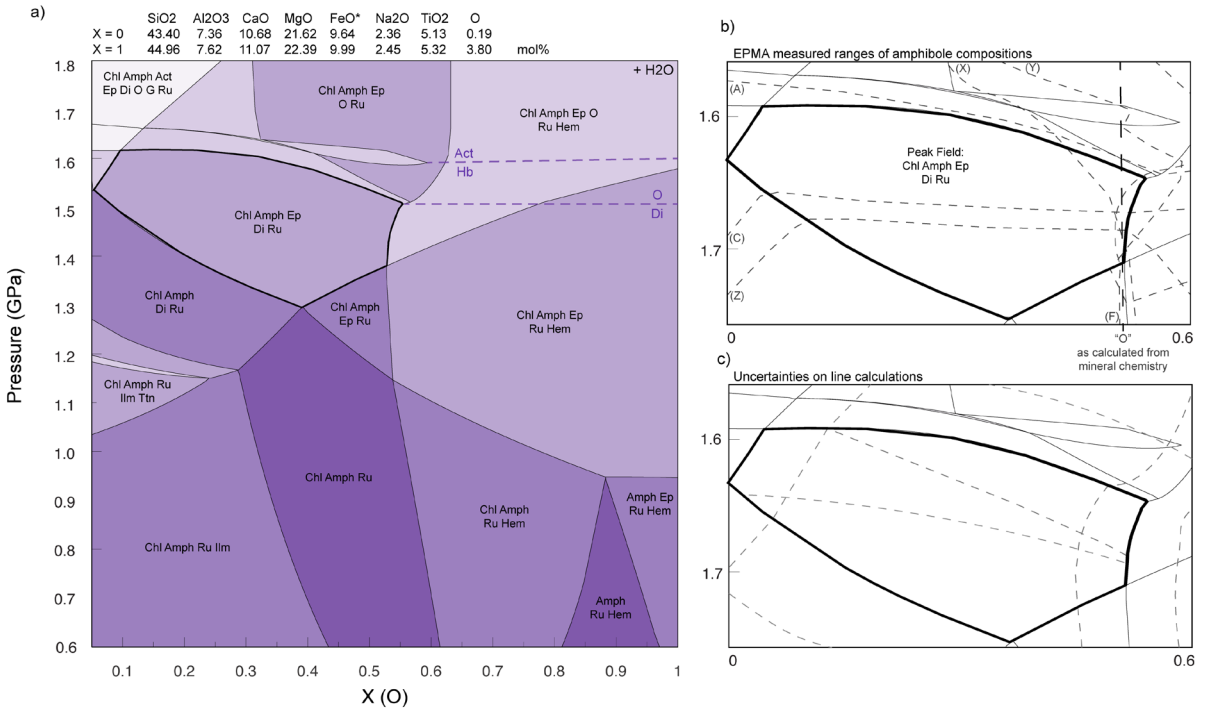
Zhao, G., Sun, M., Wilde, S. A., and Li, S. (2004). A Paleo-Mesoproterozoic supercontinent: assembly, growth and breakup. *Earth-Science Reviews, 67*(1-2), 91-123. doi:10.1016/j.earscirev.2004.02.003

Appendix 2:

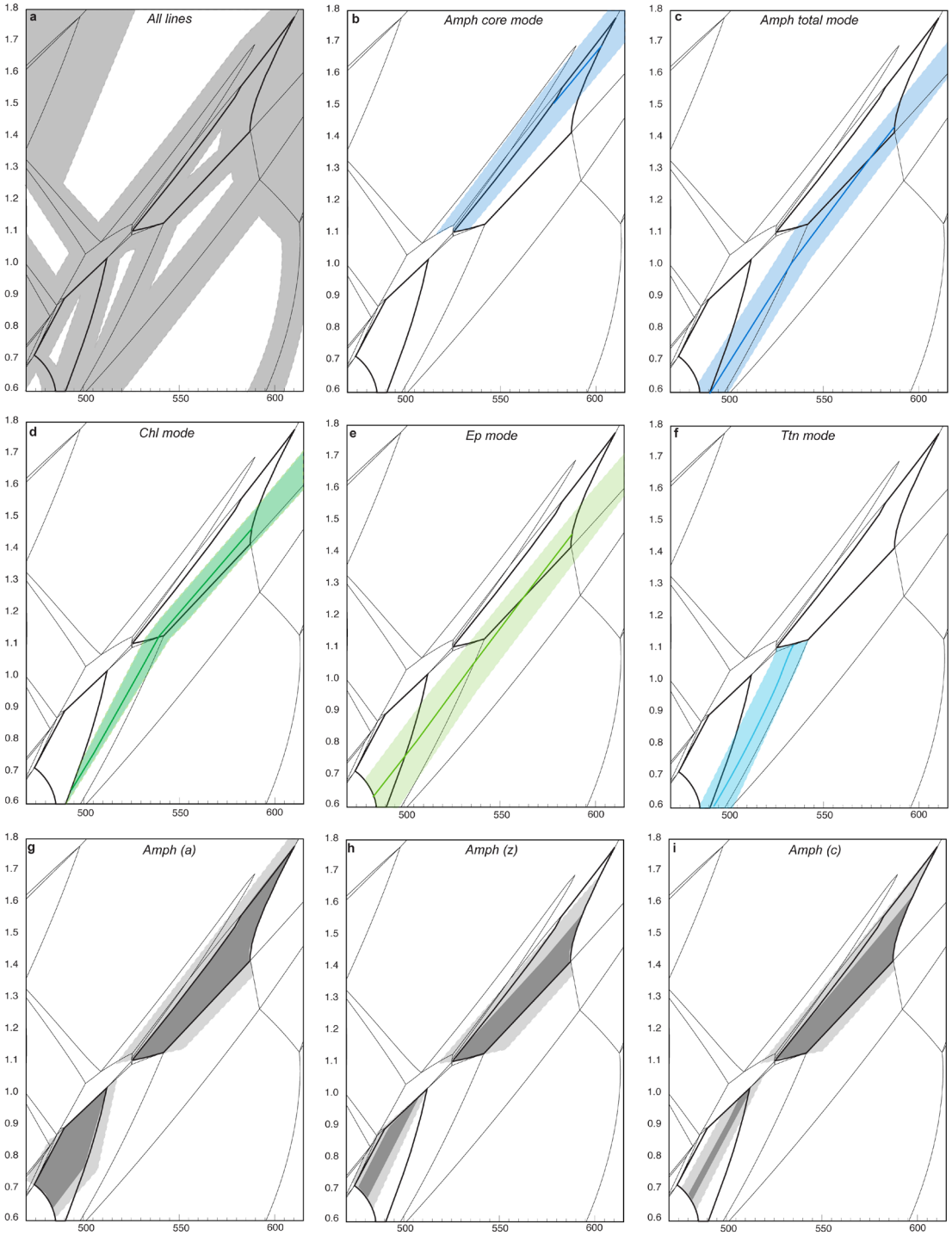
Supplementary data for Chapter 2: Blueschist from the Mariana forearc records long-lived residence of material in the subduction channel



Supplementary Figure 1: a) P–MH2O section showing changing H2O contents and pressure at a set temperature of 580 °C. Thick black line outlines the possible peak fields. Variance is coloured as v = 7 as the darkest shade and decreases in variance as the shade lightens. b) Modal proportions of minerals as measured from the sample (Supplementary Table 2) are shown as lines. Shaded grey fields are the total range of all EPMA measured amphibole core compositions A (xNa on the A site), C (xCa on the M4 site), Z (xNa on the M4 site), Y (xAl on the M2 site), F (xFe3+ on the M2 site) and X (Fe/Fe + Mg), where the entire measured range is indicated by a grey transparent field with a dashed outline. Where different compositional ranges overlap, the shading is darker. Dotted vertical lines indicate the range of H2O values that correspond to the mineral assemblage, modal proportions and amphibole compositions observed in the rock, (MH2O=0.5–1, equivalent to ~9–13 mol% H2O). Chl: chlorite, Amph: Amphibole, O: Omphacite, Di: Diopside, Ep: Epidote, Ru: Rutile, Ttn: Titanite, Act: Actinolite, Gl: Glaucophane, Q: Quartz, Ilm: Ilmenite, Hem: Hematite, Law: Lawsonite, G: Garnet.



Supplementary Figure 2: a) P–MO section showing changing oxidation state (Fe2+/Fe3+, or 'O') and pressure at a set temperature of 580 °C. Thick black line indicates interpreted peak field. Variance is coloured as v = 7 as the darkest shade and decreases in variance as the shade lightens. Purple dashed lines indicate the locations of the omphacite–diopside and actinolite–hornblende solvi. b) Zoom in to peak field, where grey dashed line indicate ranges of EPMA measured amphibole compositions A (xNa on the A site), C (xCa on the M4 site), Z (xNa on the M4 site), Y (xAl on the M2 site), F (xFe3+ on the M2 site) and X (Fe/Fe + Mg). Dotted black line indicates 'O' value calculated from mineral chemistry. C) Dashed lines indicate 2 sigma errors on line calculations as output by THERMOCALC in the peak field.



Supplementary Figure 3: 2 sigma errors on all calculations in the P–T pseudosection (Figure 7). For the modes, a solid line indicates the modal contour and the shaded error indicates the uncertainty on that contour as output by THERMOCALC. For the amphibole compositions, the dark grey field indicates the total range of EPMA measured amphibole compositions and the light grey field with dashed lines indicated the uncertainty on the highest and lowest compositions that bound the range. a) Errors of all phase assemblage fields. b) Modal proportion of amphibole cores. c) Total modal proportion of amphibole. d) Modal proportion of chlorite. e) Modal proportion of epidote. f) Modal proportion of titanite. g) Error on amphibole A compositional range (xNa on the A site). h) Error on amphibole Z compositional range (xNa on the M4 site). i) Error on amphibole C compositional range (xCa on the M4 site).

Supplementary data table 1: Representative EPMA mineral compositions used in bulk compositional calculations from Pabst et al. (2012)

	mg-hbl	mg-hast	prg	prg	edenite	mg-kat	mg-kat
SiO2	48.03	43.32	43.51	43.37	45.83	47.98	48.28
TiO2	0.48	0.5	0.67	0.47	0.53	0.52	0.43
Al2O3	7.99	12.33	12.22	12.4	10.59	8.12	7.79
Fe2O3	4.84	7.74	3.01	2.91	2.91	3.03	2.79
FeO	7.61	4.48	8.08	8.19	7.07	11.03	10.61
MnO	0.28	0.32	0.25	0.33	0.39	0.4	0.35
MgO	15.19	15.02	14.1	14.04	15.32	13.02	13.19
CaO	9.72	10.69	11.59	11.57	11.67	8.61	8.79
Na2O	2.55	2.21	2.41	2.56	2.03	3.99	3.47
K2O	0.21	0.28	0.27	0.31	0.23	0.17	0.26
H20	2.07	2	2.03	2.03	2.06	2.05	2.03
Total	98.97	98.89	98.14	98.18	98.63	98.92	97.99
	mg-hbl	mg-hast	prg	prg	edenite	mg-kat	mg-kat
SiO2	48.03	43.32	43.51	43.37	45.83	47.98	48.28
TiO2	0.48	0.5	0.67	0.47	0.53	0.52	0.43
Al2O3	7.99	12.33	12.22	12.4	10.59	8.12	7.79
FeO	11.97	11.44	10.79	10.81	9.69	13.76	13.12
MnO	0.28	0.32	0.25	0.33	0.39	0.4	0.35
MgO	15.19	15.02	14.1	14.04	15.32	13.02	13.19
CaO	9.72	10.69	11.59	11.57	11.67	8.61	8.79
Na2O	2.55	2.21	2.41	2.56	2.03	3.99	3.47
K2O	0.21	0.28	0.27	0.31	0.23	0.17	0.26
H20	2.07	2	2.03	2.03	2.06	2.05	2.03
Total	98.49	98.11	97.84	97.89	98.34	98.62	97.71
No. Oxygens	23	23	23	23	23	23	23
Si	7.697	6.894	6.999	6.962	7.325	7.717	7.851
Ti	0.058	0.060	0.081	0.057	0.064	0.063	0.053
Al	1.509	2.312	2.317	2.346	1.995	1.539	1.493
Cr	0.000	0.000	0.000	0.000	0.000	0.000	0.000
Fe3+	0.000	0.000	0.000	0.000	0.000	0.000	0.000
Fe2+	1.566	1.566	1.383	1.380	1.239	1.742	1.678
Mn2+	0.038	0.043	0.034	0.045	0.053	0.054	0.048
Mg	3.629	3.563	3.382	3.360	3.650	3.122	3.198
Zn	0.000	0.000	0.000	0.000	0.000	0.000	0.000
Ca	1.669	1.822	1.997	1.990	1.998	1.484	1.531
Na	0.792	0.682	0.752	0.797	0.629	1.244	1.094
K	0.043	0.057	0.055	0.063	0.047	0.035	0.054
Cl	0.000	0.000	0.000	0.000	0.000	0.000	0.000
F	0.000	0.000	0.000	0.000	0.000	0.000	0.000
OH-	2.000	2.000	2.000	2.000	2.000	2.000	2.000

	mg-hbl	mg-hast	prg	prg	edenite	mg-kat	mg-kat
X Ca in M4 (c)	0.752	0.833	0.909	0.908	0.904	0.670	0.687
X Na in M4 (z)	0.200	0.087	0.102	0.103	0.093	0.354	0.337
X Fe3 in M2 (f)	0.356	0.422	0.339	0.337	0.294	0.410	0.393
X Al in M2 (y)	0.148	0.208	0.239	0.248	0.215	0.179	0.195
F e / (F e +Mg) (x)	0.183	0.144	0.173	0.175	0.150	0.232	0.221
XKA + XNaA (a)	0.352	0.501	0.531	0.579	0.426	0.447	0.356

Supplementary data table 1 continued: Representative EPMA mineral compositions used in bulk compositional calculations from Pabst et al. (2012)

	chl	chl		pump	pump	pump		ep	ep
SiO2	27.9	27.85		35.83	36.14	36.8		37.72	36.51
TiO2	0.03	0.03		0.77	0.31	0.26		0.25	0.33
Al2O3	19.55	19.82		19.72	21.78	22.47		23.6	23.18
Fe2O3				10.68	8.12	7.15		14.03	12.83
FeO	15.27	14.52							
MnO	0.45	0.45		0.2	0.41	0.28		0.24	0.2
MgO	23.26	23.36		2.33	2.95	3.25		0.02	0.03
CaO	0.08	0.1		21.85	21.84	21.88		22.76	23.05
Na2O	0.01	0.04		0.22	0.18	0.25		0.06	0
K2O	0.02	0.02		0	0.01	0.01		0.01	0
H20	11.88	11.86						1.9	1.83
Total	98.45	98.05		91.6	91.74	92.35		100.59	97.96
	chl	chl		pump	pump	pump		ep	ep
SiO2	27.9	27.85		35.83	36.14	36.8		37.72	36.51
TiO2	0.03	0.03		0.77	0.31	0.26		0.25	0.33
Al2O3	19.55	19.82		19.72	21.78	22.47		23.6	23.18
FeO	15.27	14.52		9.61	7.31	6.43		12.62	11.55
MnO	0.45	0.45		0.2	0.41	0.28		0.24	0.2
MgO	23.26	23.36		2.33	2.95	3.25		0.02	0.03
CaO	0.08	0.1		21.85	21.84	21.88		22.76	23.05
Na2O	0.01	0.04		0.22	0.18	0.25		0.06	0
K2O	0.02	0.02		0	0.01	0.01		0.01	0
H20	11.88	11.86						1.9	1.83
Total	98.45	98.05		90.53	90.93	91.63		99.18	96.68
No. Oxygens	14	14		24.5	24.5	24.5		12.5	12.5
Si	2.857	2.854		5.968	5.941	5.979		2.987	2.961
Ti	0.002	0.002		0.096	0.038	0.032		0.015	0.020
Al	2.360	2.394		3.871	4.219	4.303		2.202	2.216
Cr	0.000	0.000		0.000	0.000	0.000		0.000	0.000

Fe3+	0.000	0.000		1.071	0.882	0.756		0.804	0.822
Fe2+	1.177	1.120		0.417	0.234	0.215		0.032	-0.039
Mn2+	0.039	0.039		0.028	0.057	0.039		0.016	0.014
Mg	3.551	3.569		0.579	0.723	0.787		0.002	0.004
Zn	0.000	0.000		0.000	0.000	0.000		0.000	0.000
Ca	0.009	0.011		3.899	3.846	3.809		1.931	2.003
Na	0.002	0.008		0.071	0.057	0.079		0.009	0.000
K	0.003	0.003		0.000	0.002	0.002		0.001	0.000
Cl	0.000	0.000		0.000	0.000	0.000		0.000	0.000
F	0.000	0.000		0.000	0.000	0.000		0.000	0.000
OH-	8.000	8.000		7.000	7.000	7.000		1.000	1.000
	chl	chl		pump	pump	pump		ep	ep
Fe/Fe+Mg	0.249	0.239					Si on T	2.987	2.961
Si on T2	0.857	0.854					Al on T	0.013	0.039
Al on T2	1.143	1.146					Al on M2	1.000	1.000
Y	0.571	0.573					F	0.202	0.206

Supplementary data table 1 continued: Representative EPMA mineral compositions used in bulk compositional calculations from Pabst et al. (2012)

	cpx	cpx	cpx	ru	ttn	ilm
SiO2	53.43	53.1	53.49	0	30.57	
TiO2	0.04	0.16	0.01	96.98	37.5	10.66
Al2O3	3.17	2.18	3.27	0	1	
Fe2O3				1.69	0.05	63.6
FeO	20.9	17.01	16.85			24.53
MnO	0.1	0.2	0.22	0	0.06	0.07
MgO	4.07	6.86	6.09	0	0.01	0.01
CaO	6.65	10.76	9.36	0.11	28.14	0.02
Na2O	10.15	7.67	8.67	0.01	0.02	
K2O	0	0	0	0.01	0	
H20						
Total	98.51	97.94	97.96	98.8	97.35	98.89
	cpx	cpx	cpx	ru	ttn	ilm
SiO2	53.43	53.1	53.49	0	30.57	
TiO2	0.04	0.16	0.01	96.98	37.5	10.66
Al2O3	3.17	2.18	3.27	0	1	
FeO	20.90	17.01	16.85	1.52	0.04	81.76
MnO	0.1	0.2	0.22	0	0.06	0.07
MgO	4.07	6.86	6.09	0	0.01	0.01
CaO	6.65	10.76	9.36	0.11	28.14	0.02
Na2O	10.15	7.67	8.67	0.01	0.02	
K2O	0	0	0	0.01	0	
H20						
Total	98.51	97.94	97.96	98.63	97.34	92.52

No. Oxygens	6	6	6	2	5	3
Si	2.019	2.016	2.016	0.000	1.016	0.000
Ti	0.001	0.005	0.000	0.979	0.938	0.201
Al	0.141	0.098	0.145	0.000	0.039	0.000
Cr	0.000	0.000	0.000	0.000	0.000	0.000
Fe3+	0.563	0.427	0.456	0.042	0.055	1.598
Fe2+	0.031	0.059	0.022	-0.023	-0.053	0.199
Mn2+	0.003	0.006	0.007	0.000	0.002	0.001
Mg	0.229	0.388	0.342	0.000	0.000	0.000
Zn	0.000	0.000	0.000	0.000	0.000	0.000
Ca	0.269	0.438	0.378	0.002	1.002	0.001
Na	0.743	0.564	0.633	0.000	0.001	0.000
K	0.000	0.000	0.000	0.000	0.000	0.000
Cl	0.000	0.000	0.000	0.000	0.000	0.000
F	0.000	0.000	0.000	0.000	0.000	0.000
OH-	0.000	0.000	0.000	0.000	0.000	0.000
	cpx	cpx	cpx	ru	ttn	ilm
J	0.743	0.564	0.633			
F	0.800	0.814	0.758			
X	0.120	0.132	0.061			

Supplementary data table 2: Results of volume % of metamorphic minerals as determined by pixel counting. Mineral densities were calculated based on proportions of end-member densities. These weight % values were then used in conjunction with microprobe chemistry (Supplementary data table 1) to calculate a whole rock chemistry (Supplementary data table 4).1-oxide-normalised modes are also presented, which correspond to THERMOCALC mineral modes. Whole rock geochemistry calculated for the blueschist clast and used to calculate the phase equilibria model is also given (where O represents Fe2O3)

Mineral	Vol %	Density	Wt %	1-oxide-normalised	Whole rock comp.	Mol %
Chlorite	14.87	2.78	12.96	0.1975	SiO2	44.16
Amphibole core	46.88	3.12	45.86	0.4419	Al2O3	7.49
Amphibole rim	28.29	3.35	29.71	0.2667	CaO	10.87
Amphibole total	75.17		75.57	0.7086	MgO	22
Clinozoisite core	1.86	3.21	1.87	0.0196	FeO*	9.81
Epidote rim	2.34	3.38	2.48	0.0252	Na2O	2.4
Epidote total	4.2		4.35	0.0448	TiO2	5.23
Pumpellyite	0.5	3.2	0.5	0.0039	O	1.97
Clinopyroxene	0.5	3.45	0.54	0.0042		
Rutile	3.67	4.25	4.89	0.0347		
Titanite	1.09	3.48	1.19	0.0102		

Supplementary data table 3: Secondary ionization mass spectrometry (SIMS) results for rutile and zircon

Sample/ mineral	grain	spot	Age (Ma)	Age (Ma)	Age (Ma)	Age (Ma)	Age (Ma)	Age (Ma)	% Radio-genic						
			206Pb/	206Pb/	207Pb/	207Pb/	207Pb/	207Pb/	206Pb	206Pb*/	206Pb*/	207Pb*/	207Pb*/	207Pb*/	207Pb*/
			238U	238U	235U	235U	206Pb	206Pb		238U	238U	235U	235U	206Pb*	206Pb*
				1 s.e.		1 s.e.		1 s.e.			1 s.e.		1 s.e.		1 s.e.
E1H3-4B rut	1	1	51.9	2.3	57.0	11.3	274	432	95.0	0.00809	0.00036	0.0577	0.0118	0.0518	0.0098
E1H3-4B rut	1	2	48.4	4.9	10.6	76.9	b.d.	b.d.	42.4	0.00753	0.00076	0.0105	0.0765	0.0101	0.0731
E1H3-4B rut	2	1	44.7	1.9	26.8	14.8	b.d.	b.d.	68.6	0.00695	0.00029	0.0267	0.0150	0.0279	0.0153
E1H3-4B rut	1	3	50.0	1.8	49.1	11.3	7.04	529	93.8	0.00778	0.00028	0.0495	0.0116	0.0462	0.0102
E1H3-4B rut	1	4	43.3	1.2	43.8	5.3	72.4	281	91.5	0.00674	0.00018	0.0441	0.0054	0.0475	0.0056
E1H3-4B rut	3	1	46.3	2.6	56.7	34.8	518	1320	76.9	0.00721	0.00040	0.0574	0.0362	0.0577	0.0348
E1H3-4B rut	3	2	51.3	5.0	80.0	73.0	1050	1800	81.4	0.00799	0.00078	0.0820	0.0778	0.0744	0.0664
E1H3-4B rut	4	1	55.1	2.2	61.4	7.4	314	257	92.0	0.00858	0.00035	0.0623	0.0077	0.0527	0.0060
E1H3-4B rut	1	5	49.6	2.1	44.3	37.1	b.d.	b.d.	46.8	0.00772	0.00033	0.0446	0.0382	0.0419	0.0353
E1H3-4B zrn	1	1	51.1	0.9	49.9	2.8	b.d.	b.d.	97.5	0.00796	0.00014	0.0503	0.0029	0.0459	0.0025
E1H3-4B zrn	2	2	64.9	14.1	105	168	1150	3170	58.3	0.0101	0.0022	0.109	0.184	0.0783	0.1250
E1H3-4B zrn	3	3	53.4	1.9	44.0	32.9	b.d.	b.d.	58.2	0.00832	0.00030	0.0443	0.0339	0.0387	0.0287
E1H3-4B zrn	4	4	50.1	0.9	51.7	6.4	129	287	90.6	0.00780	0.00014	0.0523	0.0066	0.0486	0.0059

Supplementary data table 3: Secondary ionization mass spectrometry (SIMS) results for rutile and zircon

Sample/mineral	grain	spot	Correlation	208Pb/	208Pb/	208Pb/	208Pb/	206Pb/	206Pb/	Th/	U	common Pb
			of Concordia	206Pb	206Pb	207Pb	207Pb	204Pb	204Pb	U		correction
			Ellipses							wt.	μg/g	
					1 s.e.		1 s.e.		1 s.e.			
E1H3-4B rut	1	1	0.4351	0.102	0.016	1.04	0.12	284	50	0.00024	16.5	208Pb
E1H3-4B rut	1	2	0.5595	1.07	0.07	2.3	0.04	32.7	1.7	b.d.	28.2	204Pb
E1H3-4B rut	2	1	0.3303	0.639	0.019	2.28	0.05	54.5	4.8	0.0000188	19.4	208Pb
E1H3-4B rut	1	3	0.4742	0.128	0.005	1.36	0.05	303	56	b.d.	21.2	204Pb
E1H3-4B rut	1	4	0.2837	0.174	0.01	1.54	0.1	190	34	0.000388	14.3	208Pb
E1H3-4B rut	3	1	0.5379	0.47	0.048	1.95	0.07	74.2	9.2	0.0000119	10.6	208Pb
E1H3-4B rut	3	2	0.6184	0.393	0.076	1.77	0.09	101	24	b.d.	28	204Pb
E1H3-4B rut	4	1	0.4099	0.162	0.009	1.43	0.09	159	28	0.00000629	14	208Pb
E1H3-4B rut	1	5	0.3538	1.08	0.02	2.37	0.04	38.9	2.1	0.0000648	19.8	208Pb
E1H3-4B zrn	1	1	0.3751	0.0532	0.0045	0.804	0.06	829	205	0.00426	1300	208Pb
E1H3-4B zrn	2	2	0.4371	0.851	0.105	2.18	0.1	44.7	6.7	0.014	398	208Pb
E1H3-4B zrn	3	3	0.6378	0.851	0.033	2.32	0.08	37.4	5.3	0.009	176	208Pb
E1H3-4B zrn	4	4	0.296	0.195	0.008	1.61	0.08	175	40	0.00839	299	208Pb

1 s.e. = standard error	
b.d. = below detection	
common Pb correction uses anthropogenic Pb for Southern California:	
206Pb/204Pb	18.86
207Pb/204Pb	15.62
208Pb/204Pb	38.34

Appenix 3:

Supplementary material for Chapter 3: Subduction and accumulation of lawsonite eclogite and garnet blueschist in eastern Australia

Supplementary File 1: Analyses of modern beach sand zircons

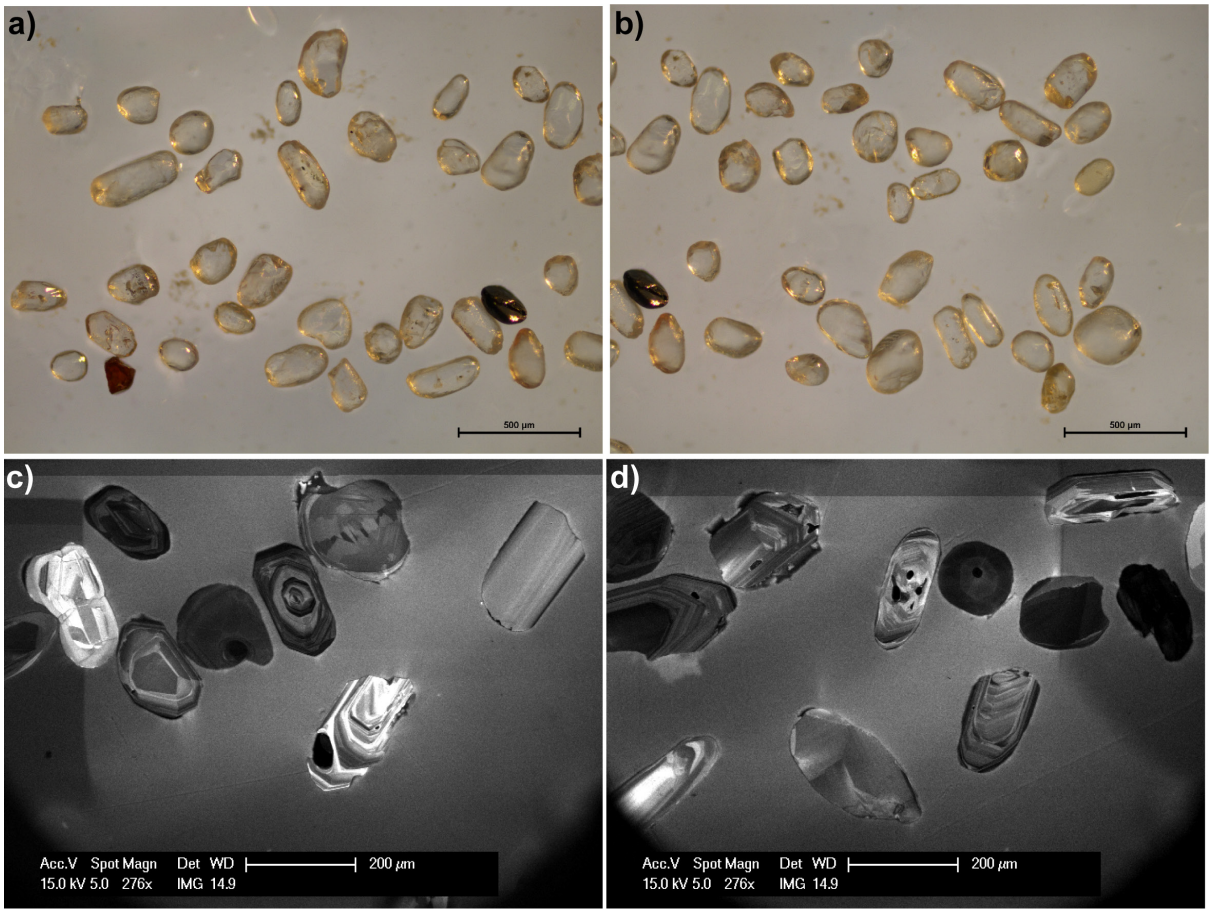
Approximately 2kg of modern beach sand was sampled from the northern end of Rocky Beach, several meters from the eclogite and blueschist boulders, and from the southern end of Town Beach approximately 1 km north of the eclogite and blueschist location. Zircons were obtained by panning and heavy liquid separation, mounted in epoxy and imaged using cathodoluminescence attached to a Quanta 600. Isotopic compositions of 204Pb, 206Pb, 207Pb, 208U, 232Th and 238U were measured using a New Wave 213 nm Nd–YAG laser, coupled with an Agilent 7500cs/7500s ICP–MS using a spot size of 30 öm was used, with 5 Hz frequency and an acquisition time of 60 seconds, including 30 seconds of background measurement and 30 seconds of ablation. Data analyses and correction for mass bias and elemental fractionation utilizing the program Glitter (Griffin, Belousova, Shee, Pearson and O'Reilly, 2004), and the primary zircon standard GJ. Instrument drift was accounted for using a linear correction and standard bracketing every 8 zircon analyses. Age calculations were done using Isoplot (Ludwig, 2003).

In both locations zircons are abundant. They display rounded morphologies (Supplementary Figure 1) consistent with vigorous mechanical action on an open ocean beach. Many of the zircons have a frosted appearance arising from abrasion. The zircons range in size between 80 and 260 microns with aspects that range from 1:1 to 1:5. CL imaging reveals a wide variety of internal structure from simple classically defined igneous-style structure to complex grains with lobate dissolution and precipitation surfaces to grains that have little internal structure (Supplementary Figure 1) and grains that have obvious metamorphic style overgrowths.

The results of beach sand zircon U-Pb age determinations are shown in Supplementary Table 6. 79 zircons were analysed from the eclogite and blueschist locality on northern Rocky Beach. 62 zircons are within ± 10% of concordia and 70 grains within ± 20%. Ages of the ± 10% concordant grains range between mid-Carboniferous (~ 335 Ma) to Mesoarchaean (~ 3000 Ma). There are well-defined age peaks at approximately 960, 560, 410 and 350 Ma. For zircons within ± 20% of concordia, apparent grain ages range between Early Triassic (~250 Ma) and Mesoarchaean (~3100 Ma), however there is no significant change to the major age populations.

73 zircons were analysed from the southern end of Town Beach. 45 are within ± 10% of concordia and 63 grains within ± 20%. Ages of the ± 10% concordant grains range between early Triassic (~ 250 Ma) to ~ Neoarchaean (~ 2600 Ma). There are prominent age peaks at approximately 960, 540, 490, 440, 400, 335 and 250 Ma. For zircons within

± 20% of concordia, apparent grain ages range between ~250 Ma and 2800 Ma however there is no significant change to the major age populations.



Supplementary Figure 1 caption: Modern beach sand zircons from Port Macquarie. a), b) Representative zircons showing abraded and rounded morphologies. c), d) Representative CL images displaying a range of internal structures.

Supplementary Data 1: Representative electron microprobe analyses for minerals in lawsonite eclogite (RB11) and garnet blueschist (RB12), as well as cations and end-member proportions. X(Fe) = Fe2+/(Fe2++Mg), O(j) = Na on the M2 site, as defined by the THERMOCALC A-X model

	RB12 Garnet rim	RB12 Garnet core	RB11 Garnet rim	RB11 Garnet core
SiO2	36.39	37.20	36.97	36.48
TiO2	0.08	0.18	0.15	0.26
Al2O3	21.56	20.97	21.51	20.90
Cr2O3	0.01	0.01	0.00	0.00
FeO	30.27	23.52	29.00	21.13
MnO	0.52	6.47	0.79	11.43
MgO	1.85	0.96	1.03	0.17
CaO	8.28	9.84	10.26	9.16
Na2O	0.01	0.31	0.02	0.01
K2O	0.00	0.00	0.01	0.00
Cl	0.00	0.00	0.00	0.00
F	0.05	0.05	0.05	0.08
TOTAL	99.06	99.56	99.76	99.61
Si	2.897	3.000	2.960	2.955
Ti	0.005	0.011	0.009	0.016
Al	2.023	1.998	2.029	1.996
Cr	0.000	0.000	0.000	0.000
Fe3+	0.000	0.001	0.024	0.043
Fe2+	2.015	1.588	1.918	1.388
Mn	0.035	0.443	0.054	0.784
Mg	0.220	0.115	0.123	0.021
Ca	0.706	0.853	0.880	0.795
Na	0.000	0.000	0.002	0.001
K	0.000	0.000	0.001	0.000
Cl	0.000	0.000	0.000	0.000
F	0.000	0.000	0.012	0.020
TOTAL	7.901	8.009	8.000	8.000
X(gt)	0.9	0.93	0.94	0.99
Almandine	0.68	0.53	0.65	0.47
Pyrope	0.07	0.04	0.04	0.01
Grossular	0.24	0.28	0.29	0.26
Spesspartine	0.01	0.15	0.02	0.26

Supplementary Data 1 continued: Representative electron microprobe analyses for minerals in lawsonite eclogite (RB11) and garnet blueschist (RB12), as well as cations and end-member proportions. X(Fe) = Fe2+/(Fe2++Mg), O(j) = Na on the M2 site, as defined by the THERMOCALC A-X model

	RB12 Omphacite in garnet	RB11 Omphacite		RB12 Phengite	RB11 Phengite
SiO2	54.10	55.59	SiO2	52.50	52.18
TiO2	0.07	0.04	TiO2	0.14	0.09
Al2O3	9.48	9.62	Al2O3	24.40	22.34
Cr2O3	0.02	0.00	Cr2O3	0.02	0.00
FeO	8.87	6.16	FeO	2.88	4.25
MnO	0.24	0.01	MnO	0.01	0.02
MgO	5.91	7.89	MgO	4.26	3.98
CaO	11.22	13.67	CaO	0.03	0.00
Na2O	8.68	6.77	Na2O	0.14	0.04
K2O	0.01	0.00	K2O	5.74	11.04
Cl	0.00	0.01	Cl	0.03	0.00
F	0.00	0.00	F	0.02	0.00
TOTAL	98.60	99.78	TOTAL	90.15	93.95
Si	1.956	1.991	Si	3.759	3.572
Ti	0.002	0.001	Ti	0.008	0.005
Al	0.404	0.406	Al	2.059	1.803
Cr	0.001	0.000	Cr	0.001	0.000
Fe3+	0.288	0.079	Fe3+	0.000	0.013
Fe2+	0.020	0.106	Fe2+	0.172	0.231
Mn	0.007	0.000	Mn	0.000	0.001
Mg	0.319	0.421	Mg	0.454	0.406
Ca	0.435	0.524	Ca	0.002	0.000
Na	0.608	0.470	Na	0.020	0.005
K	0.000	0.000	K	0.524	0.964
Cl	0.000	0.000	Cl	0.004	0.000
F	0.000	0.000	F	0.005	0.000
TOTAL	4.000	4.000	TOTAL	7.000	7.000
J(cpx)	0.61	0.47	Paragonite	0.02	0.01
Jadiete	0.36	0.39	Margarite	0	0
Diopside	0.42	0.42	Muscovite	0.38	0.34
Hedenbergite	0.03	0.11	Celedonite	0.43	0.41
Aegerine	0.25	0.08	Ferro-celedonite	0.16	0.24

Supplementary Data 1 continued: Representative electron microprobe analyses for minerals in lawsonite eclogite (RB11) and garnet blueschist (RB12), as well as cations and end-member proportions. X(Fe) = Fe2+/(Fe2++Mg), O(j) = Na on the M2 site, as defined by the THERMOCALC A-X model

	RB12 Glaucophane core	RB12 Glaucophane rim	RB11 Glaucophane	RB12 Chlorite	RB11 Chlorite
SiO2	57.00	56.44	55.53	26.36	25.79
TiO2	0.00	0.01	0.06	0.00	0.00
Al2O3	11.04	10.14	9.11	17.89	18.03
Cr2O3	0.02	0.00	0.01	0.02	0.00
FeO	10.95	13.82	17.25	28.59	30.65
MnO	0.02	0.16	0.17	0.85	1.09
MgO	9.50	8.21	6.44	13.06	10.56
CaO	0.51	0.23	0.29	0.01	0.03
Na2O	7.36	7.34	7.17	0.00	0.02
K2O	0.01	0.03	0.06	0.00	0.01
Cl	0.00	0.00	0.01	0.01	0.00
F	0.00	0.00	0.00	0.03	0.06
TOTAL	96.48	96.42	96.08	86.81	86.24
Si	7.953	7.947	8.047	5.775	2.883
Ti	0.000	0.001	0.007	0.000	0.000
Al	1.815	1.682	1.556	4.524	2.376
Cr	0.001	0.000	0.001	0.000	0.000
Fe3+	0.086	0.349	0.000	0.049	0.000
Fe2+	1.191	1.279	2.090	5.042	2.866
Mn	0.002	0.019	0.021	0.165	0.103
Mg	1.976	1.723	1.390	4.373	1.761
Ca	0.076	0.035	0.044	0.000	0.003
Na	1.991	2.003	2.013	0.008	0.004
K	0.000	0.000	0.011	0.000	0.002
Cl	0.000	0.000	0.002	0.000	0.000
F	0.000	0.000	0.000	0.050	0.023
TOTAL	15.091	15.038	15.180	19.986	10.000
X(Fe)	0.38	0.43	0.60	0.45	0.38
Aliv	0.05	0.05	0		
A1vi	1.77	1.63	1.56		
Xalvi	0.35	0.33	0.31		

Supplementary Data 1 continued: Representative electron microprobe analyses for minerals in lawsonite eclogite (RB11) and garnet blueschist (RB12), as well as cations and end-member proportions. X(Fe) = Fe2+/(Fe2++Mg), O(j) = Na on the M2 site, as defined by the THERMOCALC A-X model

	RB11 Stilpnome-lane	RB11 Lawsonite	RB11 Titanite	RB12 Rutile	RB12 Titanite
SiO2	44.60	37.14	30.32	0.00	30.31
TiO2	0.00	0.50	37.96	96.51	39.03
Al2O3	6.58	31.76	1.36	0.06	0.73
Cr2O3	0.00	0.00	0.00	0.02	0.00
FeO	25.03	0.25	0.18	0.42	0.15
MnO	1.61	0.00	0.00	0.00	0.01
MgO	6.70	0.00	0.00	0.00	0.00
CaO	0.06	17.32	28.12	0.08	28.27
Na2O	0.63	0.00	0.02	0.00	0.00
K2O	1.44	0.00	0.06	0.00	0.01
Cl	0.00	0.00	0.00	0.01	0.00
F	0.01	0.00	0.06	0.04	0.06
TOTAL	86.65	86.93	98.05	97.12	98.55
Si	7.877	1.983	1.001	0.000	1.000
Ti	0.000	0.017	0.943	0.993	0.968
Al	1.370	1.998	0.053	0.001	0.028
Cr	0.000	0.000	0.000	0.000	0.000
Fe3+	0.910	0.038	0.057	0.011	0.030
Fe2+	2.788	0.027	0.052	0.006	0.026
Mn	0.241	0.000	0.000	0.000	0.000
Mg	1.765	0.000	0.000	0.000	0.000
Ca	0.011	0.991	0.995	0.001	0.999
Na	0.215	0.000	0.001	0.000	0.000
K	0.324	0.000	0.003	0.000	0.000
Cl	0.000	0.000	0.000	0.000	0.000
F	0.004	0.000	0.006	0.002	0.007
TOTAL	15.500	5.000	3.000	1.000	3.000
X(Fe)	0.32				

Supplementary Table 2: Calculated bulk geochemistry for lawsonite eclogite and garnet blueschist samples, used for phase equilibria modelling in mol%

	Lawsonite eclogite	Garnet blueschist
SiO2	56.8	60.92
Al2O3	14.76	9.98
CaO	3.21	0.62
MgO	8.31	12.31
FeO*	10.15	8.35
K2O	4.97	2.74
Na2O	1.25	5.03
O	0.55	0.04
Total	100	100
H2O	In excess	In excess

Supplementary Table 3: Lu–Hf and Sm–Nd isotopic results for lawsonite eclogite and garnet blueschist

Sample	fraction	Sm [ppm]	2s	Nd [ppm]	2s	147Sm/144Nd	2s	143Nd/144Nd	2se
Glaucophane Eclogite	G1	2.687	0.001	7.239	0.013	0.224389	0.000417	0.512868	0.000012
RB12	G2	2.012	0.001	1.449	0.001	0.840118	0.000448	0.514938	0.000013
	G3	2.019	0	2.013	0	0.606874	0.000191	0.514217	0.000007
	WR	0.742	0	2.034	0	0.220627	0.000011	0.513051	0.000007
Lawsonite eclogite	L1-A	24.882	0.054	75.183	0.814	0.20008	0.00221	0.512627	0.000008
RB11	L1-B	26.41	0.068	78.465	0.396	0.203488	0.001152	0.512625	0.000004
	L1-C	24.075	0.053	72.665	0.614	0.200301	0.001747	0.51263	0.000007
	L2-A	30.094	0.074	93.293	1.534	0.195019	0.003241	0.512571	0.000009
	L2-B	28.674	0.114	90.025	1.094	0.192564	0.002461	0.512598	0.000009
	L2-C	31.343	0.102	93.271	0.958	0.203162	0.002188	0.512583	0.000005
	G1	2.115	0.001	3.934	0.003	0.325075	0.000304	0.513173	0.000009
	WR	12.428	0.008	64.283	0.02	0.116875	0.000082	0.512445	0.00001
Sample	fraction	Lu [ppm]	Hf [ppm]	176Lu/177Hf	2s	176Hf/177Hf	2se		Weight (mg)
Glaucophane Eclogite	G1	3.132	3.898	0.114	0.0006	0.283641	0.000005		69.38
RB12	G2	1.952	0.07	3.951	0.0198	0.317732	0.000016		75.31
	G3	1.278	0.074	2.461	0.0123	0.304656	0.000023		60.43
	WR	0.256	1.896	0.019	0.0001	0.282977	0.000007		99.8
Lawsonite Eclogite	G1	2.827	2.583	0.155	0.0008	0.284042	0.000004		73.49
RB11	L1-A	0.731	2.195	0.047	0.0002	0.283073	0.000004		71.32
	L2-A	0.777	1.911	0.058	0.0003	0.283139	0.000004		77.62
	L1-B	0.78	1.943	0.057	0.0003	0.283155	0.000004		76.66
	L2-B	0.707	1.841	0.054	0.0003	0.283132	0.000006		76.88
	L1-C	0.655	1.836	0.05	0.0003	0.283093	0.000005		76.29
	L2-C	0.85	2.238	0.054	0.0003	0.283119	0.000004		78.99
	WR	1.124	8.264	0.019	0.0001	0.282797	0.000004		100.09

Supplementary Table 4: Used In-situ U–Pb zircon geochronology results.

Analyses no.	Pb207/Pb206		Pb207/U235		Pb206/U238		Pb207/Pb206		Pb206/U238		Pb207/U235	
R4-O	0.0552	0.00497	0.60151	0.05114	0.07935	0.00269	420.3	189.35	492.2	16.04	478.2	32.42
R4-ND	0.06707	0.00673	0.80534	0.07481	0.08746	0.00374	840	196.07	540.5	22.15	599.8	42.08
R4-NB	0.05781	0.00424	0.62759	0.04375	0.07894	0.00218	522.3	153.33	489.8	13	494.6	27.3
R4-NA	0.05734	0.00822	0.65518	0.08859	0.08345	0.00441	504.3	288.28	516.7	26.23	511.7	54.34
R4-D	0.06175	0.00188	0.6597	0.01943	0.07749	0.00117	665.4	63.88	481.1	6.98	514.4	11.89
R4-B	0.06266	0.00827	0.63071	0.07688	0.07382	0.00407	696.9	258.52	459.1	24.43	496.5	47.87
R4-AG	0.05936	0.01146	0.68563	0.1258	0.08367	0.00553	580.3	371.91	518	32.87	530.2	75.78
R1A-5C	0.05886	0.00503	0.67749	0.05504	0.08396	0.00266	562.1	175.92	519.7	15.81	525.3	33.31
R1A-5BB	0.06185	0.00327	0.64226	0.0325	0.0754	0.00161	668.9	109.25	468.6	9.66	503.7	20.09
R1A-5AB	0.06044	0.00633	0.5564	0.05482	0.06703	0.00266	619.5	211.08	418.2	16.04	449.2	35.76
R1A-4A	0.05706	0.0033	0.55671	0.03073	0.07103	0.00159	493.1	123.26	442.3	9.58	449.4	20.05
R1A-10E	0.05881	0.00392	0.63798	0.04032	0.07877	0.00204	560	138.86	488.8	12.18	501.1	25
R1A-10C	0.05663	0.00292	0.66374	0.03258	0.08531	0.00182	476.5	110.74	527.8	10.8	516.9	19.89
R1A-10A	0.05592	0.00535	0.64244	0.05856	0.08346	0.00285	448.7	200	516.7	16.93	503.8	36.2
G1A-9A	0.06846	0.01169	0.75167	0.12629	0.07983	0.00303	882.4	318.17	495.1	18.07	569.2	73.2
G1A-8A	0.04904	0.00798	0.52546	0.08436	0.07814	0.0031	149.8	341.88	485	18.53	428.8	56.15
G1A-7B2	0.04803	0.00799	0.49079	0.07995	0.07414	0.00328	100.6	352.13	461	19.7	405.5	54.45
G1A-7B1	0.05484	0.02154	0.67095	0.25999	0.08878	0.00632	405.7	699.35	548.3	37.43	521.3	157.98
G1A-7A	0.05963	0.01082	0.6405	0.11367	0.07783	0.00393	590.3	351.35	483.2	23.53	502.6	70.36
G1A-5C2	0.06099	0.00771	0.62703	0.07828	0.07465	0.00244	638.9	250.92	464.1	14.61	494.2	48.85
G1A-5B1	0.06179	0.00492	0.68036	0.05308	0.08475	0.00188	666.8	161.96	524.4	11.16	527	32.08
G1A-3A2	0.0648	0.01048	0.79677	0.11425	0.09504	0.00369	767.9	308.07	585.3	21.72	595	64.56
G1A-3A1	0.06423	0.01014	0.75463	0.11677	0.08516	0.00331	749.2	302.41	526.8	19.64	570.9	67.58
G1A-15B	0.05549	0.01003	0.63446	0.11209	0.08299	0.00353	431.6	359.42	514	20.99	498.9	69.64
G1A-15A2	0.05898	0.00629	0.63987	0.06685	0.07872	0.00226	566.3	216.66	488.5	13.49	502.2	41.39
G1A-12D	0.05591	0.01119	0.61412	0.1274	0.07873	0.00387	448.4	392.33	488.5	23.14	486.2	80.14
G1A-12B	0.05592	0.00634	0.70239	0.08016	0.09104	0.00296	448.9	234.33	561.7	17.52	540.2	47.81
G1A-12A	0.0625	0.0084	0.69142	0.07802	0.08122	0.00459	691.2	263.39	503.4	27.39	533.7	46.84
G1A-10C	0.05778	0.00932	0.6275	0.09488	0.08024	0.00308	521.1	319.74	497.5	18.4	494.5	59.19
G1A-10B	0.04972	0.00758	0.49243	0.07139	0.0725	0.00287	182	320.59	451.2	17.23	406.6	48.57

Supplementary Table 4: Unused In-situ U–Pb zircon geochronology results.

Analyses no.	Pb207/Pb206		Pb207/U235		Pb206/U238		Pb207/Pb206		Pb206/U238		Pb207/U235	
R4-NC	0.09961	0.02325	1.04376	0.21321	0.07709	0.0094	1616.8	381.33	478.8	56.23	725.8	105.93
R4-L	0.0571	0.00412	0.52818	0.03599	0.06721	0.0019	495	152.23	419.3	11.48	430.6	23.91
R4-JB	0.34602	0.07598	8.98697	1.52583	0.19496	0.03232	3689.6	299.82	1148.2	174.38	2336.7	155.13
R4-JA	0.31968	0.0395	6.07242	0.59751	0.14628	0.01239	3568.3	178.09	880.1	69.66	1986.3	85.78
R4-H	0.15833	0.02288	2.8976	0.36615	0.13493	0.0107	2437.9	226.05	815.9	60.77	1381.3	95.39
R4-GB	0.19153	0.02327	6.42743	0.67586	0.25591	0.01934	2755.4	186.73	1468.9	99.28	2036	92.4
R4-GA	0.05884	0.0065	0.6978	0.0715	0.0867	0.004	561.1	224.2	536	23.76	537.5	42.76
R4-DB	0.06011	0.0054	0.66843	0.05664	0.08099	0.00279	607.5	183.24	502	16.61	519.8	34.47
R4-C	0.06042	0.00949	0.68962	0.09822	0.08282	0.00604	618.6	307.12	512.9	35.96	532.6	59.03
R4-AC	0.06127	0.00947	0.65058	0.09542	0.0772	0.00416	648.6	301.29	479.4	24.89	508.8	58.7
R4-AB	0.05349	0.01082	0.69054	0.12643	0.09328	0.00881	349.5	402.26	574.9	51.95	533.1	75.93
R4-AA	0.06439	0.00699	0.68112	0.06765	0.07674	0.00371	754.6	213.8	476.6	22.22	527.5	40.86
R1A-8AA	0.064	0.00726	1.07869	0.11555	0.1233	0.00534	741.5	223.2	749.5	30.63	743	56.44
R1A-8A	0.04882	0.00824	0.62353	0.09792	0.09208	0.00631	139.2	354.08	567.8	37.27	492.1	61.24
R1A-6B	0.09562	0.01634	0.95086	0.14942	0.07552	0.00546	1540.4	291.21	469.3	32.75	678.6	77.77
R1A-5BA	0.05962	0.00898	0.67053	0.09546	0.08236	0.00449	589.8	296.99	510.2	26.76	521	58.02
R1A-5A	0.05985	0.00813	0.63675	0.08176	0.07723	0.00383	598	269.94	479.5	22.9	500.3	50.72
R1A-2A	0.05319	0.00669	0.60879	0.07241	0.08301	0.00382	336.7	262.42	514	22.74	482.8	45.7
R1A-10EC	0.06125	0.00736	0.55628	0.06286	0.06601	0.00299	648	239.13	412.1	18.07	449.1	41.01
R1A-10EB	0.05467	0.00322	0.56463	0.03182	0.07497	0.00171	398.9	126.66	466	10.25	454.5	20.65
G1A-9B	0.14332	0.03899	1.21141	0.30079	0.0619	0.00713	2267.7	406.32	387.2	43.29	805.8	138.11
G1A-1A2	0.10294	0.04656	0.97667	0.14355	0.06855	0.00779	1677.7	662.4	427.4	46.97	691.9	223.71
G1A-1A1	0.07366	0.01411	0.78757	0.14051	0.0785	0.00536	1032.2	345.34	487.1	32.06	589.8	79.81
G1A-1A	0.05029	0.00941	0.56259	0.10094	0.08189	0.00428	208.4	384.71	507.4	25.49	453.2	65.59
G1A-12E	0.03934	0.00459	0.3867	0.04633	0.07122	0.00247	0.1	0	443.5	14.86	332	33.92

Supplementary Table 5: EPMA results from zircon analyses in lawsonite eclogite in wt%

SAMPLE	SiO2	ZrO2	HfO2	O	TOTAL
RB11a-zircon-GR-1	32.8745	64.9545	1.42052	0	99.2495
RB11a-zircon-GR-11	32.6349	63.5957	1.35038	0	97.581
RB11a-zircon-GR-12	32.6524	66.4432	1.16889	0	100.265
RB11a-zircon-GR-14	31.8928	65.6534	1.28397	0	98.8302
RB11a-zircon-GR-15	32.7224	65.6996	1.26152	0.000004	99.6836
RB11a-zircon-GR-16	32.4295	64.1059	1.19603	0	97.7315
RB11a-zircon-GT-17	32.4387	65.7032	1.30114	0	99.4431
RB11a-zircon-MT-10	32.6495	65.1539	1.118	0	98.9214
RB11a-zircon-MT-12	32.4422	65.6214	1.19085	-0.00001	99.2544
RB11a-zircon-MT-13	32.6281	65.6593	1.15147	0.000004	99.4388
RB11a-zircon-MT-15	32.298	64.6146	1.24841	0	98.161
RB11a-zircon-MT-3	32.033	66.2374	1.40782	0.000008	99.6783
RB11a-zircon-MT-4	32.2596	66.7526	1.44334	0	100.456
RB11a-zircon-MT-5	32.2817	63.8129	1.4875	0	97.5821
RB11a-zircon-MT-6	32.566	65.4846	1.13044	0	99.181
RB11a-zircon-MT-7	32.5091	64.4667	1.32259	-0.00001	98.2985
RB11a-zircon-MT-8	31.6595	67.359	1.25898	0	100.278
Average HfO2	1.2789		Gr = in garnet		
Average wt% Hf	1.0846		Mt = in matrix		

Supplementary Table 6: Detrital zircon analyses from modern beach sands at Port Macquarie. Errors are 2se

Analyses no.	Pb207/ Pb206		Pb207/ U235		Pb206/ U238		Pb208/ Th232		conc	Pb207/ Pb206		Pb206/ U238		Pb207/ U235		Pb208/ Th232	
RB17_09	0.05251	0.00142	0.05372	0.00077	0.38902	0.0105	0.01714	0.00065	109.55	307.9	60.47	337.3	4.7	333.7	7.67	343.5	12.97
RB17_40	0.05283	0.00151	0.04072	0.0006	0.29643	0.00842	0.01367	0.00042	80.08	321.3	63.53	257.3	3.74	263.6	6.6	274.5	8.43
RB17_45	0.05389	0.00196	0.05902	0.001	0.43852	0.01575	0.02005	0.00201	100.96	366.2	79.6	369.7	6.11	369.2	11.11	401.2	39.81
RB17_43	0.05395	0.00141	0.05593	0.00083	0.41604	0.01097	0.01706	0.00134	95.09	368.9	57.9	350.8	5.04	353.2	7.87	341.9	26.56
RB17_31	0.05398	0.00086	0.06768	0.00087	0.50352	0.00857	0.02158	0.00053	114.14	369.9	35.58	422.2	5.26	414.1	5.79	431.6	10.58
RB17_12	0.05405	0.00084	0.05589	0.00067	0.41651	0.00675	0.01772	0.00055	94.02	372.9	34.85	350.6	4.11	353.6	4.84	355.1	10.89
RB17_17	0.05435	0.00079	0.04978	0.00061	0.37302	0.00582	0.01663	0.00043	81.27	385.4	32.27	313.2	3.77	321.9	4.3	333.3	8.58
RB17_28	0.05466	0.00095	0.06572	0.00085	0.49514	0.00904	0.02278	0.00057	103.01	398.3	38.33	410.3	5.15	408.4	6.14	455.2	11.21
RB17_46	0.05485	0.00136	0.0548	0.0008	0.4144	0.01042	0.01699	0.00152	84.73	405.9	53.86	343.9	4.91	352	7.48	340.5	30.25
RB17_29	0.05502	0.00071	0.07012	0.00087	0.53182	0.00765	0.02404	0.00057	105.76	413.1	28.2	436.9	5.27	433	5.07	480.2	11.16
RB17_53	0.05504	0.00149	0.05294	0.00082	0.40172	0.01111	0.01721	0.00168	80.35	413.8	58.91	332.5	5.02	342.9	8.05	345	33.36
RB17_35	0.05523	0.00112	0.06536	0.00086	0.4975	0.01029	0.02302	0.00072	96.84	421.5	44.15	408.2	5.23	410	6.98	460.1	14.24
RB17_16	0.05567	0.00105	0.08419	0.0011	0.64631	0.01259	0.02706	0.00082	118.70	439	41.11	521.1	6.53	506.2	7.76	539.7	16.17
RB17_49	0.05635	0.00179	0.06884	0.00113	0.5349	0.01699	0.02195	0.00271	92.16	465.6	69.03	429.1	6.82	435.1	11.24	438.8	53.65
RB17_22	0.05647	0.00154	0.07715	0.00115	0.60054	0.01631	0.02524	0.00095	101.89	470.2	59.45	479.1	6.88	477.6	10.34	503.9	18.66
RB17_52	0.05665	0.00153	0.06311	0.00098	0.49293	0.01357	0.02176	0.00205	82.65	477.3	58.85	394.5	5.92	406.9	9.23	435	40.55
RB17_51	0.05722	0.00146	0.06831	0.00104	0.53891	0.0141	0.02219	0.00203	85.27	499.6	55.74	426	6.27	437.7	9.3	443.7	40.09
RB17_62	0.05738	0.00152	0.05183	0.00077	0.40999	0.01119	0.01874	0.00128	64.38	505.9	57.65	325.7	4.73	348.9	8.06	375.3	25.36
RB17_03	0.0575	0.00114	0.08031	0.00104	0.63684	0.01282	0.02636	0.00095	97.55	510.5	43.32	498	6.22	500.3	7.95	525.9	18.76
RB17_34	0.05758	0.00129	0.08636	0.00121	0.68536	0.0156	0.02747	0.00073	103.99	513.5	48.73	534	7.16	530	9.4	547.8	14.38
RB17_56	0.0576	0.00172	0.08556	0.00138	0.6795	0.02047	0.02717	0.00295	102.90	514.3	64.57	529.2	8.17	526.5	12.38	541.9	58.14
RB17_59	0.05764	0.00174	0.08315	0.00134	0.6608	0.02009	0.02586	0.00308	99.79	516	65.11	514.9	8	515.1	12.28	516.1	60.62
RB17_10	0.05766	0.00151	0.09192	0.00133	0.73106	0.01904	0.02927	0.00119	109.72	516.7	56.62	566.9	7.85	557.2	11.17	583.1	23.4
RB17_01	0.05783	0.00093	0.09182	0.00115	0.7322	0.01236	0.02999	0.00072	108.24	523.2	35.18	566.3	6.79	557.8	7.25	597.3	14.13
RB17_30	0.05785	0.00124	0.08623	0.00119	0.68756	0.015	0.03036	0.00113	101.81	523.7	46.47	533.2	7.05	531.3	9.03	604.5	22.19
RB17_20	0.05806	0.00094	0.08369	0.00108	0.67018	0.01162	0.02721	0.00098	97.46	531.6	35.65	518.1	6.45	520.8	7.06	542.6	19.29
RB17_11	0.05811	0.0013	0.06771	0.00093	0.54255	0.01228	0.02176	0.00085	79.20	533.3	48.69	422.4	5.63	440.1	8.08	435.1	16.82

Supplementary Table 6 continued: Detrital zircon analyses from modern beach sands at Port Macquarie. Errors are 2se

Analyses no.	Pb207/ Pb206		Pb207/ U235		Pb206/ U238		Pb208/ Th232		conc	Pb207/ Pb206		Pb206/ U238		Pb207/ U235		Pb208/ Th232	
RB17_73	0.05815	0.00113	0.09127	0.00131	0.73166	0.0155	0.02839	0.00134	105.27	534.8	42.6	563	7.73	557.5	9.09	565.9	26.29
RB17_32	0.05819	0.00078	0.0899	0.00113	0.72102	0.01071	0.02939	0.00073	103.47	536.4	29.64	555	6.67	551.3	6.32	585.4	14.4
RB17_33	0.05823	0.00076	0.09557	0.0012	0.76699	0.01122	0.03254	0.00078	109.39	537.9	28.9	588.4	7.08	578	6.45	647.3	15.21
RB17_38	0.05825	0.00079	0.09196	0.00117	0.73829	0.01117	0.03055	0.00095	105.27	538.7	29.93	567.1	6.93	561.4	6.53	608.2	18.57
RB17_48	0.05834	0.00177	0.09285	0.00146	0.74691	0.02262	0.02764	0.00271	105.63	541.9	65.85	572.4	8.62	566.4	13.15	551.2	53.39
RB17_68	0.05864	0.001	0.08511	0.00119	0.68809	0.0131	0.02857	0.00128	95.05	553.9	36.61	526.5	7.05	531.7	7.88	569.3	25.07
RB17_26	0.05871	0.00133	0.08567	0.00118	0.69327	0.01579	0.03101	0.00098	95.24	556.4	48.49	529.9	6.99	534.8	9.47	617.2	19.3
RB17_05	0.05871	0.00091	0.08676	0.00108	0.70247	0.01148	0.02511	0.00147	96.39	556.5	33.61	536.4	6.38	540.3	6.85	501.2	29.04
RB17_25	0.05876	0.00073	0.09763	0.00121	0.79078	0.01107	0.03386	0.00077	107.56	558.3	26.91	600.5	7.1	591.6	6.27	673.1	15.1
RB17_18	0.05879	0.00115	0.09159	0.0012	0.74235	0.01482	0.02915	0.00087	101.00	559.3	42.03	564.9	7.08	563.8	8.64	580.7	17.06
RB17_55	0.05884	0.00158	0.09618	0.00149	0.78027	0.02139	0.03027	0.00315	105.49	561.2	57.43	592	8.79	585.6	12.2	602.8	61.82
RB17_71	0.0589	0.00148	0.084	0.00126	0.68204	0.0177	0.0319	0.00203	92.33	563.2	53.89	520	7.48	528	10.68	634.6	39.67
RB17_47	0.0589	0.00178	0.08426	0.00132	0.68433	0.02058	0.02571	0.00243	92.53	563.6	64.51	521.5	7.86	529.4	12.4	513.2	47.8
RB17_06	0.059	0.00074	0.09682	0.00119	0.78768	0.011	0.03203	0.00084	105.08	567	26.99	595.8	6.98	589.9	6.25	637.2	16.43
RB17_37	0.05905	0.00078	0.10069	0.00128	0.81943	0.01219	0.03116	0.00075	108.70	568.9	28.62	618.4	7.48	607.7	6.81	620.3	14.67
RB17_63	0.05905	0.0011	0.08872	0.00124	0.72217	0.0146	0.02864	0.00123	96.31	568.9	40.04	547.9	7.35	551.9	8.61	570.7	24.26
RB17_23	0.05924	0.00085	0.08929	0.00112	0.72911	0.01126	0.03071	0.00071	95.73	575.9	30.78	551.3	6.61	556	6.61	611.5	14
RB17_75	0.05934	0.00114	0.09424	0.00135	0.77102	0.01617	0.03041	0.00137	100.17	579.6	41.28	580.6	7.93	580.3	9.27	605.5	26.81
RB17_44	0.05935	0.00154	0.08075	0.0012	0.66076	0.01724	0.02467	0.00202	86.33	579.9	55.34	500.6	7.15	515.1	10.54	492.6	39.91
RB17_21	0.0595	0.00102	0.09172	0.00118	0.75235	0.0135	0.03011	0.00071	96.60	585.6	36.92	565.7	6.99	569.6	7.82	599.7	13.9
RB17_64	0.05953	0.00101	0.09175	0.00127	0.75292	0.01422	0.03087	0.0013	96.50	586.4	36.49	565.9	7.48	569.9	8.24	614.5	25.5
RB17_69	0.05959	0.00131	0.09588	0.00146	0.78771	0.01873	0.03059	0.00167	100.25	588.7	46.85	590.2	8.58	589.9	10.64	609	32.71
RB17_08	0.05965	0.00106	0.08933	0.00117	0.73496	0.01357	0.02768	0.00094	93.33	591	38.08	551.6	6.9	559.5	7.94	551.9	18.46
RB17_27	0.06017	0.00111	0.10112	0.00134	0.83868	0.016	0.03552	0.001	101.85	609.7	39.25	621	7.84	618.4	8.83	705.6	19.51
RB17_15	0.06022	0.00107	0.10555	0.00131	0.87619	0.01577	0.03194	0.00107	105.74	611.7	37.76	646.8	7.64	638.9	8.54	635.6	21.02
RB17_39	0.06025	0.0014	0.0897	0.00126	0.7448	0.0175	0.02894	0.00091	90.43	612.4	49.38	553.8	7.48	565.2	10.18	576.7	17.87
RB17_58	0.06039	0.00169	0.09488	0.00149	0.79002	0.02244	0.03201	0.00367	94.59	617.7	59.15	584.3	8.8	591.2	12.73	636.8	71.83

Supplementary Table 6 continued: Detrital zircon analyses from modern beach sands at Port Macquarie. Errors are 2se

Analyses no.	Pb207/ Pb206		Pb207/ U235		Pb206/ U238		Pb208/ Th232		conc	Pb207/ Pb206		Pb206/ U238		Pb207/ U235		Pb208/ Th232	
RB17_41	0.06042	0.00134	0.09359	0.00133	0.77959	0.01776	0.02951	0.00202	93.24	618.5	47.3	576.7	7.84	585.3	10.13	587.9	39.75
RB17_72	0.06044	0.00096	0.09496	0.00132	0.79127	0.0144	0.03312	0.00149	94.41	619.4	33.85	584.8	7.75	591.9	8.16	658.6	29.18
RB17_61	0.06051	0.00106	0.10042	0.00139	0.8376	0.01616	0.03191	0.00131	99.20	621.8	37.44	616.8	8.16	617.8	8.93	635	25.62
RB17_19	0.0613	0.00136	0.09183	0.00125	0.77611	0.01729	0.02786	0.00076	87.16	649.7	46.77	566.3	7.36	583.3	9.89	555.3	15.02
RB17_42	0.06161	0.00133	0.0907	0.00129	0.77036	0.0171	0.02665	0.00192	84.75	660.4	45.47	559.7	7.6	580	9.81	531.5	37.79
RB17_66	0.06177	0.00098	0.09793	0.00134	0.83388	0.01504	0.03427	0.00146	90.41	666.1	33.63	602.2	7.89	615.8	8.33	681.1	28.45
RB17_04	0.06218	0.00083	0.09266	0.00113	0.79446	0.01153	0.02989	0.00072	83.95	680.5	28.37	571.3	6.65	593.7	6.52	595.4	14.08
RB17_60	0.0674	0.00218	0.12109	0.00205	1.12522	0.0367	0.03897	0.00492	86.67	850.1	65.8	736.8	11.78	765.5	17.54	772.6	95.81
RB17_13	0.0703	0.00114	0.1621	0.00204	1.57125	0.02661	0.05072	0.00191	103.33	937.2	33	968.4	11.34	958.9	10.51	1000	36.8
RB17_65	0.07072	0.0012	0.15708	0.00219	1.53145	0.02891	0.05142	0.00225	99.06	949.4	34.41	940.5	12.19	943.1	11.6	1013.4	43.25
RB17_67	0.0721	0.00136	0.16517	0.00236	1.64172	0.03351	0.04987	0.00221	99.66	988.8	37.83	985.4	13.04	986.4	12.88	983.7	42.64
RB17_14	0.07329	0.00093	0.15613	0.0019	1.57783	0.02213	0.05	0.00132	91.51	1022.1	25.56	935.3	10.57	961.5	8.72	986.2	25.34
RB17_74	0.07375	0.00174	0.15476	0.00237	1.57353	0.03862	0.04675	0.00249	89.66	1034.6	46.82	927.6	13.22	959.8	15.24	923.5	48.09
RB17_07	0.07536	0.00174	0.16548	0.0024	1.72007	0.03982	0.05266	0.00213	91.57	1078.1	45.59	987.2	13.29	1016.1	14.86	1037.4	40.93
RB17_02	0.12533	0.00154	0.36096	0.00442	6.23847	0.08476	0.10218	0.00227	97.70	2033.5	21.64	1986.7	20.93	2009.9	11.89	1966.4	41.7
RB17_57	0.18643	0.00497	0.42494	0.00663	10.9222	0.29776	0.12718	0.01409	84.21	2710.9	43.28	2282.9	29.97	2516.5	25.36	2419.7	252.71
RB17_50	0.21905	0.0059	0.5804	0.00881	17.53056	0.47572	0.15503	0.01657	99.22	2973.7	42.75	2950.4	35.95	2964.3	26.07	2913.1	290
RB17_70	0.27033	0.00412	0.55856	0.00783	20.81721	0.36971	0.16199	0.0077	86.48	3307.9	23.68	2860.7	32.38	3130.1	17.21	3034.6	133.99

Appendix 4:

Supplementary materials for Chapter 4: Resubduction of lawsonite eclogite within a serpentinite-filled subduction channel

Supplementary File 1

Phase mapping methods

To identify inclusions assemblages in garnet, phase maps were constructed in the Tescan Integrated Mineral Analyser (TIMA) software using data collected on a Tescan Mira3 TIMA with four PulsTor SDD X-ray detectors at the John de Laeter Center, Curtin University. Analysis was conducted in dot-mapping mode with 1 μm BSE pixel spacing. EDS analyses of 1000 counts were acquired at a regular spacing of 5 μm, and additionally at every change in BSE contrast. TIMA software was used to compare BSE intensity and EDS peaks to a custom mineral reference library and automatically classify individual mineral grains. Analytical conditions were an accelerating voltage of 25 kV, beam intensity of 19, probe current of 5.48 nA, spot size of 80 nm, and a working distance of 15 mm.

EBSD map data were collected using a Tescan Mira3 VP-FESEM with Oxford Instruments X-Max 150 SDD X-ray detector, Symmetry EBSD detector and Aztec Synergy software at the John de Laeter Center, Curtin University. Analytical conditions were an accelerating voltage of 20 kV, beam intensity of 18, and working distance of 25 mm. Stage tilt was 70° and step size was 1.22 μm. The EBSD camera was set to binning mode "Speed 1", camera exposure time was 10 ms, and the camera gain was 2. Auto background correction was used with a Hough Resolution of 40, band detection mode was "Centers", number of band detected was 11, and indexing mode was "Optimized - TDK". Band contrast and EDS maps were exported from Aztec and EDS maps were colour scaled in ImageJ.

Extended phase equilibrium modelling methods

The phase equilibria model was calculated using THERMOCALC (TC340i, Powell and Holland, 1988; Holland and Powell, 2011) using the internally-consistent thermodynamic dataset 'ds5' (filename tc-ds55.txt; November 2003 updated version of the Holland and Powell, 1998 data set) and activity–composition (a–x) models (Supp. Table 2; Holland and Powell, 1988; Holland and Powell, 2003; White et al., 2007; Green et al., 2007; Holland and Powell, 2011; Diener et al., 2012) in the chemical system NCKFMASHO. The latest thermodynamic dataset ds62 (Green et al., 2016) was not used, to allow direct comparison with the phase equilibria models of Tamblyn et al. (2019a). The Mn-rich interiors of prograde-zoned garnet were not included in the calculated local rock composition for the stage 2 mineral assemblage, so Mn was not considered in the modelled system. Ti was also not considered, due to limitations in modelling the stability of titanite at high pressure. Titanite has been reported to be the stable

Ti-bearing phase rather than rutile in systems due to the low activity of CO_2, or minor amounts of Al and Fe^{3+} in its crystal lattice (Enami et al., 1993; Castelli and Rubatto; 2002: Brovarone et al., 2011). As we did not investigate rutile/titanite stability as a function of X_{CO2}, and the current *a–x* model does not allow Al or Fe^{3+} substitution in titanite, we did not include it in the calculation of bulk compositions or the phase equilibria models. Stilpnomelane was also not predicted in the model as currently there is no *a–x* model available for it.

Water content was handled in two ways. A model for the local rock composition was calculated with water in excess, and a model for the local rock composition was calculated with a set water content, derived from the abundance of hydrous minerals (Table 2; Supp. Table 1). This was done to approximate the two 'end-members' of hydration the eclogite may have experienced, with the water content calculated from the abundance of hydrous minerals representing the minimum amount of water available in the rock system. We acknowledge this assumes essentially closed-system behaviour, i.e. does not model water flux into the rock from an external source. As we have no indication that this process occurred, we did not model such behaviour.

Oxidation state (Fe_2O_3) for the sample was constrained from the measured microprobe chemical analyses from each mineral used to calculate the metamorphic local rock composition, by using mineral stoichiometry in the calculation of cations from raw weight % oxides (Table 2; Supp. Table 1; Droop, 1987).

Extended Rb–Sr LA-QQQ-MS methods

Phengite was analysed in-situ for Rb and Sr isotopes and major and trace elements using an ESI 213 NWR (TwoVol2) laser ablation system with an attached Agilent 8800QQQ ICP-MS/MS in the Microgeochemistry Laboratory at the University of Gothenburg, Sweden, following the methods of Zack and Hogmalm (2016) and Hogmalm et al. (2017). Laser parameters were a fluence of ~ 6 Jcm^{-2} and a frequency of 10 Hz. Phengite was analysed with a spot size of 40 μm, both perpendicular and parallel to cleavage. Titanite was also analysed to obtain initial $^{87}Sr/^{86}Sr$ ratios, with a spot size of 50 μm. The ICP-MS/MS allows separating $^{87}Sr+$ from $^{87}Rb+$ where Sr+ reacts with a reaction gas (here N_2O) to form SrO+ while Rb+ does not react. Complete separation is achieved by first allowing only one specific M/Z through the first quadrupole (Q1) into the reaction cell and then collect the reacted ion through the second quadrupole (Q2). In detail, to measure ^{86}Sr, Q1 is set to M/Z 86 and Q2 to M/Z 102, while for ^{87}Sr, Q1 is 87 and Q2 is 103. Since not all Sr reacts with N_2O (only about 80%; Hogmalm et al., 2017), ^{87}Rb cannot be analysed interference-free. Instead, ^{85}Rb can be used as a proxy for ^{87}Rb, as $^{87}Rb/^{85}Rb$ can be

assumed to be constant on Earth within the precisions required for this approach. As Rb+ does not react with N2O, Q1 is set to M/Z 85 and Q2 is set to M/Z 85 as well. A range of other isotopes were collected during each analysis together with ^{85}Rb, ^{86}Sr and ^{87}Sr in order to detect and exclude contamination by other minerals, such as: ^{23}Na, ^{24}Mg, ^{27}Al, ^{28}Si, ^{39}K, ^{43}Ca, ^{48}Ti, ^{55}Mn, ^{56}Fe, ^{89}Y, ^{133}Cs, ^{137}Ba, and ^{140}Ce. Laser parameters chosen were a fluence of ~ 6 Jcm^{-2} and a frequency of 10 Hz.

References:

Brovarone, A. V., Groppo, C., Hetényi, G., Compagnoni, R., and Malavieille, J. (2011). Coexistence of lawsonite-bearing eclogite and blueschist: phase equilibria modelling of Alpine Corsica metabasalts and petrological evolution of subducting slabs. *Journal of metamorphic Geology, 29*(5), 583-600.

Diener, J., and Powell, R. (2012). Revised activity–composition models for clinopyroxene and amphibole. *Journal of metamorphic Geology, 30*(2), 131-142.

Droop, G. (1987). A general equation for estimating Fe3+ concentrations in ferromagnesian silicates and oxides from microprobe analyses, using stoichiometric criteria. *Mineralogical Magazine, 51*(361), 431-435.

Enami, M., Suzuki, K., Liou, J., and Bird, D. K. (1993). Al-Fe3+ and F-OH substitutions in titanite and constraints on their PT dependence. *European Journal of Mineralogy, 5*(2), 219-231.

Green, E., Holland, T., and Powell, R. (2007). An order-disorder model for omphacitic pyroxenes in the system jadeite-diopside-hedenbergite-acmite, with applications to eclogitic rocks. *American Mineralogist, 92*(7), 1181-1189.

Green, E., White, R., Diener, J., Powell, R., Holland, T., and Palin, R. (2016). Activity–composition relations for the calculation of partial melting equilibria in metabasic rocks. *Journal of metamorphic Geology, 34*(9), 845-869.

Hogmalm, K. J., Zack, T., Karlsson, A. K.-O., Sjöqvist, A. S., and Garbe-Schönberg, D. (2017). In situ Rb–Sr and K–Ca dating by LA-ICP-MS/MS: an evaluation of N 2 O and SF 6 as reaction gases. *Journal of Analytical Atomic Spectrometry, 32*(2), 305-313.

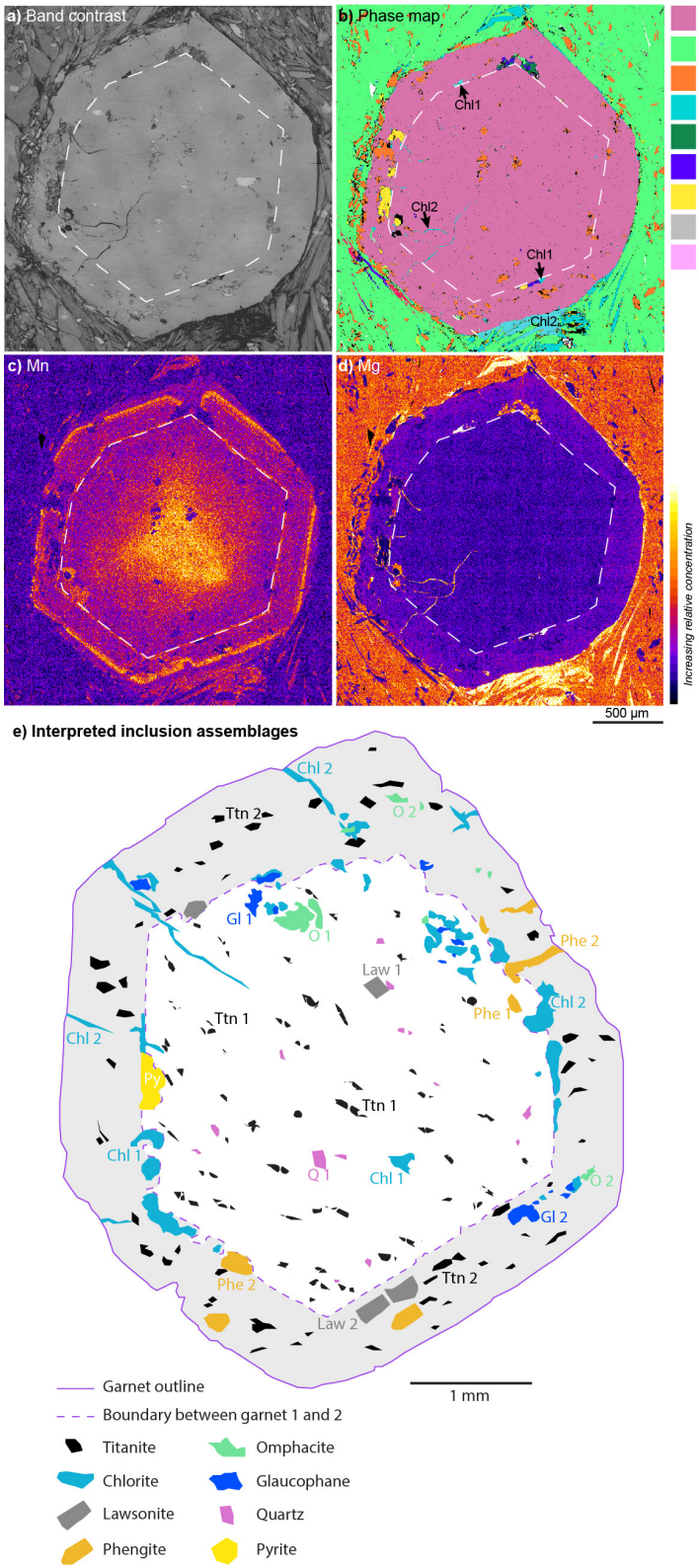
Holland, T., and Powell, R. (1998). An internally consistent thermodynamic data set for phases of petrological interest. *Journal of metamorphic Geology, 16*(3), 309-343.

Holland, T., and Powell, R. (2003). Activity–composition relations for phases in petrological calculations: an asymmetric multicomponent formulation. *Contributions to Mineralogy and Petrology, 145*(4), 492-

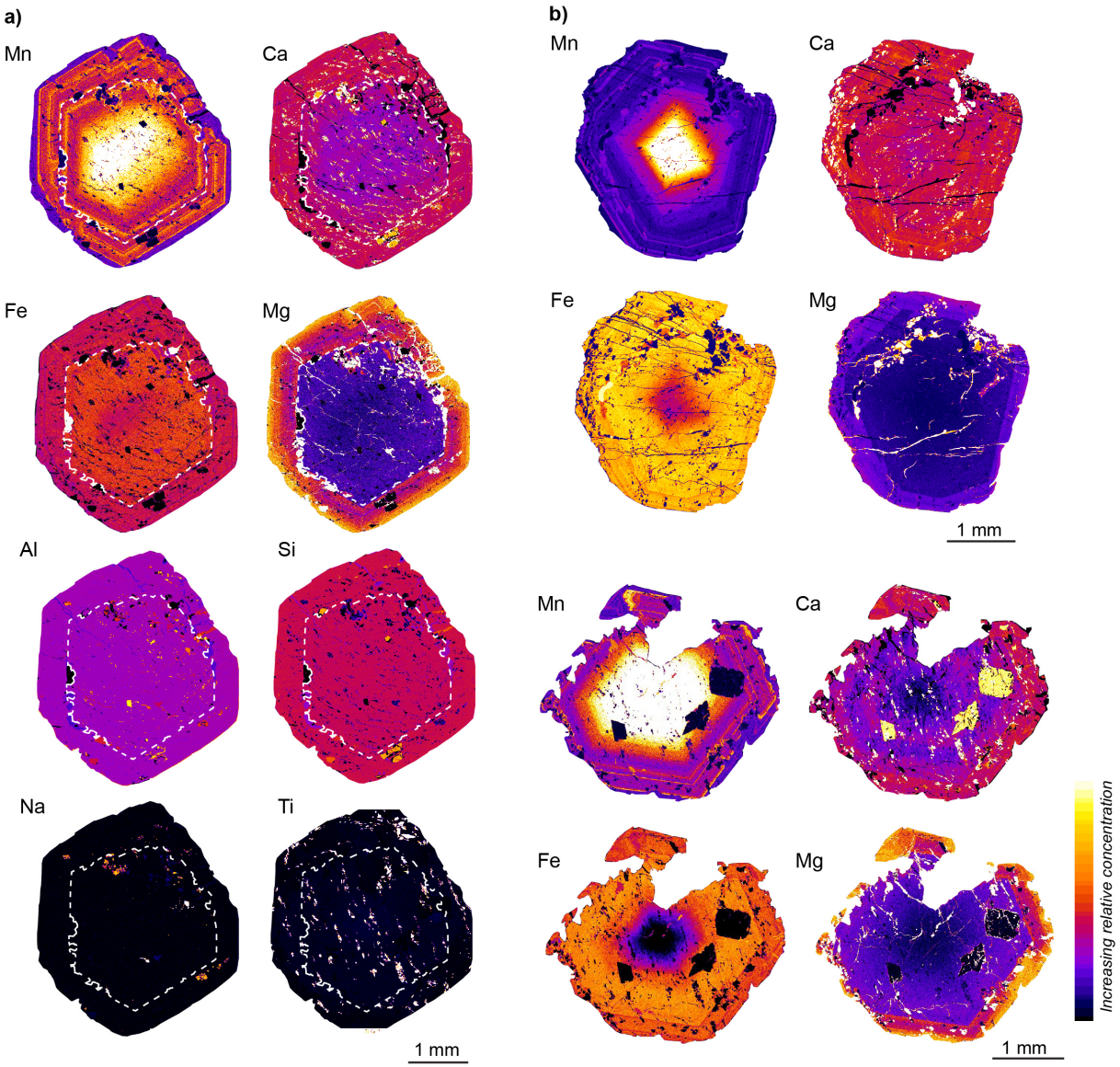
501.

Holland, T., and Powell, R. (2011). An improved and extended internally consistent thermodynamic dataset for phases of petrological interest, involving a new equation of state for solids. *Journal of metamorphic Geology, 29*(3), 333-383.

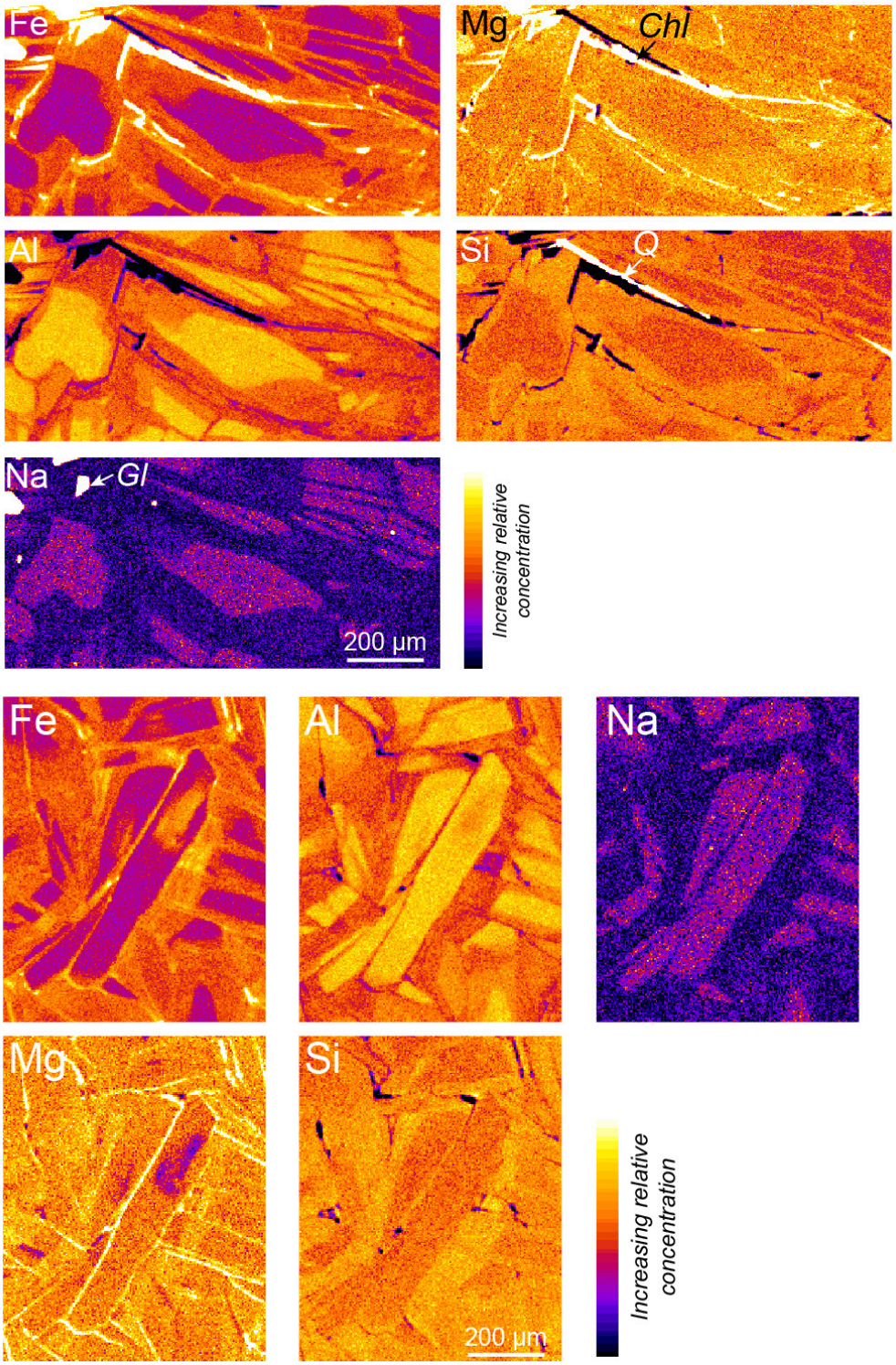
Zack, T., and Hogmalm, K. J. (2016). Laser ablation Rb/Sr dating by online chemical separation of Rb and Sr in an oxygen-filled reaction cell. *Chemical Geology, 437*, 120-133.



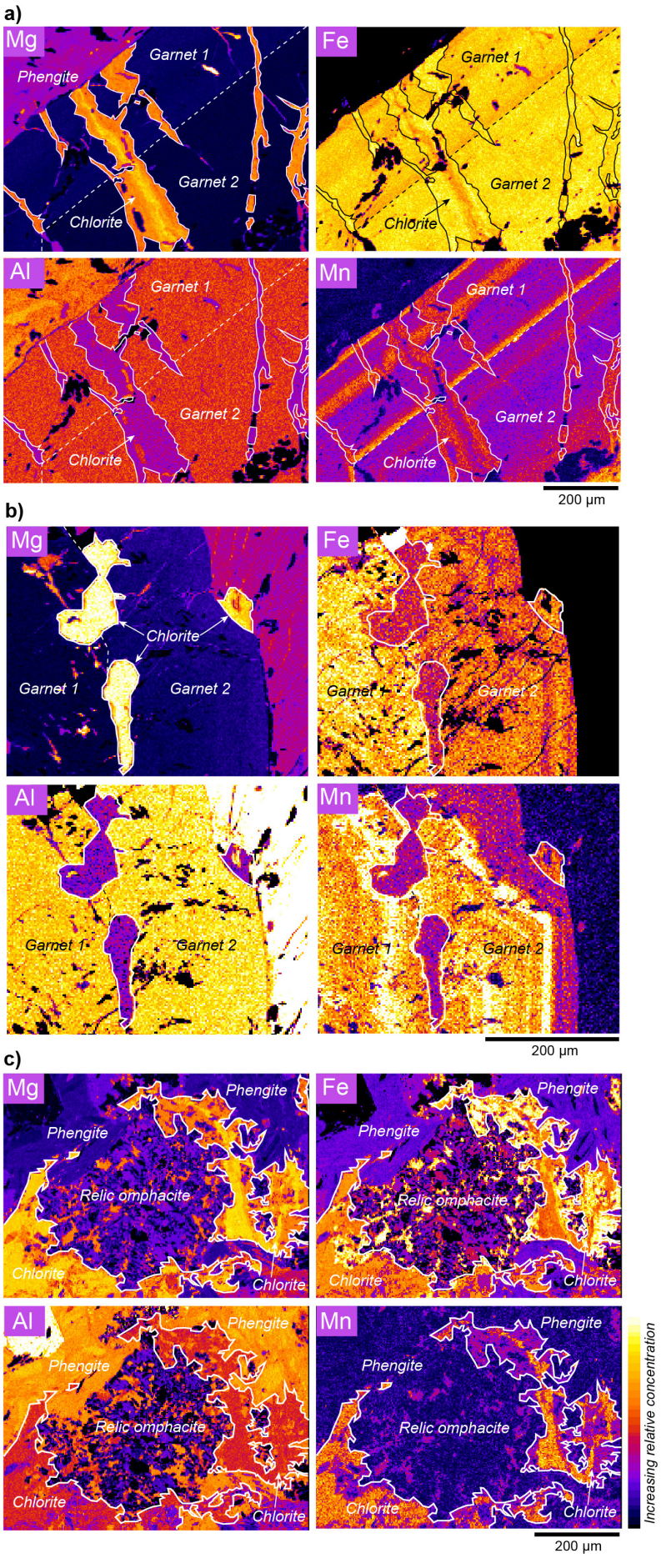
Supplementary Figure 1: Phase map and corresponding images showing an example of inclusion assemblages from garnet porphyroblast in Figure 2d. White dashed line indicates the boundary between garnet 1 and garnet 2. a) Band contrast image, showing that there are no cracks or fractures leading to the minerals included on the boundary of garnet 1 and garnet 2. b) Phase map, showing chlorite 1 trapped at the boundary of garnet 1 and garnet 2, and chlorite 2 cross-cutting the garnet porphyroblast. Phengite, omphacite, titanite, quartz and pyrite are also trapped at the boundary of garnet 1 and garnet 2. c) Mn EDS map of the garnet porphyroblast, showing the boundary between garnet 1 and garnet 2 but also deflections in the Mn zoning around inclusions, indicating they were trapped during garnet growth. d) Mg EDS map, confirming the high-Mg chlorite grains, and also showing the boundary between garnet 1 and garnet 2. e) Schematic diagram of the inclusion assemblages in garnet, traced from phase maps and EPMA compositional maps (Supp. Fig. 1; 2). Chlorite 1 is from both stage 1 prograde and stage 1 retrograde. See figure 2 for abbreviations.



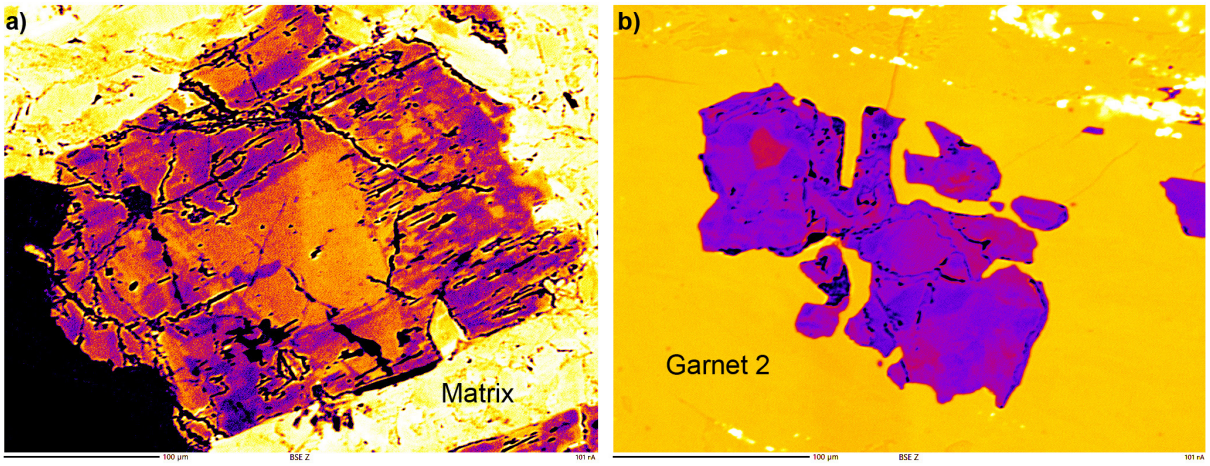
Supplementary Figure 2: Additional EPMA element maps of garnets from lawsonite eclogite. a) Maps of a different garnet that was used to trace the inclusion assemblages in Figure 4 of the main text. b) Maps of two garnets showing prograde zoning in stage 1 garnet. Stage 2 garnet is evident as rims with elevated XMg. Multiple embayments can be seen in Mn-rich oscillatory zoning.



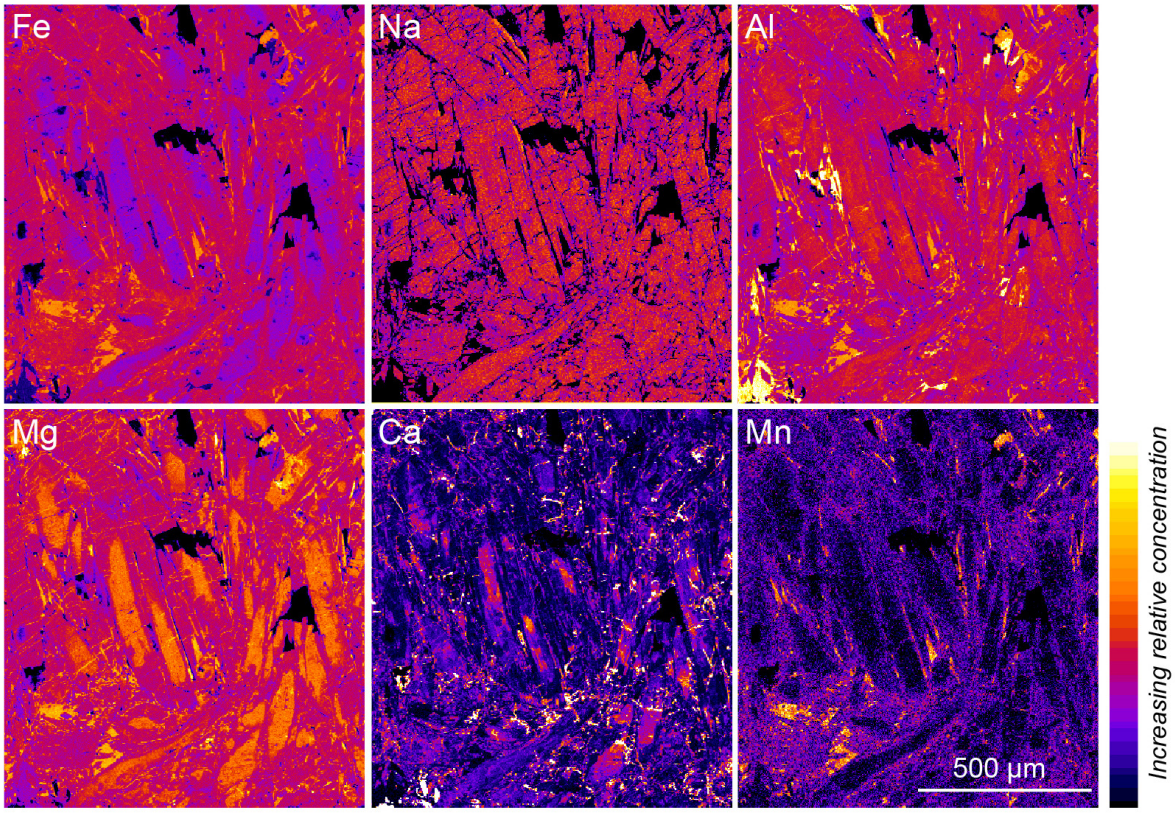
Supplementary Figure 3: Additional EPMA maps of phengite from the lawsonite eclogite, showing prograde zoning, defined by increasing Si, Fe and Mg.



Supplementary Figure 4: EPMA maps of chlorite in textural positions throughout the lawsonite eclogite, showing that chlorite composition appears related to the minerals it is forming in association with. Continuous white/black line indicates the boundary of a chlorite crystals. Dotted white/black line indicates the boundary between garnet 1 and garnet 2. a) Zoned chlorite, forming in stage 2 retrograde fractures which cross-cut both garnet 1 and garnet 2. b) Chlorite 1, trapped as inclusions between garnet 1 and garnet 2, and chlorite 2, which is consuming garnet 2. The two different stages of chlorite have different compositions. c) Chlorite 2 forming from the breakdown of omphacite in the matrix. The chlorite zoning is patchy, showing strong differences in composition throughout the maps.



Supplementary Figure 5: BSE images of omphacite, showing zoning related to Fe content. a) Coarse omphacite crystal in the matrix. b) Omphacite crystals captured in garnet 2, showing similar zoning to omphacite in the matrix.



Supplementary Figure 6: EPMA maps of texturally late glaucophane from the lawsonite eclogite, showing retrograde zoning that developed during exhumation following stage 2 burial.

Supplementary Table 1: Mineral compositions measured by EPMA used in bulk rock composition calculations, after Tamblyn et al. (2019a). Additional mineral compositions are in Supplementary Table 5.

	Lawsonite	Phengite	Chlorite	Omphacite	Glaucophane	Garnet Rim	Garnet Core
SiO2	37.14	52.18	25.79	55.59	55.53	36.97	36.48
TiO2	0.00	0.09	0.00	0.04	0.06	0.15	0.26
Al2O3	32.38	22.34	18.03	9.62	9.11	21.51	20.90
Cr2O3	0.00	0.00	0.00	0.00	0.01	0.00	0.00
FeO	0.25	4.25	30.65	6.16	17.25	29.00	21.13
MnO	0.00	0.02	1.09	0.01	0.17	1.03	11.43
MgO	0.00	3.98	10.56	7.89	6.44	0.79	0.17
ZnO	0.00	0.00	0.02	0.01	0.00	0.01	0.00
CaO	17.54	0.00	0.03	13.67	0.29	10.26	9.16
Na2O	0.00	0.04	0.02	6.77	7.17	0.02	0.01
K2O	0.00	11.04	0.01	0.00	0.06	0.01	0.00
Cl	0.00	0.00	0.00	0.01	0.01	0.00	0.00
F	0.00	0.00	0.06	0.00	0.00	0.05	0.08
Total	87.32	93.95	86.24	99.78	96.08	99.76	99.61
No. Oxygens	8	11	14	6	23	12	12
Si	1.969	3.572	2.883	1.991	9.011	2.965	2.955
Ti	0.000	0.005	0.000	0.001	0.007	0.009	0.016
Al	2.023	1.803	2.376	0.406	1.742	2.033	1.996
Cr	0.000	0.000	0.000	0.000	0.001	0.000	0.000
Fe3+	0.038	0.013	0.000	0.079	0.000	0.012	0.043
Fe2+	0.027	0.231	2.866	0.106	2.340	1.933	1.388
Mn2+	0.000	0.001	0.103	0.000	0.024	0.070	0.784
Mg	0.000	0.406	1.761	0.421	1.557	0.094	0.021
Zn	0.000	0.000	0.002	0.000	0.000	0.001	0.000
Ca	0.996	0.000	0.003	0.524	0.050	0.881	0.795
Na	0.000	0.005	0.004	0.470	2.255	0.002	0.001
K	0.000	0.964	0.002	0.000	0.012	0.001	0.000
Cl	0.000	0.000	0.000	0.000	0.002	0.000	0.000
F	0.000	0.000	0.023	0.000	0.000	0.012	0.020
Total cations (S)	5	7	10	4	17	8	8
XMg	0.00	0.63	0.38	0.70	0.40	0.05	0.01
	Paragonite	0.01	J(cpx) DS5	0.47	XFe	0.95	0.99
	Margarite	0.00	Jadiete	0.39	Almandine	0.65	0.47
	Muscovite	0.34	Diopside	0.42	Pyrope	0.03	0.01
	Celadonite	0.41	Hedenbergite	0.11	Grossular	0.29	0.26
	Ferrocele-donite	0.24	Aegerine	0.08	Spessartine	0.02	0.26

Supplementary Table 2: Modal proportions of minerals used in rock composition calculations for phase equilibrium modelling. 1-oxide-normalised modes are presented to compare with the modal proportions calculated by THERMOCALC.

	Burial 1 (Tamblyn et al., 2019)				Burial 2 (this study)			
	Volume %	Density	Weight %	1-oxide-normalised	Volume %	Density	Weight %	1-oxide-normalised
Garnet	20.1	4.07	25.41	0.1431	15.93	4.07	20.49	0.1104
Lawsonite	7.4	3.08	7.08	0.0634	2.85	3.08	2.77	0.0238
Omphacite	4.7	3.38	4.94	0.03	5.25	3.38	5.6	0.0327
Glaucophane	9.53	3.07	9.09	0.0748	10.65	3.07	10.33	0.0815
Chlorite	9.53	3.03	8.97	0.1065	10.65	3.03	10.19	0.1161
Phengite	48.74	2.93	44.51	0.5823	54.67	2.93	50.61	0.6354
Total	100		100	1	100		100	1

Supplementary Table 3: A-X models used in calculation of mineral equilibrium forward models for local bulk compositions in this study

White mica	Coggon, R. and Holland, T.J.B., 2002. Mixing properties of phengitic micas and revised garnet-phengite thermobarometers. Journal of Metamorphic Geology, 20, 683-696.
Biotite	White, RW, Powell, R and Holland, TJB (2007) Progress relating to calculation of partial melting equilibria for metapelites. Journal of Metamorphic Geology, 25, 511-527
Amphibole	Diener, JFA, Powell, R, White, RW and Holland, TJB (2007) A new thermodynamic model for clino- and orthoamphiboles in Na2O-CaO-FeO-MgO-Al2O3-SiO2-H2O-O. Journal of Metamorphic Geology, 25, 631-656.
Clinopyroxene	Green, ECR, Holland, TJB and Powell, R (2007) An order-disorder model for omphacitic pyroxenes in the system jadeite-diopside-hedenbergite-acmite, with applications to eclogite rocks. American Mineralogist, 92, 1181-1189.
Garnet	White, RW, Powell, R and Holland, TJB (2007) Progress relating to calculation of partial melting equilibria for metapelites. Journal of Metamorphic Geology, 25, 511-527
Epidote	Holland, TJB and Powell, R (1998) An internally consistent thermodynamic dataset for phases of petrological interest. Journal of Metamorphic Geology, 16, 309-343.
Chlorite	Holland, TJB, Baker, JM and Powell, R (1998) Mixing properties and activity-composition relationships of chlorites in the system MgO-FeO-Al2O3-SiO2-H2O. European Journal of Mineralogy, 10, 395-406.
Chloritiod	White, RW, Powell, R, Holland, TJB and Worley, BA (2000) The effect of TiO2 and Fe2O3 on metapelitic assemblages at greenschist and amphibolite facies conditions: mineral equilibria calculations in the system K2O-FeO-MgO-Al2O3-SiO2-H2O-TiO2-Fe2O3. Journal of Metamorphic Geology, 18, 497-511.
Talc	Holland, T.J.B., and Powell, R., 1998. An internally consistent thermodynamic data-set for phases of petrological interest. Journal of Metamorphic Geology, 16, 309-343.

Supplementary Table 4: Additional mineral compositions measured by EPMA

	Phengite 1	Phengite 1	Phengite 1	Phengite 1	Phengite 1	Phengite 1
SiO2	50.47	50.77	50.53	50.70	50.98	50.84
TiO2	0.17	0.14	0.22	0.20	0.22	0.21
Al2O3	24.15	24.60	25.04	25.28	26.05	25.75
Cr2O3	0.00	0.00	0.00	0.00	0.01	0.00
FeO	6.15	5.28	3.82	2.90	2.59	2.63
MnO	0.00	0.00	0.00	0.00	0.00	0.00
MgO	2.69	2.89	3.39	3.98	3.86	3.82
ZnO	0.00	0.00	0.04	0.02	0.00	0.01
CaO	0.00	0.00	0.00	0.00	0.00	0.00
Na2O	0.17	0.17	0.22	0.22	0.25	0.20
K2O	10.40	10.55	10.52	10.55	10.55	10.61
Cl	0.00	0.02	0.00	0.00	0.00	0.00
F	0.00	0.01	0.00	0.00	0.01	0.00
Total	94.20	94.43	93.78	93.85	94.52	94.09
No. Oxygens	11.00	11.00	11.00	11.00	11.00	11.00
Si	3.474	3.471	3.455	3.449	3.435	3.444
Ti	0.009	0.007	0.011	0.010	0.011	0.011
Al	1.959	1.982	2.018	2.027	2.068	2.055
Cr	0.000	0.000	0.000	0.000	0.001	0.000
Fe2+	0.354	0.302	0.219	0.165	0.146	0.149
Mn2+	0.000	0.000	0.000	0.000	0.000	0.000
Mg	0.276	0.295	0.345	0.404	0.388	0.386
Zn	0.000	0.000	0.002	0.001	0.000	0.001
Ca	0.000	0.000	0.000	0.000	0.000	0.000
Na	0.023	0.022	0.029	0.029	0.032	0.027
K	0.913	0.920	0.918	0.916	0.907	0.917
Cl	0.000	0.000	0.000	0.000	0.000	0.000
F	0.000	0.003	0.001	0.000	0.002	0.000
OH-	2.000	1.997	1.999	2.000	1.998	2.000
Total cations (S)	7.01	7.00	7.00	7.00	6.99	6.99
Fe + Mg PFU	0.63	0.60	0.56	0.57	0.53	0.53
XMg	0.44	0.49	0.61	0.71	0.73	0.72
x(mu) (Xfe)	0.56	0.51	0.39	0.29	0.27	0.28
y(mu)	0.43	0.45	0.48	0.48	0.51	0.51
Paragonite	0.02	0.02	0.03	0.03	0.03	0.03
Margarite	0.00	0.00	0.00	0.00	0.00	0.00
Muscovite	0.33	0.38	0.40	0.40	0.43	0.44
Celadonite	0.28	0.29	0.35	0.40	0.39	0.39

Supplementary Table 4 continued: Additional mineral compositions measured by EPMA

	Phengite 1	Phengite 1	Phengite 1	Phengite 1	Phengite 1	Phengite 1
SiO2	50.53	51.48	50.92	50.75	51.37	51.79
TiO2	0.18	0.13	0.13	0.12	0.10	0.09
Al2O3	25.65	24.47	23.97	24.03	23.91	23.70
Cr2O3	0.00	0.00	0.00	0.00	0.01	0.00
FeO	2.60	3.36	3.51	3.75	4.11	4.01
MnO	0.01	0.00	0.01	0.01	0.03	0.01
MgO	3.76	3.90	3.86	3.76	3.74	3.79
ZnO	0.00	0.00	0.02	0.00	0.00	0.00
CaO	0.00	0.00	0.00	0.00	0.00	0.00
Na2O	0.17	0.10	0.09	0.06	0.04	0.07
K2O	10.58	10.82	10.80	10.72	10.85	10.74
Cl	0.01	0.00	0.00	0.00	0.00	0.01
F	0.01	0.02	0.00	0.00	0.00	0.03
Total	93.50	94.27	93.31	93.19	94.15	94.22
No. Oxygens	11.00	11.00	11.00	11.00	11.00	11.00
Si	3.444	3.494	3.499	3.494	3.507	3.525
Ti	0.009	0.006	0.007	0.006	0.005	0.005
Al	2.060	1.957	1.941	1.949	1.923	1.902
Cr	0.000	0.000	0.000	0.000	0.000	0.000
Fe2+	0.148	0.191	0.202	0.216	0.235	0.228
Mn2+	0.000	0.000	0.001	0.001	0.002	0.000
Mg	0.383	0.394	0.395	0.385	0.380	0.385
Zn	0.000	0.000	0.001	0.000	0.000	0.000
Ca	0.000	0.000	0.000	0.000	0.000	0.000
Na	0.022	0.013	0.012	0.007	0.005	0.009
K	0.920	0.937	0.946	0.941	0.945	0.933
Cl	0.000	0.000	0.000	0.000	0.000	0.000
F	0.002	0.005	0.000	0.000	0.000	0.006
OH-	1.998	1.995	2.000	2.000	2.000	1.994
Total cations (S)	6.99	6.99	7.00	7.00	7.00	6.99
Fe + Mg PFU	0.53	0.59	0.60	0.60	0.61	0.61
XMg	0.72	0.67	0.66	0.64	0.62	0.63
x(mu) (Xfe)	0.28	0.33	0.34	0.36	0.38	0.37
y(mu)	0.51	0.46	0.44	0.44	0.43	0.44
Paragonite	0.02	0.01	0.01	0.01	0.01	0.01
Margarite	0.00	0.00	0.00	0.00	0.00	0.00
Muscovite	0.45	0.40	0.38	0.39	0.37	0.38
Celadonite	0.38	0.39	0.40	0.39	0.38	0.39

Supplementary Table 4 continued: Additional mineral compositions measured by EPMA

	Phengite 2	Phengite 2	Phengite 2	Phengite 2	Phengite 2	Phengite 2
SiO2	53.79	53.29	52.48	50.88	52.51	50.19
TiO2	0.03	0.03	0.04	0.15	0.08	0.22
Al2O3	23.03	23.79	23.25	24.62	23.66	25.81
Cr2O3	0.00	0.00	0.00	0.00	0.00	0.01
FeO	4.15	3.40	3.99	3.80	4.04	2.66
MnO	0.08	0.06	0.07	0.02	0.03	0.01
MgO	4.00	4.12	4.05	3.61	4.01	3.80
ZnO	0.00	0.00	0.04	0.04	0.00	0.02
CaO	0.00	0.00	0.00	0.00	0.00	0.00
Na2O	0.02	0.00	0.02	0.05	0.04	0.21
K2O	10.70	10.62	10.66	10.44	10.68	10.49
Cl	0.00	0.00	0.00	0.00	0.01	0.00
F	0.00	0.00	0.05	0.01	0.01	0.00
Total	95.79	95.32	94.63	93.62	95.05	93.44
No. Oxygens	11.00	11.00	11.00	11.00	11.00	11.00
Si	3.593	3.564	3.553	3.480	3.539	3.426
Ti	0.002	0.001	0.002	0.007	0.004	0.011
Al	1.813	1.875	1.855	1.984	1.879	2.076
Cr	0.000	0.000	0.000	0.000	0.000	0.001
Fe2+	0.232	0.190	0.226	0.217	0.228	0.152
Mn2+	0.004	0.004	0.004	0.001	0.001	0.000
Mg	0.398	0.411	0.408	0.369	0.403	0.387
Zn	0.000	0.000	0.002	0.002	0.000	0.001
Ca	0.000	0.000	0.000	0.000	0.000	0.000
Na	0.002	0.001	0.003	0.006	0.005	0.028
K	0.911	0.906	0.920	0.911	0.918	0.914
Cl	0.000	0.000	0.000	0.000	0.000	0.000
F	0.001	0.000	0.011	0.002	0.002	0.000
OH-	1.999	2.000	1.989	1.998	1.998	2.000
Total cations (S)	6.96	6.95	6.97	6.98	6.98	7.00
Fe + Mg PFU	0.63	0.60	0.63	0.59	0.63	0.54
XMg	0.63	0.68	0.64	0.63	0.64	0.72
x(mu) (Xfe)	0.37	0.32	0.36	0.37	0.36	0.28
y(mu)	0.44	0.48	0.43	0.48	0.44	0.51
Paragonite	0.00	0.00	0.00	0.01	0.01	0.03
Margarite	0.00	0.00	0.00	0.00	0.00	0.00
Muscovite	0.36	0.39	0.36	0.40	0.36	0.43
Celadonite	0.40	0.41	0.41	0.37	0.40	0.39

Supplementary Table 4 continued: Additional mineral compositions measured by EPMA

	Phengite 2	Phengite 2	Phengite 2	Phengite 2	Phengite 2	Phengite 2	Phengite 2
SiO2	51.09	51.15	50.26	50.52	50.77	50.64	52.27
TiO2	0.14	0.15	0.12	0.22	0.24	0.22	0.04
Al2O3	24.60	24.52	24.15	25.11	25.49	25.64	23.78
Cr2O3	0.00	0.01	0.00	0.00	0.00	0.00	0.00
FeO	5.42	6.13	5.78	4.08	3.00	2.64	4.05
MnO	0.00	0.00	0.00	0.01	0.01	0.01	0.09
MgO	2.87	2.55	2.66	3.34	3.89	3.92	3.95
ZnO	0.02	0.01	0.02	0.00	0.03	0.02	0.00
CaO	0.00	0.00	0.00	0.00	0.00	0.00	0.00
Na2O	0.15	0.13	0.14	0.12	0.21	0.22	0.04
K2O	10.49	10.43	10.38	10.68	10.47	10.57	10.78
Cl	0.00	0.01	0.00	0.00	0.00	0.01	0.00
F	0.01	0.03	0.00	0.02	0.00	0.02	0.02
Total	94.78	95.09	93.49	94.12	94.12	93.90	95.01
No. Oxygens	11.00	11.00	11.00	11.00	11.00	11.00	11.00
Si	3.479	3.481	3.478	3.449	3.443	3.439	3.529
Ti	0.007	0.007	0.006	0.011	0.012	0.011	0.002
Al	1.974	1.967	1.970	2.020	2.038	2.051	1.892
Cr	0.000	0.001	0.000	0.000	0.000	0.000	0.000
Fe2+	0.309	0.349	0.334	0.233	0.170	0.150	0.229
Mn2+	0.000	0.000	0.000	0.001	0.000	0.000	0.005
Mg	0.291	0.259	0.274	0.340	0.394	0.397	0.397
Zn	0.001	0.001	0.001	0.000	0.001	0.001	0.000
Ca	0.000	0.000	0.000	0.000	0.000	0.000	0.000
Na	0.020	0.017	0.018	0.016	0.027	0.029	0.005
K	0.911	0.906	0.916	0.930	0.906	0.916	0.928
Cl	0.000	0.000	0.000	0.000	0.000	0.000	0.000
F	0.003	0.006	0.000	0.005	0.001	0.004	0.005
OH-	1.997	1.994	2.000	1.995	1.999	1.996	1.995
Total cations (S)	6.99	6.99	6.998	7.001	6.992	6.995	6.988
Fe + Mg PFU	0.60	0.61	0.61	0.57	0.56	0.55	0.63
XMg	0.49	0.43	0.45	0.59	0.70	0.73	0.63
x(mu) (Xfe)	0.51	0.57	0.55	0.41	0.30	0.27	0.37
y(mu)	0.46	0.46	0.45	0.47	0.49	0.49	0.43
Paragonite	0.02	0.02	0.02	0.02	0.03	0.03	0.01
Margarite	0.00	0.00	0.00	0.00	0.00	0.00	0.00
Muscovite	0.38	0.38	0.37	0.41	0.41	0.42	0.36
Celadonite	0.29	0.26	0.27	0.34	0.39	0.40	0.40

Supplementary Table 4 continued: Additional mineral compositions measured by EPMA

	Glaucophane 1	Glaucophane 1	Glaucophane 1	Glaucophane 1	Glaucophane 1
SiO2	56.58	55.59	55.24	55.77	56.26
TiO2	0.01	0.01	0.02	0.01	0.00
Al2O3	9.43	8.78	8.14	9.04	9.49
Cr2O3	0.00	0.00	0.00	0.00	0.00
FeO	16.82	17.78	18.23	17.49	16.43
MnO	0.21	0.18	0.28	0.15	0.17
MgO	6.21	6.41	6.53	6.51	6.94
ZnO	0.00	0.00	0.00	0.00	0.00
CaO	0.17	0.57	1.07	0.43	0.32
Na2O	6.94	6.59	6.22	6.74	6.63
K2O	0.08	0.05	0.02	0.03	0.02
Cl	0.00	0.00	0.00	0.00	0.01
F	0.06	0.00	0.06	0.03	0.00
H2O	0.00	0.00	0.00	0.00	0.00
Cl	0.00	0.00	0.00	0.00	0.00
F	0.02	0.00	0.02	0.01	0.00
Total	96.50	95.97	95.79	96.20	96.27
No. Oxygens	23.00	23.00	23.00	23.00	23.00
Si	8.047	8.012	8.012	8.006	8.023
Ti	0.002	0.001	0.002	0.001	0.000
Al	1.581	1.491	1.391	1.529	1.595
Cr	0.000	0.000	0.000	0.000	0.000
Fe3+	0.370	0.362	0.343	0.333	0.271
Fe2+	1.631	1.781	1.868	1.767	1.688
Mn2+	0.025	0.022	0.035	0.019	0.021
Mg	1.317	1.377	1.412	1.393	1.476
Zn	0.000	0.000	0.000	0.000	0.000
Ca	0.026	0.088	0.167	0.066	0.049
Na	1.914	1.842	1.749	1.875	1.833
K	0.015	0.008	0.004	0.006	0.004
Cl	0.000	0.000	0.000	0.001	0.001
F	0.026	0.000	0.027	0.016	0.002
OH-	0.000	0.000	0.000	0.000	0.000
Total cations (S)	14.927	14.985	14.982	14.995	14.960
Fe3/Fe3+Alvi	0.19	0.20	0.20	0.18	0.15
XMg	0.45	0.44	0.43	0.44	0.47

Supplementary Table 4 continued: Additional mineral compositions measured by EPMA

	Glaucophane 1	Glaucophane 1	Glaucophane 1	Glaucophane 1	Glaucophane 1	Glaucophane 1
SiO2	54.90	56.47	56.37	56.33	54.56	55.60
TiO2	0.00	0.01	0.00	0.00	0.00	0.00
Al2O3	7.86	10.24	10.29	10.14	9.03	9.68
Cr2O3	0.00	0.00	0.00	0.00	0.00	0.00
FeO	18.64	16.43	15.84	16.03	17.14	18.29
MnO	0.27	0.14	0.15	0.15	0.18	0.27
MgO	6.49	6.41	6.43	6.84	6.06	5.18
ZnO	0.00	0.00	0.00	0.00	0.00	0.00
CaO	1.04	0.06	0.05	0.08	0.16	0.04
Na2O	6.28	6.82	6.86	6.69	6.29	6.73
K2O	0.04	0.01	0.01	0.03	0.04	0.04
Cl	0.01	0.00	0.00	0.00	0.01	0.00
F	0.06	0.02	0.01	0.04	0.09	0.02
H2O	0.00	0.00	0.00	0.00	0.00	0.00
Cl	0.00	0.00	0.00	0.00	0.00	0.00
F	0.03	0.01	0.01	0.02	0.04	0.01
Total	95.58	96.59	96.00	96.31	93.51	95.84
No. Oxygens	23.00	23.00	23.00	23.00	23.00	23.00
Si	8.000	8.025	8.033	8.021	8.048	8.035
Ti	0.000	0.001	0.000	0.000	0.000	0.000
Al	1.349	1.714	1.728	1.702	1.569	1.648
Cr	0.000	0.000	0.000	0.000	0.000	0.000
Fe3+	0.386	0.194	0.218	0.160	0.264	0.283
Fe2+	1.885	1.758	1.670	1.749	1.850	1.927
Mn2+	0.034	0.017	0.018	0.018	0.023	0.033
Mg	1.410	1.358	1.367	1.452	1.333	1.116
Zn	0.000	0.000	0.000	0.000	0.000	0.000
Ca	0.162	0.009	0.008	0.012	0.025	0.006
Na	1.774	1.878	1.896	1.847	1.800	1.886
K	0.008	0.002	0.002	0.005	0.007	0.007
Cl	0.002	0.000	0.000	0.000	0.001	0.000
F	0.028	0.008	0.005	0.017	0.040	0.008
OH-	0.000	0.000	0.000	0.000	0.000	0.000
Total cations (S)	15.009	14.956	14.940	14.966	14.918	14.942
Fe3/Fe3+Alvi	0.22	0.10	0.11	0.09	0.14	0.15
XMg	0.43	0.44	0.45	0.45	0.42	0.37

Supplementary Table 4 continued: Additional mineral compositions measured by EPMA

	Titanite 1	Titanite 2	Titanite 3	Titanite 4	Titanite 5	Titanite 6	Titanite 7	Titanite 8	Titanite 9	Titanite 10	Titanite 11
SiO2	32.37	32.40	32.28	32.06	31.55	32.27	32.65	32.18	32.18	32.29	32.08
TiO2	37.71	37.44	34.20	36.20	35.73	33.56	37.69	36.20	37.50	37.08	36.64
Al2O3	1.07	1.15	2.27	1.43	1.34	2.84	0.68	1.35	0.78	0.99	1.27
FeO	0.21	0.30	0.41	0.20	0.35	0.61	0.25	0.28	0.23	0.34	0.25
CaO	27.57	27.54	27.29	27.69	27.46	26.83	27.71	27.18	27.57	27.69	27.77
F	0.13	0.14	0.25	0.26	0.13	0.60	0.13	0.20	0.11	0.01	0.12
ZrO2	0.00	0.00	0.01	0.00	0.00	0.00	0.00	0.00	0.00	0.00	0.01
Y2O3	0.08	0.01	0.13	0.08	0.03	0.18	0.06	0.10	0.06	0.03	0.00
Nd2O3	0.00	0.06	0.11	0.00	0.07	0.07	0.00	0.00	0.02	0.00	0.00
SrO	0.00	0.02	0.00	0.00	0.01	0.00	0.00	0.00	0.00	0.00	0.01
Total	99.14	99.06	96.96	97.92	96.67	96.95	99.16	97.50	98.46	98.44	98.16
No. Oxygens	5	5	5	5	5	5	5	5	5	5	5
Si	1.059	1.060	1.073	1.059	1.055	1.074	1.068	1.068	1.060	1.061	1.057
Ti	0.928	0.921	0.855	0.900	0.899	0.840	0.927	0.904	0.930	0.916	0.908
Al	0.041	0.044	0.089	0.056	0.053	0.111	0.026	0.053	0.030	0.038	0.049
Fe2+	0.006	0.008	0.011	0.005	0.010	0.017	0.007	0.008	0.006	0.004	0.007
Ca	0.966	0.966	0.972	0.980	0.984	0.957	0.971	0.967	0.973	0.975	0.980
F	0.013	0.014	0.027	0.028	0.014	0.063	0.013	0.021	0.012	0.001	0.013
Total cations (S)	3	3	3	3	3	3	3	3	3	3	3

Supplementary Table 4 continued: Additional mineral compositions measured by EPMA

	Titanite 12	Titanite 13	Titanite 14	Titanite 15	Titanite 16	Titanite 17	Titanite 18	Titanite 19	Titanite 20	Titanite 21	Titanite 22
SiO2	32.12	31.86	31.71	31.78	31.53	32.58	32.49	32.24	32.86	32.55	33.56
TiO2	36.99	36.94	36.83	36.17	36.83	37.34	36.90	36.71	37.20	37.57	35.05
Al2O3	1.27	0.71	0.93	1.34	0.77	0.99	1.19	1.21	1.32	0.89	2.15
FeO	0.22	0.18	0.24	0.24	0.30	0.45	0.15	0.17	0.24	0.38	0.61
CaO	27.62	27.72	27.65	27.83	27.68	27.45	27.51	27.54	27.64	27.76	25.88
F	0.20	0.11	0.15	0.13	0.10	0.11	0.19	0.17	0.10	0.02	0.09
ZrO2	0.00	0.00	0.00	0.01	0.00	0.01	0.00	0.00	0.00	0.00	0.00
Y2O3	0.04	0.05	0.03	0.05	0.05	0.04	0.08	0.08	0.01	0.02	0.04
Nd2O3	0.00	0.03	0.03	0.01	0.00	0.02	0.00	0.03	0.01	0.02	0.01
SrO	0.01	0.00	0.00	0.02	0.00	0.00	0.00	0.00	0.01	0.00	0.00
Total	98.45	97.60	97.58	97.57	97.27	99.00	98.51	98.15	99.38	99.21	97.40
No. Oxygens	5	5	5	5	5	5	5	5	5	5	5
Si	1.056	1.058	1.053	1.053	1.050	1.067	1.068	1.064	1.069	1.062	1.110
Ti	0.915	0.923	0.920	0.901	0.923	0.920	0.912	0.911	0.910	0.922	0.872
Al	0.049	0.028	0.036	0.052	0.030	0.038	0.046	0.047	0.050	0.034	0.084
Fe2+	0.006	0.005	0.005	0.007	0.008	0.012	0.004	0.005	0.006	0.010	0.017
Ca	0.973	0.986	0.984	0.987	0.988	0.963	0.969	0.973	0.964	0.971	0.917
F	0.021	0.011	0.016	0.014	0.011	0.011	0.019	0.018	0.010	0.003	0.009
Total cations (S)	3	3	3	3	3	3	3	3	3	3	3

Supplementary Table 4 continued: Additional mineral compositions measured by EPMA

	Titanite 23	Titanite 24	Titanite 25	Titanite 26	Titanite 27	Titanite 28	Titanite 29	Titanite 30	Titanite 31	Titanite 32	Titanite 33
SiO2	32.73	32.59	32.08	32.40	32.38	31.23	32.26	33.05	33.02	32.11	31.54
TiO2	36.21	37.64	37.59	35.64	37.33	34.27	37.09	38.08	35.92	37.05	36.21
Al2O3	1.05	1.08	0.89	1.61	1.02	2.44	0.93	0.91	1.93	1.08	1.21
FeO	0.66	0.32	0.32	0.31	0.21	0.50	0.27	0.23	0.33	0.21	0.21
CaO	27.29	27.75	27.66	27.29	27.75	27.74	27.52	27.67	26.57	27.50	27.60
F	0.07	0.07	0.11	0.11	0.14	0.60	0.13	0.16	0.20	0.19	0.17
ZrO2	0.03	0.00	0.00	0.00	0.01	0.02	0.00	0.00	0.02	0.00	0.00
Y2O3	0.05	0.07	0.07	0.00	0.00	0.09	0.08	0.07	0.08	0.07	0.05
Nd2O3	0.00	0.04	0.03	0.02	0.03	0.11	0.06	0.07	0.01	0.02	0.06
SrO	0.00	0.00	0.00	0.04	0.02	0.00	0.00	0.01	0.00	0.01	0.02
Total	98.08	99.56	98.73	97.41	98.89	97.01	98.34	100.25	98.07	98.24	97.05
No. Oxygens	5	5	5	5	5	5	5	5	5	5	5
Si	1.079	1.061	1.054	1.073	1.061	1.041	1.064	1.071	1.088	1.060	1.052
Ti	0.898	0.921	0.929	0.888	0.920	0.859	0.920	0.928	0.890	0.920	0.908
Al	0.041	0.041	0.035	0.063	0.039	0.096	0.036	0.035	0.075	0.042	0.047
Fe2+	0.018	0.009	0.009	0.003	0.006	0.014	0.007	0.006	0.009	0.006	0.006
Ca	0.964	0.968	0.974	0.968	0.974	0.990	0.972	0.960	0.938	0.972	0.986
F	0.007	0.008	0.011	0.011	0.014	0.063	0.014	0.016	0.020	0.020	0.018
Total cations (S)	3	3	3	3	3	3	3	3	3	3	3

Supplementary Table 4 continued: Additional mineral compositions measured by EPMA

	Chl between G1-G2	Chl between G1-G2	Chl between G1-G2	Chl between G1-G2	Chl between G1-G2	Chl between G1-G2
SiO2	27.16	26.78	26.89	27.84	28.32	27.41
TiO2	0.01	0.01	0.00	0.00	0.00	0.00
Al2O3	17.38	17.12	17.35	16.95	16.96	16.46
Cr2O3	0.00	0.00	0.00	0.00	0.00	0.00
FeO	28.69	29.38	29.56	27.71	27.93	27.16
MnO	0.54	0.49	0.56	0.73	0.62	0.71
MgO	13.59	12.75	12.90	14.50	14.50	14.16
CaO	0.04	0.02	0.02	0.02	0.00	0.02
Na2O	0.03	0.01	0.00	0.00	0.00	0.00
K2O	0.00	0.00	0.01	0.00	0.01	0.01
Cl	0.02	0.01	0.00	0.01	0.00	0.00
F	0.00	0.00	0.00	0.00	0.00	0.00
Total	87.45	86.58	87.29	87.76	88.35	85.94
No. Oxygens	14	14	14	14	14	14
Si	2.928	2.932	2.920	2.974	3.001	2.990
Ti	0.001	0.001	0.000	0.000	0.000	0.000
Al	2.208	2.209	2.220	2.133	2.118	2.115
Cr	0.000	0.000	0.000	0.000	0.000	0.000
Fe2+	2.587	2.689	2.685	2.475	2.475	2.477
Mn2+	0.049	0.045	0.052	0.066	0.056	0.065
Mg	2.185	2.081	2.089	2.309	2.290	2.303
Zn	0.000	0.000	0.000	0.000	0.000	0.000
Ca	0.004	0.002	0.002	0.003	0.000	0.003
Na	0.006	0.003	0.000	0.001	0.001	0.000
K	0.000	0.000	0.001	0.000	0.001	0.002
Cl	0.003	0.002	0.000	0.001	0.000	0.000
F	0.000	0.000	0.000	0.000	0.000	0.000
OH-	7.997	7.998	8.000	7.999	8.000	8.000
XMg	0.46	0.44	0.44	0.48	0.48	0.48
Total cations (S)	9.969	9.963	9.970	9.960	9.941	9.954

Supplementary Table 4 continued: Additional mineral compositions measured by EPMA

	Chl in matrix	Chl in matrix	Chl in matrix	Chl in matrix	Chl in matrix	Chl in matrix
SiO2	25.3268	25.786	25.4335	26.0219	25.9439	25.786
TiO2	0	0	0	0	0	0
Al2O3	17.7925	17.8831	17.771	17.4605	17.9011	18.0289
Cr2O3	0	0.008666	0	0	0	0
FeO	31.6785	31.2798	30.691	30.4226	30.0452	30.654
MnO	1.24185	1.04272	1.16179	0.959382	1.0319	1.08576
MgO	9.50293	10.5961	9.86179	10.9944	10.8247	10.5647
CaO	0.001941	0.018012	0	0.027398	0.018154	0.025863
Na2O	0	0.025569	0	0.010716	0.021759	0.017162
K2O	0	0	0.004489	0	0.006724	0.010947
Cl	0.014769	0.005203	0	0	0	0.000666
F	0.069114	0.031943	0.120703	0.085858	0.048591	0.064968
Total	85.59597045	86.66248915	84.99344968	85.94752226	85.82156863	86.23525876
No. Oxygens	14	14	14	14	14	14
Si	2.861	2.862	2.876	2.898	2.887	2.867
Ti	0.000	0.000	0.000	0.000	0.000	0.000
Al	2.369	2.339	2.368	2.291	2.348	2.362
Cr	0.000	0.001	0.000	0.000	0.000	0.000
Fe2+	2.992	2.903	2.902	2.833	2.796	2.850
Mn2+	0.119	0.098	0.111	0.090	0.097	0.102
Mg	1.600	1.753	1.662	1.825	1.796	1.751
Zn	0.000	0.000	0.000	0.000	0.000	0.002
Ca	0.000	0.002	0.000	0.003	0.002	0.003
Na	0.000	0.006	0.000	0.002	0.005	0.004
K	0.000	0.000	0.001	0.000	0.001	0.002
Cl	0.003	0.001	0.000	0.000	0.000	0.000
F	0.025	0.011	0.043	0.030	0.017	0.023
OH-	7.972	7.988	7.957	7.970	7.983	7.977
XMg	0.35	0.38	0.36	0.39	0.39	0.38
Total cations (S)	9.941	9.964	9.919	9.943	9.933	9.943

Supplementary Table 4 continued: Additional mineral compositions measured by EPMA

	Omphacite	Omphacite	Omphacite	Omphacite	Omphacite	Omphacite	Omphacite
notes	Rim of porphryoblast	Rim of porphryoblast	Rim of porphryoblast	Rim of porphryoblast	Rim of porphryoblast	Rim of porphryoblast	Core of porphryoblast
SiO2	55.93	54.92	54.93	55.69	55.40	55.87	55.51
TiO2	0.02	0.05	0.05	0.04	0.02	0.03	0.05
Al2O3	9.30	9.68	10.72	9.03	9.56	9.94	8.88
Cr2O3	0.00	0.01	0.00	0.00	0.00	0.00	0.00
FeO	6.38	6.79	6.52	6.94	6.66	5.75	6.61
MnO	0.02	0.07	0.04	0.09	0.05	0.02	0.06
MgO	8.07	7.80	7.72	8.19	7.91	7.97	8.25
CaO	14.10	13.55	12.45	14.15	13.79	14.01	14.41
Na2O	6.49	6.49	6.34	6.31	6.52	6.47	6.28
K2O	0.01	0.01	0.72	0.00	0.01	0.00	0.02
Cl	0.00	0.01	0.00	0.00	0.00	0.00	0.01
F	0.00	0.00	0.00	0.00	0.00	0.00	0.00
Total	100.32	99.39	99.49	100.45	99.93	100.06	100.07
No. Oxygens	6	6	6	6	6	6	6
Si	1.998	1.982	1.977	1.991	1.987	1.998	1.991
Ti	0.001	0.001	0.001	0.001	0.001	0.001	0.001
Al	0.391	0.412	0.455	0.381	0.404	0.419	0.375
Cr	0.000	0.000	0.000	0.000	0.000	0.000	0.000
Fe3+	0.062	0.077	0.064	0.071	0.073	0.033	0.077
Fe2+	0.128	0.128	0.132	0.136	0.126	0.139	0.121
Mn2+	0.001	0.002	0.001	0.003	0.002	0.000	0.002
Mg	0.430	0.419	0.414	0.437	0.423	0.425	0.441
Zn	0.000	0.000	0.000	0.000	0.000	0.000	0.000
Ca	0.540	0.524	0.480	0.542	0.530	0.537	0.554
Na	0.450	0.454	0.442	0.437	0.453	0.449	0.436
K	0.000	0.001	0.033	0.000	0.001	0.000	0.001
Total cations (S)	4	4	4	4	4	4	4
j (cpx)	0.45	0.45	0.44	0.44	0.45	0.45	0.44
x(cpx) (Xfe)	0.23	0.23	0.24	0.24	0.23	0.25	0.22
Jadeite	0.39	0.38	0.39	0.37	0.38	0.42	0.36
Diopside	0.42	0.42	0.42	0.43	0.42	0.42	0.44
Hedenbergite	0.13	0.13	0.14	0.13	0.13	0.14	0.12
Aegerine/Acmite	0.06	0.07	0.05	0.07	0.07	0.03	0.07

Supplementary Table 4 continued: Additional mineral compositions measured by EPMA

	Omphacite	Omphacite	Omphacite	Omphacite	Omphacite	Omphacite	Omphacite
notes	Core of porphyroblast	Core of porphyroblast	Core of porphyroblast	Core of porphyroblast	Core of porphyroblast	Core of porphyroblast	Inc in Garnet 2
SiO2	55.54	55.40	55.00	55.66	55.25	55.13	53.65
TiO2	0.02	0.02	0.12	0.03	0.07	0.10	0.03
Al2O3	9.53	9.21	8.61	10.11	8.69	8.45	3.50
Cr2O3	0.00	0.00	0.00	0.01	0.00	0.01	0.00
FeO	7.21	8.87	9.67	5.99	7.92	8.07	11.26
MnO	0.02	0.03	0.08	0.03	0.06	0.06	0.12
MgO	7.37	6.69	6.35	8.00	7.65	7.49	9.15
CaO	13.49	13.11	13.53	13.26	14.44	14.31	18.76
Na2O	6.71	7.06	6.59	6.54	6.16	6.21	3.29
K2O	0.01	0.02	0.01	0.13	0.00	0.01	0.00
Cl	0.00	0.00	0.00	0.00	0.00	0.00	0.00
F	0.00	0.00	0.02	0.00	0.00	0.00	0.01
Total	99.90	100.40	99.98	99.75	100.24	99.83	99.77
No. Oxygens	6	6	6	6	6	6	6
Si	1.996	1.989	1.997	1.995	1.990	1.996	1.998
Ti	0.001	0.001	0.003	0.001	0.002	0.003	0.001
Al	0.404	0.390	0.369	0.427	0.369	0.360	0.153
Cr	0.000	0.000	0.000	0.000	0.000	0.000	0.000
Fe3+	0.071	0.124	0.092	0.042	0.077	0.078	0.087
Fe2+	0.145	0.142	0.202	0.137	0.162	0.166	0.264
Mn2+	0.001	0.001	0.002	0.001	0.002	0.002	0.004
Mg	0.395	0.358	0.344	0.427	0.411	0.404	0.508
Zn	0.000	0.000	0.000	0.000	0.000	0.000	0.000
Ca	0.520	0.504	0.526	0.509	0.557	0.555	0.748
Na	0.468	0.491	0.464	0.454	0.430	0.436	0.238
K	0.001	0.001	0.000	0.006	0.000	0.000	0.000
Total cations (S)	4	4	4	4	4	4	4
j (cpx)	0.47	0.49	0.46	0.45	0.43	0.44	0.24
x(cpx) (Xfe)	0.27	0.28	0.37	0.24	0.28	0.29	0.34
Jadeite	0.40	0.37	0.37	0.41	0.36	0.36	0.15
Diopside	0.39	0.36	0.34	0.41	0.41	0.40	0.50
Hedenbergite	0.14	0.14	0.20	0.13	0.16	0.16	0.26
Aegerine/Acmite	0.07	0.12	0.09	0.04	0.07	0.08	0.09

Supplementary Table 4 continued: Additional mineral compositions measured by EPMA

	Omphacite	Omphacite	Omphacite	Omphacite	Omphacite	Omphacite
notes	Inc in Garnet 2	Inc in Garnet 2	Inc in Garnet 2	Inc in Garnet 2	Inc in Garnet 2	Inc in Garnet 2
SiO2	54.51	53.93	54.27	54.66	54.65	54.89
TiO2	0.03	0.03	0.00	0.05	0.12	0.02
Al2O3	8.11	7.93	5.87	8.60	8.50	7.52
Cr2O3	0.01	0.00	0.01	0.00	0.00	0.02
FeO	9.12	9.64	10.12	11.23	8.38	10.10
MnO	0.05	0.06	0.11	0.05	0.01	0.04
MgO	7.40	7.17	8.51	5.82	7.74	7.29
CaO	14.31	14.12	16.55	12.91	14.19	14.63
Na2O	6.16	6.11	4.80	7.03	6.23	6.01
K2O	0.00	0.01	0.00	0.00	0.01	0.01
Cl	0.01	0.01	0.00	0.00	0.00	0.00
F	0.00	0.00	0.00	0.00	0.00	0.00
Total	99.73	99.01	100.26	100.36	99.84	100.53
No. Oxygens	6	6	6	6	6	6
Si	1.981	1.978	1.983	1.980	1.976	1.988
Ti	0.001	0.001	0.000	0.001	0.003	0.001
Al	0.347	0.343	0.253	0.367	0.362	0.321
Cr	0.000	0.000	0.000	0.000	0.000	0.001
Fe3+	0.123	0.135	0.122	0.163	0.116	0.124
Fe2+	0.154	0.160	0.187	0.177	0.138	0.182
Mn2+	0.002	0.002	0.003	0.002	0.000	0.001
Mg	0.401	0.392	0.463	0.314	0.418	0.393
Zn	0.000	0.000	0.000	0.000	0.000	0.000
Ca	0.557	0.555	0.648	0.501	0.550	0.567
Na	0.434	0.435	0.340	0.494	0.436	0.422
K	0.000	0.000	0.000	0.000	0.001	0.000
Total cations (S)	4	4	4	4	4	4
j (cpx)	0.43	0.43	0.34	0.49	0.44	0.42
x(cpx) (Xfe)	0.28	0.29	0.29	0.36	0.25	0.32
Jadeite	0.32	0.31	0.23	0.34	0.33	0.30
Diopside	0.41	0.40	0.47	0.32	0.42	0.40
Hedenbergite	0.16	0.16	0.19	0.18	0.14	0.18
Aegerine/Acmite	0.11	0.12	0.11	0.15	0.11	0.12

Supplementary Table 4 continued: Additional mineral compositions measured by EPMA

	Omphacite	Omphacite	Omphacite
notes	Inc in garnet 1	Inc in garnet 1	Inc in garnet 1
SiO2	54.78	54.87	54.97
TiO2	0.11	0.10	0.09
Al2O3	8.38	8.47	8.67
Cr2O3	0.00	0.00	0.00
FeO	8.06	8.08	9.38
MnO	0.09	0.06	0.06
MgO	7.76	7.76	6.83
CaO	14.55	14.67	13.76
Na2O	6.05	5.98	6.58
K2O	0.01	0.01	0.01
Cl	0.00	0.00	0.01
F	0.00	0.02	0.00
Total	99.79	100.01	100.35
No. Oxygens	6	6	6
Si	1.984	1.984	1.984
Ti	0.003	0.003	0.002
Al	0.358	0.361	0.369
Cr	0.000	0.000	0.000
Fe3+	0.094	0.083	0.119
Fe2+	0.150	0.161	0.165
Mn2+	0.003	0.002	0.002
Mg	0.419	0.418	0.368
Zn	0.000	0.000	0.000
Ca	0.564	0.568	0.532
Na	0.425	0.419	0.460
K	0.000	0.000	0.000
Total cations (S)	4	4	4
j (cpx)	0.42	0.42	0.46
x(cpx) (Xfe)	0.26	0.28	0.31
Jadeite	0.34	0.34	0.35
Diopside	0.42	0.42	0.37
Hedenbergite	0.15	0.16	0.17
Aegerine/Acmite	0.09	0.08	0.11

Supplementary Table 5: Summary of the approximate P–T conditions interpreted for each stage of the two burial cycles, the petrologic evidence supporting these conditions, and which P–T model was used for the interpretation.

Stage	Method constrained	P–T conditions	P–T figure	Description of model
Prograde 1	Inclusion assemblages in garnet 1 and lawsonite 1	Begins at 0.8–1.1 GPa, ~ 350 °C	Figure 8	Bulk rock composition
Peak 1	Inclusions in garnet, possible coesite, predicted garnet mode, lawsonite stability	2.9 GPa, 600 °C	Figure 8b	Bulk rock composition
Retrograde 1	Inclusions in garnet 2, reduction in garnet mode	Ends at max. conditions of 2.0 GPa, 500 °C	Figure 9b	Local rock composition, water in excess/ water set
Prograde 2	Inclusions in garnet 2, compositions of the cores of zoned minerals (garnet 2, omphacite and phengite)	Begins at max. conditions of 2.0 GPa, 500 °C	Figure 9c/Figure 10b	Local rock composition, water in excess/ water set
Peak 2	Preserved peak mineral assemblage, composition of phengite rims	2.7 GPa, 590 °C	Figure 9c/Figure 10b	Local rock composition, water in excess/ water set
Retrograde 2	Preserved retrograde assemblage, modes of minerals currently in rock	1.9 GPa, 520 °C	Figure 10c	Local rock composition, water set

Supplementary Table 6: LA-ICP-MS U-Pb titanite geochronlogical results.

	207Pb/235U	2se	206Pb/238U	2se	Error correlation	238U/206Pb	2se	207Pb/206Pb	2se
RB10_1	53.4	2.3	0.537	0.021	0.6050	1.8622	0.0728	0.7310	0.0290
RB10_2	54.8	2.4	0.543	0.017	0.4795	1.8416	0.0577	0.7380	0.0280
RB10_3	56.3	2.6	0.547	0.019	0.6149	1.8282	0.0635	0.7530	0.0300
RB10_4	63	2.8	0.624	0.019	0.2650	1.6026	0.0488	0.7340	0.0310
RB10_5	60.1	2.5	0.614	0.02	0.3217	1.6287	0.0531	0.7170	0.0280
RB10_6	31.1	2	0.34	0.017	0.7336	2.9412	0.1471	0.6670	0.0360
RB10_7	670	120	6.3	1.3	0.6414	0.1587	0.0328	0.8600	0.1100
RB10_8	37.9	2.9	0.408	0.026	0.8233	2.4510	0.1562	0.6760	0.0340
RB11a_1	26.4	1.6	0.311	0.019	0.4600	3.2154	0.1964	0.6270	0.0410
RB11a_2	4.22	0.29	0.1089	0.0039	0.2918	9.1827	0.3289	0.2820	0.0180
RB11a_3	45.3	3.6	0.463	0.044	0.6772	2.1598	0.2053	0.7320	0.0530
RB11a_4	79.2	5.3	0.734	0.04	0.6054	1.3624	0.0742	0.7850	0.0440
RB11a_5	46.8	2.1	0.478	0.022	0.3127	2.0921	0.0963	0.7170	0.0370
RB11a_6	91	7.2	0.915	0.087	0.0547	1.0929	0.1039	0.7370	0.0770
RB11a_7	129	13	1.28	0.12	0.7025	0.7813	0.0732	0.7350	0.0570
RB11a_8	124	12	1.2	0.12	0.8995	0.8333	0.0833	0.7620	0.0400
RB11a_9	76.4	7.4	0.718	0.077	0.6375	1.3928	0.1494	0.7690	0.0600
RB11a_10	66.7	5.3	0.666	0.041	0.6746	1.5015	0.0924	0.7330	0.0440
RB11a_11	18.2	2.3	0.242	0.027	0.8679	4.1322	0.4610	0.5430	0.0370
RB11a_12	41.7	4.1	0.421	0.046	0.6191	2.3753	0.2595	0.7390	0.0680
RB11a_13	3.92	0.2	0.1055	0.0032	0.3533	9.4787	0.2875	0.2690	0.0130
RB11a_14	3.63	0.18	0.0992	0.0031	0.4125	10.0807	0.3150	0.2661	0.0120
RB11a_15	10.5	1.1	0.161	0.011	0.6142	6.2112	0.4244	0.4640	0.0340
RB11a_16	15.4	1.2	0.196	0.011	0.9025	5.1020	0.2863	0.5670	0.0230
RB11a_17	39.4	2.1	0.422	0.016	0.6407	2.3697	0.0898	0.6760	0.0310
RB11a_18	3.89	0.31	0.0997	0.004	0.5827	10.0301	0.4024	0.2830	0.0200
RB11a_19	3.84	0.37	0.1023	0.0068	0.4309	9.7752	0.6498	0.2730	0.0250
RB11a_20	101.4	9.1	0.928	0.078	0.75734	1.077586	0.09057298	0.799	0.054
RB11a_21	3.68	0.21	0.1047	0.0036	0.098596	9.551098	0.3284045	0.257	0.015
RB11a_22	3	0.16	0.0946	0.0026	0.14176	10.57082	0.2905301	0.233	0.012
RB11a_23	76.4	5.5	0.761	0.049	0.63177	1.31406	0.08461099	0.745	0.046
RB11a_24	107.2	8.9	1.05	0.076	0.81751	0.952381	0.06893424	0.741	0.042
RB11a_25	32.4	1.9	0.358	0.018	0.39544	2.793296	0.1404451	0.668	0.042
RB11a_26	3.22	0.15	0.0973	0.0029	0.096407	10.27749	0.3063179	0.2385	0.011
RB11a_27	5.55	0.44	0.1175	0.007	0.53196	8.510638	0.5070167	0.348	0.025
RB11a_28	13	1.1	0.21	0.015	0.89674	4.761905	0.3401361	0.448	0.02
RB11a_29	8.78	0.94	0.1454	0.0084	0.84419	6.877579	0.3973292	0.434	0.031
RB11a_30	38	2.9	0.394	0.03	0.1965	2.538071	0.1932541	0.719	0.069
RB11a_31	32.7	3.1	0.354	0.035	0.91164	2.824859	0.2792939	0.708	0.071
RB11a_32	6.01	0.41	0.1215	0.005	0.44273	8.230453	0.3387018	0.361	0.021
RB11a_33	25.2	1.5	0.3	0.013	0.49072	3.333333	0.1444444	0.618	0.037
RB11a_34	21.8	2.1	0.254	0.023	0.79374	3.937008	0.3565007	0.613	0.043
RB11a_35	11.8	1.8	0.19	0.019	0.79207	5.263158	0.5263158	0.456	0.047
RB11a_36	326	25	2.86	0.22	0.85561	0.3496503	0.02689618	0.84	0.043
RB11a_37	460	33	4.28	0.29	0.86787	0.2336449	0.01583108	0.777	0.031
RB11a_38	11.4	2.1	0.166	0.016	0.91311	6.024096	0.5806358	0.49	0.046
RB11a_39	17.4	7.1	0.209	0.044	0.78792	4.784689	1.007303	0.55	0.15
RB11a_40	39.3	2.3	0.437	0.023	0.74776	2.28833	0.1204384	0.654	0.027
RB11a_41	29.2	6.7	0.342	0.067	0.75684	2.923977	0.5728258	0.62	0.096
RB11a_42	19.3	5.8	0.232	0.055	0.88969	4.310345	1.021849	0.544	0.07

Supplementary Table 6 continued: LA-ICP-MS U-Pb titanite geochronlogical results.

	Error correlation	204Pb ppm	2se	Approx Pb total	232Th ppm	2se	238U ppm	2se	Zr ppm	2se
RB10_1	0.6034	6.13	0.83	21.2	0.18	0.018	4.1	0.11	3.99	0.18
RB10_2	0.4671	6.9	0.96	21.59	0.17	0.022	4.11	0.091	70	13
RB10_3	0.4441	6.81	0.8	22.85	0.125	0.011	4.26	0.13	4.13	0.22
RB10_4	0.5865	6.16	0.71	20.97	0.127	0.012	3.431	0.063	3.92	0.18
RB10_5	0.6295	6.73	0.91	21.3	0.314	0.019	3.565	0.067	4.34	0.2
RB10_6	0.0439	5.9	1.3	25.73	0.92	0.15	8.63	0.56	1430	240
RB10_7	0.9982	4.3	1.6	7.96	0.167	0.027	0.169	0.023	0.1	0.055
RB10_8	-0.0137	3.84	0.68	12.75	0.672	0.046	3.52	0.2	420	150
RB11a_1	0.6060	2.8	0.73	9.27	0.119	0.021	3.5	0.15	3.75	0.38
RB11a_2	0.1940	3.2	0.85	21.07	38	1.2	31.37	0.83	6700	160
RB11a_3	0.5685	2.21	0.77	7.53	0.156	0.036	1.92	0.23	4.03	0.97
RB11a_4	0.2412	6.3	1.8	23.22	5.02	0.31	3.21	0.14	83	28
RB11a_5	0.7145	6.3	1.4	19.78	0.278	0.03	4.46	0.1	4.27	0.32
RB11a_6	0.7537	2.14	0.89	5.32	1.02	0.14	0.64	0.049	33.9	2.9
RB11a_7	0.5263	3.8	1.4	11.27	2.88	0.14	0.935	0.078	22.27	0.96
RB11a_8	0.3839	3.2	1.1	9.49	4.68	0.66	0.802	0.051	48.2	2.8
RB11a_9	0.5856	2.84	0.84	9.28	8.11	0.28	1.44	0.23	232	59
RB11a_10	0.2174	2.89	0.83	9.34	2.22	0.17	1.492	0.096	27.4	1.2
RB11a_11	-0.2781	2.02	0.93	7.07	8.3	1	3.84	0.53	830	150
RB11a_12	0.5952	1.68	0.75	8.05	3.15	0.58	2.15	0.27	410	93
RB11a_13	0.3778	3.9	0.81	24.64	36.12	0.58	38.33	0.55	9540	140
RB11a_14	0.3056	2.8	0.81	20.19	42.2	1.1	33.17	0.85	7850	180
RB11a_15	-0.0188	5	1.1	19.38	20.7	2.2	16.9	1.5	3610	380
RB11a_16	-0.3265	3.48	0.73	15.69	9.07	0.75	9.98	0.63	1930	120
RB11a_17	0.1195	5.57	0.86	18.29	1.264	0.077	4.72	0.11	118	52
RB11a_18	-0.0303	3.3	1.2	16.69	45.6	1.5	27	1	6540	260
RB11a_19	0.3665	Below LOD	Below LOD	14.02	44.7	1.8	23.4	1.3	6870	300
RB11a_20	0.50834	2.71	0.83	9.92	5.14	0.2	1.094	0.081	148	22
RB11a_21	0.43977	2.15	0.74	17.91	38.48	0.87	28.42	0.47	8130	130
RB11a_22	0.43923	3.99	0.67	23.84	71.3	1.7	42.98	0.94	11810	240
RB11a_23	0.43897	2.17	0.66	8.35	1.81	0.1	1.192	0.075	79.4	9.7
RB11a_24	0.34113	2.59	0.56	6.29	2.79	0.42	0.63	0.054	69	12
RB11a_25	0.61381	3.09	0.67	11.13	3.3	1.5	3.47	0.25	4.67	0.68
RB11a_26	0.55918	3.45	0.99	22.16	68.7	1.7	37	1.4	10840	450
RB11a_27	0.33329	1.03	0.56	7.45	13.1	0.36	9.74	0.28	1561	27
RB11a_28	-0.16573	7.4	1.2	38.19	112	23	23.8	2.5	600	170
RB11a_29	-0.35907	3.3	1.1	11.06	12.78	0.93	9.98	0.5	1960	100
RB11a_30	0.65288	1.16	0.63	5.58	0.757	0.065	1.596	0.071	34.3	2.9
RB11a_31	0.60816	Below LOD	Below LOD	3.028	0.367	0.037	0.962	0.062	31.9	1
RB11a_32	0.27541	2.34	0.77	12.9	12.06	0.65	15.6	1	2050	120
RB11a_33	0.42335	3.28	0.83	11.67	1.03	0.13	4.61	0.25	42	10
RB11a_34	0.21968	1.8	0.86	7.15	3.45	0.28	3.33	0.38	371	44
RB11a_35	-0.27552	1.1	0.51	6.71	7.84	0.82	5.54	0.82	1100	170
RB11a_36	0.47458	5.28	0.81	15.65	6.29	0.2	0.531	0.028	45.1	1.6
RB11a_37	0.37201	7.7	1.1	26.82	9.5	0.24	0.629	0.03	42.4	2.3
RB11a_38	-0.36313	4	1.5	16.61	28.8	1	12.11	0.59	5340	270
RB11a_39	-0.43314	2	0.92	5.48	2.79	0.97	5.1	1.9	1670	580
RB11a_40	0.38584	6.54	0.93	23.15	4.4	0.94	5.95	0.36	167	63
RB11a_41	0.39066	0.98	0.86	6.67	1.93	0.72	3	0.94	420	200
RB11a_42	-0.50973	1.23	0.56	6.56	8.7	1.7	5.37	0.97	1140	230

Supplementary Table 6 continued: LA-ICP-MS U-Pb titanite geochronlogical results.

	207Pb/235U	2se	206Pb/238U	2se	Error correlation	238U/206Pb	2se	207Pb/206Pb	2se
RB11a_43	89.3	9.1	0.92	0.13	0.72347	1.086957	0.1535917	0.782	0.093
RB11a2_1	5.62	0.47	0.118	0.0063	0.52701	8.474576	0.4524562	0.347	0.024
RB11a2_2	3.57	0.27	0.0994	0.0041	0.59349	10.06036	0.4149646	0.261	0.015
RB11a2_3	81.7	4.6	0.778	0.038	0.67257	1.285347	0.06278045	0.769	0.035
RB11a2_4	23.7	1.6	0.269	0.014	0.31566	3.717472	0.1934744	0.653	0.047
RB11a2_5	58.3	4.2	0.543	0.037	0.32745	1.841621	0.125488	0.778	0.055
RB11a2_6	6.45	0.35	0.1281	0.0041	0.098497	7.806401	0.2498536	0.366	0.019
RB11a2_7	147	21	1.36	0.2	0.82282	0.7352941	0.1081315	0.79	0.057
RB11a2_8	16.2	1.9	0.226	0.021	0.94603	4.424779	0.411152	0.513	0.026
RB11a2_9	102.1	7.3	0.933	0.092	0.15438	1.071811	0.1056877	0.85	0.11
RB11a2_10	42	4.7	0.416	0.054	0.58652	2.403846	0.3120377	0.744	0.077
RB11a2_11	22.6	1.8	0.392	0.025	0.80371	2.55102	0.1626926	0.42	0.022
RB11a2_12	42.6	3.1	0.452	0.031	0.47283	2.212389	0.1517347	0.698	0.055
RB11a2_13	31.7	7.2	0.346	0.068	0.88999	2.890173	0.568011	0.661	0.059
RB11a2_14	8	1.1	0.144	0.012	0.85631	6.944444	0.5787037	0.389	0.028
RB11a2_15	67.5	7.1	0.627	0.075	0.45945	1.594896	0.1907771	0.84	0.12
RB11a2_16	23.8	2.7	0.264	0.029	0.83179	3.787879	0.4160927	0.663	0.045
RB11a2_17	4.59	0.46	0.1082	0.0049	0.69499	9.242144	0.4185444	0.302	0.022
RB11a2_18	37.3	4.7	0.421	0.042	0.88242	2.375297	0.2369655	0.628	0.034
RB11a2_19	13.7	1.4	0.191	0.016	0.12055	5.235602	0.4385845	0.537	0.064
RB11a2_20	79	15	0.74	0.12	0.78389	1.351351	0.2191381	0.781	0.076
RB09a_1	16.4	1.3	0.217	0.012	0.71169	4.608295	0.2548366	0.543	0.032
RB09a_2	14.4	1.8	0.201	0.017	0.72778	4.975124	0.4207817	0.505	0.03
RB09a_3	34.3	2.8	0.407	0.027	0.81676	2.457002	0.1629952	0.616	0.034
RB09a_4	70.7	4.7	0.681	0.038	0.62309	1.468429	0.08193876	0.763	0.045
RB09a_5	47.1	3.6	0.471	0.036	0.54108	2.123142	0.1622784	0.727	0.051
RB09a_6	31	5	0.331	0.043	0.70272	3.021148	0.3924754	0.669	0.054
RB09a_7	6.72	0.44	0.1269	0.005	0.47827	7.880221	0.3104894	0.378	0.021
RB09a_8	7.2	0.59	0.1292	0.0065	0.54354	7.739938	0.3893932	0.398	0.024
RB09a_9	49.8	3.2	0.487	0.025	0.24066	2.053388	0.1054101	0.736	0.049
RB09a_10	3.55	0.22	0.0921	0.0031	0.15298	10.85776	0.3654622	0.275	0.016
RB09a_11	31.3	3.4	0.32	0.03	0.88526	3.125	0.2929688	0.698	0.042
RB09a_12	52.6	3.7	0.524	0.03	0.80728	1.908397	0.1092594	0.722	0.035
RB09a_13	18.26	1.6	0.242	0.012	0.11562	4.132231	0.204904	0.552	0.039
RB09a_14	8.25	0.54	0.1418	0.0069	0.37467	7.052186	0.34316	0.43	0.027
RB09a_15	18.2	1.4	0.227	0.013	0.41747	4.405286	0.2522851	0.586	0.041
RB09a_16	35.4	2.9	0.357	0.021	0.60063	2.80112	0.1647718	0.73	0.049
RB09a_17	18.3	1.5	0.226	0.014	0.68041	4.424779	0.2741013	0.599	0.037
RB09a_18	23.8	1.6	0.278	0.014	0.30074	3.597122	0.18115	0.638	0.042
RB09a_19	43.9	3.5	0.47	0.039	0.75073	2.12766	0.1765505	0.69	0.046
RB09a_20	41.3	2.8	0.414	0.021	0.72117	2.415459	0.1225233	0.731	0.037
RB09a_21	39.7	2.5	0.418	0.02	0.60684	2.392344	0.1144662	0.689	0.038
RB09a_22	57.5	5.2	0.537	0.043	0.76776	1.862197	0.1491145	0.769	0.056
RB09a_23	35	3.7	0.374	0.027	0.45924	2.673797	0.1930281	0.663	0.063
RB09a_24	62.2	5.3	0.556	0.041	0.8312	1.798561	0.1326277	0.794	0.05
RB09a_25	9.29	0.74	0.1369	0.0085	0.020956	7.304602	0.4535363	0.482	0.041
RB09a_26	40.2	3.9	0.406	0.033	0.61062	2.463054	0.200199	0.688	0.053
RB09a_27	41.1	2.8	0.434	0.024	0.24602	2.304147	0.1274183	0.665	0.051
RB09a_28	62.9	3.8	0.606	0.028	0.46051	1.650165	0.07624525	0.729	0.04
RB09a_29	48.9	3.2	0.499	0.024	0.48651	2.004008	0.09638516	0.696	0.039

Supplementary Table 6 continued: LA-ICP-MS U-Pb titanite geochronlogical results.

	Error correlation	204Pb ppm	2se	Approx Pb total	232Th ppm	2se	238U ppm	2se	Zr ppm	2se
RB11a_43	0.72777	2.43	0.79	5.19	1.348	0.097	0.603	0.056	59	12
RB11a2_1	0.041322	2.48	0.93	14.16	38.3	0.72	17.92	0.9	6090	330
RB11a2_2	0.031912	2.95	0.98	17.95	46.41	0.87	29.78	0.84	10450	280
RB11a2_3	0.44242	3.56	0.83	12.26	0.109	0.024	1.636	0.06	2.83	0.25
RB11a2_4	0.52612	2.92	0.77	10.33	7.5	0.4	4.24	0.24	822	64
RB11a2_5	0.59657	3.92	0.98	13.96	0.229	0.07	2.59	0.11	60	27
RB11a2_6	0.54875	2.94	0.62	15.91	35.9	1.6	17.45	0.39	5580	150
RB11a2_7	0.10201	3.6	1	12.24	3.64	0.54	1.1	0.2	183	64
RB11a2_8	-0.37009	5.5	1.3	23.26	33	5.5	13.03	0.94	2900	410
RB11a2_9	0.87987	2.86	0.88	10.55	0.988	0.063	1.177	0.066	25.6	2.6
RB11a2_10	0.72919	1.7	0.9	4.32	0.926	0.086	1.183	0.087	8.72	0.98
RB11a2_11	0.12838	5.4	1.7	31.41	118	16	10.3	1	48.3	8
RB11a2_12	0.49886	1.9	0.55	5.606	0.525	0.053	1.373	0.066	32	19
RB11a2_13	0.056164	5.2	1.6	13.08	8.5	3.5	5.1	1.2	740	380
RB11a2_14	-0.43105	2.5	0.68	11.17	23.5	1.9	11.5	1	3530	330
RB11a2_15	0.71946	1.68	0.81	4.52	0.505	0.078	0.789	0.068	22.2	2.2
RB11a2_16	0.22532	2.47	0.97	10.43	5.51	0.8	4.87	0.47	900	130
RB11a2_17	-0.25738	1.74	0.59	12.22	35.4	2	17.5	1.1	4940	350
RB11a2_18	-0.19579	3.21	0.8	10.55	8.4	1.3	3.06	0.34	660	120
RB11a2_19	0.40543	1.4	1	5.08	6.24	0.25	3.44	0.14	894	39
RB11a2_20	0.011662	1.1	0.54	6.24	2.73	0.5	1.12	0.26	171	74
RB09a_1	-0.014108	4.65	0.84	15.47	15.6	1.9	8.56	0.73	1730	170
RB09a_2	-0.37592	4.04	0.67	15.93	16.7	2.2	11.4	1.5	2920	580
RB09a_3	0.34768	3.55	0.58	13.92	12.9	2.3	3.87	0.39	39.8	8.1
RB09a_4	0.53139	2.1	0.56	8.33	0.328	0.054	1.27	0.11	16.9	3.8
RB09a_5	0.64819	3.77	0.99	12.28	0.173	0.019	2.75	0.12	2.73	0.29
RB09a_6	-0.11864	1.97	0.94	8.06	9.7	1.4	2.9	0.56	520	160
RB09a_7	0.21243	3.16	0.78	13.42	31.2	1.7	14.52	0.78	4750	450
RB09a_8	0.32726	3.18	0.78	17.33	55	1.7	17.17	0.41	5980	150
RB09a_9	0.70014	5.3	1.1	19.59	0.154	0.028	4.16	0.16	170	110
RB09a_10	0.50265	5	1.1	33.74	60.6	2.8	60.5	3.2	16750	710
RB09a_11	-0.17201	2.67	0.91	11.5	2.26	0.52	4.05	0.38	301	82
RB09a_12	0.13584	5.49	0.77	18.73	0.13	0.016	3.82	0.18	5.46	0.6
RB09a_13	0.50198	3.5	1.3	11.87	10.88	0.3	5.76	0.18	1069	27
RB09a_14	0.42232	2.04	0.63	11.76	27.6	5.3	10.83	0.57	2620	140
RB09a_15	0.51092	3.5	1	11.24	9.46	0.4	5.87	0.37	1120	100
RB09a_16	0.21737	1.24	0.5	6.61	0.0476	0.0098	2.04	0.097	27	19
RB09a_17	0.28712	2.69	0.72	9.92	1.7	1	5.29	0.39	95	51
RB09a_18	0.57755	4.1	0.95	15.22	0.326	0.034	6.26	0.24	83	25
RB09a_19	0.49192	4.1	1.1	12.12	0.873	0.083	2.88	0.15	48	26
RB09a_20	0.30504	4.42	0.79	16.27	0.454	0.099	4.08	0.18	22.4	7.9
RB09a_21	0.64723	4.2	1.1	16.17	0.155	0.025	4.15	0.21	186	75
RB09a_22	0.57298	1.64	0.49	6.56	0.097	0.013	1.13	0.089	81.5	5.6
RB09a_23	0.31935	5.6	2.1	16.32	0.301	0.055	4.94	0.54	800	440
RB09a_24	0.54394	2.53	0.64	10.05	0.338	0.034	1.799	0.094	40	1.5
RB09a_25	0.77889	3.7	1.2	14.46	1.1	0.28	14.09	0.53	12030	830
RB09a_26	0.29765	1.85	0.49	5.43	0.669	0.037	1.42	0.14	163	51
RB09a_27	0.67155	2.54	0.82	10.45	0.117	0.022	2.55	0.15	2.11	0.26
RB09a_28	0.5704	6.51	0.87	20.16	0.376	0.027	3.263	0.078	8.9	2.3
RB09a_29	0.59284	3.91	0.62	13.59	2.65	0.37	2.82	0.11	238	40

Supplementary Table 6 continued: LA-ICP-MS U-Pb titanite geochronlogical results.

	207Pb/235U	2se	206Pb/238U	2se	Error correlation	238U/206Pb	2se	207Pb/206Pb	2se
RB09a_30	22.4	1.6	0.281	0.017	0.43316	3.558719	0.2152962	0.596	0.042
RB09a_31	31.4	2.2	0.373	0.019	0.45337	2.680965	0.1365639	0.618	0.039
RB09a_32	61	3.7	0.609	0.027	0.57595	1.642036	0.07279963	0.733	0.037
RB09a_33	58.8	4.2	0.605	0.037	0.61339	1.652893	0.101086	0.722	0.045
RB09a_34	47.7	3.1	0.481	0.026	0.69456	2.079002	0.1123785	0.727	0.035
RB09a_35	45.1	3.9	0.47	0.034	0.89323	2.12766	0.1539158	0.697	0.034
RB09a_36	45.6	2.9	0.446	0.029	0.52986	2.242152	0.1457902	0.747	0.047
RB09a_37	4.39	0.61	0.106	0.0075	0.87159	9.433962	0.6674973	0.29	0.025
RB09a_38	40.4	3.2	0.42	0.022	0.51944	2.380952	0.1247166	0.681	0.051
RB09a_39	56.3	3.4	0.546	0.027	0.35028	1.831502	0.09056877	0.742	0.044
RB09a_40	35.6	2.8	0.363	0.022	0.094462	2.754821	0.1669588	0.702	0.06
RB09a_41	3.09	0.27	0.092	0.005	0.74712	10.86957	0.5907372	0.243	0.015
RB09a_42	47.7	3.1	0.503	0.032	0.49377	1.988072	0.1264777	0.7	0.043
RB09a_43	48.5	2.8	0.506	0.027	0.46619	1.976285	0.1054539	0.703	0.039
RB09a_44	90.3	7.4	0.864	0.058	0.77688	1.157407	0.07769633	0.76	0.043
RB09a_45	3.31	0.35	0.0968	0.0041	0.76222	10.33058	0.4375555	0.245	0.019
RB09a_46	47.6	3.1	0.47	0.021	0.52966	2.12766	0.09506564	0.737	0.041
RB09a_47	26.7	2.1	0.313	0.022	0.70853	3.194888	0.2245608	0.636	0.037
RB09a_48	3.66	0.45	0.0943	0.0042	0.068553	10.60445	0.4723087	0.29	0.037
RB09a_49	64.8	5.8	0.668	0.045	0.16834	1.497006	0.1008462	0.745	0.075
RB09a_50	62.9	3.9	0.647	0.032	0.61395	1.545595	0.07644365	0.737	0.038
RB09a_51	2.07	0.16	0.0868	0.0032	0.47984	11.52074	0.4247276	0.1786	0.011
RB11a_1	40.5	2.9	0.397	0.029	0.45445	2.518892	0.1839996	0.739	0.057
RB11a_2	40.1	2.1	0.503	0.02	0.3806	1.988072	0.07904857	0.57	0.024
RB11a_3	18.3	1.9	0.204	0.016	0.67564	4.901961	0.3844675	0.648	0.054
RB11a_4	33.2	3.4	0.354	0.036	0.2505	2.824859	0.2872738	0.693	0.088
RB11a_5	31.2	2.4	0.325	0.022	0.54904	3.076923	0.208284	0.679	0.051
RB11a_6	39.1	5.4	0.459	0.047	0.81465	2.178649	0.2230861	0.594	0.051
RB11a_7	26.6	2.4	0.343	0.028	0.62747	2.915452	0.2379961	0.555	0.04
RB11a_8	38.9	2.5	0.398	0.024	0.2887	2.512563	0.1515113	0.716	0.048
RB11a_9	45.3	2.7	0.46	0.022	0.2279	2.173913	0.1039698	0.714	0.041
RB11a_10	153.3	11	1.362	0.086	0.80644	0.7342144	0.04636009	0.818	0.046
RB11a_11	37.3	3.4	0.398	0.033	0.62154	2.512563	0.2083281	0.703	0.059
RB11a_12	28	3.2	0.329	0.037	0.43748	3.039514	0.3418298	0.646	0.08
RB11a_13	15.03	1	0.2019	0.01	0.0066977	4.952947	0.2453168	0.561	0.045
RB11a_14	43.9	3.4	0.434	0.029	0.56468	2.304147	0.1539638	0.75	0.05
RB11a_15	28.8	1.7	0.318	0.015	0.23678	3.144654	0.1483327	0.68	0.041
RB11a_16	36.5	2.5	0.402	0.022	0.79951	2.487562	0.1361352	0.671	0.032
RB11a_17	27.8	1.9	0.338	0.018	0.20978	2.95858	0.1575575	0.622	0.037
RB11a_18	16.1	1.4	0.222	0.021	0.17914	4.504505	0.4261018	0.564	0.043
RB11a_19	8.02	0.53	0.1426	0.0065	0.29261	7.012623	0.3196497	0.415	0.026
RB11a_20	37.5	2.8	0.388	0.031	0.51677	2.57732	0.2059199	0.726	0.054
RB11a_21	29.66	1.5	0.308	0.013	0.44971	3.246753	0.1370383	0.685	0.034
RB11a_22	144.8	8.5	1.422	0.068	0.6393	0.7032349	0.03362867	0.724	0.036
RB11a_23	28.9	2	0.298	0.018	0.22931	3.355705	0.2026936	0.687	0.053
RB11a_24	35.2	2.6	0.35	0.026	0.30992	2.857143	0.2122449	0.717	0.06
RB11a_25	73.8	6.4	0.713	0.072	0.51505	1.402525	0.1416294	0.735	0.068
RB11a_26	92	14	0.86	0.14	0.529	1.162791	0.1892915	0.79	0.13
RB11a_27	45.6	4.1	0.46	0.039	0.46201	2.173913	0.18431	0.724	0.075
RB11a_28	51	3	0.544	0.019	0.6616	1.838235	0.06420307	0.697	0.033

Supplementary Table 6 continued: LA-ICP-MS U-Pb titanite geochronlogical results.

	Error correlation	204Pb ppm	2se	Approx Pb total	232Th ppm	2se	238U ppm	2se	Zr ppm	2se
RB09a_30	0.59745	1.61	0.54	5.65	0.266	0.053	2.395	0.097	3.65	0.71
RB09a_31	0.35493	2.64	0.73	9.84	3.63	0.46	3	0.1	247	44
RB09a_32	0.65954	3.29	0.65	11.27	0.057	0.01	1.964	0.07	1.43	0.14
RB09a_33	0.52327	3.57	0.88	13.29	2.33	0.16	2.36	0.1	69	17
RB09a_34	0.32014	4.87	0.79	16.5	0.372	0.045	3.6	0.11	3.31	0.26
RB09a_35	0.061371	6.2	1.1	20.25	0.186	0.022	4.75	0.23	8.4	2
RB09a_36	0.63818	4.3	1.1	12.57	0.164	0.026	2.97	0.13	6.6	3
RB09a_37	-0.56803	4.8	1.4	27.33	78	10	41.8	4.5	13800	1300
RB09a_38	0.40265	2.1	0.75	9.13	2.22	0.37	2.33	0.12	203	40
RB09a_39	0.63335	6.6	1.3	17.21	0.74	0.062	3.27	0.1	34.5	6.5
RB09a_40	0.60353	3.64	0.97	12.96	0.81	0.073	3.95	0.23	340	140
RB09a_41	-0.010804	3.02	0.78	24.27	78.3	5.7	44.7	3.1	17000	1000
RB09a_42	0.67275	2.93	0.82	10.62	1.862	0.073	2.239	0.07	17.23	0.56
RB09a_43	0.7173	4.65	0.81	13.98	0.397	0.041	2.92	0.1	4.41	0.79
RB09a_44	0.26029	5.15	0.99	20.33	2.33	0.28	2.44	0.2	235	51
RB09a_45	-0.48582	3.4	1	26.23	101.6	6.2	43.6	2.3	14470	670
RB09a_46	0.41088	5.49	0.89	16.17	0.087	0.015	3.6	0.1	2.78	0.26
RB09a_47	0.38678	2.52	0.65	6.747	0.304	0.034	2.51	0.17	96	14
RB09a_48	0.38594	1.4	1.1	9.69	27.8	1.1	16.13	0.86	4010	310
RB09a_49	0.49606	1.76	0.7	5.114	0.802	0.041	0.806	0.043	21.21	0.5
RB09a_50	0.51786	5.83	0.84	19.05	0.177	0.02	3.09	0.12	4.42	0.47
RB09a_51	-0.051513	3.21	0.85	22.66	46.3	2.7	49.8	2.2	18850	960
RB11a_1	0.61928	2.72	0.82	9.739	0.119	0.022	2.7	0.12	18.6	7.3
RB11a_2	0.63536	8.2	1.5	31.6	5.66	0.2	7.05	0.2	26.4	3.3
RB11a_3	0.28842	1.61	0.67	7.28	2.97	0.25	4	0.22	264	20
RB11a_4	0.70631	2.05	0.99	4.58	1.52	0.13	1.475	0.096	52.1	3.1
RB11a_5	0.58068	1.69	0.6	4.92	0.801	0.07	1.625	0.068	56.9	8.4
RB11a_6	0.15323	2.78	0.98	9.99	2.35	0.28	2.32	0.24	74	17
RB11a_7	0.32949	1.68	0.58	7.15	2.65	0.2	2.39	0.13	88	16
RB11a_8	0.72857	3.7	1.2	9.53	0.574	0.059	2.67	0.18	23.4	4.5
RB11a_9	0.64925	5	1.2	17.71	1.68	0.3	4.08	0.11	111	22
RB11a_10	0.48874	6.59	0.95	22.14	11.19	0.68	1.552	0.073	70.8	3.2
RB11a_11	0.50992	2.23	0.82	8.21	3.4	1.2	2.35	0.21	8.63	0.69
RB11a_12	0.55487	1.35	0.71	5.47	3.14	0.39	1.98	0.24	227	35
RB11a_13	0.69218	3.76	0.9	13.01	12.4	1.4	7.92	0.41	1510	130
RB11a_14	0.4117	2.47	0.77	6.411	1.53	0.082	1.567	0.063	31.4	1.7
RB11a_15	0.70224	3.84	0.64	14.1	0.15	0.017	4.94	0.083	1.66	0.15
RB11a_16	0.25705	8.7	1.1	28.73	0.402	0.031	8.18	0.44	5	0.42
RB11a_17	0.71242	4.7	1.4	13.97	1.35	0.25	4.73	0.2	15.5	3
RB11a_18	0.7989	2.1	1.1	4.936	0.351	0.046	2.87	0.13	2.59	0.34
RB11a_19	0.49341	2.63	0.88	13.09	6.81	0.24	13.22	0.54	998	69
RB11a_20	0.64424	3.5	1.2	8.82	0.42	0.11	2.51	0.16	63	23
RB11a_21	0.77077	4.2	1.1	14.35	0.157	0.022	4.94	0.14	2.88	0.24
RB11a_22	0.4768	8.2	1.2	28.31	0.791	0.062	1.951	0.062	11.93	0.57
RB11a_23	0.6549	2.99	0.88	8.09	0.096	0.02	2.94	0.11	25	12
RB11a_24	0.4421	3.7	1	13.11	0.235	0.031	3.91	0.23	3.93	0.38
RB11a_25	0.81491	1.05	0.48	4.604	0.211	0.025	0.677	0.048	8.23	0.81
RB11a_26	0.41641	Below LOD	Below LOD	2.895	0.443	0.049	0.344	0.038	10.3	7.1
RB11a_27	0.63796	2.02	0.76	4.24	0.84	0.1	0.939	0.068	69	13
RB11a_28	0.20794	11.8	1.3	38.78	0.269	0.033	7.71	0.32	48	27

Supplementary Table 6 continued: LA-ICP-MS U-Pb titanite geochronlogical results.

	207Pb/235U	2se	206Pb/238U	2se	Error correlation	238U/206Pb	2se	207Pb/206Pb	2se
RB11a_29	61.5	6.1	0.592	0.053	0.64157	1.689189	0.1512281	0.776	0.064
RB11a_30	80.9	4.6	0.77	0.032	0.29281	1.298701	0.053972	0.769	0.038
RB11a_31	5.91	0.38	0.1201	0.0047	0.46733	8.326395	0.3258456	0.357	0.019
RB11a_32	22.26	1.4	0.2602	0.01	0.61557	3.843198	0.1477017	0.618	0.029
RB11a_33	58.4	7.3	0.617	0.063	0.58729	1.620746	0.1654894	0.692	0.068
RB11a_34	42.4	2.4	0.42	0.016	0.41413	2.380952	0.09070295	0.729	0.037
RB11a_35	54.7	3.1	0.541	0.025	0.36735	1.848429	0.08541723	0.736	0.041
RB11a_36	59.2	5.8	0.59	0.052	0.64777	1.694915	0.1493824	0.744	0.059
RB11a_37	39.1	4.9	0.43	0.047	0.91321	2.325581	0.2541915	0.659	0.04
RB11a_38	46.7	3.9	0.525	0.045	0.61128	1.904762	0.1632653	0.672	0.05
RB11a_39	49.5	3.4	0.505	0.03	0.46387	1.980198	0.1176355	0.727	0.05
RB11a_40	35.3	2.6	0.395	0.021	0.28644	2.531646	0.1345938	0.642	0.037
RB11a_41	27.4	2	0.306	0.016	0.38449	3.267974	0.1708744	0.655	0.044
RB11a_42	36.8	2.1	0.385	0.016	0.44596	2.597403	0.107944	0.69	0.031

Supplementary Table 6 continued: LA-ICP-MS U-Pb titanite geochronlogical results.

	Error correlation	204Pb ppm	2se	Approx Pb total	232Th ppm	2se	238U ppm	2se	Zr ppm	2se
RB11a_29	0.48578	3.5	1.2	10.08	5	1.6	1.57	0.27	175	46
RB11a_30	0.63409	4.51	0.73	14.34	0.24	0.027	1.892	0.045	15.7	2.3
RB11a_31	0.25607	2.82	0.78	13.558	29.92	0.79	16.32	0.43	6900	150
RB11a_32	0.22249	4.93	0.8	17.8	11.22	0.34	7.73	0.23	1778	70
RB11a_33	0.29467	Below LOD	Below LOD	6.55	0.74	0.2	1.18	0.18	86	32
RB11a_34	0.50982	4.54	0.71	16.54	0.2	0.018	4.069	0.096	7.12	0.48
RB11a_35	0.64392	2.93	0.72	10.002	0.379	0.034	1.923	0.054	16.86	0.8
RB11a_36	0.4153	1.98	0.78	8.07	0.46	0.14	1.52	0.13	28	10
RB11a_37	-0.31553	4	1.3	12.46	2.76	0.7	3.31	0.27	335	82
RB11a_38	0.49998	1.71	0.53	6.561	1.21	0.1	1.448	0.093	3.76	0.36
RB11a_39	0.68191	2.57	0.71	8.74	0.224	0.025	1.847	0.098	13.89	0.93
RB11a_40	0.67372	7.9	1.6	20.88	0.286	0.038	5.68	0.22	107	48
RB11a_41	0.40937	1.98	0.63	7.09	0.642	0.078	2.559	0.068	5.17	0.24
RB11a_42	0.50554	8.2	1.6	28.22	2.31	0.12	7.52	0.19	15.5	1.1

Supplementary Table 8: 40Ar/39Ar Furnace Step-Heating analytical results

Temp (˚C)	Cum.% 39Ar	40Ar (x 1 0 - 1 3 moles)	±	39Ar (x 1 0 - 1 4 moles)	±	38Ar (x 1 0 - 1 6 moles)	±	37Ar (x 1 0 - 1 6 moles)	±
Sample PM2									
J-Value = 0.032496 0.000114									
600	0.16	0.265	0.0008	0.3102	0.0008	0.0332	0.0208	0.0238	0.0021
700	2.05	3.1966	0.0098	3.744	0.0033	0.5166	0.0929	22.5241	1.3088
750	10.24	14.2047	0.0441	16.1851	0.0225	1.0984	0.4113	0.1699	0.4302
780	27.1	29.451	0.0907	33.3028	0.035	3.9403	1.1386	171.6875	49.8171
810	46.16	33.5525	0.1022	37.6683	0.061	2.666	0.9431	0.3589	0.3423
840	62.77	29.3882	0.0897	32.8234	0.0295	1.6076	1.3992	0.3591	0.2583
870	73.88	19.7717	0.0609	21.957	0.0189	3.1147	0.665	108.9781	12.3317
900	79.72	10.4518	0.0485	11.5291	0.0574	1.2522	0.3052	32.2217	10.9448
950	83.1	6.0401	0.0187	6.6825	0.0076	0.9693	0.2916	14.2295	13.0602
1000	87.3	7.5194	0.0229	8.2985	0.0127	1.0816	0.2496	44.6042	2.8328
1100	95.71	15.0029	0.046	16.6157	0.0169	1.2264	0.5542	222.1979	16.1815
1200	99.51	6.926	0.0211	7.5072	0.0033	0.8289	0.2862	432.1144	7.4636
1350	99.98	1.2252	0.0037	0.9345	0.0012	0.2435	0.0592	21.942	3.3877
1450	100	1.3567	0.0041	0.0423	0.0005	0.8395	0.0194	0.0253	0.0124
Sample PM4									
J-Value = 0.032493 0.00012									
600	0.1	0.0925	0.0003	0.0948	0.0004	0.0004	0.0245	0.1771	0.9373
700	1.91	1.5229	0.0046	1.7375	0.0022	0.2738	0.0461	0.0256	0.049
750	14.63	10.7236	0.0331	12.1796	0.013	1.2954	0.2995	28.0615	5.9766
780	24.63	8.5639	0.026	9.5815	0.0092	1.1514	0.2441	17.853	3.9651
810	37.57	11.1101	0.0338	12.3922	0.0119	1.3663	0.3182	17.863	8.8282
840	52.3	12.7142	0.0398	14.1104	0.012	1.5627	0.3524	11.5769	6.21
870	64.25	10.3839	0.0316	11.443	0.006	1.0567	0.2924	10.6689	1.9136
900	71.23	6.0724	0.0184	6.6899	0.0045	0.7872	0.2005	6.4049	3.221
950	77.27	5.2619	0.0161	5.7774	0.008	0.6942	0.1395	18.074	2.4138
1000	85	6.7583	0.0205	7.404	0.0082	0.9178	0.211	38.7782	4.9643
1100	96.41	10.0597	0.0328	10.9311	0.0129	1.5834	0.2721	167.3209	3.1903
1200	99.43	2.6528	0.0249	2.8913	0.0252	0.4688	0.1058	242.2322	5.0485
1350	99.99	0.6019	0.0019	0.538	0.0003	0.138	0.0185	128.3846	0.9523
1450	100	0.2153	0.0007	0.0095	0.0005	0.1131	0.0294	12.1138	0.4686

Supplementary Table 8 continued: 40Ar/39Ar Furnace Step-Heating analytical results

36Ar (x10-16 moles)	±	Ca/K	±	%40Ar*	40Ar*/39Ar	±	Age (Ma)	±
Sample PM2								
0.0004	0.0001	0.0013	0.0001	99.7	8.54	0.04	441.8	1.6
0.6538	0.034	0.1053	0.0061	93.7	8.02	0.04	417.9	1.8
0.6701	0.5493	0.0002	0.0005	98.3	8.65	0.1	447.1	4.8
2.0397	1.1534	0.0902	0.0262	97.7	8.66	0.11	447.5	4.9
0.0045	0.0336	0.0002	0.0002	99.7	8.91	0.03	458.6	1.4
0.6614	0.8677	0.0002	0.0001	99.1	8.89	0.08	458	3.8
1.8016	0.3045	0.0869	0.0098	97	8.76	0.05	452	2.3
0.4103	0.152	0.0489	0.0166	98.6	8.96	0.07	461	3.3
0.3304	0.2811	0.0373	0.0342	98.1	8.89	0.13	458	5.8
0.2986	0.13	0.0941	0.006	98.6	8.95	0.06	460.8	2.5
0.2369	0.3416	0.234	0.017	99.3	8.99	0.07	462.3	3.1
0.6498	0.2188	1.0073	0.0174	97	8.97	0.09	461.5	4.1
1.2177	0.0447	0.4109	0.0634	70.5	9.26	0.15	474.6	6.6
4.4643	0.0632	0.0105	0.0051	2.8	8.87	4.53	456.8	205.9
Sample PM4								
0.0546	0.016	0.0327	0.173	82.4	8.05	0.5	419.3	23.3
0.2152	0.044	0.0003	0.0005	95.6	8.4	0.08	435.3	3.7
0.7178	0.1089	0.0403	0.0086	97.8	8.63	0.04	446	1.8
0.3105	0.0647	0.0326	0.0072	98.7	8.84	0.03	455.6	1.6
0.2963	0.0431	0.0252	0.0125	98.9	8.89	0.03	458	1.4
0.2932	0.0748	0.0144	0.0077	99.1	8.95	0.03	460.5	1.5
0.1082	0.0445	0.0163	0.0029	99.4	9.05	0.03	464.9	1.4
0.2415	0.031	0.0168	0.0084	98.6	8.97	0.03	461.4	1.4
0.2004	0.0296	0.0547	0.0073	98.6	9.01	0.03	463	1.5
0.2453	0.0672	0.0917	0.0117	98.7	9.03	0.04	464.2	1.8
0.7854	0.0331	0.2679	0.0051	97.4	8.99	0.03	462.4	1.5
0.286	0.0474	1.4661	0.0331	96.6	8.88	0.13	457.5	5.7
0.3326	0.0146	4.176	0.031	83.5	9.36	0.09	479.1	3.9
0.6983	0.0244	22.4001	1.5233	4.2	9.51	7.69	485.7	344.2

Supplementary Table 8: In-situ LA-ICP-QQQ Rb-Sr results for phengite and titanite analyses. Struck out analyses were not used in age calculations

Mineral	Analyses No.	87Rb/86Sr	2se	87Sr/86Sr	2se
Phengite cores	RB10_MuC_1	13.21	0.18	0.7833	0.0091
	RB10_MuC_2	25.15	0.78	0.854	0.015
	RB10_MuC_3	98	29	1.34	0.19
	RB10_MuC_4	74	16	1.19	0.11
	RB10_MuC_5	37.62	0.72	0.938	0.015
	RB10_MuC_6	29.6	2.5	0.891	0.02
	RB10_MuC_7	16.4	0.31	0.8095	0.0077
	RB10_MuC_8	12.81	0.86	0.7863	0.0081
	RB10_MuC_9	11.85	0.14	0.7808	0.0069
	RB10_MuC_10	16.35	0.15	0.8044	0.0089
	RB10_MuC_11	21.34	0.26	0.847	0.011
	RB10_MuC_12	13.57	0.16	0.7944	0.0081
	RB10_MuC_13	14.37	0.26	0.8021	0.0087
	RB10_MuC_14	17.02	0.23	0.8075	0.009
	RB10_MuC_15	76.3	2.9	1.18	0.039
	RB10_MuC_16	13.1	1	0.79	0.013
Phengite rims	RB10_MuGtR_1	36.32	0.86	0.929	0.014
	RB10_MuGtR_2	15.39	0.33	0.8056	0.0093
	RB10_MuGtR_3	39.1	1.2	0.949	0.013
	RB10_MuGtR_4	36.94	0.5	0.938	0.01
	RB10_MuR_1	55.7	5.5	1.041	0.037
	RB10_MuR_2	117	14	1.438	0.094
	RB10_MuR_3	561	51	4.33	0.35
	RB10_MuR_4	243	22	2.24	0.14
	RB10_MuR_5	311	21	2.5	0.15
	RB10_MuR_6	37.7	1.7	0.956	0.022
	RB10_MuR_7	25.14	0.9	0.867	0.019
	RB10_MuR_8	426	24	3.39	0.18
	RB10_MuR_9	296	29	2.57	0.18
	RB10_MuR_10	2020	230	13.4	1.4
	RB10_MuR_11	42.9	1.1	0.963	0.016
	RB10_MuR_12	1003	93	6.72	0.55
	RB10_MuR_13	735	50	5.61	0.41
	RB10_MuR_14	347	30	2.98	0.22
Titanite	RB10_Ttn_1	0.068	0.015	0.7015	0.008
	RB10_Ttn_2	0.049	0.011	0.712	0.0086
	RB10_Ttn_3	0.063	0.023	0.7098	0.0093
	RB10_Ttn_4	0.53	0.14	0.7	0.0086
	RB10_Ttn_5	0.066	0.012	0.719	0.014
	RB10_Ttn_6	0.444	0.033	0.704	0.014
	RB10_Ttn_7	0.0025	0.0029	0.707	0.031
	RB10_Ttn_8	0.8	0.14	0.733	0.02
	~~RB10_Ttn_9~~	~~2~~	~~1.1~~	~~0.737~~	~~0.026~~

Appendix 5:

Supplementary materials for Chapter 5: The 2 Ga eclogites of central Tanzania: directly linking age and metamoprhism

Supplementary file 1

LA–ICP–MS titanite U–Pb geochronology methods

Titanite grains were separated using conventional techniques and mounted in epoxy resin and polished to expose their cross section. They were then imaged using a Quanta600 SEM to identify exsolution or mineral inclusions. They were analysed for U–Pb isotopes and trace element concentrations using an ASI m50 LA–ICP with an attached 7700 MS at Adelaide Microscopy. Grains were ablated using a spot size of 51 μm, a frequency of 5 Hz, and an intensity of 3.5 Jcm-2, with an acquisition time of 70 s for each analysis including 30 s of background measurement and 40 s of ablation. The primary reference titanite MKED-1 was used to correct for elemental fractionation, mass bias and instrument drift over the courses of analyses (Spandler et al., 2016), and a titanite grain from Mt Painter (442.6 ± 1.8 Ma; Elburg et al., 2003) was used as the secondary standard. The synthetic glass standard NIST610 was used to correct for trace element concentrations. Corrections were done using the software Iolite (Paton et al., 2011) and age calculations were done using IsoplotR (Vermeesch, 2018). The secondary standard returned a weighted mean $^{206}Pb/^{238}U$ age of 442.3 ± 2.4 Ma (MSWD = 0.35, n = 14) throughout the course of the analyses.

Titanite U–Pb geochronology results

Titanite geochronology was conducted on grain separates from T01-40 (Supplementary Fig. 5; Supplementary Table 7). Sample T06-09 did not yield titanite. Titanite is restricted to 30–60 μm grains within garnet cores in T01-40 and is therefore texturally prograde. Ninety-eight analyses show a common Pb trend, intersecting at ca. 1780 Ma (error ellipses are 2σ; $^{207}Pb/^{206}Pb0 = 0.4259 \pm 0.0503$). However, it is evident the titanite has experienced Pb loss, and the data points are being pulled to higher $^{238}U/^{206}Pb$ ratios (Fig 10). Thus, this lower intercept has been affected by the Pb loss event, and the intercept age is meaningless. However it is evident that prior to the lead loss event, the lower intercept would have been older, consistent with the presence of titanite as inclusions in ca. 2000 Ma garnet.

References:

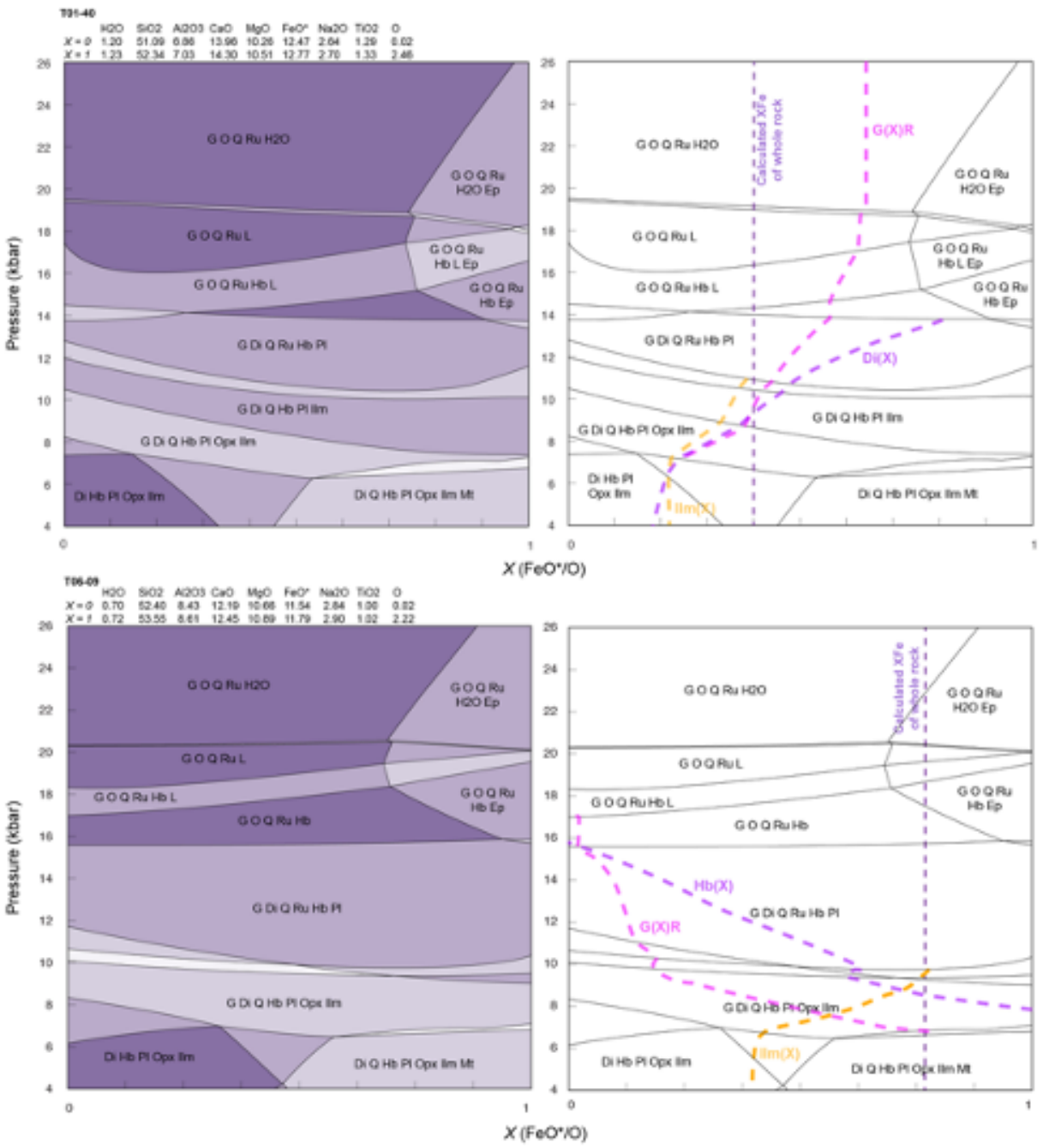
Elburg, M., Bons, P., Foden, J., and Brugger, J., 2003, A newly defined Late Ordovician magmatic-thermal event in the Mt Painter Province, northern Flinders Ranges, South Australia: Australian Journal of Earth Sciences, v. 50, no. 4, p. 611-631.

Paton, C., Hellstrom, J., Paul, B., Woodhead, J., and Hergt, J., 2011, Iolite: Freeware for the visualisation and processing of mass spectrometric data: Journal of Analyti-

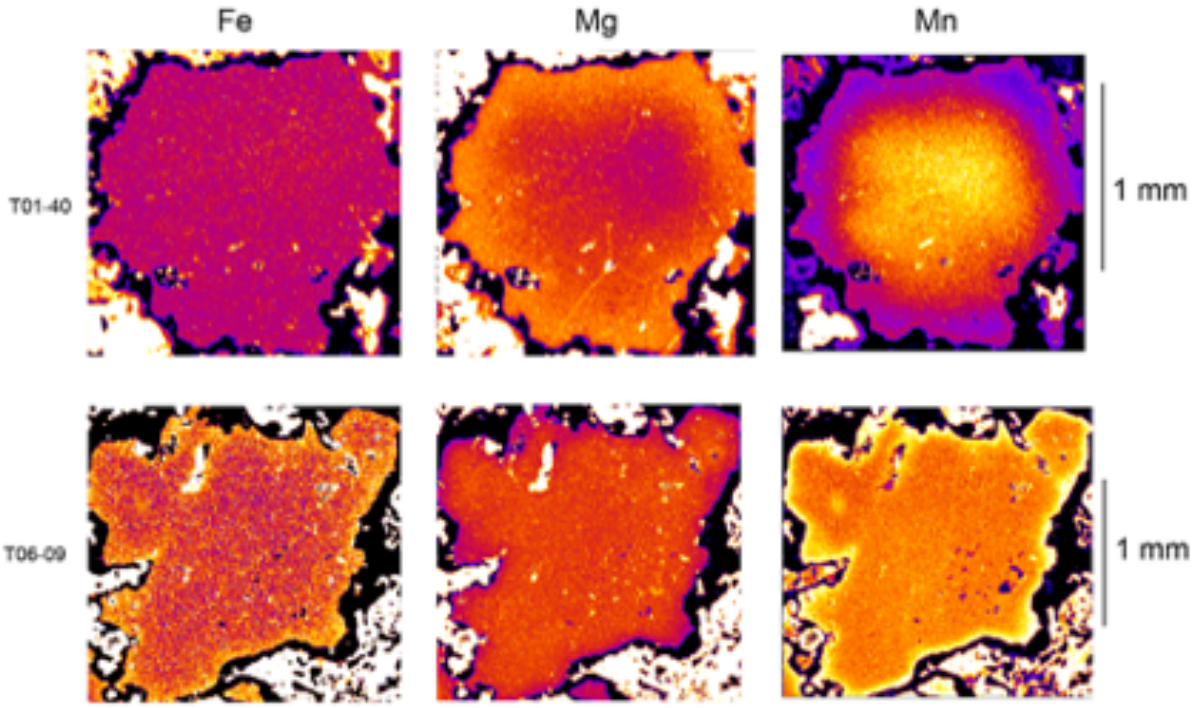
cal Atomic Spectrometry, v. 26, no. 12, p. 2508-2518.

Spandler, C., Hammerli, J., Sha, P., Hilbert-Wolf, H., Hu, Y., Roberts, E., and Schmitz, M., 2016, MKED1: a new titanite standard for in situ analysis of Sm–Nd isotopes and U–Pb geochronology: Chemical Geology, v. 425, p. 110-126.

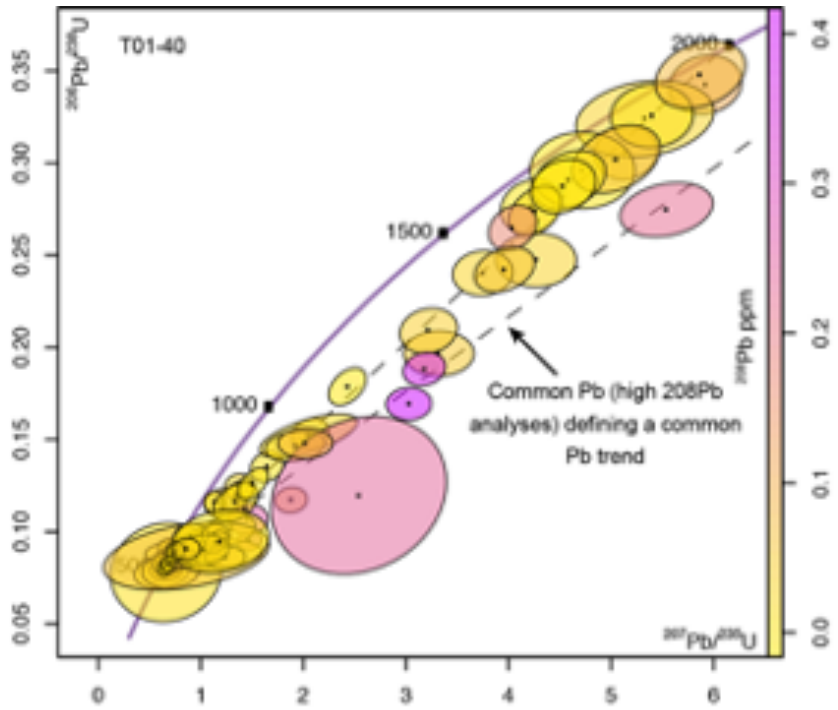
Vermeesch, P., 2018, IsoplotR: a free and open toolbox for geochronology: Geoscience Frontiers, v. 9, no. 5, p. 1479-1493.



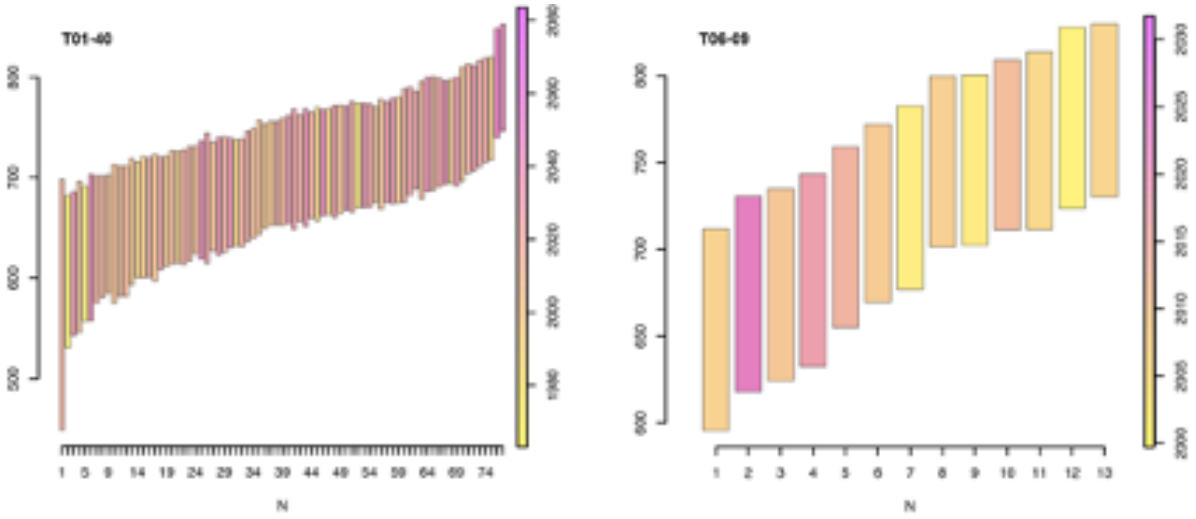
Supplementary Figure. 1: Pressure-composition models for samples T01-40 and T06-09, varying FeO*/O on the X-axis, calculated at 750 °C. Dashed lines indicate compositions of minerals used to constrain oxidation state; Di(X) = Fe/Fe+Mg, Hb(X) = Fe/Fe+Mg, G(X) = Fe/Fe+Mg, Ilm(X) = proportion of ilmenite. The calculated XFe of the bulk rock, constrained from combining modes of minerals with their measured EPMA chemistry is shown as a purple dashed line. Abbreviations: Di: Diopside, Ep: Epidote, G: Garnet, Hb: Hornblende, Ilm: Ilmenite, L: Liquid (melt), Mt: Magnetite, O: Omphacite, Opx: Orthopyrxoene, Pl: Plagioclase, Q: Quartz, Ru: Rutile.



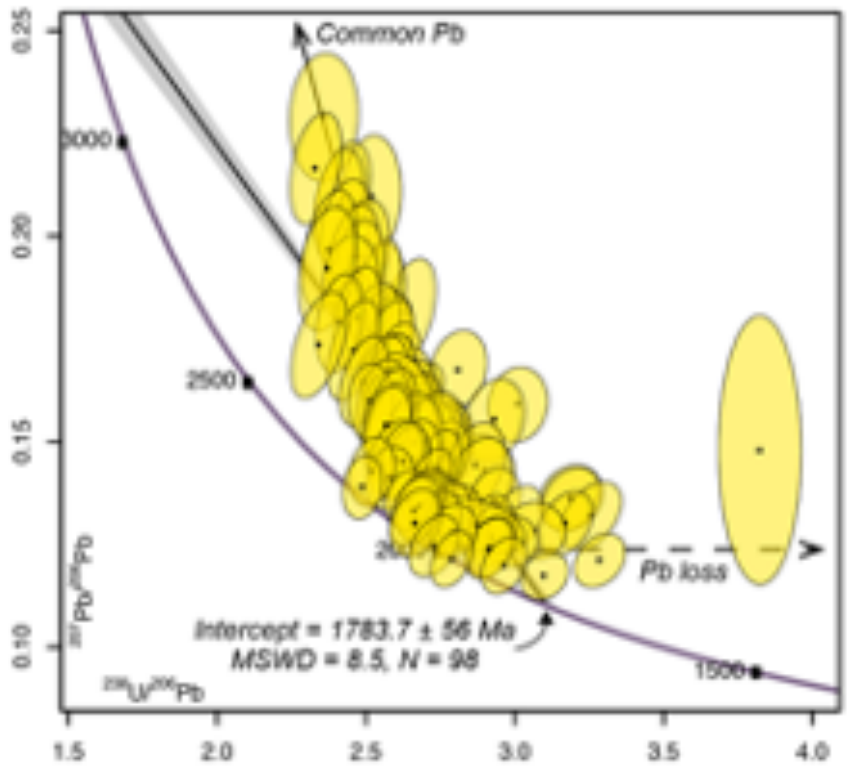
Supplementary Figure. 2: Additional major element maps of garnets of similar sizes in T01-40 and T06-09, measured by LA-ICP-MS.



Supplementary Figure. 3: All U–Pb rutile data in T01-40, showing high 208Pb analyses (in pink) that define a common lead trend. These analyses were not used in age calculations.



Supplementary Figure 4: Ti in zircon temperatures coloured by 207Pb/206Pb age.



Supplementary Figure 5: Titanite U–Pb results from T01-40. The combined effect of common Pb and Pb loss is evident. Potentially, prior to Pb loss the common Pb trend defined a lower intercept close to 2 Ga.

Supplementary Table 1: Whole rock geochemistry of T01-40 and T06-09 measured by XRF. Major elements are in wt% and trace elements are in ppm.

Specimen	T01-40	T06-09
SiO2	49.00	49.70
TiO2	1.65	1.26
Al2O3	11.17	13.57
Fe2O3T	15.89	14.55
MnO	0.17	0.21
MgO	6.60	6.78
CaO	12.50	10.79
Na2O	2.61	2.78
K2O	0.03	0.02
P2O5	0.18	0.15
LOI	1.12	0.82
FeO	8.78	8.17
Fe2O3	6.13	5.47
Total	99.80	99.81
Rb	<0.5	<0.5
Sr	103.00	53.00
Y	28.90	28.20
Zr	95.00	77.00
V	505.00	362.00
Ni	67.00	93.00
Cr	104.00	150.00
Nb	4.30	4.70
Ga	17.50	17.80
Cu	155.00	261.00
Zn	144.00	148.00
Co	59.00	53.00
Ba	7.00	33.00
La	11.00	12.00
Ce	18.00	16.00
U	<0.5	<0.5
Th	0.70	<0.5
Sc	43.00	39.00
Pb	<1	<1

Supplementary Table 2: Mineral compositions measured by EPMA in T01-40 and T06-09.

	T01-40			T06-09	
	Garnet core	Garnet inner rim	Garnet resorbed rim	Garnet core	Garnet rim
SiO2	36.87	36.59	37.55	36.35	36.91
TiO2	0.01	0.08	0.08	0.05	0.06
Al2O3	21.44	21.59	21.45	21.48	21.64
Cr2O3	0.03	0.03	0.00	0.00	0.00
FeO	27.14	26.06	26.95	23.75	25.78
MnO	2.52	1.02	1.07	0.58	0.94
MgO	3.28	4.88	4.21	6.60	4.87
ZnO	0.00	0.00	0.04	0.03	0.00
CaO	8.17	8.45	8.23	8.75	8.28
Na2O	0.00	0.04	0.01	0.00	0.02
K2O	0.00	0.00	0.00	0.00	0.00
Cl	0.00	0.00	0.01	0.00	0.00
F	0.00	0.00	0.00	0.00	0.00
H2O	0.00	0.00	0.00	0.00	0.00
Total	99.45	98.73	99.61	98.94	98.51
No. Oxygens	12	12	12	12	12
Si	2.931	2.893	2.960	2.871	2.924
Ti	0.000	0.005	0.005	0.003	0.004
Al	2.008	2.012	1.993	1.999	2.020
Cr	0.002	0.002	0.000	0.000	0.000
Fe3+	0.128	0.196	0.079	0.254	0.126
Fe2+	1.676	1.527	1.698	1.315	1.582
Mn2+	0.170	0.068	0.071	0.039	0.063
Mg	0.388	0.575	0.495	0.777	0.575
Zn	0.000	0.000	0.003	0.002	0.000
Ca	0.696	0.716	0.695	0.741	0.703
Na	0.000	0.006	0.002	0.000	0.003
K	0.000	0.000	0.000	0.000	0.000
Cl	0.000	0.000	0.001	0.000	0.000
F	0.000	0.000	0.000	0.000	0.000
OH-	0.000	0.000	0.000	0.000	0.000
Total cations	8	8	8	8	8
x(g)	0.8119	0.7264	0.7742	0.6287	0.7333
Almandine	0.5721	0.5291	0.5737	0.4580	0.5412
Pyrope	0.0687	0.1015	0.1281	0.1437	0.1339
Grossular / z(g)	0.2375	0.2479	0.2349	0.2579	0.2405
Spessartine / m(g)	0.0579	0.0236	0.0240	0.0136	0.0215
p(kho) (or f(g))	0.0638	0.0978	0.0393	0.1268	0.0629

Supplementary Table 2 continued: Mineral compositions measured by EPMA in T01-40 and T06-09.

	T01-40		T06-09		T01-40	T06-09
	Clinopyroxene	Clinopyroxene in garnet	Clinopyroxene		Amphibole	Amphibole
SiO2	50.84	51.59	51.05	SiO2	42.00	42.66
TiO2	0.27	0.50	0.39	TiO2	1.36	1.45
Al2O3	2.99	5.48	4.29	Al2O3	11.93	11.52
Cr2O3	0.01	0.04	0.01	Cr2O3	0.00	0.07
FeO	9.48	9.07	6.60	FeO	15.44	16.12
MnO	0.10	0.05	0.04	MnO	0.07	0.06
MgO	12.92	11.40	13.84	MgO	11.18	10.64
ZnO	0.00	0.02	0.00	ZnO	0.03	0.07
CaO	20.88	20.50	22.33	CaO	11.30	11.11
Na2O	1.05	1.55	0.83	Na2O	2.21	2.09
K2O	0.04	0.00	0.00	K2O	0.24	0.22
Cl	0.01	0.00	0.00	Cl	0.13	0.72
F	0.00	0.00	0.00	F	0.02	0.00
H2O	0.00	0.00	0.00	H2O	0.00	0.00
Total	98.60	100.17	99.39	Total	95.89	96.56
No. Oxygens	6	6	6	No. Oxygens	23	23
Si	1.913	1.910	1.889	Si	6.265	6.339
Ti	0.008	0.014	0.011	Ti	0.153	0.162
Al	0.133	0.239	0.187	Al	2.097	2.017
Cr	0.000	0.001	0.000	Cr	0.000	0.008
Fe3+	0.103	0.026	0.073	Fe3+	0.851	0.808
Fe2+	0.195	0.255	0.131	Fe2+	1.075	1.194
Mn2+	0.003	0.001	0.001	Mn2+	0.009	0.007
Mg	0.725	0.629	0.763	Mg	2.486	2.358
Zn	0.000	0.000	0.000	Zn	0.004	0.008
Ca	0.842	0.813	0.885	Ca	1.806	1.769
Na	0.076	0.111	0.060	Na	0.638	0.603
K	0.002	0.000	0.000	K	0.046	0.042
Cl	0.001	0.000	0.000	Cl	0.033	0.183
F	0.000	0.000	0.000	F	0.011	0.000
OH-	0.000	0.000	0.000	OH-	0.000	0.000
Total cations	4	4	4	Total cations	15.429	15.315
j	0.0763	0.1111	0.0596	x(amp)	0.3018	0.3362
f	0.4361	0.0961	0.2810	y(amp)	0.1809	0.1780
x	0.2124	0.2886	0.1463	z(amp)	0.1277	0.1648
Jadeite	0.0430	0.1004	0.0429	a(amp)	0.4291	0.3151
Diopside	0.7275	0.6324	0.8028	k(amp)	0.0976	0.1175
Hedenbergite	0.1961	0.2565	0.1376	c(amp)	0.9030	0.8847
Aeg/Ac	0.0333	0.0107	0.0167	f(amp)	0.4254	0.4041
				t(amp)	0.0765	0.0809

Supplementary Table 2 continued: Mineral compositions measured by EPMA in T01-40 and T06-09.

	T01-40				T06-09	
	Plagioclase co-ronae	Plagioclase co-ronae	Plagioclase in garnet	Plagioclase in garnet	Plagioclase co-ronae	Plagioclase co-ronae
SiO2	62.33	63.91	60.16	59.93	60.85	58.38
TiO2	0.01	0.00	0.01	0.01	0.00	0.04
Al2O3	24.86	23.31	24.11	23.83	24.38	25.66
Cr2O3	0.00	0.01	0.00	0.00	0.01	0.00
FeO	0.09	0.07	0.43	0.39	0.13	0.17
MnO	0.00	0.00	0.00	0.01	0.00	0.00
MgO	0.00	0.00	0.01	0.01	0.00	0.00
ZnO	0.00	0.00	0.00	0.00	0.02	0.00
CaO	5.68	4.10	5.42	5.29	5.55	7.16
Na2O	8.70	9.48	8.71	8.85	8.63	7.62
K2O	0.03	0.04	0.04	0.04	0.06	0.04
Cl	0.00	0.00	0.00	0.00	0.01	0.01
F	0.01	0.01	0.02	0.00	0.00	0.00
H2O	0.00	0.00	0.00	0.00	0.00	0.00
Total	101.72	100.93	98.87	98.32	99.64	99.07
No. Oxygens	8	8	8	8	8	8
Si	2.718	2.797	2.694	2.694	2.705	2.623
Ti	0.000	0.000	0.000	0.000	0.000	0.001
Al	1.278	1.202	1.272	1.262	1.277	1.358
Cr	0.000	0.000	0.000	0.000	0.000	0.000
Fe3+	0.000	0.000	0.000	0.000	0.000	0.000
Fe2+	0.003	0.003	0.016	0.015	0.005	0.006
Mn2+	0.000	0.000	0.000	0.000	0.000	0.000
Mg	0.000	0.000	0.000	0.000	0.000	0.000
Zn	0.000	0.000	0.000	0.000	0.001	0.000
Ca	0.265	0.192	0.260	0.255	0.264	0.345
Na	0.736	0.804	0.756	0.771	0.744	0.664
K	0.002	0.002	0.002	0.002	0.004	0.002
Cl	0.000	0.000	0.000	0.000	0.001	0.000
F	0.001	0.001	0.003	0.000	0.000	0.000
OH-	0.000	0.000	0.000	0.000	0.000	0.000
Total cations	5	5	5	5	5	5
ca(pl)	0.2647	0.1924	0.2555	0.2479	0.2612	0.3409
k(pl)	0.0017	0.0024	0.0021	0.0020	0.0036	0.0022
p(abh)	0.7336	0.8052	0.7424	0.7500	0.7351	0.6569
p(an)	0.2647	0.1924	0.2555	0.2479	0.2612	0.3409
p(san)	0.0017	0.0024	0.0021	0.0020	0.0036	0.0022

Supplementary Table 2 continued: Mineral compositions measured by EPMA in T01-40 and T06-09.

	T01-40	T06-09		T01-40	T06-09
	Ilmenite	Ilmenite		Magnetite	Magnetite
SiO2	0.02	0.00	SiO2	0.04	0.02
TiO2	49.55	46.95	TiO2	0.06	0.05
Al2O3	0.04	0.09	Al2O3	0.39	0.37
Cr2O3	0.01	0.02	Cr2O3	0.13	0.61
FeO	47.83	51.05	FeO	90.24	91.94
MnO	0.17	0.13	MnO	0.01	0.02
MgO	1.02	0.96	MgO	0.03	0.06
ZnO	0.03	0.05	ZnO	0.02	0.00
CaO	0.02	0.00	CaO	0.07	0.13
Na2O	0.01	0.00	Na2O	0.03	0.00
K2O	0.01	0.00	K2O	0.00	0.00
Cl	0.00	0.00	Cl	0.00	0.01
F	0.00	0.00	F	0.00	0.00
H2O	0.00	0.00	H2O	0.00	0.00
Total	98.69	99.25	Total	91.02	93.20
T01-40	3	3	No. Oxygens	4	4
Si	0.000	0.000	Si	0.002	0.001
Ti	0.943	0.886	Ti	0.002	0.002
Al	0.001	0.003	Al	0.018	0.017
Cr	0.000	0.000	Cr	0.004	0.018
Fe3+	0.113	0.225	Fe3+	1.974	1.960
Fe2+	0.899	0.847	Fe2+	0.993	0.993
Mn2+	0.004	0.003	Mn2+	0.000	0.001
Mg	0.038	0.036	Mg	0.002	0.003
Zn	0.000	0.001	Zn	0.001	0.000
Ca	0.001	0.000	Ca	0.003	0.005
Na	0.001	0.000	Na	0.003	0.000
K	0.000	0.000	K	0.000	0.000
Cl	0.000	0.000	Cl	0.000	0.000
F	0.000	0.000	F	0.000	0.000
OH-	0.000	0.000	OH-	0.000	0.000
Total cations	2	2	Total cations	3	3
i(ilm)	0.9436	0.8861	x(sp, mt)	0.9981	0.9968
g(ilm	0.0383	0.0358	y(sp, mt)	0.0091	0.0084
m(ilm	0.0036	0.0028	z(sp, mt)	0.0019	0.0015
p(ilm	0.9017	0.8475	p(herc)	0.0072	0.0052
p(hem)	0.0564	0.1139	p(sp)	0.0019	0.0032
			p(mt)	0.9890	0.9901
			p(usp)	0.0019	0.0015

Supplementary Table 2 continued: Mineral compositions measured by EPMA in T01-40 and T06-09.

	T06-09			T01-40
	Orthopyroxene	Orthopyroxene		Titanite
SiO2	50.99	51.42	SiO2	29.60
TiO2	0.05	0.00	TiO2	38.27
Al2O3	0.98	0.95	Al2O3	1.43
Cr2O3	0.01	0.01	Cr2O3	0.00
FeO	26.56	25.29	FeO	0.53
MnO	0.31	0.23	MnO	0.01
MgO	19.37	20.57	MgO	0.00
ZnO	0.08	0.10	ZnO	0.01
CaO	0.35	0.27	CaO	27.50
Na2O	0.01	0.03	Na2O	0.01
K2O	0.00	0.00	K2O	0.00
Cl	0.01	0.01	Cl	0.02
F	0.00	0.00	F	0.39
H2O	0.00	0.00	H2O	0.00
Total	98.69	98.88	Total	97.59
No. Oxygens	6	6	No. Oxygens	5
Si	1.962	1.959	Si	0.987
Ti	0.001	0.000	Ti	0.959
Al	0.044	0.043	Al	0.056
Cr	0.000	0.000	Cr	0.000
Fe3+	0.029	0.040	Fe3+	0.010
Fe2+	0.825	0.766	Fe2+	0.005
Mn2+	0.010	0.007	Mn2+	0.000
Mg	1.111	1.169	Mg	0.000
Zn	0.002	0.003	Zn	0.000
Ca	0.014	0.011	Ca	0.982
Na	0.000	0.002	Na	0.001
K	0.000	0.000	K	0.000
Cl	0.001	0.001	Cl	0.001
F	0.000	0.000	F	0.042
OH-	0.000	0.000	OH-	0.000
Total cations	4	4	Total cations	3
x(opx)	0.4261	0.3958		
y(opx)	0.0060	0.0018		
m(opx) = p(mnopx)	0.0050	0.0036		
f(opx) = p(fopx)	0.0292	0.0402		
c(opx) = p(odi)	0.0144	0.0111		
p(mgts)	0.0060	0.0018		
p(en)	0.5276	0.5532		
p(fs)	0.4090	0.3777		
p(fm)	0.0150	0.0166		

Supplementary Table 3: Garnet rare earth element compositions measured by LA-ICP-MS

	La_ppm	Error (2SE)	Ce_ppm	Error (2SE)	Pr_ppm	Error (2SE)	Nd_ppm	Error (2SE)	Sm_ppm	Error (2SE)
T01-40-1 - 1	BLOD	BLOD	0.0259	0.0077	0.0118	0.0061	0.142	0.041	0.117	0.042
T01-40-1 - 2	BLOD	BLOD	0.063	0.016	0.0356	0.0086	0.49	0.1	0.61	0.12
T01-40-1 - 3	BLOD	BLOD	0.048	0.011	0.05	0.01	1.36	0.15	2.53	0.22
T01-40-1 - 4	BLOD	BLOD	0.082	0.017	0.051	0.012	1.21	0.13	2.06	0.17
T01-40-1 - 5	BLOD	BLOD	0.063	0.012	0.062	0.011	1.14	0.14	1.75	0.19
T01-40-1 - 6	0.0051	0.0039	0.053	0.013	0.044	0.01	0.879	0.099	1.85	0.18
T01-40-1 - 7	BLOD	BLOD	0.063	0.014	0.0565	0.0095	1.01	0.1	2.38	0.21
T01-40-1 - 8	BLOD	BLOD	0.146	0.022	0.095	0.013	1.64	0.16	1.36	0.15
T01-40-1 - 9	0.0076	0.0046	0.092	0.014	0.079	0.014	1.57	0.14	2.57	0.19
T01-40-1 - 10	BLOD	BLOD	0.083	0.014	0.073	0.012	1.58	0.14	2.2	0.18
T01-40-1 - 11	0.0128	0.0065	0.173	0.022	0.11	0.018	1.7	0.17	0.94	0.12
T01-40-1 - 12	BLOD	BLOD	0.06	0.014	0.061	0.014	1.32	0.13	1.93	0.16
T01-40-1 - 13	BLOD	BLOD	0.069	0.016	0.0448	0.0099	1.05	0.12	2.46	0.2
T01-40-1 - 14	BLOD	BLOD	0.104	0.017	0.066	0.012	1.11	0.11	1.44	0.15
T01-40-1 - 16	0.0068	0.0045	0.085	0.017	0.055	0.011	0.651	0.088	0.61	0.1
T01-40-1 - 17	0.0063	0.0044	0.137	0.021	0.1	0.014	1.45	0.15	0.95	0.12
T01-40-1 - 18	0.0066	0.0043	0.06	0.011	0.057	0.011	1.01	0.11	1.52	0.16
T01-40-1 - 19	BLOD	BLOD	0.099	0.015	0.066	0.014	1.3	0.13	1.31	0.12
T01-40-1 - 20	BLOD	BLOD	0.069	0.016	0.035	0.01	0.322	0.063	0.258	0.063
T01-40-2 - 1	0.0101	0.0053	0.12	0.021	0.069	0.011	1.01	0.13	1.03	0.11
T01-40-2 - 2	BLOD	BLOD	0.059	0.013	0.05	0.012	0.85	0.1	0.92	0.13
T01-40-2 - 3	0.0036	0.0034	0.087	0.013	0.0317	0.0072	0.373	0.073	0.354	0.07
T01-40-2 - 4	0.008	0.0053	0.12	0.016	0.058	0.011	1.01	0.11	0.84	0.11
T01-40-2 - 5	0.0057	0.004	0.089	0.015	0.0501	0.0096	0.771	0.089	0.8	0.11
T01-40-2 - 6	BLOD	BLOD	0.052	0.01	0.0386	0.0092	0.99	0.12	2.39	0.19
T01-40-2 - 7	0.0095	0.0047	0.075	0.015	0.055	0.01	1.05	0.12	2.57	0.2
T01-40-2 - 8	BLOD	BLOD	0.101	0.017	0.056	0.011	0.815	0.095	0.479	0.091
T01-40-2 - 9	BLOD	BLOD	0.042	0.011	0.0378	0.0093	0.609	0.075	1.42	0.15
T01-40-2 - 10	BLOD	BLOD	0.083	0.012	0.0502	0.0094	0.72	0.11	0.81	0.11
T01-40-2 - 11	0.0087	0.0054	0.073	0.016	0.0632	0.0097	1.1	0.1	2.45	0.22
T01-40-2 - 12	BLOD	BLOD	0.0144	0.0059	BLOD	BLOD	0.116	0.038	0.13	0.044
T01-40-2 - 13	BLOD	BLOD	0.0091	0.0048	0.0036	0.003	0.025	0.019	0.1	0.036
T01-40-2 - 14	0.0076	0.0047	0.046	0.011	0.0238	0.0073	0.291	0.062	0.351	0.085
T01-40-2 - 15	0.046	0.018	0.201	0.043	0.085	0.016	1.45	0.13	1.87	0.16
T01-40-2 - 16	BLOD	BLOD	0.116	0.021	0.08	0.016	1.2	0.14	0.71	0.12
T01-40-2 - 18	0.0067	0.0042	0.167	0.02	0.091	0.013	1.16	0.11	0.84	0.12
T01-40-2 - 19	BLOD	BLOD	0.062	0.013	0.0456	0.0099	1.17	0.13	2.91	0.22
T01-40-2 - 20	BLOD	BLOD	0.042	0.01	0.0104	0.005	0.159	0.045	0.111	0.04
T01-40-3 - 1	BLOD	BLOD	0.059	0.014	0.051	0.01	1.11	0.13	2.18	0.21
T01-40-3 - 2	0.0098	0.005	0.118	0.017	0.094	0.016	1.63	0.12	1.7	0.2
T01-40-3 - 3	BLOD	BLOD	0.112	0.019	0.089	0.013	1.34	0.13	1.51	0.17
T01-40-3 - 4	BLOD	BLOD	0.0375	0.0096	0.0281	0.0066	0.758	0.092	1.61	0.16
T01-40-3 - 6	BLOD	BLOD	0.044	0.012	0.049	0.012	0.783	0.095	1.79	0.16
T01-40-3 - 7	BLOD	BLOD	0.073	0.014	0.0498	0.0095	1.33	0.16	2.86	0.21
T01-40-3 - 8	0.0029	0.0033	0.036	0.01	0.0138	0.0057	0.172	0.049	0.257	0.063
T01-40-3 - 9	0.0086	0.0047	0.097	0.015	0.078	0.014	1.16	0.13	1.12	0.11
T01-40-3 - 10	BLOD	BLOD	0.072	0.015	0.0429	0.0097	0.97	0.11	2.37	0.19
T01-40-3 - 11	0.0241	0.0095	0.184	0.032	0.092	0.015	1.11	0.13	0.75	0.13
T01-40-3 - 12	BLOD	BLOD	0.083	0.016	0.0388	0.0094	0.423	0.058	0.335	0.084
T01-40-3 - 13	0.0072	0.0045	0.084	0.015	0.076	0.013	1.48	0.15	2.12	0.19

Supplementary Table 3 continued: Garnet rare earth element compositions measured by LA-ICP-MS

	Eu_ppm	Error (2SE)	Gd_ppm	Error (2SE)	Tb_ppm	Error (2SE)	Dy_ppm	Error (2SE)	Ho_ppm	Error (2SE)
T01-40-1 - 1	0.15	0.023	1.29	0.13	0.787	0.042	14.82	0.36	6.04	0.13
T01-40-1 - 2	0.456	0.041	2.39	0.19	0.887	0.042	12.19	0.38	4.117	0.088
T01-40-1 - 3	1.218	0.065	7.06	0.31	1.537	0.058	12.54	0.35	2.661	0.072
T01-40-1 - 4	0.769	0.05	2.97	0.23	0.652	0.043	9.21	0.33	4.149	0.093
T01-40-1 - 5	0.508	0.045	2.32	0.19	0.664	0.032	9.3	0.29	2.53	0.065
T01-40-1 - 6	0.904	0.05	6.03	0.29	1.492	0.046	10.55	0.33	1.704	0.073
T01-40-1 - 7	1.112	0.062	6.44	0.28	1.507	0.057	13.76	0.35	3.164	0.09
T01-40-1 - 8	0.389	0.039	1.53	0.13	0.549	0.033	10.28	0.38	4.1	0.11
T01-40-1 - 9	1.174	0.076	7.15	0.36	1.592	0.056	10.37	0.31	1.431	0.062
T01-40-1 - 10	0.676	0.05	3.28	0.23	0.768	0.042	11.16	0.32	5.18	0.12
T01-40-1 - 11	0.171	0.027	0.62	0.1	0.298	0.025	6.75	0.27	3.681	0.093
T01-40-1 - 12	0.636	0.052	4.12	0.24	1.229	0.057	15.75	0.42	3.988	0.096
T01-40-1 - 13	1.357	0.072	9.06	0.41	2.24	0.1	17.67	0.85	3.86	0.25
T01-40-1 - 14	0.609	0.055	2.57	0.2	0.567	0.024	7.22	0.28	2.999	0.09
T01-40-1 - 16	0.22	0.031	1.43	0.12	0.729	0.042	14.34	0.37	5.02	0.11
T01-40-1 - 17	0.24	0.027	0.92	0.13	0.255	0.021	4.4	0.21	1.914	0.071
T01-40-1 - 18	0.796	0.052	4.27	0.24	1.289	0.048	13.56	0.4	3.196	0.088
T01-40-1 - 19	0.576	0.047	1.99	0.18	0.707	0.045	15.16	0.35	8.38	0.14
T01-40-1 - 20	0.127	0.023	0.464	0.08	0.266	0.023	5.33	0.24	2.237	0.066
T01-40-2 - 1	0.379	0.037	1.28	0.14	0.434	0.032	7.54	0.28	2.515	0.076
T01-40-2 - 2	0.563	0.048	3.06	0.2	0.849	0.045	8.9	0.3	2.336	0.083
T01-40-2 - 3	0.132	0.026	0.98	0.12	0.605	0.035	13.17	0.35	6.01	0.14
T01-40-2 - 4	0.273	0.035	1	0.12	0.308	0.028	6.49	0.25	3.63	0.1
T01-40-2 - 5	0.257	0.027	1.14	0.12	0.52	0.034	9.84	0.32	3.913	0.092
T01-40-2 - 6	1.149	0.084	6.51	0.32	1.409	0.06	9.23	0.33	1.615	0.051
T01-40-2 - 7	1.334	0.071	8.06	0.33	1.681	0.057	11.58	0.3	1.886	0.053
T01-40-2 - 8	0.147	0.023	0.87	0.12	0.535	0.031	12.17	0.34	6.096	0.099
T01-40-2 - 9	0.795	0.056	6.39	0.29	1.529	0.053	13.2	0.33	2.964	0.08
T01-40-2 - 10	0.404	0.042	2.31	0.2	0.855	0.042	11.56	0.4	3.49	0.1
T01-40-2 - 11	1.168	0.06	6.34	0.28	1.439	0.05	11.37	0.31	2.213	0.072
T01-40-2 - 12	0.116	0.019	1.58	0.13	0.955	0.046	13.45	0.4	3.338	0.097
T01-40-2 - 13	0.087	0.018	1.37	0.15	0.955	0.044	18.3	0.36	5.42	0.1
T01-40-2 - 14	0.141	0.027	1.34	0.14	0.726	0.041	13.74	0.32	5.18	0.11
T01-40-2 - 15	0.821	0.053	3.52	0.21	0.721	0.039	5.88	0.24	1.371	0.051
T01-40-2 - 16	0.217	0.03	0.658	0.096	0.252	0.022	5.72	0.23	3.114	0.091
T01-40-2 - 18	0.256	0.031	0.8	0.11	0.283	0.021	4.93	0.2	2.082	0.056
T01-40-2 - 19	1.311	0.077	8.78	0.39	2.089	0.062	14.21	0.39	1.901	0.079
T01-40-2 - 20	0.046	0.012	0.605	0.083	0.394	0.031	8.86	0.3	3.753	0.095
T01-40-3 - 1	1.004	0.066	6.29	0.36	1.341	0.059	9.28	0.3	1.575	0.067
T01-40-3 - 2	0.577	0.061	1.79	0.16	0.351	0.027	4.23	0.21	1.614	0.06
T01-40-3 - 3	0.453	0.045	2.54	0.2	0.7	0.042	9.13	0.32	2.783	0.078
T01-40-3 - 4	0.89	0.072	5.28	0.31	1.346	0.061	10.71	0.33	2.03	0.073
T01-40-3 - 6	0.81	0.058	6.16	0.33	1.361	0.062	8.6	0.3	1.045	0.049
T01-40-3 - 7	1.37	0.085	6.4	0.34	1.149	0.051	7.36	0.28	1.245	0.049
T01-40-3 - 8	0.149	0.024	1.65	0.16	1.041	0.048	18.68	0.45	5.71	0.12
T01-40-3 - 9	0.426	0.041	1.52	0.14	0.398	0.034	6.26	0.24	2.672	0.081
T01-40-3 - 10	1.088	0.074	7.5	0.36	1.715	0.065	12.87	0.44	2.16	0.081
T01-40-3 - 11	0.233	0.031	0.487	0.084	0.155	0.022	3.94	0.2	2.233	0.076
T01-40-3 - 12	0.124	0.023	1.01	0.11	0.616	0.035	10.39	0.31	3.612	0.098
T01-40-3 - 13	0.911	0.058	4	0.24	0.847	0.049	12.18	0.32	4.474	0.094

Supplementary Table 3 continued: Garnet rare earth element compositions measured by LA-ICP-MS

	Er_ppm	Error (2SE)	Tm_ppm	Error (2SE)	Yb_ppm	Error (2SE)	Lu_ppm	Error (2SE)
T01-40-1 - 1	23.61	0.43	3.506	0.088	20.96	0.56	2.654	0.088
T01-40-1 - 2	12.85	0.35	1.464	0.052	7.53	0.25	0.843	0.045
T01-40-1 - 3	6.3	0.19	0.733	0.042	4.01	0.21	0.535	0.026
T01-40-1 - 4	20.08	0.36	3.495	0.085	23.73	0.52	3.261	0.086
T01-40-1 - 5	6.91	0.23	0.88	0.043	4.57	0.21	0.594	0.037
T01-40-1 - 6	3.46	0.19	0.403	0.034	2.4	0.17	0.28	0.026
T01-40-1 - 7	7.56	0.25	0.848	0.043	4.36	0.21	0.525	0.034
T01-40-1 - 8	14.66	0.29	2.095	0.075	13.02	0.4	1.626	0.06
T01-40-1 - 9	2.33	0.13	0.246	0.025	1.08	0.11	0.146	0.018
T01-40-1 - 10	25.31	0.45	4.43	0.1	29.66	0.58	3.935	0.099
T01-40-1 - 11	20.09	0.37	3.94	0.1	29.17	0.66	3.99	0.12
T01-40-1 - 12	9.89	0.26	1.094	0.047	5.2	0.23	0.613	0.036
T01-40-1 - 13	10.79	0.7	1.64	0.15	10.18	0.96	1.38	0.15
T01-40-1 - 14	14.01	0.35	2.574	0.096	19.54	0.51	3.01	0.1
T01-40-1 - 16	15.1	0.37	1.839	0.063	10.15	0.36	1.222	0.061
T01-40-1 - 17	8.29	0.24	1.367	0.054	9.73	0.37	1.445	0.06
T01-40-1 - 18	7.08	0.21	0.759	0.045	3.87	0.24	0.493	0.032
T01-40-1 - 19	41.28	0.53	7.11	0.13	43.22	0.82	5.23	0.1
T01-40-1 - 20	9.6	0.24	1.511	0.054	10.16	0.38	1.37	0.064
T01-40-2 - 1	7.95	0.24	1.06	0.048	6.37	0.28	0.829	0.05
T01-40-2 - 2	7.41	0.22	1.022	0.054	6.56	0.24	0.837	0.042
T01-40-2 - 3	26.06	0.49	3.984	0.081	25.25	0.49	3.366	0.097
T01-40-2 - 4	20.17	0.48	3.74	0.1	25.98	0.53	3.525	0.092
T01-40-2 - 5	14.58	0.31	2.016	0.06	11.31	0.33	1.392	0.053
T01-40-2 - 6	3.53	0.13	0.406	0.027	2.2	0.15	0.285	0.025
T01-40-2 - 7	4.03	0.16	0.459	0.035	2.87	0.17	0.354	0.029
T01-40-2 - 8	28.6	0.43	5.2	0.12	37.44	0.75	5.61	0.13
T01-40-2 - 9	7.76	0.24	0.854	0.04	4.24	0.17	0.478	0.032
T01-40-2 - 10	11.03	0.34	1.452	0.064	8.13	0.33	0.97	0.045
T01-40-2 - 11	4.41	0.16	0.476	0.032	2.42	0.16	0.277	0.022
T01-40-2 - 12	7.91	0.24	0.816	0.042	3.84	0.18	0.401	0.029
T01-40-2 - 13	14.35	0.3	1.674	0.051	8.81	0.27	1.112	0.057
T01-40-2 - 14	19.11	0.46	2.54	0.088	13.27	0.37	1.507	0.059
T01-40-2 - 15	4	0.13	0.527	0.029	2.58	0.17	0.275	0.024
T01-40-2 - 16	16.96	0.27	3.405	0.082	24.2	0.56	3.681	0.095
T01-40-2 - 18	8.49	0.23	1.329	0.058	8.45	0.33	1.142	0.056
T01-40-2 - 19	2.97	0.14	0.254	0.024	1.16	0.12	0.137	0.017
T01-40-2 - 20	14.41	0.34	2.184	0.074	14.1	0.44	2.066	0.074
T01-40-3 - 1	3.42	0.16	0.382	0.03	1.7	0.14	0.208	0.024
T01-40-3 - 2	6.61	0.28	1.042	0.045	5.83	0.27	0.669	0.048
T01-40-3 - 3	9.34	0.28	1.315	0.058	7.53	0.22	0.924	0.047
T01-40-3 - 4	4.4	0.18	0.486	0.035	2.56	0.17	0.312	0.027
T01-40-3 - 6	1.67	0.11	0.151	0.02	0.63	0.085	0.052	0.015
T01-40-3 - 7	2.34	0.14	0.233	0.023	1.15	0.12	0.129	0.017
T01-40-3 - 8	15.16	0.35	1.672	0.065	8.4	0.28	0.906	0.043
T01-40-3 - 9	10.39	0.31	1.622	0.045	10.85	0.39	1.433	0.075
T01-40-3 - 10	4.46	0.22	0.461	0.032	2.39	0.18	0.281	0.026
T01-40-3 - 11	11.88	0.34	2.175	0.079	15.72	0.51	2.195	0.094
T01-40-3 - 12	11.93	0.34	1.672	0.06	10.24	0.37	1.489	0.061
T01-40-3 - 13	15.62	0.31	2.1	0.072	12.17	0.39	1.437	0.059

Supplementary Table 3 continued: Garnet rare earth element compositions measured by LA-ICP-MS

	La_ppm	Error (2SE)	Ce_ppm	Error (2SE)	Pr_ppm	Error (2SE)	Nd_ppm	Error (2SE)	Sm_ppm	Error (2SE)
T01-40-3 - 14	0.008	0.0046	0.055	0.013	0.061	0.01	1.03	0.11	2.44	0.23
T01-40-3 - 15	0.0061	0.0043	0.075	0.014	0.0496	0.0098	0.84	0.11	1.93	0.18
T01-40-3 - 16	0.0077	0.0047	0.089	0.018	0.053	0.011	0.9	0.11	1.51	0.17
T01-40-3 - 17	BLOD	BLOD	0.105	0.015	0.058	0.012	1.33	0.16	1.92	0.17
T01-40-3 - 18	BLOD	BLOD	0.074	0.015	0.052	0.012	1.37	0.11	2.63	0.22
T01-40-3 - 19	0.0052	0.0041	0.066	0.016	0.0441	0.0087	1.3	0.12	3.22	0.22
T01-40-3 - 20	0.0096	0.0061	0.115	0.02	0.084	0.014	1.35	0.13	1.88	0.19
T01-40-4 - 1	BLOD	BLOD	0.104	0.018	0.063	0.013	1.48	0.16	2.46	0.2
T01-40-4 - 2	0.0092	0.0051	0.129	0.021	0.059	0.011	0.84	0.11	0.71	0.12
T01-40-4 - 3	BLOD	BLOD	0.078	0.017	0.0376	0.0099	0.635	0.092	0.85	0.13
T01-40-4 - 4	BLOD	BLOD	0.053	0.011	0.0382	0.0088	0.93	0.11	2.36	0.2
T01-40-4 - 5	BLOD	BLOD	0.066	0.013	0.064	0.012	1.33	0.14	2.3	0.22
T01-40-4 - 6	BLOD	BLOD	0.061	0.014	0.0346	0.0083	0.622	0.087	0.57	0.085
T01-40-4 - 8	0.004	0.0039	0.061	0.014	0.045	0.012	1.16	0.13	2.84	0.21
T01-40-4 - 9	BLOD	BLOD	0.044	0.012	0.0474	0.0093	0.619	0.091	0.63	0.13
T01-40-4 - 10	0.0082	0.0048	0.116	0.023	0.073	0.012	1.23	0.13	2.44	0.21
T01-40-4 - 11	0.0046	0.004	0.098	0.018	0.0319	0.0079	0.69	0.11	1.02	0.14
T01-40-4 - 12	0.0062	0.0049	0.083	0.016	0.083	0.014	1.41	0.14	2.46	0.18
T01-40-4 - 13	BLOD	BLOD	0.045	0.013	0.0289	0.009	0.536	0.09	1.43	0.16
T01-40-4 - 14	0.086	0.081	0.23	0.14	0.075	0.017	1.36	0.14	2.36	0.2
T01-40-4 - 15	BLOD	BLOD	0.099	0.016	0.069	0.013	1.05	0.13	1.63	0.18
T01-40-4 - 16	BLOD	BLOD	0.095	0.016	0.06	0.012	1.44	0.16	2.37	0.19
T01-40-4 - 17	0.0074	0.0048	0.052	0.011	0.0376	0.0092	0.517	0.092	1.12	0.17
T01-40-4 - 18	0.0078	0.0046	0.096	0.018	0.062	0.012	0.88	0.1	0.94	0.13
T01-40-4 - 19	BLOD	BLOD	0.07	0.016	0.051	0.012	1.25	0.11	2.82	0.24
T01-40-4 - 20	0.0084	0.0053	0.067	0.015	0.047	0.01	0.77	0.1	1.45	0.13
T06-09-1 - 1	0.00153	0.00062	0.00367	0.00094	0.00125	0.00052	0.0203	0.0046	0.092	0.012
T06-09-1 - 2	0.00188	0.00083	0.0095	0.0018	0.00333	0.00091	0.0722	0.0088	0.236	0.019
T06-09-1 - 3	0.00304	0.00087	0.016	0.0024	0.0065	0.0013	0.132	0.012	0.262	0.017
T06-09-1 - 4	0.00103	0.00045	0.00411	0.00093	0.00182	0.00063	0.0398	0.0071	0.176	0.016
T06-09-1 - 5	BLOD	BLOD	0.0021	0.00068	0.00191	0.00062	0.0606	0.0094	0.213	0.015
T06-09-1 - 6	0.00103	0.00055	0.0054	0.0012	0.00332	0.00082	0.0795	0.0091	0.249	0.021
T06-09-1 - 7	0.0064	0.0039	0.0115	0.0063	0.0019	0.0006	0.0379	0.0071	0.178	0.02
T06-09-1 - 8	0.00067	0.00042	0.0057	0.0015	0.00252	0.00077	0.077	0.011	0.208	0.019
T06-09-1 - 9	BLOD	BLOD	0.005	0.0013	0.00558	0.0009	0.135	0.012	0.28	0.017
T06-09-1 - 10	0.0021	0.001	0.0108	0.0027	0.00503	0.00096	0.112	0.012	0.26	0.019
T06-09-1 - 11	0.00144	0.00062	0.006	0.0013	0.00359	0.0008	0.067	0.0085	0.22	0.017
T06-09-1 - 12	0.00114	0.00046	0.00412	0.00088	0.00156	0.00055	0.0393	0.0062	0.181	0.017
T06-09-1 - 13	0.00159	0.00067	0.0042	0.0013	0.00173	0.00063	0.0541	0.0069	0.22	0.018
T06-09-1 - 14	0.00245	0.00076	0.0093	0.002	0.00304	0.00074	0.078	0.011	0.188	0.014
T06-09-1 - 15	0.00113	0.0006	0.0059	0.0014	0.00395	0.00086	0.069	0.01	0.199	0.017
T06-09-1 - 16	0.00072	0.0004	0.00298	0.00081	0.0015	0.0006	0.0398	0.0065	0.18	0.017
T06-09-1 - 17	BLOD	BLOD	0.0043	0.0012	0.00298	0.00066	0.0611	0.007	0.194	0.017
T06-09-1 - 18	0.00195	0.0006	0.0058	0.0013	0.00225	0.00063	0.0457	0.0069	0.149	0.014
T06-09-1 - 19	BLOD	BLOD	0.00379	0.00097	0.00193	0.00061	0.0508	0.0079	0.185	0.016
T06-09-1 - 20	0.0016	0.0011	0.0041	0.0017	0.00219	0.00069	0.0451	0.0071	0.159	0.014
T06-09-2 - 1	0.00117	0.00051	0.0085	0.0013	0.00532	0.0009	0.152	0.013	0.266	0.019
T06-09-2 - 2	0.0044	0.0012	0.0123	0.0019	0.00266	0.00066	0.0492	0.0066	0.167	0.016
T06-09-2 - 3	0.00098	0.00049	0.0058	0.0014	0.00324	0.0008	0.0746	0.0082	0.207	0.018
T06-09-2 - 4	0.00202	0.00078	0.0094	0.0015	0.00469	0.00097	0.109	0.011	0.249	0.018

Supplementary Table 3 continued: Garnet rare earth element compositions measured by LA-ICP-MS

	Eu_ppm	Error (2SE)	Gd_ppm	Error (2SE)	Tb_ppm	Error (2SE)	Dy_ppm	Error (2SE)	Ho_ppm	Error (2SE)
T01-40-3 - 14	1.269	0.085	7.11	0.28	1.51	0.064	11.7	0.39	2.032	0.063
T01-40-3 - 15	1.127	0.08	7.45	0.42	1.769	0.065	14.28	0.34	3.234	0.075
T01-40-3 - 16	0.945	0.066	5.8	0.31	1.253	0.053	7.35	0.27	1.016	0.051
T01-40-3 - 17	0.802	0.06	4.63	0.33	1.373	0.065	13.4	0.42	2.901	0.091
T01-40-3 - 18	1.345	0.072	8.08	0.32	1.784	0.062	12.32	0.38	2.048	0.069
T01-40-3 - 19	1.623	0.078	9.01	0.39	1.733	0.065	11.67	0.34	2.667	0.079
T01-40-3 - 20	0.732	0.058	3.74	0.21	1.033	0.048	13.46	0.33	3.8	0.11
T01-40-4 - 1	1.121	0.064	5.92	0.28	1.345	0.058	9.25	0.28	1.414	0.054
T01-40-4 - 2	0.277	0.036	1.66	0.15	0.808	0.044	11.34	0.29	2.809	0.091
T01-40-4 - 3	0.388	0.042	1.87	0.2	0.691	0.041	11.33	0.32	4.68	0.12
T01-40-4 - 4	1.205	0.084	7.77	0.39	1.648	0.064	11.54	0.41	2.007	0.081
T01-40-4 - 5	1.109	0.072	5.83	0.27	1.419	0.049	12.49	0.31	2.618	0.078
T01-40-4 - 6	0.386	0.042	2.24	0.19	0.935	0.05	12.92	0.33	3.612	0.079
T01-40-4 - 8	1.373	0.084	7.07	0.36	1.291	0.052	8.27	0.29	1.421	0.053
T01-40-4 - 9	0.445	0.045	2.22	0.16	0.594	0.038	7.29	0.26	3.04	0.1
T01-40-4 - 10	1.425	0.08	8.28	0.41	1.843	0.076	11.08	0.34	1.273	0.056
T01-40-4 - 11	0.388	0.043	2.62	0.23	1.037	0.045	12.79	0.36	3.024	0.091
T01-40-4 - 12	1.224	0.076	6.35	0.3	1.269	0.05	8.28	0.29	1.224	0.058
T01-40-4 - 13	0.757	0.06	5.58	0.3	1.339	0.057	11.42	0.35	2.86	0.1
T01-40-4 - 14	1.247	0.076	6.26	0.33	1.43	0.055	13.69	0.43	3.645	0.081
T01-40-4 - 15	0.615	0.051	2.88	0.19	0.914	0.043	9.95	0.31	2.009	0.075
T01-40-4 - 16	0.987	0.065	4.33	0.22	0.936	0.043	11.42	0.3	3.81	0.094
T01-40-4 - 17	0.629	0.042	4.15	0.28	0.967	0.044	7.89	0.27	1.59	0.065
T01-40-4 - 18	0.365	0.037	1.39	0.14	0.522	0.036	8.48	0.32	3.048	0.093
T01-40-4 - 19	1.379	0.085	8.6	0.38	1.878	0.07	14.92	0.38	2.848	0.088
T01-40-4 - 20	0.742	0.059	4.66	0.35	1.341	0.061	11.6	0.34	2.031	0.071
T06-09-1 - 1	0.0602	0.0042	0.538	0.028	0.114	0.0044	0.82	0.027	0.1712	0.005
T06-09-1 - 2	0.1138	0.0062	0.531	0.024	0.1062	0.0039	0.788	0.026	0.1719	0.0061
T06-09-1 - 3	0.1225	0.0058	0.584	0.028	0.1256	0.0043	0.835	0.027	0.1532	0.0051
T06-09-1 - 4	0.1023	0.0052	0.511	0.023	0.1007	0.0046	0.725	0.023	0.154	0.0057
T06-09-1 - 5	0.1125	0.0062	0.519	0.028	0.0996	0.0036	0.727	0.026	0.159	0.0054
T06-09-1 - 6	0.1189	0.0067	0.499	0.025	0.0918	0.0036	0.706	0.023	0.148	0.0062
T06-09-1 - 7	0.1041	0.0057	0.51	0.024	0.0895	0.0037	0.662	0.019	0.1456	0.0058
T06-09-1 - 8	0.1039	0.0069	0.52	0.025	0.1006	0.0049	0.725	0.026	0.1668	0.0059
T06-09-1 - 9	0.141	0.0071	0.571	0.028	0.1017	0.0047	0.73	0.024	0.1588	0.0056
T06-09-1 - 10	0.1213	0.0065	0.598	0.026	0.1187	0.0048	0.831	0.029	0.1579	0.0058
T06-09-1 - 11	0.1095	0.0063	0.497	0.025	0.0912	0.0041	0.668	0.026	0.1462	0.005
T06-09-1 - 12	0.1087	0.0066	0.547	0.025	0.0997	0.0039	0.734	0.024	0.1509	0.005
T06-09-1 - 13	0.103	0.0057	0.58	0.028	0.1039	0.0052	0.782	0.025	0.1616	0.0053
T06-09-1 - 14	0.0944	0.0061	0.503	0.027	0.1006	0.0047	0.769	0.024	0.1665	0.0044
T06-09-1 - 15	0.1211	0.0066	0.562	0.029	0.1025	0.0044	0.759	0.026	0.1633	0.0056
T06-09-1 - 16	0.0934	0.0065	0.532	0.024	0.1041	0.0037	0.725	0.022	0.1549	0.0068
T06-09-1 - 17	0.1006	0.007	0.496	0.029	0.095	0.0037	0.745	0.027	0.1625	0.0052
T06-09-1 - 18	0.0999	0.0055	0.531	0.026	0.1061	0.0039	0.792	0.026	0.1709	0.006
T06-09-1 - 19	0.0937	0.0067	0.543	0.026	0.1113	0.0045	0.781	0.025	0.1616	0.0067
T06-09-1 - 20	0.0832	0.0062	0.48	0.028	0.0967	0.0038	0.72	0.024	0.1676	0.0057
T06-09-2 - 1	0.1258	0.0073	0.509	0.022	0.0858	0.0044	0.616	0.025	0.1384	0.005
T06-09-2 - 2	0.0972	0.0058	0.47	0.023	0.0954	0.0044	0.719	0.026	0.1572	0.0049
T06-09-2 - 3	0.1183	0.0055	0.49	0.028	0.0943	0.0044	0.677	0.024	0.1544	0.0061
T06-09-2 - 4	0.1161	0.0059	0.499	0.024	0.0962	0.0046	0.699	0.024	0.1572	0.0051

Supplementary Table 3 continued: Garnet rare earth element compositions measured by LA-ICP-MS

	Er_ppm	Error (2SE)	Tm_ppm	Error (2SE)	Yb_ppm	Error (2SE)	Lu_ppm	Error (2SE)
T01-40-3 - 14	4.31	0.19	0.431	0.034	2.35	0.18	0.28	0.029
T01-40-3 - 15	10.24	0.3	1.44	0.062	8.49	0.35	0.981	0.044
T01-40-3 - 16	1.67	0.1	0.148	0.017	0.595	0.08	0.0622	0.0099
T01-40-3 - 17	6.72	0.23	0.762	0.041	3.49	0.18	0.357	0.029
T01-40-3 - 18	3.7	0.14	0.353	0.028	1.79	0.15	0.202	0.021
T01-40-3 - 19	9.13	0.26	1.649	0.059	13.27	0.41	2.255	0.075
T01-40-3 - 20	10.47	0.26	1.215	0.054	6.77	0.26	0.855	0.044
T01-40-4 - 1	2.47	0.12	0.231	0.022	1.17	0.11	0.152	0.019
T01-40-4 - 2	7.05	0.21	0.881	0.045	5.89	0.27	0.834	0.047
T01-40-4 - 3	18.35	0.48	2.724	0.071	16.71	0.4	2.183	0.077
T01-40-4 - 4	4.68	0.2	0.574	0.038	3.45	0.19	0.416	0.032
T01-40-4 - 5	5.49	0.2	0.556	0.034	2.56	0.17	0.312	0.028
T01-40-4 - 6	8.79	0.24	0.967	0.05	4.46	0.23	0.521	0.035
T01-40-4 - 8	2.93	0.17	0.34	0.03	1.93	0.15	0.264	0.024
T01-40-4 - 9	14.94	0.38	2.813	0.083	19.78	0.42	2.682	0.083
T01-40-4 - 10	1.89	0.11	0.18	0.021	0.765	0.089	0.072	0.013
T01-40-4 - 11	6.86	0.23	0.751	0.035	3.8	0.2	0.45	0.029
T01-40-4 - 12	2.23	0.15	0.244	0.024	1.44	0.14	0.184	0.02
T01-40-4 - 13	8.67	0.27	1.206	0.053	6.92	0.27	0.991	0.048
T01-40-4 - 14	10.75	0.3	1.394	0.057	8.03	0.27	1.045	0.057
T01-40-4 - 15	3.98	0.17	0.408	0.03	1.91	0.12	0.231	0.024
T01-40-4 - 16	13.42	0.29	1.805	0.056	10.02	0.38	1.137	0.051
T01-40-4 - 17	3.36	0.18	0.383	0.026	2.1	0.15	0.286	0.023
T01-40-4 - 18	10.48	0.28	1.489	0.049	8.25	0.29	0.993	0.052
T01-40-4 - 19	5.6	0.2	0.528	0.033	2.14	0.16	0.23	0.024
T01-40-4 - 20	4.03	0.19	0.402	0.03	1.93	0.12	0.195	0.023
T06-09-1 - 1	0.485	0.014	0.0703	0.0035	0.475	0.021	0.0668	0.0035
T06-09-1 - 2	0.502	0.022	0.075	0.0042	0.511	0.016	0.0757	0.004
T06-09-1 - 3	0.386	0.016	0.0469	0.003	0.291	0.016	0.0342	0.0021
T06-09-1 - 4	0.455	0.019	0.0688	0.0035	0.475	0.021	0.0684	0.0038
T06-09-1 - 5	0.458	0.017	0.0655	0.0033	0.43	0.02	0.0595	0.0034
T06-09-1 - 6	0.427	0.018	0.0615	0.0036	0.382	0.016	0.0561	0.003
T06-09-1 - 7	0.421	0.016	0.0562	0.0035	0.325	0.016	0.0432	0.0028
T06-09-1 - 8	0.487	0.019	0.0732	0.0043	0.486	0.023	0.0701	0.0041
T06-09-1 - 9	0.47	0.015	0.0665	0.0037	0.493	0.023	0.0715	0.0035
T06-09-1 - 10	0.422	0.017	0.0595	0.0033	0.369	0.015	0.0498	0.0031
T06-09-1 - 11	0.453	0.017	0.0712	0.0035	0.475	0.021	0.0819	0.0045
T06-09-1 - 12	0.467	0.015	0.0686	0.0037	0.46	0.02	0.0668	0.0036
T06-09-1 - 13	0.491	0.017	0.0686	0.0034	0.465	0.022	0.069	0.0042
T06-09-1 - 14	0.506	0.018	0.0748	0.004	0.502	0.022	0.0705	0.0038
T06-09-1 - 15	0.476	0.015	0.0703	0.0039	0.489	0.023	0.0682	0.0036
T06-09-1 - 16	0.46	0.017	0.0655	0.0032	0.448	0.021	0.0665	0.0042
T06-09-1 - 17	0.488	0.019	0.072	0.0039	0.507	0.023	0.074	0.004
T06-09-1 - 18	0.498	0.017	0.0717	0.0033	0.49	0.019	0.0708	0.0035
T06-09-1 - 19	0.483	0.015	0.0709	0.0033	0.489	0.02	0.0672	0.0036
T06-09-1 - 20	0.484	0.014	0.0723	0.0042	0.483	0.019	0.0746	0.0036
T06-09-2 - 1	0.46	0.015	0.0713	0.0035	0.509	0.024	0.079	0.0037
T06-09-2 - 2	0.462	0.016	0.0657	0.0036	0.445	0.016	0.059	0.0035
T06-09-2 - 3	0.447	0.015	0.0657	0.0034	0.402	0.018	0.0575	0.0033
T06-09-2 - 4	0.484	0.019	0.0768	0.0034	0.547	0.023	0.0829	0.0053

Supplementary Table 3 continued: Garnet rare earth element compositions measured by LA-ICP-MS

	La_ppm	Error (2SE)	Ce_ppm	Error (2SE)	Pr_ppm	Error (2SE)	Nd_ppm	Error (2SE)	Sm_ppm	Error (2SE)
T06-09-2 - 5	0.0017	0.00079	0.0074	0.0016	0.00177	0.00053	0.0512	0.0068	0.159	0.013
T06-09-2 - 6	0.0039	0.0026	0.0117	0.0035	0.00483	0.00093	0.093	0.01	0.237	0.021
T06-09-2 - 7	0.00176	0.00071	0.0067	0.0014	0.00356	0.0008	0.1	0.012	0.252	0.016
T06-09-2 - 8	0.00243	0.00096	0.0103	0.0023	0.0049	0.001	0.111	0.013	0.289	0.021
T06-09-2 - 9	0.00067	0.0004	0.0045	0.0011	0.00438	0.00095	0.148	0.014	0.289	0.023
T06-09-2 - 10	0.0139	0.0083	0.025	0.012	0.0071	0.0018	0.147	0.013	0.264	0.022
T06-09-2 - 11	0.00121	0.00056	0.0056	0.0011	0.0051	0.001	0.096	0.012	0.232	0.017
T06-09-2 - 12	0.054	0.029	0.067	0.037	0.0084	0.0024	0.104	0.011	0.247	0.02
T06-09-2 - 13	0.0041	0.0017	0.0103	0.0029	0.00413	0.00085	0.0883	0.0099	0.211	0.017
T06-09-2 - 14	0.00098	0.00051	0.0058	0.0016	0.00252	0.00068	0.062	0.0093	0.203	0.016
T06-09-2 - 15	0.00213	0.00089	0.0097	0.003	0.0057	0.0011	0.139	0.014	0.355	0.024
T06-09-2 - 16	0.00048	0.00036	0.00347	0.00084	0.00381	0.00091	0.0831	0.0094	0.266	0.02
T06-09-2 - 17	0.00102	0.00054	0.0051	0.0012	0.0053	0.0012	0.132	0.012	0.239	0.019
T06-09-2 - 18	0.0023	0.00084	0.0062	0.002	0.00207	0.0007	0.0478	0.0082	0.164	0.015
T06-09-2 - 19	0.00258	0.0008	0.0065	0.0012	0.00214	0.00061	0.0478	0.0074	0.16	0.014
T06-09-2 - 20	0.0041	0.0013	0.0129	0.0028	0.00448	0.00093	0.115	0.013	0.241	0.018
T06-09-3 - 1	0.00083	0.00052	0.0071	0.0014	0.00495	0.00099	0.106	0.012	0.237	0.019
T06-09-3 - 2	0.02	0.011	0.025	0.012	0.00364	0.00096	0.0552	0.007	0.205	0.015
T06-09-3 - 3	0.00043	0.00035	0.0043	0.001	0.00245	0.00066	0.047	0.0066	0.17	0.016
T06-09-3 - 4	0.007	0.0042	0.025	0.012	0.0056	0.0017	0.111	0.012	0.284	0.02
T06-09-3 - 5	0.00049	0.00036	0.0039	0.001	0.0025	0.00073	0.076	0.011	0.216	0.016
T06-09-3 - 6	0.00101	0.00056	0.0039	0.0012	0.00203	0.00059	0.0457	0.0092	0.197	0.015
T06-09-3 - 7	0.00144	0.00063	0.0038	0.0011	0.00115	0.00048	0.0308	0.0051	0.121	0.013
T06-09-3 - 8	BLOD	BLOD	0.00302	0.00078	0.00312	0.00075	0.0594	0.0074	0.178	0.014
T06-09-3 - 9	0.00061	0.00039	0.00319	0.00082	0.00383	0.00095	0.11	0.013	0.252	0.017
T06-09-3 - 10	0.00088	0.00045	0.0046	0.0011	0.00277	0.00079	0.0568	0.0072	0.19	0.016
T06-09-3 - 11	0.0066	0.0013	0.0176	0.0021	0.0035	0.00093	0.0625	0.0084	0.181	0.016
T06-09-3 - 12	0.00105	0.00048	0.0057	0.0013	0.00352	0.00072	0.091	0.01	0.223	0.019
T06-09-3 - 13	0.00152	0.00064	0.0053	0.0011	0.00214	0.00063	0.0708	0.0096	0.197	0.017
T06-09-3 - 14	0.00177	0.00074	0.0085	0.0015	0.00408	0.00098	0.098	0.012	0.243	0.019
T06-09-3 - 15	0.00055	0.00036	0.0062	0.0013	0.0061	0.001	0.158	0.014	0.197	0.016
T06-09-3 - 16	0.00082	0.00042	0.00409	0.00084	0.00322	0.00084	0.0769	0.0085	0.214	0.014
T06-09-3 - 17	0.0022	0.0012	0.0058	0.0022	0.00285	0.00074	0.0747	0.0085	0.198	0.014
T06-09-3 - 18	BLOD	BLOD	0.0078	0.0014	0.0071	0.0012	0.156	0.012	0.263	0.019
T06-09-3 - 19	0.00047	0.00035	0.0036	0.00093	0.00384	0.00083	0.092	0.01	0.241	0.016
T06-09-3 - 20	0.0008	0.00046	0.00327	0.00095	0.00245	0.00071	0.0637	0.0087	0.179	0.019
T06-09-4 - 1	0.0073	0.0057	0.0151	0.0089	0.0043	0.001	0.0917	0.009	0.242	0.019
T06-09-4 - 2	0.044	0.025	0.047	0.026	0.0045	0.0013	0.0713	0.0087	0.238	0.02
T06-09-4 - 3	0.0299	0.0097	0.084	0.026	0.0107	0.0031	0.071	0.015	0.14	0.016
T06-09-4 - 4	0.00059	0.00038	0.00306	0.00098	0.00346	0.00075	0.094	0.011	0.247	0.019
T06-09-4 - 5	0.00197	0.00066	0.0072	0.0014	0.00189	0.00059	0.0489	0.0077	0.16	0.015
T06-09-4 - 6	0.00049	0.00037	0.004	0.0011	0.00332	0.00076	0.096	0.012	0.25	0.019
T06-09-4 - 7	0.00104	0.00053	0.0038	0.0011	0.00191	0.00064	0.0388	0.0066	0.184	0.017
T06-09-4 - 8	0.00148	0.00062	0.007	0.0013	0.00364	0.00082	0.069	0.0082	0.238	0.022
T06-09-4 - 9	0.0023	0.00081	0.0103	0.002	0.00332	0.00083	0.071	0.01	0.25	0.021
T06-09-4 - 10	0.00081	0.00047	0.0073	0.0013	0.00461	0.00095	0.105	0.011	0.254	0.021
T06-09-4 - 11	0.00071	0.00043	0.0042	0.001	0.00278	0.00078	0.0556	0.0074	0.186	0.019
T06-09-4 - 12	0.00088	0.00045	0.0051	0.0011	0.00134	0.00052	0.0351	0.0069	0.124	0.013
T06-09-4 - 13	0.0089	0.0016	0.0274	0.0025	0.0089	0.0012	0.156	0.011	0.259	0.019
T06-09-4 - 14	0.0096	0.0018	0.0287	0.0031	0.0059	0.0014	0.1023	0.0094	0.259	0.018

Supplementary Table 3 continued: Garnet rare earth element compositions measured by LA-ICP-MS

	Eu_ppm	Error (2SE)	Gd_ppm	Error (2SE)	Tb_ppm	Error (2SE)	Dy_ppm	Error (2SE)	Ho_ppm	Error (2SE)
T06-09-2 - 5	0.0876	0.0054	0.539	0.024	0.1118	0.0043	0.849	0.025	0.1706	0.0049
T06-09-2 - 6	0.1284	0.0058	0.534	0.028	0.0912	0.0042	0.708	0.028	0.1521	0.005
T06-09-2 - 7	0.1313	0.0073	0.477	0.027	0.088	0.0038	0.682	0.028	0.1436	0.0062
T06-09-2 - 8	0.1443	0.0082	0.58	0.03	0.1047	0.0042	0.748	0.025	0.1688	0.0053
T06-09-2 - 9	0.1381	0.0066	0.532	0.027	0.0975	0.0041	0.738	0.023	0.1628	0.0049
T06-09-2 - 10	0.121	0.0063	0.465	0.026	0.0952	0.0041	0.774	0.023	0.1829	0.0067
T06-09-2 - 11	0.1201	0.0065	0.534	0.027	0.0985	0.0048	0.724	0.025	0.1592	0.0059
T06-09-2 - 12	0.1262	0.0062	0.526	0.028	0.1002	0.0043	0.78	0.025	0.1796	0.0058
T06-09-2 - 13	0.1108	0.0064	0.482	0.024	0.093	0.0043	0.68	0.024	0.1516	0.0063
T06-09-2 - 14	0.1113	0.007	0.509	0.026	0.0955	0.0042	0.714	0.024	0.1553	0.0048
T06-09-2 - 15	0.1635	0.0079	0.632	0.031	0.1127	0.0047	0.774	0.03	0.1596	0.0052
T06-09-2 - 16	0.1189	0.0053	0.515	0.027	0.0994	0.0037	0.736	0.025	0.1583	0.006
T06-09-2 - 17	0.1216	0.006	0.525	0.027	0.0936	0.0039	0.666	0.027	0.1284	0.0043
T06-09-2 - 18	0.0991	0.0053	0.503	0.028	0.1029	0.0039	0.757	0.029	0.1582	0.0048
T06-09-2 - 19	0.1013	0.0072	0.525	0.025	0.1003	0.0041	0.72	0.022	0.147	0.0045
T06-09-2 - 20	0.1214	0.0064	0.501	0.026	0.0878	0.0043	0.611	0.021	0.1273	0.0046
T06-09-3 - 1	0.1205	0.0059	0.505	0.026	0.0961	0.0039	0.719	0.027	0.1492	0.0058
T06-09-3 - 2	0.1064	0.0058	0.539	0.027	0.1025	0.0049	0.745	0.024	0.1592	0.0061
T06-09-3 - 3	0.1002	0.0056	0.496	0.025	0.0938	0.0041	0.648	0.024	0.1439	0.0063
T06-09-3 - 4	0.1472	0.0065	0.641	0.026	0.1073	0.0042	0.745	0.027	0.1502	0.0044
T06-09-3 - 5	0.1086	0.0068	0.501	0.027	0.0936	0.0038	0.668	0.024	0.1354	0.0051
T06-09-3 - 6	0.1085	0.0065	0.516	0.026	0.0968	0.0045	0.709	0.022	0.1509	0.0053
T06-09-3 - 7	0.0759	0.0053	0.502	0.027	0.0977	0.0045	0.709	0.026	0.1527	0.0057
T06-09-3 - 8	0.0862	0.0053	0.631	0.028	0.1333	0.0053	1.016	0.039	0.2083	0.0073
T06-09-3 - 9	0.1283	0.0078	0.517	0.023	0.0966	0.0037	0.701	0.023	0.1573	0.0051
T06-09-3 - 10	0.0999	0.0057	0.642	0.038	0.1112	0.0048	0.804	0.028	0.163	0.0058
T06-09-3 - 11	0.0871	0.0054	0.577	0.028	0.1229	0.0046	0.889	0.023	0.1849	0.0058
T06-09-3 - 12	0.1133	0.0059	0.584	0.026	0.1085	0.004	0.771	0.024	0.1643	0.0055
T06-09-3 - 13	0.0959	0.0059	0.531	0.026	0.099	0.005	0.725	0.031	0.1567	0.0061
T06-09-3 - 14	0.1225	0.0057	0.496	0.023	0.0934	0.0046	0.682	0.02	0.1491	0.0052
T06-09-3 - 15	0.0853	0.0057	0.318	0.02	0.0885	0.004	0.845	0.026	0.201	0.0067
T06-09-3 - 16	0.1142	0.0074	0.525	0.028	0.0962	0.0047	0.693	0.027	0.1416	0.0053
T06-09-3 - 17	0.0988	0.0059	0.556	0.027	0.1083	0.0045	0.781	0.026	0.1638	0.0049
T06-09-3 - 18	0.1285	0.0067	0.546	0.024	0.1125	0.0053	0.844	0.028	0.1744	0.0061
T06-09-3 - 19	0.1169	0.0063	0.541	0.026	0.0972	0.0044	0.677	0.025	0.1349	0.0051
T06-09-3 - 20	0.1001	0.0065	0.625	0.035	0.1263	0.0057	0.887	0.028	0.19	0.0067
T06-09-4 - 1	0.1153	0.0074	0.459	0.022	0.0802	0.0036	0.577	0.024	0.1199	0.0048
T06-09-4 - 2	0.1316	0.0065	0.643	0.031	0.1186	0.005	0.75	0.028	0.1464	0.0054
T06-09-4 - 3	0.0853	0.006	0.692	0.025	0.1505	0.0048	1.138	0.034	0.2282	0.0077
T06-09-4 - 4	0.123	0.0065	0.526	0.024	0.099	0.005	0.694	0.02	0.1507	0.0057
T06-09-4 - 5	0.088	0.0057	0.525	0.024	0.1157	0.0051	0.866	0.031	0.1802	0.0063
T06-09-4 - 6	0.115	0.0057	0.519	0.029	0.0926	0.0044	0.655	0.022	0.143	0.0058
T06-09-4 - 7	0.0939	0.0058	0.566	0.03	0.1192	0.0044	0.852	0.027	0.1768	0.0064
T06-09-4 - 8	0.1146	0.0067	0.521	0.025	0.0964	0.0044	0.713	0.027	0.1613	0.006
T06-09-4 - 9	0.132	0.0071	0.569	0.027	0.1054	0.0043	0.749	0.024	0.1531	0.0062
T06-09-4 - 10	0.1244	0.006	0.605	0.028	0.0976	0.0041	0.718	0.031	0.1389	0.0047
T06-09-4 - 11	0.1079	0.0064	0.578	0.027	0.1097	0.0055	0.779	0.032	0.1558	0.0061
T06-09-4 - 12	0.0856	0.0064	0.607	0.025	0.1333	0.0048	0.993	0.034	0.2018	0.0057
T06-09-4 - 13	0.1253	0.0073	0.502	0.022	0.088	0.0038	0.631	0.02	0.1244	0.0046
T06-09-4 - 14	0.1262	0.0066	0.503	0.031	0.0982	0.0044	0.679	0.025	0.1526	0.0061

Supplementary Table 3 continued: Garnet rare earth element compositions measured by LA-ICP-MS

	Er_ppm	Error (2SE)	Tm_ppm	Error (2SE)	Yb_ppm	Error (2SE)	Lu_ppm	Error (2SE)
T06-09-2 - 5	0.515	0.017	0.0716	0.0036	0.46	0.02	0.0676	0.004
T06-09-2 - 6	0.474	0.016	0.0711	0.0036	0.443	0.022	0.0669	0.0039
T06-09-2 - 7	0.404	0.015	0.061	0.0037	0.4	0.017	0.059	0.0038
T06-09-2 - 8	0.52	0.021	0.0756	0.003	0.532	0.019	0.0764	0.004
T06-09-2 - 9	0.514	0.015	0.0724	0.0041	0.493	0.023	0.0716	0.0033
T06-09-2 - 10	0.583	0.022	0.0933	0.0043	0.643	0.026	0.0978	0.0044
T06-09-2 - 11	0.468	0.015	0.0673	0.0035	0.461	0.019	0.0663	0.0043
T06-09-2 - 12	0.543	0.018	0.0795	0.0042	0.524	0.023	0.0754	0.0036
T06-09-2 - 13	0.456	0.015	0.0681	0.0045	0.461	0.019	0.071	0.0037
T06-09-2 - 14	0.439	0.016	0.0652	0.0042	0.437	0.02	0.0612	0.0035
T06-09-2 - 15	0.486	0.019	0.0723	0.0043	0.489	0.016	0.072	0.0037
T06-09-2 - 16	0.468	0.017	0.0634	0.0035	0.49	0.02	0.0717	0.0035
T06-09-2 - 17	0.333	0.014	0.0437	0.0029	0.267	0.017	0.0335	0.0022
T06-09-2 - 18	0.485	0.015	0.0675	0.0033	0.478	0.022	0.07	0.004
T06-09-2 - 19	0.456	0.016	0.0678	0.0038	0.434	0.018	0.0661	0.0036
T06-09-2 - 20	0.398	0.016	0.0672	0.003	0.485	0.02	0.0781	0.0043
T06-09-3 - 1	0.45	0.015	0.0674	0.0034	0.474	0.024	0.0633	0.0031
T06-09-3 - 2	0.457	0.016	0.0684	0.0037	0.456	0.018	0.069	0.003
T06-09-3 - 3	0.403	0.018	0.0593	0.0031	0.394	0.021	0.054	0.0033
T06-09-3 - 4	0.413	0.018	0.0578	0.0032	0.368	0.016	0.0505	0.0035
T06-09-3 - 5	0.386	0.014	0.0522	0.0031	0.374	0.014	0.0505	0.0034
T06-09-3 - 6	0.465	0.017	0.069	0.0043	0.433	0.024	0.0655	0.0034
T06-09-3 - 7	0.467	0.018	0.0696	0.0038	0.46	0.019	0.0657	0.0036
T06-09-3 - 8	0.568	0.023	0.0787	0.0043	0.493	0.026	0.0707	0.0039
T06-09-3 - 9	0.47	0.016	0.0685	0.0035	0.458	0.017	0.0669	0.0037
T06-09-3 - 10	0.475	0.018	0.0696	0.0034	0.46	0.019	0.067	0.0037
T06-09-3 - 11	0.531	0.02	0.0742	0.0035	0.509	0.021	0.0745	0.0041
T06-09-3 - 12	0.469	0.017	0.0679	0.0032	0.478	0.018	0.0732	0.0039
T06-09-3 - 13	0.47	0.016	0.0681	0.0035	0.456	0.02	0.0645	0.004
T06-09-3 - 14	0.43	0.012	0.0646	0.0036	0.426	0.018	0.0644	0.0036
T06-09-3 - 15	0.637	0.021	0.0924	0.0046	0.659	0.027	0.099	0.0046
T06-09-3 - 16	0.389	0.015	0.0549	0.0031	0.358	0.02	0.05	0.0031
T06-09-3 - 17	0.47	0.017	0.0715	0.0038	0.453	0.022	0.0682	0.0038
T06-09-3 - 18	0.5	0.016	0.066	0.0045	0.438	0.021	0.062	0.004
T06-09-3 - 19	0.378	0.013	0.0508	0.0028	0.364	0.019	0.0541	0.003
T06-09-3 - 20	0.558	0.023	0.088	0.0042	0.577	0.026	0.0856	0.0042
T06-09-4 - 1	0.329	0.014	0.0469	0.003	0.32	0.018	0.0439	0.0031
T06-09-4 - 2	0.422	0.013	0.0575	0.0034	0.372	0.019	0.0555	0.0038
T06-09-4 - 3	0.621	0.021	0.0863	0.0041	0.529	0.023	0.0763	0.0034
T06-09-4 - 4	0.461	0.016	0.0669	0.0036	0.422	0.02	0.0636	0.0039
T06-09-4 - 5	0.543	0.02	0.0816	0.0045	0.537	0.027	0.0805	0.0039
T06-09-4 - 6	0.428	0.016	0.0614	0.0035	0.412	0.018	0.0657	0.0037
T06-09-4 - 7	0.488	0.018	0.0696	0.0033	0.436	0.019	0.0634	0.003
T06-09-4 - 8	0.468	0.021	0.0694	0.0032	0.472	0.02	0.066	0.0046
T06-09-4 - 9	0.42	0.019	0.0607	0.0036	0.403	0.021	0.06	0.0036
T06-09-4 - 10	0.384	0.014	0.0523	0.0032	0.353	0.016	0.0498	0.0033
T06-09-4 - 11	0.45	0.015	0.0647	0.0031	0.431	0.022	0.0594	0.0029
T06-09-4 - 12	0.577	0.021	0.0786	0.0041	0.51	0.024	0.0756	0.0039
T06-09-4 - 13	0.336	0.016	0.0448	0.0034	0.289	0.015	0.0401	0.0031
T06-09-4 - 14	0.472	0.017	0.0729	0.004	0.555	0.021	0.0797	0.0046

Supplementary Table 3 continued: Garnet rare earth element compositions measured by LA-ICP-MS

	La_ppm	Error (2SE)	Ce_ppm	Error (2SE)	Pr_ppm	Error (2SE)	Nd_ppm	Error (2SE)	Sm_ppm	Error (2SE)
T06-09-4 - 15	0.00119	0.00052	0.0051	0.0014	0.00328	0.00088	0.0662	0.0086	0.197	0.018
T06-09-4 - 16	0.001	0.00046	0.0047	0.0011	0.00231	0.00066	0.0418	0.0081	0.171	0.015
T06-09-4 - 17	0.0097	0.0016	0.0256	0.0024	0.00424	0.00091	0.049	0.0085	0.154	0.017
T06-09-4 - 18	0.00085	0.00042	0.0052	0.0013	0.00314	0.00082	0.0597	0.0087	0.202	0.017
T06-09-4 - 19	0.0066	0.0039	0.021	0.01	0.00474	0.00092	0.102	0.012	0.241	0.019
T06-09-4 - 20	0.00077	0.00044	0.0039	0.001	0.00217	0.00066	0.0628	0.0099	0.186	0.014
	Eu_ppm	Error (2SE)	Gd_ppm	Error (2SE)	Tb_ppm	Error (2SE)	Dy_ppm	Error (2SE)	Ho_ppm	Error (2SE)
T06-09-4 - 15	0.0994	0.007	0.627	0.03	0.1126	0.0048	0.761	0.028	0.1609	0.005
T06-09-4 - 16	0.0942	0.0054	0.648	0.031	0.123	0.0051	0.81	0.03	0.1571	0.006
T06-09-4 - 17	0.0814	0.0052	0.608	0.031	0.1412	0.0056	1.169	0.036	0.2263	0.0073
T06-09-4 - 18	0.1091	0.0061	0.531	0.024	0.1029	0.0043	0.747	0.022	0.1755	0.0064
T06-09-4 - 19	0.1202	0.0062	0.535	0.028	0.1085	0.0051	0.767	0.027	0.1635	0.0064
T06-09-4 - 20	0.0949	0.0067	0.571	0.031	0.1145	0.0049	0.844	0.025	0.1835	0.0069
	Er_ppm	Error (2SE)	Tm_ppm	Error (2SE)	Yb_ppm	Error (2SE)	Lu_ppm	Error (2SE)		
T06-09-4 - 15	0.465	0.017	0.0645	0.0037	0.423	0.022	0.0622	0.0038		
T06-09-4 - 16	0.429	0.015	0.0575	0.0036	0.392	0.019	0.0544	0.0038		
T06-09-4 - 17	0.637	0.02	0.0873	0.0042	0.555	0.019	0.0812	0.0041		
T06-09-4 - 18	0.509	0.016	0.0766	0.0038	0.528	0.022	0.0796	0.0041		
T06-09-4 - 19	0.474	0.018	0.0641	0.0034	0.426	0.018	0.0652	0.0037		
T06-09-4 - 20	0.55	0.019	0.0814	0.0033	0.556	0.023	0.0793	0.0043		

Supplementary Table 4: Lu–Hf geochronology results, measured by TIMS. Italized analyses were not used in the age calculations.

Sample ID	Fraction	mg	Lu ppm	Hf ppm	176Lu/177Hf	2s	176Hf/177Hf	2s
T01-40	G1	73.70	1.877	0.097	2.7984	0.0140	0.389373	0.000011
T01-40	G2	73.16	1.835	0.081	3.2606	0.0163	0.407197	0.000016
T01-40	G3	71.66	1.561	0.097	2.3226	0.0116	0.371100	0.000014
T01-40	G4	75.74	1.572	0.129	1.7406	0.0087	0.320728	0.000006
T01-40	*WR*	*100.48*	*0.296*	*0.931*	*0.0450*	*0.0002*	*0.284935*	*0.000003*
T06-09	G1	72.66	1.114	0.150	1.0606	0.0053	0.321538	0.000009
T06-09	G2	79.34	1.023	0.158	0.9201	0.0046	0.316318	0.000009
T06-09	G3	72.08	0.996	0.169	0.8389	0.0042	0.313279	0.000008
T06-09	*G4*	*69.65*	*1.235*	*0.137*	*1.2930*	*0.0065*	*0.366087*	*0.000012*
T06-09	WR	99.91	0.757	0.726	0.1473	0.0007	0.284638	0.000004

Supplementary Table 5: U-Pb and trace element compostions of zircons in T01-40 and T06-09.

Included in age calculations		Final U238/ Pb206 mean	Final U238/ Pb206 2SE(prop)	Final Pb207/ U235 mean	Final Pb207/ U235 2SE(prop)	Final Pb207/ Pb206 mean	Final Pb207/ Pb206 2SE(prop)
	T01-40						
	T0140 - 1	2.85701223	0.175643606	6.220908851	0.419629835	0.124797357	0.001856929
	T0140 - 2	2.874535237	0.21827807	6.22919818	0.498249205	0.123447317	0.002323776
	T0140 - 3	2.894284877	0.215299468	5.981158474	0.377013222	0.123755742	0.00272082
	T0140 - 4	2.869526808	0.182006391	5.99911604	0.365101983	0.12391727	0.003425404
	T0140 - 5	2.806814291	0.135325441	6.265780778	0.308439044	0.124781609	0.001871988
	T0140 - 6	2.814335409	0.245923318	6.187676999	0.472139816	0.124048419	0.002796337
	T0140 - 7	2.723307121	0.052770457	6.324515634	0.155959094	0.123492695	0.000915184
x	T0140 - 8	3.04682584	0.221565011	5.960609423	0.497700355	0.126424183	0.003143075
	T0140 - 10	2.610824722	0.198726736	6.841407262	0.706553147	0.125434789	0.002558645
	T0140 - 11	2.762681319	0.111721634	6.309457401	0.273261966	0.124106025	0.002338317
	T0140 - 12	2.800719312	0.201832744	6.320993167	0.449388042	0.126628748	0.002571038
	T0140 - 14	2.72791006	0.145805403	6.336131756	0.376479249	0.123122203	0.001924705
	T0140 - 15	2.776146943	0.122532642	6.273600508	0.405294283	0.124315317	0.002358604
	T0140 - 16	2.778594121	0.074097225	6.139431487	0.185112455	0.123211103	0.001209263
	T0140 - 17	2.761436961	0.272265435	6.335153079	0.631697322	0.124324326	0.003334937
	T0140 - 18	2.727718486	0.201293865	6.338352175	0.548690656	0.12122793	0.00298196
	T0140 - 19	2.675939732	0.270330154	6.617353132	0.799117919	0.121089315	0.003214944
	T0140 - 21	2.814269144	0.127991202	6.114480513	0.354119326	0.122898421	0.002042037
	T0140 - 22	2.769407882	0.180596724	6.489928758	0.440797065	0.127134806	0.002957782
	T0140 - 23	2.693685808	0.26318056	6.502699418	0.556402066	0.12452408	0.003987046
	T0140 - 24	2.504339649	0.22611277	7.009791148	0.581078022	0.125446317	0.003618943
	T0140 - 25	2.662189337	0.259894882	6.973374278	0.819362913	0.126032199	0.003485613
	T0140 - 26	2.835586256	0.187745738	6.310391175	0.496864248	0.12587269	0.002180368
	T0140 - 27	2.820050102	0.159200267	6.259105532	0.385448756	0.125244218	0.002363908
	T0140 - 28	2.781279504	0.178622315	6.353930474	0.419900413	0.125141907	0.002896014
	T0140 - 29	2.866038514	0.325855693	6.465606872	0.74699129	0.124503277	0.002654699
x	T0140 - 30	2.988189015	0.191863756	6.021321267	0.451397672	0.12692386	0.002847271
	T0140 - 31	2.826890261	0.208057903	6.132654368	0.524517135	0.120385963	0.002435089
	T0140 - 33	2.753307574	0.316869817	6.819501107	0.919143846	0.12450637	0.003646808
	T0140 - 34	2.646091448	0.206945573	6.403463095	0.423159899	0.122653528	0.002693683
	T0140 - 35	2.728656243	0.057580228	6.349409977	0.177323856	0.125027358	0.001326709
	T0140 - 36	2.788508613	0.117918318	6.130028597	0.22301021	0.123808343	0.001180288
	T0140 - 37	2.700416672	0.328278713	6.605245189	0.76540834	0.123097193	0.003596045
	T0140 - 38	2.843562164	0.296770853	6.743812674	0.874227621	0.128098139	0.002857626
	T0140 - 41	2.70220757	0.234275923	6.868519397	0.773869303	0.127326039	0.00406862
	T0140 - 42	2.856893226	0.196289744	6.122135885	0.512168888	0.125867098	0.004116989
x	T0140 - 43	2.817842398	0.054092634	6.208541579	0.187334508	0.125136893	0.000923663
x	T0140 - 44	2.832739099	0.060959243	6.099806138	0.176440875	0.124719556	0.001317382
	T0140 - 45	2.841392657	0.1353869	6.163951859	0.284302702	0.125387917	0.002562533
	T0140 - 46	2.866906536	0.22676517	6.079711167	0.466501598	0.124987181	0.002835493
	T0140 - 47	2.759514186	0.327649201	6.894644471	0.825641424	0.127250526	0.003371236
	T0140 - 48	2.669064669	0.184795673	6.435769684	0.4403254	0.126909527	0.002737428
	T0140 - 50	2.855451947	0.231243413	6.298570844	0.634981274	0.125201518	0.002472045
	T0140 - 51	2.698830528	0.157715213	6.482957003	0.515769524	0.12686133	0.003033344
	T0140 - 52	2.655396318	0.462171322	6.932464323	1.057472814	0.124054441	0.003184109
	T0140 - 53	3.0119259	0.352268548	6.21662271	0.712539006	0.125631261	0.002871925
	T0140 - 54	2.867721153	0.236971237	6.328415363	0.599526887	0.125778639	0.002909872
	T0140 - 55	2.83267935	0.228732255	6.281300991	0.550593229	0.123864907	0.00268632
	T0140 - 56	2.999159269	0.353919816	6.029993182	0.708524849	0.12569327	0.004132953

Supplementary Table 5 continued: U-Pb and trace element compostions of zircons in T01-40 and T06-09.

	Final U/Th mean	Final U/Th 2SE(int)	Approx U PPM mean	Approx U PPM 2SE(int)	Approx Th PPM mean	Approx Th PPM 2SE(int)
T01-40						
T0140 - 1	5.492373384	0.909560983	8.074193544	0.554004803	1.690516507	0.258008751
T0140 - 2	4.918180516	2.567480595	5.89466433	0.422617631	1.239847533	0.317566553
T0140 - 3	6.000160081	1.665621121	6.824677025	0.418323978	1.360052789	0.225390451
T0140 - 4	11.62106738	6.612630601	5.435370957	0.426133421	0.87158508	0.248417396
T0140 - 5	6.387992767	0.834822157	11.07534149	0.642294038	1.89288916	0.241497299
T0140 - 6	6.773892987	2.496101853	5.754889588	0.670167014	0.650526677	0.237297164
T0140 - 7	1.269223073	0.031543309	47.07756842	1.661586065	36.96748953	1.077242754
T0140 - 8	7.317390251	6.055559719	5.406110839	0.441361028	0.742466183	0.299531606
T0140 - 10	4.142940892	3.516894205	6.082972595	0.596356145	1.19305349	0.315409775
T0140 - 11	4.026238907	0.477529786	11.52610046	0.862260372	2.986150548	0.247334096
T0140 - 12	5.584078357	2.146068296	9.483505178	1.848278152	1.429502461	0.449492876
T0140 - 14	7.632247143	1.703465567	10.41376394	1.26527753	1.592955123	0.326982472
T0140 - 15	6.147291429	3.014950213	7.358206322	0.37753475	1.248709631	0.314343145
T0140 - 16	4.833025184	0.368072028	24.66542994	1.245025224	5.191974381	0.497384819
T0140 - 17	2.911824108	0.61562455	6.658634775	0.528682898	2.478411342	0.33322763
T0140 - 18	6.641081222	5.27243158	5.161895454	0.40933368	1.165125469	0.304979617
T0140 - 19	5.709580732	1.19762382	5.184386333	0.557059086	1.035949993	0.253251724
T0140 - 21	8.330630346	3.262331797	10.39378868	0.908097797	1.577132174	0.29739971
T0140 - 22	3.293252548	1.871898667	6.895189278	0.45420255	1.790032015	0.348575522
T0140 - 23	-1.583496766	7.150287431	4.15119036	0.435030691	0.688150379	0.266915184
T0140 - 24	3.043549728	8.310764389	3.517807302	0.475889029	0.551086134	0.289712141
T0140 - 25	8.126078482	10.34516899	5.26023059	0.617179824	0.830550099	0.25849446
T0140 - 26	4.163167802	3.980101987	5.288816882	0.469231481	0.983688303	0.232075066
T0140 - 27	11.05174888	6.60108634	7.292870179	0.472636314	1.260213576	0.303030561
T0140 - 28	4.447428357	0.620378342	7.115299223	0.4850671	1.633117266	0.237344533
T0140 - 29	6.236453714	4.861128287	4.725733658	0.5551109	0.803054522	0.314418481
T0140 - 30	8.770038547	3.252441556	6.566504696	0.589404139	1.174037034	0.304144069
T0140 - 31	8.611956096	13.78821505	4.710421006	0.353670367	0.704219444	0.261173647
T0140 - 33	3.819928143	13.62589652	4.278431683	0.502028491	0.636471427	0.289988055
T0140 - 34	3.753313621	0.799250517	6.811539824	0.487636186	2.033390167	0.291340622
T0140 - 35	3.676949675	0.236322427	22.92102304	1.051466288	6.095214776	0.460599911
T0140 - 36	4.96455725	0.492278292	15.13030886	0.973747666	3.168900661	0.295515917
T0140 - 37	3.337463121	7.05544075	4.20570607	0.560799572	0.639813539	0.262627397
T0140 - 38	3.640370278	5.85332786	4.118983556	0.455521297	0.877839388	0.29241597
T0140 - 41	6.542287478	6.62183584	4.309228896	0.50218696	0.930486788	0.303937886
T0140 - 42	5.425654688	3.081765943	4.913512137	0.457039317	0.958320205	0.392292409
T0140 - 43	3.531760199	0.191859816	48.22586909	3.239003054	14.16795151	1.678007759
T0140 - 44	4.398959633	0.283846547	26.08874247	1.458251566	5.969695153	0.600115924
T0140 - 45	4.879350655	0.884487065	8.799029702	0.344546555	1.928835721	0.280652022
T0140 - 46	-15.37894589	50.41357216	5.442269157	0.546624913	0.046377924	0.219902423
T0140 - 47	3.109503297	4.627666494	4.174262504	0.577920708	0.07934796	0.2614735
T0140 - 48	4.488615065	1.980915529	8.693079449	2.018325354	1.804081114	0.564682405
T0140 - 50	6.201461015	1.33946038	5.991486522	0.489888324	1.141382924	0.22097151
T0140 - 51	9.074094549	8.226904573	5.133687552	0.312485303	0.507502141	0.274360225
T0140 - 52	2.078252618	3.801883205	3.516355654	0.61848168	0.709987861	0.291405998
T0140 - 53	8.41254762	8.264851757	4.510105937	0.493330057	0.631547503	0.190842947
T0140 - 54	3.694275756	4.555473824	5.788346827	0.521656582	0.932067439	0.259101034
T0140 - 55	2.720869528	3.73758633	5.621868498	0.504585281	0.818040616	0.2732308
T0140 - 56	8.333871094	10.87188947	4.749960926	0.569842548	0.663126107	0.309416551

Supplementary Table 5 continued: U-Pb and trace element compostions of zircons in T01-40 and T06-09.

	Ti ppm m49	2SE	Y ppm m89	2SE	S m p p m m147	2SE	Eu ppm m153	2SE	G d p p m m157	2SE	Tb ppm m159	2SE	D y p p m m163	2SE
T01-40														
T0140 - 1	6.4	2.5	35.2	1.3	0.12	0.1	0.126	0.052	1.25	0.31	0.42	0.065	4.9	0.47
T0140 - 2	7.8	1.9	30.57	0.95	0	1	0.058	0.034	0.8	0.23	0.264	0.066	3.43	0.37
T0140 - 3	6.1	2.2	25.21	0.8	0	1	0.056	0.033	0.82	0.23	0.233	0.054	2.83	0.34
T0140 - 4	4	1.7	25.77	0.65	0	1	0	1	0.68	0.2	0.23	0.046	2.66	0.34
T0140 - 5	4.2	2	13.65	0.55	0	1	0.052	0.031	0.13	0.12	0.152	0.041	1.14	0.25
T0140 - 6	4.8	2	12.65	0.55	0	1	0.041	0.028	0.25	0.12	0.06	0.026	0.74	0.17
T0140 - 7	6.3	2.2	32	1	0.97	0.21	0.428	0.089	3.26	0.45	0.83	0.11	5.8	0.59
T0140 - 8	0.2	1.3	10.31	0.37	0	1	0	1	0.16	0.1	0.032	0.018	0.9	0.25
T0140 - 10	6.3	2.2	26.8	1.1	0	1	0.053	0.032	0.75	0.25	0.273	0.062	2.79	0.34
T0140 - 11	4.6	1.8	27.11	0.74	0.14	0.11	0.177	0.064	1.64	0.32	0.557	0.092	3.95	0.44
T0140 - 12	8	2.4	35.3	1.7	0	1	0.104	0.047	0.66	0.21	0.308	0.048	3.4	0.41
T0140 - 14	4.2	1.9	19.3	1.1	0	1	0.069	0.036	0.64	0.22	0.189	0.042	1.88	0.28
T0140 - 15	5.6	2.4	22.81	0.81	0	1	0.024	0.023	0.55	0.2	0.208	0.05	2.14	0.36
T0140 - 16	3.7	2.2	19.07	0.83	0.39	0.17	0.179	0.065	1.91	0.36	0.557	0.07	3.87	0.55
T0140 - 17	6	3	21.74	0.94	0	1	0	1	0.33	0.16	0.123	0.039	1.87	0.26
T0140 - 18	7.7	2.7	32.6	1	0	1	0.052	0.033	0.67	0.19	0.252	0.055	2.93	0.39
T0140 - 19	1.8	1.6	15.65	0.49	0	1	0	1	0.13	0.1	0.086	0.03	1.25	0.26
T0140 - 21	7.2	2.7	19.63	0.76	0.072	0.081	0.114	0.054	0.47	0.16	0.177	0.047	1.86	0.29
T0140 - 22	5	2.2	34.18	0.95	0	1	0.089	0.037	1.03	0.24	0.295	0.053	3.04	0.34
T0140 - 23	2.2	2.3	12.17	0.65	0	1	0.013	0.018	0.2	0.13	0.131	0.039	1.27	0.22
T0140 - 24	3.7	2.1	16.34	0.76	0	1	0.041	0.029	0.45	0.17	0.086	0.034	1.49	0.33
T0140 - 25	3.9	1.8	20.18	0.84	0	1	0.024	0.023	0.32	0.15	0.145	0.034	1.94	0.36
T0140 - 26	9.1	2.3	24.53	0.84	0	1	0.069	0.039	0.49	0.19	0.173	0.047	2.35	0.31
T0140 - 27	2.8	1.8	25.15	0.76	0	1	0.011	0.015	0.6	0.24	0.199	0.047	2.27	0.27
T0140 - 28	4.9	2.6	33.3	1.1	0.14	0.11	0.056	0.031	0.93	0.24	0.388	0.065	4.44	0.44
T0140 - 29	3.1	2.3	31.27	0.88	0	1	0.047	0.03	0.7	0.23	0.283	0.049	2.65	0.35
T0140 - 30	7.7	2.7	33.1	1.4	0.16	0.11	0.073	0.036	0.8	0.21	0.283	0.05	3.22	0.41
T0140 - 31	2.3	1.6	13.42	0.59	0	1	0.006	0.012	0.17	0.11	0.048	0.023	0.91	0.26
T0140 - 33	3	1.5	23.7	1.2	0.022	0.045	0.084	0.037	0.51	0.19	0.169	0.048	1.86	0.31
T0140 - 34	5	1.9	30.1	1.3	0	1	0.054	0.032	1.13	0.28	0.309	0.07	3.27	0.37
T0140 - 35	4.4	2.2	60.3	1.3	1.18	0.35	0.47	0.11	5.62	0.58	1.57	0.15	12.41	0.77
T0140 - 36	7.4	3	32.3	1.1	0	1	0.131	0.052	0.81	0.24	0.281	0.059	3.49	0.43
T0140 - 37	3.6	1.8	11.02	0.52	0	1	0	1	0.17	0.11	0.082	0.028	0.93	0.22
T0140 - 38	7.1	2.7	31.39	0.78	0	1	0.08	0.037	0.65	0.21	0.279	0.059	3.2	0.33
T0140 - 41	2	1.6	29.31	0.68	0	1	0.051	0.031	0.39	0.15	0.232	0.053	2.62	0.35
T0140 - 42	4.2	2.1	21.52	0.95	0	1	0.006	0.011	0.39	0.17	0.179	0.04	1.99	0.31
T0140 - 43	9	3.1	46	1	0.63	0.2	0.323	0.093	3.01	0.49	0.874	0.088	7.57	0.72
T0140 - 44	10.1	3.5	36.3	1.2	0.51	0.21	0.29	0.08	2.62	0.39	0.679	0.076	6.35	0.45
T0140 - 45	6.7	2.6	32.64	0.87	0.065	0.073	0.085	0.037	1.06	0.25	0.385	0.07	3.86	0.5
T0140 - 46	2.9	1.6	38.5	1.4	0	1	0.047	0.03	0.42	0.18	0.251	0.045	3.5	0.38
T0140 - 47	4.8	2.7	31.93	0.99	0	1	0.006	0.011	0.28	0.14	0.168	0.05	2.53	0.36
T0140 - 48	8.1	2.9	27.6	2	0.18	0.12	0.101	0.04	1.44	0.34	0.37	0.071	3.64	0.41
T0140 - 50	1.1	2	17.73	0.95	0	1	0.011	0.016	0.17	0.11	0.122	0.039	1.36	0.26
T0140 - 51	7.5	2.6	40.6	2.8	0	1	0.114	0.039	0.72	0.25	0.364	0.083	4.1	0.51
T0140 - 52	3.7	2.6	7.49	0.42	0	1	0	1	0.18	0.11	0.071	0.027	0.84	0.18
T0140 - 53	6.9	2.6	10.72	0.54	0	1	0.011	0.015	0.18	0.11	0.094	0.03	1.06	0.21
T0140 - 54	5.4	2.4	15.77	0.61	0	1	0.012	0.017	0.3	0.13	0.104	0.038	1.01	0.2
T0140 - 55	3.5	2.4	19.04	0.81	0	1	0.005	0.011	0	1	0.097	0.038	1.5	0.33
T0140 - 56	5	2	27.7	1.5	0	1	0.023	0.022	0.49	0.19	0.157	0.043	2.49	0.33

Supplementary Table 5 continued: U-Pb and trace element compostions of zircons in T01-40 and T06-09.

	Ho ppm m165	2SE	Er ppm m166	2SE	Tm ppm m169	2SE	Yb ppm m173	2SE	Lu ppm m175	2SE	Hf ppm m178	2SE
T01-40												
T0140 - 1	1.27	0.11	3.32	0.38	0.39	0.063	2.49	0.3	0.387	0.067	8640	230
T0140 - 2	0.81	0.11	2.56	0.31	0.401	0.075	3.3	0.55	0.5	0.068	8430	230
T0140 - 3	0.68	0.095	2.47	0.3	0.405	0.078	3.07	0.59	0.475	0.081	8590	190
T0140 - 4	0.72	0.1	2.72	0.25	0.391	0.079	2.9	0.54	0.596	0.084	8440	210
T0140 - 5	0.432	0.065	1.49	0.22	0.377	0.073	2.7	0.45	0.557	0.062	7300	140
T0140 - 6	0.328	0.075	1.1	0.21	0.292	0.058	2.58	0.43	0.412	0.049	8230	190
T0140 - 7	1.03	0.1	2.01	0.25	0.226	0.047	1.6	0.3	0.235	0.048	7250	140
T0140 - 8	0.265	0.052	1.01	0.2	0.165	0.043	1.44	0.26	0.275	0.054	8240	160
T0140 - 10	0.815	0.079	2.21	0.21	0.375	0.056	2.8	0.5	0.472	0.071	8190	180
T0140 - 11	0.76	0.11	2.13	0.29	0.295	0.059	2.35	0.47	0.334	0.059	8030	180
T0140 - 12	1.04	0.11	3.92	0.41	0.805	0.09	6.07	0.61	1.02	0.12	8060	160
T0140 - 14	0.531	0.068	1.89	0.26	0.328	0.059	2.63	0.55	0.448	0.089	8270	210
T0140 - 15	0.67	0.1	2.05	0.23	0.357	0.07	3.09	0.48	0.461	0.064	8180	160
T0140 - 16	0.648	0.093	1.18	0.21	0.095	0.036	0.39	0.2	0.047	0.022	7810	130
T0140 - 17	0.505	0.079	2.41	0.43	0.473	0.078	4.34	0.44	0.6	0.1	8260	140
T0140 - 18	1.09	0.1	3.67	0.39	0.726	0.083	5.86	0.67	1.01	0.12	8430	200
T0140 - 19	0.372	0.073	1.65	0.28	0.347	0.055	2.57	0.56	0.464	0.086	8470	160
T0140 - 21	0.639	0.071	2.03	0.25	0.403	0.052	3.13	0.61	0.502	0.074	7900	180
T0140 - 22	1.02	0.14	3.03	0.3	0.533	0.094	4.76	0.71	0.81	0.11	8870	200
T0140 - 23	0.346	0.065	1	0.19	0.111	0.044	1.51	0.4	0.234	0.038	8400	210
T0140 - 24	0.467	0.097	1.79	0.23	0.266	0.051	2.24	0.38	0.429	0.068	8960	180
T0140 - 25	0.517	0.09	2.08	0.26	0.359	0.056	3.48	0.61	0.478	0.081	8430	120
T0140 - 26	0.638	0.093	2.51	0.3	0.469	0.08	2.97	0.51	0.466	0.073	8510	180
T0140 - 27	0.7	0.12	2.18	0.31	0.388	0.086	3.14	0.5	0.654	0.09	8420	180
T0140 - 28	1.03	0.12	3.11	0.42	0.452	0.057	4.21	0.45	0.532	0.075	8910	150
T0140 - 29	0.986	0.092	3.12	0.33	0.501	0.077	5.05	0.65	0.766	0.096	8140	150
T0140 - 30	0.94	0.11	3.1	0.28	0.537	0.087	5.28	0.63	0.845	0.082	8250	160
T0140 - 31	0.334	0.061	1.34	0.23	0.196	0.052	1.75	0.38	0.356	0.063	8900	250
T0140 - 33	0.671	0.09	2.53	0.26	0.377	0.075	2.97	0.61	0.453	0.072	8420	150
T0140 - 34	0.81	0.12	2.52	0.33	0.361	0.065	2.34	0.47	0.351	0.057	8540	170
T0140 - 35	2.13	0.15	3.58	0.41	0.333	0.06	1.81	0.31	0.177	0.053	8210	200
T0140 - 36	1.08	0.12	3.35	0.35	0.618	0.085	5	0.67	0.95	0.1	8550	140
T0140 - 37	0.269	0.059	0.93	0.2	0.113	0.033	0.98	0.24	0.183	0.048	8140	190
T0140 - 38	1.02	0.12	3.26	0.33	0.603	0.071	5.69	0.75	0.95	0.11	8690	160
T0140 - 41	0.899	0.097	3.31	0.37	0.635	0.086	5.51	0.66	0.95	0.11	8390	180
T0140 - 42	0.654	0.092	1.81	0.25	0.26	0.059	2.22	0.42	0.278	0.059	8440	180
T0140 - 43	1.519	0.091	3.68	0.39	0.458	0.082	2.74	0.39	0.432	0.065	8360	180
T0140 - 44	1.2	0.13	3.04	0.31	0.33	0.061	2.02	0.39	0.28	0.063	7990	150
T0140 - 45	0.97	0.11	2.87	0.33	0.402	0.079	3.02	0.48	0.525	0.069	8950	210
T0140 - 46	0.95	0.12	3.15	0.3	0.415	0.074	2.61	0.46	0.268	0.058	8560	150
T0140 - 47	0.85	0.1	2.52	0.3	0.316	0.061	1.35	0.37	0.231	0.051	8230	190
T0140 - 48	0.92	0.13	2.52	0.34	0.24	0.061	2.37	0.44	0.367	0.082	8720	200
T0140 - 50	0.477	0.089	2.14	0.25	0.413	0.068	4.16	0.58	0.68	0.1	7890	170
T0140 - 51	1.21	0.14	3.62	0.33	0.642	0.074	4.91	0.57	0.672	0.092	8230	150
T0140 - 52	0.205	0.054	0.57	0.14	0.058	0.023	0.74	0.28	0.091	0.034	9130	180
T0140 - 53	0.231	0.055	0.91	0.18	0.126	0.034	1.35	0.32	0.144	0.047	8360	150
T0140 - 54	0.456	0.073	2.23	0.26	0.38	0.08	3.63	0.44	0.568	0.084	8170	180
T0140 - 55	0.545	0.073	2.42	0.34	0.3	0.053	3.46	0.54	0.524	0.069	8630	220
T0140 - 56	0.88	0.13	2.92	0.34	0.505	0.068	4.58	0.71	0.814	0.096	8170	150

Supplementary Table 5 continued: U-Pb and trace element compostions of zircons in T01-40 and T06-09.

Included in age calculations		Final U238/ Pb206 mean	Final U238/ Pb206 2SE(prop)	Final Pb207/ U235 mean	Final Pb207/ U235 2SE(prop)	Final Pb207/ Pb206 mean	Final Pb207/ Pb206 2SE(prop)
	T0140 - 57	2.982975601	0.35821859	5.989174978	0.648764716	0.126346288	0.002576166
	T0140 - 58	2.882275329	0.282736137	6.099010291	0.567381737	0.124157054	0.002264006
	T0140 - 59	2.750337631	0.058951022	6.213267954	0.189201092	0.124691545	0.001555751
	T0140 - 60	2.791552961	0.072935962	6.129708779	0.18456636	0.12356878	0.001383196
	T0140 - 61	2.738899849	0.043588486	6.205692665	0.157289479	0.123654178	0.001010059
	T0140 - 62	2.74637018	0.048297022	6.318773347	0.143349575	0.125631258	0.001186102
	T0140 - 63	2.856733378	0.177163342	6.037523021	0.367687964	0.122445622	0.002113814
	T0140 - 64	2.771356993	0.214909743	6.169595782	0.456236697	0.123294567	0.002873095
	T0140 - 65	2.69517053	0.06443178	6.518923766	0.24046847	0.125735204	0.001518452
	T0140 - 66	2.822154095	0.168815081	6.374682072	0.408030792	0.127824644	0.002856711
	T0140 - 67	2.699141058	0.078363785	6.473147107	0.254197988	0.125179881	0.001696931
	T0140 - 69	2.911045577	0.315631248	6.16303933	0.612081917	0.125114935	0.002561323
	T0140 - 71	2.804565291	0.235253969	6.508375858	0.508491655	0.127746448	0.003035837
	T0140 - 72	2.590669477	0.31387547	7.086953194	1.103733664	0.126691614	0.003204392
	T0140 - 73	3.136331311	0.42637322	6.165198831	0.874898031	0.126404046	0.003092165
	T0140 - 74	2.777999629	0.079991664	6.309880135	0.218818106	0.125838543	0.002104109
x	T0140 - 75	2.820223665	0.056243271	6.151511353	0.153199151	0.124886523	0.001198459
	T0140 - 77	2.852439794	0.253304634	6.613066929	0.708155911	0.128914687	0.00304022
	T0140 - 78	2.758014607	0.186783772	6.574186542	0.489295384	0.127146011	0.002717626
	T0140 - 79	2.818321347	0.12485442	6.203710455	0.282768753	0.124902826	0.00265471
	T0140 - 81	2.897389828	0.245512092	6.244540337	0.536648256	0.125482332	0.002761294
x	T0140 - 82	3.00430516	0.204257973	5.847764436	0.374152336	0.126654241	0.002782447
	T0140 - 83	2.742158224	0.222285634	6.514879416	0.624696016	0.128354549	0.004319968
	T0140 - 84	2.77271218	0.282856262	6.457858215	0.549593743	0.126998798	0.003995209
	T0140 - 85	2.647519544	0.258918752	6.832825986	0.690901924	0.125587787	0.002075973
	T0140 - 86	2.734023186	0.0385057	6.17554146	0.130600187	0.123666322	0.001078688
	T0140 - 87	2.793600776	0.22817263	6.444902793	0.651258745	0.125360652	0.002794472
	T0140 - 88	2.629814377	0.271076525	6.492345613	0.696863404	0.126933653	0.003738756
	T0140 - 89	2.844730295	0.151721873	6.253710331	0.348576677	0.127704371	0.002872642
x	T0140 - 90	3.374323956	0.066113778	4.864329248	0.111338332	0.119520235	0.00162553
	T0140 - 91	2.769494646	0.365392222	6.660225633	1.082456752	0.127557725	0.004008787
	T0140 - 92	2.925314119	0.22426346	6.118670989	0.470268039	0.126278309	0.002268961
	T0140 - 93	2.755574558	0.237737082	6.360305644	0.727285451	0.124145493	0.002856842
	T0140 - 94	2.896123185	0.298853634	6.088057006	0.564963331	0.126235334	0.002323718
	T0140 - 96	2.927476961	0.175863815	5.971227594	0.397105906	0.124679614	0.002181641

* An x indicates the analysis was not used in age calculations.

Supplementary Table 5 continued: U-Pb and trace element compostions of zircons in T01-40 and T06-09.

	Final U/Th mean	Final U/Th 2SE(int)	Approx U PPM mean	Approx U PPM 2SE(int)	Approx Th PPM mean	Approx Th PPM 2SE(int)
T0140 - 57	4.364009659	4.339009067	4.439574785	0.567801215	0.952126236	0.279672793
T0140 - 58	2.450507328	5.606514588	5.63880765	0.57598063	1.00748757	0.292231852
T0140 - 59	3.917642261	0.174746196	26.17526994	1.473144503	6.757793866	0.523583542
T0140 - 60	4.727319752	0.26682223	18.32525531	1.010536037	3.904354763	0.234102032
T0140 - 61	1.737097316	0.030205904	42.39756448	1.279452955	24.20297425	0.73776438
T0140 - 62	0.633878287	0.02372419	38.06211632	1.642904365	60.17242429	2.323284552
T0140 - 63	3.761437495	0.507402146	8.161437811	0.597760247	2.269474572	0.27672177
T0140 - 64	7.638552891	3.554524582	6.67439585	0.753928455	1.107327083	0.230196757
T0140 - 65	2.619944887	0.602434824	15.76032915	3.324981478	7.413171639	1.897655148
T0140 - 66	4.061113604	0.560258702	6.967860482	0.478076402	1.882620344	0.236140153
T0140 - 67	5.508235116	0.762467591	16.82052639	1.792219252	3.316560491	0.456518143
T0140 - 69	4.577993074	4.022252358	4.738511021	0.614621488	0.666089557	0.270621116
T0140 - 71	-2.314533878	16.5562033	4.840405052	0.471983776	0.613167086	0.351015138
T0140 - 72	6.718191881	3.708351164	3.752881723	0.577875769	0.637687089	0.287048389
T0140 - 73	-7.624168162	15.63333195	5.281925216	0.765678165	0.480997995	0.325169385
T0140 - 74	4.10203313	0.2888616	14.6671734	1.169212463	3.645670887	0.366038041
T0140 - 75	1.37660689	0.142565941	33.2815828	2.250813984	26.11212391	3.661472311
T0140 - 77	1.540670277	12.81365255	5.2790469	0.571383391	0.837580107	0.265184912
T0140 - 78	5.407982271	2.191700429	6.348511159	0.44143619	1.596800348	0.346766336
T0140 - 79	5.761941295	8.026892349	6.79653169	0.509277446	1.142260495	0.310683387
T0140 - 81	-4.651389116	18.55294753	6.056586294	0.547743279	0.812978046	0.234767029
T0140 - 82	4.039437861	1.448075246	6.368756428	0.608366297	1.558148825	0.355491206
T0140 - 83	4.805643469	2.122363826	5.949646206	0.745420485	1.099602131	0.316143879
T0140 - 84	2.949454796	3.146069954	4.533335946	0.486604354	1.052326231	0.271021477
T0140 - 85	5.902708486	1.465112217	5.071263147	0.539716165	0.972204697	0.191912904
T0140 - 86	0.70627793	0.007308597	65.65025734	3.984168758	93.31198432	5.214723469
T0140 - 87	5.227682811	7.104180507	4.768099467	0.685432977	0.561245754	0.24079546
T0140 - 88	5.910306686	1.453450022	4.890256872	0.694568266	1.043150118	0.217706971
T0140 - 89	4.033343962	19.48531105	6.324118643	0.253618245	0.652424137	0.247741955
T0140 - 90	5.825587026	0.322801329	23.73720263	1.014763025	4.142770412	0.224388877
T0140 - 91	-22.66785187	36.34407112	3.379730371	0.457241411	0.47842374	0.314382956
T0140 - 92	4.69837406	1.099912186	6.783660696	0.536543943	1.736364668	0.30932078
T0140 - 93	7.596923027	4.037706412	5.442875005	0.64691822	1.039516935	0.288528724
T0140 - 94	3.321165006	5.104516692	5.311998421	0.733927221	1.179524889	0.346716136
T0140 - 96	5.854341973	2.580117257	6.990171828	0.542106681	1.706026493	0.318148321

Supplementary Table 5 continued: U-Pb and trace element compostions of zircons in T01-40 and T06-09.

	Ti ppm m49	2SE	Y ppm m89	2SE	S m p p m m147	2SE	Eu ppm m153	2SE	G d p p m m157	2SE	Tb ppm m159	2SE	D y p p m m163	2SE
T0140 - 57	7.7	2.6	23.47	0.96	0	1	0	1	0.18	0.11	0.042	0.022	1.42	0.23
T0140 - 58	3	2.7	17.99	0.84	0	1	0.046	0.03	0.17	0.11	0.102	0.043	1.22	0.23
T0140 - 59	3.1	2.3	43.9	1.7	0.56	0.19	0.356	0.079	4.62	0.67	1.22	0.13	9.1	0.53
T0140 - 60	10	3.2	40.65	0.93	0.28	0.13	0.278	0.073	1.75	0.31	0.429	0.086	4.62	0.46
T0140 - 61	8.2	3	27.02	0.88	0.25	0.13	0.192	0.056	2.25	0.37	0.519	0.064	4.08	0.46
T0140 - 62	12.5	3.9	24.51	0.77	1.1	0.32	0.63	0.14	4.22	0.55	0.88	0.11	5.74	0.59
T0140 - 63	7	3.4	21.02	0.8	0	1	0.012	0.016	0.4	0.16	0.181	0.042	1.94	0.29
T0140 - 64	12.7	3.7	31.99	0.91	0	1	0.144	0.055	0.81	0.24	0.289	0.045	3.11	0.38
T0140 - 65	9.9	3.9	24.8	1.1	0.22	0.12	0.134	0.049	1.6	0.27	0.467	0.071	3.39	0.37
T0140 - 66	4.6	2.6	24.79	0.99	0	1	0	1	0.57	0.2	0.128	0.033	2.18	0.35
T0140 - 67	8.6	4	35.5	1.1	0.07	0.079	0.183	0.069	1.5	0.29	0.556	0.097	5.04	0.52
T0140 - 69	9.8	4.5	22.13	0.71	0.018	0.037	0.084	0.036	0.54	0.2	0.263	0.053	2.54	0.39
T0140 - 71	9.9	3.2	19.99	0.99	0	1	0	1	0.38	0.16	0.101	0.037	1.66	0.29
T0140 - 72	11.5	3.8	24.37	0.95	0	1	0.044	0.028	0.41	0.16	0.164	0.046	2.28	0.36
T0140 - 73	9	3.5	48.3	1.3	0.02	0.041	0.2	0.062	1.22	0.24	0.451	0.081	4.94	0.5
T0140 - 74	7.6	3.3	28.42	0.9	0.102	0.087	0.108	0.051	1.18	0.32	0.345	0.062	3.55	0.35
T0140 - 75	8.2	4.1	21.29	0.8	0.36	0.19	0.191	0.05	2.08	0.35	0.442	0.083	3.5	0.42
T0140 - 77	16.3	5.5	26.5	1.3	0	1	0.089	0.043	0.79	0.27	0.244	0.047	2.63	0.36
T0140 - 78	6.7	3.7	42.1	1.1	0.19	0.12	0.083	0.036	0.83	0.24	0.344	0.077	3.49	0.37
T0140 - 79	9.1	4.7	27.3	0.76	0	1	0.047	0.031	0.97	0.26	0.321	0.064	3.43	0.46
T0140 - 81	11.4	4.4	33.3	1.1	0	1	0.071	0.037	0.49	0.18	0.217	0.056	3.04	0.43
T0140 - 82	9.4	4	36.1	1.3	0.3	0.14	0.125	0.042	0.9	0.28	0.384	0.069	3.78	0.4
T0140 - 83	17.2	5.2	36	1.2	0.19	0.11	0.145	0.055	1.27	0.29	0.402	0.064	3.99	0.38
T0140 - 84	10	3.9	25.02	0.68	0.023	0.047	0.101	0.041	0.69	0.22	0.308	0.055	2.91	0.33
T0140 - 85	12	4.1	17.72	0.7	0	1	0.081	0.036	0.53	0.19	0.193	0.046	2.19	0.34
T0140 - 86	7.8	3.3	41.7	1.2	1.38	0.32	0.8	0.13	5.7	0.68	1.18	0.13	8.3	0.54
T0140 - 87	7.2	3.4	14.97	0.56	0	1	0.0045	0.0091	0.21	0.12	0.043	0.02	1.1	0.16
T0140 - 88	6.6	2.7	31.7	1.2	0.021	0.043	0.055	0.033	0.44	0.2	0.228	0.064	2.47	0.4
T0140 - 89	2.5	2.5	18.41	0.88	0	1	0.036	0.028	0.24	0.13	0.102	0.036	1.42	0.24
T0140 - 90	4.9	3.6	35.1	1.3	0.46	0.18	0.355	0.074	3.5	0.57	0.95	0.12	6.62	0.55
T0140 - 91	9.7	4.5	29.78	0.9	0	1	0.011	0.016	0.31	0.15	0.133	0.031	2.39	0.33
T0140 - 92	4.7	3.7	27.9	1	0	1	0.075	0.037	0.88	0.25	0.329	0.061	3.48	0.36
T0140 - 93	10.8	4.9	38.19	0.83	0	1	0.086	0.036	0.77	0.22	0.227	0.046	3.33	0.38
T0140 - 94	6.6	3.9	27.14	0.99	0.099	0.095	0.037	0.028	0.57	0.2	0.223	0.063	2.52	0.28
T0140 - 96	10.4	3.9	26.88	0.87	0	1	0.045	0.029	0.83	0.24	0.231	0.048	2.42	0.37

Supplementary Table 5 continued: U-Pb and trace element compostions of zircons in T01-40 and T06-09.

	Ho ppm m165	2SE	Er ppm m166	2SE	Tm ppm m169	2SE	Yb ppm m173	2SE	Lu ppm m175	2SE	Hf ppm m178	2SE
T0140 - 57	0.639	0.089	4.29	0.58	1.65	0.15	39.3	2.6	17.9	0.99	9350	190
T0140 - 58	0.422	0.069	1.71	0.25	0.348	0.062	3.05	0.41	0.715	0.088	8190	150
T0140 - 59	1.54	0.15	2.89	0.29	0.333	0.058	2.01	0.36	0.261	0.046	8360	140
T0140 - 60	1.29	0.12	4.23	0.44	0.696	0.083	6.35	0.69	1.066	0.099	8270	150
T0140 - 61	0.878	0.084	2.24	0.3	0.324	0.059	2.01	0.42	0.295	0.057	7710	190
T0140 - 62	0.73	0.1	1.47	0.28	0.146	0.041	0.67	0.27	0.092	0.032	7850	150
T0140 - 63	0.619	0.067	1.93	0.25	0.316	0.061	2.3	0.44	0.44	0.085	8660	160
T0140 - 64	0.72	0.1	3.51	0.32	0.528	0.09	5.86	0.66	0.84	0.1	9010	160
T0140 - 65	0.77	0.1	2.27	0.33	0.336	0.067	2.35	0.5	0.379	0.072	7820	190
T0140 - 66	0.69	0.11	2.54	0.27	0.406	0.069	3.5	0.48	0.553	0.079	9000	190
T0140 - 67	1.18	0.12	2.55	0.27	0.434	0.076	2.2	0.43	0.328	0.08	9080	170
T0140 - 69	0.618	0.086	2	0.24	0.252	0.052	2.17	0.44	0.263	0.068	7710	160
T0140 - 71	0.52	0.081	2.44	0.3	0.403	0.067	3.6	0.64	0.547	0.074	8160	170
T0140 - 72	0.759	0.087	2.43	0.3	0.401	0.072	3.7	0.55	0.711	0.074	8270	180
T0140 - 73	1.37	0.099	4.32	0.41	0.704	0.085	6.36	0.69	0.98	0.11	8490	160
T0140 - 74	0.87	0.1	2.23	0.35	0.338	0.062	2.6	0.45	0.328	0.063	7710	180
T0140 - 75	0.73	0.1	1.78	0.25	0.216	0.061	1.03	0.25	0.178	0.05	8350	170
T0140 - 77	0.738	0.083	2.36	0.37	0.374	0.078	3.8	1	0.68	0.16	8360	210
T0140 - 78	1.23	0.12	4.85	0.38	0.798	0.092	6.43	0.8	1.136	0.083	8410	220
T0140 - 79	0.81	0.073	2.23	0.29	0.345	0.047	2.09	0.39	0.301	0.058	8320	160
T0140 - 81	0.919	0.092	3.32	0.29	0.66	0.11	5.23	0.64	0.83	0.12	8720	150
T0140 - 82	1.09	0.11	3.36	0.38	0.595	0.081	4.89	0.64	0.691	0.099	8990	190
T0140 - 83	1.08	0.12	3.23	0.36	0.539	0.066	3.97	0.49	0.521	0.074	7800	150
T0140 - 84	0.7	0.11	2.41	0.28	0.371	0.068	2.68	0.48	0.267	0.059	7650	170
T0140 - 85	0.492	0.07	1.34	0.2	0.238	0.056	1.73	0.35	0.239	0.051	7980	220
T0140 - 86	1.45	0.13	3.52	0.33	0.382	0.067	2.23	0.39	0.282	0.06	7670	120
T0140 - 87	0.365	0.059	1.53	0.27	0.33	0.069	2.36	0.47	0.41	0.084	8500	210
T0140 - 88	0.99	0.13	3.74	0.39	0.694	0.081	7.02	0.83	1.15	0.1	8050	150
T0140 - 89	0.487	0.085	1.83	0.21	0.367	0.068	3.42	0.57	0.464	0.086	7900	180
T0140 - 90	1.05	0.11	2.3	0.31	0.237	0.043	1.5	0.4	0.118	0.039	8650	180
T0140 - 91	0.83	0.11	3.72	0.29	0.667	0.069	5.56	0.55	0.759	0.097	8080	140
T0140 - 92	0.82	0.11	2.35	0.32	0.243	0.054	2.08	0.37	0.267	0.056	8300	190
T0140 - 93	1.019	0.092	4.07	0.32	0.867	0.096	8.34	0.83	1.25	0.14	9050	170
T0140 - 94	0.79	0.12	3.09	0.25	0.477	0.079	4.01	0.68	0.8	0.12	8080	150
T0140 - 96	0.756	0.098	2.22	0.23	0.437	0.081	3.36	0.43	0.544	0.064	8670	160

Supplementary Table 5 continued: U-Pb and trace element compostions of zircons in T01-40 and T06-09.

Included in age calculations		Final U238/ Pb206 mean	Final U238/ Pb206 2SE(prop)	Final Pb207/ U235 mean	Final Pb207/ U235 2SE(prop)	Final Pb207/ Pb206 mean	Final Pb207/ Pb206 2SE(prop)
	T06-09						
	T0609 - 2	2.743129901	0.029091081	6.216069279	0.10382438	0.12358244	0.000821314
x	T0609 - 3	2.879322013	0.039929597	6.023951653	0.116030515	0.125644261	0.00088188
	T0609 - 4	2.724214314	0.029477257	6.268590583	0.112196236	0.12375068	0.000670657
x	T0609 - 5	2.787474201	0.033919432	6.153720006	0.115433221	0.124335718	0.000844805
x	T0609 - 6	2.76348346	0.031309523	6.287032782	0.122179866	0.125427027	0.000960378
	T0609 - 7	2.754975263	0.02869508	6.195348622	0.107349508	0.123714817	0.000970981
x	T0609 - 9	2.779708672	0.041937296	6.143532447	0.104134075	0.124128048	0.000639945
x	T0609 - 11	2.761444422	0.027775666	6.244037533	0.107048175	0.124645353	0.000705768
	T0609 - 12	2.684168825	0.039472872	6.438544329	0.129712536	0.125247759	0.001027529
	T0609 - 13	2.755414738	0.046720149	6.196741396	0.128207191	0.12381663	0.000668894
	T0609 - 14	2.718698203	0.027444452	6.245508956	0.105824	0.123249619	0.000700628
	T0609 - 15	2.721709845	0.028883005	6.28937751	0.107579495	0.124272675	0.000761936
x	T0609 - 18	2.759668728	0.026965224	6.22376662	0.10234462	0.124675241	0.000601813
	T0609 - 19	2.741100292	0.025296698	6.198238679	0.100858137	0.123633091	0.000668668
x	T0609 - 20	2.798533204	0.036762024	6.100462265	0.139742458	0.124378306	0.000795348
x	T0609 - 21	2.771708134	0.026796635	6.220870603	0.104254877	0.125151402	0.00072038
	T0609 - 23	2.719844703	0.032482777	6.287827219	0.116243646	0.124078805	0.000670565
x	T0609 - 24	2.679634378	0.028990945	6.336073564	0.106875893	0.123321056	0.000517024
x	T0609 - 25	2.920511721	0.045186765	5.885166398	0.11420668	0.124601058	0.000625048
	T0609 - 26	2.725564778	0.033599998	6.234134597	0.112020612	0.123209662	0.000695863
	T0609 - 27	2.744855507	0.032828075	6.262391258	0.114111464	0.124645984	0.000932296
	T0609 - 28	2.748100287	0.035255275	6.244269679	0.103786693	0.123908626	0.000591704
x	T0609 - 29	2.662982107	0.032274906	6.464622664	0.11774972	0.12480555	0.000917911
x	T0609 - 31	2.795251022	0.035952562	6.249392635	0.118432636	0.125587097	0.000794357
x	T0609 - 32	2.679338731	0.027842899	6.441418234	0.10757587	0.124115788	0.000753069
	T0609 - 34	2.762258417	0.028498084	6.19966367	0.106605634	0.123115316	0.000629303
x	T0609 - 36	2.678774425	0.027429696	6.414346748	0.106396798	0.123531922	0.000742174

Supplementary Table 5 continued: U-Pb and trace element compostions of zircons in T01-40 and T06-09.

	Final U/Th mean	Final U/Th 2SE(int)	Approx U PPM mean	Approx U PPM 2SE(int)	Approx Th PPM mean	Approx Th PPM 2SE(int)
T06-09						
T0609 - 2	2.199509089	0.02537263	104.1633367	5.921915816	47.02067306	2.334390465
T0609 - 3	23.32543802	2.958887227	38.05854844	0.752993075	1.702038163	0.284065798
T0609 - 4	2.682604947	0.0233632	137.6880471	6.390472892	51.0061515	2.100137155
T0609 - 5	2.92846028	0.09758572	73.88873523	4.781581671	25.5634595	2.381866703
T0609 - 6	11.76769053	1.727830378	59.75078089	6.298256764	5.899746512	1.464592312
T0609 - 7	32.85555363	4.879330976	82.7095472	4.285747957	2.548102048	0.499880042
T0609 - 9	3.482191425	0.111104619	106.375953	7.300036805	30.66776182	2.442023738
T0609 - 11	9.666850096	1.446360945	96.88710693	5.40054058	11.78511537	2.136028901
T0609 - 12	35.39778223	9.77466851	38.78441054	1.627438245	1.332987995	0.232764812
T0609 - 13	7.145414779	0.400030278	116.919869	9.144623131	16.63575881	1.528294877
T0609 - 14	2.539921442	0.027036198	156.2537338	7.06560968	61.38366756	2.208153612
T0609 - 15	20.45152567	2.596275204	84.57572861	5.639143402	4.716005658	0.839899822
T0609 - 18	2.528867714	0.028676361	142.9254218	6.156435196	56.41400926	1.950666243
T0609 - 19	1.842518398	0.088693711	167.4951769	9.412088913	93.45174558	9.086884365
T0609 - 20	2.99704053	0.048500251	153.7213003	1.790158797	50.97542408	0.779544545
T0609 - 21	3.275587398	0.023565781	117.0729305	4.915058165	35.76106511	1.589452799
T0609 - 23	1.872970875	0.063069811	194.3230813	3.318133212	103.412347	4.932367555
T0609 - 24	2.530404462	0.023660405	201.8733688	11.07765515	79.99394601	4.918043659
T0609 - 25	3.072043317	0.033450904	196.5032605	5.115660726	63.9386	1.354352192
T0609 - 26	3.569080535	0.044264352	132.3240104	6.538171721	37.09823778	1.902721612
T0609 - 27	23.81227501	3.409773049	67.06576908	3.068590134	2.947534705	0.514869521
T0609 - 28	7.252111723	0.709343472	104.5710499	9.064006819	15.74924958	2.426303972
T0609 - 29	8.489348588	1.52578104	70.86625027	11.10132704	12.09919033	4.008029406
T0609 - 31	18.81957623	0.794717526	110.5264564	3.894244812	5.745195224	0.313433722
T0609 - 32	2.197182821	0.045443058	140.2610959	3.977797933	63.67040292	1.788536235
T0609 - 34	2.690171262	0.07428148	132.2476132	3.744515949	49.01400898	0.967395827
T0609 - 36	3.54775878	0.143562632	103.1719758	6.5631952	29.67330305	1.192719263

Supplementary Table 5 continued: U-Pb and trace element compostions of zircons in T01-40 and T06-09.

	Ti ppm m49	2SE	Y ppm m89	2SE	S m p p m m147	2SE	Eu ppm m153	2SE	G d p p m m157	2SE	Tb ppm m159	2SE	D y p p m m163	2SE
T06-09														
T0609 - 2	11.9	3.5	20.6	0.84	0.54	0.22	0.179	0.059	1.33	0.3	0.298	0.06	2.39	0.29
T0609 - 3	4.6	2.2	74	4.1	0	1	0.176	0.064	1.89	0.39	0.89	0.11	8.26	0.73
T0609 - 4	10.5	2.7	20.5	0.83	0.45	0.21	0.233	0.066	1.5	0.34	0.292	0.062	2.81	0.37
T0609 - 5	11	2.4	13.89	0.54	0.17	0.12	0.134	0.055	1	0.25	0.188	0.045	1.72	0.26
T0609 - 6	6.1	2	37.1	1.4	0.043	0.06	0.173	0.063	2.97	0.5	0.757	0.09	5.67	0.52
T0609 - 7	3.4	1.7	35	2	0.15	0.12	0.379	0.097	2.69	0.58	0.572	0.099	3.95	0.49
T0609 - 9	10.4	2.4	19.64	0.97	0.23	0.13	0.198	0.05	1.51	0.33	0.33	0.067	2.43	0.37
T0609 - 11	4.1	1.7	39.4	1.3	0.46	0.19	0.378	0.096	2.58	0.41	0.636	0.088	4.51	0.53
T0609 - 12	4.4	2.1	21.95	0.95	0.2	0.12	0.18	0.062	3.11	0.41	0.61	0.095	3.29	0.43
T0609 - 13	7.6	2.5	20.49	0.95	0.33	0.16	0.263	0.064	1.94	0.42	0.367	0.073	2.38	0.38
T0609 - 14	10.6	2.7	37.1	1	1.18	0.3	0.42	0.11	2.73	0.51	0.621	0.064	4.85	0.44
T0609 - 15	6.5	2.3	18.16	0.4	0.3	0.15	0.161	0.053	1.72	0.34	0.439	0.069	2.39	0.32
T0609 - 18	13.4	3.6	39.9	1.1	1.35	0.34	0.51	0.11	3.55	0.4	0.845	0.076	5.03	0.53
T0609 - 19	14.2	3.5	39.3	1.5	0.88	0.28	0.563	0.092	3.19	0.52	0.73	0.11	5.61	0.59
T0609 - 20	10.1	2.7	17.26	0.88	0.79	0.25	0.325	0.077	1.06	0.34	0.344	0.067	2.1	0.32
T0609 - 21	11.7	2.7	27.7	1.1	0.85	0.28	0.364	0.098	2.23	0.42	0.448	0.07	3.12	0.46
T0609 - 23	11.6	2.8	31.4	1.9	1.36	0.32	0.5	0.11	3	0.48	0.575	0.095	4.26	0.54
T0609 - 24	12.3	3.1	39.6	1.2	1.37	0.3	0.694	0.087	3.82	0.47	0.831	0.088	5.68	0.39
T0609 - 25	14.7	3.6	28.6	1.3	1.01	0.31	0.55	0.12	2.55	0.36	0.483	0.084	3.23	0.43
T0609 - 26	8.4	3.1	19.4	1.7	0.48	0.21	0.277	0.068	1.5	0.36	0.309	0.071	2.75	0.33
T0609 - 27	5.2	2.4	16.02	0.75	0.25	0.13	0.173	0.062	1.55	0.39	0.288	0.063	2.19	0.34
T0609 - 28	4.7	2.1	23.99	0.92	0.22	0.12	0.178	0.056	1.14	0.29	0.392	0.063	2.63	0.42
T0609 - 29	7.1	2.1	25.98	0.98	0.3	0.14	0.205	0.073	1.9	0.37	0.403	0.081	3.58	0.36
T0609 - 31	17	22	38	1.1	0.48	0.2	0.321	0.082	3.39	0.5	0.697	0.095	4.76	0.54
T0609 - 32	8.3	2.7	24.14	0.95	0.43	0.21	0.235	0.066	1.81	0.33	0.391	0.062	2.91	0.36
T0609 - 34	13.6	4.2	29.6	1	0.85	0.21	0.473	0.081	1.89	0.32	0.399	0.077	3.84	0.45
T0609 - 36	7.8	2.6	19.46	0.63	0.43	0.18	0.293	0.071	1.91	0.38	0.346	0.068	2.42	0.36

Supplementary Table 5 continued: U-Pb and trace element compostions of zircons in T01-40 and T06-09.

	Ho ppm m165	2SE	Er ppm m166	2SE	Tm ppm m169	2SE	Yb ppm m173	2SE	Lu ppm m175	2SE	Hf ppm m178	2SE
T06-09												
T0609 - 2	0.691	0.065	2.32	0.28	0.36	0.062	2.78	0.5	0.441	0.072	8740	170
T0609 - 3	2.36	0.25	8.11	0.78	1.26	0.1	9.1	1.2	1.43	0.15	12990	240
T0609 - 4	0.603	0.078	2.03	0.26	0.36	0.062	2.25	0.41	0.4	0.063	8520	170
T0609 - 5	0.417	0.078	1.33	0.24	0.253	0.056	1.65	0.32	0.331	0.057	9130	330
T0609 - 6	1.01	0.13	3.24	0.32	0.54	0.067	3.86	0.54	0.474	0.086	13350	330
T0609 - 7	1.19	0.12	3.6	0.37	0.611	0.094	4.89	0.66	0.798	0.086	11320	280
T0609 - 9	0.717	0.094	1.82	0.3	0.355	0.064	2.56	0.48	0.497	0.077	9910	180
T0609 - 11	1.08	0.13	3.81	0.36	0.631	0.093	5.93	0.69	0.92	0.11	10740	190
T0609 - 12	0.621	0.084	1.81	0.28	0.211	0.051	1.67	0.34	0.211	0.044	13510	240
T0609 - 13	0.597	0.089	2.04	0.26	0.411	0.073	2.83	0.5	0.462	0.078	11070	220
T0609 - 14	1.23	0.14	4.17	0.47	0.511	0.081	5.4	0.73	0.703	0.081	8610	180
T0609 - 15	0.535	0.075	1.59	0.28	0.278	0.058	2.37	0.41	0.397	0.073	12150	260
T0609 - 18	1.45	0.16	4.29	0.36	0.722	0.099	5.66	0.68	0.91	0.1	8650	180
T0609 - 19	1.17	0.14	3.75	0.39	0.66	0.11	4.92	0.61	0.75	0.1	8350	170
T0609 - 20	0.55	0.074	1.71	0.29	0.251	0.06	2.19	0.4	0.363	0.062	8490	190
T0609 - 21	0.94	0.11	3.08	0.36	0.435	0.066	3.68	0.6	0.476	0.075	8520	180
T0609 - 23	0.99	0.13	2.99	0.32	0.47	0.08	2.93	0.49	0.539	0.092	8580	190
T0609 - 24	1.28	0.13	3.91	0.33	0.614	0.08	4.61	0.6	0.571	0.065	9530	270
T0609 - 25	0.77	0.098	3.07	0.35	0.493	0.067	3.54	0.66	0.599	0.087	8920	150
T0609 - 26	0.662	0.077	1.61	0.29	0.326	0.066	2.41	0.39	0.342	0.073	9340	190
T0609 - 27	0.332	0.073	1.31	0.25	0.155	0.044	1.41	0.34	0.219	0.05	13370	400
T0609 - 28	0.693	0.09	2.34	0.3	0.41	0.082	3.54	0.57	0.523	0.07	12490	300
T0609 - 29	0.764	0.097	2.64	0.33	0.318	0.062	2.86	0.48	0.539	0.077	11770	440
T0609 - 31	1.12	0.12	3.92	0.35	0.6	0.1	4.91	0.53	0.818	0.09	10790	230
T0609 - 32	0.82	0.092	2.74	0.36	0.398	0.075	3.71	0.47	0.516	0.069	8470	160
T0609 - 34	0.96	0.11	3.15	0.29	0.412	0.074	3.99	0.51	0.537	0.096	8680	210
T0609 - 36	0.6	0.1	1.83	0.25	0.324	0.06	2.29	0.37	0.402	0.068	10710	310

Supplementary Table 6: U-Pb and trace element data from rutile in T01-40 and T06-09.

	207Pb/235U	2SE	206Pb/238U	2SE	Error Correlation	Si_ppm	2SE	Zr_ppm	2SE	Pb208_ppm	2SE	U238_ppm	2SE
T01-40 Rutile													
T01_40_65	0.772	0.065	0.0887	0.004	0.15602	109	19	1027.9	7.7	-0.0004	0.0023	7.738	0.066
T01_40_31	1.138	0.087	0.1159	0.0049	0.0098935	97	19	854.6	7.1	-0.0003	0.0027	7.554	0.073
T01_40_71	4.59	0.29	0.2908	0.013	0.29865	278	32	516.7	4.7	-0.0001	0.0023	4.253	0.046
T01_40_89	0.645	0.05	0.0802	0.0036	0.093066	125	21	500.6	4.5	0	0.0024	8.937	0.095
T01_40_37	0.675	0.075	0.0835	0.0042	0.042194	123	19	1140.9	9	0.0006	0.0027	4.895	0.056
T01_40_35	0.701	0.067	0.0813	0.0038	0.070206	119	21	454.9	4.5	0.0014	0.0031	6.337	0.075
T01_40_34	2.43	0.15	0.1787	0.0083	0.42392	92	24	1222	12	0.0016	0.0037	9.72	0.12
T01_40_60	0.674	0.064	0.0839	0.004	0.12503	115	19	442	4.1	0.0028	0.003	5.765	0.075
T01_40_85	4.53	0.26	0.2874	0.012	0.20887	121	24	515.8	4.1	0.0028	0.0028	4.471	0.058
T01_40_87	0.734	0.06	0.0879	0.0039	0.22382	131	23	308.1	6.1	0.0033	0.0031	11.34	0.12
T01_40_84	1.19	0.39	0.0947	0.014	0.18549	220	100	518.6	7.3	0.0038	0.0063	2.45	0.048
T01_40_12	0.75	0.076	0.0874	0.0042	0.11677	184	31	380.2	3.1	0.0045	0.0034	5.952	0.058
T01_40_41	0.745	0.085	0.0885	0.0047	0.047755	96	20	706.7	9.2	0.0045	0.0033	3.645	0.055
T01_40_16	0.685	0.069	0.0821	0.0037	0.25514	105	22	584.7	8.2	0.0052	0.0045	9.059	0.075
T01_40_4	0.69	0.11	0.0783	0.0035	0.083763	93	20	1068.4	7.8	0.0057	0.0058	8.432	0.073
T01_40_63	0.627	0.079	0.0828	0.0048	0.028122	115	21	587.3	4.5	0.0061	0.0044	3.351	0.037
T01_40_19	0.66	0.13	0.0793	0.0047	0.057711	97	23	435.3	4.7	0.0062	0.0044	4.392	0.06
T01_40_6	0.665	0.092	0.0855	0.0047	0.011777	139	26	821.7	7.3	0.0064	0.0036	3.438	0.043
T01_40_86	1.51	0.12	0.126	0.007	0.48707	122	21	843.4	7.8	0.0065	0.0043	8.477	0.091
T01_40_46	4.72	0.42	0.296	0.017	0.0040918	136	35	454.8	4.5	0.0067	0.0053	2.331	0.047
T01_40_44	5.4	0.33	0.3256	0.014	0.046636	1410	110	455.6	7.8	0.007	0.0036	4.504	0.085
T01_40_15	0.621	0.22	0.0781	0.0073	0.1792	155	36	592.3	9.2	0.0076	0.0078	9.59	0.16
T01_40_13	4.22	0.24	0.2764	0.012	0.15809	121	23	579.5	9	0.0089	0.0048	4.947	0.085
T01_40_91	0.682	0.055	0.0823	0.0037	0.16941	119	22	824	12	0.0096	0.0042	9.09	0.12
T01_40_8	0.715	0.065	0.0792	0.0038	0.065454	117	21	913.3	9.4	0.0102	0.0048	6.761	0.072
T01_40_57	0.727	0.091	0.0847	0.0046	0.02159	125	21	556.7	5	0.0107	0.0067	4.144	0.054
T01_40_18	1.645	0.13	0.1353	0.0066	0.17515	200	120	368.5	4	0.0117	0.005	6.007	0.069
T01_40_47	0.705	0.074	0.0819	0.0037	0.084105	88	25	315.1	3.1	0.0117	0.0046	6.895	0.08
T01_40_39	0.76	0.04	0.0885	0.0035	0.19812	102	19	1031	17	0.0123	0.0042	41.71	0.61
T01_40_59	0.756	0.097	0.0862	0.0045	0.067997	288	45	583	6	0.0133	0.0053	3.412	0.045
T01_40_77	1.34	0.18	0.1159	0.0087	0.38441	280	27	390.8	3.8	0.0135	0.0051	2.003	0.033
T01_40_88	0.753	0.074	0.0891	0.0044	0.053743	136	21	421.9	3.8	0.0137	0.0051	6.102	0.069
T01_40_5	0.66	0.44	0.0779	0.022	0.052957	246	41	1077	17	0.0145	0.009	8.71	0.12
T01_40_62	0.792	0.081	0.0854	0.0039	0.0042425	166	30	732.6	7.9	0.0146	0.0071	8.623	0.081
T01_40_76	0.91	0.14	0.097	0.0059	0.027146	168	29	532.8	5.6	0.0152	0.0047	2.343	0.038
T01_40_92	1.44	0.93	0.1122	0.024	0.14414	910	280	2860	810	0.0163	0.0072	2.852	0.052
T01_40_73	4.26	0.21	0.2738	0.011	0.36406	465	95	688.8	5.7	0.0167	0.0062	18.66	0.17
T01_40_40	0.708	0.23	0.0789	0.0078	0.081864	133	25	686.2	6.5	0.0183	0.0071	7.4	0.11
T01_40_48	0.85	2	0.0812	0.019	0.12092	129	41	462.9	6.5	0.0187	0.0087	3.474	0.081
T01_40_50	0.98	0.12	0.0948	0.0048	0.061048	224	47	492.5	7.1	0.021	0.012	5.456	0.089
T01_40_54	1.92	0.24	0.1464	0.0068	0.21094	199	36	443.2	6.6	0.0218	0.0097	4.586	0.069
T01_40_36	0.816	0.19	0.092	0.0044	0.020348	116	24	193.5	2	0.022	0.0073	6.394	0.072
T01_40_66	1.35	0.13	0.1195	0.007	0.49239	131	24	1161	12	0.0222	0.0098	7.44	0.11
T01_40_23	0.735	0.079	0.0835	0.0039	0.073596	131	21	664.7	5.4	0.0244	0.0074	8.357	0.071
T01_40_52	2.05	0.39	0.152	0.0097	0.63724	129	36	402.3	4.4	0.0267	0.0094	3.615	0.073
T01_40_61	0.84	0.14	0.087	0.0051	0.23108	88	25	478.2	6	0.029	0.012	3.841	0.066
T01_40_32	1.054	0.097	0.0997	0.0051	0.57646	362	55	365.5	3.2	0.0301	0.0073	6.068	0.069
T01_40_10	2.07	0.15	0.1529	0.007	0.16247	693	53	616.3	6.7	0.0304	0.0065	4.783	0.066

Supplementary Table 6 continued: U-Pb and trace element data from rutile in T01-40 and T06-09.

	207Pb/235U	2SE	206Pb/238U	2SE	Error Correlation	Si_ppm	2SE	Zr_ppm	2SE	Pb208_ppm	2SE	U238_ppm	2SE
T01_40_64	3.75	0.24	0.2402	0.01	0.062583	109	28	801.5	9.2	0.0339	0.0085	4.485	0.056
T01_40_90	0.861	0.11	0.0906	0.0048	0.069306	369	49	519.3	7.8	0.0339	0.0082	4.133	0.073
T01_40_21	0.817	0.091	0.0882	0.0045	0.14053	450	49	901.5	8.2	0.0349	0.0072	4.523	0.052
T01_40_55	1.3	0.19	0.1016	0.007	0.18141	74	22	492.3	6.1	0.0359	0.0079	2.021	0.039
T01_40_53	1.38	0.12	0.1243	0.0058	0.0043276	104	24	457.6	4.5	0.0363	0.0074	5.133	0.056
T01_40_1	0.883	0.088	0.0854	0.0041	0.17748	120	21	969.2	9.6	0.037	0.0089	5.612	0.069
T01_40_28	5.33	0.55	0.324	0.017	0.1963	145	30	656	13	0.037	0.011	2.664	0.066
T01_40_83	1.03	0.2	0.0902	0.0067	0.15341	167	29	1163	12	0.037	0.011	3.208	0.053
T01_40_17	4.27	0.32	0.2474	0.012	0.00072356	134	34	605.6	8.1	0.039	0.016	7.52	0.13
T01_40_25	0.97	0.12	0.0939	0.005	0.036736	156	23	678.9	7.5	0.039	0.03	4.405	0.074
T01_40_9	1.03	0.47	0.0884	0.007	0.067783	160	30	294.2	6.1	0.04	0.011	4.487	0.069
T01_40_27	0.81	1.5	0.083	0.024	0.06828	114	36	755.6	9.7	0.042	0.014	8.6	0.12
T01_40_69	3.22	0.23	0.209	0.01	0.13272	241	37	632.6	8	0.047	0.0096	6.079	0.073
T01_40_24	0.85	0.12	0.0858	0.0044	0.0068051	129	29	919	15	0.051	0.013	5.074	0.076
T01_40_3	5.14	0.25	0.3057	0.012	0.06375	157	25	1191	14	0.0513	0.0094	9.88	0.13
T01_40_79	1.14	0.11	0.098	0.005	0.020378	276	35	722.5	9.6	0.053	0.012	4.745	0.078
T01_40_49	0.98	0.11	0.0845	0.0047	0.15533	734	91	1016	12	0.0531	0.0087	3.316	0.048
T01_40_20	3.32	0.28	0.1966	0.01	0.0057804	255	43	538.1	5.6	0.056	0.024	2.756	0.048
T01_40_30	0.76	0.054	0.0829	0.0034	0.20845	702	75	255.6	4.3	0.058	0.012	13.57	0.21
T01_40_75	3.96	0.24	0.2422	0.01	0.29152	179	29	1118	17	0.059	0.013	8.55	0.12
T01_40_26	0.815	0.081	0.0895	0.0043	0.070857	580	42	1057.9	9.5	0.063	0.012	7.743	0.093
T01_40_67	0.861	0.66	0.0867	0.015	0.34616	180	36	201.9	3.1	0.066	0.02	11.84	0.19
T01_40_58	5.05	0.35	0.302	0.015	0.3316	2910	260	455.7	5.5	0.068	0.012	2.713	0.053
T01_40_68	1.24	0.16	0.0861	0.0049	0.052161	180	26	440.3	6.4	0.07	0.014	4.363	0.07
T01_40_81	1.148	0.094	0.0944	0.0048	0.33692	257	39	393	5.4	0.07	0.011	7.79	0.09
T01_40_82	0.828	0.11	0.085	0.0039	0.13296	560	220	1138	10	0.079	0.023	9.09	0.1
T01_40_45	5.87	0.36	0.348	0.015	0.28	691	56	464	10	0.08	0.018	4.63	0.1
T01_40_78	2.02	0.22	0.1479	0.0068	0.0098766	351	42	1000	11	0.081	0.017	7.361	0.088
T01_40_22	1.24	0.17	0.1154	0.0067	0.065772	326	29	748.2	9.2	0.082	0.014	2.795	0.048
T01_40_51	1.022	0.076	0.0951	0.0041	0.034263	335	39	399.6	4.2	0.092	0.015	8.99	0.1
T01_40_2	1.171	0.098	0.0955	0.0049	0.26917	2070	300	536	8	0.106	0.015	5.379	0.07
T01_40_33	3.59	2.7	0.1908	0.028	0.10497	1427	81	541.6	9.2	0.11	0.019	3.872	0.094
T01_40_11	5.92	0.29	0.3425	0.013	0.11274	238	43	816	11	0.114	0.017	7.213	0.098
T01_40_56	1.099	0.085	0.0902	0.0039	0.1643	516	54	1052	11	0.115	0.013	8.52	0.11
T01_40_42	1.88	0.13	0.1172	0.0057	0.069984	393	33	908.3	8.4	0.127	0.014	6.092	0.076
T01_40_38	0.833	0.044	0.0898	0.0034	0.27095	1540	280	1234	16	0.173	0.016	43.48	0.5
T01_40_74	4.04	0.19	0.2648	0.01	0.23761	2757	83	9870	290	0.173	0.018	15.58	0.46
T01-40 analyses omitted because of high Pb208 (defined a common lead trend)													
T01_40_80	5.54	0.37	0.2746	0.012	0.24217	300	60	747.1	6.4	0.219	0.022	4.233	0.045
T01_40_7	1.474	0.098	0.0951	0.0041	0.13846	679	62	1064	14	0.232	0.02	9.02	0.1
T01_40_72	2.54	0.7	0.1197	0.035	0.17214	1570	210	527	10	0.234	0.025	4.816	0.097
T01_40_29	1.46	0.16	0.1068	0.0069	0.0085006	3280	830	1314	16	0.25	0.064	6.54	0.17
T01_40_70	3.18	0.17	0.1882	0.0075	0.15655	21510	440	264.6	2.7	0.367	0.032	12.03	0.15
T01_40_14	3.03	0.18	0.1693	0.0072	0.02834	13850	220	549.5	4.9	0.401	0.03	6.965	0.078

Supplementary Table 6 continued: U-Pb and trace element data from rutile in T01-40 and T06-09.

	207Pb/235U	2SE	206Pb/238U	2SE	Error Correlation	Si_ppm	2SE	Zr_ppm	2SE	Pb208_ppm	2SE	U 2 3 8 _ ppm	2SE
T06-09 Rutile													
T06_09_7	176	38	1.49	0.3	0.99931	310	47	1130	15	119	24	25.7	0.3
T06_09_6	3.44	4.5	0.1572	0.12	0.59742	2.80E+03	1.30E+03	771	31	4.05	0.52	77.4	3.5
T06_09_9	3.23	2.5	0.1536	0.063	0.52933	780	250	370.8	5.4	2.58	0.14	55.23	0.54
T06_09_8	1.294	0.73	0.1059	0.011	0.0038955	222	30	1087	13	0.169	0.019	15.57	0.14
T06_09_11	3.19	0.37	0.185	0.016	0.72427	3820	680	1143	18	0.67	0.12	17.97	0.5
T06_09_5	1.93	0.34	0.143	0.017	0.67807	135	25	1023.3	8.2	0.0275	0.007	13.81	0.11
T06_09_3	1.83	0.29	0.1111	0.0079	0.030659	20380	670	1007	24	0.443	0.054	15.34	0.65
T06_09_4	1.069	0.16	0.0984	0.0089	0.54402	576	60	1021	12	0.15	0.019	13.53	0.15
T06_09_10	1.397	0.11	0.1053	0.0046	0.32695	312	38	955.8	8.4	0.251	0.023	14.41	0.14
T06_09_2	1.377	0.098	0.1046	0.0045	0.040384	257	40	297.3	4.8	0.364	0.044	20.23	0.23

Supplementary Table 7: U-Pb data from titanite in T01-40.

	207Pb/235U	2SE	206Pb/238U	2SE	Error Correlation	Pb204_ppm	2SE
T01_40_T_1	6.73	0.34	0.3751	0.0098	0.21697	0.72	0.25
T01_40_T_2	8.9	0.44	0.3844	0.01	0.12641	1.32	0.31
T01_40_T_3	12.8	0.63	0.429	0.013	0.22392	1	0.28
T01_40_T_4	6.12	0.28	0.3434	0.0077	0.13204	1.08	0.39
T01_40_T_5	5.89	0.3	0.3135	0.0085	0.38461	0.51	0.29
T01_40_T_7	6	0.26	0.3586	0.0075	0.088944	0.55	0.4
T01_40_T_8	8.75	0.46	0.3975	0.01	0.43121	0.84	0.25
T01_40_T_9	8.9	0.43	0.3885	0.011	0.27592	1.16	0.4
T01_40_T_10	8.24	0.4	0.3883	0.01	0.013763	0.46	0.22
T01_40_T_11	7.08	0.33	0.3784	0.0088	0.37805	0.78	0.26
T01_40_T_12	6.46	0.33	0.3567	0.0092	0.31939	0.55	0.28
T01_40_T_13	6.17	0.29	0.3393	0.0084	0.27864	1.05	0.36
T01_40_T_14	6.9	0.35	0.3719	0.0092	0.13259	0.42	0.23
T01_40_T_15	10.65	0.58	0.404	0.012	0.31112	0.85	0.29
T01_40_T_16	5.86	0.27	0.3432	0.0076	0.11155	0.72	0.32
T01_40_T_17	10.93	0.56	0.407	0.012	0.21115	0.86	0.31
T01_40_T_18	9.65	0.49	0.4067	0.012	0.024897	0.5	0.26
T01_40_T_19	6.37	0.32	0.3411	0.0082	0.28308	0.81	0.29
T01_40_T_20	11.17	0.7	0.422	0.014	0.20987	0.8	0.32
T01_40_T_21	6.29	0.29	0.3665	0.0093	0.14109	0.33	0.23
T01_40_T_22	7.29	0.35	0.3618	0.0089	0.19405	0.81	0.28
T01_40_T_23	6.56	0.3	0.3643	0.0083	0.26476	0.45	0.26
T01_40_T_24	5.218	0.22	0.3226	0.0069	0.31183	0.52	0.22
T01_40_T_25	7.47	0.37	0.3617	0.0088	0.38654	1.01	0.35
T01_40_T_26	11.91	0.6	0.413	0.013	0.21125	1.06	0.33
T01_40_T_27	7.66	0.44	0.3709	0.014	0.079287	0.63	0.33
T01_40_T_28	6.88	0.31	0.3687	0.0091	0.21055	0.77	0.28
T01_40_T_29	7.53	0.36	0.3873	0.0097	0.38079	0.91	0.31
T01_40_T_30	6.6	0.5	0.3487	0.012	0.061628	0.59	0.34
T01_40_T_31	10.03	0.54	0.3916	0.01	0.26418	0.87	0.31
T01_40_T_32	8.23	0.37	0.3734	0.0095	0.14846	0.96	0.28
T01_40_T_33	9.22	0.48	0.3889	0.011	0.0062778	0.83	0.33
T01_40_T_34	8.1	0.41	0.3752	0.01	0.10861	0.59	0.21
T01_40_T_35	6.9	0.33	0.3733	0.0091	0.20332	0.44	0.23

Supplementary Table 7 continued: U-Pb data from titanite in T01-40.

	207Pb/235U	2SE	206Pb/238U	2SE	Error Correlation	Pb204_ppm	2SE
T01_40_T_37	8.35	0.53	0.3877	0.011	0.38431	0.93	0.25
T01_40_T_38	7.74	0.54	0.3752	0.011	0.34025	0.7	0.33
T01_40_T_39	10.63	0.58	0.408	0.013	0.50644	1.2	0.3
T01_40_T_40	5.88	0.27	0.3136	0.0078	0.26366	1.07	0.32
T01_40_T_41	9.31	0.5	0.3891	0.011	0.10006	0.81	0.35
T01_40_T_42	7.57	0.36	0.3792	0.0091	0.21042	0.51	0.22
T01_40_T_43	8.32	0.68	0.381	0.013	0.5867	1.17	0.34
T01_40_T_44	8.22	0.56	0.387	0.011	0.012805	0.83	0.39
T01_40_T_45	8.39	0.47	0.383	0.01	0.10845	0.57	0.26
T01_40_T_46	8.26	0.42	0.3891	0.01	0.25755	0.49	0.23
T01_40_T_47	7.28	0.38	0.3321	0.0091	0.45122	0.67	0.25
T01_40_T_48	7.68	0.37	0.3689	0.009	0.20943	1.05	0.25
T01_40_T_49	9.62	0.53	0.3962	0.012	0.1808	1.03	0.27
T01_40_T_50	6.22	0.46	0.348	0.016	0.85776	0.42	0.2
T01_40_T_51	5.87	0.27	0.3425	0.0077	0.13313	0.35	0.21
T01_40_T_52	8.86	0.47	0.3895	0.0098	0.26624	0.87	0.29
T01_40_T_53	7.54	0.39	0.3755	0.0098	0.18495	0.93	0.27
T01_40_T_54	9.46	0.51	0.3786	0.011	0.062085	1.2	0.28
T01_40_T_55	7.53	0.4	0.3641	0.011	0.33992	0.56	0.24
T01_40_T_56	5.077	0.22	0.3043	0.0066	0.18583	0.25	0.23
T01_40_T_57	5.81	0.28	0.3349	0.0086	0.54403	0.85	0.27
T01_40_T_58	8.21	0.41	0.3558	0.01	0.39238	1.03	0.47
T01_40_T_59	7.73	0.4	0.3847	0.011	0.25352	0.56	0.25
T01_40_T_60	5.58	0.26	0.3071	0.008	0.074477	0.5	0.23
T01_40_T_61	7.3	0.4	0.3412	0.0096	0.31687	1.16	0.54
T01_40_T_62	7.52	0.37	0.3622	0.0093	0.1824	0.98	0.34
T01_40_T_63	8.6	0.46	0.3919	0.011	0.19937	1.15	0.36
T01_40_T_64	5.569	0.25	0.3373	0.0072	0.12801	0.49	0.23
T01_40_T_65	11.42	0.57	0.4109	0.012	0.31049	1.01	0.33
T01_40_T_66	5.98	0.29	0.3421	0.0081	0.19274	0.39	0.24
T01_40_T_67	10.11	0.51	0.3949	0.011	-0.049871	1.34	0.4
T01_40_T_68	7.06	0.35	0.3691	0.0092	-0.038236	0.48	0.19
T01_40_T_69	7.62	0.4	0.3809	0.0098	0.18001	0.69	0.28
T01_40_T_70	7.74	0.39	0.368	0.0095	0.21346	0.99	0.3
T01_40_T_71	6.52	0.35	0.36	0.0082	0.20704	0.4	0.22
T01_40_T_72	11.85	0.64	0.4148	0.012	0.24245	0.92	0.28
T01_40_T_73	10.21	0.54	0.427	0.014	0.034411	0.75	0.3
T01_40_T_74	5.76	0.3	0.3258	0.009	0.54673	0.52	0.21
T01_40_T_75	8.19	0.4	0.3789	0.01	0.2866	1.2	0.43
T01_40_T_76	6.32	0.28	0.3577	0.0084	0.41861	0.41	0.23
T01_40_T_77	8.81	0.43	0.3874	0.0097	0.017212	0.66	0.35
T01_40_T_78	7.22	0.35	0.365	0.0089	0.073062	0.66	0.24
T01_40_T_79	5.33	0.98	0.2615	0.0078	0.16787	1.16	0.39
T01_40_T_80	10.05	0.53	0.4047	0.011	0.11824	0.83	0.25
T01_40_T_81	6.93	0.39	0.3484	0.0095	0.1751	0.65	0.28
T01_40_T_82	13.38	0.89	0.424	0.017	0.54988	0.86	0.26
T01_40_T_83	10.22	0.55	0.4147	0.011	0.2111	1.08	0.31
T01_40_T_84	8.29	0.44	0.3779	0.01	0.13671	0.79	0.3
T01_40_T_85	5.65	0.26	0.3153	0.0073	0.11974	0.58	0.23

Supplementary Table 7 continued: U-Pb data from titanite in T01-40.

	207Pb/235U	2SE	206Pb/238U	2SE	Error Correlation	Pb204_ppm	2SE
T01_40_T_86	8.09	0.42	0.3754	0.01	0.21919	0.88	0.28
T01_40_T_87	7.8	0.39	0.3967	0.01	0.31842	0.88	0.25
T01_40_T_88	7.38	0.43	0.3606	0.0093	0.19492	0.71	0.26
T01_40_T_89	8.24	0.39	0.3863	0.0096	0.38042	0.5	0.22
T01_40_T_90	7.69	0.36	0.4018	0.0091	0.30585	0.47	0.27
T01_40_T_92	6.01	0.28	0.3327	0.0082	0.097025	0.59	0.27
T01_40_T_93	6.79	0.32	0.3667	0.0088	0.31786	0.45	0.21
T01_40_T_94	6.81	0.4	0.345	0.01	0.58711	0.43	0.3
T01_40_T_95	11.41	0.64	0.4209	0.013	0.12401	1.01	0.27
T01_40_T_96	11.47	0.74	0.397	0.013	0.4289	0.58	0.21
T01_40_T_97	8.52	0.46	0.3797	0.011	0.35555	0.73	0.26
T01_40_T_98	6.89	0.33	0.3757	0.0092	0.090038	0.53	0.22
T01_40_T_99	9.1	0.45	0.4011	0.011	0.095361	0.77	0.25
T01_40_T_100	10.85	0.62	0.404	0.014	0.24771	0.94	0.31
T01_40_T_101	88.3	5.6	1.071	0.064	0.4618	0.62	0.15

Appendix 6:

Supplementary materials for Chapter 6: Mantle heating at ca. 2 Ga driven by crustal growth: evidence from granites and eclogites

Supplementary file 1

Extended methods

Geochemical analyses and filtering

The geochemical database by Gard et al. (2019) used in this study is a whole-rock database of major and trace elements and age. The data originate from the GEOROC compilation, a number of national and provincial survey datasets and open-file reports, and numerous individual publications. The dataset supplements GEOROC data particularly in Precambrian terranes and geographic regions outside of the United States.

The database was processed in Matlab® by first converting all Fe to Fe2+ and then normalizing to the following major elements without LOI: SiO2, TiO2, Al2O3, Cr2O3, FeOT, NiO, MnO, MgO, CaO, BaO, Na2O, K2O, and P2O5. The normalized compositions of igneous and metaigneous rocks were then assigned total-alkali silica (TAS) plutonic names using a the IUGS classification scheme. From these samples, we then extract all the granites and (alkalic+subalkalic) basalts for analysis. Only continental samples were used in our analysis. While granites are typically assigned names based on their modal mineralogy and the quartz-alkali feldspar-plagioclase (QAP) method, we opt for the TAS geochemical classification method because it ensures a like-for-like comparison of samples based on chemistry and the modal data do not generally exist to perform a QAP analysis. Furthermore, names provided by authors do not always relate to the QAP scheme, or the estimation of modal mineralogy on hand samples typically has significant uncertainty. For normalization of Eu* and Sr* and the trace element compatibility diagram (Supp. Fig. 1) we use NMORB by Gale et al. (2013).

Province age-area analysis

To perform the age-area analysis, we started with a set of geological province polygons by Hasterok et al. (in prep). The provinces polygons were defined from georeferenced province boundaries published in the literature and refined using a variety of datasets including but not limited to elevation (ETOPO1; Amante and Eakins, 2009), magnetics (EMAG2_V3, WDMAM; Dyment et al., 2020; Meyer et al., 2016), seafloor age (Seton et al., 2020), geochemistry sample ages (Gard et al., 2019) and recent volcanic centers (Venzke, 2013). Province areas were computed in QGIS using the province polygons.

Two datasets were used for igneous crystallization dates: Puetz et al. (2018), a zircon U–Pb compilation; and Gard et al. (2019), with individual geochemical sample dates. Dates in Gard et al. (2019) are derived from a variety of methods including Pb-Pb, U–Pb, Th–Pb, Rb–Sr, K–Ar, and Ar–Ar,

where the vast majority are from U–Pb dates on zircons and the K–Ar and Ar–Ar dates are generally only used for young samples. A few dates (n = 218) are based on stratigraphic relationships or estimated from nearby co-genetic/co-generational plutons. While the two datasets include some overlap in samples, it is not feasible at this stage to remove duplicates. There are significant differences between the two datasets geographically such that a combination of the two yields a larger set of provinces available for analysis. Because the probability of the peaks are not used in the sorting or continental growth calculation the duplication of data will not affect the overall result, although there is some chance that it will affect the proper identification of the most significant age peak. The analysis was performed on each dataset individually and provides similar results for all but the younger provinces where few zircon U–Pb dates exist. The results from each individual analysis are provided in Supplementary Fig. 5 for comparison.

A kernel density estimate (KDE) was produced for the crystallization dates of igneous and metaigneous samples within each geologic province using a bandwidth of 50 Ma. The peaks in the age spectrum were identified by the point where the slope changed from positive to negative. Only peaks with a number of samples greater than the 50% cumulative probability as determined by a binomial distribution were considered significant. To determine the number of data for this threshold, we divide number of total data of any age within a province by the number of 50 Ma bins required to span the range of ages within a province.

There are some significant differences between the two age datasets (Supp. Fig. 5), but the overall pattern is older than 0.7 Ga is similar, especially in the interval surrounding 2 Ga of interest to this study. Because U–Pb dating is less accurate near 0 Ma, there is a significant difference in the number of samples estimated at these ages. There are also differences in the locations of the sample which leads to differences in provinces used in each analysis (see supplementary data file). Another source of difference comes from the fact that zircons are typically much higher in concentration in felsic igneous rocks. As a result the Puetz et al. (2018) zircon compilation likely oversamples these felsic rocks, whereas the Gard et al. (2019) database includes a more balanced range of igneous rock compositions.

Growth rate is determined within a 100 Ma window by dividing the province areas created within an interval by 100 Ma. The province areas are entirely assigned to the first igneous event. While this may overestimate the area of a province grown within a given time interval, we assume that the first igneous event was large enough to construct the bulk of the crust upon which future magmatic events were added. We believe this assumption is reasonable in many cases because the first igne-

ous event is frequently the largest peak in the age spectrum.

The large peaks near 0 Ma using the Gard et al. (2019) dataset probably result from sampling bias of young igneous rocks because the cover over most of the older rocks or are the target of the vast majority of studies. This bias is quite clear in North America where many of the terranes in the western US are largely underlain by Precambrian basement are instead estimated near 0 Ma in age. There has been no attempt to rectify this bias in the dataset because it is beyond the scope of this study, and unlikely to change the interpretation as the Puetz et al. (2018) data are not biased in this same way and yield a broadly similar result.

References:

Amante, C., and Eakins, B. W., 2009, ETOPO1 arc-minute global relief model: procedures, data sources and analysis.

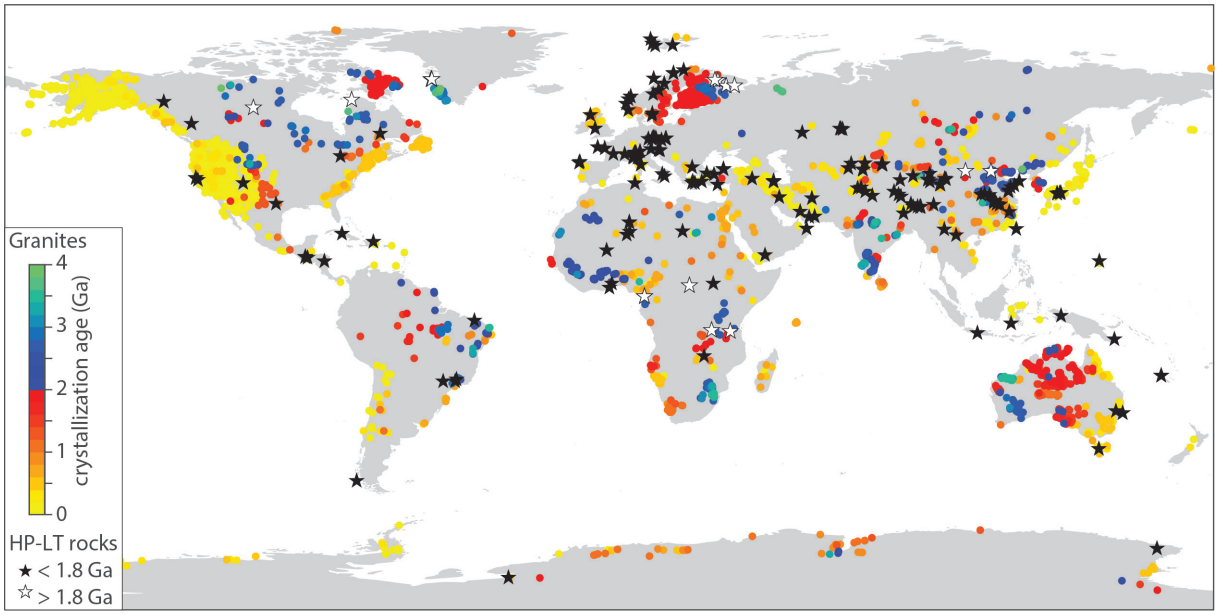
Dyment, J., Choi, Y., Lesur, V., Garcia-Reyes, A., Catalan, M., Ishihara, T., Litvinova, T., and Hamoudi, M., The World Digital Magnetic Anomaly Map: version 2.1, *in* Proceedings EGU General Assembly Conference Abstracts2020, p. 22098.

Gale, A., Dalton, C. A., Langmuir, C. H., Su, Y., and Schilling, J. G., 2013, The mean composition of ocean ridge basalts: Geochemistry, Geophysics, Geosystems, v. 14, no. 3, p. 489-518.

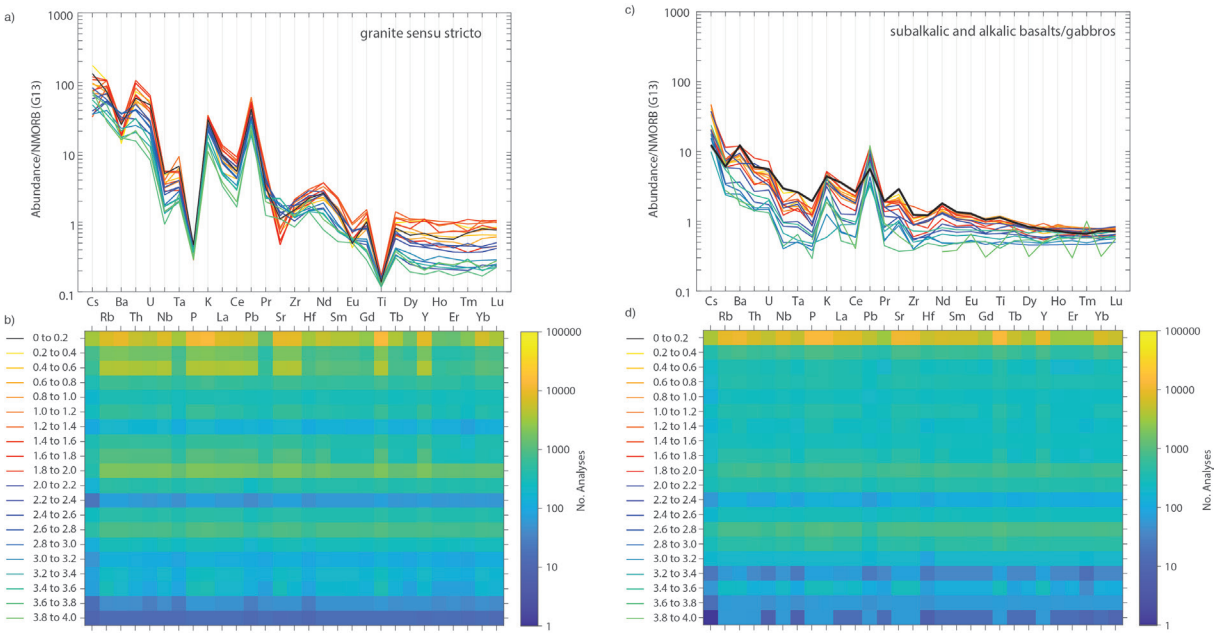
Meyer, B., Saltus, R., and Chulliat, A., 2016, EMAG2: Earth Magnetic Anomaly Grid (2-arc-minute resolution) Version 3. Model, National Centers for Environ-mental Information, NOAA.

Seton, M., Müller, R. D., Zahirovic, S., Williams, S., Wright, N. M., Cannon, J., Whittaker, J. M., Matthews, K. J., and McGirr, R., 2020, A Global Data Set of Present-Day Oceanic Crustal Age and Seafloor Spreading Parameters: Geochemistry, Geophysics, Geosystems, v. 21, no. 10, p. e2020GC009214.

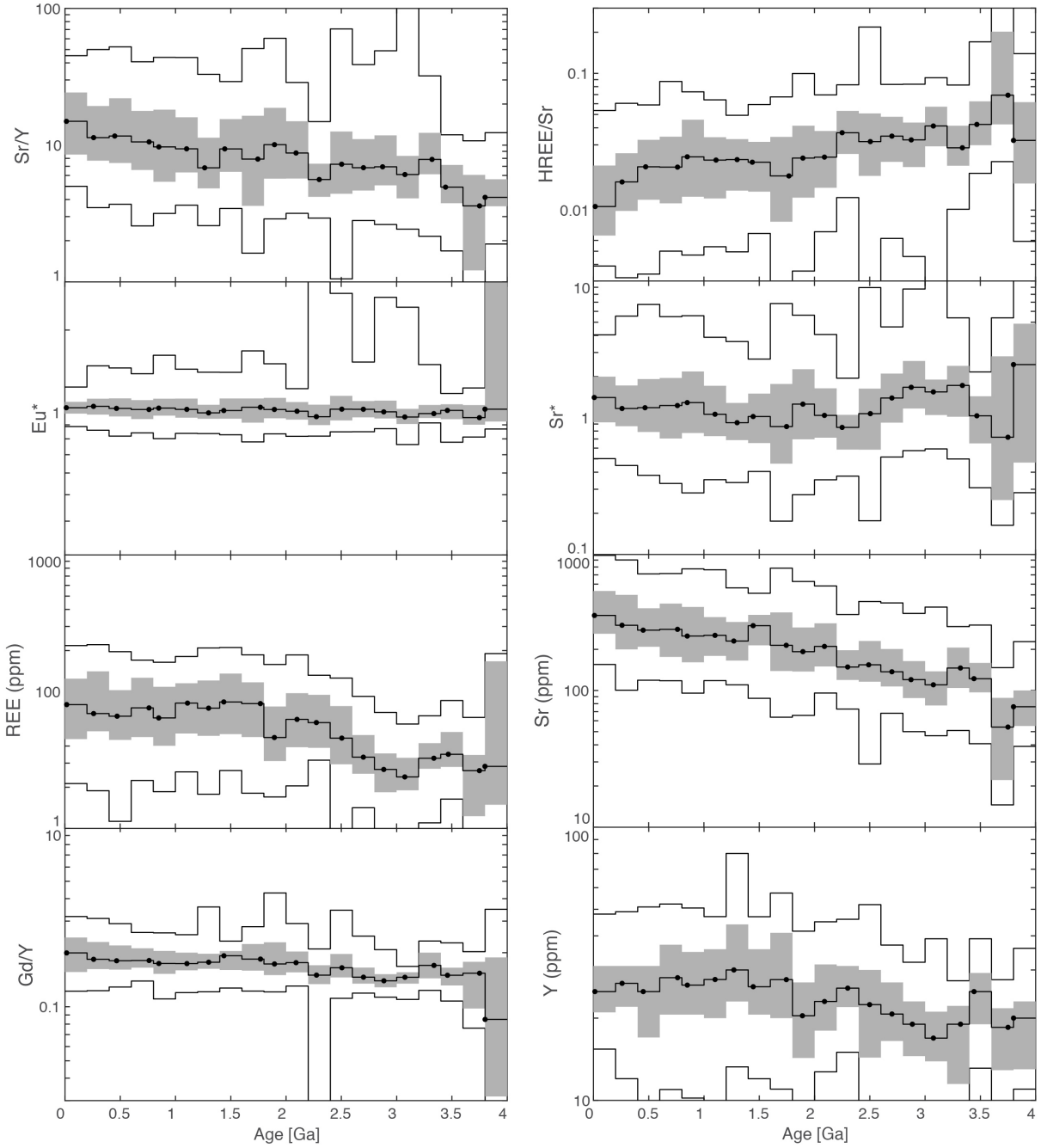
Venzke, E., 2013, Global Volcanism Program, 2013. Volcanoes of the World, v. 4.5. 2, Smithson. Institution, Natl. Museum Nat. Hist.



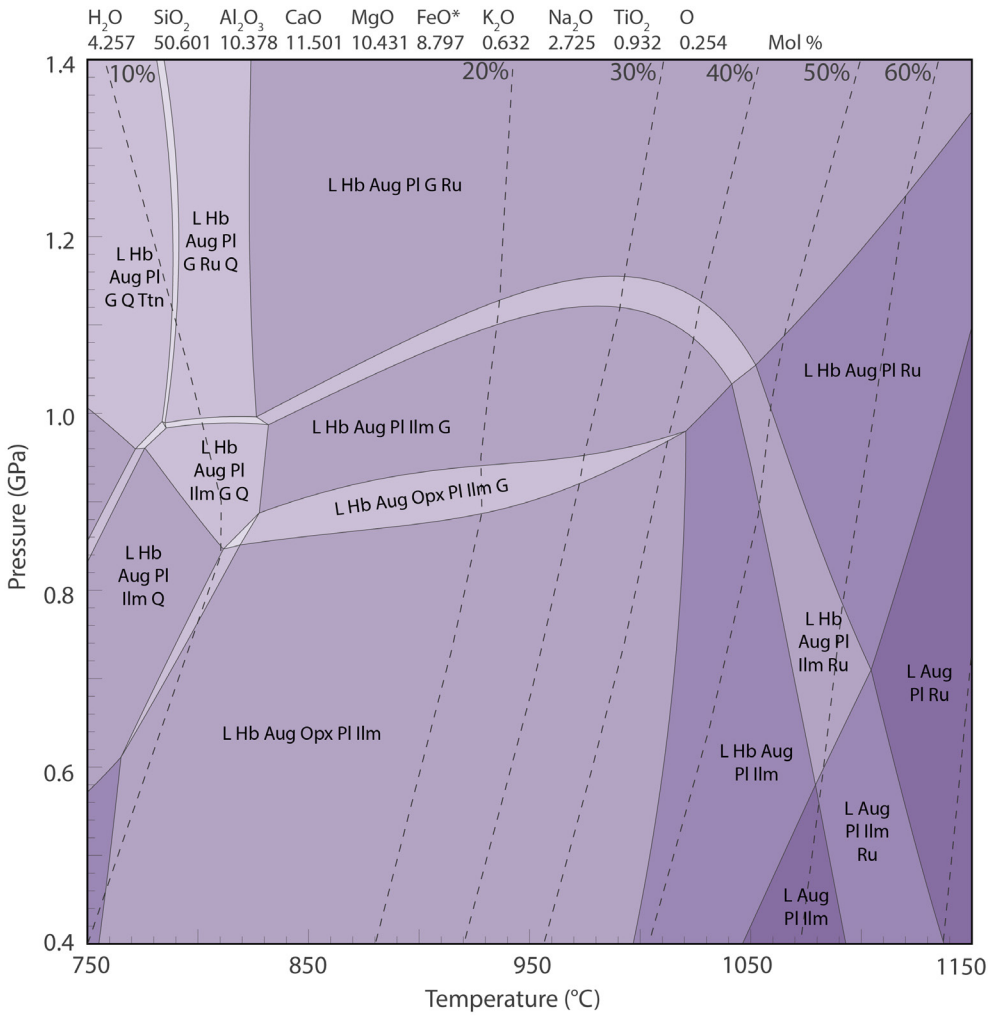
Supplementary Figure 1: Locations of granites (circles) and high-pressure low-temperature (HP-LT) rocks (stars) in the databases of this study. Some HP-LT rocks were added to the pre-existing database. The granite data has good spatial coverage across the continents, with some bias towards younger (< 200 Ma) igneous systems.



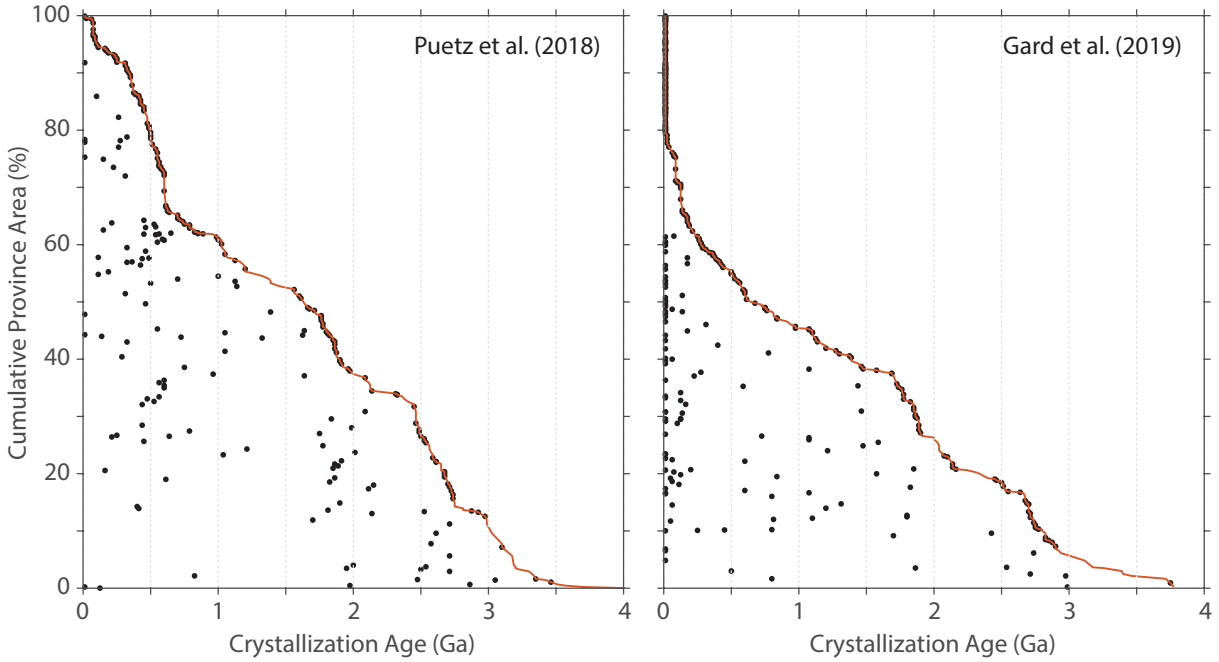
Supplementary Figure 2: a) Trace element compatibility plot (or spider plot) of granite chemistry from 4 Ga until present, in 0.2 Ga age bins, normalised to MORB (Gale et al., 2013). Note the development of Sr and Eu anomalies at ca. 2 Ga, and the corresponding increase in Y and HREEs. b) Number of data in each 0.2 Ga age bin for each element. c) Trace element compatibility plot of basalt chemistry. All basalts show a positive Pb anomaly. c) Number of data in each 0.2 Ga age bin for each element.



Supplementary Figure 3: Ratios, anomalies and elements of interest in basaltic rocks through time. The heavy centre line represents the median value, and the grey field the interquartile range (25th to 75th quantiles). The point shows the median age of each 0.2 Ga age bin. No change points were identified by Pettitt's tests at 2 Ga.



Supplementary Figure 4: Mineral equilibria model calculated with THERMOCALC for the average basaltic composition in the dataset. Dashed lines represent liquid modes. Abbreviations: L: Liquid, Hb: Hornblende, Aug: Augite, Pl: Plagioclase, G: Garnet, Opx: Orthopyroxene, Q: Quartz, Ru: Rutile, Ilm: Ilmenite, Ttn: Titanite.



Supplementary Figure 5: Cumulative ages-area models using the igneous samples from Puetz et al. (2018) U–Pb zircon compilation (left) and Gard et al. (2019) sample ages (right). Individual points identify the age of the largest peak in the age-spectrum and the line identifies the age of the first recorded igneous event.

Supplementary Table 1 is too large to be placed into thesis format, however is available upon request.

It's getting strange in here

And it gets stranger every year